R-08-91

Bedrock hydrogeolology
Model testing and synthesis

Site descriptive modelling
SDM-Site Laxemar

Ingvar Rhén, Torbjörn Forsmark
SWECO Environment AB

Lee Hartley, Steve Joyce, David Roberts
Serco Technical and Assurance Services

Björn Gylling, Niko Marsic
Kemakta Konsult AB

November 2009

Svensk Kärnbränslehantering AB
Swedish Nuclear Fuel
and Waste Management Co

Box 250, SE-101 24 Stockholm
Phone +46 8 459 84 00

ISSN 1402-3091
SKB Rapport R-08-91

Bedrock hydrogeolology
Model testing and synthesis

Site descriptive modelling
SDM-Site Laxemar

Ingvar Rhén, Torbjörn Forsmark
SWECO Environment AB

Lee Hartley, Steve Joyce, David Roberts
Serco Technical and Assurance Services

Björn Gylling, Niko Marsic
Kemakta Konsult AB

November 2009

Keywords: Laxemar, Hydrogeology, Hydrochemistry, Modelling, Calibration.

Summary

The Swedish Nuclear Fuel and Waste Management Company (SKB) has conducted site investigations at two different locations, the Forsmark and Laxemar-Simpevarp areas, with the objective of siting a final repository for spent nuclear fuel according to the KBS-3 concept. Site characterisation should provide all data required for an integrated evaluation of the suitability of the investigated site and an important component in the characterisation work is the development of a hydrogeological model. The hydrogeological model is used by repository engineering to design the underground facility and to develop a repository layout adapted to the site. It also provides input to the safety assessment. Another important use of the hydrogeological model is in the environmental impact assessment.

The current report (R-08-91) is a level III report that describes the hydrogeological conceptual model and the regional scale numerical groundwater flow modelling. In a second level III report the analysis of the primary data and the hydrogeological conceptualisation of deterministic deformation zones as hydraulic conductor domains (HCD) and the bedrock in between as hydraulic rock domains (HRD) is presented (R-08-78). There the HRD are parameterised in terms of a hydrogeological DFN model. In a concluding level II report (R-08-92) the analysis and results of the two level III reports are summarised.

Hydrogeological conceptual model

HCD model:

The key interpreted characteristics are:

- A clear trend of decreasing transmissivity with depth.
- A positive correlation between interpreted “size” and transmissivity. Size here corresponds to interpreted trace length on the surface.
- Indications that the transmissivity of HCDs is dependent on the orientation of deformation zones. E-W zones appear more conductive than zones of other orientations.
- Significant lateral heterogeneity with a suggested standard deviation of Log(T) of 1.4. (standard deviation of log10(T) of the entire sample of HCD transmissivities is 1.4 and standard deviation of log10(T) of transmissivities within individual zones is in the range 0.5 to 2.).

The confirmatory testing with the regional groundwater flow model has shown that in general the initial assessed transmissivity models for the HCD (based on the hydraulic test results) complies with the confirmatory model testing performed, however with a general slightly lower transmissivity (Multiplication factors of 1.0, 0.3 and 0.1 of original values were assessed between ground surface down to –150 m, between –150 to –650 m and below –650 m, respectively.) included in the SDM-Site base case (in this report for the SDM-Site Laxemar modelling *Base case* corresponds to *deterministic base model simulation* in the SDM-Site Forsmark modelling).

The role of N-S dolerite dykes associated with ZSMNS001A-C and ZSMNS059A (along with some other dolerite-affected minor HCD) as flow barriers appears confirmed by differences in measurements in natural head and interference tests across/along these zones. A similar effect arising from clayey fracture infills or fault gouge in ZSMEW002A and ZSMNW042A-west also appears to be confirmed by the natural head data. This behaviour is introduced by modelling these structures as strongly anisotropic, i.e. large contrast between longitudinal (in plane) hydraulic conductivity and transverse hydraulic conductivity. Particle tracking has shown that this anisotropy has significant impact on groundwater flow patterns, in at least, the western part of Laxemar local model area.

The palaeohydrogeological calibration suggested introduction of a methodology for deriving kinematic porosity and fracture surface area per unit volume based on the intensity of conductive fractures within the HCD, rather than using a scaling relationship between aperture and transmissivity.

HRD model:

Regional scale groundwater flow and solute transport simulation of palaeohydrogeology, natural head measurements and hydraulic interference test data have confirmed that hydrogeological properties, as given by the hydrogeological DFN model base case /Rhén et al. 2008/ (based on all open and partly open fractures and semi-correlated transmissivity model) together with the HCD parameterisation provide an appropriate description of the hydrogeological situation in the bedrock. Only relatively minor modifications were considered necessary to obtain an acceptable match between the flow model results and field data.

A slight reduction (1/3 of initial assessed values) in hydraulic conductivity (horizontal and vertical) below –150 m elevation improved the palaeohydrogeological calibration, and hence was included in the SDM-Site *base case model*.

Sensitivity studies suggested that a slight increase (a factor 3) in the horizontal hydraulic conductivity above –150 m elevation improved the match relative to natural groundwater head data and the match to hydrogeochemistry measured in some boreholes (These changes have not been implemented in the SDM-Site *base case model*).

The appropriateness of kinematic porosity based on conductive fracture intensity (as calculated by the hydrogeological DFN model) and transport aperture was confirmed by the palaeohydrogeological simulations, although it was necessary to include the contribution to kinematic porosity from small fractures down to the $r = 0.28$ m size.

HSD model:

The applied hydraulic conductivities based on hydraulic tests comply with the results of confirmatory testing, but it was considered appropriate to generally decrease the vertical hydraulic conductivities to 1/10 of the originally suggested values (isotropic), to be able to reproduce the head difference between the soil and the near-surface bedrock.

Hydrogeological boundary conditions (i.e. groundwater level, -recharge and -discharge):

The natural (undisturbed) groundwater levels generally follow the topography. In the Quaternary deposits, the depth to the groundwater table is expected to be within a few metres from the ground surface, with maximum depth at topographic highs and minimum depths in the valleys, as shown by measurements. The natural (undisturbed) groundwater level in the upper bedrock behaves similarly, but there is a noticeable downward gradient in the upper 200 m of bedrock noted in about 50% of the core-drilled boreholes, the rest showing low and variable (upwards or downwards) vertical hydraulic gradients.

According to the regional groundwater flow modelling, discharge takes place in the larger valleys and near the sea. This is in accordance with measured heads which are consistently at ground surface throughout the seasonal cycle in low lying areas and the distribution of surface water.

Palaeohydrogeological model

Combining the interpretation of hydraulic characteristics of the bedrock from report /Rhén et al. 2008/ with the understanding gained from simulating the palaeohydrogeological evolution, the hydrogeological situation for groundwater flow and solute transport is summarised in the table below.

Solute transport model

Above c. –150 m the evolution of hydrochemistry is sufficiently rapid that the simulated results are non-sensitive to the initial condition.

In the interval –150 to –600 m the results are however dependent on the hydraulic parameters, solute transport parameters (fracture surface area in particular) and pre-Holocene conditions. In this depth range the simulation results are to some extent stable with regard to heterogeneity, since when fracture intensity is low, advective transport is reduced, but when fracture intensity is increased then both advection and exchange with the matrix is increased, and so solute transport is retarded more by RMD.

Depth zone	General characteristics
dZ1: > –150 m	Advection dominated – high groundwater flow rates with sub-horizontal fracturing giving $K_h > K_v$ in many areas. Flushed by post-glacial meteoric water. High fracture intensity implies matrix blocks 1–2 m in size, which gives equilibrium between fracture and matrix on timescales of ~1,000 years.
dZ2: –150 m to –400 m	Some advection, but rock matrix diffusion (RMD) retards post-glacial meteoric penetration. Fracture intensity is generally much lower, reducing groundwater flux and increasing matrix blocks to typically ~5 m in size, such that porewater chemistry lags behind that of the fracture water by 1,000s years. In more fractured areas, RMD is more effective, and consequently slows down mixing.
dZ3: –400 m to –650 m	Low advection. RMD important because advective flow rates are small. Fracture intensity lower still, with typical matrix blocks ~10 m in size, such that porewater chemistry lags behind that of fracture water ~10,000 years. Expect some difference between fracture and porewater chemistries.
dZ4: < –650 m	Very low advection. RMD dominates Fracture intensity very low, with typical matrix blocks ~100 m in size, such that porewater chemistry lags behind that of fracture water ~100,000 years. Differences between fracture and porewater chemistries are to be expected.

Sensitivities to assigned parameters in the HCD model:

Strong hydraulic anisotropy in ZSMNS001A-C, ZSMNS059A, and KLX19_DZ5-8, which are associated with interpreted dolerite dykes, is essential to reproduce the interference test with pumping in HLX28 and the 'jumps' in natural heads observed in the southern part of HRD_W.

Anisotropy in ZSMNW042A-west and ZSMEW002A is also required for similar reasons, although attributed to the effects of fault gouge.

Varying the HCD transmissivity half an order of magnitude has some noticeable effect on both hydrochemistry and natural heads. Using a general reduction of the transmissivity by a multiplication factor of 0.3 below –150 m was found beneficial to the calibration.

Introduction of lateral heterogeneity (stochastic variation) in the HCDs, which is considered more realistic than the SDM-Site base case (homogeneous), generally caused more flushing of the system and in some cases pushed the post-glacial meteoric flushing well below the measured hydrochemical concentrations. The discharge areas for particles released in the potential repository area are dispersed considerably more for the ten stochastic realisations of the HCD and HRD than for the homogeneous base case.

A sensitivity case without anisotropy in the HCD confirms the strong influence of the dolerite dykes on the flow conditions and transport in HRD_W mainly. Without hydraulic anisotropy, paths starting beneath the lower lying areas in HRD_W tend to move eastwards rather than south, and they are longer and go deeper.

Sensitivities to assigned parameters in the HRD model:

The initial HRD properties, without the multiplication factor 1/3 decrease in hydraulic conductivity below –150 m as in the SDM-Site base case, gave little change in natural groundwater heads, but produced worse match to hydrogeochemistry data.

Increasing the horizontal conductivity of HRD in the top –150 m reduces post-glacial meteoric flushing below –150 m and hence improves the match. Such a scenario is within the uncertainty in the interpretation of the measured data, which are sparse in the top 100 m of bedrock. If such a change was made to the SDM-Site base case, it would improve the match to both natural groundwater head and hydrochemistry.

The effects of heterogeneity on groundwater chemistry are most evident in the depth zone –150 m to –400 m where pockets of brackish-glacial water tend to occur in areas of relatively low hydraulic conductivity. In reality, such areas are likely to occur also at higher elevation given the expected variation in intensity of conductive fractures.

Sensitivities to assigned parameters in the HSD model:

The assigned hydraulic conductivities affect the modelled head in the Quaternary deposits on land but do not affect the calibration in other ways. However, the hydraulic conductivity of the sea sediments is important for the description of how the bedrock connects hydraulically to the sea.

Sensitivities to the conceptual model for palaeohydrogeology:

Sensitivities to the considered variants in boundary and initial conditions were found to be relatively small compared to those due to changes in hydraulic or transport properties. Hence, it is concluded that although these conditions are quite uncertain, as long as they are defined based on careful conceptual considerations, the simulation results are not overshadowed by their uncertainty.

Likewise, the hydrogeochemical composition of the porewater at depth is uncertain, but plausible alternatives can be accommodated within the conceptual model without large implications for the results.

Unresolved issues

It has been shown that the deformation zones associated with dolerite dykes locally, in the south-western part of the local model area, act as flow barriers. However, it is not known if the dolerite dykes within the two large deformation zones ZSMNS001C and ZSMNS059A are continuous along the extents of these zones. According to the geological model there may also be other, probably small, dolerite dykes within the local model domain. These possible smaller dolerite dykes are not believed to have any significant effect on the flow field, but this has not been tested in the flow model.

The hydrogeological DFN models used are based on the assumption that all mapped open fractures are possible flowing features, the so called OPO case (Open and Partly Open fractures, including mapping classes; certain, probable and possible) and a semi-correlated transmissivity-size model was used. There are other hydrogeological DFN models reported in /Rhén et al. 2008/, judged to fit data less good but still considered plausible, that have not been tested in the regional groundwater flow model.

The fracture set dominant for flow is the subvertical, steeply dipping WNW set. Since boreholes are either vertical or steeply dipping, the intensity and transmissivity of fractures of this set are more uncertain than the subhorizontal set. Efforts have been made in the hydrogeological DFN modelling, cf /Rhén et al. 2008/ to compensate for this bias, but the resulting interpretation is still more sensitive to the methodology than to the subhorizontal set itself.

The modelling indicates that the assignment method for transport properties, e.g. the connected open fracture surface area and kinematic porosity, in a continuum model should be improved and possibly be more directly linked to the fracture intensity models in HCDs and HRDs.

Contents

1 Introduction

1.1 Background

The Swedish Nuclear Fuel and Waste Management Company (SKB) has undertaken site investigations at two different locations, the Forsmark and Laxemar-Simpevarp areas, with the objective of siting a geological repository for spent nuclear fuel. The investigations are conducted in campaigns punctuated by data freezes. After each data freeze, the site data are analysed and site descriptive modelling work is carried out. A site descriptive model (SDM) is an integrated model for geology, rock mechanics, thermal properties, hydrogeology, hydrogeochemistry and transport properties, and a description of the surface system.

So far, three full versions of a site descriptive model have been completed, Simpevarp 1.1 and 1.2 and Laxemar 1.2. Version 0 /SKB 2002/ established the state of knowledge prior to the site investigation. Simpevarp version 1.1 /SKB 2004b/, which essentially constituted a training exercise, was completed during 2004 and Simpevarp version 1.2 during 2005 /SKB 2005a/. The latter formed the basis for a preliminary safety evaluation (PSE) of the Simpevarp subarea /SKB 2005b/ and completed the initial site investigation stage (ISI) in the Simpevarp subarea. A preliminary repository layout (D1) for the Simpevarp subarea was presented in 2006 /SKB 2006a/. SDM-Site Laxemar version 1.2 was presented 2006 /SKB 2006b/ and that this preliminary site descriptive model completed the initial site investigation stage (ISI). It formed the basis for a PSE of the Laxemar subarea /SKB 2006c/, a preliminary repository layout /SKB 2006d/, and the first evaluation of the long-term safety of this layout for KBS-3 repository layout in the context of the SR-Can project /SKB 2006e/.

After the completion of the initial site investigations of the Simpevarp and Laxemar subareas /SKB 2005a, 2006b/, an evaluation of the site data from the two subareas, results from site modelling, repository layouts and preliminary safety evaluations were carried out. Based on this evaluation, a decision was made to continue with the complete site investigation (CSI) in the central, southern and western parts of the Laxemar subarea /SKB 2007a/, the so-called focused area. Three modelling stages were initially planned for the complete site investigation work. An important component of each of these planned stages was to address and continuously try to resolve uncertainties of importance for repository engineering and safety assessment. However, due to re-planning of the modelling work, neither the modelling stage 2.1 nor 2.2 included an official delivery of any updated versions of the geological models for Laxemar. The primary objective of the geological modelling during stage Laxemar 2.1 /SKB 2006f/, was to analyse available new data at data freeze Laxemar 2.1 (June 30, 2005) to provide feedback to ensure that adequate geological information was obtained during the complete site investigation stage at Laxemar /SKB 2006g/. However, in order to maximise the feedback to the site investigation, a successive evaluation of data that became available in the time period between June 30, 2005 and the end of March 2006 were also included in the Laxemar 2.1 modelling work. Based on an integrated analysis of all available site data, a decision was made at the turn of the year 2006–2007 to expand the focused area of the site investigation to the south to include also an additional area south of the Laxemar subarea. This decision also raised an urgent need for a complementary cored borehole to minimise the uncertainty in the final geological models in the focused area/volume. The outcome of the drilling of this complementary borehole has been considered in the geological modelling of rock domains and deformation zones presented here. Hence, due to projected lack of critical data from southern Laxemar at the time for data freeze Laxemar 2.2 (December 31, 2006), a decision was made to allow inclusion of data from the final data freeze Laxemar 2.3 (August 31, 2007) in the concluding site-descriptive modelling work. This modelling work, based on the data available at data freeze Laxemar 2.3, is referred to as modelling stage SDM-Site Laxemar. The detailed hydrogeological reporting of the SDM-Site Laxemar is reported in /Rhén et al. 2008/ and in the current report (both level III reports in the SDM report structure) and is ultimately summarised in the concluding Level II document /Rhén and Hartley 2009/.

1.2 Scope and objectives

The primary objectives of the work reported here are to:

- provide a 3D regional groundwater flow model of Laxemar and its surrounding area to allow quantitative assessment and illustration of the conceptual understanding of the site,
- build confidence in the flow modelling work by testing the 3D model against a variety of field data, such as interference tests, palaeohydrogeology (hydrogeochemistry) and near-surface hydrogeology,
- provide a parameterised hydrogeological 3D description and modelling of Laxemar needed for the end users Repository Engineering, Safety Assessment and Environmental Impact Assessment.

The descriptions should especially focus on the hydraulic properties of deformation zones (HCDs) and the naturally fractured rock between the deformation zones (HRDs) in the potential repository volumes. This requires consideration of how to construct and parameterise the models of HCDs and the hydrogeological DFN models representative of the HRDs, applicable to the entire regional scale 3D groundwater flow domain, a volume of c. 600 km^3 (The corresponding local model volume is c. 20 km^3.), cf Section 1.3. Part of this is achieved by deriving specific:

- HCD models for deformation zones that cover the regional model domain /Rhén et al. 2008/ based on geological models presented by /Wahlgren et al. 2008/.
- Hydrogeological DFN models for the hydraulic domains /Rhén et al. 2008/ defined on the basis of defined fracture domains, covering the local model volume and where the defined rock domains account for the remaining part of the regional model. The geological fracture domain model is presented by /LaPointe et al. 2008/ and the rock domains in /Wahlgren et al. 2008/, as summarised briefly in Chapter 3.

/Rhén et al. 2008/ also provide recommendations as to how to model the deformation zones hydrogeologically (e.g. representative hydrogeological thickness, hydrogeological barrier etc) and how to represent the upper part of bedrock (100 m or so) which is generally characterised to a much lesser degree by cored boreholes, but is known to generally be more permeable than below 100 m depth.

The principal prerequisites for the modelling presented in this report are the data and results presented in /Rhén et al. 2008/, providing hydrogeological properties for HCDs and HRDs based on borehole data. That conceptualisation and parameterisation are in this report tested by use of a regional scale groundwater flow model, imposing a variety of different boundary and initial conditions.

1.2.1 Disposition

This remainder of the report is organised as follows:

- Chapter 2 presents SKB's systems approach to groundwater flow and solute transport in fractured crystalline rocks as attempted in the SDM. This chapter constitutes an important premise for Chapters 4 through 11.
- Chapter 3 presents an overview of the modelled deterministic deformation zones and the fracture domains derived for SDM-Site Laxemar. This chapter is important for the work presented in Chapters 4, 5 and 7 through 10.
- Chapter 4 presents the hydrogeological conceptual model development and the integral parts of the hydrogeological conceptual model.
- Chapter 5 presents an overview of the borehole monitoring data, the hydraulic interference tests carried out up till data freeze Laxemar 2.3 for SDM-Site Laxemar and essential hydrochemistry data for the modelling presented in Chapter 9.
- Chapter 6 presents the calibration targets used in the regional groundwater flow modelling.
- Chapter 7 describes the implementation of the conceptual model in the numerical groundwater flow model.

- Chapter 8 presents the calibration of the numerical groundwater flow model based on natural groundwater level data, drawdown induced by the near-by Äspö laboratory and interference tests conducted in Laxemar.
- Chapter 9 presents the calibration of the numerical groundwater flow model based on hydrochemical data and simulation of the period since latest glaciation (this process is denoted Palaeohydrogeology throughout this report.)
- Chapter 10 presents some exploration simulations focused mainly on flow paths to and from the tentative repository layout.
- Chapter 11 summarises the conclusions related to the hydrogeological conceptual model, the results of the groundwater flow and transport models and also provides a summary of the conceptual and parameter uncertainty and the lists remaining unresolved issues.

1.3 Regional and local model areas

The regional and local model areas employed for model version SDM-Site Laxemar are shown in Figure 1-1. The *Laxemar-Simpevarp regional (scale) model area/volume* (Later in the report referenced as *Regional model area/volume*) for SDM-Site Laxemar is the same as the one used in model version Laxemar 1.2.

The coordinates outlining the surface area of the Regional model volume, cf Figure 1-1 are (in metres):

RT90 (RAK) system: (Easting, Northing):
(1539000, 6373000), (1560000, 6373000), (1539000, 6360000), (1560000, 6360000).

RHB 70; elevation: +100 m.a.s.l. –2,100 m.a.s.l.

Volume: $21 \times 13 \times 2.3$ km^3 = 600.6 km^3.

The coordinates defining the *Laxemar local (scale) model area/volume* (Later in the report referenced as *Local model area/volume*) for model version SDM-Site Laxemar are (in metres):

RT90 (RAK system: (Easting, Northing): (1546150, 6368200), (1550390, 6368200), (1550390, 6364250), (1546150, 6364250).

RHB 70: elevation: +100 m.a.s.l. –1,100 m.a.s.l.

Volume: $4.24 \times 3.95 \times 1.2$ km^3 = 20.1 km^3.

Focused area/volume is the central, southern and western parts of the local model area, cf Figure 1-1.

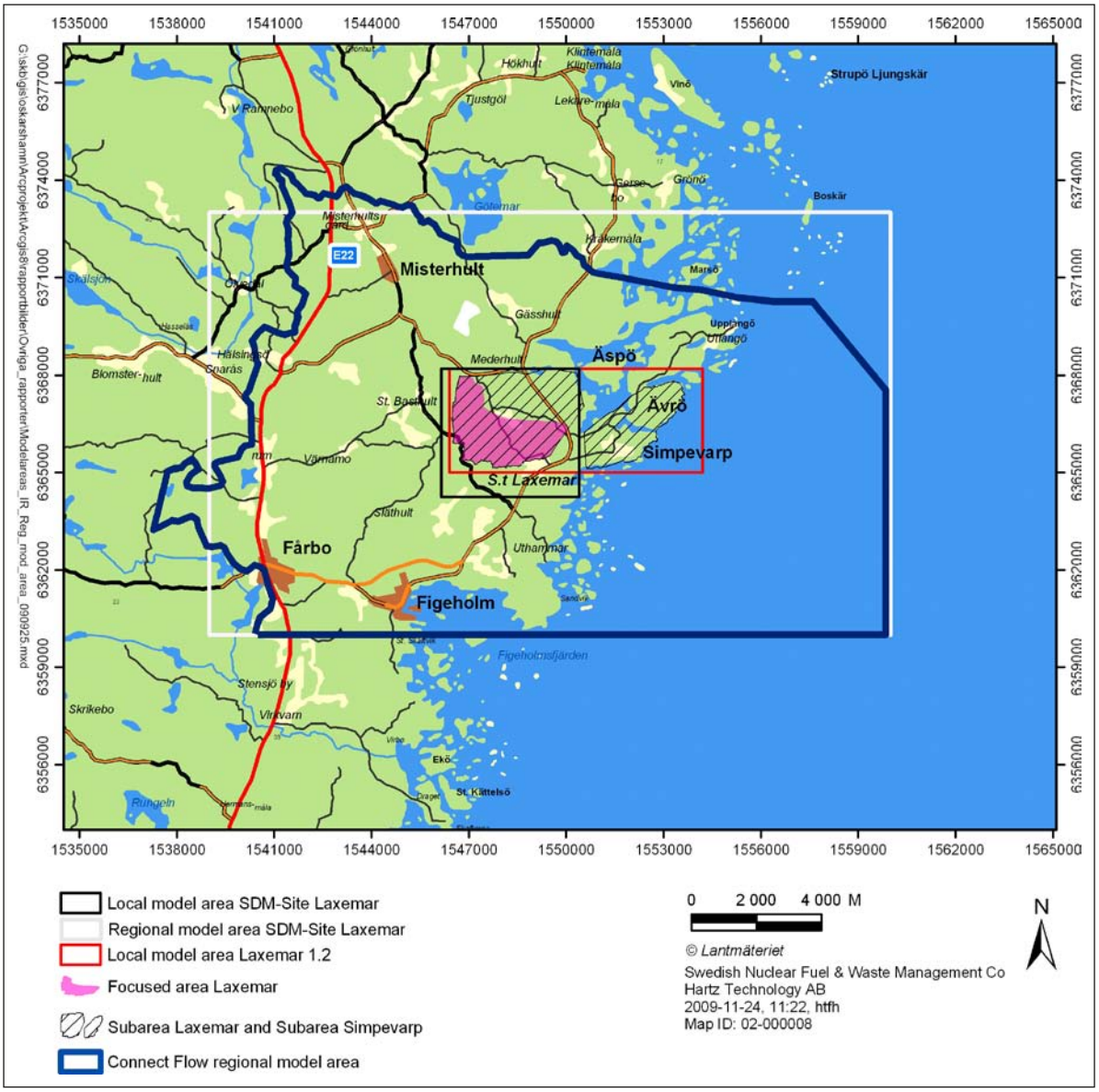

Figure 1-1. *Regional and local model areas used for model version SDM-Site Laxemar. The area coverage of the regional model is the same as that employed in previous model versions, whereas the local model area is significantly reduced compared to that employed in model version Laxemar 1.2. Laxemar subarea and Simpevarp subarea defined the investigations areas during the initial stage of the site investigations. ConnectFlow regional model area defines the boundaries for the regional groundwater flow simulations.*

2 SKB's systems approach to hydrogeological modelling in the SDM

2.1 General

The hydrogeological SDM modelling is conducted on different scales, regional scale as well as local scale. In model version SDM-Site Laxemar, particular attention is paid to the local model volume, see Section 1.3. In order to meet the objectives listed in Section 1.1 the groundwater system is divided into different hydraulic domains. Figure 2-1 illustrates schematically SKB's systems approach as employed in the hydrogeological SDM for Laxemar. The groundwater system consists of three basic hydraulic domain types, namely HSD, HCD and HRD, where:

- HSD represents the Quaternary deposits.
- HCD represents deformation zones (or "hydraulic conductors").
- HRD represents the fractured bedrock between the deformation zones.

The systems approach constitutes the basis for the conceptual modelling, the site investigations and the numerical simulations carried out in support of the hydrogeological SDM.

Besides the three hydraulic domains shown in Figure 2-1, the groundwater flow and solute transport model analysed in this work consists of three additional elements:

- A solute (salt) transport model for the modelling of advective transport and matrix diffusion.
- Initial conditions for groundwater flow and hydrochemistry.
- Boundary conditions for groundwater flow and hydrochemistry.

The parameterisation of the six elements is based on of altogether 13 different submodels, see Table 2-1.

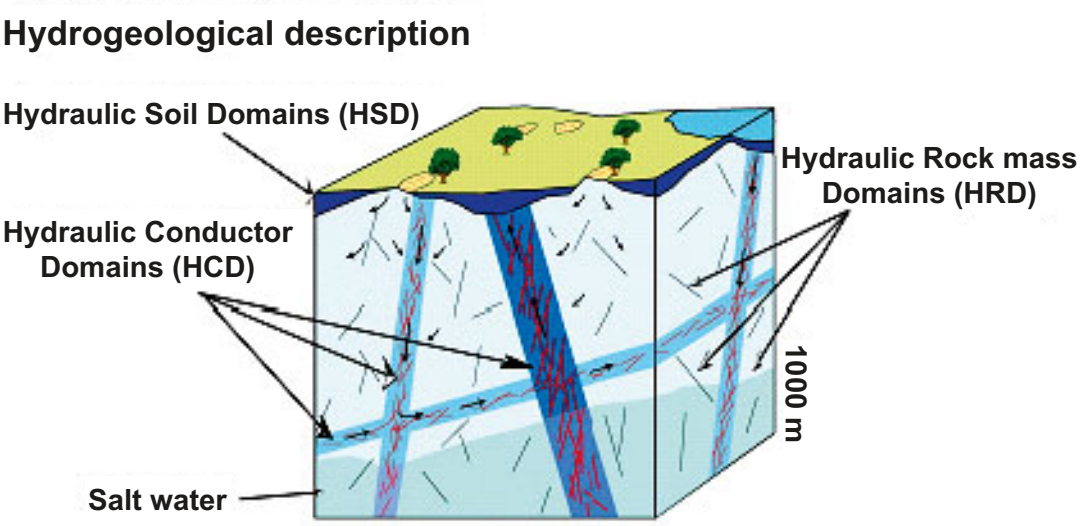

Figure 2-1. *Cartoon showing the division of the crystalline bedrock and the overburden (Quaternary deposits) into hydraulic domains. Within each domain, the hydraulic properties are represented by equivalent values, or by spatially distributed statistical distributions /Rhén et al. 2003/.*

Table 2-1. The groundwater flow and solute transport modelling with the ConnectFlow code is based on altogether 13 different submodels. The shaded fields show the key field/laboratory data used to conceptualise and parameterise the six elements listed in the top row. (Modified after /Follin 2008/.)

HCD, Hydraulic conductor domain model	HRD, Hydraulic rock mass domain model	HSD, Hydraulic soil domain model	Solute (salt) transport model	Initial conditions	Boundary conditions
2. Deformation zone (DZ) model	1. Rock domain model	8. Quaternary deposits model	7. Hydrogeological DFN model	10. Palaeo-hydrological model	3. Digital elevation model
5. Bedrock hydrogeological description of DZ	4. Fracture domain model	3. Digital elevation model	13. Bedrock transport properties model		11. Shore level displacement model
	5. Bedrock hydrogeological description of rock between DZ	9. Quaternary deposits hydro-geological model			12. Baltic Sea salinity model
	6. Geological DFN model				
	7. Hydro geological DFN model				
Single-hole hydraulic tests (PSS, HTHB and PFL), Interference tests	Single-hole hydraulic tests (PSS, HTHB and PFL)	Slug-tests, Interference tests	Single-hole hydraulic tests (PFL)	Hydrochemical database	Hydrochemical database
Borehole core description	Borehole fracture data		Dilution tests, SWIW tests, In situ tracer tests, Laboratory tests (sorption/ diffusion)		Hydrological monitoring data

The hydrogeological investigations/site-descriptive modelling of the groundwater system is divided up between the *surface systems* and *bedrock hydrogeology*, where the former treat the near-surface system (surface hydrology and the hydrogeology of surface rock and HSD), and the latter analyses the deeper (bedrock hydrogeology and hydraulic properties of the HCD and HRD), cf Section 2.3. However, the hydrogeology modelling group also uses hydraulic properties of HSDs and interacts with the surface systems modelling group in the assessment of the hydraulic properties of HSDs. This division is purely pragmatic and the interface between the different descriptions is seamless from a conceptual modelling point of view. For instance, the hydraulic properties of the bedrock and the head distribution at the bottom boundary of the near-surface hydrogeological system are provided by the numerical flow modelling undertaken for the entire system. A description of the approach taken by SKB for the near-surface hydrogeological modelling for Laxemar model version 1.2 is found in /Bosson 2006/. The shallow groundwater system is modelled so as to include the part of the bedrock down to c. 600 m depth with flow conditions that are consistent with the bedrock hydrogeological model, see Figure 2-2.

2.2 Methodology

As part of the preliminary Site Descriptive Modelling (SDM) for the Initial Site Investigation (ISI) phases at Forsmark, Simpevarp and Laxemar, a methodology was developed for constructing hydrogeological models of the crystalline bedrock at the studied sites. The methodology combined a deterministic representation of major deformation zones with a stochastic representation of the less fractured bedrock between these zones using a Discrete Fracture Network (DFN) concept, the latter subsequently upscaled in regional scale flow models.

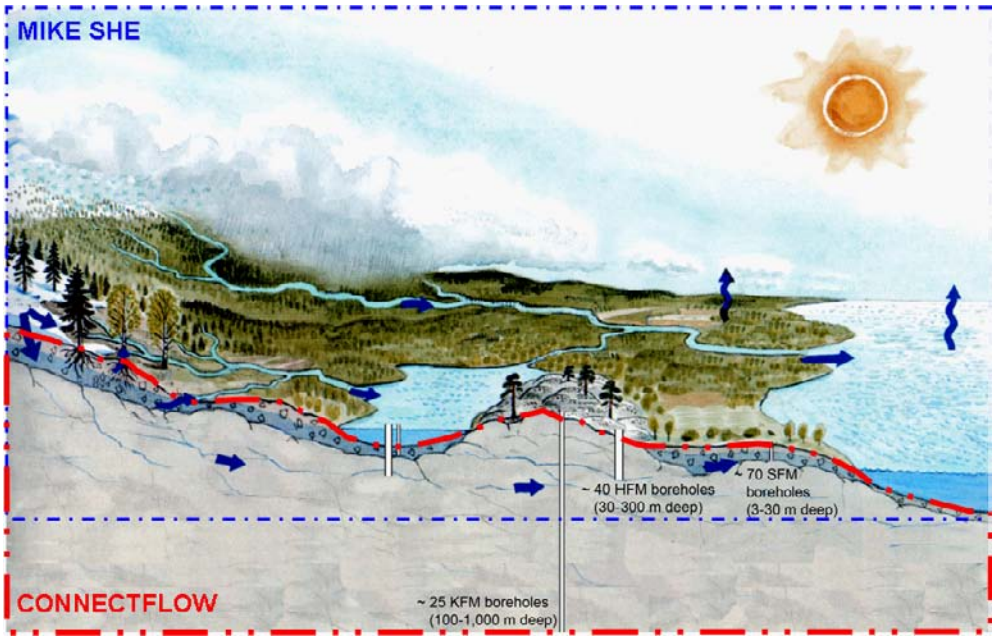

Figure 2-2. *Schematic illustration of how the modelling of the hydrologic cycle is divided into a surface-based system and a bedrock-based system. The former is modelled with the MIKE SHE code and the latter with the ConnectFlow code. Reproduced from /Follin et al. 2007c/.*

The deterministic deformation zones and fracture network (between the deterministic deformation zones) are parameterised hydraulically with data from single-hole Posiva Flow Log (PFL) pumping tests, single-hole Pipe String System (PSS) injection tests and single-hole pump tests with Hydraulic Test System for Percussion Boreholes (HTHB), see e.g. /Pöllänen et al. 2007, Enachescu et al. 2006b/ and /Rahm and Enachescu 2004/. The hydrogeological descriptions of the deterministic deformation zones and the less fractured bedrock outside/between these zones are referred to as Hydraulic Conductor Domains (HCD) and Hydraulic Rock Domains (HRD), respectively, according to SKB's systems approach to bedrock hydrogeology /Rhén et al. 2003/.

The hydraulic properties of the HCD and DFN models form the basis of constructing regional-scale Equivalent Continuum Porous Medium (ECPM) flow models, cf Chapter 7, which are e.g. used to simulate the palaeohydrogeological evolution over the last 10,000 years (Holocene), cf Chapter 4 and 9. This modelling is conducted as a coupled process between variable density groundwater flow and the hydrodynamic transport of several reference waters, taking into account the process of rock-matrix diffusion. Results obtained from these simulations include prediction of hydrochemical constituents (e.g. major ions and environmental isotopes) for the present-day situation along boreholes, which is subsequently compared with results of groundwater samples acquired from the corresponding boreholes/borehole sections. By comparing the model predictions with measurements, the models developed can be partially calibrated to improve model parameterisation, thus improving our understanding of principal controls of the hydrogeological system, thereby building confidence in the conceptual models developed for the studied site, cf Chapters 8 through 10. As the calibration results are dependent on the conceptual models, these models should be hydrogeologically relevant and sound.

The methodology has achieved reasonable success given the restricted amounts, and types of data available at the time of models preceding the SDM-Site models. Notwithstanding, several issues of concern have surfaced following the reviews of the preliminary site descriptions of the Simpevarp and Laxemar subareas conducted internally by SKB's modelling teams /SKB 2005a, SKB 2006b/, by SKB's external review group (SIERG) and by the SKI's international review group (INSITE) /SKI 2005/. Moreover, the safety implications of the preliminary site descriptions have been assessed in the Preliminary Safety Evaluations (PSE) /SKB 2005b, SKB 2006c/ and in SR-Can /SKB 2006e, Hartley et al. 2006b/.

It is recognised that the main reason for uncertainties of the geometrical descriptions of domains and their hydraulic properties in the model version 1.2 site descriptive model (SDM) of Laxemar /SKB 2006b/ were associated with relatively limited number of hydraulic observations compared to the large volume investigated and the high variability found in the existing data.

For the complete site investigation (CSI) phase, the integrated use of geological, hydrogeological, hydrogeochemical and transport models has identified the need for more robust, discipline-consistent models to be produced by the final stage of the site descriptive modelling. As part of the solution for obtaining more robust models, an integrated strategy forward has been formulated, see Figure 2-3. This "updated strategy" is not an entirely new direction in methodology, but rather a refocusing on and clarification of the key aspects of the hydrogeological SDM, i.e.:

- assessing the current understanding of the hydrogeology at the analysed site, and
- provision of the hydrogeological input descriptions needed for the end users; design, safety assessment and environmental impact assessment. These input descriptions should especially focus on the hydraulic properties in the potential repository volumes of the explored sites and assessment of the distribution of flow paths at potential repository depth.

/Follin et al. 2007a/ proposed a procedure for integrating four kinds of data in the groundwater flow (GWF) modelling of the final SDM, see Figure 2-4, as a means of approaching the issue of confirmatory testing of the developed models (Step 4 in Figure 2-3).

At Laxemar the hydrogeological HCD and DFN-based models for the HRDs derived as part of model version Laxemar 1.2 and the hydrogeological and hydrochemical information from data freeze Laxemar 2.1 were used to explore some specific hydrogeological issues raised in the reviews of Laxemar version 1.2. The aim was not a full SDM update, but rather to provide preparatory modelling studies of regional boundary conditions, cf /Holmén 2008/ that was based on /Ericsson et al. 2006/, as well as modelling studies intended to provide insight into new aspects of the suggested procedure and the use of field data (e.g. interference tests) and the possible effects in Laxemar of the nearby underground laboratory Äspö Hard Rock Laboratory (Äspö HRL) /Hartley et al. 2007/, thereby providing premises and support for the subsequent work reported here.

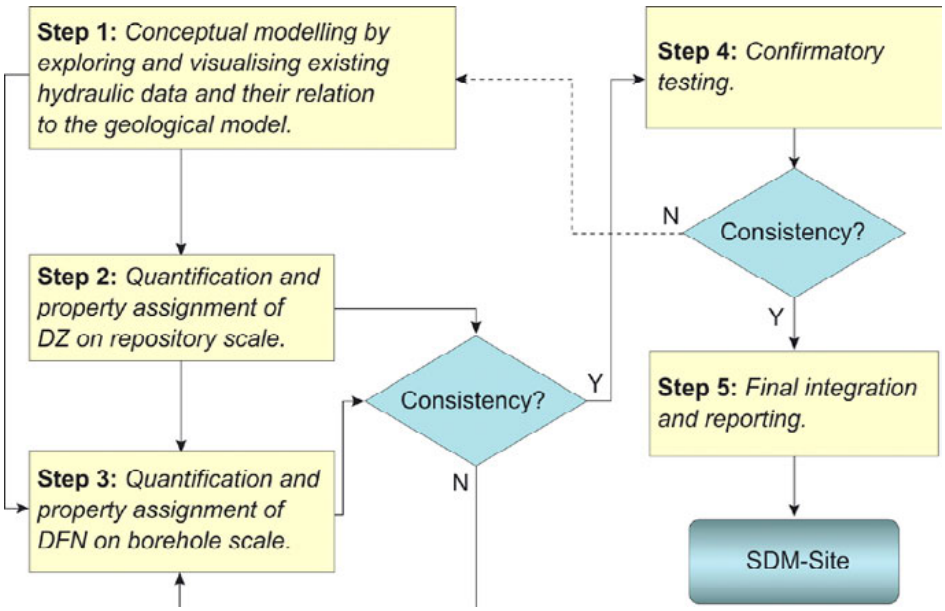

Figure 2-3. *Flow chart of the five steps suggested for the hydrogeological modelling of the complete site investigation (CSI) phase.*

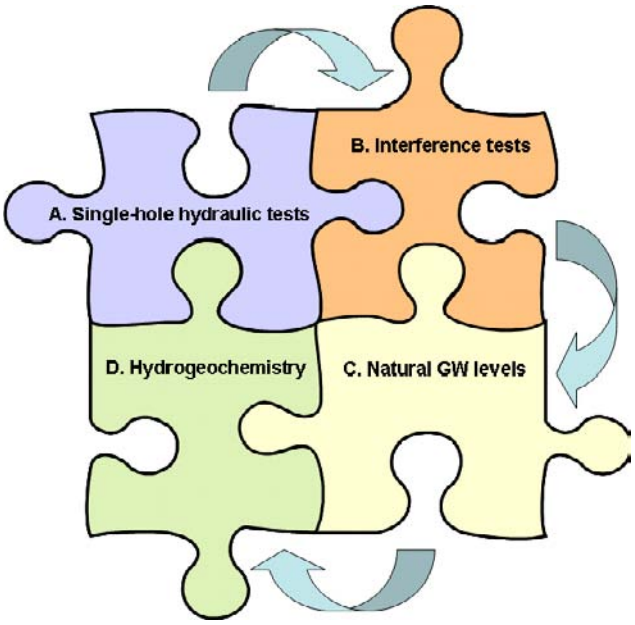

Figure 2-4. *Four kinds of data are used in the numerical groundwater flow modelling of the final SDM as a means of approaching the issue of confirmatory testing, cf Step 4 in Figure 2-3: A) Hydraulic properties of deformation zones and discrete fracture networks as deduced from single-hole hydraulic tests (this report); B) Interference tests; C) Natural groundwater levels; D) Hydrogeochemistry (see /Follin et al. 2007b/).*

It is noted that an underlying idea behind Figure 2-4 is that the same GWF model is used for each type of simulation to make it transparent that a single implementation of the conceptual model can be calibrated against all four types of field observation (although A is rather used for conditioning the borehole near-field and B-D are the basis for confirmatory testing), although it might have been possible to improve the model performance further in relation to a particular data type by refining, e.g. the geometry or material property distribution around a particular observation borehole.

2.3 Bedrock hydrogeology

A cornerstone of the bedrock hydrogeological description concerns the hydraulic characterisation of the deterministic deformation zones (HCD) and the fractured bedrock between these zones (HRD). The approach taken by SKB combines a deterministic representation of the major deformation zones with a stochastic representation of the fractured bedrock between these zones using a Discrete Fracture Network (DFN) concept. The hydraulic description of the deformation zones is particularly important for Repository Engineering whereas the hydraulic description of the less fractured bedrock between the deformation zones is especially important for Safety Assessment. The hydraulic characterisation of the fractured bedrock between the deterministic deformation zones at repository depth is a vital, yet complex task given the relatively minute number of data available at this depth. The hydrogeological SDM is based on data from investigations in vertical to steeply inclined cored boreholes drilled from the surface, typically extending to depths between 300 to 1,000 m. The current understanding of the groundwater system at depth is constrained by this fact, where the subvertical boreholes also tend to favour sampling of subhorizontal structures.

The hydraulic characterisation of the deformation zones is fairly straightforward. All hydraulic data between the upper and lower bounds of an interpreted deformation zone interval in a borehole, as described in the single-hole geological interpretation, are considered, regardless of the hydraulic test method used. The hydraulic data collected are pooled, i.e. lumped together, to form an integrated single transmissivity value for the particular borehole interval for any given method and means of test evaluation employed.

Figure 2-5 illustrates the principal structural-hydraulic approach taken by SKB in the hydrogeological modelling within SDM-Site Laxemar for modelling deformation zones and also identifying the maximum size for hydraulic features modelled stochastically (L ≤ 1,000 m). The methods and methodology for assessing properties of the HCDs and HRDs from boreholes data are discussed in /Rhén et al. 2008/.

2.4 The ECPM approach

Any numerical groundwater model is a simplified representation of geometry, material properties parameterisation and boundary and initial conditions of a real physical groundwater system. The Equivalent Continuous Porous Medium (ECPM) approach is used in the current hydrogeological SDM for the transformation of geometrical and hydraulic properties of a modelled system consisting of 2D discrete features (HCD and hydrogeological DFN features) into a 3D continuous porous medium, see Figure 2-6.

In the regional scale modelling presented in this report, different hydrogeological DFN models are defined for all defined HRDs and the ECPM cell-properties are calculted from the hydraulic properties of the flowing fractures defined by the respective hydrogeological DFN models and the properties of the HCDs. Since each ECPM model studied is based on a particular underlying stochastic DFN realisation, the ECPM models are inherently also stochastic. It should be mentioned that within the subsequent Safety Assessment, the hydrogeological DFN is used to model the flow pattern within the repository volume, and not the ECPM devised by in the SDM work. The ECPM is also needed for palaeohydrogeological regional simulations, as shown in this report, cf Chapter 9, but also for the hydrochemical simulations within the Safety Assessment.

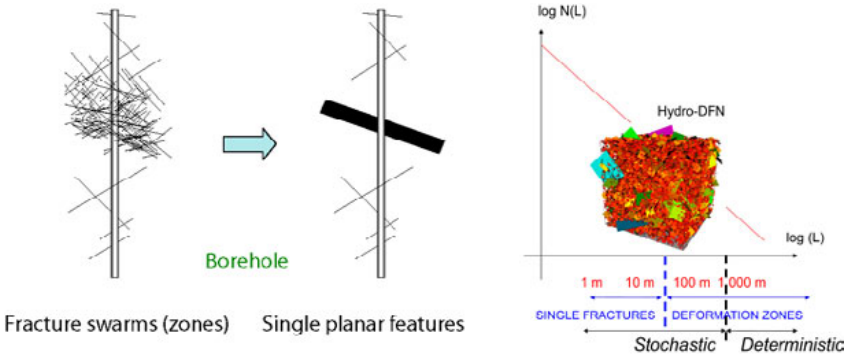

Figure 2-5. *Schematic illustrations showing the structural-hydraulic approach in the hydrogeological SDM used for the treatment of the deterministic deformation zones and minor deformation zones, the latter modelled stochastically in the hydrogeological SDM. Left: The hydraulic data collected between the upper and lower bounds of an interpreted deformation zone interval in a borehole are lumped together to form one single integrated transmissivity value for the zone in that interval. In the same fashion all fractures in the deformation zone interval are also lumped together, to form one single planar feature with an integrated transmissivity made up of the sum of individual fracture transmissivities. Right: A tectonic continuum is envisaged where the number of features/fractures of different sizes follows a power law relationship. Features up to r = 564 m in size (corresponding to a 1,000×1,000 m square) are regarded as uncertain and are consequentially treated stochastically using the Hydrogeological DFN concept. Reproduced from /Follin et al. 2007c/.*

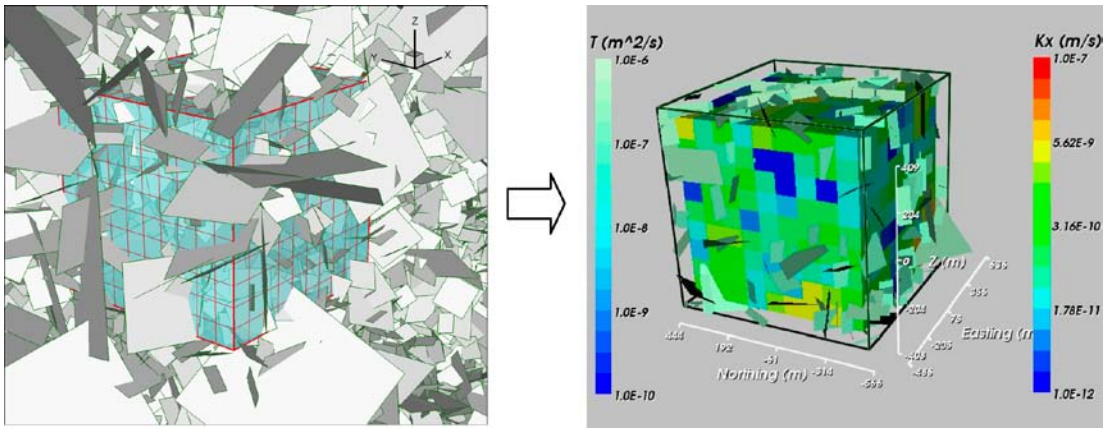

Figure 2-6. *Illustrations showing of the ECPM concept. Geometrical and hydraulic properties of modelled 2D discrete features (deformation zones and DFN) are transformed into a 3D equivalent continuous porous medium. Reproduced from /Follin et al. 2007c/*

3 Geological setting

3.1 Overview of the investigated area

The investigated area is close to the coast, cf Figure 3-1. The topography is fairly flat (regional topographic gradient in the order of 4%) but with relatively distinct valleys, cf Figure 3-2. The investigation area is located within a crystalline basement, mostly covered by a rather thin till in the elevated areas and with glaciafluvial sediments in the larger valleys. The site-average annual precipitation and specific discharge are estimated to be on the order of 600 mm and 160–170 mm, respectively /Werner et al. 2008, Larsson-McCann et al. 2002/ and the area is covered with a fairly large number of small stream and lakes, cf Figure 3-1. The Äspö Hard Rock laboratory is located below the Äspö island, cf Figure 3-1, which is an underground research facility that affects the groundwater flow locally in the area. The Simpevarp penisula hosts the Clab interim facility and there is inflow to the rock caverns near the surface, but it has a very local affect on the groundwater flow. The geology of the area is described in more detail in the rest of Chapters 3 and 4.

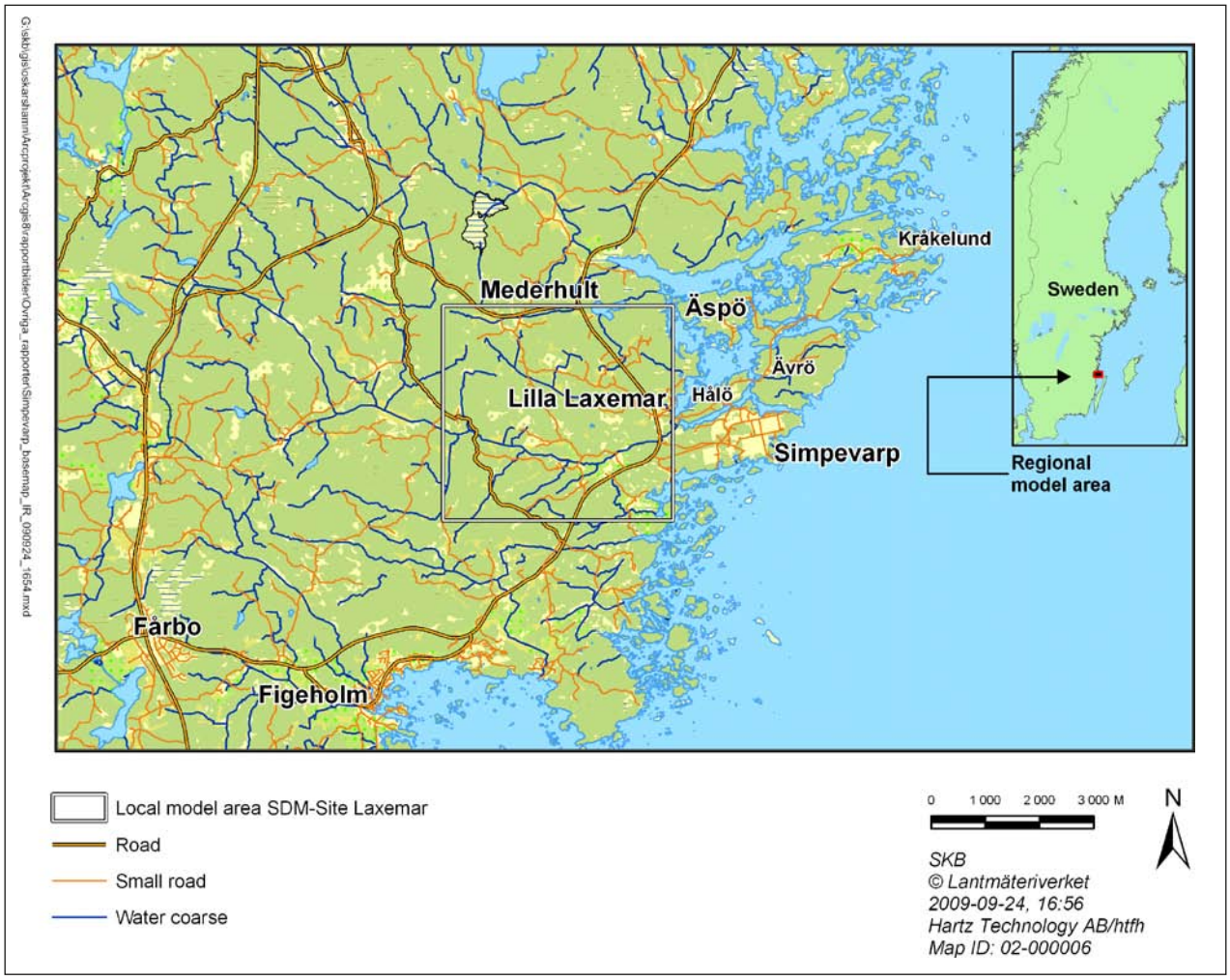

Figure 3-1. *Overview map of the Laxemar-Simpevarp regional model area with the SDM-Site Laxemar local model area indicated.*

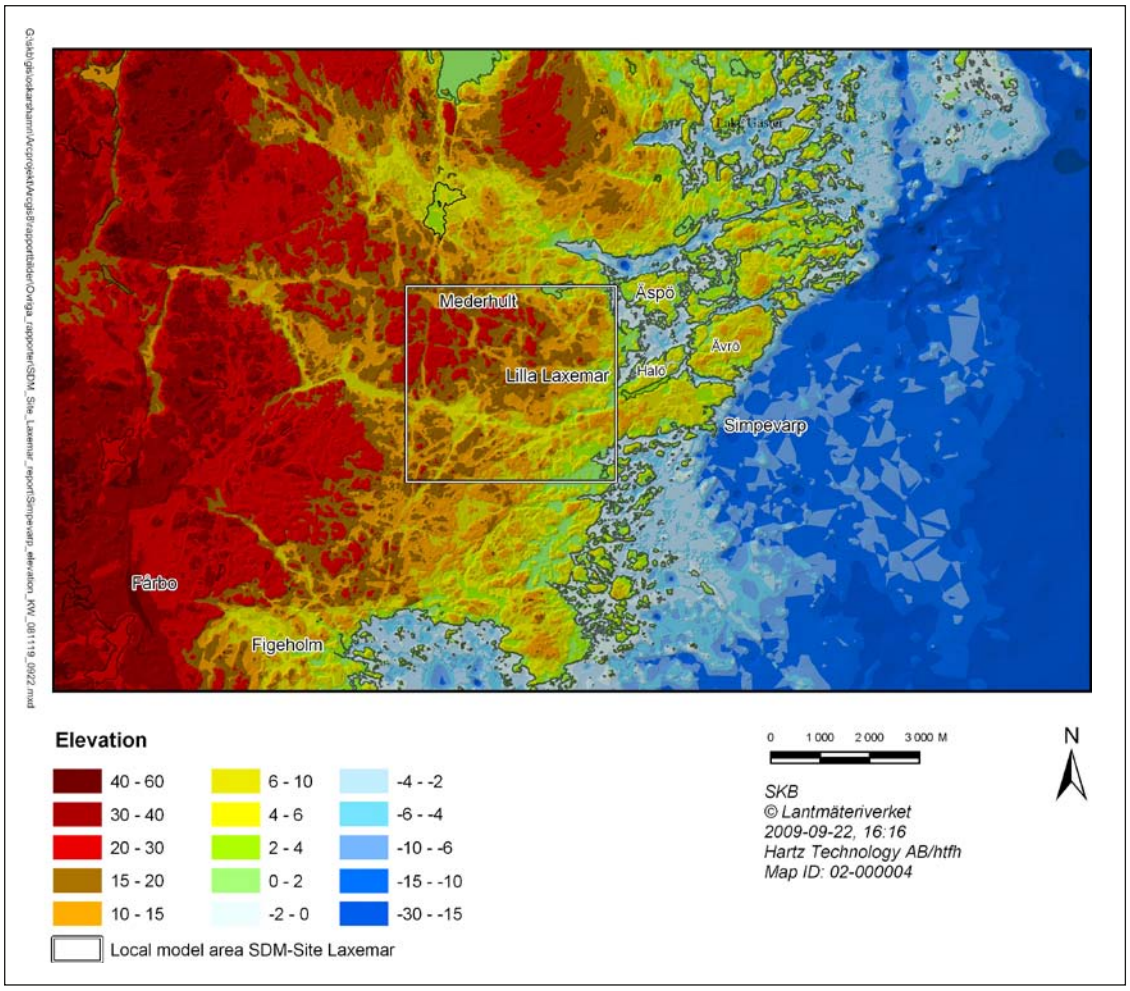

Figure 3-2. *Overview map illustrating the ground-surface topography (m.a.s.l.) in an area roughly corresponding to the Laxemar-Simpevarp regional model area, including the bathymetry of lakes and the sea.*

The investigations made within the Laxemar-Simpevarp regional model area, cf Figure 1-1 and Figure 3-1, cover the Laxemar local model area, the Simpevarp peninsula and the Ävrö Island. Figure 3-3 and Figure 3-4 show the Laxemar local model area and the eastern part of the regional model area with the boreholes available for interpretation of the bedrock properties and conditions in the area. Figure 3-5 and Figure 3-6 illustrate the drilled groundwater monitoring wells that in part have helped to define the bedrock surface, but mainly provide input to the model of the Quaternary deposits (HSD) within the regional model area and groundwater head data in the Quaternary deposits.

During the site investigations in Laxemar, boreholes have mainly been drilled within the Laxemar local model area (HLX10-43, KLX03-29A), cf Figure 3-3. Boreholes have previously also been drilled on the Simpevarp peninsula (HSH01-06, KSH01-KSH03B) and on the Ävrö island (HLX09-14, KAV04A,B) as part of investigations of the Simpevarp subarea, cf Figure 3-4. The additional boreholes shown, e.g. KLX01 and KLX02 (cf Figure 3-3) were drilled during projects preceding the site investigations in the Laxemar-Simpvarp area. The boreholes completed before the site investigations generally provide less geological and hydrogeological data and are sometimes based on methodologies other than those employed in the current site investigations. Data from cored borehole KLX27A, cf Figure 3-3, drilled late in complete site investigations, have not been used for the geological DFN and hydrogeological DFN models, as the corresponding data became available late in the project. However, the hydrogeological DFN model of HRD_W was used to predict the fracturing and inflow in this borehole and subsequently compared with measured data, see /Rhén et al. 2008, cf Appendix 10 therein/

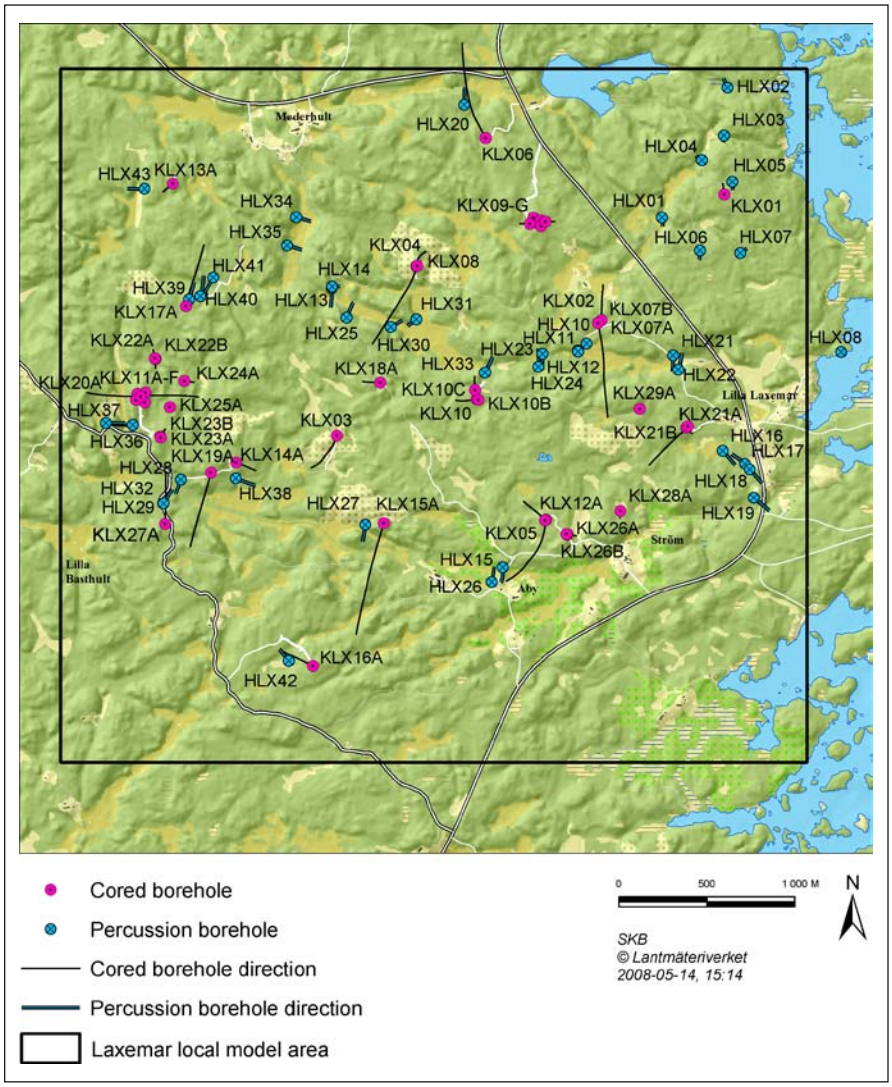

Figure 3-3. *Cored and percussion-drilled boreholes within and close to the Laxemar local model area. Borehole KLX27A has not been used for primary data analysis and for hydrogeological DFN model as the data was available late in the project. (Other cored and percussion-drilled boreholes, cf Figure 3-4.)*

3.2 Overview of the bedrock geology

The Laxemar-Simpevarp regional model area is dominated by a geological unit referred to as the Transscandinavian Igneous Belt (TIB). The bedrock is dominated by well preserved c. 1.8 Ga intrusive rocks varying in composition between granite-syenitoid-dioritoid-gabbroid. Although a non-uniformly distributed faint to weak foliation, is present, the most prominent ductile structures at Laxemar are discrete, low-temperature, brittle-ductile to ductile shear zones of mesoscopic to regional character, which are related to the waning stages of the Svecokarelian orogeny. Subsequently the rock mass has been subjected to repeated phases of brittle deformation, under varying regional stress regimes, involving reactivation along earlier formed structures. There are indications that the ductile anisotropy, including both larger ductile shear zones as well as the weak to faint foliation, minor shear zones and mylonites, has had an influence on the later brittle deformation. With a few exceptions, the deterministically modelled deformation zones at Laxemar are characterised by brittle deformation although virtually all the zones have their origin in an earlier ductile regime. The brittle history of the Laxemar-Simpevarp area is complex and involves a series of reactivation events that have prevented the construction of a consistent simplistic model covering their development. /Wahlgren et al. 2008/.

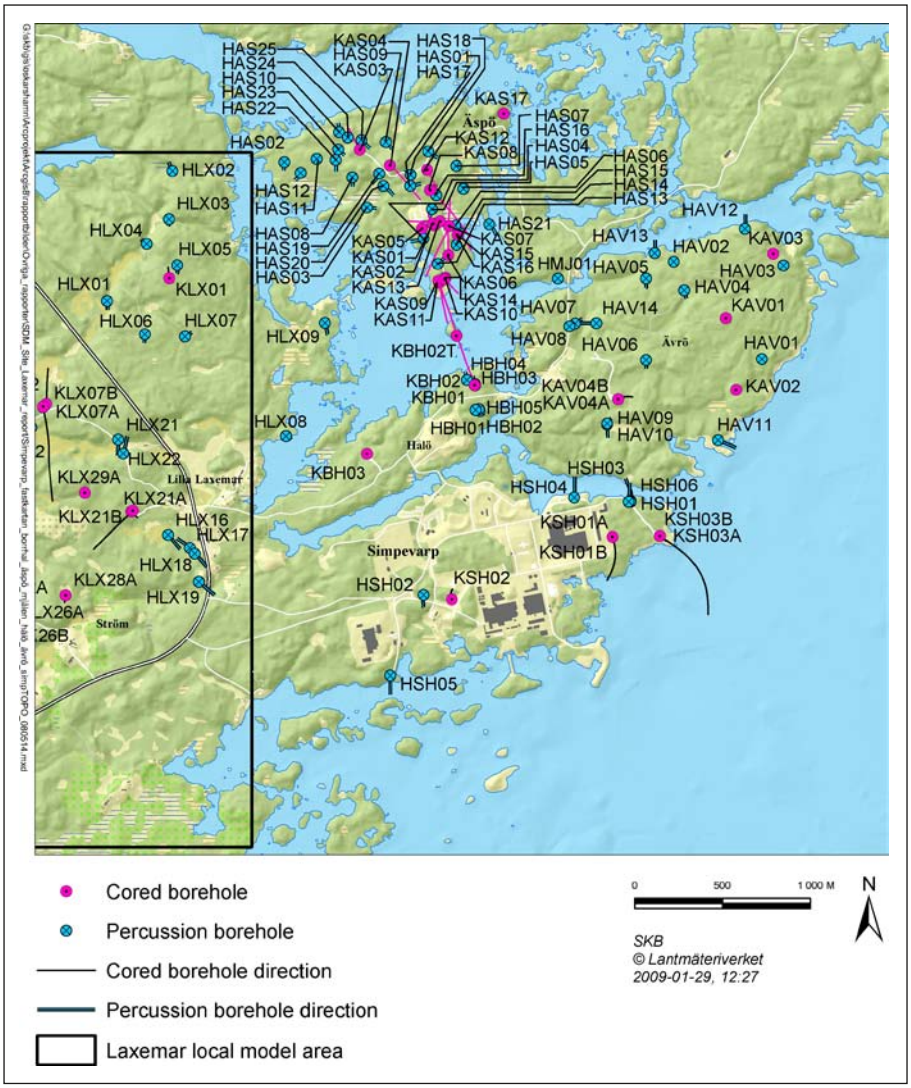

Figure 3-4. *Cored and percussion boreholes within the regional model area covering Äspö, Hålö, Ävrö, Mjälen and Simpevatp peninsula (i.e. parts of the Simpevarp subarea) .(Other cored and percussion-drilled boreholes, cf Figure 3-3.)*

3.3 Overview of the deformation zone model

Deformation zones are important hydrogeological objects as they generally are more conductive than the surrounding rock but may also occasionally act as hydraulic barriers.

3.3.1 General

The term deformation zone is used in all phases of the geological work, bedrock surface mapping, surface based interpretations, single-hole geological and hydrogeological interpretations and 3D modelling. Hence, a deformation zone is a general term referring to an essentially 2D structure along which there is a concentration of brittle, ductile or combined brittle and ductile deformation. Table 3-1 presents the terminology for brittle structures based on trace length and thickness as presented in /Andersson et al. 2000/. The geometric boundaries between the different structures are highly approximate.

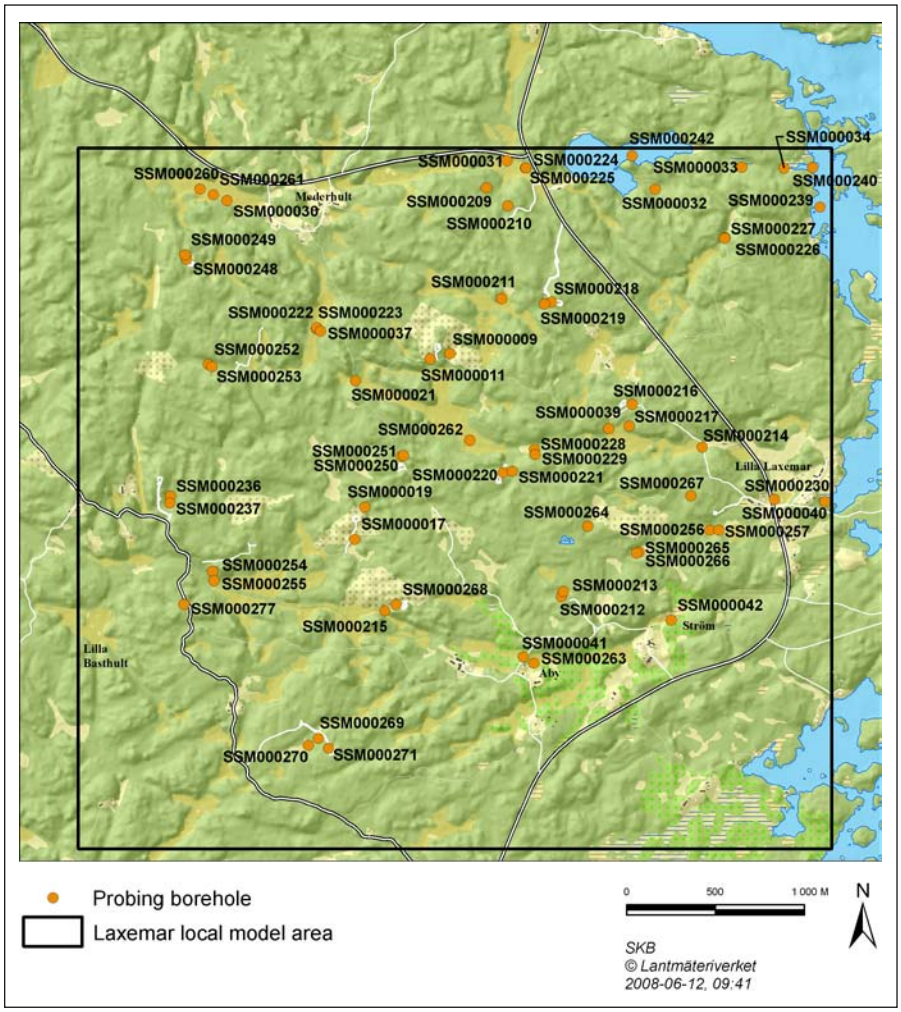

Figure 3-5. *Groundwater monitoring wells within and close to the Laxemar local model area. (Other monitoring wells, cf Figure 3-6.)*

Table 3-1. Terminology and general description (length and width are approximate) of brittle structures /modified after Andersson et al. 2000/.

Terminology	Length	Width	Geometrical description
Regional deformation zone	> 10 km	> 100 m	Deterministic
Local major deformation zone	1 km–10 km	5 m–100 m	Deterministic (with description of uncertainty
Local minor deformation zone	10 m–1 km	0.1–5 m	Statistical (if possible, deterministic)
Fracture	< 10 m	< 0.1 m	Statistical

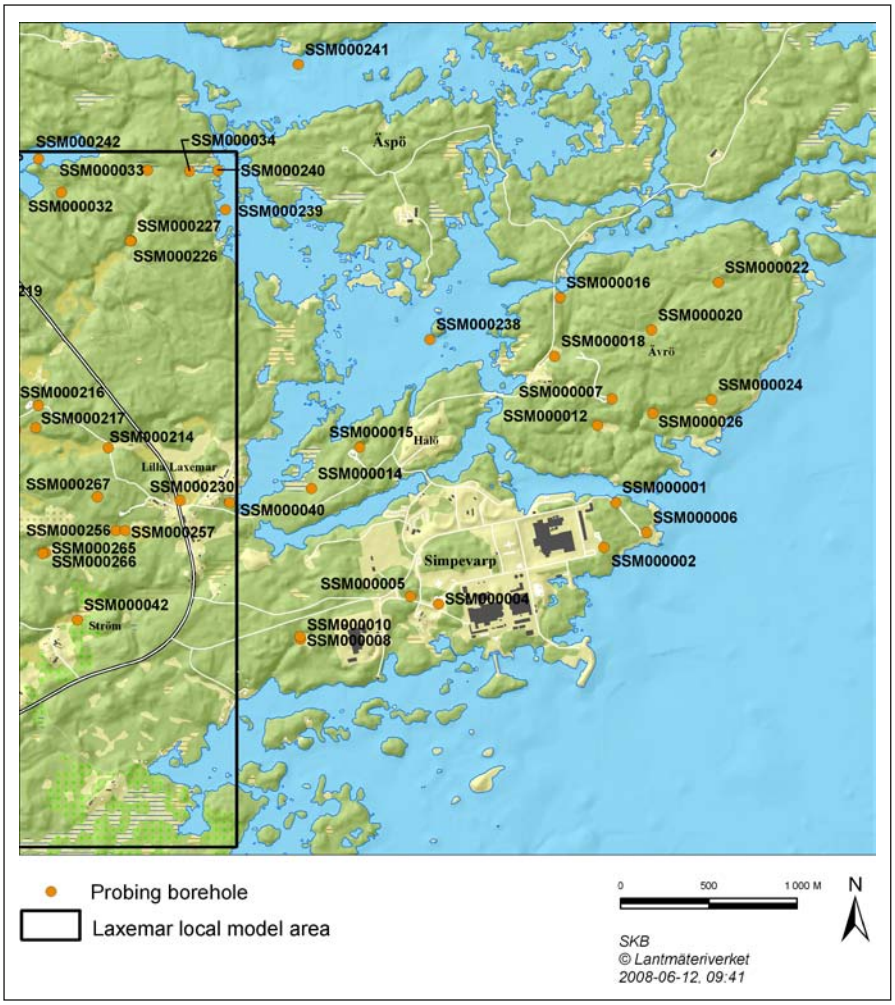

Figure 3-6. *Groundwater monitoring wells within the regional model area covering Äspö, Hålö, Ävrö, Mjälen and Simpevatp peninsula (i.e. parts of the Simpevarp subarea). (Other monitoring wells, cf Figure 3-5.)*

3.3.2 Deformation zone model

The regional scale ductile deformation zones according to the SDM-Site Laxcemar deformation zone model strike NNE-SSW and NE-SW, are subvertical and are characterised by sinistral (left-lateral) strike-slip displacements, while E-W oriented zones, although more strongly overprinted by brittle deformation, display moderate to steep dips to the south or north, cf Figure 3-7. The kinematics of the latter are not resolved at Laxemar, but E-W ductile shear zones in the Simpevarp subarea show complex kinematics, including both reverse and normal dip-slip as well as sinistral and dextral strike-slip displacements. The N-S striking deformation zones are steeply dipping, with a tendency to dip to the west with a sinistrial strike-slip displacement. Both the N-S and the NE-SW zones have possibly experienced a reversed strike-slip movement at a later stage. It should be noted that the regional and local major deformation zones, although the majority have a ductile precursor, are mainly brittle in character /Wahlgren et al. 2008/.

The focused volume is bounded in the west by the N-S oriented, steeply dipping deformation zone ZSMNS001C, in the south by the WNW-ESE oriented, moderately south-dipping ZSMNW042A, in the north by the E-W oriented, moderately north-dipping ZSMEW007A and in the east by the NE-SW oriented, steeply to subvertically dipping ZSMNE005A, the latter of which corresponds to the rock domain RSMP01. All these zones, with the exception of ZSMNE005A, are mainly brittle in character and ZSMNS001C in the west is associated with a dolerite dyke. The focused volume is transected by a series of smaller deformation zones with a variety of orientations and with dips varying from subvertical to subhorizontal. Apart from a characteristic increase in fracture frequency,

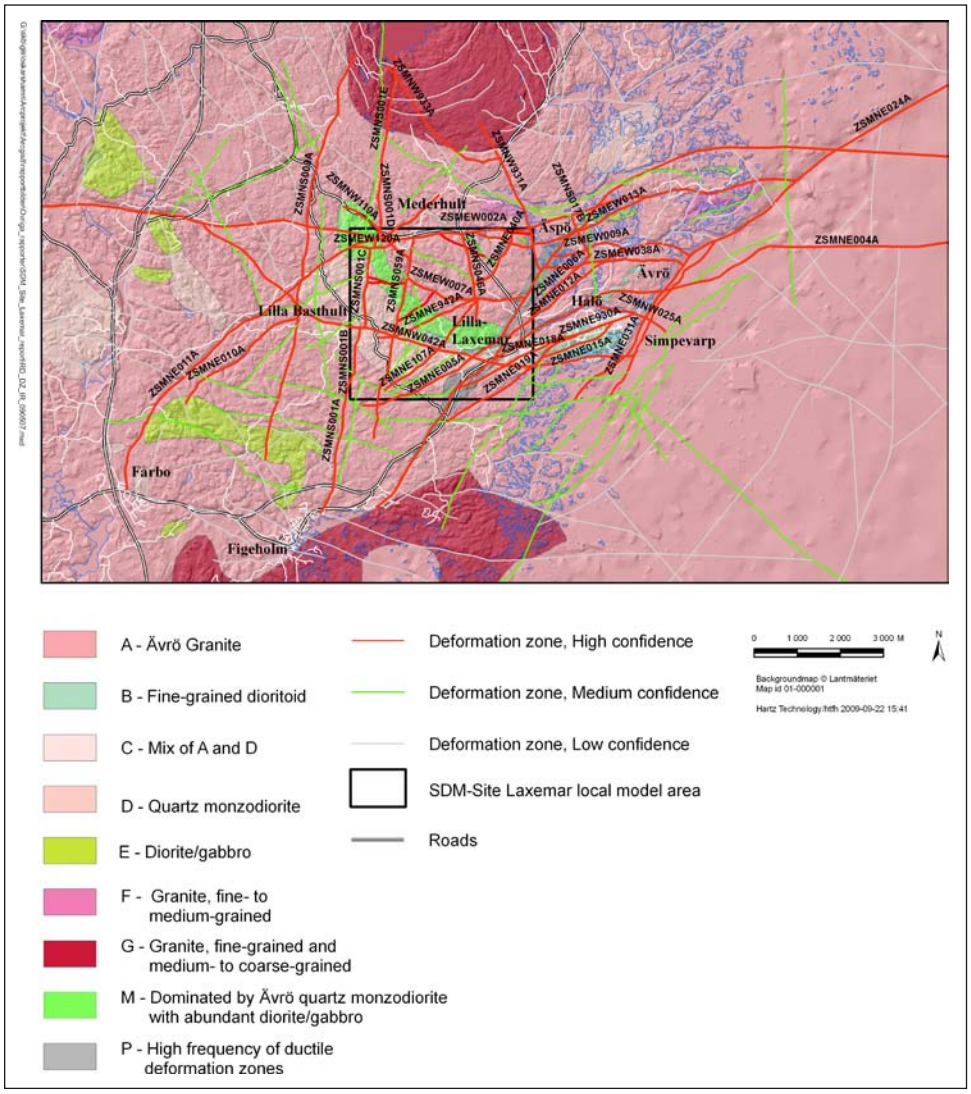

Figure 3-7. *Deformation zones and rock domains in the regional model area. Modified after /Wahlgren et al. 2008/.*

most of the deformation zones in Laxemar commonly contain associated fault rocks, such as different types of cataclasites, breccias and fault gouge. All available evidence indicates that multiple episodes of deformation took place within a broadly-defined brittle regime under different physical conditions /Wahlgren et al. 2008/.

The true thicknesses of the deformation zones, including the transition zone and core, inside the focused volume are up to a few tens of metres. It is judged that the presence of undetected deformation zones inside the focused volume, which are significantly longer than 3 km, is highly unlikely /Wahlgren et al. 2008/.

Within the local model volume, see Figure 3-8, the deterministically modelled deformation zones are of modelled size (trace length at surface) of 1 km or longer whereas within the regional model volume, see Figure 3-7, but outside the local model volume, deterministic zones are modelled with a size of 1.6 km or longer /Wahlgren et al. 2005, 2008/.

The regional scale 3D deformation zone model for SDM-Site Laxemar /Wahlgren et al. 2008/ contains 189 (if deformation zone elements with the same name but with extension A, B etc are counted as one deformation zone, e.g. ZSMNS001A, ZSMNS001B etc) deterministically modelled deformation zones within the regional model volume, of which 70 deformation zone elements (64 if deformation zone elements with the same name and extension A, B are counted as one deformation zone) are included in the local model volume, see Figure 3-7 to Figure 3-8. Most of these

deterministic deformation zones are referred to as ZSMxxx. However, a subset (N = 25) of the deterministic zones are interpreted on the basis of one single borehole intercept but being devoid of an associated surface lineament. In doing so, only those zones with an interpreted true thickness of 10 m or more in a borehole are interpreted to have a size (length) in excess of 1,000 m. These deformation zones are named *Borehole-ID_DZ-unit*, where the DZ-unit is defined in the geological single-hole interpretation (e.g. KLX07_DZ9). The latter 25 deformation zones are modelled deterministically as discs with radius 564.2 m (based on an equal area of 1×1 km^2). The size of these modelled discs are considered very uncertain.

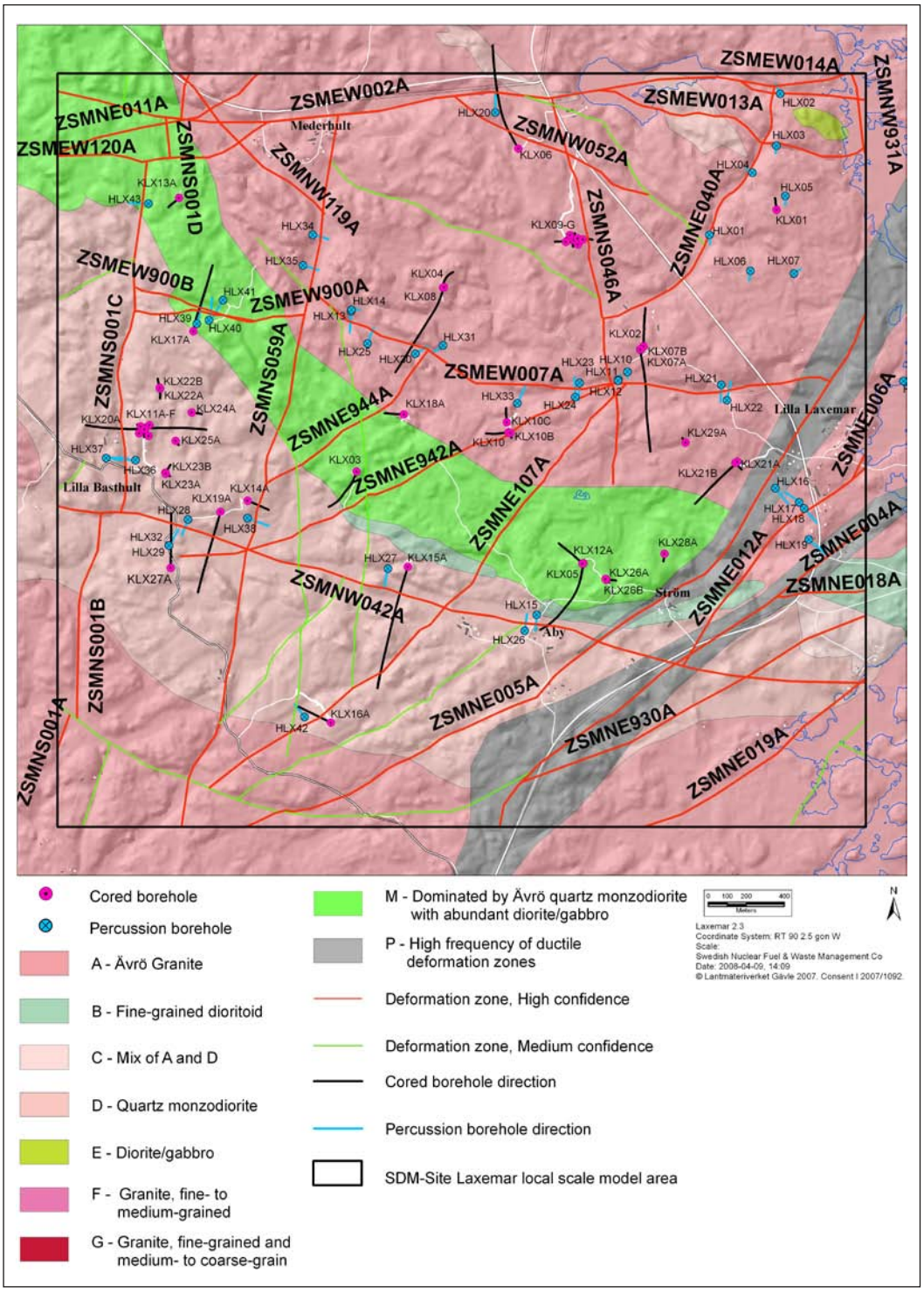

Figure 3-8. *Interpreted deterministic deformation zones and rock domains within the local model area, cf /Wahlgren et al. 2008/.*

Deformation zones are primarily of hydraulic importance as planar conductive elements with higher permeability than the surrounding rock. However, some deformation zones may in fact act as partial hydraulic barriers by geological inference, e.g. through association to dolerite dykes or existence of fault gouge, both of low hydraulic conductivity, cf Chapter 4 and /Rhén et al. 2008/.

Minor deformation zones (MDZ) are not modelled determinstically by geology /Hermanssson et al. 2008/. These were analysed hydraulically and incorporated in the hydrogeological DFN model /Rhén et al. 2008/. A few of the MDZ of the defined stochastically by Geology were modelled deterministically by Hydrogeology. Their identification and the rationale for their special treatise by Hydrogeology is provided by /Rhén et al. 2008, cf Chapter 7 and Appendix 3 therein/.

Deformation zones associated with dolerite dykes

Dolerite has not been observed in outcrop within Laxemar, but has been observed on the Äspö Island and north of the area, in conjunction with the Götemar Granite, cf Figure 3-7 (Rock domain G in the northern part of the regional model area). However, observations have been made of dolerite in a number of cored and percussion boreholes in western Laxemar, namely KLX14A and HLX38 (along deformation zone ZSMNS059A); KLX20A, HLX36, HLX37 and HLX43 (along deformation zone ZSMNS001C), plus additional observations in KLX19A and HLX13. The dolerite dykes in HLX38 are very thin /Triumf 2007/. The probable and possible dolerite dykes, according to the geophysical investigations and the borehole observations /Triumf 2007/, are shown in Figure 3-9. Only a few of the interpretations of possible dolerite dykes based on geophysics have been confirmed by borehole observations. Three of these dolerite dykes have been modelled deterministically by Geology /Wahlgren et al. 2008/:

- ZSMNS001.
- ZSMNS059A.
- KLX19_DZ5-8_dolerite (devoid of associated surface expression, assumed to me 1,000 m in size, with strip/dip: 185/81).

Thicker dolerite dykes, associated with ZSMNS001C and ZSMNS059A, are of hydraulic importance as they, at least locally, act as hydraulic barriers, due to the low-permeable characteristics of the dolerite. However, the rock bordering the dolerite dykes may be quite permeable. The hydraulic implications of these dolerite dykes are discussed more in Chapter 4 and by /Rhén et al. 2008/.

3.4 Overview of the rock domain model

The hydraulic properties of the rock between the deterministic deformation zones may vary considerably depending on rock domain, as defined below. Rock domains may have different hydraulic properties due to differences in composition, grain size, texture, homogeneity and ductile structures between rock domains, but above all due to presence of deformation zones and degree of fracturing, cf /Rhén et al. 2008, 2006c/. It is therefore important to assess the hydraulic data in relation to rock domains.

3.4.1 Rock domain model for SDM-Site Laxemar

The rock domains are defined on the basis of a combination of composition, grain size, texture, homogeneity and ductile structural overprinting. The rock domain model is discussed in detail by /Wahlgren et al. 2008/ and is shown here in Figure 3-7, Figure 3-8 and Figure 3-10 The Ävrö granite is dominant in the regional model area (Domain A), whereas Domain M (dominated by Ävrö quartz monzodiorite with abundant diorite/gabbro) and Domain D (dominated by quartz monzodiorite) make up larger parts of the local model volume, /Wahlgren et al. 2008/.

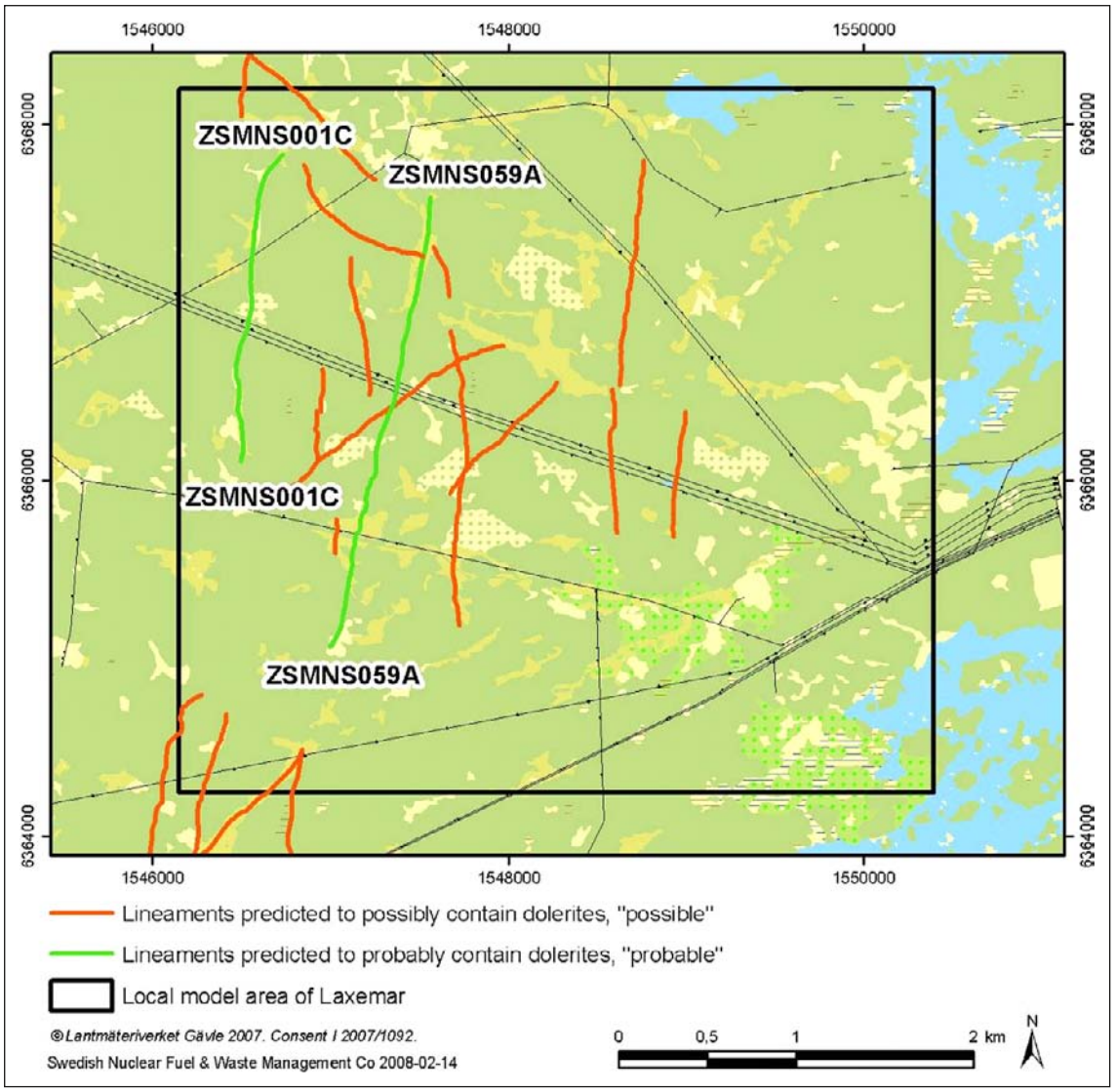

Figure 3-9. *Interpretations of possible dolerite dykes based on geophysics. Two lineaments (green line) are predicted as "probable" regarding their potential content of dolerite in the Laxemar area – they coincide with the deformation zones ZSMNS001C and ZSMNS059A. The lineaments (red line) are predicted as "possible" regarding their potential content of dolerite as part of their sources /Triumf 2007/.*

The rock domains have been given different codes where domains denominated with the same capital letter are dominated by the same characteristics as displayed below:

RSM**A**-domain: dominated by Ävrö granite;

RSM**B**-domain: dominated by fine-grained dioritoid;

RSM**BA**-domain: characterised by a mixture of Ävrö granite and fine-grained dioritoid;

RSM**C**-domain: characterised by a mixture of Ävrö granite and quartz monzodiorite;

RSM**D**-domain: dominated by quartz monzodiorite;

RSM**E**-domain: dominated by diorite/gabbro;

RSM**G**-domain: dominated by the Götemar type granite;

RSM**M**-domain: characterised by a high frequency of minor bodies to small enclaves of diorite/gabbro in particularly Ävrö quartz monzodiorite;

RSM**P**-domain: characterised by a high frequency of low-grade ductile shear zones in the above mentioned rock types.

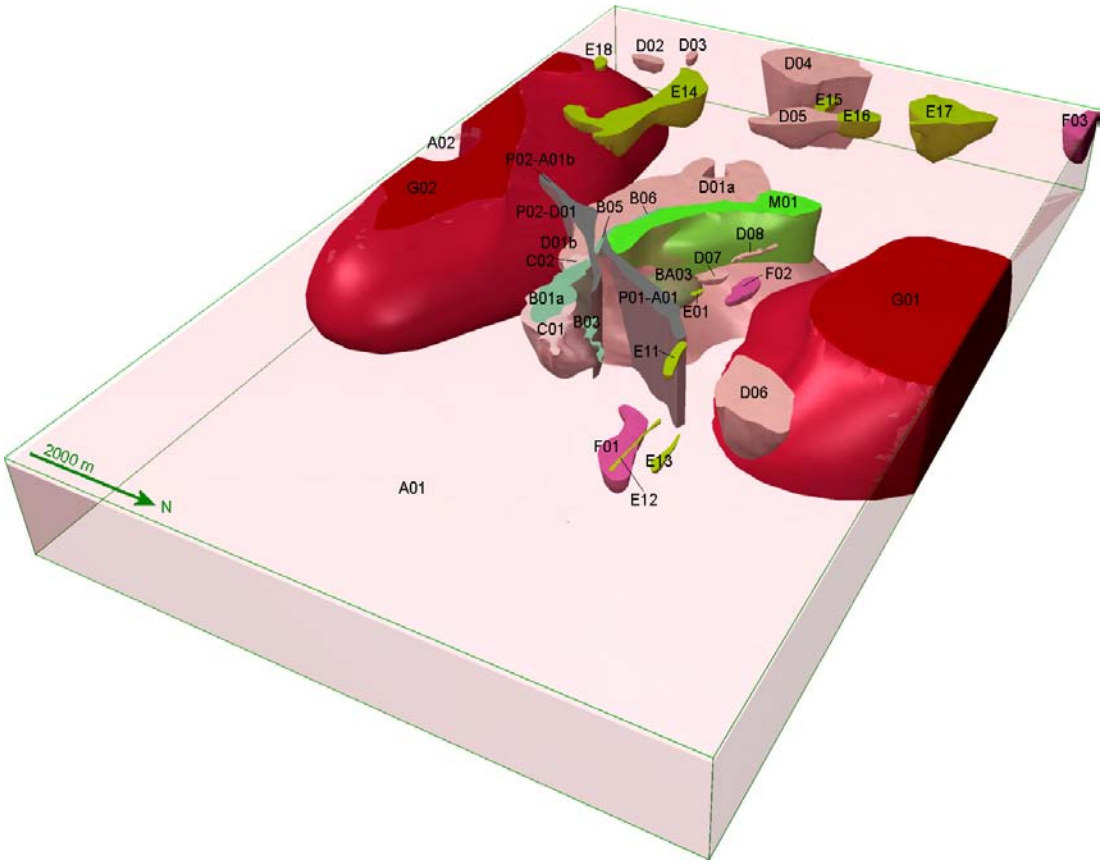

Figure 3-10. *Rock domains visulised in 3D in the regional model area. Ävrö granite shown transparent, /Wahlgren et al. 2008/.*

One rock domain, RSMBA03, characterised by a mixture of Ävrö granite and fine-grained dioritoid, intersects only borehole KLX02 at borehole length 540.0–960.0 m, and is geologically modelled as an ellipsoidal body. It is located in the northern part of the model and occupies a rather small volume.

3.5 Overview of the fracture domain model

The fracture domains and rock domains have been the base geometrical models for the study of the spatial variation of hydraulic properties and for the subsequent definition of hydraulic rock domains (HRD), cf /Rhén et al. 2008/. Fracture domains are potentially hydraulically significant as the intensity and orientations of open fractures, a subset of all fractures, are responsible for the permeability of the rock.

3.5.1 Fracture domain model

Fracture domains provide a local scale conceptual framework for describing spatial heterogeneity in rock fracturing in SDM-Site Laxemar. The six identified fracture domains in Laxemar (FSM_C, FSM_EW007, FSM_N, FSM_NE005, FSM_S, and FSM_W) are for the most part bounded by deformation zones, and were defined based on identified contrasts in relative fracture frequencies between orientation sets and between open and sealed fractures, cf Figure 3-11 through Figure 3-13. The fracture domains exist inside a volume (the ‘fracture domain envelope’) which is smaller than the local model volume. Patterns of relative fracture intensity inside each domain appear to correspond well to the tectonic history interpreted as part of the deformation zone modelling, cf /Wahlgren et al. 2008/.

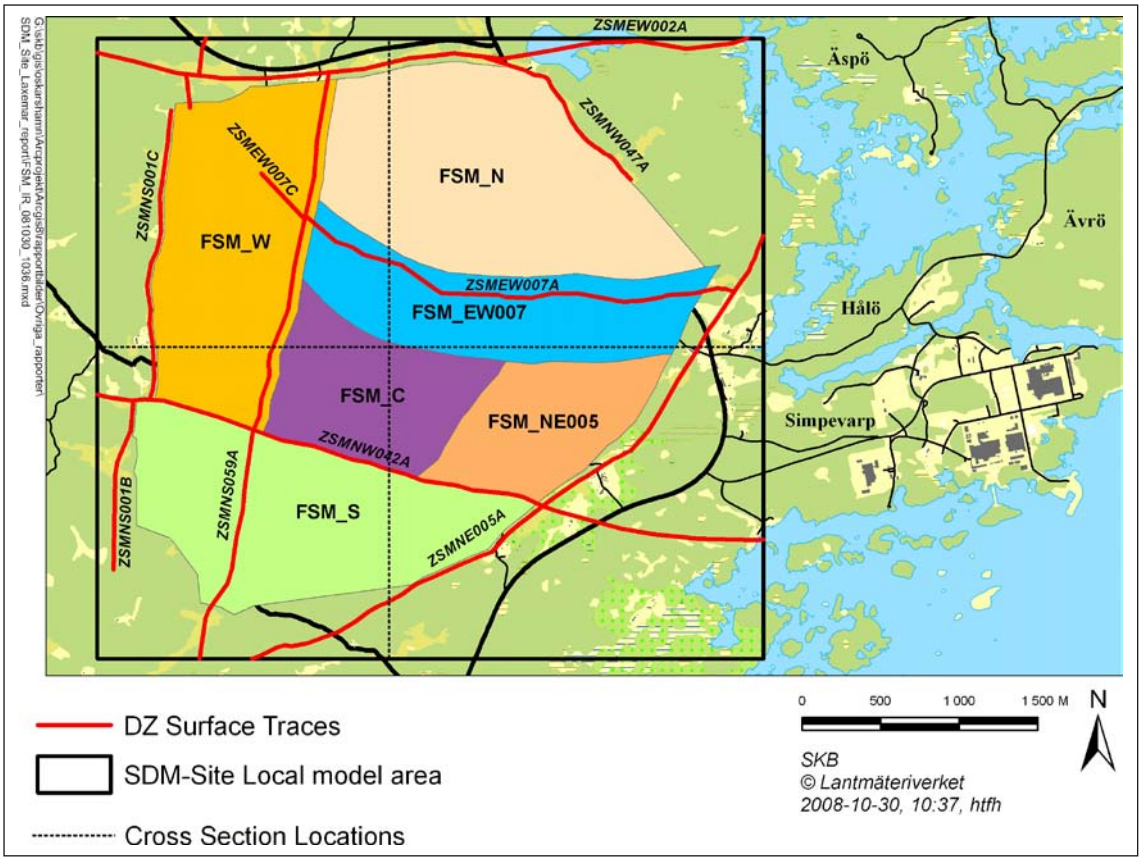

Figure 3-11. *Illustration of the SDM-Site Laxemar Fracture Domain Model, based on /La Pointe et al. 2008/.*

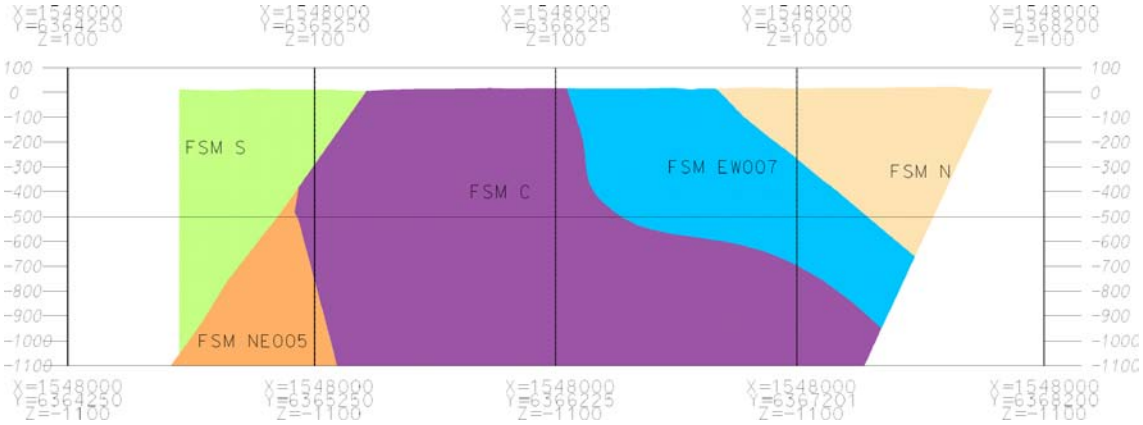

Figure 3-12. *RVS cross-section, oriented north-south through the middle of the Laxemar local model volume, of identified fracture domains. Vertical section from south (left) to north at Easting's X = 154,800 m, cf /La Pointe et al. 2008/.*

Bedrock fracturing between deterministic deformation zones in Laxemar can be described in terms of four distinct orientation sets: A subvertically-dipping, N-S striking set that appears to be the oldest; an ENE-WSW striking subvertically-dipping set; a WNW-ESE striking subvertically-dipping set; and a subhorizontally- to moderately-dipping fracture set that generally strike N-S to NNW (SH set). Fracture sizes are described according to a power-law (Pareto) distribution of equivalent radii, with parameters dependent on which set of model assumptions employed. The majority of the fractures in the Laxemar cored boreholes are sealed, whereas open and partly open fractures make up between 15–45% of the fracture population in most cored boreholes, cf /Wahlgren et al. 2008/.

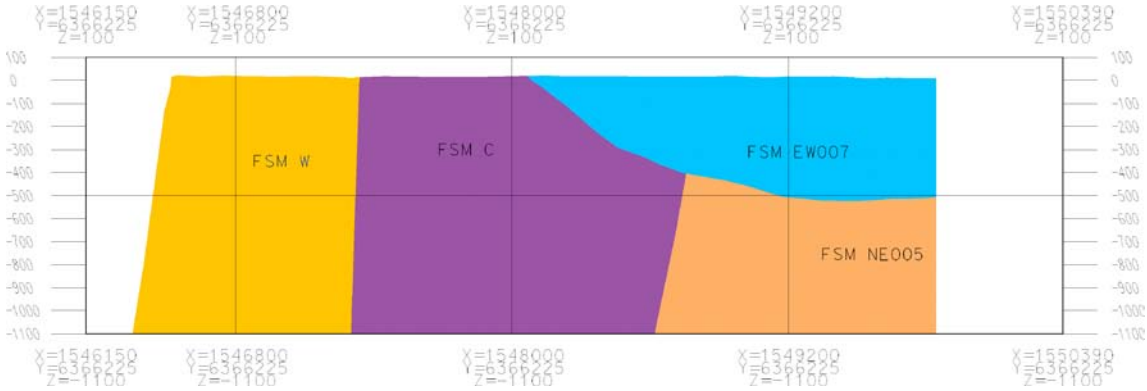

Figure 3-13. *RVS cross-section, oriented east-west through the centre of the Laxemar local model volume, of identified fracture domains. Vertical section from west (left) to east at Northing's Y = 6,366,225 m, cf /La Pointe et al. 2008/.*

The intensity of fracturing within a given fracture domain is described in terms of the average volumetric intensity P_{32} of a given orientation set. The spatial variability of the fracture intensity between deterministic deformation zones follows either a Gamma or a Weibull distribution at scales greater than 9 m for the N-S, SH, and WNW sets, and at scales greater than 15 m for the ENE set. The intensity of all fractures (Sealed + open + partly open fractures) was not found to be a function of depth or rock domain at a given statistical significance level, although weak to moderate correlations between fracture intensity and specific lithologies were noted. Fracture locations can be approximated using a Poisson point process, and fracture sizes appear to scale in an Euclidean fashion, cf /Wahlgren et al. 2008/.

Detailed analysis of the spatial distribution of fractures and other geological characteristics motivated the definition of fracture domains /La Pointe et al. 2008/. The fracturing of the near surface rock is also discussed in /Söderbäck and Lindborg eds. 2009/.

3.6 Quaternary deposits

The Quaternary deposits are generally much more permeable than the average crystalline rock and a large part of the groundwater infiltration will only flow through the Quaternary deposits to its discharge point. Depending of the type of hydrogeological problem studied, the hydraulic properties of the Quaternary deposits may be of large or small importance.

3.6.1 Model of Quaternary deposits

The data and concepts for description of the Quaternary deposits and other sediments in the Laxemar-Simepvarp regional model area are given in /Sohlenius and Hedenström 2008/ and a more detailed description of the 3D-modelling of the Quaternary deposits is reported by /Nyman et al. 2008/. The hydraulic properties of the different types of Quaternary deposits are discussed in /Werner et al. 2008/. In this section the description of the Quaternary deposits are summarised.

All Quaternary deposits in the Laxemar area have most probably been deposited during or after the latest deglaciation during which.the ice sheet in the area advanced from the north-west. The Baltic Sea completely covered the investigated area after the latest deglaciation c. 12,000 BC. Land uplift was fastest during the first couple of thousand years following the deglaciation and has subsequently decreased to the present rates of c. 1 mm/year. Older Quaternary deposits have been eroded in areas exposed to waves and currents and the material has later been re-deposited. Fine-grained sediments have been deposited on the floor of bays and in other sheltered positions. Peat has accumulated in many of the wetlands situated in topographically low positions. The groundwater table in many of the former wetlands has been artificially lowered to obtain land for forestry and agriculture, which has caused the peat to partly or completely oxidise. As land uplift proceeds, some new areas are being subjected to erosion at the same time as other new areas are becoming lakes and sheltered bays where fine-grained sediments can accumulate.

The geographical distribution and depth of the Quaternary deposits is largely determined by the topography of the underlying bedrock. Areas with outcrop bedrock and a thin till cover dominate the whole regional model area, including the sea floor. These areas are transected by a number of fissure valleys where the cover of Quaternary deposits is considerably thicker. Glacial clay with a thin cover of sand is the dominating surface deposit in the valleys on the sea floor. In the bays and land areas, the valleys are dominated by clay gyttja, which at many locations in the terrestrial areas is covered by a thin layer of peat. There are several glaciofluvial deposits, with a northerly strike, in the investigated area. The Tuna esker in the western part of the regional model area is the largest of these deposits. In a morphological sense, this esker is the most significant Quaternary deposit in the model area. In certain areas the till has a more coherent distribution than in the area in general. These areas are characterised by hummocks, which are probably not due to the morphology of the underlying bedrock.

The properties of Quaternary constituents have been classified at sites representing ten land classes. These are not discussed further here. The reader is referred to /Sohlenius and Hedenström 2008/ for a detailed discussion.

Most data on the total depth of the Quaternary deposits cover were obtained from geophysical investigations. The stratigraphical distribution of Quaternary deposits was obtained from drilling and excavations. The results show that the stratigraphical distribution of Quaternary deposits in the investigated area is rather uniform. Till is the oldest Quaternary deposit in the area, and is consequently resting directly upon the bedrock surface. The till in the valleys is often overlain by glacial clay, which in many valleys is overlain by a thin layer of sand followed by clay gyttja and peat.

The chemical composition of the Quaternary deposits in the Laxemar-Simpevarp area are close to the Swedish averages. The petrographical and mineralogical composition of the till reflects that of the local bedrock even though the till has been transported from the north. Since the till has been subjected to chemical weathering, the chemical composition of the till differs slightly from that of the bedrock. The mineralogy of the clay is different from that of the bedrock since the clays have a high content of clay minerals, which were formed by chemical weathering of primary rock-forming minerals. The chemical composition of the clay is also affected by the environmental conditions prevailing during deposition.

/Nyman et al. 2008/ present a depth and stratigraphic model of the Quaternary deposits (here abbreviated RDM) of the Laxemar-Simpevarp area. These models are based on the detailed digital elevation model of the area (with a horizontal resolution of 20 m by 20 m), the detailed map of the Quaternary deposits, and a large amount of geological and geophysical data. The RDM takes into account site investigation data available in the Laxemar 2.2 data freeze (Dec. 31, 2006). The RDM developed by /Nyman et al. 2008/ contains six layers of Quaternary deposits, denoted Z1–Z6; Z1 represents the upper layer of the Quaternary deposits. These layers, illustrated in the cross section in Figure 3-14, are defined and described as follows /Nyman et al. 2008, Sohlenius and Hedenström 2008/:

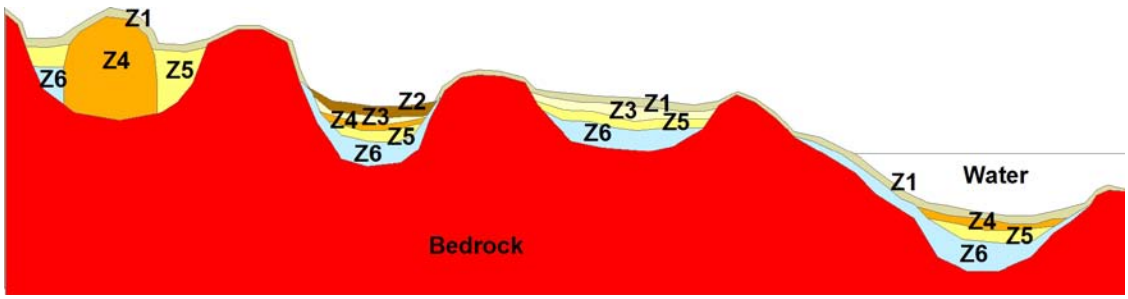

Figure 3-14. *The stratigraphical model which was used for modelling stratigraphy and total depth of Quaternary deposits in the Laxemar-Simpevarp regional model area /Sohlenius and Hedenström 2008/.*

Layer Z1 represents a thin **surface(-affected) layer**. It is present both on land, below lakes and below the sea. The exception is areas with peat on the surface; in those areas, layer Z2 is the upper layer. In the RDM, the layer thickness is set to 0.10 m in areas with shallow/exposed rock (i.e. rock outcrops on the map of Quaternary deposits), and to 0.60 m in other areas. If the total depth (thickness) of the Quaternary deposits depth is less than 0.60 m, Z1 is the only layer (i.e. there are no Z2–Z6 layers). In the terrestrial areas, layer Z1 is assumed to be affected by soil-forming processes.

Layer Z2 represents **(fen or bog) peat**. This layer is only present in land areas where the map of Quaternary deposits shows peat. Hence, layer Z2 is not present below lakes and the sea. The peat areas are further divided into "shallow" and "deep" peat areas. In the shallow peat areas, layer Z2 is directly underlain by layer Z6 (till; see below), which implies that there are no Z3–Z5 layers in those areas. In deep peat areas, Z2 is underlain by layers Z3–Z6. The thickness of Z2 is set equal to the calculated average thickness of peat in the area (0.85 m).

Layer Z3 represents **postglacial clay, clay gyttja/gyttja clay, gyttja or recent fluvial sediments**. The Z3 layer is only present in areas where clay gyttja is shown on the map of Quaternary deposits, and where layer Z2 is present (i.e. in the "deep" peat areas). Layer Z3 is always underlain by layers Z4–Z6.

Layer Z4 represents **postglacial sand/gravel, glaciofluvial sediments or artificial fill**, and is hence only present in areas where these types of Quaternary deposits or peat (underlain by postglacial clay in layer Z3 and postglacial sand/gravel in layer Z3) are shown on the map of Quaternary deposits. Note that glaciofluvial sediments and artificial fill rest directly on the rock (which is located below layer Z6), which means that there are no Z5 or Z6 layers in those areas. In areas with postglacial sand/ gravel in layer Z4, this layer is underlain by glacial clay (layer Z5) and till (layer Z6).

Layer Z5 represents **glacial clay**. The Z5 layer is present where the map of Quaternary deposits shows post-glacial sand/gravel, glacial clay or peat (in the "deep" peat areas).

Layer Z6 represents **(glacial) till**, which is directly underlain by rock. Layer Z6 has zero thickness is exposed/shallow rock areas (i.e. areas with a total depth (thickness) of Quaternary deposits less than 0.60 m), and in areas where layer Z4 directly overlies the rock. The lower level of layer Z6 in the RDM can hence be considered as a "digital elevation model" of the rock surface. The thickness of layer Z6 is estimated by the calculated average thickness of till in the area, except for areas in which till is shown on the map of Quaternary deposits.

With the exception of layer Z1, the lower boundary of all layers is produced by kriging. The lower boundary of layer Z1 is calculated based on the DEM, the elevation of the rock surface and assigned rules for the layer thickness. In order to enable the construction of the RDM, /Nyman et al. 2008/ divided the area into 3 type areas (denoted I–III) and 9 domains, see Figure 3-15. Figure 3-16 shows the modelled distribution of total overburden depth in the Laxemar-Simpevarp regional model area. As can be seen the depth of the overburden is in general just 0–3 m. Figure 3-17 illustrates the variable depth of the Quaternary deposits along a vertical north-south section accross the Mederhult zone (ZSMEW002A). Appendix 4 summarises the Quaternary deposits RDM layer definitions, including notations on which layers that are present "locally", given different types of deposits on the map of Quaternary deposits. In addition, the table presents average thicknesses of the individual layers.

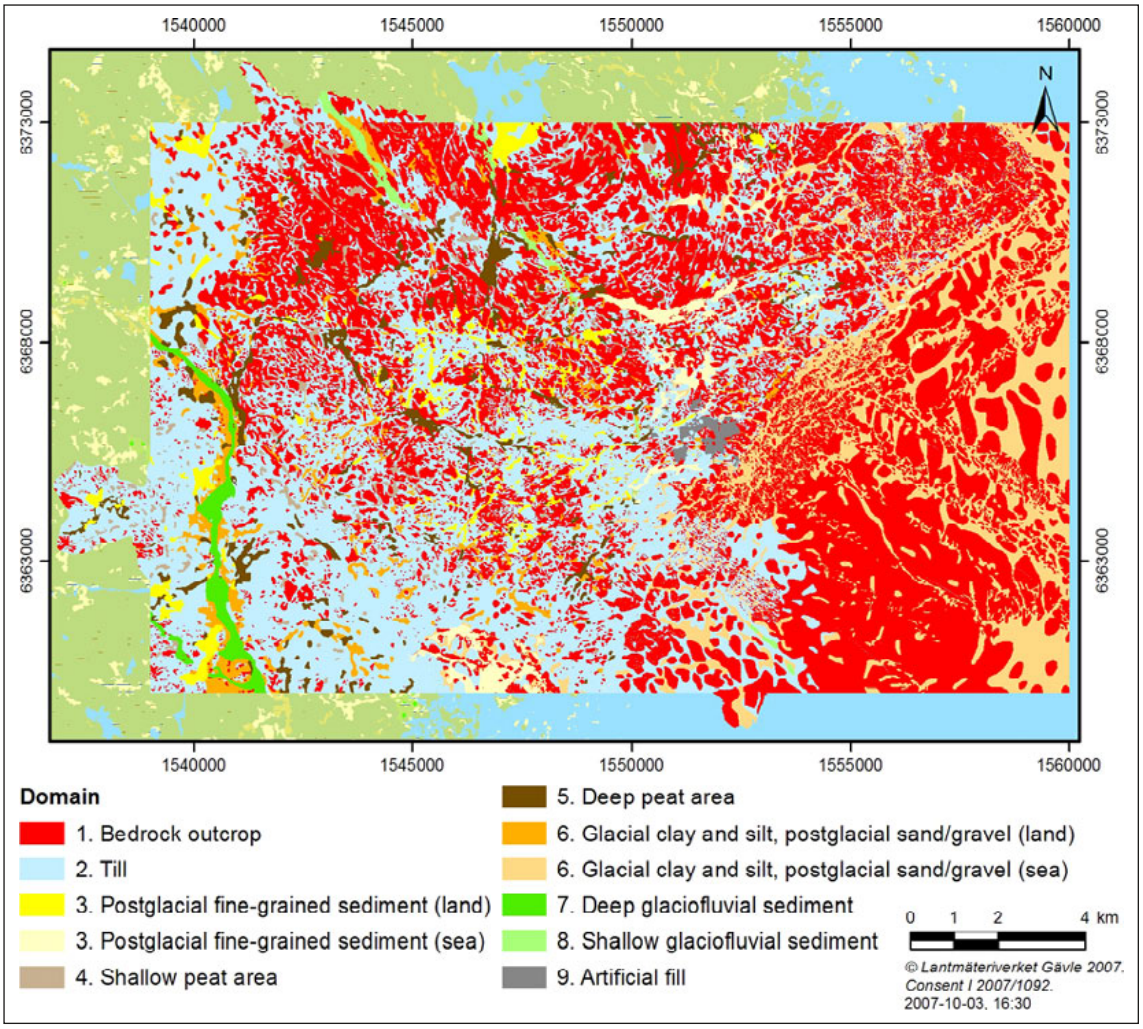

Figure 3-15. *The model area classified in nine types of domains, which were used in the depth and stratigraphy models of the Quaternary deposits /Sohlenius and Hedenström 2008/.*

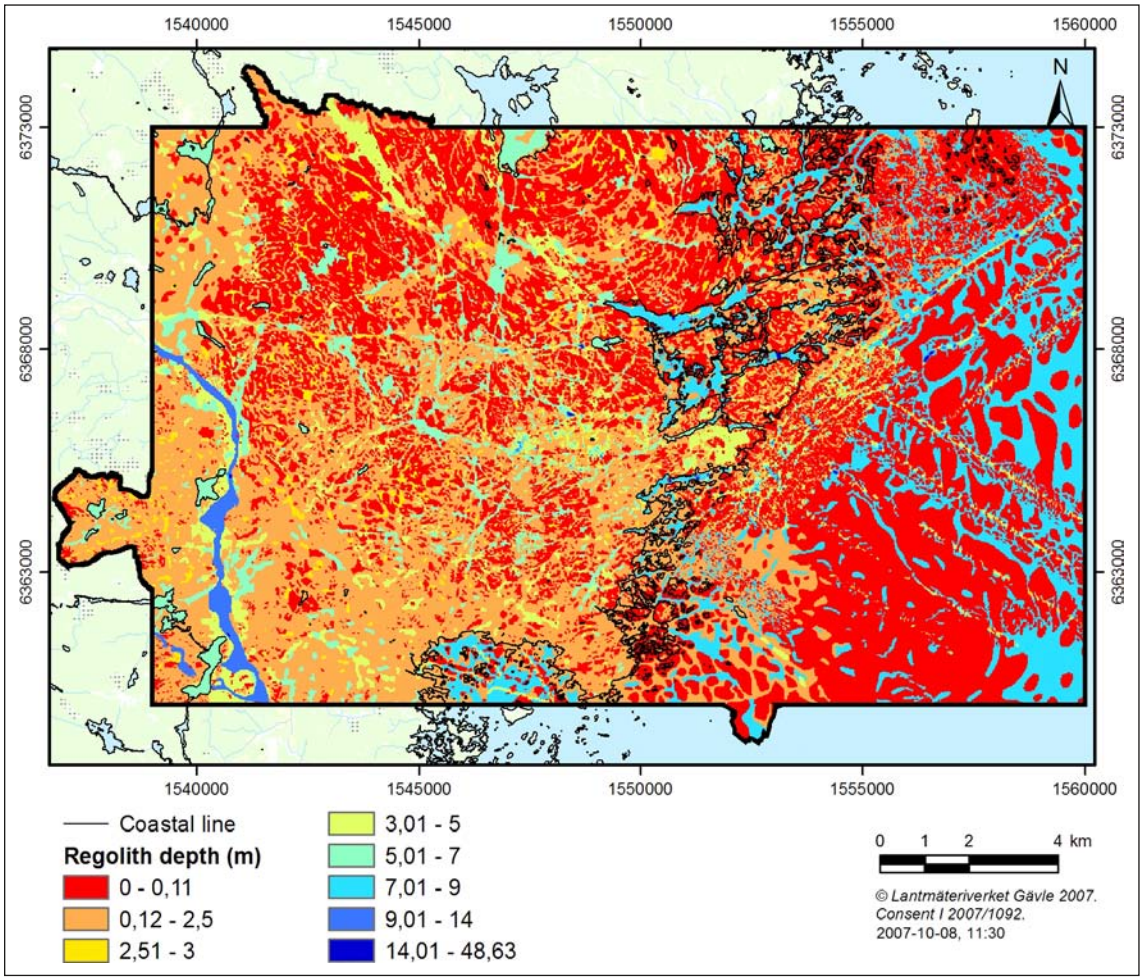

Figure 3-16. *The modelled distribution of total depths of the Quaternary deposits in the Laxemar-Simpevarp area /Sohlenius and Hedenström 2008/.*

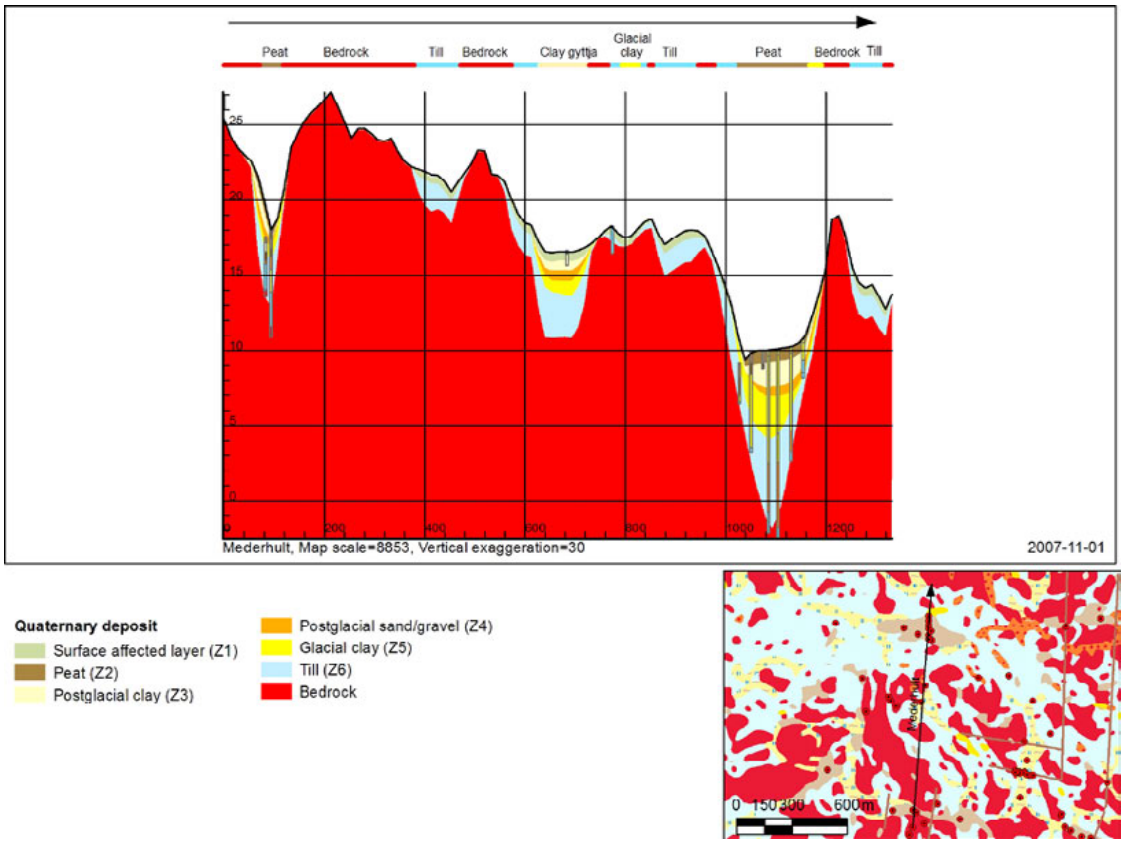

Figure 3-17. *The profile shows the total depth and stratigraphy of the Quaternary deposits in a north-south profile close to Mederhult. The valley in the right part of the profile (between 1,000 and 1,200 on the horizontal scale) is one of the largest lineaments in the area (ZSMEW002A in Figure 3-7) /Sohlenius and Hedenström 2008/.*

4 Conceptual model development

This chapter presents the hydrogeological conceptual models in terms of basic geometry of the underlying deformation zone model (HCD), the hydraulic rock domains (HRD) and their hydraulic parameterisation. This is followed by descriptions of basic data important for the formulation of hydraulic boundary conditions. A considerable effort is furthermore placed on the description of the palaeohydrogeological development as a basis for formulating hydrogeochemical boundary and initial conditions.

4.1 Hydrogeological description and conceptual model

In this section the components of hydrogeological conceptual models are presented including some of the data that constitute the basis for these models. The component conceptual models constitute the integral parts for the construction of the numerical groundwater flow models and modelling as reported in Chapters 7 through 11.

4.1.1 General

The Laxemar-Simpevarp regional model area is in general characterised by an undulating bedrock surface covered with a thin cover of Quaternary deposits, mainly till on the top of the hills and thicker Quaternary deposits in the valleys that are made up of till overlain by postglacial deposits. The crystalline bedrock is transected by a number of deformation zones, mainly steeply dipping, with less fractured bedrock between these zones. The bedrock in-between the HCDs is in the hydrogeological model called Hydraulic Rock Domains (HRD). Hydraulically, the deformation zones, denoted Hydraulic Conductor Domains (HCD) in the hydrogeological model, are generally more conductive than the bedrock in-between. The general tendency within the Laxemar-Simpevarp regional model volume is that the hydraulic conductivity decreases with depth in both HCDs and HRDs. Figure 4-1 shows a generalised vertical section illustrating the overall hydrological and hydrogeological conceptual model of the Laxemar-Simpevarp area. The hydrogeological characteristics of the HCDs and HRDs are further described below in Sections 4.1.2 and 4.1.3 and details are found in /Rhén et al. 2008/.

4.1.2 Hydraulic conductor domains (HCD)

Overview

The HCD geometrical model is based on the deformation zone model presented by /Wahlgren et al. 2008/ and is discussed in brief in Section 3.3.2. A selection of the main HCDs within the regional model domain is shown in Figure 4-2.

/Rhén et al. 2008/ summarise the main characteristics of the HCDs:

- A clear trend of decreasing transmissivity with depth.
- A positive correlation between interpreted “size” and transmissivity. Size here corresponds to interpreted trace length on surface.
- Indications that the transmissivity of HCDs is dependent on the orientations of deformation zones. E-W zones appear more conductive to zones of other orientations.
- The variability of transmissivity within a HCD is large considering the individual hydraulic tests performed in different parts of a HCD.
- Some HCDs are conceptualised as being anisotropic, beingless permeable across the HCD plane compared to along the plane due to a core of dolerite or fault gouge.

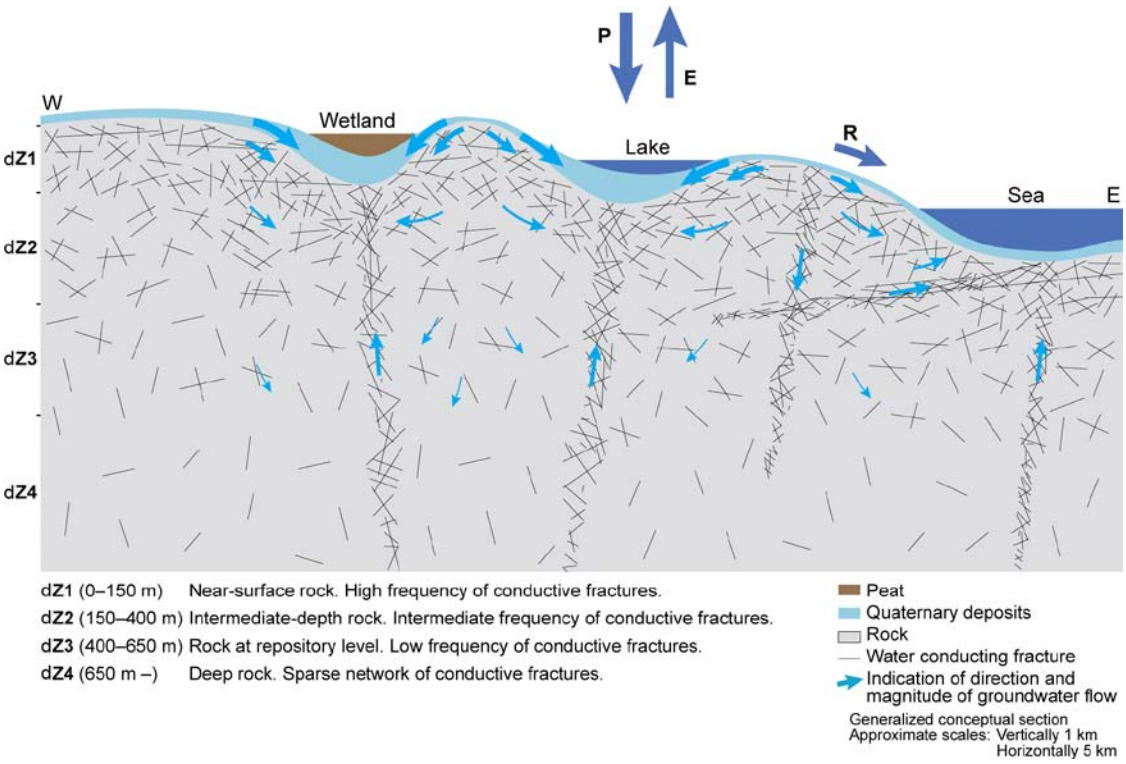

Figure 4-1. *Generalised conceptual section illustrating the conceptual model of hydrology and hydrogeology in Laxemar. Note the different horizontal (5 km) and vertical (1 km) scales. Furthermore, the thickness of the Quaternary deposits is exaggerated in the figure.*

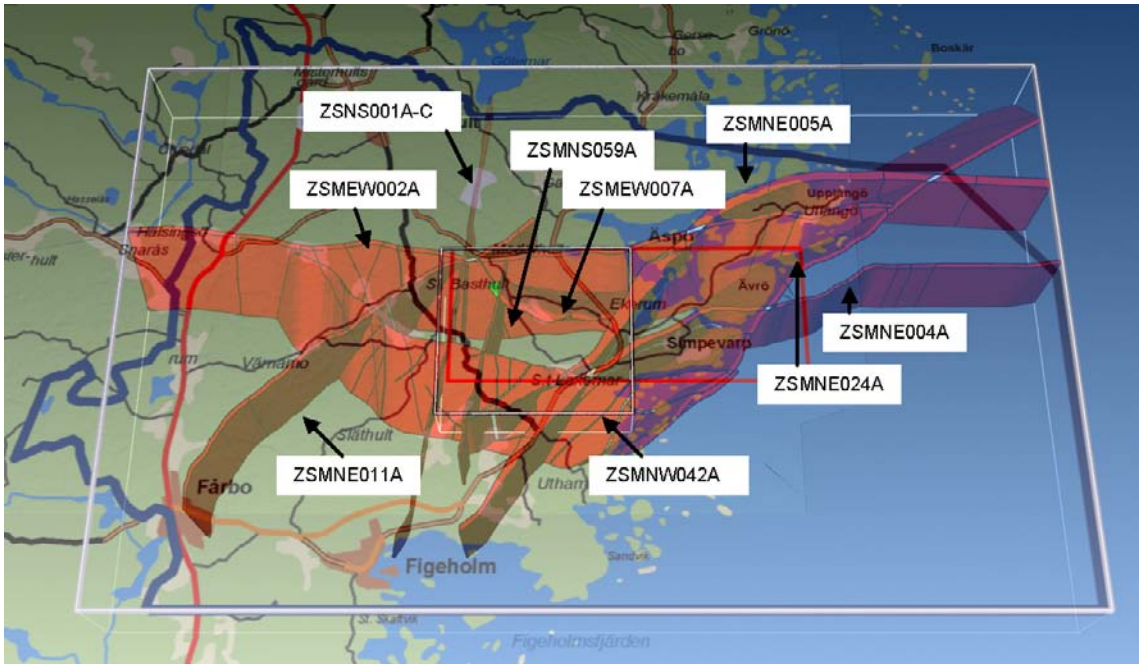

Figure 4-2. *Perspective view of some of the main HCDs (ZSMNE011A, ZSMEW002, ZSMEW007, ZSMNS001A;B;C, ZSMNS059A, ZSMNE005, ZSMNE004, ZSMNW042 and ZSMNE24A) within the Laxemar-Simpevarp regional model volume. The regional model boundaries for the groundwater flow model and the local model area are shown in Chapters 7–11 shown as blue and black lines respectively.*

Supporting data for geometries of the HCDs

The geometries of the HCDs are based on the geological deformation zone model but is some cases interference tests have provided support for the suggested geometries. The best example is the geometry of the deformation zone ZSMEW007A, where interference tests indicated that it should dip to the north and probably not having any vertical or south dipping splays, cf Figure 4-2, Section 5.3 and Appendix 1. The interpretation of the geometry and hydraulic properties of zone ZSMNS001C was also sustained by interference tests, cf Figure 4-2, Section 5.4 and Appendix 1

Trend models for transmissivity in HCDs

The data and the general models suggested for the initial assignment of hydraulic properties to HCDs in the groundwater flow modelling are presented in Figure 4-3, Figure 4-4 and Appendix 5, cf a detailed account in /Rhén et al. 2008/. The variability in transmissivity is large but considering mean values for depth zones employed in the HRDs modelling, cf Section 4.1.3, the transmissivity decreases with depth, cf Figure 4-4. There is also a tendency that the transmissivity is positively correlated to the interpreted lineament length of the HCD and also that HCDs with E-W orientations are slightly more transmissive than HCDs with other orientations, Figure 4-3 and /Rhén et al. 2008/. The general models suggested for HCD transmissity are shown in Figure 4-3.

However, some of the HCDs are intersected by several boreholes at variable depths and it was judged that there were enough data for assessment of zone-individual trend functions for seven of the HCDs, cf /Rhén et al. 2008/. These HCDs and their trend functions are shown in Appendix 5.

Supporting data for anisotropic properties in HCDs

Several interference tests have shown that dolerite dykes may act as hydraulic barriers, at least locally, and the best example relates to the HCD ZSMNS001C, associated with a core of dolerite, cf Section 5.4 and Appendix 1. Both interference tests and monitoring data show fairly large differences in hydraulic head on either side of the dyke suggesting that the two HCDs interpreted by Geology are associated with dolerite dykes, ZSMNS059A and the KLX19_DZ5-8_dolerite, also acting as hydraulic barriers, but probably to a lesser degree where the dykes become thinner. The dolerite dykes are discussed more below in this section and in Section 3.3.2.

Mapping of the cored boreholes and outcropping deformation zones has shown that fault gouge is present in at least ZSMEW002A (KLX06), ZSMEW007A (observation in trench), ZSMNW042A (KLX27A) /Wahlgren et al. 2008/. This implies that these HCDs can exert some hydraulic barrier effect, most likely highly localised. The evaluation of monitoring data and the simulations shown in Chapter 8 indicates that both ZSMEW002A and ZSMNW042A western part (i.e. west of ZSMNS059A) need to be modelled with a lower permeability across the HCD compared to the permeability along their planes. Difference in heads along KLX06 cannot be reproduced in the simulations unless parts of ZSMEW002A acts as a barrier, cf Chapter 8. Beside the observation of fault gauge in KLX27A, the lack of hydraulic responses south of ZSMNW042A during pumping in HLX28 indicates that there is a barrier effect in ZSMNW042A, cf Section 5.4 and Chapter 8. It is not known if the eastern part of ZSMNW042A has any barrier effect. Anistropic conditions for specific zones, as implemented in the numerical groundwater flow model, are shown i Table 7-1.

Dolerite dykes

Dolerite dykes in Laxemar seem to be steep and be mainly oriented N-S and are also expected to have a low hydraulic conductivity, but still heavily fractured and the wall rock outside the dolerite dykes is fairly transmissive along the sides of the dyke. The hydraulic conductivity of the dolerite core is expected to be less than 10^{-9} m/s, cf /Rhén et al. 2008/. The transmissivity of the flanking contacts or the dolerite-associated deformation zones is significantly higher, varying between $1.2 \cdot 10^{-5}$ m^2/s and $4.8 \cdot 10^{-4}$, m^2/s suggesting significant anisotropy.

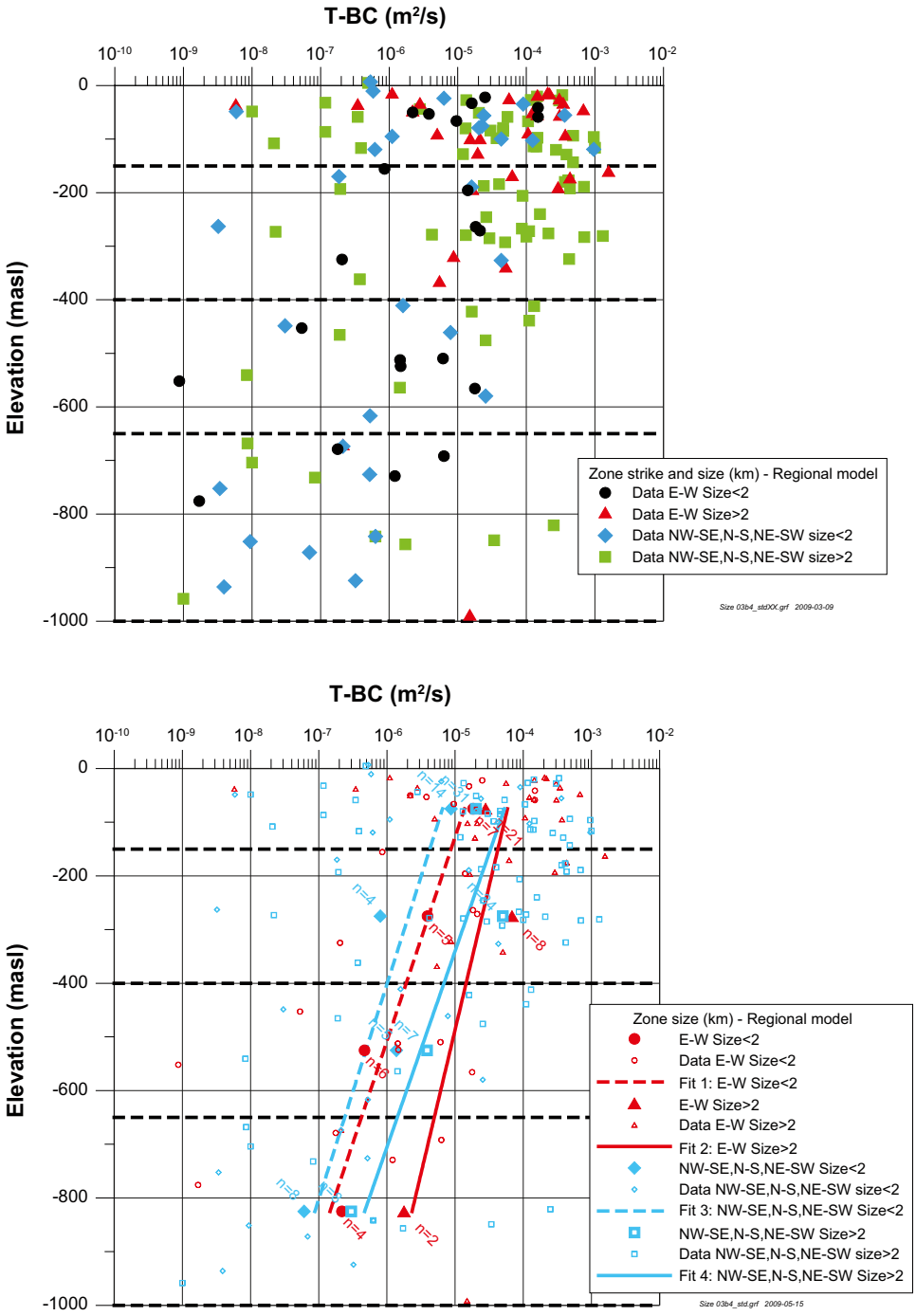

Figure 4-3. *Deformation zone transmissivity (T) related to deformation zone orientations in the horizontal plane and size, versus elevation. Mean of log10(T), plotted as well as the number of observations (n). (Top: Data in regional model. Bottom: Regression line and data, regional model.)*

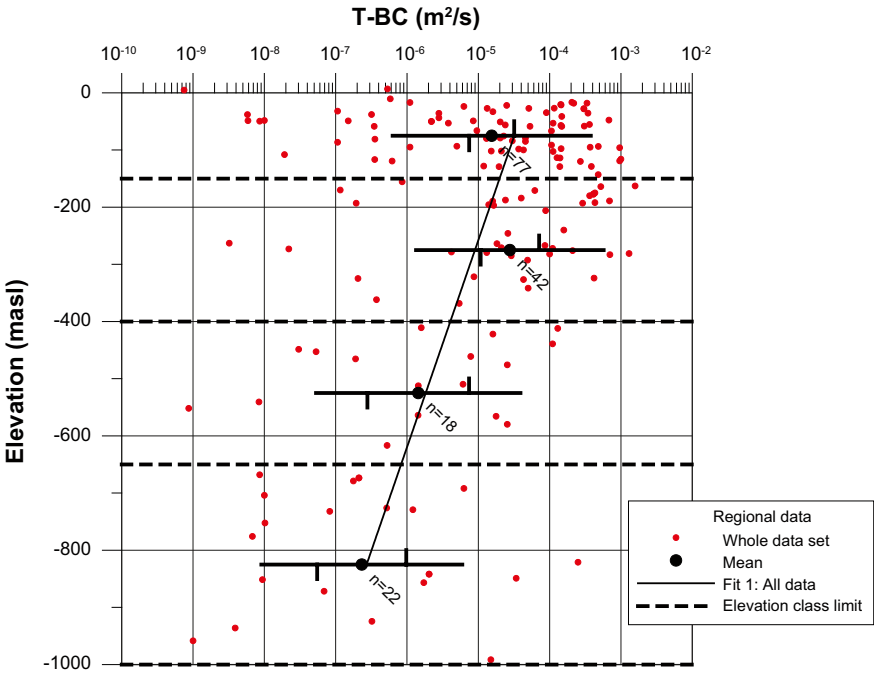

Figure 4-4. *Deformation zone transmissivity (T) for elevation intervals: the number of observations (n) for elevation intervals, geometric mean T, confidence limits for mean log10(T) (vertical bars on horizontal line) and ±1 standard deviation log10(T) (entire horizontal line) are plotted. The line is fitted to the 4 geometric mean values (Data from the regional model volume).*

Of special interest are a few dolerite dykes within the Laxemar local model area, cf Chapter 3 and /Rhén et al. 2008/:

- ZSMNS001C (It is not known if the entire ZSMNS001, A-E, has a core of dolerite).
- ZSMNS059A.
- KLX19_DZ5-8_(dolerite devoid of associated surface expression, assumed to be 1,000 m in size).

The thicknesses of the listed dolerite dykes are estimated as follows:

- ZSMNS001C can be assumed to be c. 30 ±10 m thick.
- ZSMNS059A can be assumed to be c. 5 ±5 m thick.
- KLX19_DZ5-8_dolerite can be assumed to be c. 5 ±5 m thick.

Internal variability in HCD properties

The variability of transmissivity of HCDs is readily apparent by studying the entire sample of HCD transmissivities, cf Figure 4-4. The standard deviation of log10(T) of the corresponding transmissivity data is c. 1.4 /Rhén et al. 2008/. However, as there are a number of HCDs which individually have been subjected to several hydraulic tests at multiple locations, the standard deviation related to individual HDCs is of interest in comparison with that of all data shown in Figure 4-4. In Figure 4-5 the standard deviation versus elevation is shown for the HCDs included in the regional model volume subjected to several hydraulic tests, cf Appendix 5 for presentation of transmissivity values of the HCDs with several borehole intercepts. As can be seen from Figure 4-5 the standard deviation is in the range 0.5 to 2. The estimated standard deviations are based on generally small samples and the highest standard deviations are based on very small samples and are not considered good measures for the range of standard deviation of HCD transmissivity.

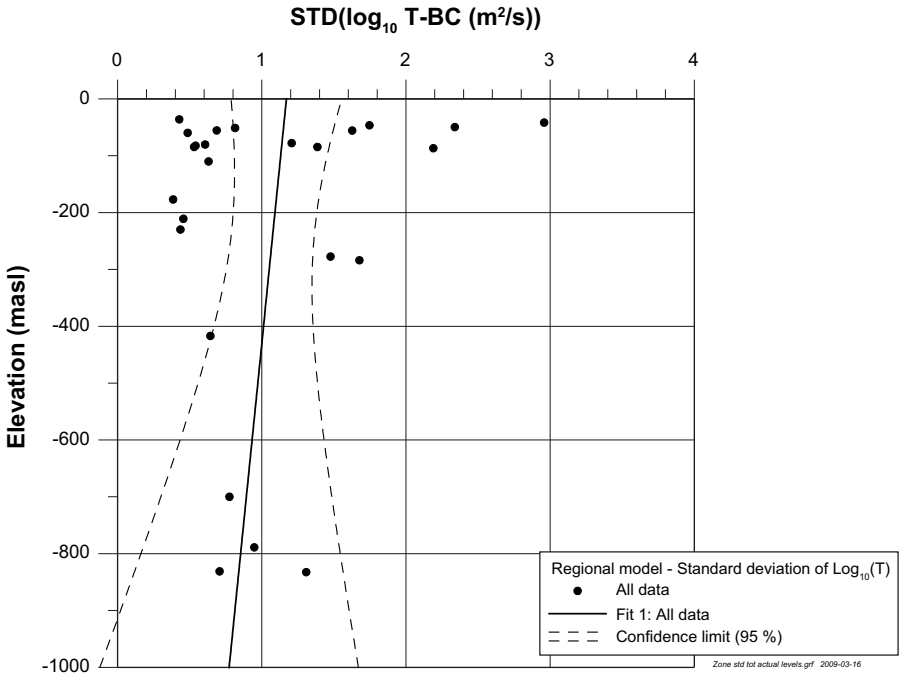

Figure 4-5. *Standard deviation of HCD transmissivity (T) versus elevation based on zones with several observations of transmissivity within a single HCD. Confidence intervals for fitted lines are shown (Data from the regional model volume)*

The internal variability in HCD properties was also studied in terms of frequencies of PFL-f features (mostly equivalent with flowing fractures) and fracture transmissivity in /Rhén et al. 2008/ and below main results are summarized.

- The range of the true thickness of a HCD is c. 10–100 m, with mean around c. 20–40 m and a standard deviation of c. 20-40 m.
- The number of flowing features increases when the total transmissivity of the HCD increases.
- The range of the number of PFL-f features(n): N and N-corr (Terzhagi corrected numbers of PFL-f features. For description of Terzaghi correction, see /Rhén et al. 2008, cf Chapter 9 therein/) within a HCD is c. 1–140 and c. 1–400, respectively, with mean around c. 5–25 and 10–50 respectively and a standard deviation of c. 5–30 and 10–100, respectively. The range for the P_{10} and $P_{10,corr}$ (Terzaghi corrected intensity of P_{10} of PFL-f features) within a HCD is c. 0.05–1 m^{-1} and 0.05–2 m^{-1} respectively, with mean around 0.2–0.5/0.3–1 m^{-1} and a standard deviation of c. 0.15–0.25/0.2–0.6 m^{-1}.
- The total transmissivity (sum over the apparent thickness, as given by a given interpreted bore-hole intercept) of a HCD decreases with depth, but not the standard deviation of the log10(sum T-PFL-f). The range of the mean of log10(sum T-PFL-f) within a HCD is c. –8 to –3 with mean around –5 to –6.6 and a standard deviation of c. 0.7–1.1 (T-PFL-f: m^2/s).
- The statistical distribution of transmissivity of the individual PFL-f features within a HCD (as calculated for the depth zones defined for HRDs) does not decrease with depth. The range of the mean of log10(T-PFL-f) within a HCD is c. –8.5 to –4.3 with a mean around –7.3 to –7 (T-PFL-f: m^2/s).
- The statistical distribution of standard deviation of the transmissivity (as established for the depth zones defined for HRDs) of the individual PFL-f features within a HCD seems to decrease with depth, but the confidence limits do not support this depth dependence. The range for the standard deviation of log10(T-PFL-f) within a HCD is c. 0.1–2.2 with mean around 0.5–0.9 (T-PFL-f: m^2/s).

Storage coefficient and transport aperture

/Rhén et al. 2008/ estimated the storage coefficient as function of the transmissivity for HCDs from a large number of interference tests, and the established correlation is presented in Appendix 4. This relation is considered useful for initial assignment of the storage coefficient when modelling of interference tests.

/Rhén et al. 2008/ also present assessments of transport aperture compiled as a base for initial assignment of flow porosity in the groundwater flow modelling.

4.1.3 Hydraulic rock domains (HRD)

Overview

Hydraulic rock domains are defined based on the spatial distribution of hydraulic properties in space, and analysis have shown that some of the fracture domains can be used directly as hydraulic domains, whereas some fracture domains in combination may be designated as hydraulic rock domains, cf /Rhén et al. 2008/. Figure 4-6 through Figure 4-8 show the HRDs (HRD_N, HRD_EW_007, HRD_C, HRD_W) corresponding to fracture domains and the detailed motivation for their individual formation is provided in /Rhén et al. 2008/. Some essential data and considerations that formed the base for defining the HRDs are discussed below.

Given that fracture domains are not defined outside the bounds of the envelope as defined in Figure 3-14, the hydraulic rock domains outside this envelope, cf Figure 3-10, are motivated and based on the hydraulic properties of geological rock domains as outlined in /Rhén et al. 2006/, see brief discussion.

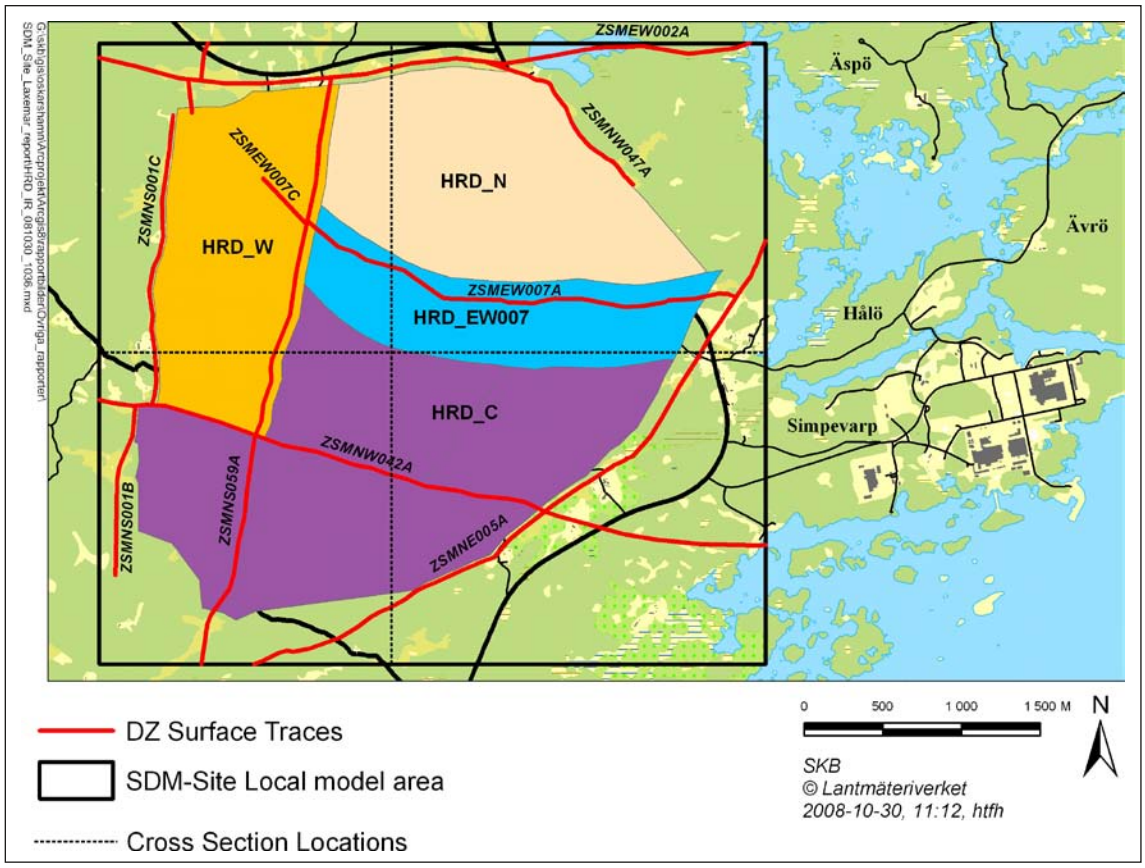

Figure 4-6. *Illustration of the SDM-Site Laxemar Hydraulic Rock Domain Model.*

Figure 4-7. *Illustration of the SDM-Site Laxemar Hydraulic Rock Domain Model, vertical section from south (left) to north at Easting's X = 154,800 m, cf Figure 4-6.*

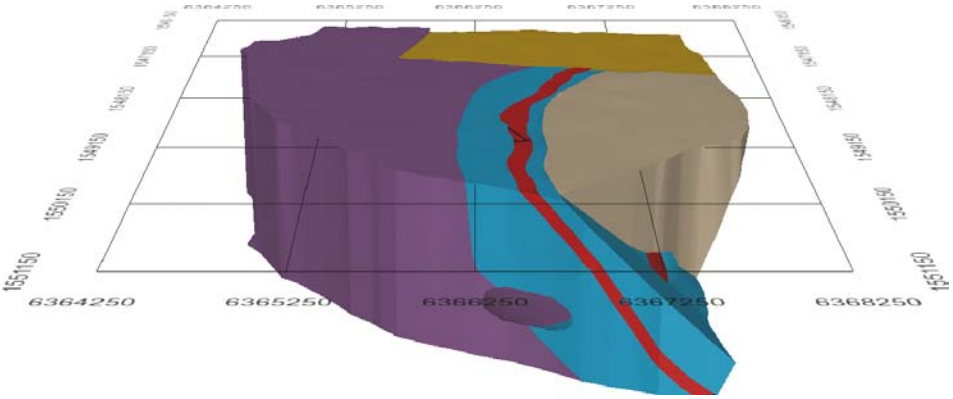

Figure 4-8. *Illustration of the SDM-Site Laxemar Hydralic Rock Domain Model, 3D view looking westward.*

Basis for assignment of HRD properties

The geological description of the bedrock between deformation zones is reported in /Wahlgren et al. 2008/ and /La Pointe et al. 2008/. The evaluation of the HRD properties in terms of general characteristic and developed hydrogeological DFN models is reported in /Rhén et al. 2008/. The hydraulic rock domains are parameterised in terms of a stochastic DFN model, by calibration against available hydraulic data mainly from the PFL-tests. The hydrogeological DFN modelling is based on the assumption that:

$$P_{10,all} \geq P_{10,open} \geq P_{10,cof} \geq P_{10,PFL} \qquad (4\text{-}1)$$

where $P_{10,cof}$ denotes the frequency of "connected open fractures", a key property of any hydrogeological DFN model. $P_{10,all}$ is the frequency of "all fractures"(sealed and open fractures) intersecting the borehole, $P_{10,open}$ is the frequency of "open fractures", $P_{10,cof}$ is the frequency of "connected open fractures" and $P_{10,PFL}$ is the frequency of "flowing connected open fractures" identified with the PFL-f method, cf /Rhén et al. 2008/ for details.

Below some principal geological and hydrogeological characteristics of the HRDs are outlined, cf /Rhén et al. 2008/:

- The flowing fractures can be grouped in four orientation sets; steep ENE, WNW, N-S and a subhorizontal set, cf Figure 4-9 and Figure 4-10.
- A clear decreasing frequency of flowing features with depth but generally with a similar transmissivity distribution of the flowing features for the specific depth interval studied (as measured by PFL-f, cf Figure 4-11 and Figure 4-12).
- As a consequence – a resulting clear trend of decreasing hydraulic conductivity with depth, cf Figure 4-13 (test scale 100 m) may be observed.
- The hydraulic conductivity is c. 10 times lower in HRDs than that of the HCDs (test scale 100 m), cf Figure 4-14.

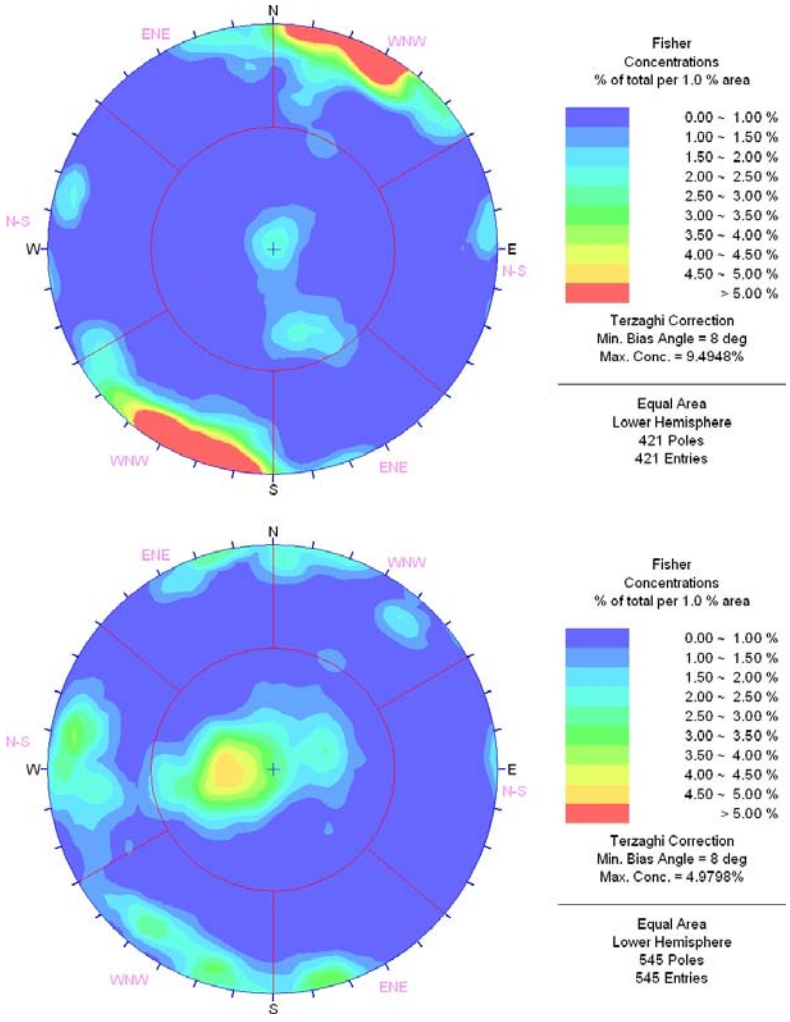

Figure 4-9. *Stereonets for FSM_EW007 (top) and FSM_W (bottom): Terzaghi-corrected intensity for PFL-f features /Rhén et al. 2008/, which corresponds to HRD_EW007 and HRD_W.*

The orientations of the sets of flowing fractures roughly correspond to the main orientation groupings of the deterministic deformation zones, see /Wahlgren et al. 2008, cf Chapter 5 therein/.

Figure 4-14 illustrates the depth trend and difference in hydraulic conductivity between HCDs and HRDs and Figure 4-13 shows the hydraulic conductivity of all HRDs pooled into one single population, based on transient tests performed in Laxemar with test scale 100 m.

The fracture orientations are not uniformly distributed, but clustered around particular orientations. It was argued in /Rhén et al. 2008/ that the fractures of every HRD could be divided in four fracture sets:

- a set striking roughly N-S,
- a set striking roughly ENE,
- a set striking roughly WNW,
- a sub-horizontal (SH) set.

The exact boundaries between the different fracture sets are not precise and vary slightly between different HRDs.

After careful inspection of the results of the analyses of intensities of fracture types (open, partly open, PFL features), individual fracture sets and all fracture sets combined, as subdivided in 50 m depth intervals, cf /Rhén et al. 2008/, it was decided that a reasonable choice of defined depth zones applicable to all HRDs should be: ground surface down to –150 m, –150 to –400 m, –400 to –650 m and below –650 m.

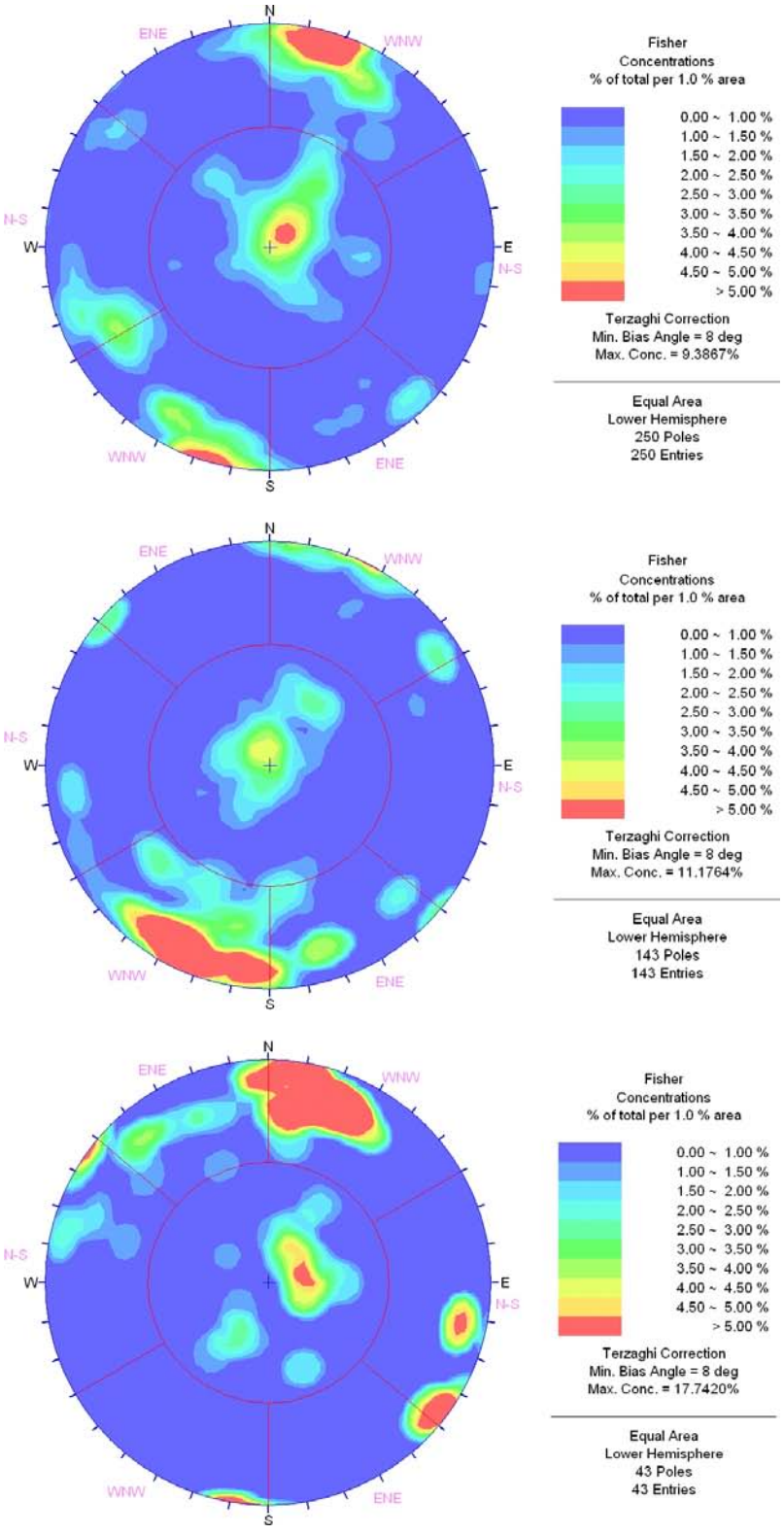

Figure 4-10. *Stereonets for FSM_NE005 (top), FSM_C (bottom) and FSM_S (bottom), and: Terzaghi-corrected intensity for PFL-f features /Rhén et al. 2008/, which in combination correspond to HRD_C.*

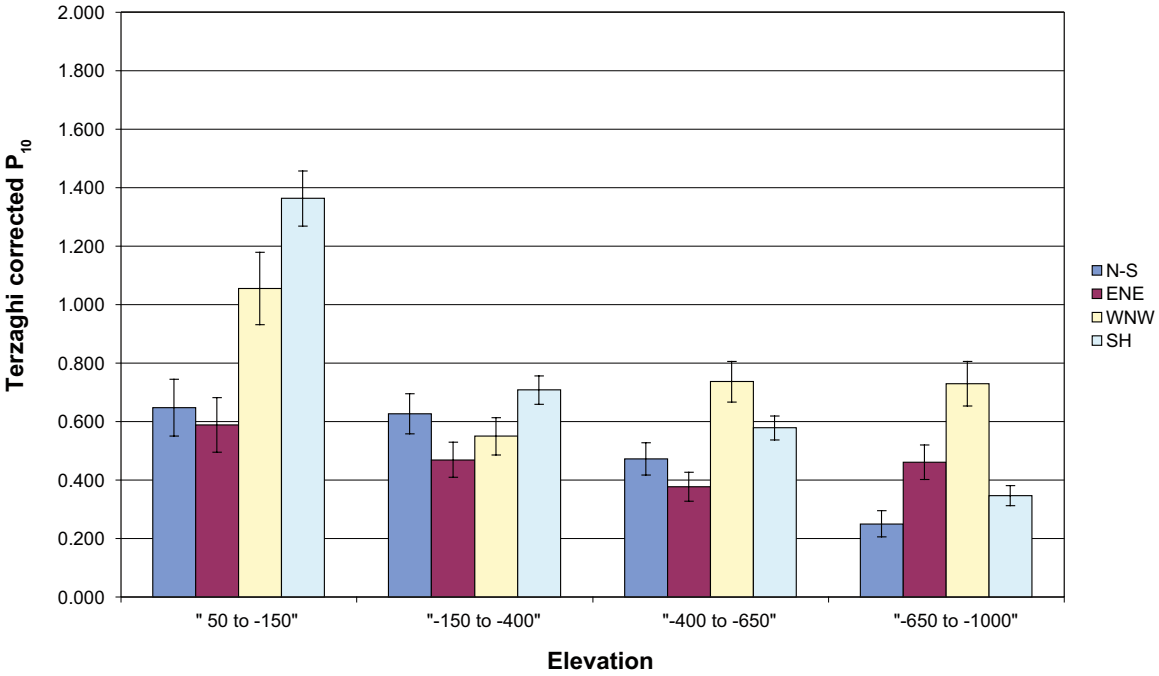

Figure 4-11. *Variation with depth of the Terzaghi-corrected fracture intensity for OPO fractures for the fully characterised sections of boreholes penetrating Hydraulic Rock Domain HRD_C /Rhén et al. 2008/.*

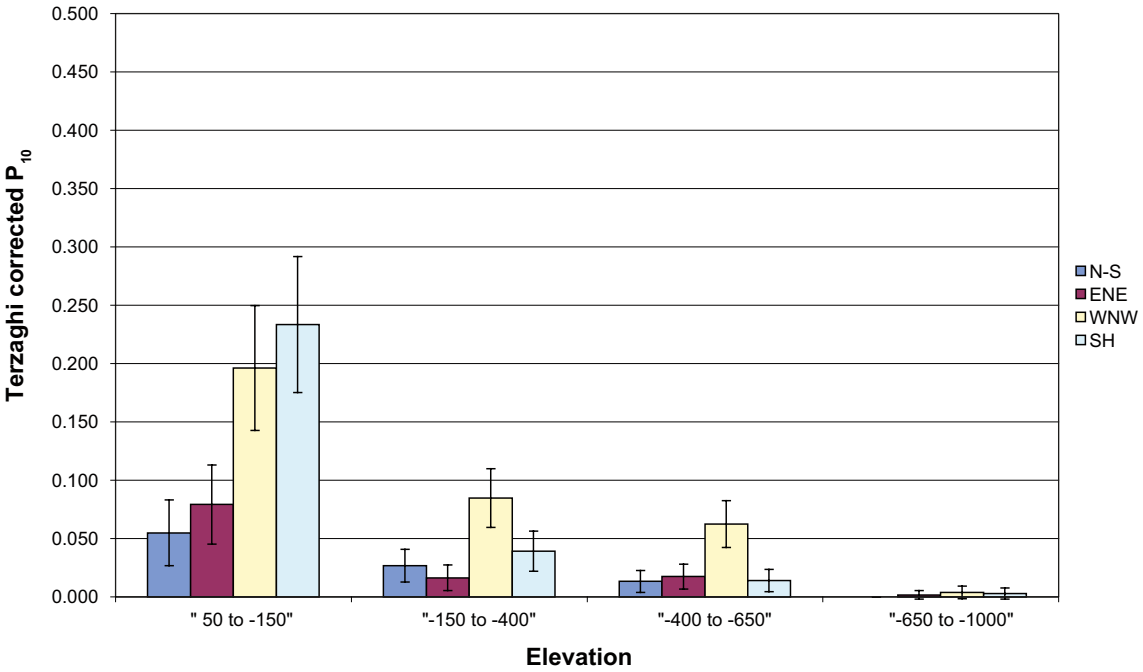

Figure 4-12. *Variation with depth of the Terzaghi-corrected fracture intensity for PFL-f features for the fully characterised sections of boreholes penetrating Hydraulic Rock Domain HRD_C /Rhén et al. 2008/.*

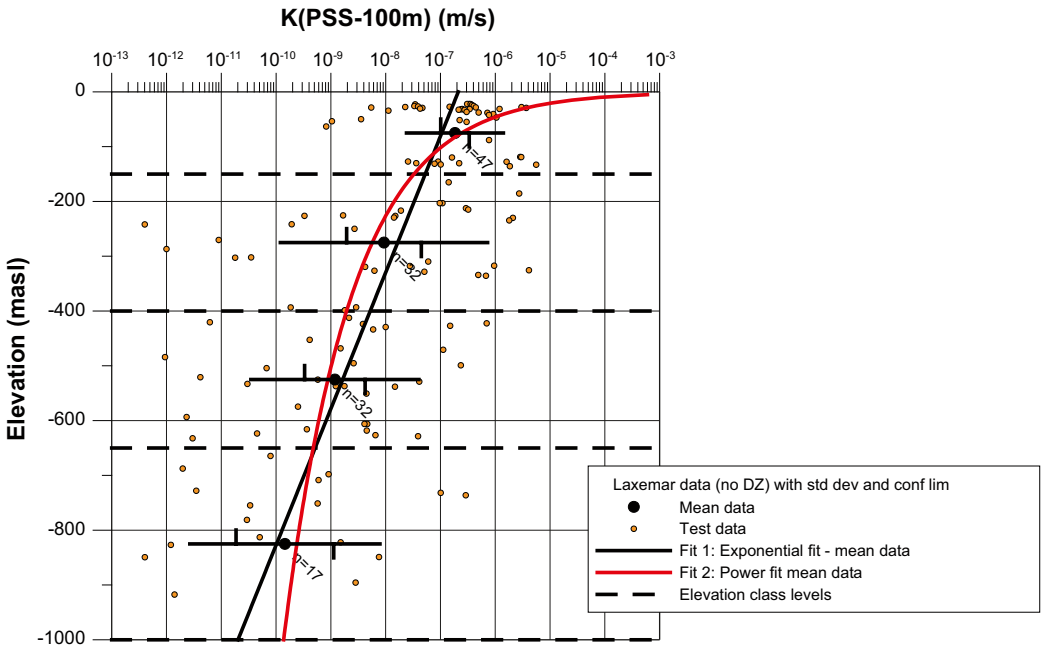

Figure 4-13. *Hydraulic conductivity (K) versus elevation (test scale 100 m). Data from test sections between deterministic deformation zones. Data from local model area. For the defined depth zones; geometric mean K, confidence limits for mean log10(K) (vertical bars on horizontal line) and ±1 standard deviation log10(K) (entire horizontal line) are plotted. Curves are fitted to the calculated four geometric mean values (black).*

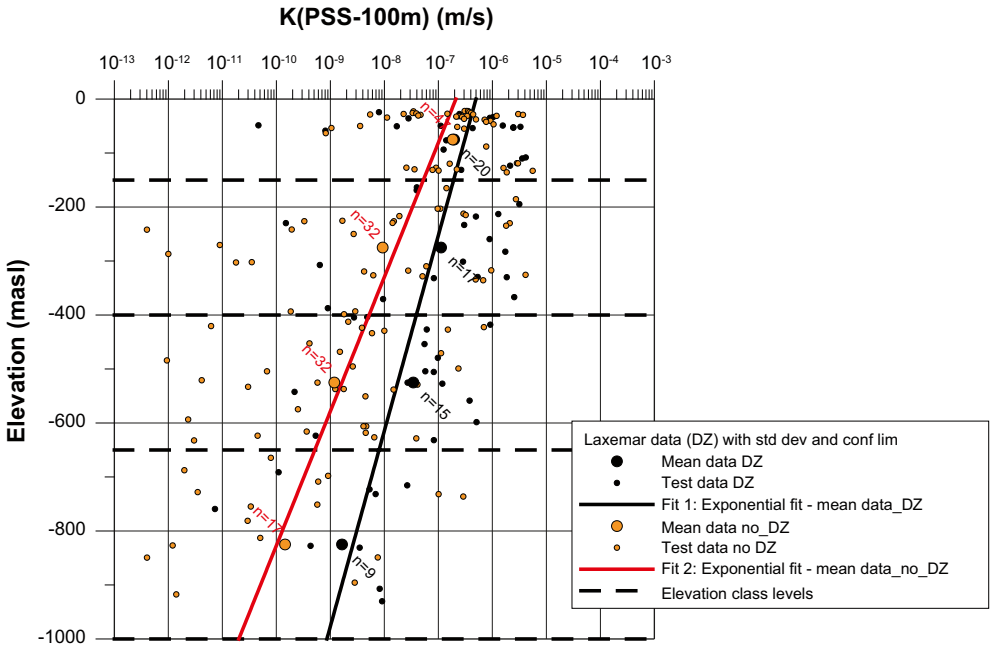

Figure 4-14. *Hydraulic conductivity (K) versus elevation (test scale 100 m). K shown for test sections between HCDs (DZ in figure) and test sections intersected by a HCD. Data from local model area. For depth zones; geometric mean K, confidence limits for mean log10(K) (vertical bars on horizontal line) and ±1 standard deviation log10(K) (entire horizontal line) are plotted. Curves are fitted to the 4 geometric mean values.*

The depth intervals, here denoted dZ1-dZ4 (cf Figure 4-1), can be described as follows:

- dZ1 (0 to –150 m): Near-surface rock, characterised by a high frequency of conductive fractures. Sub-horizontal and steeply dipping fractures striking WNW dominate.
- dZ2 (–150 to –400 m): Intermediate-depth rock, characterised by an intermediate frequency of conductive fractures. Steeply dipping fractures striking WNW dominate. Steeply dipping fractures striking WNW dominate except for HRD_W where no set is clearly dominant and the subhorizontal set is also important in HRD_N and FSM_C.
- dZ3 (–400 to –650 m): Rock at repository level, characterised by a low frequency of conductive fractures. Steeply dipping fractures striking WNW dominate except for HRD_W where no set is clearly dominant.
- dZ4 (< –650 m): Deep rock, characterised by a sparse network of conductive fractures. Steeply dipping fractures striking WNW dominate except for HRD_W where no set is clearly dominant (however rather few data within dZ4).

There is no unique best choice for the depth zones. The above choice enables a good representation of the main features of the distribution of fracture intensity. The top zone allows the higher fracture intensity and specifically the higher intensity for the SH fracture set in the near-surface rocks to be represented. The deepest zone allows the much lower intensity of PFL-f features below about –650 m to be represented. The division of the intervening bedrock into two depth zones allows the noted weak trend with elevation over this range to be represented. Furthermore, depth zone dZ3 effectively straddles the typical repository elevation at –500 m.

The change in intensity with depth and fracture set is illustrated by an example for FSM_C, a domain corresponding to a potential deposition volume, in Figure 4-11 and Figure 4-12

For a more detailed account of the key findings of the analysis of basic statistical measures of flowing fracture intensity and transmissivity as detected by the PFL method, and their relation to definition of HRDs and depth zones, the reader is referred to /Rhén et al. 2008, cf Sections 9.3 through 9.5 therein/.

Near surface rock

As pointed out above, there is a clear decrease in the frequency of flowing features and a smaller decrease of open fractures with depth. Some near-surface data were explored more comprehensively in /Söderbäck and Lindborg eds. 2009/. These data also show a depth trend but also indicate that there is a significant decrease of open fractures from surface down to c. 100 m depth. This suggests the possibility that the uppermost 10–20 m of the bedrock, where hardly any hydraulic tests have been performed, may be more conductive than suggested by the hydraulic tests above –150 m that constitute the base for the calibration of the Hydrogeological DFN models. The key results from /Söderbäck and Lindborg eds. 2009/ are provided below.

The analyses of the variation in fracture frequency in the upper 100 m of the bedrock, excluding deformation zones as defined in the extended single-hole interpretation, indicates a slight gradual increase in the frequency of open fractures from an elevation of –100 m and upwards towards the ground surface, cf Figure 4-15. In this context it should be noted that the amount of data is restricted in the uppermost part of existing drill cores since mapping is generally only carried out in sections with corresponding BIPS images. However, fractures have also been mapped in some sections that lack BIPS images. The increase in open fracture frequency appears to be coupled to a decrease in frequency of sealed fractures, cf Figure 4-15. This might indicate that at least some of the open fractures constitute reactivated sealed fractures. Furthermore, there is a tendency of an increase of subhorizontal to gently dipping open fractures towards the ground surface, cf Figure 4-16.

The calculated fracture frequency is mainly based on borehole data from fracture domain FSM_W (KLX11B-F, KLX14A, KLX22A-B, KLX23A-B, KLX24A, KLX25A) and fracture domain FSM_N (KLX07B, KLX09B-G), since available data are concentrated to these domains. For definition of fracture domains, see Chapter 3. The analysis presented by /Söderbäck and Lindborg eds. 2009/ indicates that FSM_W in the upper 100 m displays a higher frequency of open fractures and lower

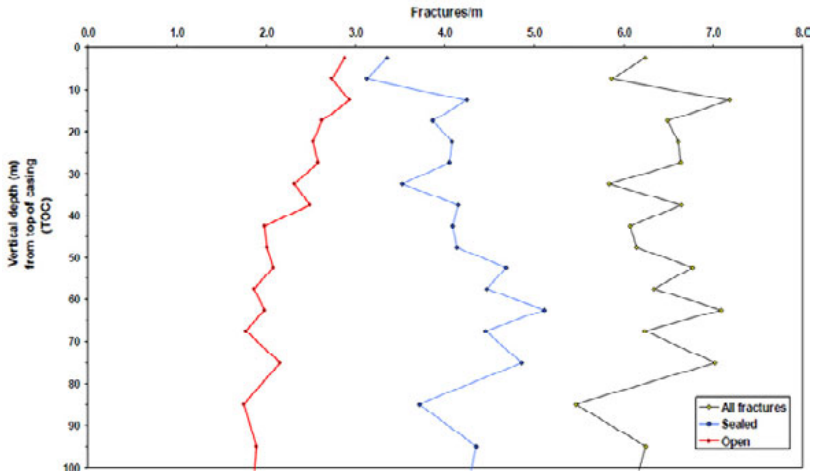

Figure 4-15. *Open fractures, sealed fractures and total number of fractures per metre for 5 metre intervals in the uppermost 100 m of the bedrock /Söderbäck and Lindborg eds. 2009/.*

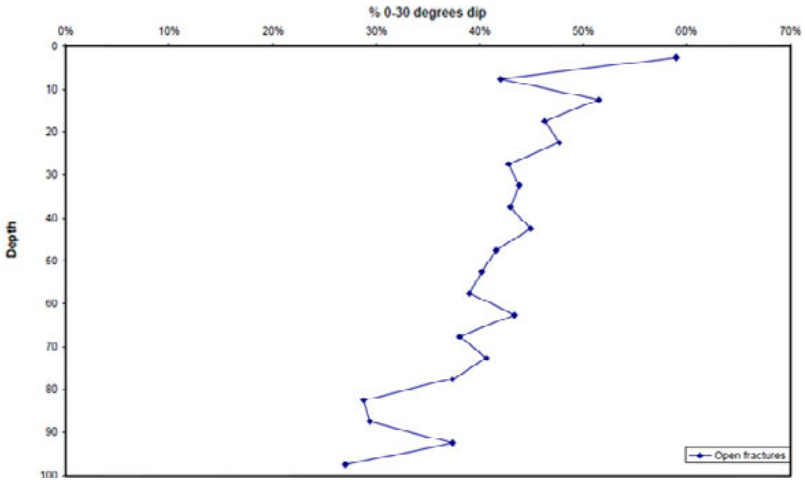

Figure 4-16. *Subhorizontal to gently dipping fractures per metre for 5 m intervals in the uppermost 100 m of the bedrock /Söderbäck and Lindborg eds. 2009/.*

frequency of sealed fractures compared with FSM_N. In addition, there is a tendency for decreasing frequency of open fractures and increasing frequency of sealed fractures towards the ground surface in FSM_W, while FSM_N shows the opposite relation, though only for the upper 60 m for sealed fractures.

For a detailed accounting of results, cf /Söderbäck and Lindborg eds. 2009/.

Hydraulic properties of HRD domains

According to /Rhén et al. 2008/, four separate hydraulic rock domains (HRD) should be modelled, cf Chapter 3:

- **HRD_C**: Corresponding to FSM_C, FSM_NE005 and FSM_S in combination.
- **HRD_EW007**: Corresponding to FSM_EW007.
- **HRD_N**: Corresponding to FSM_N.
- **HRD_W**: Corresponding to FSM_W with justified (and argumented for) exclusion of data from KLX13A.

The relatively small lens-shaped rock domain RSMBA03 has not been modelled as a defined fracture domain /La Pointe et al. 2008/. However, RSMBA03 is modelled as part of HRD_C (RSMBA03 is surrounded by FSM_C and FSM_EW007) as the few data for RSMBA03 indicate that it is fairly low-conductive it is reasonable to incorporate it to HRD_C.

The rock mass in the regional model, outside the defined FSMs, is based on the material property assignments made in model version Laxemar 1.2 /SKB 2006b, Rhén et al. 2006/ (summarised in Appendix 4) and assessments of similarities between those regional HRDs and the newly developed HRDs inside the Laxemar local model volume.

The subdivision in hydraulic rock domains and the superimposed additional division in depth zones within the local model volume have also been employed for presentation of statistics of basic hydraulic test data, cf Table 4-1 and Table 4-2. In the depth zone –400 to –650 m, the true average spacing between conductive fractures in HRD_C is c. 9 m, which is nearly half of the corresponding average spacing in HRD_W. The lower conductive fracture intensity in the rock mass of HRD_W is more than compensated by an average hydraulic conductivity ($\Sigma T/L$) of $2.8 \cdot 10^{-8}$ m/s in the same depth interval, which is close to a factor 8 higher than in the corresponding depth interval in HRD_C.

Table 4-1. Summary of intensity statistics of flowing features detected by PFL for the borehole intervals outside of interpreted deterministic deformation zones. MDZ are included in these statistics, but the numbers of individual PFL-f features are summed up within an MDZ such that each zone is treated as one single feature. (Length = Mapped length minus length of deterministic deformation zone, Mapped borehole length is approximated with a straight line for each domain in the calculations.) Modified after /Rhén et al. 2008/.

Domain	Depth zone (m)	Length (m)	Count	PFL $P_{10,corr}$ (m^{-1})	PFL P_{10} (m^{-1})
FSM_	50 to –150	279	107	0.816	0.384
EW007/	–150 to –400	1,001	241	0.550	0.241
HRD_	–400 to –650	843	72	0.225	0.085
EW007	–650 to –1,000	213	0	0.000	0.000
SM_	50 to –150	371	167	0.820	0.451
NE005	–150 to –400	806	62	0.169	0.077
	–400 to –650	615	17	0.071	0.028
	–650 to –1,000	434	4	0.013	0.009
FSM_N/	50 to –150	933	331	0.773	0.355
HRD_N	–150 to –400	608	115	0.339	0.189
	–400 to –650	441	20	0.115	0.0385
	–650 to –1,000	177	9	0.082	0.051
FSM_C	50 to –150	204	48	0.350	0.235
	–150 to –400	579	40	0.103	0.069
	–400 to –650	1,040	51	0.129	0.0389
	–650 to –1,000	950	4	0.006	0.004
FSM_W/	50 to –150	1,282	379	0.499	0.296
HRD_W	–150 to –400	904	33	0.078	0.037
	–400 to –650	677	23	0.060	0.034
	–650 to –1,000	272	1	0.005	0.004
FSM_S	50 to –150	166	21	0.254	0.126
	–150 to –400	65	20	0.655	0.308
	–400 to –650	N/A	N/A	N/A	N/A
	–650 to –1,000	N/A	N/A	N/A	N/A
HRD_C	50 to –150	741	236	0.564	0.319
	–150 to –400	1,451	122	0.164	0.084
	–400 to –650	1,655	68	0.107	0.0381
	–650 to –1,000	1,384	8	0.008	0.006

Table 4-2. Selected statistics of flowing features detected by PFL for the borehole intervals outside of interpreted deterministic deformation zones. (Note that each MDZ is considered to be a single feature, even if it corresponds to several PFL within a borehole.) (Length = Mapped length minus length of deterministic deformation zone, Mapped borehole length is approximated with a straight line for each domain in the calculations.) Modified after /Rhén et al. 2008/.

Domain	Depth zone (m)	Length (m)	PFL $P_{10,corr}$ (m^{-1})	Sum *T*/L Length (m/s)	Min *T* (m^2/s)	Max *T* (m^2/s)
FSM_	50 to –150	279	0.816	$3.1 \cdot 10^{-07}$	$4.4 \cdot 10^{-10}$	$3.2 \cdot 10^{-05}$
EW007/	–150 to –400	1,001	0.550	$1.2 \cdot 10^{-07}$	$3.1 \cdot 10^{-10}$	$3.7 \cdot 10^{-05}$
HRD_	–400 to –650	843	0.225	$1.2 \cdot 10^{-08}$	$7.9 \cdot 10^{-10}$	$1.8 \cdot 10^{-06}$
EW007	–650 to –1,000	213	0.000	$0.0 \cdot 10^{+00}$	$0.0 \cdot 10^{+00}$	$0.0 \cdot 10^{+00}$
FSM_	50 to –150	371	0.820	$2.4 \cdot 10^{-07}$	$3.9 \cdot 10^{-10}$	$1.4 \cdot 10^{-05}$
NE005	–150 to –400	806	0.169	$4.0 \cdot 10^{-09}$	$3.7 \cdot 10^{-10}$	$1.2 \cdot 10^{-06}$
	–400 to –650	615	0.071	$2.2 \cdot 10^{-09}$	$3.3 \cdot 10^{-10}$	$8.1 \cdot 10^{-07}$
	–650 to –1,000	434	0.013	$1.6 \cdot 10^{-10}$	$1.5 \cdot 10^{-09}$	$6.1 \cdot 10^{-08}$
FSM_N/	50 to –150	933	0.773	$6.7 \cdot 10^{-07}$	$7.7 \cdot 10^{-10}$	$6.5 \cdot 10^{-05}$
HRD_N	–150 to –400	608	0.339	$2.1 \cdot 10^{-07}$	$8.3 \cdot 10^{-10}$	$3.6 \cdot 10^{-05}$
	–400 to –650	441	0.115	$1.5 \cdot 10^{-08}$	$1.1 \cdot 10^{-09}$	$5.2 \cdot 10^{-06}$
	–650 to –1,000	177	0.082	$4.1 \cdot 10^{-10}$	$1.3 \cdot 10^{-09}$	$2.6 \cdot 10^{-08}$
FSM_C	50 to –150	204	0.350	$1.0 \cdot 10^{-07}$	$2.4 \cdot 10^{-09}$	$9.4 \cdot 10^{-06}$
	–150 to –400	579	0.103	$3.4 \cdot 10^{-08}$	$4.1 \cdot 10^{-10}$	$1.2 \cdot 10^{-05}$
	–400 to –650	1,040	0.129	$4.2 \cdot 10^{-09}$	$3.9 \cdot 10^{-10}$	$1.1 \cdot 10^{-06}$
	–650 to –1,000	950	0.006	$7.3 \cdot 10^{-10}$	$1.4 \cdot 10^{-08}$	$4.4 \cdot 10^{-07}$
FSM_W/	50 to –150	1,282	0.499	$2.8 \cdot 10^{-07}$	$3.7 \cdot 10^{-10}$	$4.6 \cdot 10^{-05}$
HRD_W	–150 to –400	904	0.078	$2.9 \cdot 10^{-08}$	$1.1 \cdot 10^{-09}$	$1.0 \cdot 10^{-05}$
	–400 to –650	677	0.060	$2.8 \cdot 10^{-08}$	$6.7 \cdot 10^{-10}$	$9.2 \cdot 10^{-06}$
	–650 to –1,000	272	0.005	$1.4 \cdot 10^{-11}$	$3.7 \cdot 10^{-09}$	$3.7 \cdot 10^{-09}$
FSM_S	50 to –150	166	0.254	$2.9 \cdot 10^{-07}$	$1.3 \cdot 10^{-10}$	$3.8 \cdot 10^{-05}$
	–150 to –400	65	0.655	$1.9 \cdot 10^{-07}$	$3.3 \cdot 10^{-11}$	$6.7 \cdot 10^{-06}$
	–400 to –650	N/A	N/A	N/A	N/A	N/A
	–650 to –1,000	N/A	N/A	N/A	N/A	N/A
HRD_C	50 to –150	741	0.564	$2.1 \cdot 10^{-07}$	$3.9 \cdot 10^{-10}$	$3.8 \cdot 10^{-05}$
	–150 to –400	1,451	0.164	$2.4 \cdot 10^{-08}$	$3.7 \cdot 10^{-10}$	$1.2 \cdot 10^{-05}$
	–400 to –650	1,655	0.107	$3.4 \cdot 10^{-09}$	$3.3 \cdot 10^{-10}$	$1.1 \cdot 10^{-06}$
	–650 to –1,000	1,384	0.008	$5.5 \cdot 10^{-10}$	$1.5 \cdot 10^{-09}$	$4.4 \cdot 10^{-07}$

Hydraulic anisotropy

/Rhén et al. 2008/ presents results of block modelling made using the derived hydrogeological DFN models to study scaling issues and the anisotropy of rock blocks of grid cells size of 5, 20 and 100 m, respectively. It was found that:

- Median value of the ratio K_{hmax}/K_{hmin} were in the range 5 to 9 for HRD_C and HRD_EW007 and c. 2–4 for HRD_W. The ratio K_{hmax}/K_z was 1–1.6 for HRD_C and HRD_EW007 and c. 1–2 for HRD_W, for all grid sizes tested. (K_h: Horizontal hydraulic conductivity, K_z: Vertical hydraulic conductivity).
- The estimated strike interval of K_{max} for HRD_C, HRD_W and HRD_EW007 were; c. 90–150, 100–180, 80–150 respectively, for all grid sizes tested.
- There seems to be a tendency that the anisotropy becomes more pronounced the larger the block is. The explanation is that the larger, but few, conductive fractures/features from a certain fracture set on average become more dominant for lager blocks, but are less common in the smaller blocks. Thus, the mean anisotropy may change with scale considered.

The magnitude of the anisotropy calculated above is lower than comparable inference made based on probe boreholes sampling subvertical fractures in the nearby Äspö HRL access tunnel. It was found that the highest conductivity in the horizontal direction is WNW-NW, but also N-S direction showed high conductivity /Rhén et al. 1997/. The ratio between the maximum and the minimum hydraulic conductivity in the horizontal plane was c. 100, which is considerably higher than the corresponding ratios estimated for the blocks of the Laxemar local model volume discussed above.

Evaluation of hydraulic data from the Prototype Repository at Äspö HRL shows similar results to those obtained in the Äspö access tunnel, but also indicates that the most conductive fracture set is subvertical, with an approximate WNW strike /Rhén and Forsmark 2001/. It was also shown that the hydraulic conductivity was c. 100 times less in vertical boreholes compared to horizontal boreholes, indicating that subvertical fractures are the dominant conductive fractures at Äspö.

Anisotropy in Laxemar may be even higher than indicated by the block modelling as the up-scaling from the hydrogeological DFN models to ECPM has some tendency to average out heterogeneities, but possibly also due to the fact that it is difficult to fully capture the true nature of anisotropy from a limited set of single borehole tests using the above procedure. The possibility to evaluate the anisotropic conditions from the site-investigation field data are possibly also restricted due to the fact that most boreholes are more or less vertical.

As a part of the multidisciplinary site descriptive model of Laxemar, the rock mechanics model for model version SDM-Site Laxemar is presented by /Hakami et al. 2008/. It can be concluded that the orientation of the maximum principal stress in WNW-ESE corresponds well to one of the main sets of conductive hydraulic features and that also the change in the minimum principal stress to be lower than the vertical stress below c. 200–400 m corresponds well to decrease by depth in the horizontal conductive feature frequency

A numerical modelling was performed in /Hakami et al. 2008/ to analyse the potential influence of the interpreted major deformation zones in the area on the stress field. It was concluded that the rock above deformation zones ZSMEW007A and ZSM002A, cf Figure 4-6, has lower stress level compared to other rock blocks between major deformation zones. Other studied borehole sections seemed to show no major change in the stress field due to nearby or intersecting deformation zones in the Laxemar local model volume.

4.1.4 Properties of hydraulic soil domains (HSD)

Regional scale quantitative water-flow modelling requires a parameterisation of the hydraulic properties to the Quaternary deposits. Based on /Werner et al. 2008/, the assignment follows the geometrical representation of the Quaternary deposits according to the stratigraphic model of the Quaternary deposits /Nyman et al. 2008/, cf Section 3.6. Appendix 5 presents the assignment of hydrogeological properties (hydraulic conductivity and storage parameters) to each layer defined in the stratified model of the Quaternary deposits (RDM).

The interpreted thicknesses of the layers of the Quaternary deposits and the hydraulic conductivities of these layers are presented in Table 4-3, based on data from Appendix 5 and illustrated in Figure 3-14. As can be seen in the table, the Quaternary deposits layers are relatively thin but the assigned hydraulic conductivities are generally much higher than the interpreted mean hydraulic conductivity of the superficial bedrock with the exception of Gyttja that has a hydraulic conductivity as the superficial bedrock.

It should be noted that the hydrogeological properties assignment given in Appendix 5 should be considered as a starting point for the quantitative water-flow modelling. Parameter values in the numerical model could be subject to change as a result of the flow model calibration. The pre-modelling mentioned in Chapter 1 indicated that the sea sediments should be less conductive compared to what was proposed on the basis of Laxemar model version 1.2 /Hartley et al. 2007/.

Table 4-3. Description of the layers used in the model of depth of Quaternary deposits and the interpreted hydraulic conductivities proposed to be used as initial assignments, cf a detailed accounting in Appendix 5 and Section 3.6. The stratigraphic distribution of the Z-layers is shown in Figure 3-14.

Layer	Description	Thickness (m)	Hydraulic conductivity (m/s)
Z1	This layer represents the uppermost Quaternary deposits and is present within the entire modelled area, except in areas covered by peat. On bedrock outcrops, the layer is set to 0.1 metre and in other areas to 0.6 metre. If the Quaternary depth is less than 0.6 m, Z1 will be the only layer. In the terrestrial areas, **this layer is supposed to be affected by soil forming processes.** (Mostly till but in minor areas also postglacial shingle, boulder deposits, peat, sand-gravel, artificial fill, cf Appendix 4.)	0.1–0.6	Till: $K_h = 4 \cdot 10^{-4}$ m/s $K_h/K_v = 1$ Other: $K_h = 3 \cdot 10^{-6}$–$1 \cdot 10^{-2}$ m/s $K_h/K_v = 1$
Z2	This layer is present where ***peat*** is shown on the map of Quaternary deposits. The peat areas have been sub-divided into deep and shallow peatlands (see Table 3-2).	0.85	$K_h = 3 \cdot 10^{-6}$ m/s $K_h/K_v = 1$
Z3	The layer represents ***postglacial clay gyttja, gyttja*** or ***recent fluvial sediments***.	1.6–1.7	Gyttja clay/clay gyttja: $K_h = 1 \cdot 10^{-7}$ m/s $K_h/K_v = 1$ Gyttja: $K_h = 1 \cdot 10^{-8}$ m/s $K_h/K_v = 1$
Z4	This layer represents ***postglacial coarse-grained sediments (mostly sand and gravel), artificial fill*** and ***glaciofluvial sediments***. Z4 is equivalent to artificial fill or glaciofluvial sediments in areas shown as these deposits on the map of Quaterenary deposits. In all other areas, Z4 represents the postglacial sediments. Two different average depths were used for the glaciofluvial deposits. One value for the Tuna esker and another value for the other shallower deposits. The glaciofluvial sediment and artificial fill rest directly upon the bedrock. The postglacial sand and gravel are always underlain by glacial clay (Z5) and till (Z6). Post glacial sand/gravel is the most common deposit in this layer.	Postglacial sand/gravel: 0.7–0.8 Glaciofluvial sediments: 3.5–13.2 Artificial fill: 4.4	Postglacial gravel: $K_h = 1 \cdot 10^{-2}$ m/s $K_h/K_v = 1$ Postglacial sand: $K_h = 1 \cdot 10^{-3}$ m/s $K_h/K_v = 1$ Glacifluvial sediments, **postglacial sand/gravel:** $K_h = 5 \cdot 10^{-3}$ m/s $K_h/K_v = 1$ Postglacial fine sand: $K_h = 5 \cdot 10^{-4}$ m/s $K_h/K_v = 1$ Artificial fill: $K_h = 4 \cdot 10^{-5}$ m/s $K_h/K_v = 1$
Z5	The layer represents ***glacial clay***. Z5 is always overlain by postglacial sand/gravel (Z4).	1.3–2.6	Glacial clay: $K_h = 1 \cdot 10^{-8}$ m/s $K_h/K_v = 1$
Z6	This layer represents ***glacial till***, which is the most common Quaternary deposits in the model area. Z6 is 0 if the total Quaternary depth is < 0.6 metre (e.g. at bedrock outcrops) or if Z4 (see above) rests directly on the bedrock surface. The lower limit of Z6 represents the bedrock surface, i.e. Z6 represents the DEM for the bedrock surface.	2.0–3.6	Glacial till: $K_h = 4 \cdot 10^{-5}$ m/s $K_h/K_v = 1$ Where Quaternary deposits depth > 10 m: $K_h = 4 \cdot 10^{-4}$ m/s $K_h/K_v = 1$

4.1.5 Groundwater table and natural pointwater heads

The natural (undisturbed) groundwater level follows the topography of the ground surface, as shown in Figure 4-17 and /Werner et al. 2008/. In the Quaternary deposits the depth to the water table is expected to be up to a few metres, with maximum depths at topographic heights and minimum depths in the valleys. The natural (undisturbed) groundwater level in the upper bedrock is also expected to follow the topography as shown in Figure 4-18, but artesian conditions can be expected occasionally in valleys. The implication of these observations is that topography should be a good indicator for defining the groundwater table and also for defining groundwater divides.

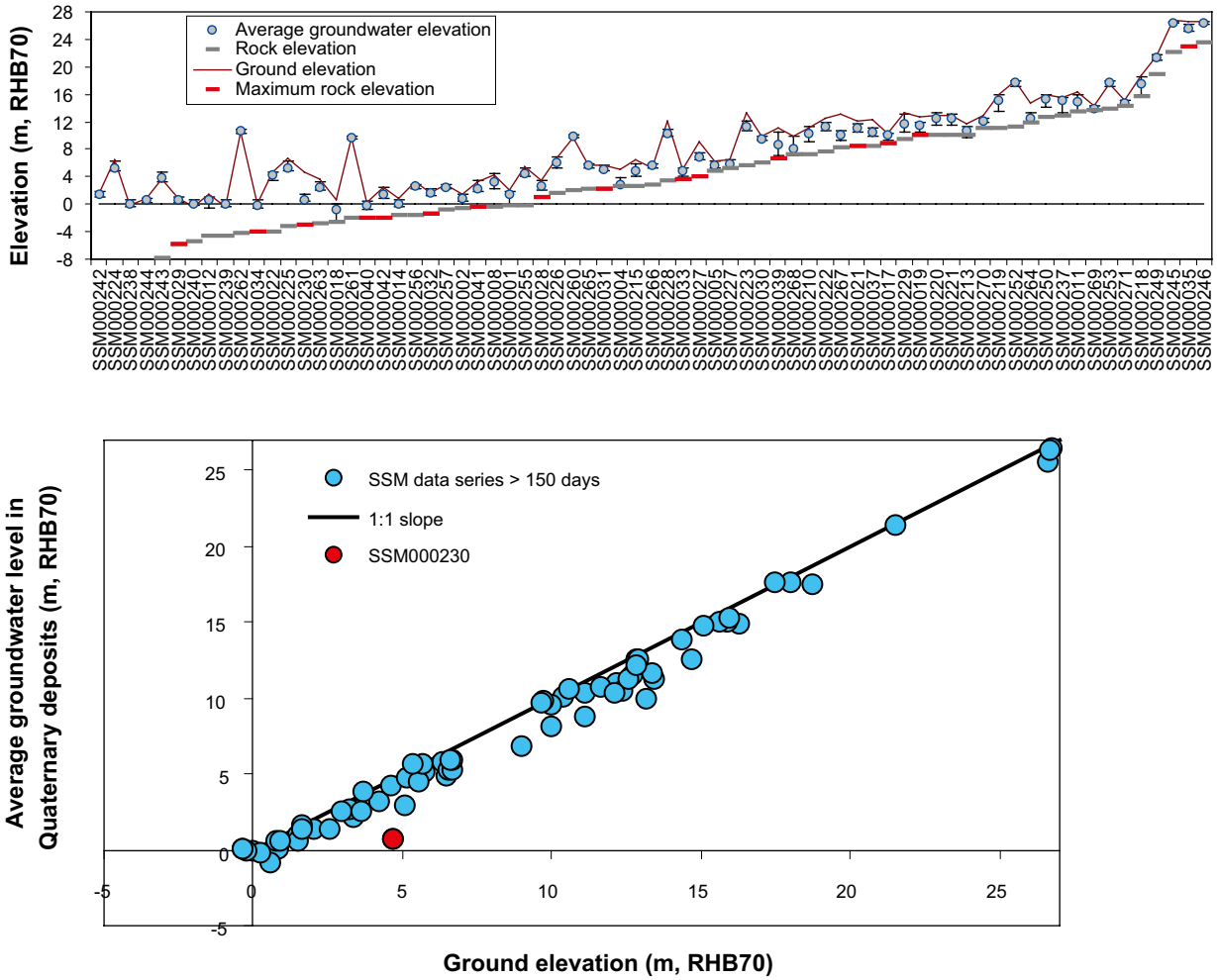

Figure 4-17. Top: Plots of averages, minimum and maximum point-water heads in monitoring wells, ground-surface elevations, and rock-surface elevations. Bottom: Mean groundwater levels (of daily mean) in Laxemar local model area. Monitoring wells in Quaternary deposits with data period longer than 150 days /Werner et al. 2008/.

Generally, boreholes at lower ground elevations show pointwater heads closer to the ground surface while boreholes at higher elevations indicate lower heads at elevations c. 5 m below the bedrock surface, cf Figure 4-18.

4.1.6 Recharge, discharge and water balance components

Sandy-gravely till is overlying the bedrock in almost the whole area. The hilly areas are dominated by shallow/exposed rock (Quaternary deposit depth less than c. 0.5 m), where groundwater recharge occurs. Groundwater discharge is conceptualised to take place in the low-altitude "valley" type areas. The latter are characterised by thicker overburden, possibly as thick as 50 m, including, from bedrock surface; till, glacial clay, postglacial sand/gravel and postglacial clay. The infiltration capacity of the Quaternary deposits in Laxemar is generally considered to exceed the rainfall intensity and the snowmelt intensity /Werner et al. 2008/.

Groundwater discharge mainly takes place in valleys and low-altitude areas. Except for a few wetlands, the surface waters (lakes, streams and wetlands) are located to low-altitude areas /Werner et al. 2008/. The interaction between the lakes and the groundwater is expected to be in the near-shore area /Werner et al. 2008/.

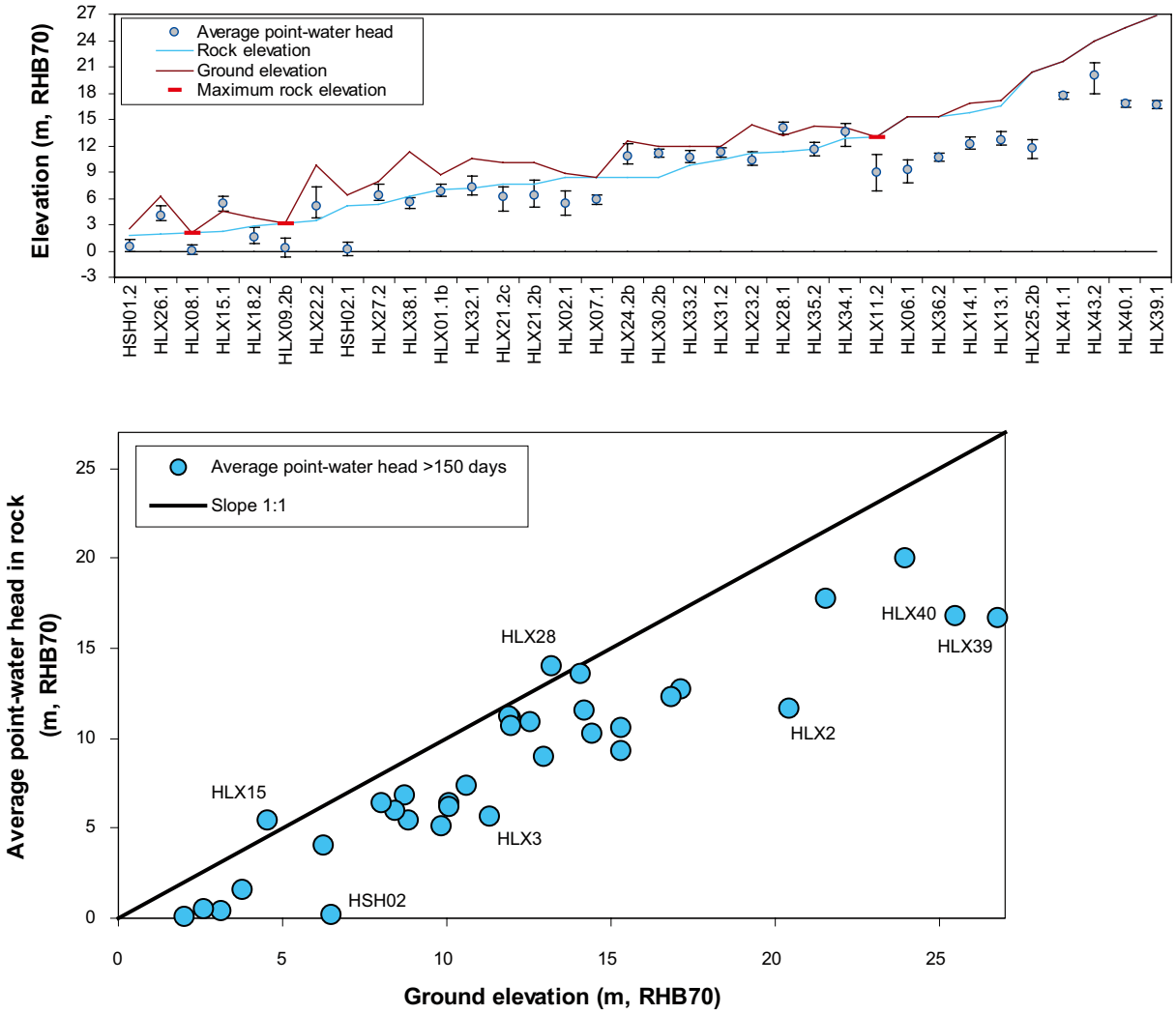

Figure 4-18. *Top: Plots of averages, minimum and maximum point-water heads in percussion boreholes, ground-surface elevations, and rock-surface elevations. Bottom: Plot of average pointwater heads (of daily mean) in percussion boreholes versus ground elevation. Note that for boreholes with packers, data are used for the upper borehole section. Also note that only borehole sections with more than 150 days of data collection are shown /Werner et al. 2008/.*

Joint evaluations of groundwater levels in the Quaternary deposits and pointwater heads in boreholes in the bedrock indicate that groundwater discharge from the superficial rock/Quaternary deposits part of the system to the surface (surface waters) is strongly influenced by the geometry and the hydrogeological properties of the Quaternary deposits overlying the till. Moreover, there is also an influence on this process by the hydrogeological properties of the superficial rock (including the deformation zones). Locally, there is a fractionation into groundwater that discharges to the surface and groundwater that flows horizontally along the valley in the upper rock/Quaternary deposits system; groundwater discharge to the surface is facilitated in areas where there are no layers of glacial clay and postglacial sediments above the till. The varying discharge conditions are illustrated in Figure 4-19 through Figure 4-21. For a detailed discussion of the presented conceptual sections, cf /Söderbäck and Lindborg eds. 2009/.

The site-average long-term annual precipitation at the Laxemar site can be approximated to c. 600 mm/year and the precipitation is somewhat higher inland compared to coastal sites /Werner et al. 2008/. The specific-discharge is estimated to be in the order of 160–170 mm/year (5.3–5.6 L/(s·km^2)), cf /Werner et al. 2008/. The regional estimate is 150–180 mm/year (4.9–5.9 L/(s·km^2)), cf /Larsson-McCann et al. 2002/. The evapotranspiration is thus estimated to be slightly higher than 400 mm/year.

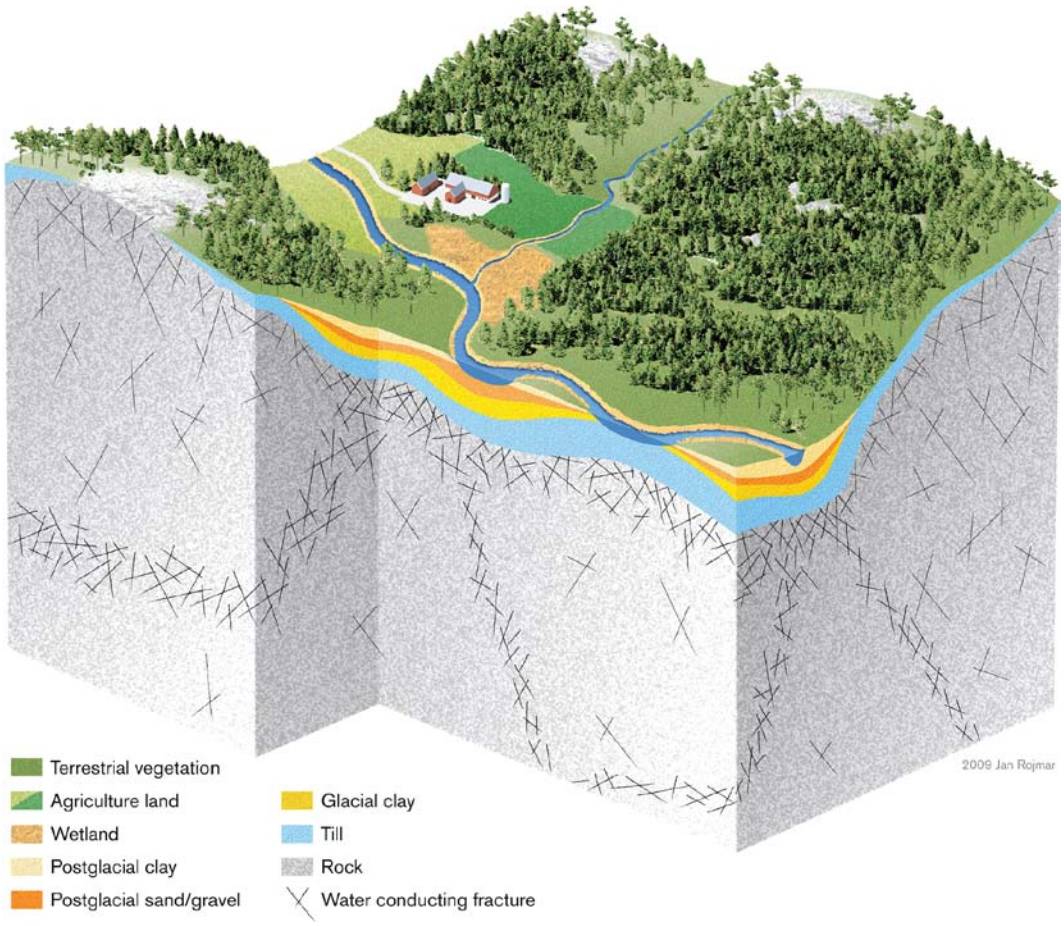

Figure 4-19. *Conceptual view of a typical large east-west valley in Laxemar.*

4.1.7 Baltic sea level and salinity

The present Baltic sea level varies with time but generally not more than c. ±0.5 m from mean sea level /Wijnbladh et al. 2008, cf Section 3.2.5 therein/ and /Werner et al. 2008, cf Section 2.3.1 therein/ and the present salinity varies with time and depth in the range 6–8‰ near Oskarshamn, /Wijnbladh et al. 2008, cf Section 3.1.2 therein/ and /Tröjbom et al. 2008, cf Appendix E therein/. Data compilation of similar character from period before the site investigations started can be found in /Larsson-McCann et al. 2002/.

4.2 Palaeohydrogeological conceptual model

The essential components of the palaeohydrogeological development presented in this section are the shoreline displacement and the different stages of the Baltic Sea. The geological evolution, palaeo-climate and historical development of the Laxemar-Simepvarp area are described in /Söderbäck ed. 2008/. Below, the parts essential to hydrogeology and palaeohydrogeology are summarised. The groundwater evolution in Laxemar is expected to have been influenced by these climate changes and development of the Baltic Sea.

Figure 4-22 illustrates some important phases in the climate (interglacials, stadials and interstadials) after the Eem interglacial.

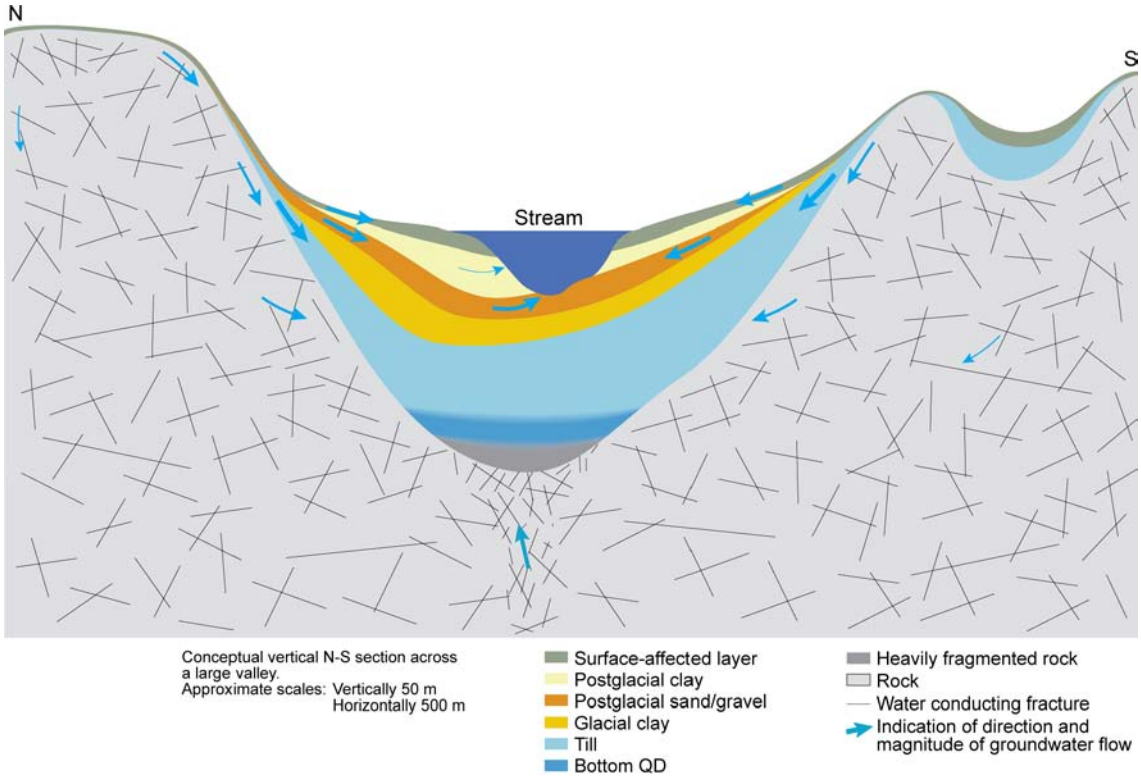

Figure 4-20. *Conceptual vertical N-S section across a typical large valley in Laxemar. Note the different horizontal (1 km) and vertical (50 m) scales in the figure.*

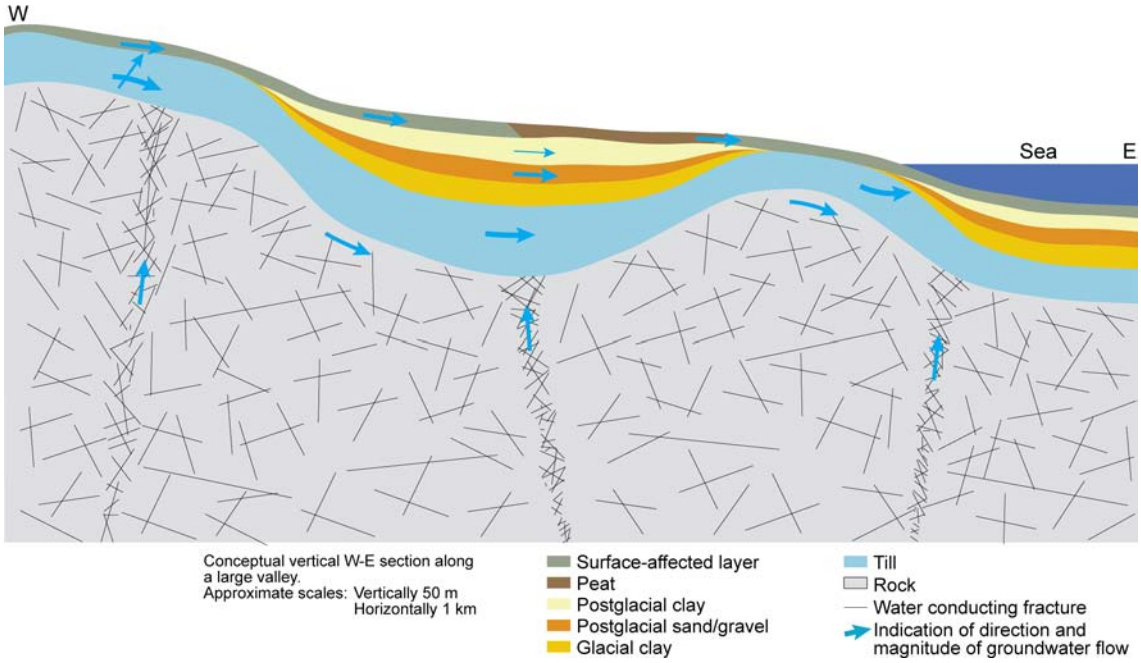

Figure 4-21. *Conceptual vertical W-E section* ***along*** *a typical large valley in Laxemar. Note the different horizontal (1 km) and vertical (50 m) scales in the figure. (The deep recharge is assumed to be mainly perpendicular to the plane shown and originating mainy from the nearby hills, cf Figure 4-19 and Figure 4-20.)*

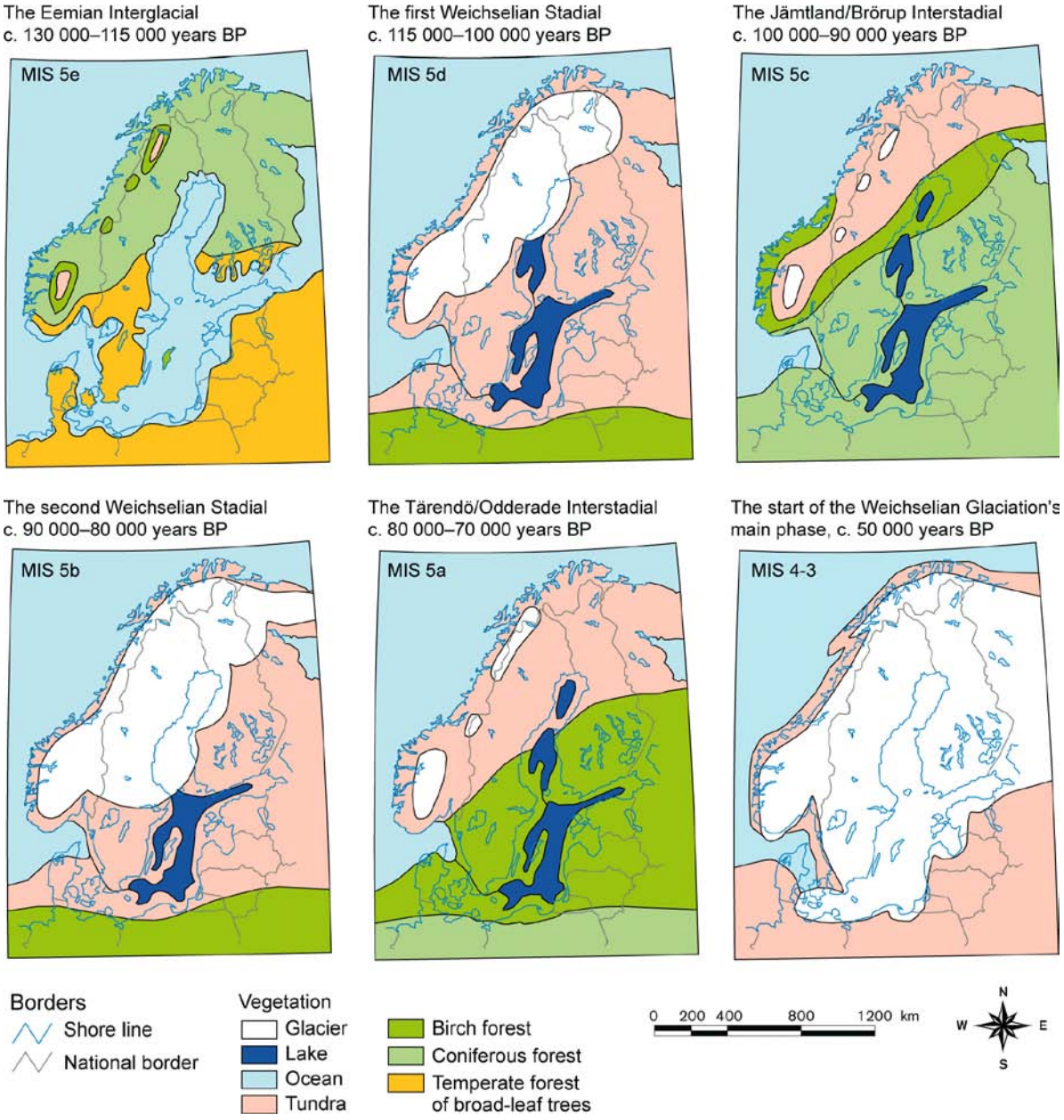

Figure 4-22. *The development of vegetation and ice cover in northern Europe during the latest interglacial (Eem) and first half of the latest ice age (Weichsel). The different periods have been correlated with the Marine Isotope Stages (MIS). The maps should be regarded as hypothetical due to the lack of well dated deposits from the different stages /from Fredén ed. 2002/, cf /Söderbäck ed. 2008/.*

The illustrations suggest that the Laxemar-Simpevarp area has been subjected to meteoric, glacial and marine/lacustrine water influences for relatively long periods of time prior to the start of the main phase of the most recent glaciation, the Weichselian. A major crustal phenomenon that has affected, and continues to affect northern Europe, following the melting of the Weichselian glaciation, is the interplay between isostatic rebound of the Earth's crust, on the one hand, and eustatic sea-level variations on the other. During the main phase of the Weichselian glaciation, the global sea level was in the order of 120 m lower than at present, due to the large amounts of water stored in the ice sheet /Fairbanks 1989/. In northern Sweden, the heavy continental ice depressed the Earth's crust by as much as 800 m below its present elevation. A marked improvement in climate took place about 18,000 years ago, shortly after the latest glacial maximum and the ice started to retreat, a process that was completed after some 10,000 years. There was a major standstill and, in some areas, a re-advance of the ice front during a cold period c. 13,000–11,500 years ago. The end of this period marked the onset of the present interglacial, the Holocene (the last 10,000 years).

The changes in the salinity of the aquatic systems in the Baltic basin during the Holocene are closely coupled to the shore-line displacement. The changes are divided into four main stages /Björck 1995, Fredén ed. 2002/ as summarised in Figure 4-23, Figure 4-24 and Table 4-4. The most saline period during the Holocene occurred c. 4500–3000 BC, when the superficial water salinity of the Littorina Sea south of Åland was 10–15‰ compared with approximately 7‰ in the current Baltic Sea /Westman et al. 1999/, see Figure 4-25. The period of the brackish Yoldia Sea was probably short, 100–150 years, which suggests that the intrusion of denser saline water into the bedrock was limited compared to the effect during the Littorina Sea period. Accordingly, the effect of the Yoldia Sea has not been simulated in the current modelling, cf Chapter 9.

The range of salinity in the Baltic Sea, excluding Yoldia Sea, in the vicinity of Laxemar is shown in Figure 4-25. It is suggested that the curve to be used for the palaeohydrogeological simulations should be contained in the indicated interval; SDM-min to SDM-max in the figure. The influence of salinity has been investigated in the palaeohydrogeology simulations (see Chapter 9) by considering SDM-site Alt1 in the base case, and Alt.2 as a variant.

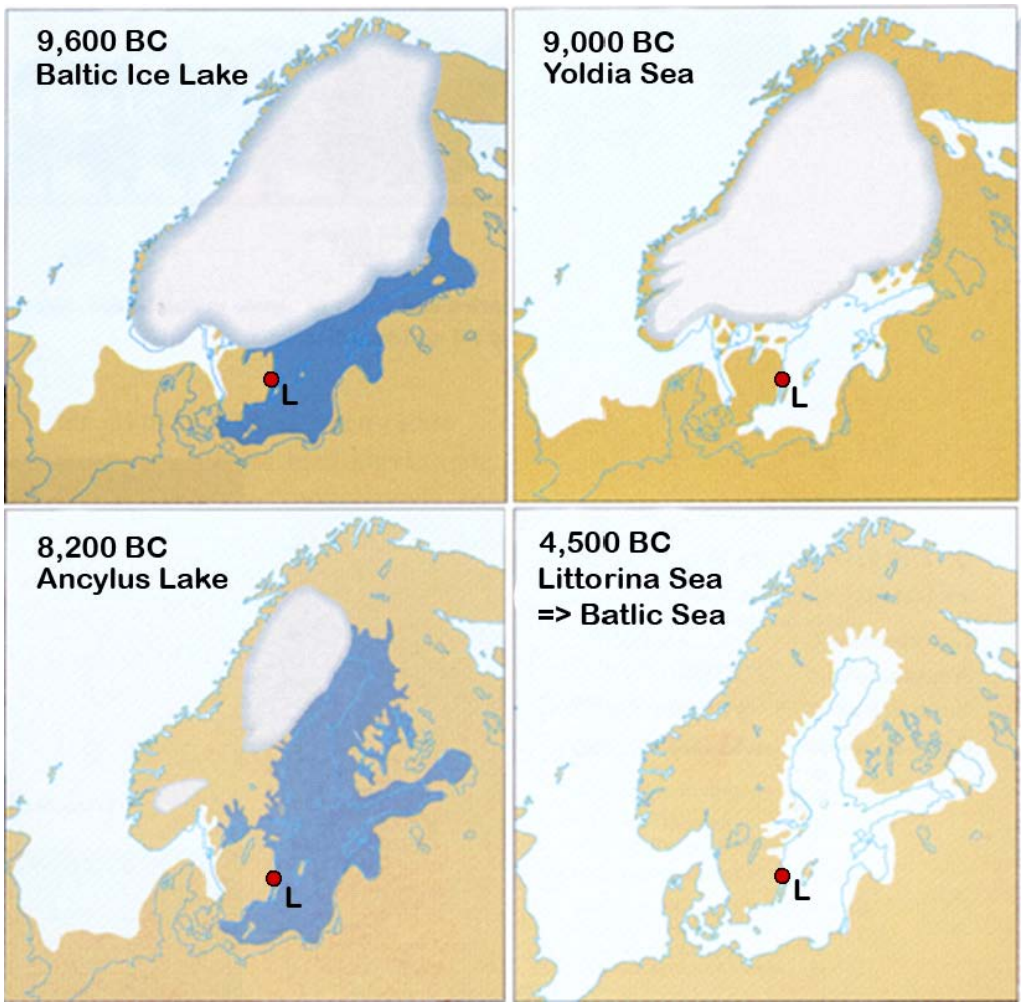

Figure 4-23. *Map of Fennoscandia with some important stages during the Holocene period. Four main stages characterise the development of the aquatic systems in the Baltic basin since the latest deglaciation: the Baltic Ice Lake (9600 to 9500 BC), the Yoldia Sea (9500 to 8800 BC), the Ancylus Lake (8800 to 7500 BC) and the Littorina Sea 7500 BC–present (the figure shows the maximum salinity at 4500 BC during the Littorina Sea stage). Fresh water is symbolised with dark blue and marine/brackish water with light blue for the present shoreline). Modified from /Söderbäck ed. 2008/. Laxemar (indicated L) was already situated in an ice free area during the Baltic Ice Lake stage.*

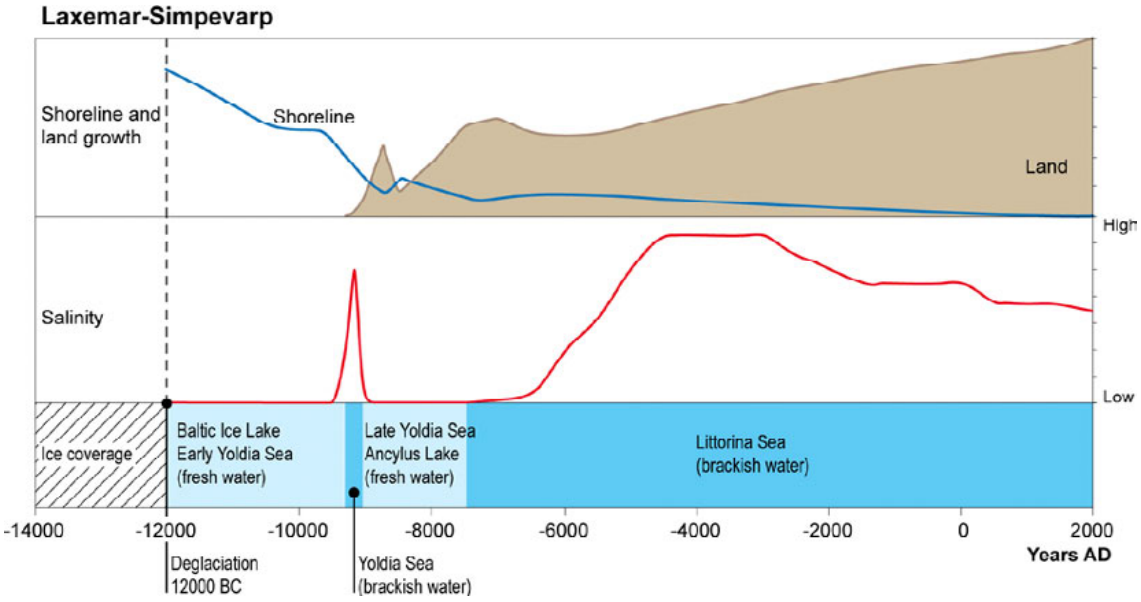

Figure 4-24. *The development of shoreline and salinity in the Laxemar-Simpevarp area from the latest deglaciation to the present time. The red curve shows the variation in salinity of the Baltic Sea at the site (the Baltic proper for Laxemar-Simpevarp), from /Söderbäck ed. 2008/.*

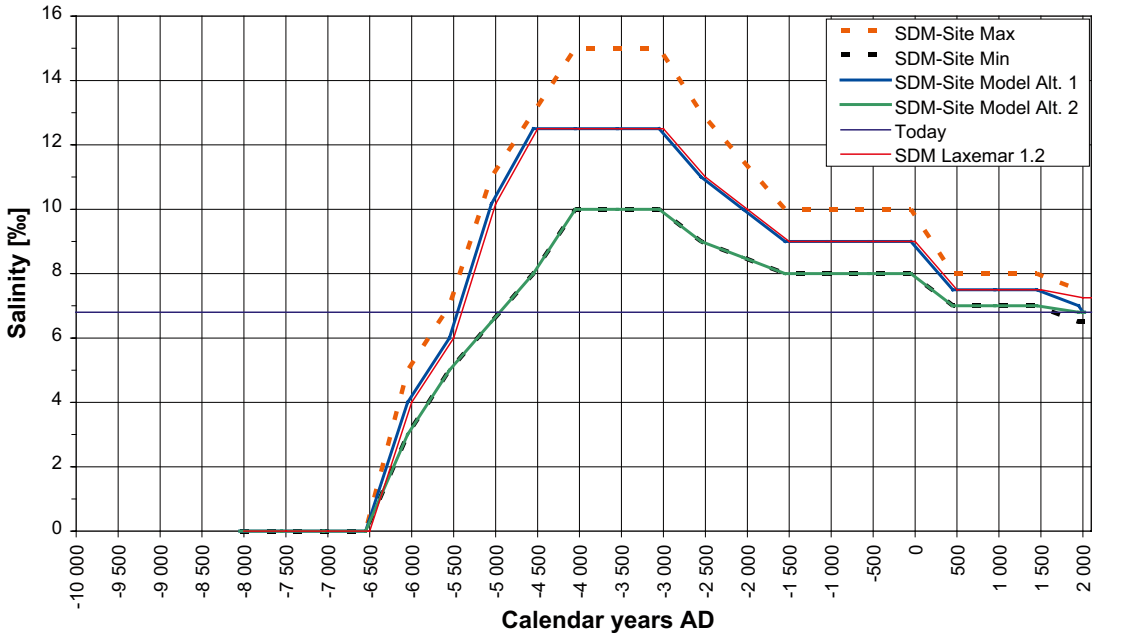

Figure 4-25. *The range in the salinity of the aquatic systems in the Baltic basin specified for SDM-Site Laxemar and version 1.2. (SDM-Site Laxemar 1.2 is equal to SDM-Site Alt. 1 and SDM-Site Min is equal to SDM-Site Model Alt. 2.) Based on /Westman et al. 1999/, cf /Söderbäck ed. 2008/.*

Table 4-4. Summary of the stages in the development of the Baltic Sea, presented as years before present. Note that the altitudes and ages are approximate values. Based on data reported by /Björck 1995, Fredén ed. 2002, Westman et al. 1999/.

Baltic stage	Calendar year BC	Salinity	Environment in Laxemar
Baltic Ice Lake	13,000–9500	Glacio-lacustrine	Laxemar-Simpevarp area covered by the Baltic Ice Lake. Small areas in Laxemar above lake level at the end of the period.
Yoldia Sea	9500–8800	Lacustrine/ Brackish (100–150 years)/Lacustrine	Laxemar-Simpevarp area covered by the Yoldia sea. Small areas in Laxemar above sea level.
Ancylus Lake	8800–7500	Lacustrine	Regressive shore level from c. +30 m RHB 70.
Littorina Sea (→ Baltic Sea)	7500–present	Brackish	Regressive shore level from c. 20–0 m RHB 70. Most saline period 4500–3000 BC Present-day Baltic Sea conditions have prevailed during the last c. 2,000 years.

The ice retreated more or less continuously during the early part of the Holocene. As soon as the vertical stress started to decrease, due to thinner ice coverage, the crust started to rise (isostatic land uplift). The net effect of the interplay between isostatic recovery on the one hand and eustatic sea-level variations on the other that results in shore level displacement, a process modelled by e.g. /Påsse 1996, 1997, 2001, Morén and Påsse 2001/.

The shore level displacement started before the final deglaciation and is still an active process throughout Sweden. For instance, the displacement rate in the Laxemar-Simpevarp area, around 10,000 years ago, was very rapid at about 2–3 cm per annum, but has now reduced to about 1 mm per annum. About 10,000 years from today the accumulated remaining displacement is predicted to be c. 6 m, assuming that the model developed by /Påsse 2001/ is valid. Thus, the present-day hydrogeological conditions in the Laxemar-Simpevarp regional model area are not at steady-state and the site will not be a coastal site in the future provided that the current shore-level displacement process continues.

Figure 4-26 shows the shore level displacement specified for SDM-Site Laxemar. In comparison with the curve used previously for version Laxemar 1.2, the displacement rate for SDM-Site Laxemar is slightly reduced at later times, but shows a sharp peak between 8700 to 7200 BC. The data points for the interpreted shoreline curve shown in /Söderbäck ed. 2008/ indicate that there are uncertainties in the actual position of the curve and it is also pointed out in this reference that there are uncertainties in the shoreline curve, especially for the last 9,500 years. This uncertainty justifies tests with alternatives of the shore level displacement, cf Figure 4-26, and Chapter 9, and. The simulation results presented in Chapter 9 indicate that the *SDM-Site Laxemar, Alt. 1* works better than the curve *SDM-Site Laxemar* shown in Figure 4-26 since it allows for some infiltration of Littorina sea water over a larger area of the site. For the *SDM-Site Laxemar* shore line curve, only very limited areas of the Laxemar-Simpevarp area are below sea level during the Littorina maximum 4500 to 3000 BC.

The *SDM-Site Laxemar* shore level curve was used to map out in detail how the shoreline changes with time within the Laxemar-Simpevarp area, cf Figure 4-27 for an illustration of the denser saline Littorina water intrusion along larger valleys, mixing with older glacial and brackish groundwater. The figure also illustrates that the larger parts of Laxemar-Simpevarp area (central and western part at higher elevations) have been exposed of Meteoric water since the latest glaciation. It can be stated that the Meteoric water has since the latest glaciation been infiltrating successively larger areas and has mixed and flushed out older waters in the upper part of the bedrock. The western part of the regional model area has, however, never been exposed to Littorina sea water as it rose early above the sea, cf Figure 4-28. However, some of the valleys in the west have an elevation indicating that Littorina could have been present but possibly the Littorina seawater in such long bays could be diluted by freshwater streams from the west.

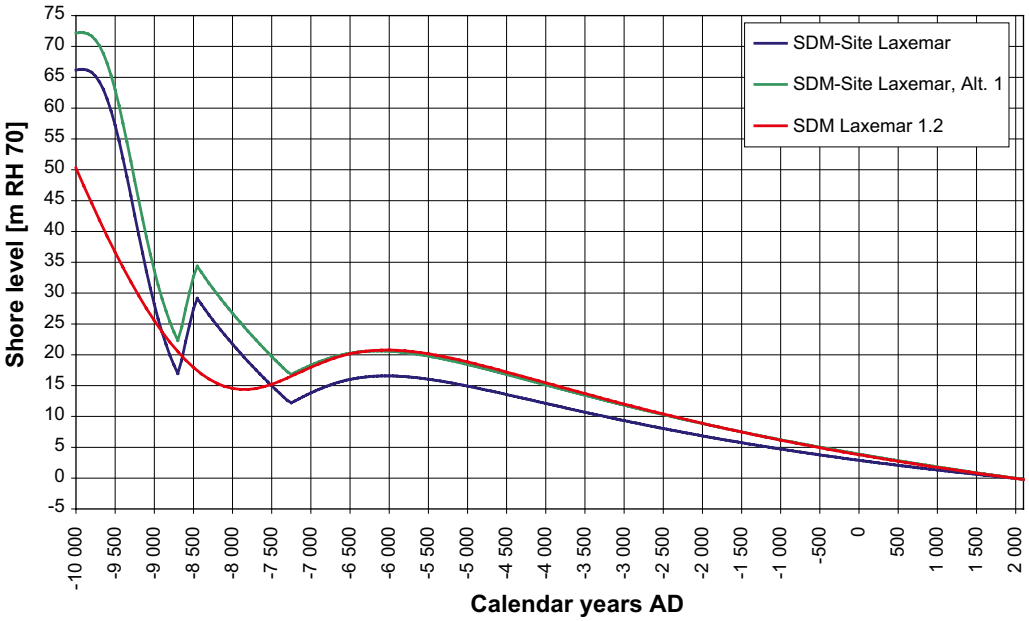

Figure 4-26. *Shore level displacement specified for SDM-Site Laxemar and compared to the evolution used in version 1.2. Based on /Påsse 1997, 2001/. In addition, an alternative model is presented.*

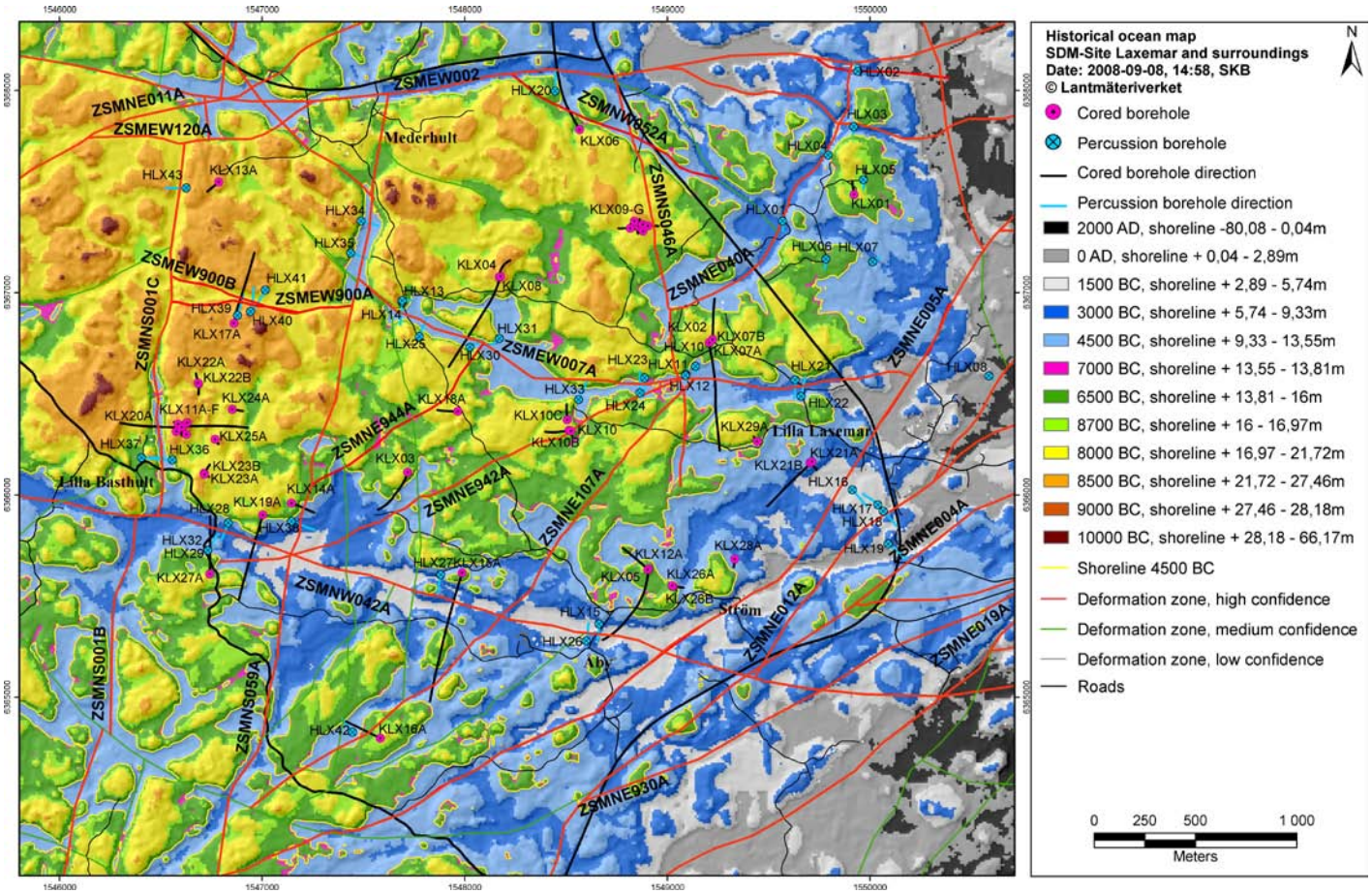

Figure 4-27. *Shoreline changes in the Laxemar-Simpevarp area during the Littorina period (based on the SDM-Site Laxemar curve, cf Figure 4-26, applicable to the Laxemar local model area. The maximum salinity in the Baltic during the Littorina period occurred between 4500 BC and 3000 BC (Blue and grey areas indicate the coverage of the Littorina sea 4500–1500 BC).*

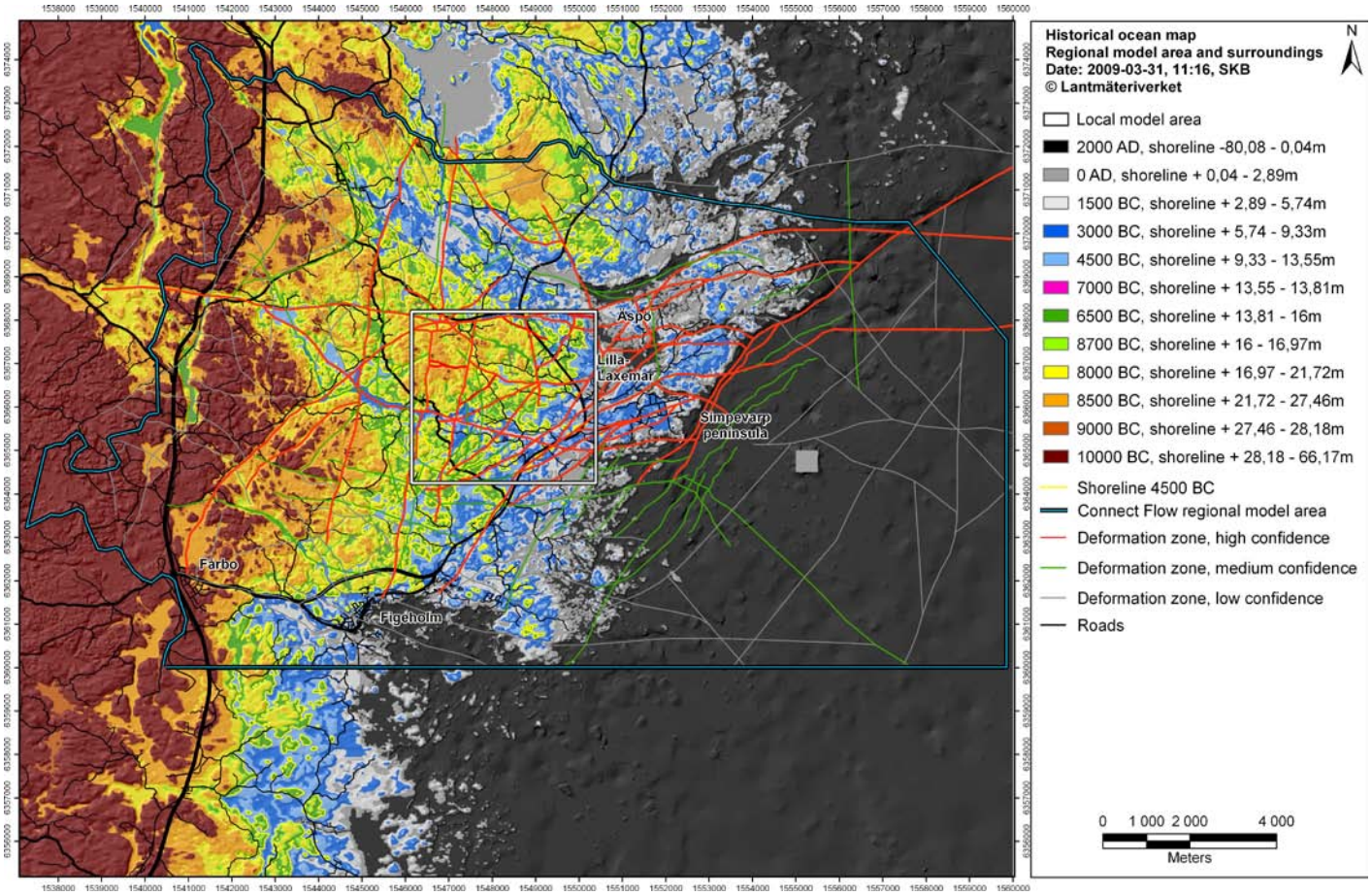

Figure 4-28. *Shoreline changes in the Laxemar-Simpevarp area during the Littorina period (based on the SDM-Site Laxemar curve, cf Figure 4-26), The maximum salinity in the Baltic during the Littorina period occurred between 4500 BC and 3000 BC (Blue and grey areas indicate the coverage of the Littorina sea 4500–1500 BC).*

Solute transport and reference waters

Coupled groundwater flow and solute transport is conceptualised in terms of the evolution of a number of groundwater constituents in order to understand the hydrochemical evolution in terms of the mixing of groundwaters of different origin. In the fracture water mixing takes place through the processes of advection, dispersion, diffusion (including rock matrix diffusion), while porewater composition is assumed to evolve only as a result of rock matrix diffusion. Groundwater composition is described in terms of mixtures of references waters, consistent with the concepts used for interpretation of hydrogeochemistry as described in Section 5.4, and based on the SDM-Site Laxemar hydrochemistry description /Laaksoharju et al. 2009/. Fracture water is assumed to be a mixture of the following 4 reference waters whose composition characteristics can be described in terms of chloride, magnesium bicarbonate and $\delta^{18}O$ as:

Deep Saline Water

Strong saline source → high chloride content (> 6,000 mg/L).

Non-marine origin → low magnesium content (< 20 mg/L).

Non-post-glacial meteoric → low bicarbonate content (< 50 mg/L). Enriched in $\delta^{18}O$.

Glacial Melt Water

Non-saline source → low chloride content (< 8 mg/L).

Non-marine origin → low magnesium content (< 8 mg/L).

Non-post-glacial meteoric → low bicarbonate content (< 50 mg/L).

Significantly depleted $\delta^{18}O$.

Littorina Sea Water

Brackish saline source → moderate chloride content (max ~5,500 mg/L).

(The chloride content of the present-day *Baltic Sea Water* is ~3,000 mg/L).

Marine origin → high magnesium content (max 250–350 mg/L).

Non-post-glacial meteoric → low bicarbonate content (< 100 mg/L).

Enriched $\delta^{18}O$ (> –10‰ SMOW).

Altered Meteoric Water

Non-saline source → low chloride content (< 200 mg/L).

Non-marine origin → low magnesium content (< 50 mg/L).

Post-glacial meteoric → high bicarbonate content (> 50 mg/L).

Intermediate $\delta^{18}O$ (–12 to –11‰ SMOW).

An additional fifth reference water is introduced in the palaeohydrogeological modelling to illustrate some conceptual thinking on how the composition of the porewater may evolve in areas of the rock matrix away from the connected flowing fracture system:

Inter-glacial Porewater

Possible saline source → low-moderate chloride content (< 5,000 mg/L).

Non-post-glacial marine origin → low magnesium content (< 50 mg/L).

Non-post-glacial meteoric → low bicarbonate content (< 50 mg/L).

Enriched $\delta^{18}O$ (> –10‰ SMOW).

This reference water is considered likely to be a very old water residing primarily in the matrix composed of meteoric and brackish waters from periods before the Weichselian glaciation. Examples of the existence of such a reference water are considered to come from porewater samples obtained in rock of low fracture intensity found from about –400 m to –600 m elevation and below, and more than about 5 m from a water conducting fracture. Small proportions of *Inter-glacial Porewater* may enter the fractures by out-diffusion from the matrix giving a slight dilution of the 4 main fracture reference waters. As indicated in the description above the origin of this reference water is by its nature uncertain being subject to long-term transients – climate evolution and rock matrix diffusion. For the palaeohydrogeological modelling, a base scenario is considered in which it is of freshwater meteoric composition (Cl, 200 mg/L), with a more brackish composition considered as a variant.

Within the palaeohydrogeological model the chemical composition at any point and time is then described in terms of the mass fractions of these five reference waters. The reference waters contain both conservative and non-conservative species, but the flow modelling assumes a conservative behaviour of these species, i.e. no chemical reactions are involved in the modelling. However, it is the conservative species that are considered important in the flow calibration and the non-conservative species are simply used as indicators of relative changes with depth in groundwater signatures. The assumption is that reference water mixing is the dominant process for the evolution

of the groundwaters composition below the uppermost part of the bedrock /Laaksoharju et al. 2009/. The compositions of reference waters are defined in terms of the major ions (Br, Ca, Cl, HCO_3, Mg, Na, K and SO_4) and the two isotopes of interest to hydrogeology are δ^2H and $\delta^{18}O$ (see Table 5-8). Assuming that the components behave conservatively, it is then straightforward to convert between the mass fraction composition at a given position (and time) and concentrations of ions or isotope ratios by linear combinations of the reference water fractions multiplied by their composition. However, only some of the major ions mentioned above behave conservative, as will be discussed later in the text, cf Section 5.6.3.

The formulation of the solute transport equations in terms of mass fractions is described in Section 7.8. Using mass fractions as the transported entities makes the definition of boundary and initial conditions intuitive since they relate directly to the hydrogeochemical conceptual model of water origin. Likewise it is useful to interpret the result in terms of the dilution or penetration of the different reference waters.

Palaeohydrogeological simulations start at 8000 BC at which time it assumed that fracture and porewater are a mixture of *Deep Saline Water*, *Glacial Melt Water* and *Inter-glacial Porewater*, i.e. these enter the model via the definition of the initial conditions. *Littorina Sea Water* and *Altered Meteoric Water* only enter the model via the boundary conditions that describe the evolution to the present-day. A more comprehensive numerical description of boundary and initial conditions is presented in Section 7.8.

4.3 Bedrock temperature

The temperature of the bedrock is of hydrogeological interest as viscosity and density of water are temperature dependent, cf Section 7.8.1. The SDM-Site Laxemar thermal site descriptive model applicable to the Laxemar local model volume is reported in /Sundberg et al. 2008/.

Figure 4-29 and Table 4-5 present the calculated gradients for the investigated boreholes. Sections with high gradient are commonly associated with interpreted deformation zones, where water bearing fractures are likely to exist. Despite these type of anomalies, the average gradient tends to remain constant with depth, generally being between 12 to 15°C/km from –200 m to –800 m elevation.

According to /Holzbecher 1998/ the dynamic viscosity (μ) and the density (ρ_{fw}) of freshwater can for Laxemar conditions be expressed as follows:

Near surface: c. +7°C, $\mu = 1.42 \cdot 10^{-3}$ Pa·s, $\rho_{fw} = 999.9$ kg/m^3

Depth 1,000 m: c. +23°C, $\mu = 0.93 \cdot 10^{-3}$ Pa·s, $\rho_{fw} = 997.6$ kg/m^3

Table 4-5. Equations fitted to the temperature profiles for the investigated boreholes. /Sundberg et al. 2008/.

Borehole	Equation (linear fit)	Calculated from data in elevation interval, m
KLX02 (2003)	Temp. = –0.0149 z + 7.4786	–46 to –1,005
KLX05	Temp. = –0.0148 z + 7.5633	–80 to –878
KLX08	Temp. = –0.016482 z + 6.3864	–63 to –823
KLX18A	Temp. = –0.015817 z + 6.8625	–79 to –580
KLX20A	Temp. = –0.013042 z + 7.6520	–51 to –309

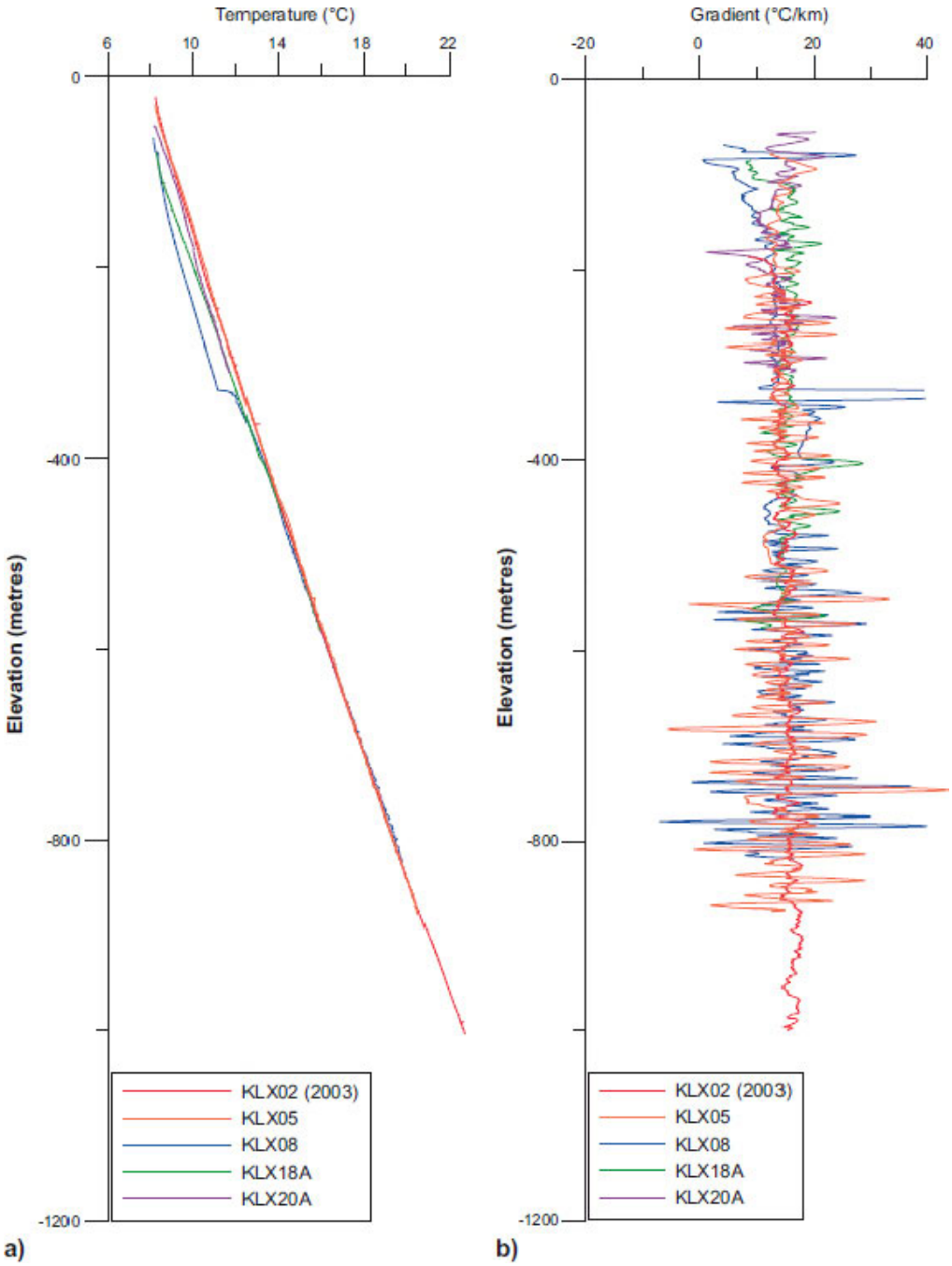

Figure 4-29. *Summary of temperature (a) and gradient calculated for nine metre intervals (b) for the four boreholes in Laxemar. Results from "approved" fluid temperature loggings only /Sundberg et al. 2008/.*

5 Monitoring data and hydraulic interference tests

This chapter provides an overview of:

- the analysis of the interference caused by the underground facility of the Äspö Hard Rock Laboratory (Äspö HRL) being kept drained continuously,
- available interference tests made during the site investigations,
- monitoring methodology of groundwater levels and available groundwater level data, and
- hydrochemical data including major ions, isotopes and mixing fractions relevant to fracture waters and matrix porewaters considered important for the palaeohydrogeological groundwater flow modelling.

The corresponding data related to the above four points are used for the calibration of the regional groundwater flow model, cf Chapters 6, 8 and 9.

5.1 Drawdown caused by Äspö HRL

The Äspö Hard Rock Laboratory (Äspö HRL) is situated below the Äspö island north-east of the Laxemar local model area, cf Figures 3-1 and Appendix 2, Figure A2-2. The recorded drawdown and tunnel inflow data have been used by SKB to test and calibrate numerical groundwater flow models as part of the construction phase of the Äspö HRL /Rhén et al. 1997/, as part of the SKB organised "Task Force on modelling of groundwater flow and transport of solutes" /Rhén and Smellie 2003/, as part of the on-going work at Äspö HRL /Vidstrand 2003/ and as part of model testing for the site investigation subsequent to model version Laxemar 1.2 /Hartley et al. 2007/.

In the current SDM-Site Laxemar work the influence of the Äspö HRL is tested in the flow modelling using the updated geometric models and parameterisations in a manner similar to that of /Hartley et al. 2007/.

It is not expected that the interim storage facility (Clab) on the Simevarp peninsula, will have anything but a very local effect on the groundwater flow pattern given its superficial depth (c. 50 m of rock cover) and the fairly low inflow rate compared with that to the Äspö HRL. The inflow rate to the Clab facility during the period 1981 to 1986 was recorded at c. 100 m^3/day, decreasing to c. 40 m^3/day in the year 2000. In contrast, in the year 2000 the maximum inflow to Äspö HRL was recorded at c. 1,900 m^3/day. The groundwater flow pattern may also locally be affected on the Simepvarp peninsula by drainage to shafts of limited depth extent associated with the foundations of the nuclear power plants east of the Clab facility.

5.1.1 Tunnel geometry

The names of the different Äspö HRL tunnel objects are given in Table 5-1 and Table 5-2. Additional information and visualisation is found in Appendix A2 (cf Figure A2-1).

Table 5-1. The main tunnel objects included in the model.

Name	Object
TASA	The main tunnel, A
TASH	Elevator shaft, H
TASV	Ventilation-in shaft, V
TASW	Ventilation-out shaft, W

Table 5-2. The diameters of the full-face drilled parts.

Object	Diameter
TBM tunnel	5.0 m
Elevator shaft, H	3.8 m
Ventilation-in shaft, V	1.5 m
Ventilation-out shaft, W	1.5 m

5.1.2 Inflow to the Äspö HRL

Inflow to the access tunnel is measured at a number of weir positions distributed along the tunnel. This gives information on the total inflow, and inflow at different sections of the HRL as monthly averages. Data are available from the time of excavation of the Äspö HRL to the operational phase of Äspö HRL, i.e. from May 1991 until December 2004. The excavation phase continued up to 1995.

The total inflow to the HRL is shown in Figure 5-1, the remainder of the weir measurements are given in Appendix A2.

5.1.3 Drawdown

The maximum drawdown on Äspö is estimated to c. 80–90 m /Rhén et al. 1997/. Drawdown observations inland that may be related to the inflow to the Äspö HRL, have been measured in the western part of Ävrö and close to the southern coast of Laxemar. Significant drawdown at the western part of Ävrö, about 2–5 m, and in the strait between Ävrö and Mjälen, about 8.5 m, have been observed in 1996. Subsequently there is a slight recovery in the drawdown, and the drawdown in the strait reduces to 7 m in the year 2000 (Mjälen is located north-west of Ävrö).

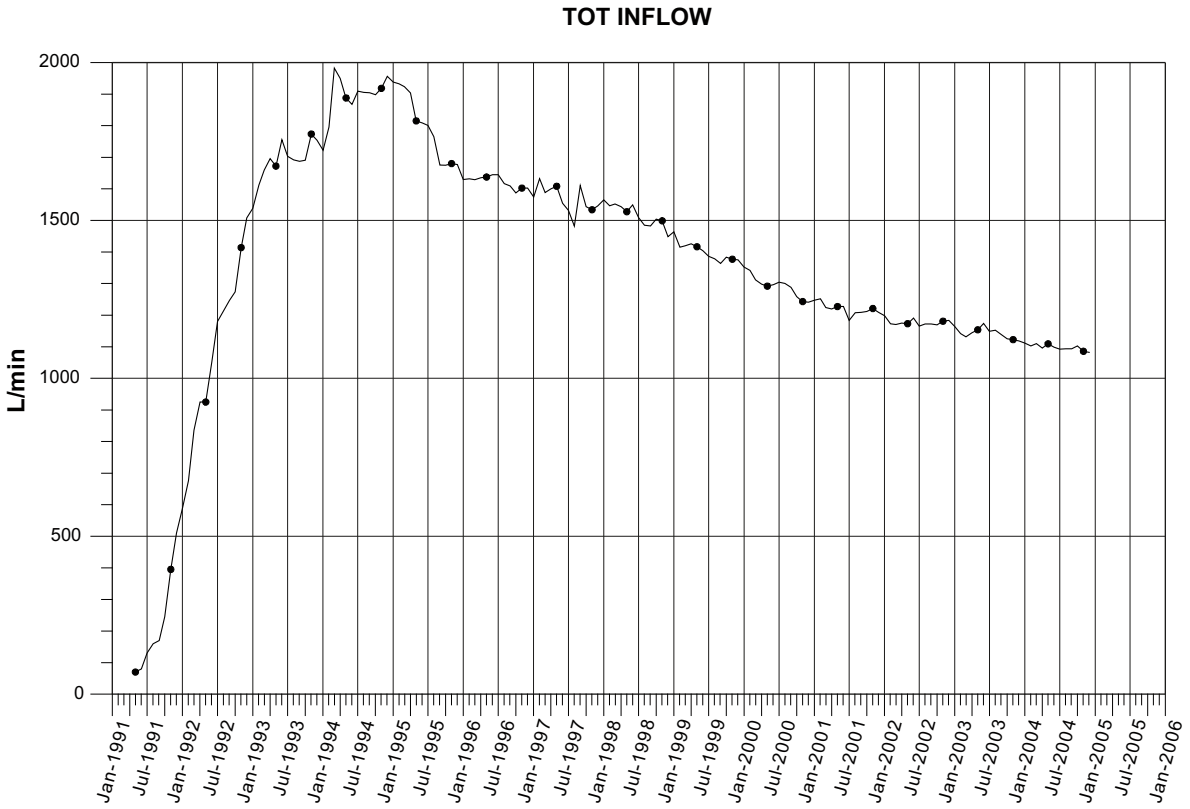

Figure 5-1. *The evolution of total water inflow to the Äspö HRL tunnel.*

In percussion borehole HLX02, which intersects the Mederhult zone (ZSMEW002A) near Äspö, cf Figure 3-4 and Figure 3-8, there is a drawdown of 0.5 m. HLX09, cf Figure 3-4, indicating a maximum drawdown of 1.5–1.9 m. No other percussion boreholes in the Laxemar subarea seem to show any significant drawdown due to the Äspö HRL. Estimated water levels and calculated drawdowns are given in Appendix 2.

Overall, the effect of Äspö HRL in Laxemar is minimal, which is also reproduced by the modelling of /Hartley et al. 2007/.

5.2 Interference tests – Site Investigation

Interference tests during the site investigations in the Laxemar-Simpevarp area have been performed in a number of boreholes and are reported in /Enachescu et al. 2006a, Enachescu et al. 2007a, b, Enachescu et al. 2008a, Gokall-Norman and Ludvigson 2007, Gustafsson and Ludvigson 2005, Harrström et al. 2007, Morosini and Wass 2006, Morosini and Jönsson 2007, Morosini et al. 2009, Rahm and Enachescu 2004, Svensson et al. 2007, Thur et al. 2007, Walger et al. 2007/. Interference test data involving observations in KLX27A /Enachescu et al. 2008b/ were not available.

Some of these tests have been of fairly short duration (a day up to a few days) and involving only a few observation sections in boreholes. However, some tests have employed both a long duration and involved several observation (monitoring) sections, thus of interest from the current flow modelling work point of view. In Appendix 1, several of the more interesting interference tests are described and analysed.

Two of the interference tests were chosen for model testing and calibration as the number of observation sections is fairly large, the pumping durations fairly long and as the tests were situated in two areas of interest for a possible deep repository. The two interference tests are here referred to as the HLX28 and the HLX33 interference test, respectively.

5.3 Interference test HLX33

5.3.1 Tested HCD

The HLX33 interference test focuses on testing the character of the deformation zone ZSMEW007A, cf Figure 5-2.

A few single-hole and cross-hole (interference) tests have been performed along the interpreted surface outcrop of deformation zone ZSMEW007A, cf Figure 5-2, and provided insight in the geometry and hydraulic character of the zone. These tests support the geological interpretation of the structure dipping towards the north, as described in Appendix 1. For instance, an earlier made pumping test in HLX10, cf Appendix A.1.7, shows a very clear responses in one of the monitoring sections in KLX02 (borehole length c. 200–300 m). This fits well with the geologically interpreted geometry of the zone ZSMEW007A /Wahlgren et al. 2008/, as the zone ZSMEW007A is interpreted to be a feature more conductive than the surrounding rock.

Early interference tests using KLX02 as pumping hole provides insight in the geometry of deformation zone ZSMEW007A. Interference tests performed between 1992–1995 involving pumping of the entire length of KLX02 (201–1,700 m) indicated hydraulic responses in KLX01 (mainly below 700 m borehole length) /Ekman 2001/. A closer look at KLX02 /Andersson et al. 2002/ indicated that in KLX02 borehole section 200–400 m the flowing features were oriented in WNW-NW and that the transmissivity in the upper 500 m of KLX02 was considerably higher than below 500 m. These observations indicate that ZSMEW007A may be one of the important structures providing hydraulic connection between KLX02 and the lower part of KLX01. Furthermore, the deformation zone model /Wahlgren et al. 2008/ projects that KLX01 should intersect ZSMEW007A between 1,000–1,020 m borehole length.

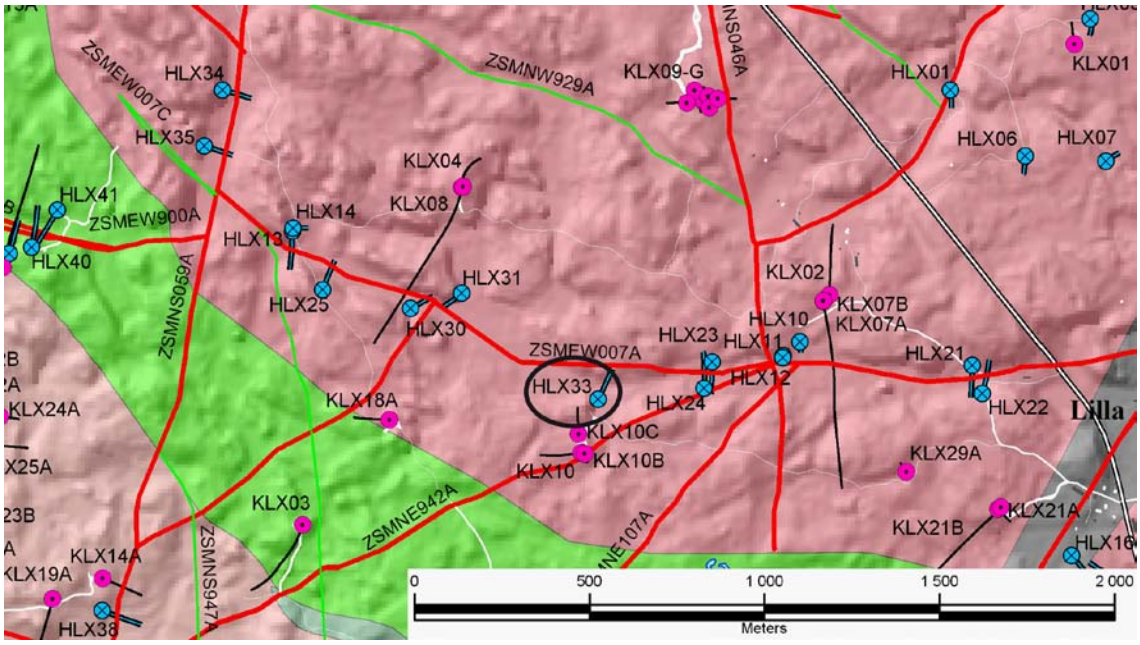

Figure 5-2. *Overview of boreholes involved in the interference test run in June–August 2006 using HLX33 as pumping borehole. The projected trajectories of the cored boreholes are shown as black lines. Rock domains shown in background, cf Figure 3-8.*

Later tests during the site investigations provide additional verification that the hydraulic features along ZSMEW007A should be steep, striking approximately E-W. The reason for this conclusion is the distribution of responses along borehole KLX07A when borehole HLX33 was pumped. As there were no responses in the deeper part of KLX07A, there exist no indications of splays to ZSMEW007A (or other conductive zones dipping south being in hydraulic contact with ZSMEW007A) dipping to the south. Later, pumping tests along KLX07A confirmed this picture as a pumping of the deeper sections in KLX07A did not seem to generate hydraulic responses towards the north.

5.3.2 Test description

Two pumping tests were performed in HLX33, one of which is used for the calibration in this work as there were more observation sections available.

The HLX33 interference test used for calibration was performed between June 28th 2006 and August 7th 2006 (c. 40 days; 960.7 hrs) with HLX33 as the pumping well. Hydraulic observations were made in boreholes (the number of sections is shown within parentheses): HLX11 (2), HLX23 (2), HLX24 (2), HLX25 (2), HLX30 (2), HLX31 (1), HLX33 (1), KLX02 (8), KLX04 (8), KLX07A (8) and KLX07B (2).

The pumping of HLX33 was performed in the borehole interval 9.0–202.1 m with a final flow rate of Q_p = 1.62 L/s and a final drawdown of s_p = 13.46 m in the pumping well. HLX33 is a borehole with a high transmissivity and is judged to be well connected to the deformation zone ZSMEW007 /Morosini et al. 2009/.

The pumping of HLX33 was influenced by the simultaneous pumping of HLX14, which was used for drilling-water supply to ongoing drilling of boreholes. The pumping of HLX14 started May 22nd 2006, i.e. c. 40 days before the start of the pumping of HLX33. The flow rate of the pumping of HLX14 was c. 0.82 L/s with a sudden increase to 0.92 L/s on June 27th 2006. The pumping in HLX14 was stopped on October 27th 2006.

Calculated response indexes are shown in Figure 5-3 and a distance-drawdown plot is presented in Figure 5-4. In Figure 5-3 the size of the discs along the boreholes indicates the magnitude of the index and lack of response is indicated with a grey sphere. The larger the index value, the better the hydraulic contact can be anticipated. The pumped borehole is also indicated by a disc, which is black if the response index is not plotted.

As can be seen, no responses are seen in the lower parts of KLX07A and KLX02. More details of the interference test are provided in Appendix 1.

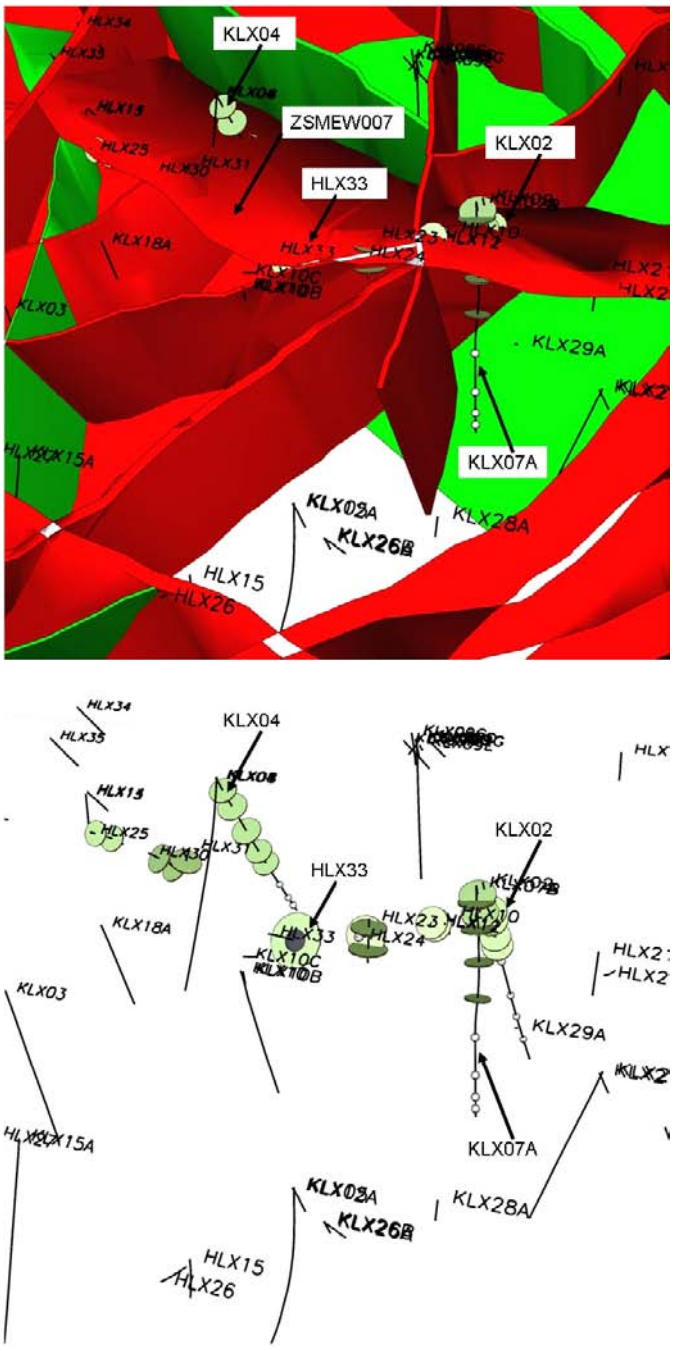

Figure 5-3. *Test in June–August 2006 with HLX33 as pumping borehole. Top of figures: north part of local model area, view from SSE. Response indexes are mapped on the boreholes. Pumping hole plotted as a black disc. The larger the disc (green) for a response index is, the better hydraulic contact with pumped borehole section can be assumed. No response is indicated by a grey sphere. A borehole without discs or spheres have not been measured. Deformation zones have been removed in lower figure to enable display of responses. (Index 2 shown: (s_p/Q_p), cf Appendix 1.)*

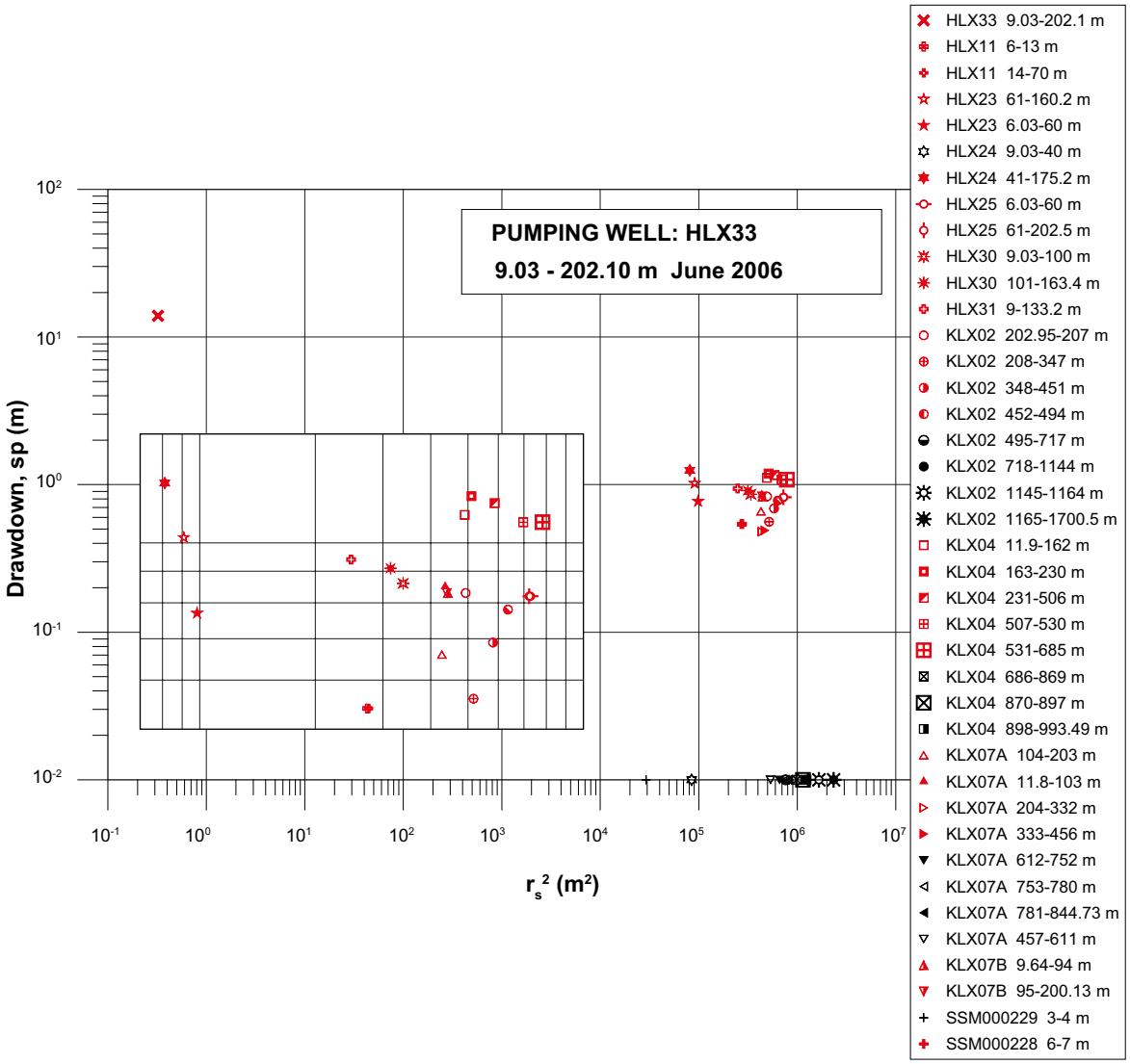

Figure 5-4. *Distance-drawdown plot (including blow-up) related to June–August 2006 interference test with HLX33 as pumping borehole. Drawdown at pump stop is shown. No response is plotted as a 0.02 m drawdown with black symbols, cf lower right of main plot.)*

5.4 Interference test HLX28

5.4.1 Tested HCDs

The HLX28 interference test focuses on testing the character of the HCDs near HLX28; (ZSMEW42A, ZSMNS001C, ZSMNS059A, KLX19_DZ5-8_dolerite and HLX28_DZ1 cf Figure 5-5) The last two HCDs can not be seen in the figure as they are modelled as subsurface discs without surface outcrops.

Deformation zone ZSMNS001C is of particular interest since it is associated with a dolerite dyke, and as such, a potential hydraulic barrier as thicker dolerite dykes are expected to be low-conductive, cf Section 4.1.2. As reported in Appendix 1, two earlier pumping tests were conducted in KLX20A verifying the expected character and behaviour of the dolerite dyke. Due to some practical considerations; KLX19A was also pumped during the same period as the tests in KLX20A, cf Figure 5-5 for location of boreholes, which however also confirms the barrier character of ZSMNS001C, cf Appendix 1. During these tests, observations were made in two packed-off percussion boreholes; HLX37 and HLX43, cf Figure 5-5. It is concluded from the responses that ZSMNS001C must have a tight core but permeable flanking wall rock on either side, at least in the southern part of ZSMNS001C near KLX20A see Appendix 1 for further details.

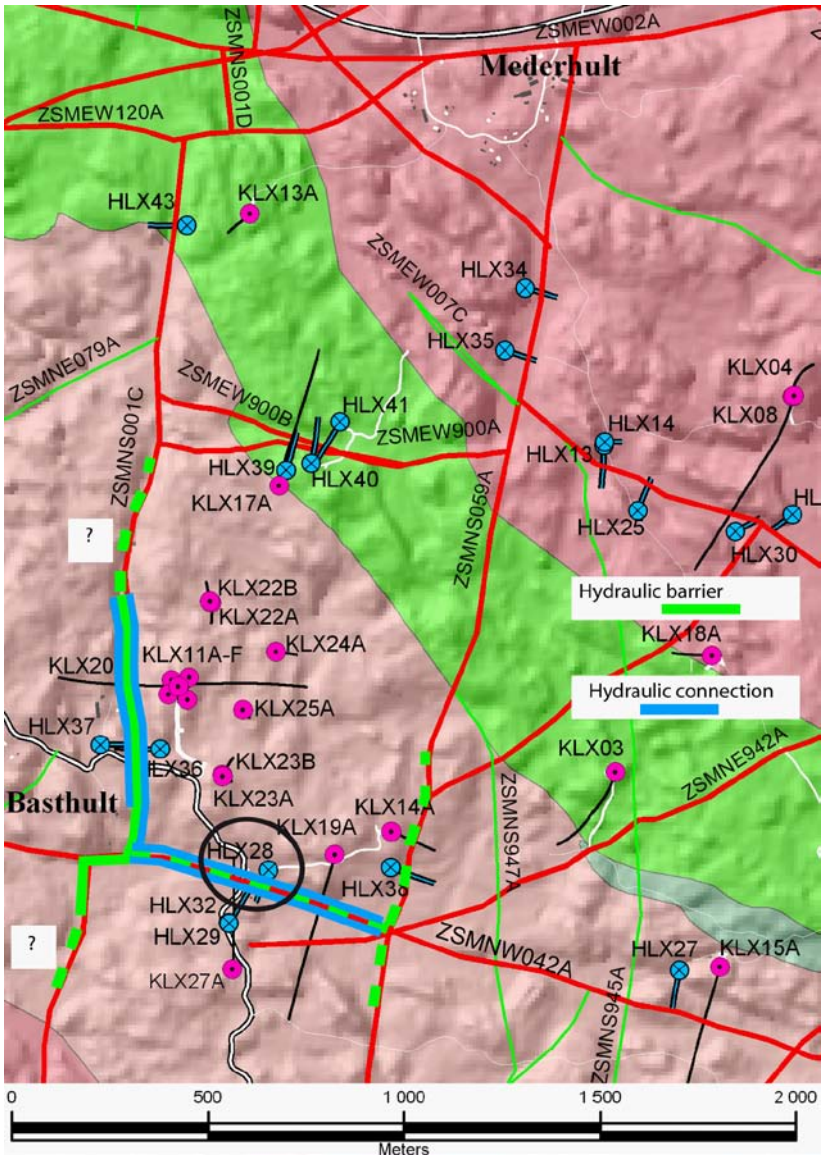

Figure 5-5. *Overview of boreholes involved in the interference test run in April 2007 using HLX28 as pumping borehole. KLX20A intersects ZSMNS01, KLX14A intersects ZSM059A and KLX19A, HLX27A and others intersects ZSMNW042A. The borehole trajectories of the cored boreholes are shown as lack lines. The background colour shows the rock domains, cf Figure 3-8.*

5.4.2 Test description

The HLX28 interference test was performed between April 5th 2007 and April 10th 2007 (c. 4.75 days) with HLX28 as the pumping well. Hydraulic observations were made in boreholes (the number of sections is show within parentheses): KLX19A (8), KLX20A (1), KLX14A (3), HLX32 (1), HLX36 (2), HLX37 (3) and HLX38 (1).

HLX28 is a borehole of high transmissivity and is interpreted to be hydraulically well connected to deformation zone ZSMNW042A, although not directly intersecting the zone. The pumping of HLX28 was performed in the borehole interval 6.03–154.2 m with a final flow rate of Q_p = 1.6 L/s and a final drawdown of s_p = 11.1 m in the pumping well /Harrström et al. 2007/.

The calculated response-indexes are shown in Figure 5-6 and a distance drawdown plot in Figure 5-7. There are clear responses in the uppermost section in KLX14A, KLX19A (sections between 98.8 to 517 m borehole length), KLX20A (open borehole conditions), HLX37 (two bottom sections), HLX36 and in HLX28. There are small responses in HLX32 and HLX38, but no responses in KLX14A (two lowest sections), KLX19A (two lowest sections) and HLX37 (uppermost section).

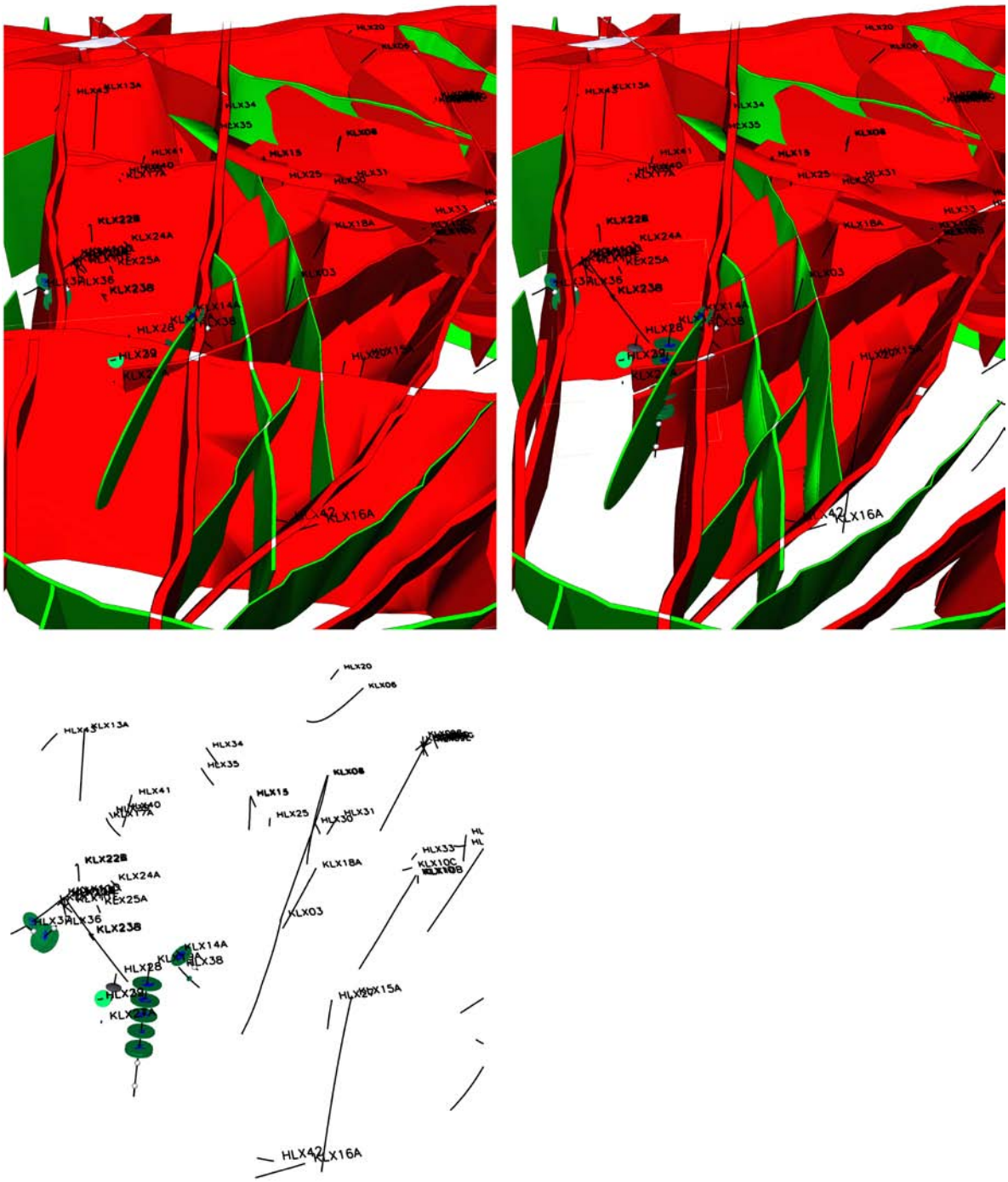

Figure 5-6. *Test in April 2007 using HLX28 as pumping borehole. Top of figures: west part of local model area, view from S. Response indexes are mapped on the boreholes. Pumping hole plotted as a black disc. The larger the disc (green) for a response index is, the better hydraulic contact with pumped borehole section can be assumed. No response is indicated by a grey sphere. A borehole without discs or spheres have not been measured. Deformation zone ZSMNW042A and HLX28_DZ1 (a subhorizontal disc intersection HLX28) are removed in the upper right figure to better show responses. Deformation zones have been removed in lower figure to enable display of responses. A steeply dipping dolerite dyke striking NNE intersects KLX19A below the responses in the borehole.*

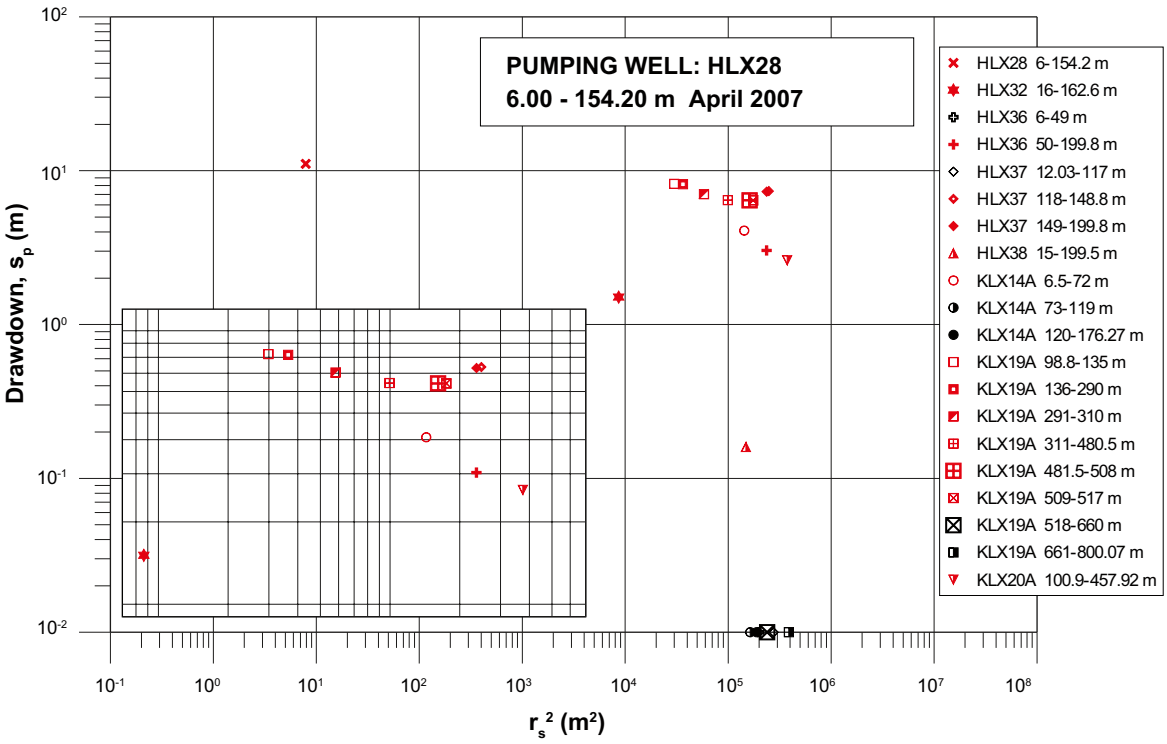

Figure 5-7. *Distance-drawdown plot (including blow-up) of April 2007 test using HLX28 as a pumping borehole. Drawdown at pump stop is shown. No response is plotted as 0.02 m drawdown with black symbols, cf lower right of main plot.*

The test demonstrates that ZSMNS001C acts as a hydraulic barrier (due to the lack of response in the uppermost section in HLX37, situated west of the dolerite dyke). These responses also indicate that the deformation zone HLX28_DZ1, intersecting HLX28 (cannot be seen in the Figure 5-5 as it is modelled as a disc without surface outcrop), is probably not intersecting ZSMNS001C for the same reason. It also appears that ZSMNS059A acts as a hydraulic barrier due to the poor response in KLX14A east of the zone and that also that the lower dolerite dyke in KLX19A (Part of HCD KLX19_DZ5-8, cf Section 4.1.2) acts as a barrier as no response is seen in observation boreholes east of this dyke. The small responses south of ZSMNW042A in HLX32 also indicated that ZSMNW042A acts as a barrier to some extent, at least in its western part,

Possibly both HLX28_DZ1 and ZSMNW042 transmit the hydraulic response to the eastern part of ZSMNS001C.

More details on the HLX28 interference test are reported in Appendix 1.

5.5 Groundwater level monitoring – site investigation

The monitoring of the variation in groundwater levels is carried out within the groundwater monitoring programme, which is one of the activities performed within the site investigation in the Laxemar-Simpevarp area. The overall objective of the groundwater monitoring programme is to further support the hydrogeological characterisation of the area and to document base-line groundwater conditions before the possible excavation of a final repository. The monitoring data are stored in the Sicada data base and are reported regularly in progress reports, see e.g. /Nyberg et al. 2005, Nyberg and Wass 2005, 2007a, b, 2008/.

The groundwater monitoring programme related to the current site investigation programme started December 2002 and the number of boreholes monitored has continuously increased during the course of the site investigations. The number of monitored boreholes are shown in Figure 3-3 through Figure 3-6 indicate the cored boreholes, percussion boreholes and groundwater monitoring wells (the SSM boreholes in Quaternary deposits). Note: Boreholes located on the Äspö island are not part of the site investigation programme and are thus not included in Table 5-3 but are shown in the figures mentioned above.

5.5.1 Instrumentation

The boreholes in the Laxemar-Simpevarp area have generally been equipped with monitoring devices to collect data at regular intervals. In percussion boreholes and cored boreholes, single- or multiple-packer systems have been installed to facilitate monitoring of groundwater levels at different depths.

Table 5-4 shows the maximum number of sections that can be installed in each type of borehole. If circulation sections (requiring two hoses) are excluded, a few more sections for water levels (groundwater pressure) can be installed. The actual instrumentation of a borehole depends on interpreted geology and hydrogeology along the borehole and the overall purpose with the borehole.

Figure 5-8 and Figure 5-9 illustrate the monitoring principles in cored boreholes, percussion boreholes and groundwater monitoring wells. The monitoring sections are numbered sequentially from the bottom of the borehole and upwards. For example, the borehole HAV06 has two monitoring sections: HAV06:1 and HAV06:2.

Table 5-3. Monitored boreholes in the Laxemar-Simpevarp regional model area (August 2007), cf /Nyberg et al. 2005, Nyberg and Wass 2005, 2007a, b, 2008/.

Time Period	Object	Maximum number of boreboreholes	Maximum number of monitored sections
November 2004 to June 2005	Core-drilled boreholes	14	53
	Percussion-drilled boreholes	29	43
	Groundwater monitoring wells	21	21
July 2005 to December 2006	Core-drilled boreholes	35	134
	Percussion-drilled boreholes	44	63
	Groundwater monitoring wells	66	66
January 2007 to August 2007	Core-drilled boreholes	35	155
	Percussion-drilled boreholes	43	62
	Groundwater monitoring wells	70	70
September 2007 to September 2008	Core-drilled boreholes	40	211
	Percussion-drilled boreholes	41	73
	Groundwater monitoring wells	70	70

Table 5-4. Monitored boreholes within the Laxemar-Simpevarp regional area. Maximum monitored sections as standard.

Object	Open sections for measuring groundwater levels	Closed sections for measuring groundwater levels	Sections for circulation or water sampling
Core-drilled boreholes (Telescoped drilled: upper wide part and diameter 76 mm lower part)	1	9	2
Percussion-drilled boreholes (diameter 140 mm)	1	3	1
Groundwater monitoring wells	1	0	1

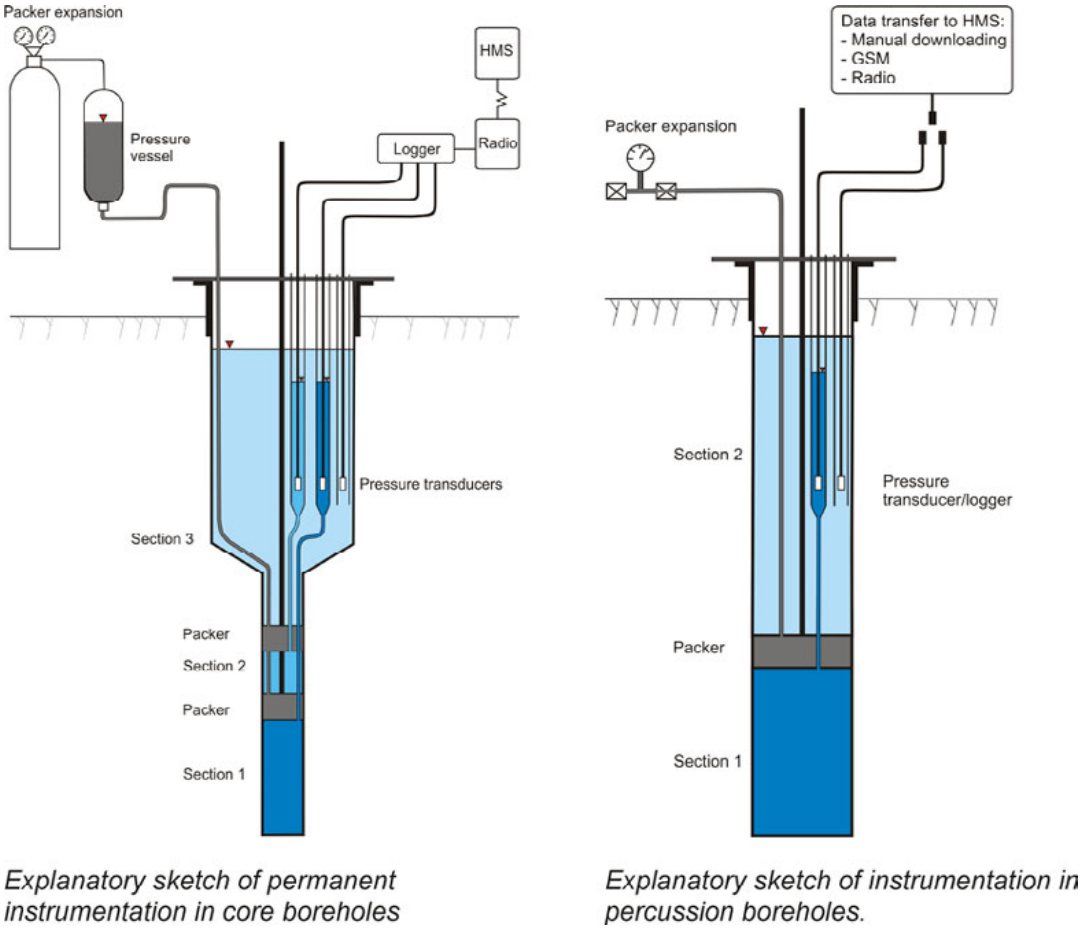

Figure 5-8. *Instrumentation in cored boreholes and percussion boreholes /Nyberg and Wass 2007b/.*

When the packers are installed, the fluid density of the water in the standpipes from the packed of measurement sections is estimated in the following way:

1. The system of packers is lowered into the borehole and the packers are inflated.
2. Each packer interval in the cored and percussion borehole is equipped with a standpipe (piezometer tube). The tubes and the groundwater monitoring wells are pumped until a stable level of the electrical conductivity of the pumped water is reached, but at least three times the volume of the groundwater monitoring well or the standpipe down to the measurement section in core or percussion boreholes.
3. A water sample is taken for a laboratory determination of the water density and the EC of the abstracted water. The laboratory determinations are made at 25°C. Therefore, the field water temperature is also documented.
4. If the water yield of packed-off section is very low (as indicated by hydraulic tests), the piezometer stand pipe is pumped before the packers are inflated. This means that probably the EC measured and sample taken is not representative for the formation water at the depth for such a pack-off section, but is relevant for estimating the pressure in the packed-off sections from level measurements in the standpipes.

The actual instrumentation of a borehole depends on interpreted geology and hydrogeology along the borehole and purpose with the borehole.

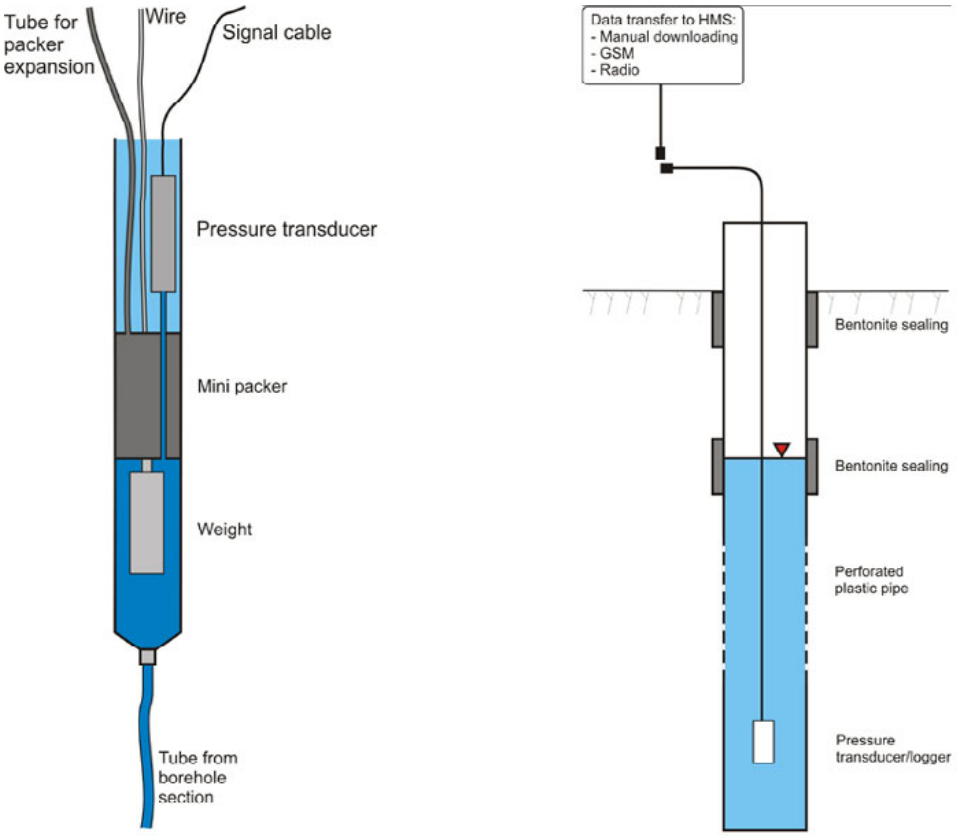

Explanatory sketch of instrumentation in standpipes in core and percussion boreholes.

Explanatory sketch of instrumentation in groundwater monitoring wells.

Figure 5-9. *Instrumentation in standpipes (in percussion and core boreholes) and groundwater monitoring wells (in Quaternary deposits) (Groundwater monitoring wells also called "soil stand pipes" in some reports.) /Nyberg and Wass 2007b/.*

5.5.2 Data collection and calibration

The HMS (Hydro Monitoring System) consists of two measurement stations (computers) which communicate with and collect data from a number of dataloggers. The computers are connected to the SKB Ethernet LAN. All data are collected by means of different transducers connected to different types of data loggers: Minitroll, LevelTroll, Mitec and Datataker /Nyberg and Wass 2007b/.

Manual levelling of all sections is made, normally once every month, in order to calibrate registrations from the data loggers. The logger data are converted to water levels using calibration constants. All collected data are subjected to a quality check, during which obviously erroneous data are removed and calibration constants are corrected such that the monitored data are consistent with the manual levelling. When manual levelling is made, the status of the equipment is also controlled and service may be initiated /Nyberg and Wass 2007b/.

Measurements of the groundwater level are normally made with one-minute intervals for percussion and core boreholes and with five-minute intervals for soil wells. Measured values are not stored unless they differ from the previously stored value by more than 0.1 m for percussion and core boreholes, and 0.05 m for soil wells. In addition to this, a value is always stored every two hours. However, in some boreholes the recording intervals are shortened since they are located in areas of high interest /Nyberg and Wass 2007b/.

The way the groundwater levels are measured imply that they generally represent so called pointwater heads, cf Appendix 3.

5.5.3 Groundwater levels

Monitoring data from groundwater monitoring wells completed in Quaternary deposits are presented in /Werner et al. 2008/, covering meteorological, hydrological and hydrogeological monitoring as well as near-surface hydrogeological properties. The data set for groundwater levels spans the period December 4th 2002 to December 31st 2007 for groundwater monitoring wells in Quaternary deposits and January 1st 2004 to December 31st 2007 for cored and percussion-drilled boreholes, i.e. three months after Laxemar data freeze 2.3. In order to estimate natural (undisturbed) groundwater levels, data were screened to remove periods with hydraulic disturbances due to e.g. drilling or hydraulic testing (data were not screened for the period 1st Sept.–31st Dec. 2007, as it was judged that the potential disturbance after data freeze i August 2007 was assumed to be small.). For details on the screening, see /Werner et al. 2008/. Some of the screened time series are rather short, which may imply that the min, max, and average values of pointwater heads re uncertain (ideally at least one annual cycle should be available). Therefore, borehole sections with 150 data days or more (i.e. more than c. five data months) have generally been used for calibration of the current flow model. The measured head data are considered representing the section mid-elevations, which are calculated simply as the average of the upper and lower section elevations.

Figure 5-10 through Figure 5-13 show the groundwater monitoring wells co-plotted with the interpreted Quaternary deposits and corresponding depths to illustrate the environment for the monitoring.

Groundwater levels in groundwater monitoring wells

The groundwater levels in Quarternary deposits, as measured in groundwater monitoring wells in Laxemar, are shown in Figure 4-17 and Figure 5-14 (cf /Werner et al. 2008/ for boreholes on Ävrö and Simpevarp peninsula). According to the performed slug tests in the groundwater monitoring wells where the well screen is located in the till or sand/gravel (i.e. strata located directly on top of the bedrock), the dataset can be divided into two groups:

- Groundwater monitoring wells located in Quaternary deposits with hydraulic conductivity of c. 10^{-6} to 10^{-5} m/s.
- Groundwater monitoring wells located in more permeable Quaternary deposits with hydraulic conductivity of c. 10^{-4} to 10^{-3} m/s. These include SSM15, 16, 18, 31, 215, 220, 221 (due to very high hydraulic conductivity in SSM223–225, the response was too fast for an evaluation of the slug test), 226, 228, 230, 238, 239, 240, 243, 244, 252, 256, 260, 262, 263, 265, 267, 268 and 270.

Only a few of the SSM groundwater monitoring wells have their well screen located in the transition zone between the Quaternary deposits and the bedrock (SSM10, 20, 42, 13, 16, 251, 260, and 263–269). However, there is no general indication in the data from these standpipes suggesting the presence of a tight layer preventing a good contact between the quaternary deposits and the bedrock.

Groundwater levels in percussion and core boreholes

In Figure 4-18 and Figure 5-15 the groundwater levels in rock in the percussion drilled boreholes and cored boreholes in Laxemar are shown (cf /Werner et al. 2008/ for boreholes on Ävrö and Simpevarp peninsula). In total data from 44 percussion boreholes and 37 core boreholes were available. The number of monitored observations sections has varied; at the time of data freeze Laxemar 2.3 in August 31st 2007 some 37 percussion borehole sections and 132 sections in cored boreholes were being monitored and in December 31st the corresponding figures were 35 and 120 respectively.

For the SDM-Site Laxemar regional scale modelling, data from 31 cored boreholes distributed between different areas have been obtained:

- 27 boreholes in Laxemar (KLX02–06, 07A–B, 08–10, 11A–18A, 11E, 20A, 21B, 23A, 24A and 26A–28A).
- 2 boreholes at Simpevarp (KSH01A and KSH02).
- 2 boreholes at Ävrö (KAV01 and KSH04A).

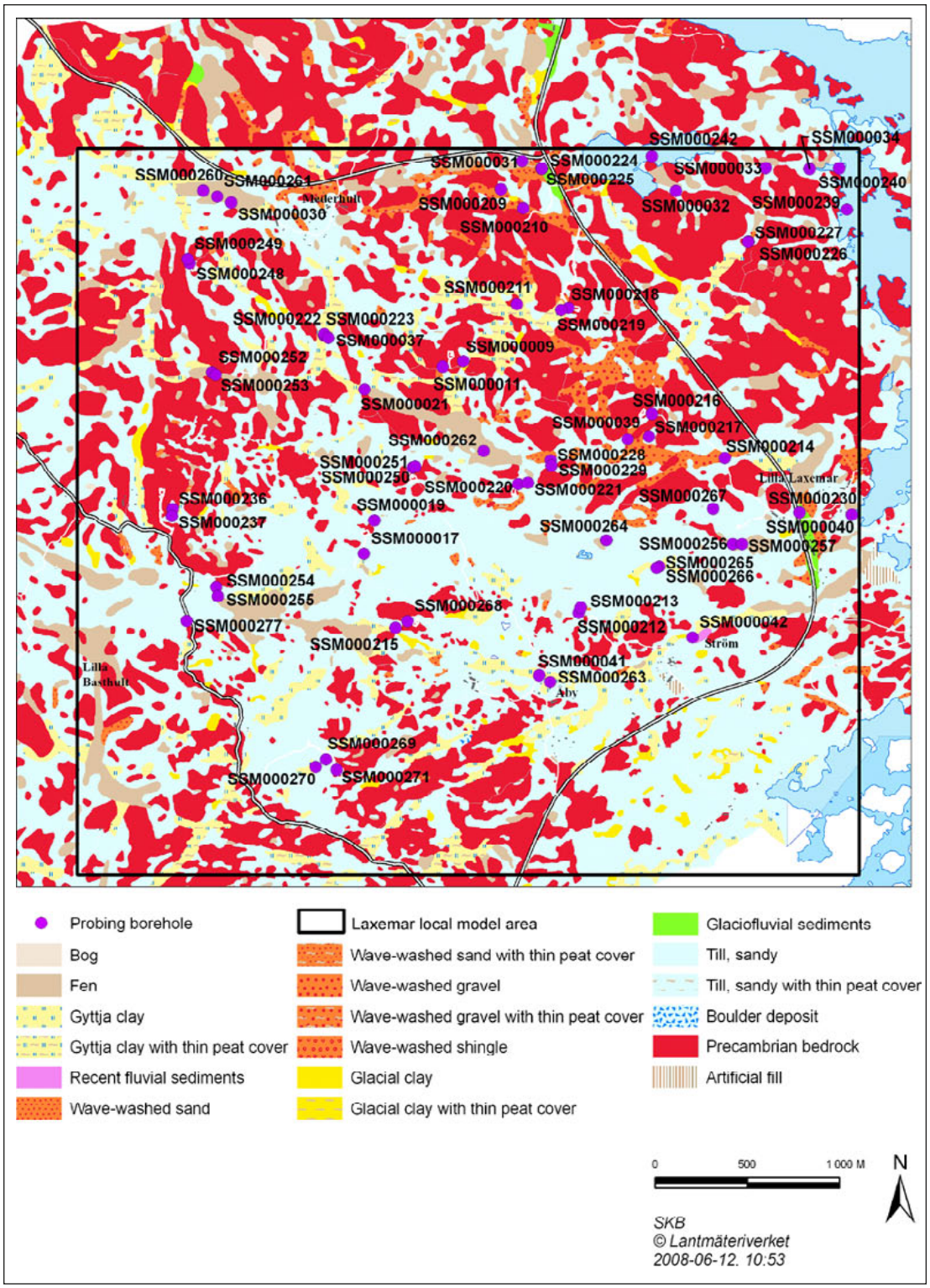

Figure 5-10. *Plot of SSM groundwater monitoring wells at Laxemar, inside the SDM-Site Laxemar local model area superimposed on the map of Quaternary deposits, see also Figure 5-12.*

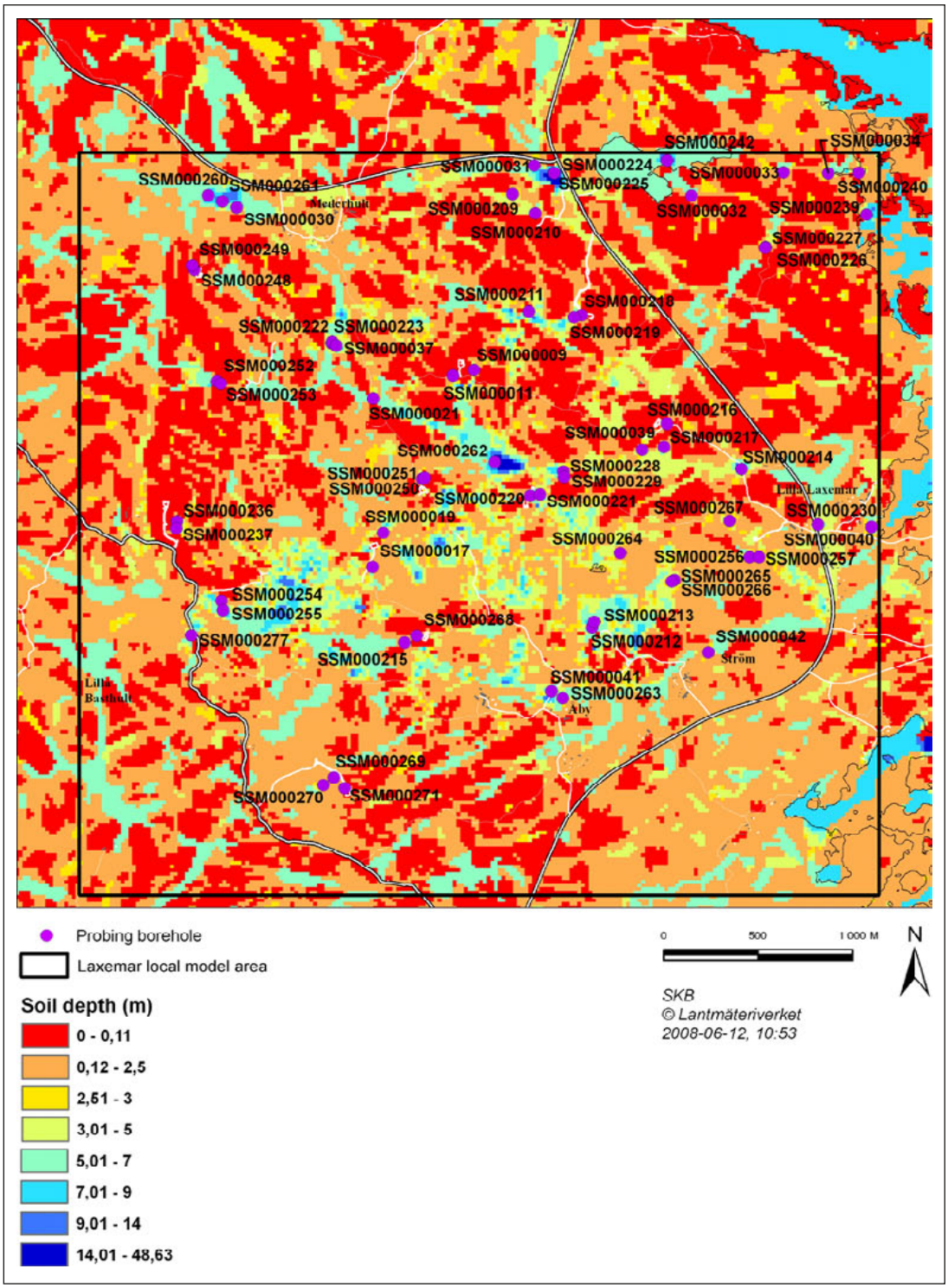

Figure 5-11. *Plot of SSM groundwater monitoring wells at Laxemar, inside the SDM-Site Laxemar local model area superimposed on the map of thickness of Quaternary deposits, see also Figure 5-13.*

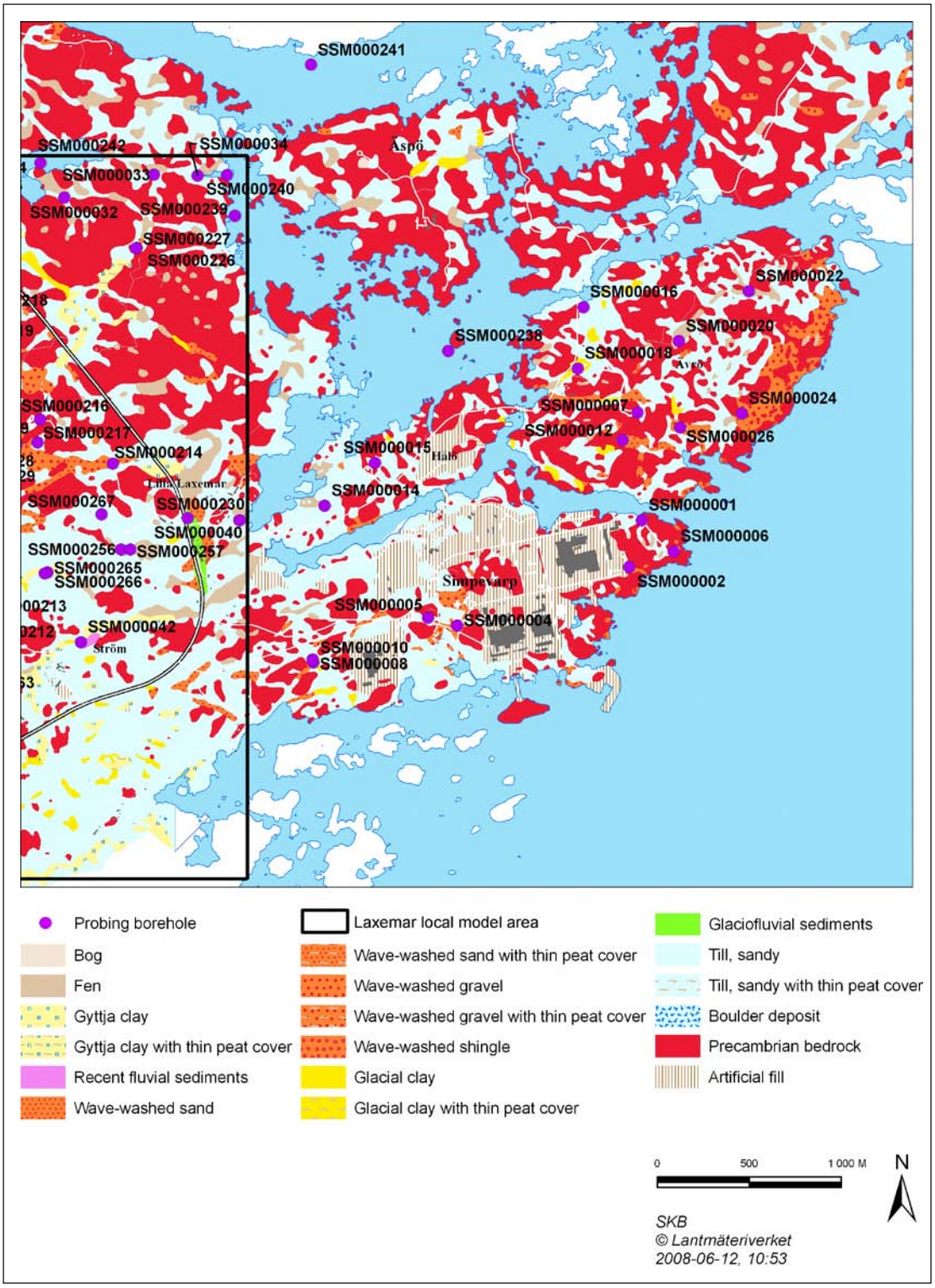

Figure 5-12. *Plot of SSM groundwater monitoring wells at Simpevarp, Ävrö and Hålö superimposed on the map of Quaternary deposits, outside the SDM-Site Laxemar local model area, see also Figure 5-10.*

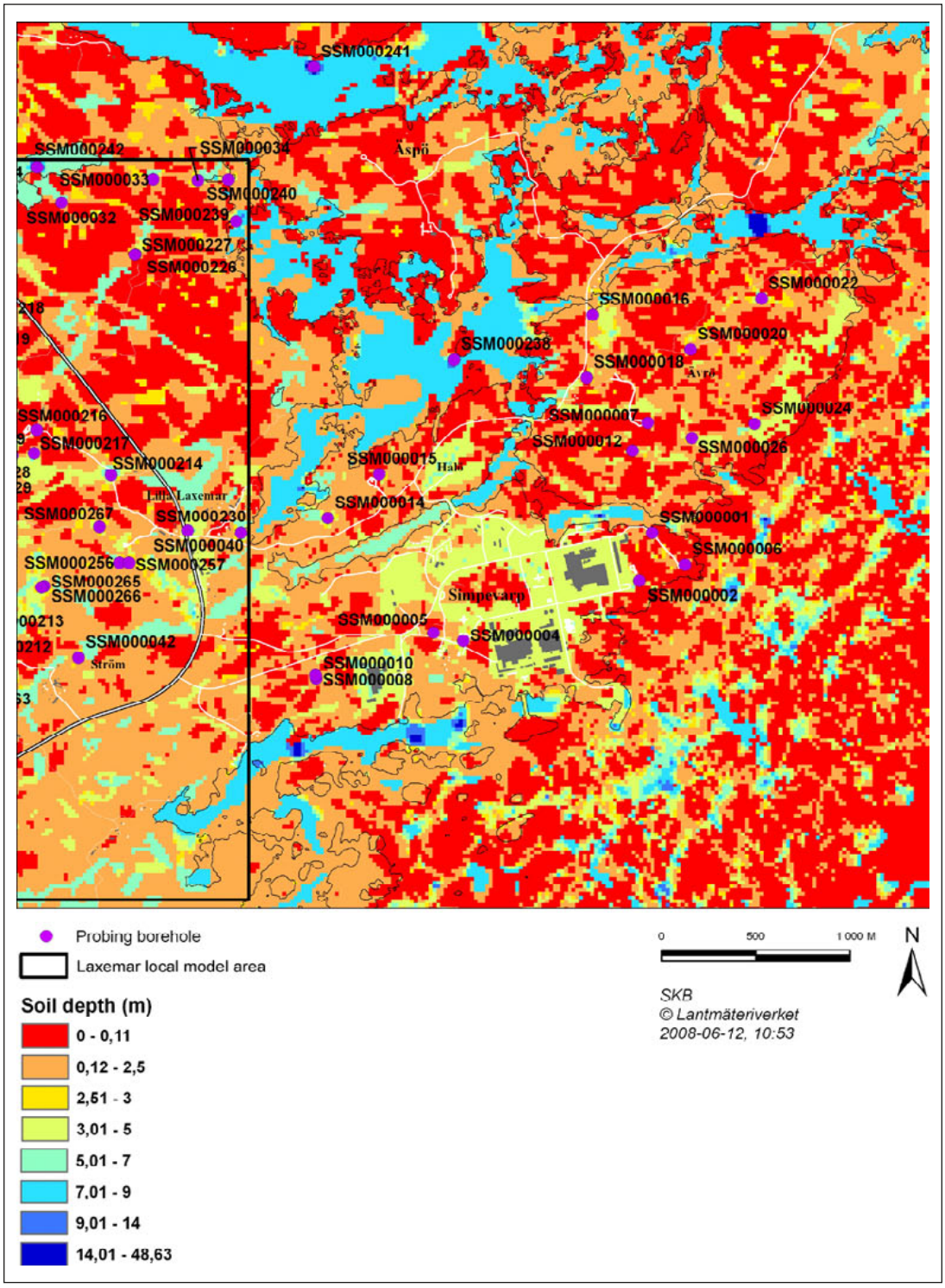

Figure 5-13. *Plot of SSM groundwater monitoring wells at Simpevarp, Ävrö and Hålö superimposed on the map of the thickness of the Quaternary deposits, outside the SDM-Site Laxemar local model area, see also Figure 5-11.*

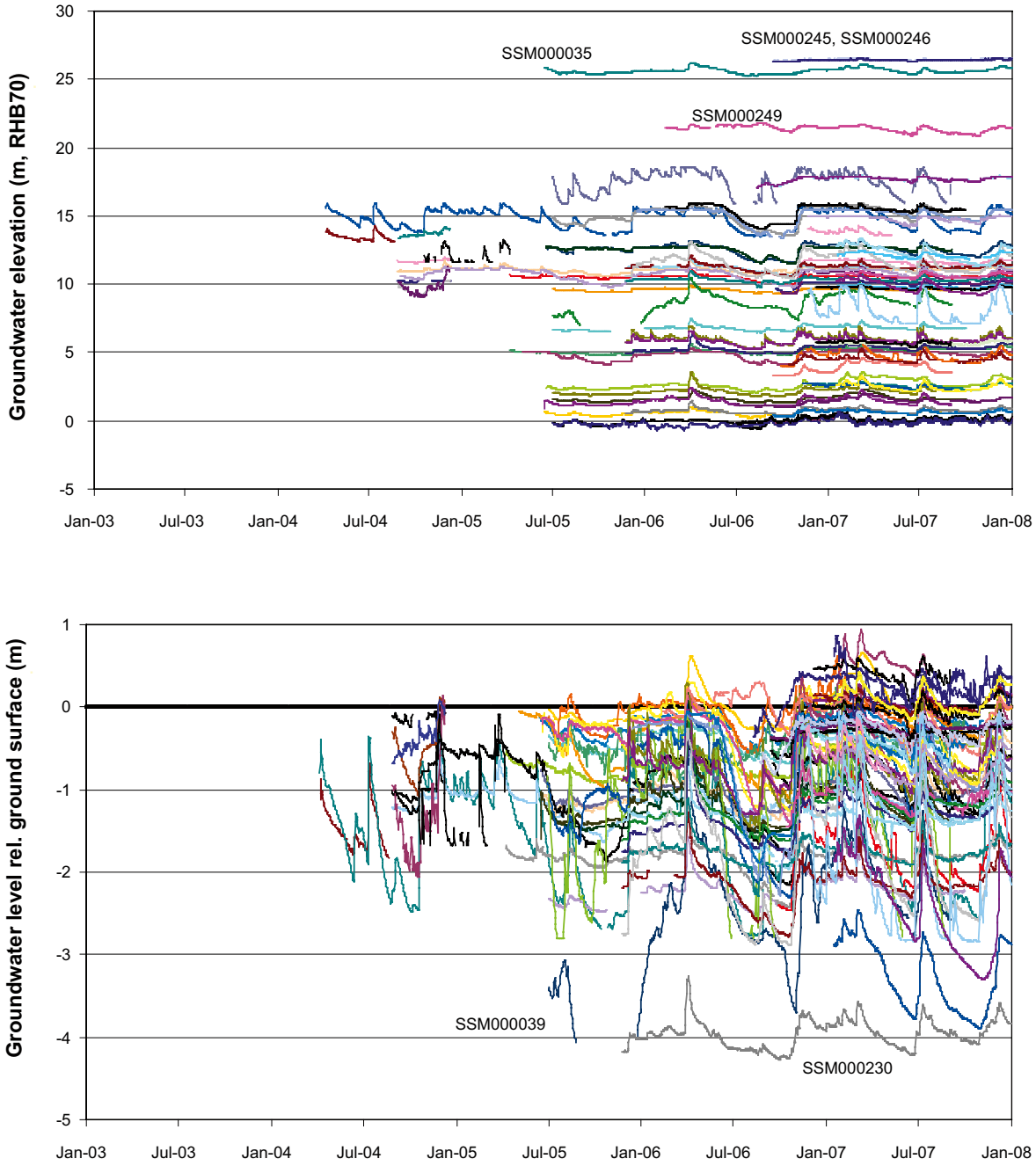

Figure 5-14. *Groundwater levels (daily mean) in Laxemar local model area – screened data. Monitoring wells in Quaternary deposits. Top: Groundwater levels (m.a.s.l.). Bottom: Groundwater levels (m.a.g.s.) /Werner et al. 2008/.*

These boreholes are equipped with multiple-packer systems, dividing them into sections (borehole section numbering starting from the bottom). Groundwater densities have been measured on water sampled from the borehole sections. For some boreholes or borehole sections, there are no density data available. However, in a few of these boreholes electrical conductivity (EC) data are available, and the density was estimated using an empirical relationship /Werner et al. 2008/. When considered appropriate, calculated density values have been used to compensate for missing measured density data /Werner et al. 2008/.

As described in Section 5.5.2 the measured, and stored data value, is the water level in the standpipes, and it represents a *pointwater head (PWH)* (cf Appendix 3) assuming that the density is constant in the standpipe and in the tubes down to the observation section. Assuming that the density in the standpipes represents the density of the formation water at the level of the observation section, it is possible to calculate the *environmental-water head (EWH),* or shorter just *environmental head* (cf Appendix 3) for the section, using the density profile for all sections up to surface, cf Appendix 3. The usefulness of EWH is that along the borehole, the vertical hydraulic gradient can be judged in a medium that is hydraulically well-connected vertically and horizontally. It turns out that generally the difference between EWH and PWH is small but at very deep levels the difference can be significant due to increasing salinity of the groundwater, which renders lower PWH than EWH. As indicated in Section 5.5.1 the pumping of the water in the standpipes may not always provide a density that can be expected to be similar to the formation water at the level of the observations section. This means that densities useful for calculation of EWH must be carefully examined and generally estimated from different sources, e.g. chemical sampling and geophysical logging of fluid electrical conductivity. This has not been possible to do during the site investigations and as a consequence EWH below elevation c. –800 m should not be used for calibration purposes. Therefore these data will not be included in the figures used to present the comparison of the modelled results to measured and calculated heads.

Due to lack of necessary data (such as density data from all sections in a particular borehole), EWH series have been calculated only for 19 of the drilled boreholes (18 cored boreholes and one percussion borehole (HLX21). The calculations show small or no differences between measured PWHs and calculated EWHs. Overall, density compensations were primarily made for the lower-most sections of the boreholes /Werner et al. 2008/.

For the following cored boreholes; KLX04, 11A, 11E, 14A, 16A, 17A, 20A, 21B, 23A, 24A and 26A–28A, only PWH data were delivered and therefore used instead of EWH data in the model calibration: In addition, for KLX04, 21B, 26A and 28A, the delivered data were considered uncertain.

The vertical hydraulic gradient along a borehole can be calculated from the head difference between two consecutive borehole sections. Such calculations indicate that the bedrock near some of the boreholes behave differently. There are boreholes (e.g. KLX09) where there are small or no vertical gradients between all consecutive borehole sections, both in terms of PWH and EWH. In other boreholes (e.g. KLX05), the direction of the hydraulic gradient in terms of PWH can be reversed compared to the direction given by EWH. The calculated EWH suggest that there are no core-drilled boreholes displaying a continuous upward or downward head gradient along the whole length of the borehole.

The yearly amplitude in groundwater head is c. 1.9 m in the percussion boreholes and c. 1.5 m in the cored boreholes, using data with at least a data series of 150 days /Werner et al. 2008/. As can be seen in Figure 4-18 there is a tendency that also the groundwater levels in the percussion boreholes follow the ground surface elevation. One can also see that there are two wells indicating artesian conditions (HLX15 and HLX28).

Figure 5-15 indicates that some pointwater heads are negative. The reason is that the density in the standpipes generally becomes higher than the average formation density in the deep observation sections, as each standpipe from an observation section is pumped and filled with water from that observation section. These cases with higher density in the standpipes compared to average (in a vertical column) formation density, are generally borehole sections below elevation c. –400 m, and high salinity values in the standpipes are generally found below c. –800 m.

The basis for the calibration of the regional groundwater flow model is the mean pointwater head (or environmental head) and in Chapter 6 the min, mean and max pointwater head are presented in monitored percussion boreholes for the time period available. The corresponding data from cored boreholes are exemplified for one borehole only in Chapter 6.

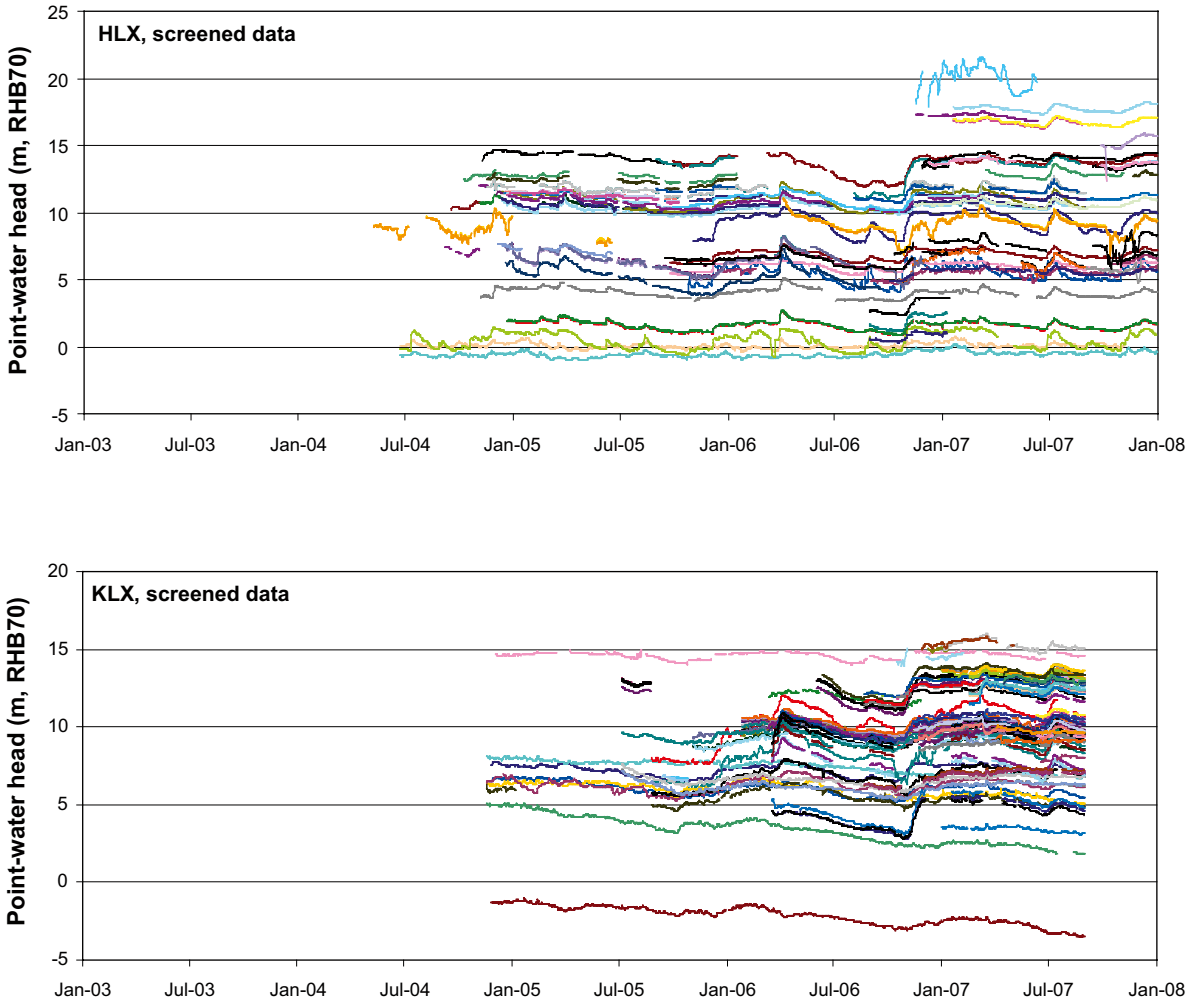

Figure 5-15. *Groundwater levels (daily mean) in Laxemar local model area area – screened data. Monitoring wells in bedrock /Werner et al. 2008/.*

5.6 Hydrogeochemistry

The spatial distribution of some of the hydrogeochemical components can be expected to be strongly linked to the evolution of the groundwater flow system and therefore the hydrogeochemical data can provide insights in the flow system and the modelling of the groundwater flow may mutually provide essential inputs for the discussion of hydrogeochemical processes.

In this section essential data are presented that are useful for the palaeohydrogeological conceptualisation and simulations presented in Section 4.2, Section 7.8.1 and in Chapter 9, respectively. The bedrock hydrogeochemistry of the Laxemar-Simpevarp area is described in detail in /Laaksoharju et al. 2009/.

5.6.1 Hydrochemical data

The hydrochemistry data delivery for SDM-Site Laxemar includes samples collected from bedrock groundwater, near surface groundwater, seawater, lake water, stream water, precipitation, wells, pits, ditches etc.

The hydrochemistry data delivery consists of measurements of major ions, isotopes, porewater data and calculated M3 mixing fractions. The major ions considered in the groundwater flow model calibration are Br, Ca, Cl, HCO_3, Mg, Na, K and SO_4. The two isotopes of interest to hydrogeology are δ^2H and $\delta^{18}O$. Appendix 4 provides a summary of the constituents and boreholes (core-drilled and percussion-drilled boreholes) considered in the model calibration for SDM-Site Laxemar. It should

be mentioned that porewater data were collected in only three boreholes; KLX03, KLX08 and KLX17A. A full list of the constituents encompassed by the hydrochemical programme providing data for SDM-Site Laxemar is given in /Laaksoharju et al. 2009/.

The hydrochemistry data delivery has been sorted into five major categories, where Categories 1 and 2 represent high quality samples, Category 3 intermediate quality samples and Categories 4 and 5 intermediate to low quality samples. The final selection of data that best represent the sampled borehole section (i.e. Categories 1 and 2) is based on:

1. Identifying as near as possible a complete set of major ion and isotope analytical data (particularly δ^2H and $\delta^{18}O$, plus tritium and carbon isotopes when available/suitable).
2. Acceptable charge balance (±10% for surface/shallow waters at < 50 mg/L Cl, deeper groundwaters ±5%).
3. Low drilling water content < 1–5%.
4. Good time-series data coverage.
5. Reliable redox values and, if present.
6. Satisfactory coverage of trace element data (including U, Th and REEs (Rare earth elements)), and dissolved gas, microbe and organic/colloid data.

Appendix 4 provides details on the criteria used for categorisation of samples for core-drilled and percussion-drilled boreholes in all the five categories. Compared to the earlier quality assured datasets related to previous model versions, this modified approach provides a more sensitive subdivision in relation to those data of intermediate to low quality and addresses more closely some of the requirements of the hydrogeological modelling programme. For details on the selection of representative data, cf /Laaksoharju et al. 2009/.

In Table 5-5, the number of samples and the location of sampled data in each category are shown. As can be seen from the table, categories 3 and 4 are important to get some spatial resolution of the hydrochemical data. Category 5 data were not used for comparison of the hydrogeological modelling results presented in Chapter 9. The Category 4 data are discussed in more detail below.

Limiting the selection of data used in the modelling to only those that fulfil criteria such as a low level of drilling water residue and full coverage of major ions and isotopes would leave a large number of samples not used. Some of these samples are found at elevations where data of higher quality are missing. It was therefore decided to use some of Category 4 samples as supplementary data in the SDM-Site Laxemar groundwater flow modelling in order to provide more data for the comparison. Samples with drilling water residue less than 20% and a charge balance less than ±10% were selected, but only if there were no other data available for that particular elevation (Cf Appendix 4 for discussion on how drilling water composition was used to adjust the sample concentrations). Even if all samples were corrected for the drilling water residue (where possible), samples having such high contents of drilling water must be used with great caution and may serve only as indicative data. In Figure 5-16 the drilling water residue and charge balance respectively is shown for all Category 4 data. As can be seen in the figure all data samples except two fulfil the criteria of a drilling water residue less than 20%. All data are within a charge balance of ±10%. The charge balance was calculated using the PHREEQC code.

Table 5-5. Number of samples and location of sampled data in each category in the extended hydrochemistry data freeze Laxemar 2.3.

Category	Number of samples and position
Category 1	3 samples (2 in KLX03, 1 in KSH02)
Category 2	4 samples (1 in KLX05, 1 in KLX08, 1 in KLX15A, 1 in KSH01A)
Category 3	58 samples (11 in percussion-drilled boreholes, 47 in core-drilled boreholes)
Category 4	48 samples (17 in percussion-drilled boreholes, 31 in core-drilled boreholes)
Category 5	322 samples (9 in percussion-drilled boreholes, 313 in core-drilled boreholes)

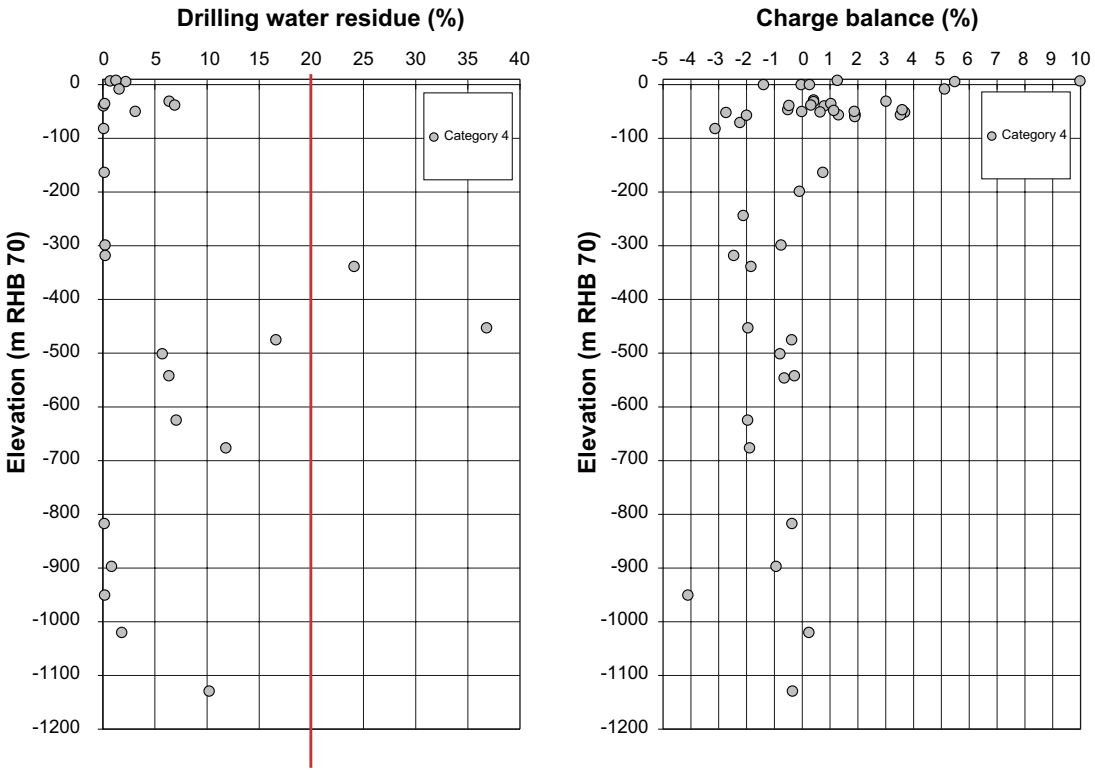

Figure 5-16. *Plot of Drilling water residue and Charge balance respectively for all Category 4 data available in the extended data freeze Laxemar 2.3.*

In the model calibration, cf Chapter 9, data from cored boreholes and percussion boreholes were used. Since the samples from the percussion boreholes are obtained from water pumped from the entire borehole length, they are subject to more disturbances by the sample acquisition.

Salinity

In the present study, the focus is on the results for salinity (expressed as TDS), Cl, Br/Cl-ratio, Na, Ca, Mg, HCO_3 and $\delta^{18}O$. Salinity is a very important natural tracer because variations in salinity lead to one of the driving forces for groundwater flow.

One of the main comparison of the results of the flow model with measured observations is a visual one where the simulated trends of salinity are co-plotted along the boreholes with interpreted field data, cf Chapter 9. The comparison is made in this way, rather than in terms of a quantitative measure defined at the data points.

The salinity for a given water composition in the groundwater flow model is calculated as the sum of the products of each reference water fraction and the salinity of that reference water (i.e. Br, Ca, Cl, HCO_3, K, Mg, Na and SO_4). The modelled salinities were compared with those observed through a visual comparison of the profiles along the boreholes, comparing the trends and major features in the boreholes.

There are different approaches for estimating the total dissolved solids (TDS) in the groundwater (in the following all concentrations are given in mg/L and eletrical conductivty EC in mS/m). A very rough method of calculating the TDS is to simply take the sum of all ions that have been considered in the groundwater flow model:

$$TDS(sum\,of\,ions) = \sum \{Br + Ca + Cl + HCO_3 + K + Mg + Na + SO_4\} \qquad (5\text{-}1)$$

Since chloride is the main anion in the groundwater in Laxemar, a strong correlation between chloride concentrations and groundwater salinity expressed as TDS, is to be expected. This correlation may be used to estimate approximate values of chloride concentrations if TDS is known,

and vice-versa. An empirical relation has been established when analysing groundwater chemistry samples from Forsmark, Laxemar, Simpevarp and Äspö/Ävrö /Auqué et al. 2006/:

$$TDS(Cl) = 1.65 \cdot Cl \qquad (5\text{-}2)$$

The TDS can also be calculated from the electric conductivity (EC) using the following empirical relation based on laboratory measurements during the investigations for Äspö Laboratory /Rhén et al. 1997/:

$$TDS(EC) = (4.67/0.741) \cdot EC \qquad (5\text{-}3)$$

The method used here, which is considered the most accurate for estimating the TDS, makes use of the PHREEQC results of total element contents and calculates the sum of all constituents observed:

$$TDS(PHREEQC) = \sum \begin{Bmatrix} Br + C + Ca + Cl + F + Fe + I + K + Li + \\ Mg + Mn + N + Na + P + S + S(6) + Si + Sr \end{Bmatrix} \qquad (5\text{-}4)$$

In Figure 5-17 a comparison of the different approaches for estimating the TDS is presented. The first three approaches discussed above, as well as the pure chloride fraction, are all compared to the TDS obtained from calculations with the computer software PHREEQC. It is clear that pure chloride concentration and TDS based on chloride consequently are lower than the TDS values calculated with PHREEQC. The TDS calculated from electric conductivity however is generally slightly higher than that obtained from PHREEQC. This is also the case for TDS calculated as the "sum of ions". This discrepancy also depends upon the scale of presentation. In this case, a logarithmic scale is used, which emphasises the differences in the lower end of the range of values. In the model calibration only the TDS values calculated with PHREEQC were used as observation data. As seen in Figure 5-17 this estimate is in the middle of the range of values computed using the different methods presented above.

See Figure 5-18 for a summary plot of all available salinity data for the cored boreholes in Laxemar.

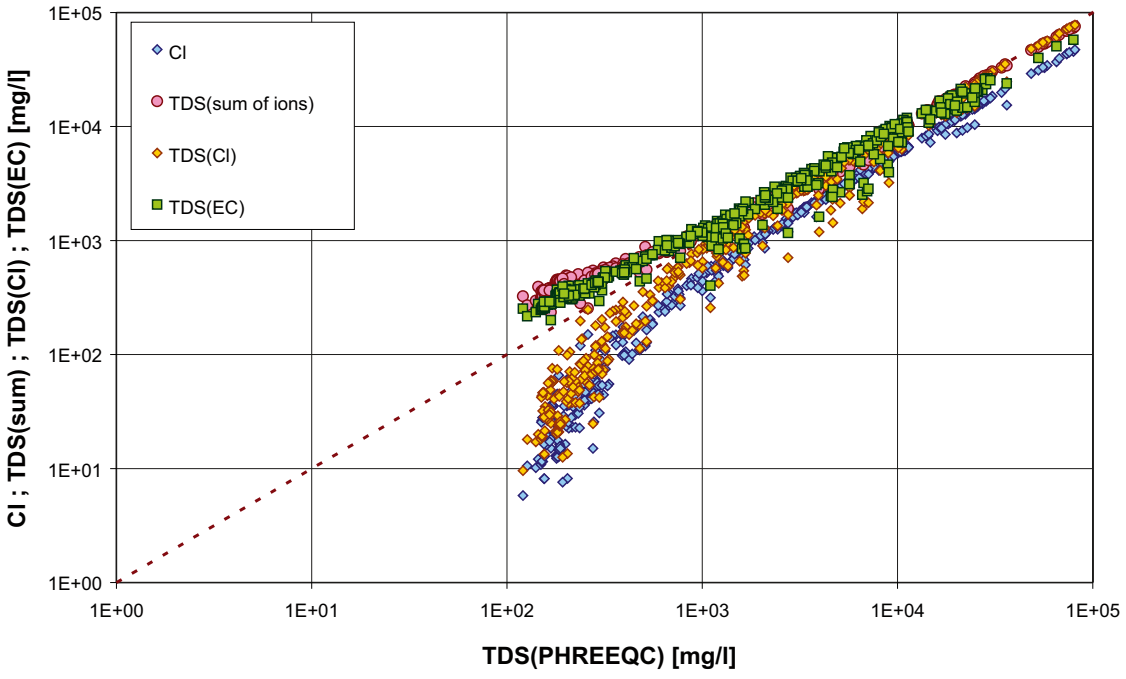

Figure 5-17. *Comparison of four different approaches for estimating the total dissolved solids, TDS, in the groundwater. (TDS values calculated with PHREEQC: TDS(sum of ions)).*

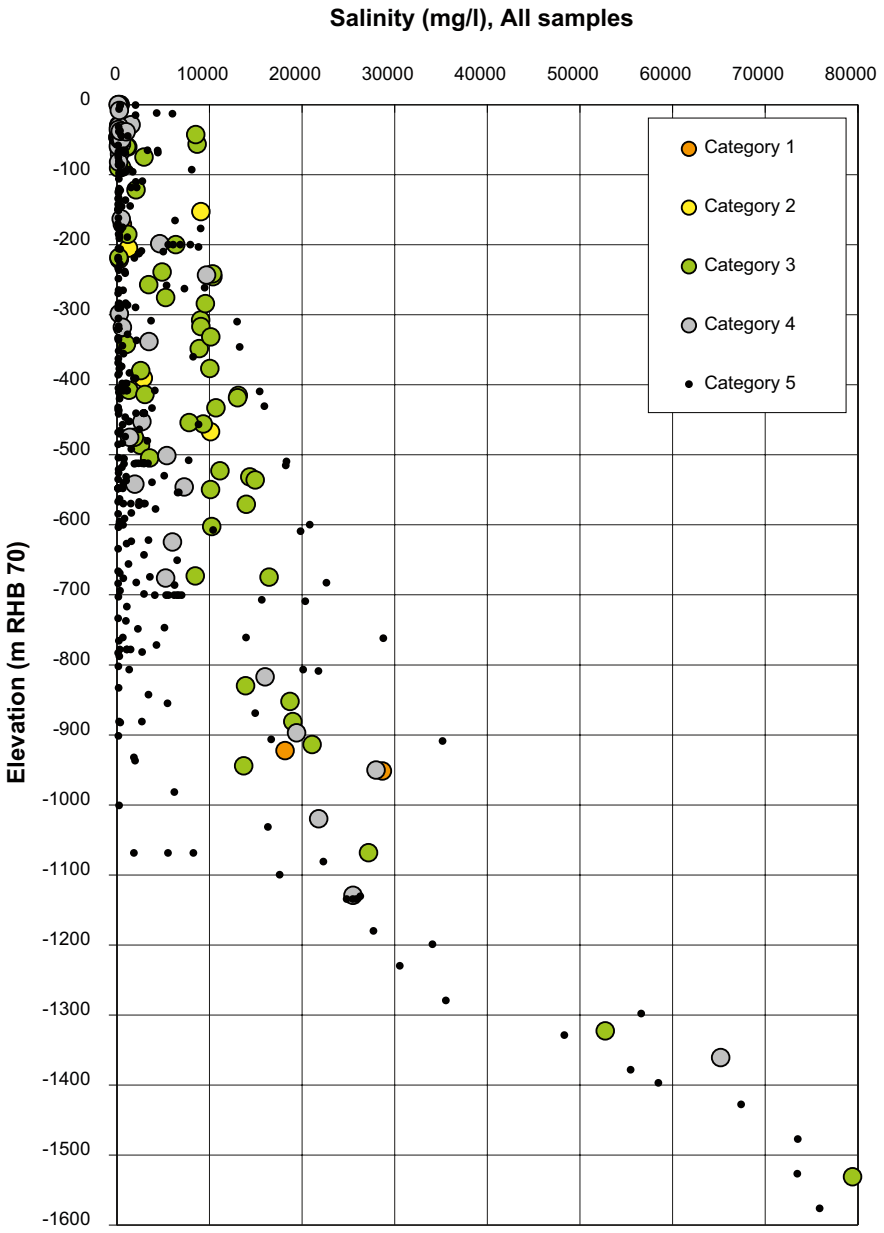

Figure 5-18. *Plot of all available data from the core-drilled boreholes and percussion-drilled boreholes in Laxemar sorted according to quality category. For the sake of comparison, the reference water salinities (TDS)(mg/L) are: Deep Saline Water = 76,291; Inter-glacial Porewater = 280; Glacial Melt Water = 2; Littorina Sea Water = 11,912; Altered Meteoric Water = 452.*

Plotting of data

For ease of presentation, and to allow results for different boreholes to be combined in a unified colour plot to distinguish the values for the different boreholes, a modified scheme is employed here, cf Figures 5-20 to 5-22, and in Chapter 9:

- Fracture water data samples in **Categories 1, 2 and 3** (orange, yellow and green colour coding), considered to be of High or Intermediate quality, were grouped together and indicated by **large filled squares** in the figures.
- Fracture water data samples in **Category 4** (grey colour coding), considered to be of Intermediate to Low quality, were indicated by **small filled circles** in the plots.

The **porewater data** are indicated by **unfilled circles** having the same border colour as is used for that particular borehole (for those boreholes where such data were available).

Because of the assessed hydrogeological diffrences, the boreholes were split into nine main groups for presentation purposes, see Figure 5-19 and Table 5-6. The division of boreholes into different groups was based on the different geological conditions (fracture domains) including judged differences in flow situation (recharge/discharge).

Table 5-6. Suggested division of the boreholes used in the model calibration.

Boreholes (KBH and HBH)	Hydraulic domain/area	Flow direction
KLX(6) + HLX(2)	HRD_N-d	Mainly discharge area but recharge in some areas in upper bedrock.
KLX(1, 9, 9B–F) + HLX(1, 3–7)	HRD_N-r	Recharge area.
KLX(2, 4, 7A–B, 8A, 10, 10B–C, 29A) + HLX(10–14, 21–25, 30–31, 33–35)	HRD_EW007	Complicated due to several interacting deformation zones but recharge is likely in the upper bedrock.
KLX(13A, 17A) + HLX(39–41, 43)	HRD_W-r	Recharge area but possibly discharge in some areas in upper bedrock.
KLX(11A–F, 14A, 19A, 22A–B, 23A–B, 24A, 25A, 27A) + HLX(28–29, 32, 36–38)	HRD_W-d	Recharge area but possibly discharge in some areas in upper bedrock.
KLX(3, 5, 12A, 15A, 16A, 21B, 26A–B, 28A) + HLX(15–19, 26–27, 42)	HRD_C	Mainly discharge area but recharge in some areas in upper bedrock.
KAV(1, 4) + HAV(4–7)	Ävrö	Recharge or Discharge dependent on borehole.
KAS(2–4, 6) + HAS(2–3, 5, 7, 13)	Äspö	Recharge or Discharge dependent on borehole.
KSH(1–3) + HSH(2–3)	Simpevarp	Recharge or Discharge dependent on borehole.

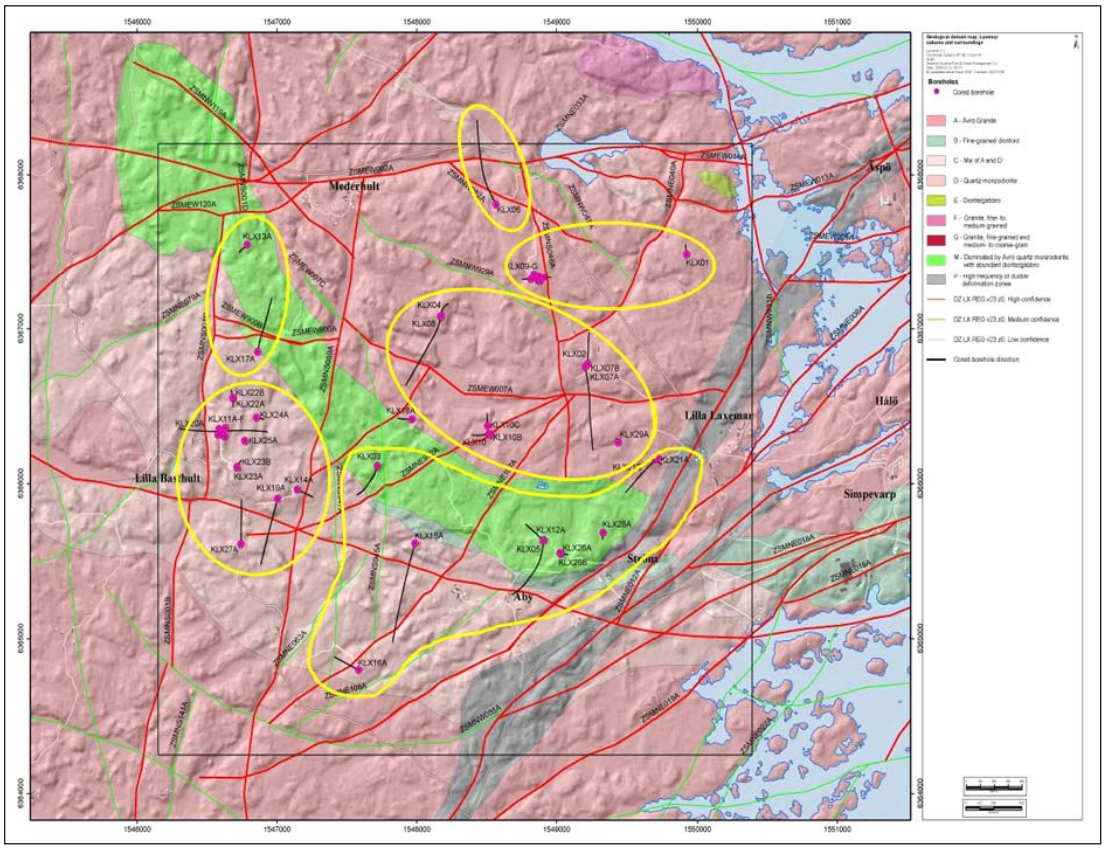

Figure 5-19. *Core-drilled boreholes in the Laxemar subarea grouped according to Table 5-6.*

5.6.2 Major ions and isotope data

The water samples collected in boreholes represent water from hydraulically connected fractures that were transmissive enough to enable sampling of water within reasonable time. These samples are assumed mainly representative of water found in the fracture system with medium to high transmissivities. The porewater samples originate from cores analysed in the laboratory and samples are only available from three cored boreholes; KLX03, KLX08 and KLX17A. The porewater from fresh core samples is here referred to as matrix porewater, i.e. water in the connected pore space of the rock matrix that is accessible for diffusion-dominated interaction with groundwater circulating in nearby (micro) fractures /Waber and Smellie 2008a/.

Fracture groundwater and porewater

Major ions but also Cl in fracture groundwater and porewater are shown in Figure 5-20 through Figure 5-22 and the areas for the plotted borehole groups are visualised in Figure 5-19. Other modelled components are shown in Chapter 9. The $\delta^{18}O$ component is also shown for all Laxemar boreholes in Figure 5-23.

As seen in Figure 5-20 the Cl contents are low in the near surface bedrock but increase towards depth, as was also shown for the TDS in Figure 5-18. Data indicate fresh recharge groundwaters (< 200 mg/L Cl) down to a depth of c. –250 m. Within the depth interval –250 to –600 m the Laxemar groundwaters are characterised mainly by brackish glacial types with some examples of brackish non-marine and transition types. The depth interval –600 to –1,200 m marks the transition from brackish non-marine to saline groundwater type, characterised by a steady increase in chloride to about 16,000 mg/L /Laaksoharju et al. 2009/.

The compiled $\delta^{18}O$ data for the Laxemar local model volume shows a wide spread, indicating a significant heterogeneity, but also clear indications of groundwater with a glacial component recognised by their low $\delta^{18}O$ (< –13.0‰ V-SMOW) /Laaksoharju et al. 2009/ around –300 to –600 m depth. In Figure 5-21 and Figure 5-25 the available $\delta^{2}H$ and $\delta^{18}O$ data for modelling are presented and in Figure 5-23 all $\delta^{18}O$ are plotted together.

Porewater data

The hydrochemistry delivery for SDM-Site Laxemar model contained matrix porewater data for the components Cl, $\delta^{2}H$ and $\delta^{18}O$ extracted from matrix core samples collected in KLX03, KLX08 and KLX17A. /Waber et al. 2009/ provides a extensive summary of the porewater analysis. An interpretation of the palaeohydrogeological aspects of the matrix porewater data is provided by /Laaksoharju et al.2009, cf Section 4.9 therein/, summarised in parts below.

For KLX03, a depth profile of 14 matrix porewater samples, down to an elevation of –932 m has been reported for the chloride concentration and 11 samples for the isotopes $\delta^{18}O$ and $\delta^{2}H$, see Table 5-7, Appendix 4 and Figure 5-20 through Figure 5-22. Down to a depth of c. 600 m of KLX03 is located in Ävrö granite. At greater depths, diorite and quartz monzodiorite are found

For KLX08, a depth profile of 18 matrix porewater samples, down to an elevation of –817 m, has been reported for the chloride concentration and 15 samples for the isotopes $\delta^{18}O$ and $\delta^{2}H$, see Table 5-7, Appendix 4 and Figure 5-20 through Figure 5-22. Down to a depth of c. 750 m, KLX08 is located in Ävrö granite. At greater depths, quartz monzodiorite are also found. Diorite/gabbro sequences are found below depth of c. 500 m.

For KLX17A, a depth profile of 25 matrix porewater samples, down to an elevation of –520 m, has been reported for the chloride concentration and 22 samples for the components $\delta^{18}O$ and $\delta^{2}H$, see Table 5-7, Appendix 4 and Figure 5-20 through Figure 5-22. KLX17A is located in Ävrö granite rock solely.

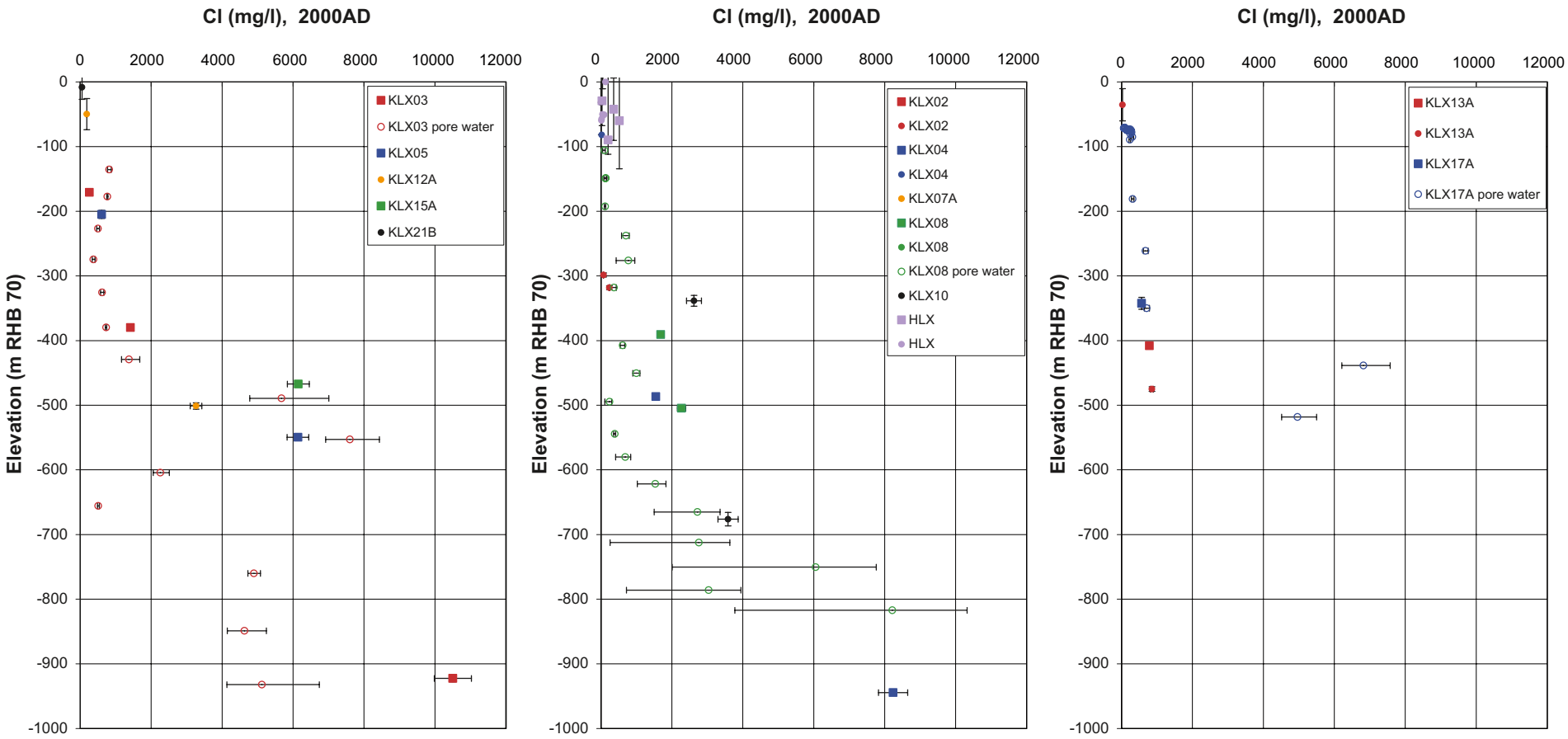

Figure 5-20. *Fracture water and porewater from KLX and HLX holes and porewater data showing the chloride content of the samples for KLX03, KLX08 and KLX17A. For the sake of comparison, the reference water chloride concentrations (mg/L) are: Deep Saline Water = 47,200; Inter-glacial Porewater = 23; Glacial Melt Water = 0.5; Littorina Sea Water = 6,500; Altered Meteoric Water = 5. The data samples considered representative (or somewhat less representative) are indicated by large filled squares, the supplementary data are indicated by small filled circles, and the porewater data are indicated by unfilled circles (for those boreholes where such data are available). The estimated uncertainty is indicated by horizontal errorbars and vertical errorbars indicates borehole section for sample.*

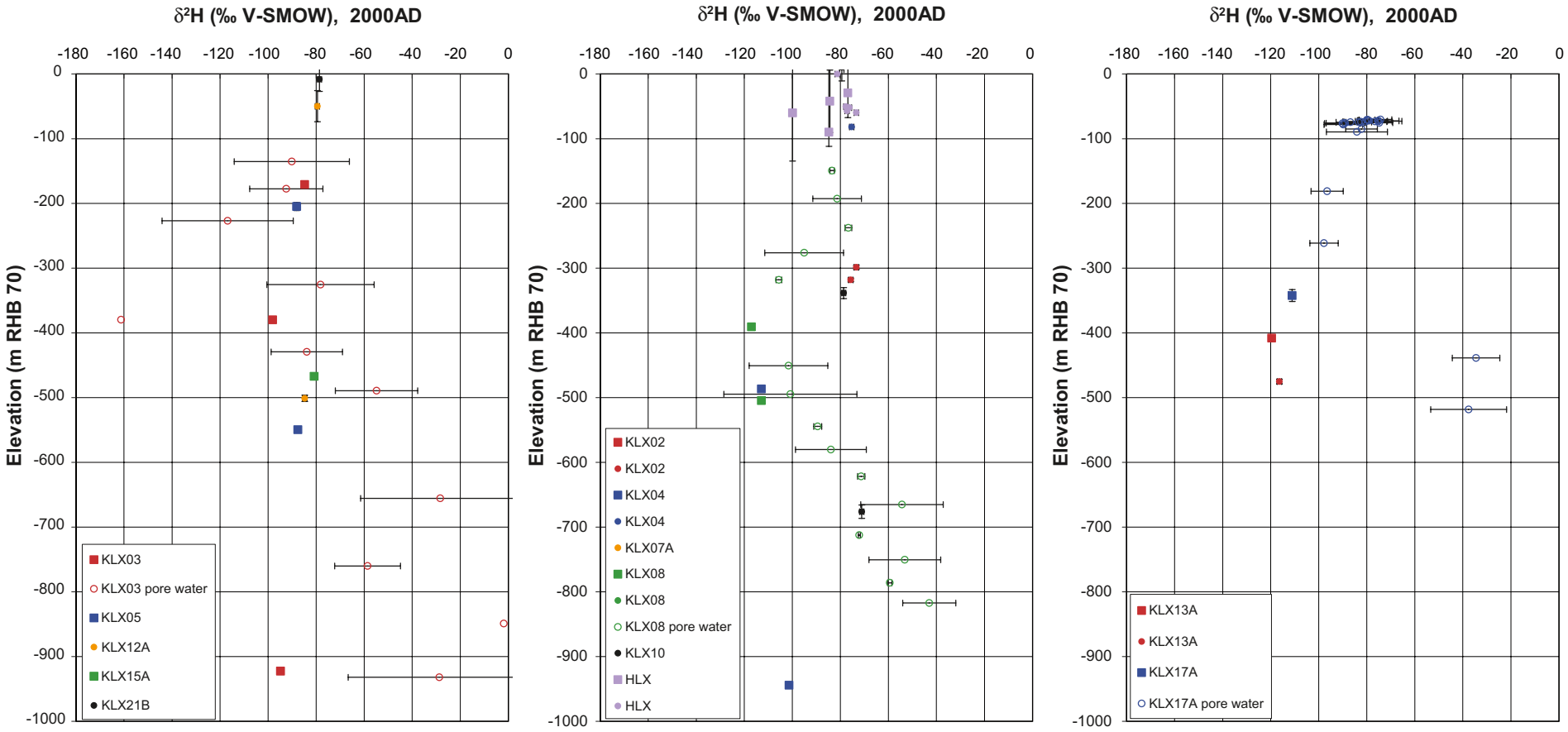

Figure 5-21. *Fracture water and porewater from KLX and HLX holes showing the δ^2H content in the samples for KLX03, KLX08 and KLX17A. For the sake of comparison, the reference water δ^2H values (‰ V-SMOW) are: Deep Saline Water = –44.9 Inter-glacial Porewater = –50.0; Glacial Melt Water = –158.0; Littorina Sea Water = –37.8; Altered Meteoric Water = –74.4. The data samples considered representative (or somewhat less representative) are indicated by large filled squares, the supplementary data are indicated by small filled circles, and the porewater data are indicated by unfilled circles (for those boreholes where such data are available). The estimated uncertainty is indicated by horizontal errorbars and vertical errorbars indicates borehole section for sample.*

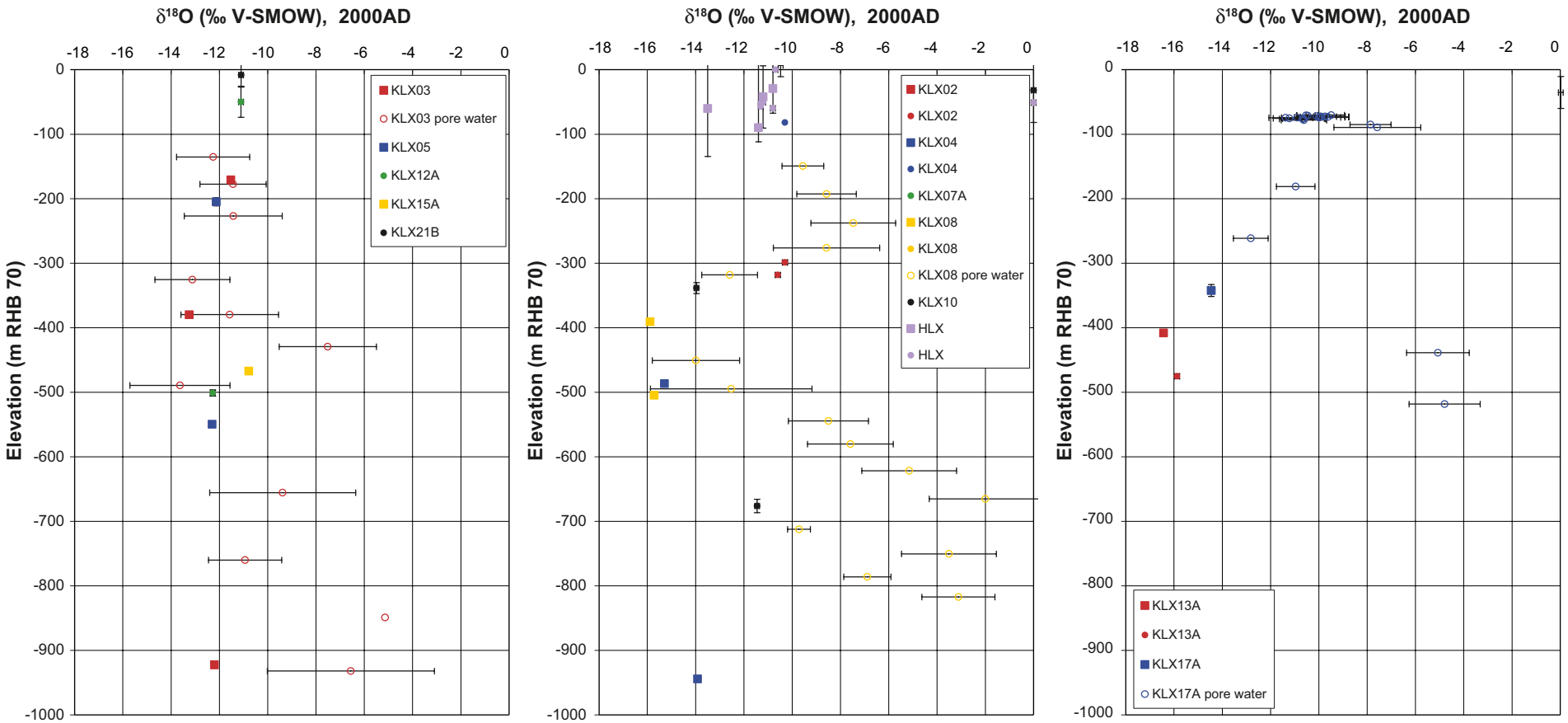

Figure 5-22. *Fracture water and porewater from KLX and HLX holes showing the $\delta^{18}O$ content in the samples for KLX03, KLX08 and KLX17A. For the sake of comparison, the reference water $\delta^{18}O$ values (‰ V-SMOW) are: Deep Saline Water = –8.9; Inter-glacial Porewater = –5.0; Glacial Melt Water = –21.0; Littorina Sea Water = –4.7; Altered Meteoric Water = –9.7. The data samples considered representative (or somewhat less representative) are indicated by large filled squares, the supplementary data are indicated by small filled circles, and the porewater data are indicated by unfilled circles (for those boreholes where such data are available). The estimated uncertainty is indicated by horizontal errorbars and vertical errorbars indicates borehole section for sample.*

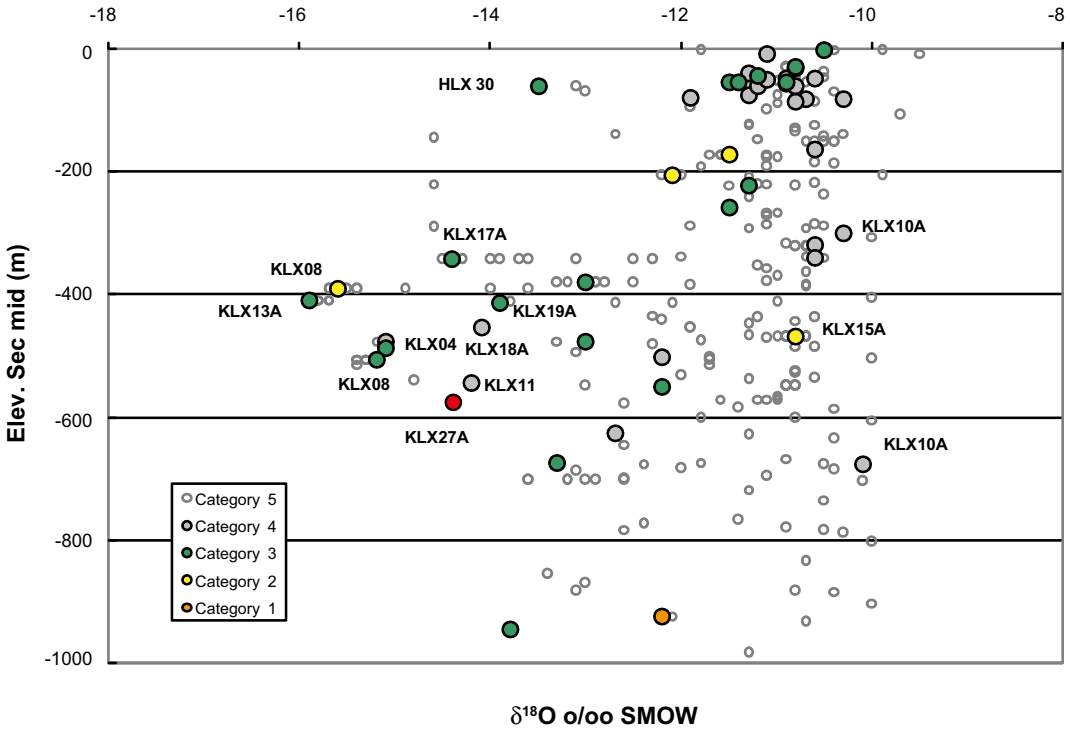

Figure 5-23. *Fracture water data with $\delta^{18}O$ versus elevation based on Category 1–5 data from all percussion and cored boreholes. The results from borehole KLX27A are also included for comparison, /Laaksoharju et al. 2009/.*

Table 5-7. Matrix porewater data collected in the Laxemar local scale model volume. The porewater measurement error of the studied components for each sample is specified in Section 6.7.

Borehole	Number of samples for each component			Elevation
	Cl	δ^2H	$\delta^{18}O$	(m)
KLX03 [1)]	14	11	11	–135 to –932
KLX08 [2)]	18	15	15	–106 to –817
KLX17A [3)]	25	22	22	–100 to –600

[1)] /Waber and Smellie 2006a, b/.

[2)] /Waber and Smellie 2006c/.

[3)] /Waber and Smellie 2008b/.

The porewater data shown, cf Figure 5-24 and Figure 5-25, indicate a depth trend but also a distinction between bedrock characterised by high transmissivity and a high frequency of water-conducting fractures at shallow to intermediate depth, and bedrock characterised by low transmissivity and a low frequency of water-conducting fractures at greater depth, cf Figure 4-12 for general trends. The frequency of flowing fractures is decreasing with depth resulting in "larger blocks" with depth and therefore longer diffusion lengths. Due to this, some water samples of porewater collected at larger depth may have a long distance to a flowing fracture and the porewater samples possibly represent a very old water that is different from the fracture groundwater at similar depth.

In boreholes KLX03 and KLX17A, generally comparable chloride contents and oxygen isotope compositions are observed for porewaters and fracture groundwaters in the transmissive shallow to intermediate depth interval down to at least about 360 m (depending on location), indicating mostly a steady-state between fracture groundwater and porewater. Two samples, however, indicate a difference between porewater and fracture groundwater and thus a transient state.

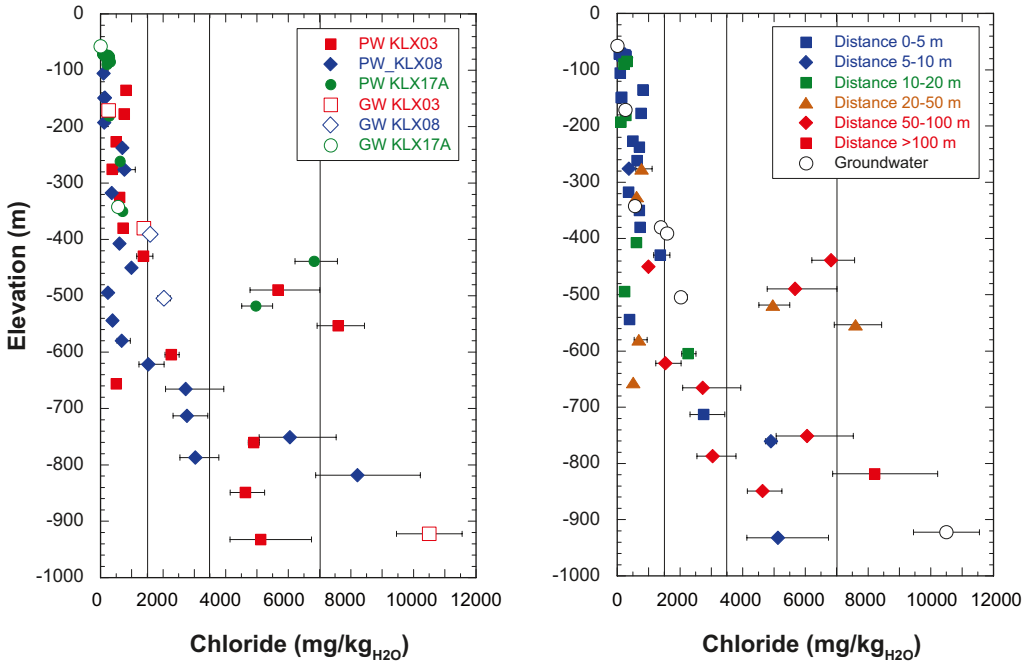

Figure 5-24. *Chloride concentration in porewater (PW, closed symbols) and related. Category 1–3 groundwaters of boreholes KLX03, KLX08 and KLX17A (left), distances of the porewater samples in relation to from the nearest water-conducting fracture (right), cf /Laaksoharju et al. 2009/.*

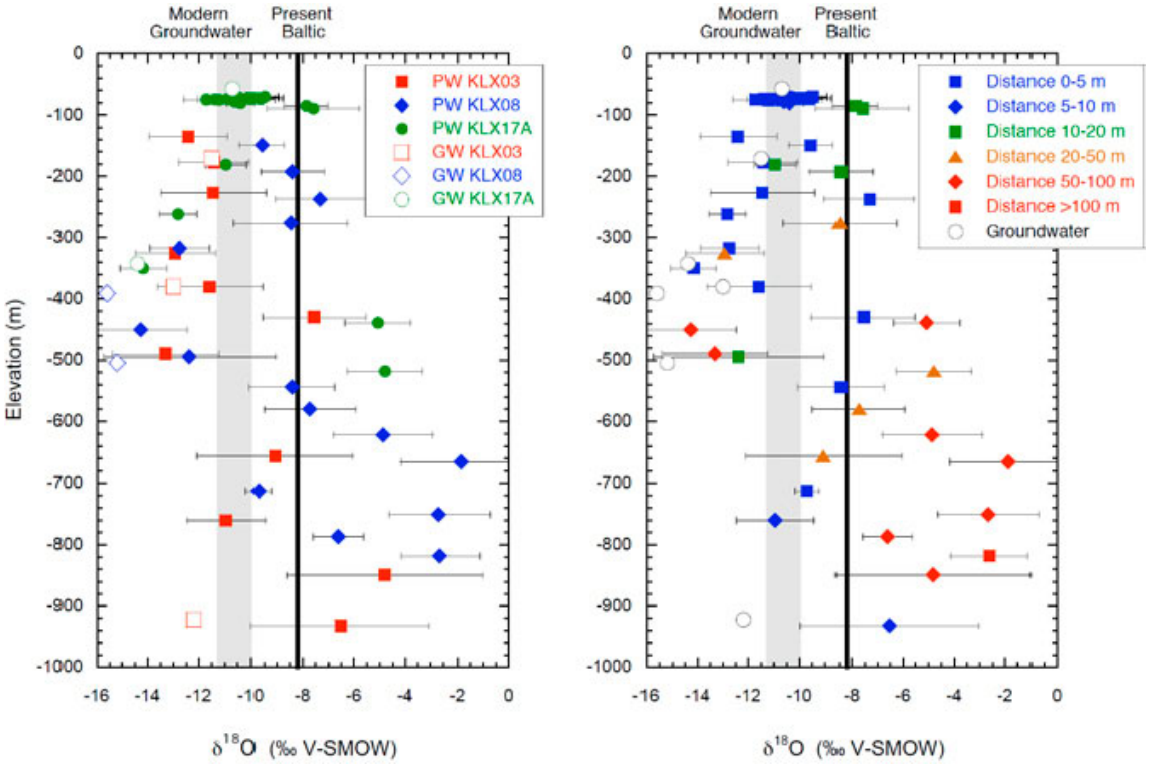

Figure 5-25. *Oxygen isotope composition, $\delta^{18}O$, of porewater (PW, closed symbols) and related groundwater (GW, open symbols, Category 1–3 data) from boreholes KLX03, KLX08 and KLX17A (left), Distances of the porewater samples from the nearest water-conducting fracture on the right /Laaksoharju et al. 2009/.*

Between –360 to –430 m in boreholes KLX03 and KLX17A, porewater and fracture groundwater have almost equally negative $\delta^{18}O$ values suggesting a close to steady-state situation, whereas the chloride content of the porewater is only half that of the fracture groundwater indicating a transient state. In borehole KLX08, a similar situation is established down to at least 500 m depth. Here, the difference in chloride content between dilute porewater and moderately mineralised fracture groundwater is even more pronounced, whereas the ^{18}O isotope signature is still similar within the uncertainty band.

Towards greater depth, fracture groundwater data are limited to one single analysis in borehole KLX03 at about 920 m depth.

5.6.3 Mixing fractions

In addition to measurements of major ions, isotopes and porewater data, the hydrochemistry data delivery for SDM-Site Laxemar includes calculated M3 mixing fractions for the four reference waters: *Deep Saline Water*, *Littorina Sea Water*, *Glacial Melt Water* and *Altered Meteoric Water*, cf Table 5-8. The calculated mixing fractions are available for all Category 1 and 2 data. For Category 3 data, calculated mixing fractions are missing in three samples for percussion-drilled boreholes and in three samples for core-drilled boreholes. For Category 4 data, calculated mixing fractions are missing in five samples for percussion-drilled boreholes and in six samples for core-drilled boreholes. The calculation of M3 mixing fractions did not consider the Inter-glacial Porewater used in the hydrogeological modelling. Any component of such a water present in groundwater samples would most probably be interpreted as part of the *Altered Meteoric Water* fraction by M3 analysis.

For the delivered M3 mixing fractions, a general uncertainty of ±10% was used /Laaksoharju et al. 1999/.

The transport of reference waters is simulated as chemically conservative (non-reactive) fluids in the groundwater flow model, cf Chapter 9. The reference water compositions in the fracture system are given in Table 5-8. Four main hydrochemical indicators were used in the palaeohydrogeological calibration:

- Cl – since it is conservative and indicates the locations of *Littorina Sea Water* and *Deep Saline Water*.
- Br/Cl ratio – since both are conservative and their ratio can be used to determine where the origin of saline water changes from a *Littorina Sea Water* to *Deep Saline Water* when the ratio increases from around 0.004 to 0.007, or more.
- $\delta^{18}O$ – since this is conservative over the timescales considered in the simulations and indicates any remnants of *Glacial Melt Water* when $\delta^{18}O < -13$ /Laaksoharju et al. 2009/.
- HCO_3 – because we model the infiltration of an *Altered Meteoric Water* into the bedrock. The HCO_3 is used as a signature for infiltrating post-glacial meteoric water (although it is a non-conservative species), this signature can also be traced by the low Cl content. (The reference water composition of *Altered Meteoric Water* takes into account the major changes that meteoric water has undergone in the Quaternary deposits and the uppermost part of the bedrock such as organic decomposition and calcite dissolution. Mixing is important for the groundwater components in Altered Meteoric Water but still the HCO_3 content can also be dependent on reactions.)

The concentrations of the major ions and the isotope ratios (and the salinity) can be readily determined from the fractions of the reference waters. In this study, these concentrations are compared with those observed, which represent in a sense measured data. In addition to this, the modelled mixing fractions of the reference waters are compared with the M3 mixing fractions inferred from the data (using a principal component analysis).

It is perhaps worth noting that ConnectFlow could have directly simulated the transport of the major ions and isotopes. However, it is more convenient (computational effective) to specify the boundary and initial conditions in terms of the reference waters, cf Section 7.8.1 for more details. Furthermore, although some chemical constituents, such as Cl, Br and $\delta^{18}O$, are transported conservatively (i.e. no chemical reaction takes place during transport), others are likely to be non-conservative, such as HCO_3 and SO_4, which can be affected by chemical and microbial processes. Mg is not a conservative

tracer either, but it is a useful indicator to differentiate between *Deep Saline Water* at depth and shallower *Littorina Sea Water* near the top surface of the model domain. However, because of the ion exchange mechanisms involving Mg, great caution should be taken when using these non-conservative tracers for model calibration purposes. In fact, even a qualitative evaluation might be misleading. The Br/Cl ratio can and should be used as a better alternative to indicate the transition zone from *Littorina Water* to *Deep Saline Water*. The environmental isotopes δ^2H and $\delta^{18}O$ provide guidance to differentiate between *Glacial Melt Water* and meteoric reference waters such as *Old Meteoric Waters* (from periods before latest glaciation) and *Inter-glacial Porewater.*

Reactive solute transport is discussed more in /Laaksoharju et al. 2009, Section 5.3 therein/ and /Molinero et al. 2009/.

Table 5-8. Composition of the reference waters selected for the mixing calculations in the Laxemar area. Data provided for hydrochemistry data delivery for SDM-Site Laxemar. All concentrations are in mg/L, except for pH (units) and δ^2H (‰ VSMOV) and $\delta^{18}O$ (‰ VSMOV).

	Deep Saline water	Littorina sea water	Altered Meteoric water	Glacial melt water	Inter-glacial Porewater	
					Case 1	Case 2
pH	8	7.6	8.17			8
HCO_3	14.1	92.5	265.0	0.12	265.0	10
Cl	47,200	6,500	23.0	0.5	23.0	5,000
SO_4^{2-}	906.0	890	35.8	0.5	35.8	375
Br	323.66	22.2	0		0	34
Ca	19,300	151	11.2	0.18	11.2	1,585
Mg	2.12	448	3.6	0.1	3.6	2
Na	8,500	3,674	110.0	0.17	110.0	1,440
K	45.5	134	3.0	0.4	3.0	4
Si	2.9	3.94	7.0	–	–	–
Fe^{2+}	–	0.002 (Fe tot)	0.08		–	–
S^{2-}	–	–	–		–	–
δ^2H (‰)	–44.9	–37.8	–76.5	–158.0	–50	–50
$\delta^{18}O$ (‰)	–8.9	–4.7	–10.9	–21.0	–5	–5

6 Regional model – calibration targets

6.1 Modelling concepts and methodology

The work reported here focuses on studying the gross performance and sensitivity of an ECPM flow model representation (cf Figure 2-6) to different model assumptions and settings of material properties, boundary and initial conditions. Single realisations are studied, representing different scenarios. Hence, the objective is not to propose a best fit model, but rather to try to discriminate among alternative major assumptions (what controls affect the modelled system) and look for major sensitivities and/or potential sources of errors in the hydrogeological conceptual model development as presented in Chapter 4.

Forward model calibration consists of changing values of model input parameters in an attempt to approximately match field conditions. The general approach here is to use the same groundwater flow and solute transport model in terms of grid discretisation and parameter settings for simulating (matching) the three types of field data associated with Tasks B–D in Figure 2-4. By comparing the model predictions with different types of field data/measurements, the overall model development can be partially calibrated to improve the parameterisation, improve our understanding of the hydrogeological system, and help build confidence in the hydrogeological conceptual model of (mainly) the Laxemar local model volume.

However, to become a meaningful activity applied to a heterogeneous and anisotropic medium such as the crystalline bedrock in the Laxemar local model area, the ECPM model calibration with regard to groundwater flow and solute transport requires that the structural-hydraulic conditions be properly characterised and implemented, cf Chapter 7. Lack of a proper structural-hydraulic numerical implementation may result in a calibrated groundwater flow and solute transport model that is not representative for use in other applications/scenarios /Konikow and Bredehoeft 1992/. Therefore, an initial model calibration step was applied in this study (Task A in Figure 2-4) prior to the modelling of the three major calibration targets focusing on groundwater flow and solute transport (Tasks B–D in Figure 2-4). The initial step, Task A, is referred to as “Local conditioning of HCD properties on single-hole hydraulic tests”.

6.2 Single-hole hydraulic tests

6.2.1 Data selected for conditioning

The evaluated transmissivities of each borehole intercept of a hydraulic conductor domain (HCD) is presented in /Rhén et al. 2008/. The HCD properties used for the ECPM flow modelling work are prescribed according to /Rhén et al. 2008/ based on the transmissivity of the borehole intercept with the HCD and within a specified distance from the borehole within the geometry of the HCD. The approximate distance used and the actual implementation is described in Chapter 7.

6.2.2 Calibration targets

The local conditioning of the transmissivity based on the local estimates of the transmissivity and assessed radius of influence can in principle be tested by simulations of the hydraulic tests. This has however not been made as it is judged that is has minor influence on the results compared to other factors studied, and that simply introducing local estimates of the transmissivity based on local measurements will anyhow be positive for how the borehole are hydraulically connects to the surroundings.

6.2.3 Uncertainties in data

Measurement uncertainties

The uncertainties in the estimated transmissivity values are discussed in /Rhén et al. 2008/. It can here be pointed out that the transmissivities for the HCDs at the borehole intercepts are based mainly on 5 m PFL-s pumping test measurements for long core boreholes. The uncertainty of these individual PFL-s estimated transmissivities are c. ±10%, based on uncertainties of flow rates and head measurements /Rhén et al. 2008/. The transient tests performed by 20 m PSS indicate that on average the transmissivities are slightly greater (c. 3 times) than the assessment based on PFL-s, cf /Rhén et al. 2008/. This difference between methods may be regarded as an indication of the average uncertainty in the value used for local conditioning. However, it should be kept in mind that the PFL-s test data represent a much larger radius of influence than the PSS test data, cf /Rhén et al. 2008/ where the methods are discussed.

Handling of uncertainties

The lateral spatial variability of the transmissivity within a HCD is large, cf /Rhén et al. 2008/ and Section 4.1.2, compared to the estimated uncertainty of the local estimate of the HCD transmissivity. The uncertainty of the local estimate of transmissivity of the HCD used for conditioning is not treated but the effect of spatial variability within HCD is tested, see Chapter 11.

6.2.4 Expected contribution to calibration

It is expected that local conditioning of the transmissivity near the boreholes will provide a more realistic situation when hydrogeochemical data are used for testing and calibrating the model, as assignment of e.g. very low transmissivities for a HCD borehole intercept using stochastic assignment of transmissivity within the HCD knowing that the transmissivity is high, is not a realistic case.

6.3 Äspö HRL drawdown

6.3.1 Data selected for calibration

Groundwater monitoring data (PWH) from 1989 up to 2004 have been used for estimation of natural (undisturbed) groundwater levels for period 1989–1990, groundwater levels during max inflow to the Äspö HRL tunnel (1993–1995) and recent groundwater levels (200–2004), see Appendix 2.

6.3.2 Calibration targets

Calibration targets are the measured drawdowns measured in a number of observation wells, which have long time series and are judged to have reliable data. Drawdown data from seven percussion boreholes located on Ävrö, Mjälen and Laxemar are used, cf Appendix 2. The drawdown on Äspö is also checked based on the interpretation of the water table on the Äspö island after the construction of the Äspö HRL, but is considered less important for the calibration, which has a focus on mainly testing the effect of the sea sediments, as they provide control on the possibility for a drawdown cone to reach the surrounding areas around Äspö /Hartley et al. 2007/.

6.3.3 Uncertainties in data

Measurement uncertainties

There are few boreholes outside the Äspö Island that have long time series, and the monitoring data for the time period during the site investigations for Äspö HRL and during the construction of the Äspö HRL suffer from disturbances mainly from drilling and hydraulic tests. Data up to December 1996 were screened within the framework of data preparation for the Äspö Task Force Task 5 modelling /Rhén and Smellie 2003/ and subsequent data were screened as part of the data preparation for the Laxemar 2.1 “Pre-modelling exercises” /Hartley et al. 2007/.

The data set for calibration is limited compared to the natural head data (PWH). The drawdown data related to Äspö HRL is estimated/judged to be within c. ±0.5 m, cf Appendix 2.

The accuracy of the measured flow rates into the tunnel has been estimated ±5%, cf /Almén and Stenberg 2005/.

Handling of uncertainties

Monitoring data indicate a clear but limited drawdown in the eastern part of the Laxemar local model area and a significant drawdown on the island of Mjälen and western Ävrö. As the uncertainty in the drawdown for the entire period 1989 to 2004 is significant, it is reasonable to accept simulated drawdown in the range ±0.5 to 1 m in relation to the measured drawdown.

The accuracy of the measured inflow rates to the tunnel segments is judged to be of high accuracy. Hence, it is considered not necessary to conduct a sensitivity study related to the uncertainty in the inflow rates.

6.3.4 Expected contribution of calibration

The main contribution of this calibration is the proper appraisal of the hydraulic conductivity of the sea sediments. It also provides a test of the assigned transmissivities to HCDs and the assigned HRD properties around Äspö, the latter which, however, is of lesser importance for the Laxemar local model area.

6.4 HLX28 Interference test

6.4.1 Data selected for calibration

Groundwater monitoring data collected during the interference test are used calculate drawdown. Drawdowns in the following boreholes are used for the calibration (No of sections within parenthesis): KLX19A (8), KLX20A (1), KLX14A (3), HLX32 (1), HLX36 (2), HLX37 (3) and HLX38 (1). The maximum drawdown for each observation section during the pumping period is shown in Figure 5-7.

6.4.2 Calibration targets

The drawdown as a function of time of the borehole sections measured is used for the calibration.

6.4.3 Uncertainties in data

Measurement uncertainties

According to the SKB Measurement Description for Monitoring (internal SKB document) the accuracy of the water levels in the standpipes in percussion boreholes and core boreholes is estimated to ±0.2 m. In the groundwater monitoring wells the accuracy is estimated to ±0.07 m. The accuracy of the calculated drawdown for periods from days to a few months can be expected to be lower than that for the measured water levels in the standpipes.

The pumping was made with a submersible pump and a separate flow gauge. The accuracy of the flow rates is estimated to ±10% of measured value (SKB Measurement Description for interference tests (internal SKB document).

Handling of uncertainties

The uncertainties in the measured water levels in the standpipes and the measured flow rates are small in relation to conceptual uncertainties and should not be a base for sensitivity cases. As pointed out in Section 5.5.3 there are uncertainties related to estimated densities in the standpipes for deep test sections. As only drawdown is studied, this uncertainty does not affect the calibration in any significant way.

6.4.4 Expected contribution of calibration

The calibration is expected to confirm ZSMNS001C as a hydraulic barrier in the south-western part of the Laxemar local model volume. It also expected that the HCDs (ZSMEW42A, ZSMNS059A, KLX19_DZ5-8_dolerite and HLX28_DZ1) close to HLX28 can explain much of the responses, as HCDs are more conductive elements than the HRDs, although in possibly three cases also acting as hydraulic barriers.

6.5 Interference test at HLX33

6.5.1 Data selected for calibration

Groundwater monitoring data collected during the interference test are used calculate the drawdown. Drawdowns in the following boreholes are used for the calibration: HLX11 (2), HLX23 (2), HLX24 (2), HLX25 (2), HLX30 (2), HLX31 (1), HLX33 (1), KLX02 (8), KLX04 (8), KLX07A (8) and KLX07B (2). The maximum drawdown for each observation section during the pumping period is shown in Figure 5-4.

6.5.2 Calibration targets

The drawdown as a function of time of the borehole sections measured is used for calibration.

6.5.3 Uncertainties in data

Measurement uncertainties

According to the SKB Measurement Description for Monitoring (internal SKB document) the accuracy of the water levels in the standpipes in percussion boreholes and core boreholes is estimated at ±0.2 m. In the groundwater monitoring wells the accuracy is estimated at ±0.07 m. The accuracy of the calculated drawdown for periods from days to a few months can be expected to be lower than the accuracy for water levels in the standpipes.

The pumping in HLX33 was made with a submersible pump and a separate flow gauge. The simultaneous pumping in HLX14 was also made with a submersible pump and a separate flow gauge. The accuracy of the flow rates is estimated to ±10% of measured value (SKB Measurement Description for interference tests (internal SKB document)).

Handling of uncertainties

The uncertainties in the measured water levels in the standpipes and the measured flow rates are small in relation to conceptual uncertainties and should not constitute a base for sensitivity cases. As pointed out in Section 5.5.3 there are uncertainties related to estimated densities in the standpipes for deep test sections. As only drawdown is studied, this uncertainty does not affect the calibration in any significant way.

It is expected that HLX14 pumping have affected the drawdown and the recovery of the interference test in HLX33 and therefore the simulation has been included the HLX14 pumping in the modelling.

6.5.4 Expected contribution of calibration

The calibration is expected to contribute to the estimate of the transmissivity of the HCD ZSMEW007 and to confirm the assessed geometry of the HCD, but also to indicate if the assessed anisotropy of HRD_EW007 and the hydraulic contrast between HRD_EW007 and HRD_C, based on the hydrogeological DFN models, is reflected in the test. The calibration will also indicate the magnitude of the storage coefficient of ZSMEW007.

6.6 Natural groundwater heads

6.6.1 Data selected for calibration

The natural (undisturbed) pointwater heads in the Quaternary deposits and the near-surface bedrock used for the calibration are shown in Figure 6-1 and Figure 6-2. The observation points are arranged with regard to the elevation of the bedrock (dark red line with orange markers). The ground elevation is shown as a green line and light green markers. The bars show the observed spread of the maximum and minimum head values. Some of the boreholes have been marked with a * in front of the name. These boreholes are all situated outside the refined mesh area in the model cf Chapter 7 (boreholes, HLX08, HLX09, HSH01 and HSH02, and a few SSM boreholes are all situated outside the refined mesh area in the model). This could potentially lead to a more difficult calibration due to the coarser grid.

It stands clear from the data that there are large local variations in measured pointwater head across the area. Two of the percussion boreholes, HLX15 and HLX28, show pointwater heads above the ground elevation (artesian). It is also worth noting that there seems to be a zone of unsaturated rock along some boreholes, i.e. locations where the pointwater head is below the rock surface. Overall, there seems to be less correlation between pointwater heads in the upper parts of the rock and the ground surface elevation, compared to the groundwater levels in the Quaternary deposits, see Figure 6-1.

In the present groundwater flow modelling, the delivered measured pointwater heads and environmental heads for cored boreholes are used for comparisons with the corresponding calculated heads from the groundwater flow modelling. The comparison is presented in separate plots for each cored borehole. In the plots, the measured head are displayed as blue crosses, where the centre of the cross indicates the midpoint of the section, the vertical line indicates the extent of the section (seclow-secup) and the horizontal line indicates the temporal variation (min-max) of the measured heads. Where available, the delivered calculated environmental heads have been used in the plots, otherwise, measured pointwater heads were used instead. Figure 6-3 shows an example from KLX08 of the presentation of measured and modelled head data.

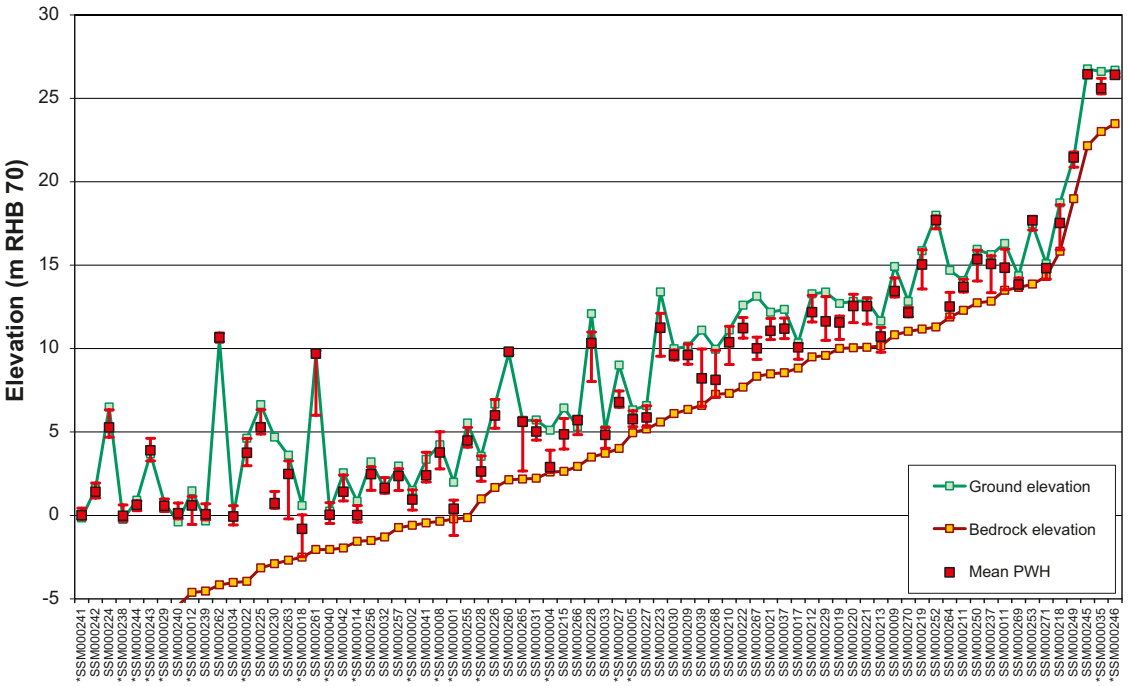

Figure 6-1. *Mean pointwater head measured in groundwater monitoring wells completed in Quaternary deposits in the Laxemar local model area available for application in the SDM-Site Laxemar flow modelling. Daily mean natural (undisturbed) head, bars indicate observed minimum and maximum levels). Boreholes marked by a * are outside the Laxemar local model area.*

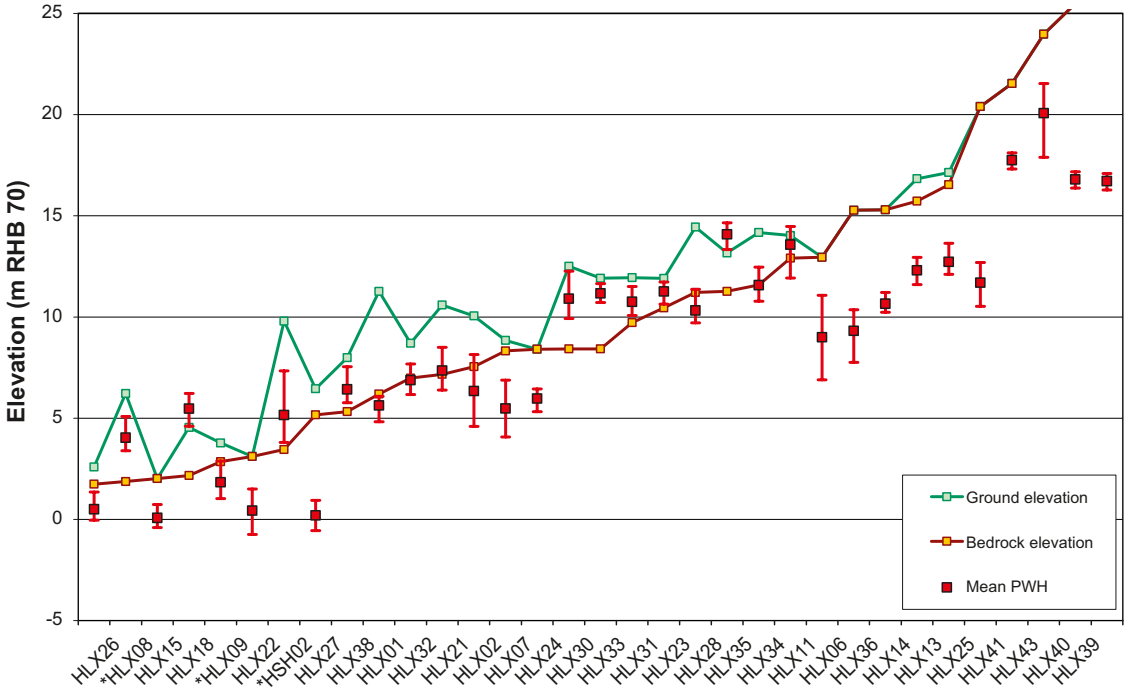

Figure 6-2. *Daily mean natural (undisturbed) pointwater head in percussion boreholes available for application in the SDM-Site Laxemar flow modelling. Note that for boreholes with packers, data are used for the upper borehole section. Bars indicate min and max. Boreholes marked by a * are outside the Laxemar local model area.*

6.6.2 Calibration targets

The 'objective function' is here to reproduce the spatial distribution of natural mean pointwater head in the Quaternary deposits as well as the near-surface bedrock and in the rock down to –800 m. This can judged by comparing graphs such as Figure 6-1 through Figure 6-3 with model predictions, as well as by calculating functions such as the root-mean-square of difference in heads.

6.6.3 Uncertainties in data

Measurement uncertainties

According to the SKB Measurement Description for Monitoring (internal SKB document) the accuracy of the water levels in the standpipes in percussion boreholes and core boreholes is estimated to be within ±0.2 m. In the groundwater monitoring wells the accuracy is estimated to ±0.07 m.

Two examples of measurement uncertainties related to estimated mean values and estimates of min and max values are: (*i*) uncertainties associated with the collection of representative pointwater head data in a heterogeneous groundwater system with a spatially varying fluid density, and (*ii*) uncertainties associated with the computation of representative mean pointwater head data in a heterogeneous groundwater system subjected to disturbances due to seasonal variations, limited data sets considering time period for measurements, precipitation events, nearby pumping, etc. Concerning point (*i*) it was decided that no data below elevation 800 m should be used for calibration.

These aspects are discussed in /Werner et al. 2008/. The mean value data utilised in the work reported here represent the best data available considering the listed uncertainties.

Handling of uncertainties

The available measurements of the water levels in the standpipes are considered to have good measurement accuracy compared to e.g. the uncertainties related to the seasonal variation. The uncertainty in the data from the Quaternary deposits and the upper 200–300 m of bedrock is more

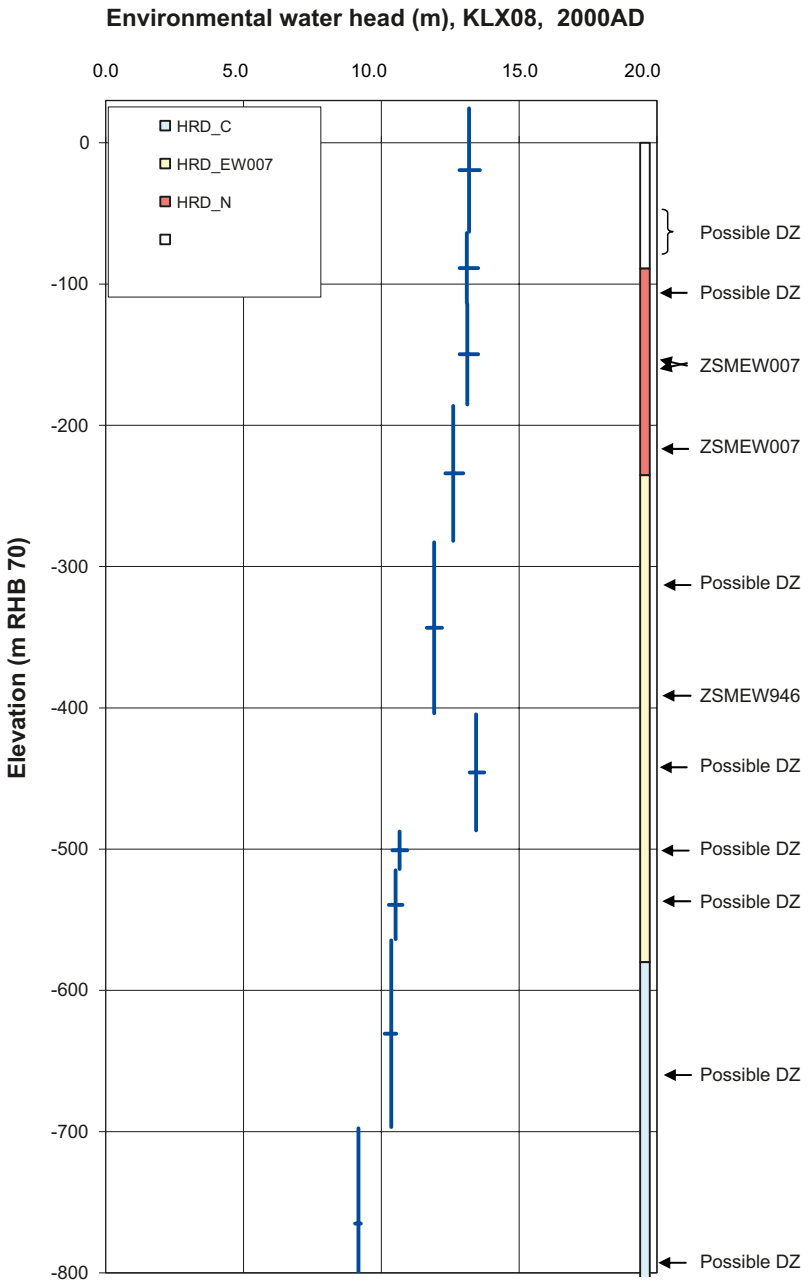

Figure 6-3. *Environmental head in KLX08 based on measured pointwater head data in sections along the borehole. The centre of each blue crossed line shows the midpoint of the section, the vertical line shows the extent of the section and the length of horizontal line shows the temporal variation of the measured head. At the right hand side, the prevailing hydraulic rock domains are shown as coloured bars along the borehole. Detected fractures/deformation zones are indicated at their intersection depth in the borehole.*

related to the time period for measurements and disturbing activities. The mean values and estimated min and max values are therefore considered uncertain. It is also important to recognise the spatial heterogeneity of properties in the Quaternary deposits and bedrock that will affect both the measured and the simulated groundwater levels. The latter can be studied by producing results based on different realisations of properties, but the spatial heterogeneity of properties suggests that one should not expect (or strive for) exact matches between model and measured data.

An example of a pertinent issue of uncertainty is: How shall the comparison be made between heads observed in a packed off multi-packer monitoring system and the pressures representing variable-density flow in a numerical continuum model grid? This aspect is discussed in Chapter 8.

6.6.4 Expected contribution to calibration

The natural pointwater head measurements are located in the Quaternary deposits and upper bedrock, and hence calibration on this type of data is expected to inform the interaction between the groundwater in the superficial bedrock and the groundwater in the Quaternary deposits, in particular the discussion about the net recharge to the bedrock and the distribution of recharge and discharge. Therefore, Task C (cf Figure 2-4) is likely to be focused on the hydraulic properties of the HSD and superficial parts of HRD, as well as providing confirmatory testing of the hydraulic boundary conditions. The pointwater head measured in the deeper part of the cored boreholes are expected to indicate similar trends and can locally possibly indicate that the hydraulic properties should be modified.

6.7 Palaeohydrogeology

6.7.1 Data selected for calibration

In the present work, the objective is to calibrate the regional groundwater flow model to match simulated hydrochemical data at 2000 AD, to the extent possible, using the following measured entities: salinity (expressed as TDS), Cl, Br/Cl-ratio, Na, Ca, Mg, HCO_3, $\delta^{18}O$ and $\delta^{2}H$. Examples of data used, value ±error (or uncertainty estimate), for Cl, $\delta^{18}O$ and $\delta^{2}H$ are shown in Figure 5-20 through Figure 5-22.

6.7.2 Uncertainties in data

Measurement uncertainties

In the Extended data freeze Laxemar 2.3, cf /Laaksoharju et al. 2009/, analytical uncertainties associated with major ions and isotopes in all groundwater samples (fracture water and porewater) were provided. In Table 6-1 a summary is provided of the analytical uncertainties in groundwater samples. For some of the components (Cl, Br, HCO_3 and SO_4) the range over which the given uncertainty is valid is also shown. However, since no other data were available, the same analytical uncertainty was used regardless of the magnitude of the value of the measured entity.

The relative analytical uncertainty for the major ions in groundwater samples ranges from ±4% to ±15%. The analytical uncertainty for TDS (or salinity) is specified for PHREEQC, which was used for the calculation of TDS. The absolute analytical uncertainty, given for the isotopes $\delta^{2}H$ and $\delta^{18}O$ in groundwater samples, is ±0.9‰ (V-SMOW) and ±0.1‰ (V-SMOW), respectively.

Table 6-1. Analytical uncertainties of elements and isotopes of analysed in groundwater samples (fracture water and porewater), as stated in conjunction with the Extended data freeze Laxemar 2.3, cf /Laaksoharju et al. 2009/.

Component	Analytical uncertainty	Type of uncertainty
Cl	±5% [70–710 mg/L] [1)]	Relative
Cl, porewater	According to data in Appendix 4 and [2)]	Absolute
$\delta^{2}H$	±0.9‰ V-SMOW [1)]	Absolute
$\delta^{2}H$, porewater	According to data in Appendix 4 and [2)]	Absolute
$\delta^{18}O$	±0.1‰ V-SMOW [1)]	Absolute
$\delta^{18}O$, porewater	According to data in Appendix 4 and [2)]	Absolute
Br	±15% [0.5–9 mg/L] [1)]	Relative
Br/Cl	±16% [3)]	Relative
Ca	±12% [1)]	Relative
Na	±13% [1)]	Relative
Mg	±12% [1)]	Relative
HCO_3	±4% [1–122 mg/L] [1)]	Relative
SO_4	±12% [0.5–70 mg/L] [1)]	Relative
TDS	±15% [3)]	Relative

[1)] Oskarshamn site investigation. Quality of hydrochemical analyses (DF version 2.3). /Nilsson 2009/.

[2)] Laxemar DF 2.3 Porewater data /Waber and Smellie 2006a, b, c, 2008b/.

[3)] Uncertainties in chemistry samples. (Fractional uncertainty, Cl and Br samples assumed independent and random.)

For the delivered M3 mixing fractions, a general uncertainty in the M3-modelled values of ±10% was used /Laaksoharju et al. 1999/.

Other examples of measurement uncertainties are:

- Sampled data are outside of the measurement range for which the analytical uncertainty is specified.
- The observed salinity (TDS) is calculated from the PHREEQC results of total element contents as the sum of totals Br+C+Ca+Cl+F+Fe+I+K+Li+Mg+Mn+N+Na+P+S+S(6)+Si+Sr.
- Drilling water contamination. Reliability in the uranine analyses and corrections applied to the sampled data.
- Positioning of the porewater samples with regard to the location of flowing fractures.
- Upconing of *Deep Saline Water* (elevation, lateral spatial extent).
- Drawdown of superficial waters.
- The estimation of the representative volume (radius of influence, shape of volume) of a given hydrochemical sample is associated with uncertainty. However, scoping suggest that a water sample has a capture zone (radius) extending at least some tens m, possibly in many cases up to c. 50 m from the pumped section (for the case of a total pumped volume of 15 m^3 [1]).

Handling of uncertainties

Some examples of handling uncertainties are:

(i) Delivered hydrochemistry data (from the ChemNet group by way of Sicada) have been divided into several representativity groups indicating uncertainties due to e.g. charge balance and drilling water content.

(ii) All sampled data for Cl, Br, $\delta^{18}O$ and TDS have been corrected with respect to the drilling water residue.

(iii) The analytical uncertainty is indicated by error bars on the data samples in the figures.

(iv) The "error" in elevation of the individual sample is taken as the upper and lower elevations of the sampled borehole section reported in the hydrochemistry data delivery for SDM-Site Laxemar modelling. The sample is actually reflecting the entire interval that is pumped rather than just a point in the middle of the interval. For presentation purposes, all data samples are placed at an elevation corresponding to the mid point of the packer section.

The components forming the base for the TDS are considered conservative tracers. This is a simplification, particularly considering HCO_3 and Mg, which are highly reactive components. However, conservative tracers are expected to normally dominate TDS.

It is also recognised that using a ECPM with 40 to 100 m blocks will tend to make the regional groundwater flow model less heterogeneous concerning hydraulic properties than the underlying hydrogeological DFN model, and most likely less heterogeneous than what can be expected in the bedrock. The hydrochemistry modelled by flow modelling will thus probably be less heterogeneous than what should be expected.

6.7.3 Expected contribution to calibration

The modelling of the palaeoclimotology and the historic development of the hydrological and hydrogeochemical conditions at the surface and its effects on the groundwater system during the Holocene (last 10,000 years) is an essential part of the SDM. In this context, the calibration on hydrochemistry is fundamental to the understanding of the hydrogeological processes in the fractured rock, assessing

[1] Assuming a kinematic porosity of 10^{-4}–10^{-3}, spherical flow and a pumped volume of 15 m^3 before collecting the water sample, the capture zone (radius from pumped section) is c. 15–33 m. If radial flow is assumed within a formation with thickness 10 m, with corresponding porosity and pumped volume as for the spherical flow example, the capture zone (radius from pumped section) is c. 22–69 m.

the impact of variable-density flow, and assessing the solute transport interaction between the fracture system and matrix.

During the Littorina Sea phase (with a fairly well defined time period), salinity infiltrated the bedrock and sank vertically. The model parameters governing this process are primarily the vertical hydraulic conductivity of the HRDs and HCDs and the transport properties (kinematic porosity and RMD parameters). Hence, salinity data are likely to provide a good basis for provision of boundary conditions and serving as a basis for calibration of the HRD and HCD hydraulic and transport properties.

The calibration of major ions and isotopes in fracture water provides a further test of these model components, while the porewater, as a remnant of past hydrogeological and hydrogeochemical conditions, provides an insight into appropriate initial conditions. It is assumed that a significant amount of the groundwater in the fracture system should be of glacial origin (with low $\delta^{18}O$ signature) directly after the latest glaciation has retreated from the Laxemar-Simpevarp regional model area. Given that there are a number of chemistry samples indicating glacial water signature, the regional groundwater model must be able to retain some glacial water up to 2000 AD. Hydraulic conductivity of the HRDs and HCDs and the transport properties (kinematic porosity and RMD parameters) are expected to control this process.

Chemistry data from fractures and matrix can possibly also confirm (or indicate) the spacing between flowing fractures, i.e. the conductive fracture frequency (CFF), as an important parameter for the modelling of matrix diffusion.

Apart from the salinity, the main focus is also on Cl, $\delta^{18}O$, Br/Cl-ratio, Mg and HCO_3, primarily in boreholes. Several of these components are (in combination) indicators of Littorina Sea water, which makes them valuable for comparison between measured and simulated concentrations. Because of the conservative nature of Cl and $\delta^{18}O$, they can be used quantitatively in the model calibration. The use of Mg, HCO_3 and potentially other ions, must be used in a more qualitative way. The main comparison of the results of the flow model with observation is a visual comparison of the trends of these major ions along the boreholes with interpreted field data.

7 Regional flow modelling – implementation of the hydrogeological conceptual model

Regional modelling of groundwater flow and solute transport is required to test the hydrogeological conceptual model of the site against different types of field observations. The comparison is made to establish whether the conceptual model behaves consistently with the observations, or whether the model needs to be adjusted. This is essentially a process of calibrating the flow model, and may require changes to the conceptual model, hydrogeological features, such as deformation zones, hydrogeological flow and transport parameters, or boundary conditions. The calibration process does not necessarily lead to a unique model, and therefore, as well as trying to calibrate the model, it is important to quantify how sensitive the calibration process is to model features and parameters, thereby indicating what has been determined or confirmed by the use of field data, along with what remains undetermined or uncertain. Single-hole geologic interpretations and hydraulic tests have been used in the conceptual model development to parameterise initial HCD and HRD models, and flow modelling has been essential in the development of the concluding SDM-Site Laxemar conceptual model (as presented in Chapter 4). The initial numerical model was calibrated against present-day hydrogeological conditions as measured by:

- Natural (undisturbed) groundwater pressures – point water head measurements in packed-off intervals in deep core-drilled boreholes, and in the uppermost bedrock and Quaternary deposits;
- Groundwater level responses (drawdowns in pointwater head) in the bedrock observed during interference tests in HLX33 and HLX28, and drawdowns induced by keeping the underground openings of the Äspö HRL drained; and

by simulations of;

- Palaeohydrogeology during the Holocene (last 10,000 years) testing conceptual ideas of boundary and initial conditions of the distribution of hydrochemistry and how it has evolved over time. Comparison with present-day hydrochemical samples (fracture water and matrix porewater) from deep boreholes.

A numerical demonstration of the conceptual model is necessary in order to establish credibility for the site descriptive model in general and the site hydrogeological description in particular. This is important since the numerical models developed are to serve as a basis for describing the present-day hydrogeological conditions as well as for predicting future hydrogeological conditions and transport pathways. Equally important is a need to illustrate the role of field data in reducing uncertainty. These requirements imply a testing of the following modelling components:

- Hydraulic properties and geometries of the major deformation zones (HCD).
- Hydraulic properties of the rock between the major deformation zones (HRD).
- Hydraulic properties of the Quaternary deposits (HSD).
- Flow boundary conditions and the hydraulic connection between the HSD and HRD.
- Initial and boundary conditions for hydrochemistry and hydrogeology.

This section describes the numerical implementation of the conceptual model described in Chapter 4. The initial parameterisation of the model was based on the data interpretation given in /Rhén et al. 2008/. Some changes to the parameterisation and other modelling settings were made as part of a calibration process against the calibration targets described in Chapter 6. In order to keep the description of the flow modelling brief, the approach used in this report is to describe the hydrogeological parameters and settings for the calibrated base case flow model in this chapter, then in Chapters 8 and 9 where the matching to data is demonstrated, additional results for sensitivity variants on the calibrated model are presented to illustrate why key steps in the calibration process were made.[2] That is, rather than present all the trials and sensitivities considered in the evolution of

[2] "Base case", in this report accounting for the SDM-Site Laxemar modelling, corresponds to "Deterministic base model simulation" in the SDM-Site Forsmark modelling /Follin 2008/.

the model from initial parameter settings to the calibrated model, the parameterisation of calibrated model is presented here, and then sensitivity cases are constructed *a posteriori* to demonstrate why the more important changes to the model were made. Additional variant simulations were made as sensitivity studies to scope some of the remaining uncertainties, such as spatial heterogeneity, and are described in Chapters 8 and 9. The hydrogeological parameterisation of the initial flow model prior to calibration is that recommended in /Rhén et al. 2008/.

7.1 General approach and flow modelling assumptions

The general flow modelling approach is to use the same groundwater flow model in terms of grid discretisation and parameter settings for simulating all three types of field data: interference tests, natural (undisturbed) point-water heads, and hydrochemistry. The same flow model with regard to geometries and hydraulic properties was used for each type of simulation to make it transparent that a single implementation of the conceptual model could be sufficiently calibrated against all three types of field observations, although it may have been possible to improve the flow modelling of a particular data type by refining the implementation (discretisation) around a relevant observation borehole, for example. Of necessity, some features of the flow model such as initial and boundary conditions had to be changed according to the situation being modelled.

All the groundwater flow and transport modelling described in this report were implemented in the ConnectFlow code /Hoch and Jackson 2004, Marsic et al. 2001, Serco 2009a, b, c/. ConnectFlow has capabilities for constructing models using either the discrete fracture network (DFN) and continuum porous medium (CPM) conceptual models, or combinations of the two.

An equivalent continuum porous medium (ECPM) approach was used for modelling regional-scale groundwater flow and solute transport. The ECPM approach concept assigns hydraulic parameters that represent an underlying discrete fracture network (DFN) model. The approach is to first generate a stochastic realisation of a hydrogeological DFN model within the regional model domain, and then for each grid element of the ECPM model to calculate a set of continuum parameters that corresponds in an equivalent behaviour, in terms of quantities such as total flux or advective travel time, to the underlying fracture network within that element. Discrete features are generated in the size range 5.6 m to 564 m radius (cf Section 7.5). For comparison, the size of the finite-elements used in the regional flow model on which ECPM properties are represented is 40–120 m. Therefore, the ECPM properties may represent a network of many sub-element scale fractures, and hence the method is one of upscaling. The derived parameters are a full hydraulic conductivity tensor, kinematic porosity and the connected fracture area per unit volume used in transport calculations.

A parameterisation of a hydrogeological DFN was developed using fracture geometrical and hydraulic data for SDM-Site Laxemar /Rhén et al. 2008/. The hydrogeological DFN characterises statistics of the geometry, intensity and hydraulic properties of fractures outside of mapped deformation zones (HCD) for each of the hydraulic rock domains (HRD) defined in /Rhén et al. 2008/. One or more realisations of the hydrogeological DFN model are generated within the regional model domain, and then upscaled according to the finite-element grid to derive ECPM properties describing the HRD fracturing for that realisation. The hydrogeological properties of the ECPM grid are then modified to incorporate a representation of the larger scale deterministic HCDs in an implicit manner by adjusting the properties of the finite-elements which their volume crosses. The length of the HCDs (kilometres) is much longer than the size of the finite-elements (40–120 m) for all HCD.

Since the HRD properties are based on stochastic realisations of a DFN, then ideally a Monte-Carlo approach should be used to scope the effect of the variability between realisations. Since the size of stochastic fractures ranges from 5.6 m to 564 m radius, which is much smaller than the regional model size, over 10 km, then one would not expect the regional flow to vary greatly between realisations, although there may be significant differences in the simulated flows and solute concentrations at individual locations such as boreholes. The conceptual model suggests the hydraulic properties of the HCD to demonstrate significant spatial heterogeneity within the plane, suggesting that even if their position can be considered deterministic from a structural and geometric point of view their hydraulic properties may have to be treated stochastically. Since the HCD are often several kilometres in length, spatial variability in their properties (transmissivity) may have a greater impact

on regional-scale flow than that in the HRD. Hence, the sensitivity to lateral spatially variability within HCD is one of the uncertainties quantified in this study. However, for practical purposes only a single realisation of the HRD is used in developing the base case flow model and quantifying other uncertainties, and the properties of the HCD are deterministic, varying only with depth (apart from local conditioning to borehole measurements of transmissivity).

Key assumptions and simplifications made in the modelling are summarised below as:

- The deterministic deformation zone model provided by Geology /Wahlgren et al. 2008/ represents modelled hydraulically active features.
- The longitudinal (in plane) transmissivity (T), expressed as $\log_{10}(T)$, of each deterministic deformation zone (HCD) varies linearly (in log10(T)) with depth, but is here assumed to be uniform horizontally i.e. no lateral heterogeneity in the base case (though conditioned locally around every borehole with measured hydraulic data).
- The statistical parameters of the hydrogeological DFN are uniform within each HRD, but may vary with depth in terms of four depth zones delimited at the elevations –150 m, –400 m and –650 m /Rhén et al. 2008/.
- Flow and solute transport within the network of fractures can be represented by an equivalent ECPM approach on an appropriate computational grid. Hexahedral grid elements of 40 m size are used around the Laxemar local model area and an area around Äspö, cf Figure 7-2, and 120 m size on the outside of this area on a regional scale.
- Properties of the HRD outside those defined within the local model volume are based on analogy to those inside, which have been comparatively well characterised.
- The hydraulic properties of the modelled Quaternary deposits are homogeneous within each type of deposit, and the hydraulic properties of layers of different types of deposits can be represented by an effective hydraulic conductivity in the horizontal and vertical directions for a finite-element.
- The top surface flow boundary condition can be specified as an average flux over an appropriate timescale. A uniform and constant effective recharge to the saturated zone of 180 mm/year /Werner et al. 2008/ is used for the palaeohydrogeology, head and Äspö drawdown simulations. The flux is reduced or allowed to be negative (i.e. discharge) where the calculated head is at or above ground surface. For the shorter timescale of the HLX33/HLX28 interference test, the flux should be adjusted in proportion to the average precipitation during the duration of the test. The flow model does not represent surface run-off or flow within the unsaturated zone.
- Initial and boundary conditions for the simulations of hydrochemistry are best conceptualised in terms of 5 reference water types (*Altered Meteoric Water*, *Deep Saline Water*, *Littorina Sea Water*, *Glacial Melt Water*, and *Inter-glacial Porewater* (cf Sections 4.2 and 5.6.3).
- The chemical composition of reference waters is derived by a principal component analysis using the Multivariate Mixing and Mass-balance (M3) analysis /Laaksoharju et al. 2009/. This is used to make a straightforward conversion between mass fractions, concentrations of individual ions, and/or environmental isotope ratios ($\delta^{18}O$, δD), and fluid density.
- The reference water mass fractions are transported as conservative entities by advection with groundwater flow and dispersion within the fracture system. Diffusion into the matrix porewater is included, i.e. rock matrix diffusion (RMD), but there is no advection within the matrix.
- Palaeohydrogeology simulations are calibrated primarily against borehole measurements of Cl, Br/Cl, and $\delta^{18}O$, which are considered to be conservative tracers. HCO_3 is used as a signature for infiltrating post-glacial meteoric water (although it is a non-conservative species); this signature can also be traced by the low Cl content, cf Section 5.6.3 for more details.
- Analysed groundwater samples vary in their integrity as representative indicators of natural conditions according to the level of contamination by drilling water and achieved charge balance. Those samples with a low contamination and a good charge balance are given more credence as quantitative calibration targets, but since such samples are quite sparse, then additional measurements are used as a secondary qualitative guide of hydrogeochemical conditions.

- Porewater measurements of Cl and $\delta^{18}O$ are also considered as calibration targets. In the simulations, the model of RMD calculates a spatial profile of solute concentrations within each idealised matrix volume, which could vary considerably from the surface of the fracture to the centre of the matrix volume. However, for simplicity the average concentration within the matrix volume is compared with the measured porewater concentration irrespective of how far the analysed core sample may have been from a water-bearing fracture. Some more detailed assessments of the variability within the matrix blocks are made to illustrate this uncertainty.
- The palaeohydrogeology simulations were started at 8000 BC and the evolution of hydrogeochemistry was calculated according to changes in sea-level and salinity. At this stage only small areas in the western part of the Laxemar local model area were above sea level, cf Section 4.2. At c. 9300 BC the western most part of the regional model area rose above the shore-level.

7.2 Topography and model domain geometry

The full Laxemar-Simpevarp regional model area used in the site descriptive geological modelling is about 21 km by 13 km and 2.2 km deep. The lateral boundaries of the flow modelling domain were based on identified surface water divides. As shown in Figure 7-1, this required extension of the model domain outside the Laxemar-Simpevarp regional model area in some parts and limiting the extent slightly in others. The bottom elevation of the model was set at –2,160 m, which is far below the top demarcation of the lowest hydraulic depth zone interpreted at –650 m in the hydrogeological DFN modelling. Flowing features below –650 m are generally rare and HCD have a maximum transmissivity of less than around $4 \cdot 10^{-6}$ m^2/s at elevation –1,000 m. For the HRD, the intensity of PFL-f features is less than 1 per 100 m and the mean hydraulic conductivity for boreholes sections outside of deformation zones below –650 m is less than 10^{-9} m/s, apart from possibly in HRD_EW007. Taking this into account together with the high salinities in excess of about 20 g/L TDS seen below about –1,000 m, then little flow of any significance is expected to circulate below –1,000 m, and hence the vertical and horizontal extent of the regional model domain is expected to be entirely adequate for describing groundwater flow within the Laxemar local model area.

The comparative study /Holmén 2008/ considered a similar and much larger regional model domain based on model version Laxemar 1.2, and demonstrated that the weakly developed surface water divide employed for delimiting the western regional model boundary is in fact not a groundwater divide for the groundwater flow at greater depth. Hence, deep groundwater flow that passes below the weakly developed surface water divide in the larger model will not be included in the current model. Given that the deep groundwater flow across the western boundary is not included in the current model, this model may underestimate groundwater flow at repository depth, and overestimate both lengths of flow paths as well as the breakthrough times of flow paths from the repository area. However, the comparison by /Holmén 2008/ estimated these differences as being small (within a factor of c. 1.5), since the deep groundwater flow missing in the small model is not large. Given the strong depth trends in hydraulic properties interpreted in SDM-Site Laxemar, it is expected that the results presented here will be even less sensitive to deep groundwater flow across the western boundary of the model.

Within the local model area and down to an elevation of –1,200 m, an embedded finer grid of 40 m elements was nested within a coarser grid of 120 m elements on the regional scale. The embedded grid covers the Laxemar local model area and Äspö, and is roughly 4 km square. For the SDM-Site Forsmark hydrogeological modelling, the corresponding fine-scale embedded grid was 20 m and covered an area of about 2–3 km in horizontal extent, and about 700 m deep, and hence the embedded grid volume used for Laxemar is about four times that of Forsmark, but less refined. Since, both the regional- and site-scale domains were larger compared to Forsmark, then the hydrogeological simulations were computationally more demanding at Laxemar.

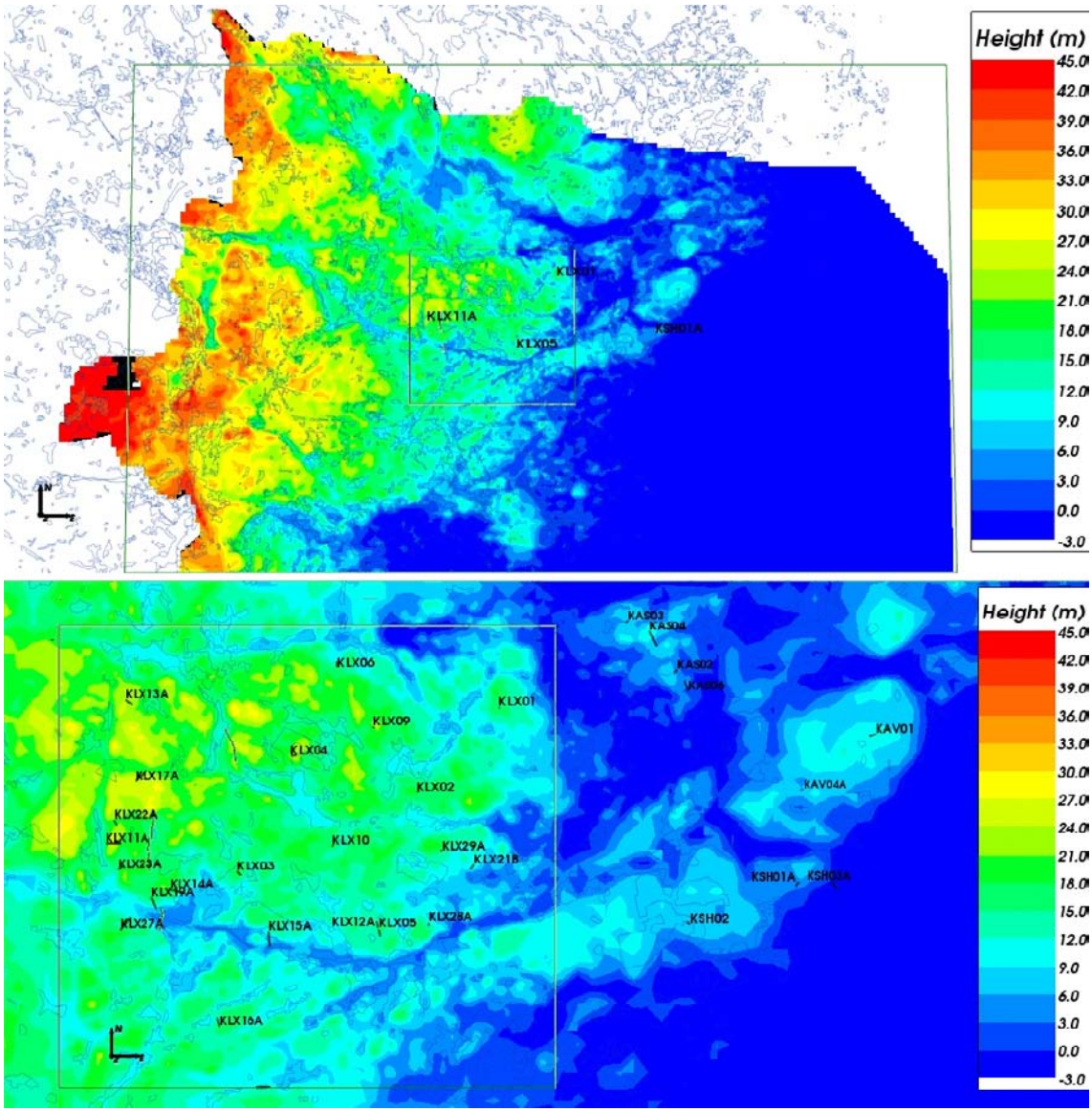

Figure 7-1. *Representation of topography on the regional scale hydrogeological model (top), and around the Laxemar local scale model area (bottom). The extent of the regional scale model area is shown by the outer green line in the top figure. The local scale model area is shown by the inner green line shown in both plots. The locations of some core-drilled boreholes are shown for reference. © Lanmäteriverket Gävle 2007 Consent I 2007/1092.*

7.3 Selection of grid resolution

Since data on the topography, fracture domains and Quaternary deposits data were supplied on a 20 m scale, then the appropriate finite-element size were chosen as multiples of 20 m. Due to the volume of the local-scale model, c. 16 km^3, a computational grid of 40 m was used to make the palaeo-hydrogeological simulations tractable, since these require around 500 time-steps (i.e. 20 y/step for a 10,000 year simulation period) of coupled flow and transport of several reference waters. As mentioned above the facility in ConnectFlow to have refined sub-domains embedded within a coarser grid was used, which apply appropriate conditions at the interface to ensure conservation of fluxes and continuity of variables.

A horizontal slice through the embedded grid around the Laxemar local model area and an area around Äspö, is shown in Figure 7-2. As can be seen, the 40 m grid covers all core-drilled boreholes in the Laxemar subarea and those around Äspö for the simulations of drawdown resulting from the HRL construction. Examples of how the properties, such as HCD transmissivity, are mapped onto this grid are given in the following sections. Many local HCDs have been identified in the mapping within the Laxemar local model area. Figure 7-2 demonstrates how the fine-scale grid gives a reasonable delimits the HCD from the HRDs, and hence can represent contrasts between their hydraulic properties. The figure also shows the borehole locations and HCDs that were considered in choosing an appropriate grid refinement.

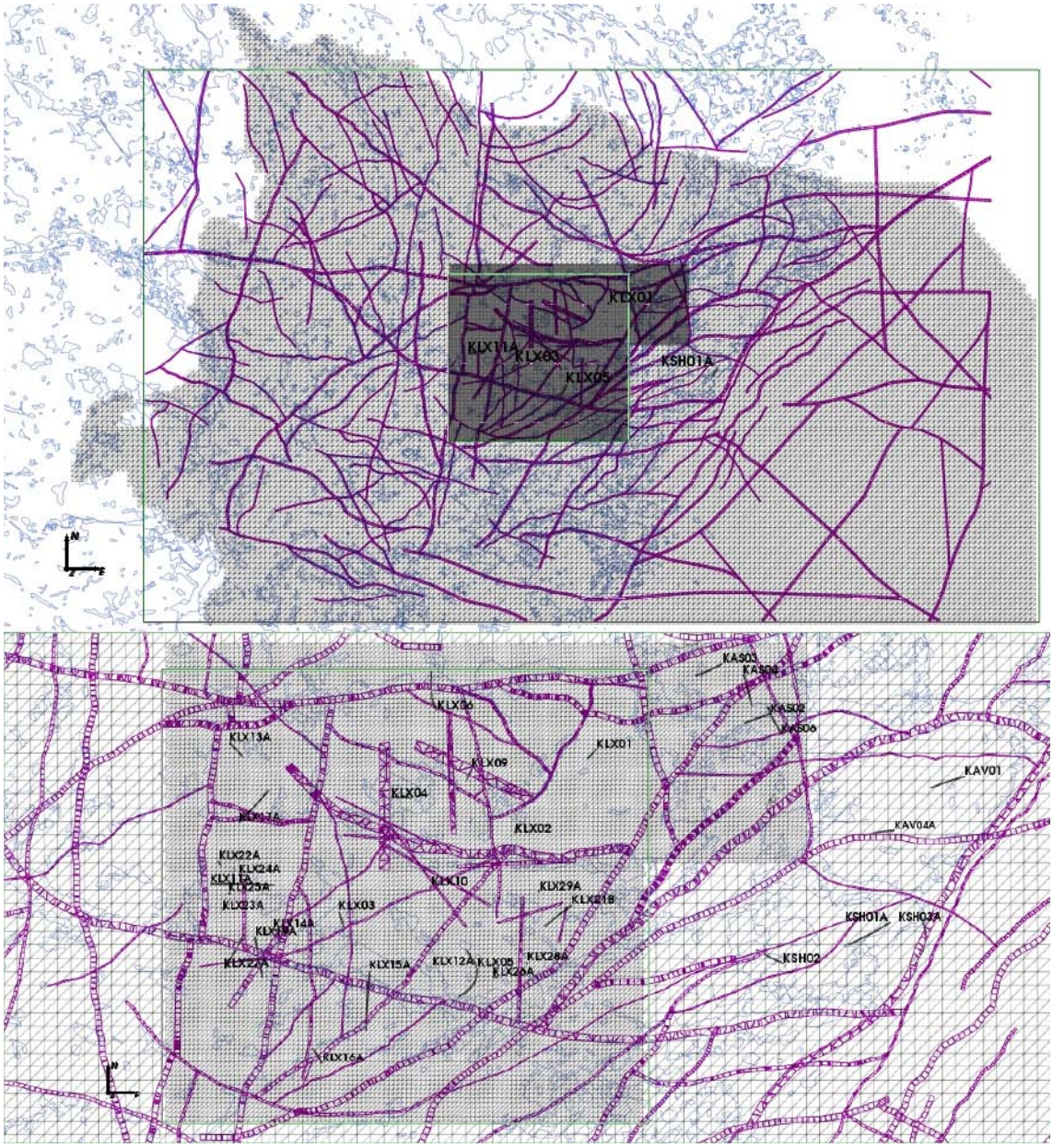

Figure 7-2. *Embedded refined finite-element grid around the Laxemar local model area and an area around Äspö, with size 40 m square. A 120 m grid was used on the regional-scale outside the local scale model area. The elements have a square horizontal cross-section, but are visualised here as artificially split into 2 triangles. The positions of the core-drilled boreholes are shown, and a horizontal slice at elevation 0 m through the deformation zone model is superimposed (purple).*

7.4 Hydraulic conductor domain (HCD) model

The Hydraulic Conductor Domains (HCD) are included in the flow model using their geometrical description provided by the Geology team and the hydraulic property assignment suggested in /Rhén et al. 2008/.

There are rather few HCDs with well characterised hydraulic properties (only 7, cf /Rhén et al. 2008/) such that they have individual T versus depth trend functions (referred to as category "App 5" in Table 7-1, i.e. referencing Appendix 5). Most of the HCD are described by using generalised depth dependencies. The HCD are divided into four main categories based on orientation and size. The four categories are denoted by: E-W orientation with size < 2 km; E-W orientation with size > 2 km; other orientations with size < 2 km; other orientations with size > 2 km, cf /Rhén et al. 2008/). For the *base case model*, transmissivity was assigned according to a depth trend defined for each HCD with no lateral heterogeneity (apart from some localised conditioning to measurement values). Initially, the prescription for HCD transmissivities defined in /Rhén et al. 2008/ was implemented as described in Table 7-1. The HCD are defined as surfaces defined by a set of points. For the purposes of the flow modelling the HCD surfaces were triangulated based on an appropriate scale, 100 m was used. Transmissivity values were then associated with each triangle to represent the defined depth trend, or in a stochastic case, the transmissivities were sampled randomly from a log-normal distribution with a mean and standard deviation that may vary with depth. The final step was to modify the transmissivities of any triangles within a specified distance away from any borehole interval in which a transmissivity has been interpreted. Again, a 100 m search radius was used around the measurement points. Transmissivity characterises flow in the plane of the HCD, but can also be defined equivalently in terms of a longitudinal hydraulic conductivity and thickness. In order to represent the dolerite dykes as hydraulic barriers (see Section 3.3.2) it is necessary to also define the flow perpendicular to the plane of the HCD in terms of a transverse hydraulic conductivity. Hence, the result of the above process is to obtain a discrete description of the HCD as a triangulated surface with each triangle having an assigned thickness, hydraulic conductivity (longitudinal and transverse), kinematic porosity and fracture surface area per unit volume. This may then be used in either an ECPM or DFN flow model. For the ECPM approach used here, ConnectFlow reads in each triangle, identifies which finite-elements are intersected by the HCD volume, and modifies the hydraulic properties accordingly to combine the background properties of the HRD with a representation of one or more HCD (see /Follin et al. 2008/).

The palaeohydrogeological simulations suggested that the HCD transmissivities should generally be reduced below –150 m (see Section 9.1.4). The default factors for the reduction are shown in Table 7-2. However, based on natural head measurements and interference tests it was found that for a few specific HCD other factors were needed. These exceptions from the general treatment are shown in Table 7-3. Hence, the final calibrated *base case model* is constructed by first using Table 7-1, then applying the factors given in Table 7-2 apart from a few specific zones where the factors specified in Table 7-3 should be used instead.

The distribution of the mean transmissivity in the HCD for the base case is shown in Figure 7-3 and Figure 7-4 from two different view points. For stochastic realisations with lateral heterogeneity, these values are used as the mean sampled value for a log-normal distribution with specified standard deviation, but truncated at ±2 standard deviations. Equivalent plots for one example realisation of the HCD with spatial variability, standard deviation in Log(T) = 1.4, is shown in Figure 7-5 and Figure 7-6. In both cases, the heterogeneous transmissivity field is conditioned to measured values at the intercept with borehole intervals where measurements are available.

In order to simulate the interference test in HLX33 and HLX28 a homogeneous specific storage coefficient around 10^{-7} m^{-1} was used for all of the bedrock.

Table 7-1. Summary of HCD and their inferred depth dependent transmissivity. It is assumed that no zone is thicker than 50 m within the flow model. The depth dependency is calculated using $T = 10^{(a+BZ)}$, where Z is elevation. Zones that are marked with * are anisotropic (e.g. dolerites). The categories are taken from /Rhén et al. 2008/ but also shown in Appendix 5 in this report. In addition the trace length and the equivalent hydraulic conductivity (K = T/thickness) for the uppermost depth zone i.e. Z > –150 m, are given.

HCD (prefixed ZSM)	Thickness in the flow model (m)	Trace Length (km)	Category	a	B	Equivalent K > –150 m (m/s)
EW002A*	50	30.0	R20	–4.049	0.0019	$1.3 \cdot 10^{-06}$
EW007A	50	3.3	App 5	–3.996	0.002158	$1.4 \cdot 10^{-06}$
EW007C	50	0.5	App 5	–3.996	0.002158	$1.4 \cdot 10^{-06}$
EW009A	12	1.7	R19	–4.910	0.00209	$7.1 \cdot 10^{-07}$
EW013A	45	4.4	R20	–4.049	0.0019	$1.4 \cdot 10^{-06}$
EW020A	50	5.8	R20	–4.049	0.0019	$1.3 \cdot 10^{-06}$
EW038A	10	3.2	R20	–4.049	0.0019	$6.4 \cdot 10^{-06}$
EW076A	31	3.1	R20	–4.049	0.0019	$2.1 \cdot 10^{-06}$
EW114A	25	2.5	R20	–4.049	0.0019	$2.6 \cdot 10^{-06}$
EW120A	50	1.2	R19	–4.910	0.00209	$1.7 \cdot 10^{-07}$
EW129A	20	2.0	R20	–4.049	0.0019	$3.3 \cdot 10^{-06}$
EW190A	17	1.7	R19	–4.910	0.00209	$5.2 \cdot 10^{-07}$
EW200A	18	1.7	R19	–4.910	0.00209	$4.9 \cdot 10^{-07}$
EW230A	18	1.8	R19	–4.910	0.00209	$4.8 \cdot 10^{-07}$
EW240A	50	5.5	R20	–4.049	0.0019	$1.3 \cdot 10^{-06}$
EW305A	19	1.9	R19	–4.910	0.00209	$4.5 \cdot 10^{-07}$
EW316A	30	2.4	R20	–4.049	0.0019	$2.1 \cdot 10^{-06}$
EW904A	50	6.1	R20	–4.049	0.0019	$1.3 \cdot 10^{-06}$
EW905A	21	2.1	R20	–4.049	0.0019	$3.0 \cdot 10^{-06}$
EW906A	50	5.7	R20	–4.049	0.0019	$1.3 \cdot 10^{-06}$
EW907A	50	12.0	R20	–4.049	0.0019	$1.3 \cdot 10^{-06}$
EW936A	11	1.1	R19	–4.910	0.00209	$7.8 \cdot 10^{-07}$
NE004A	50	15.7	R22	–4.157	0.00255	$9.0 \cdot 10^{-07}$
NE005A	50	16.0	R22	–4.157	0.00255	$9.0 \cdot 10^{-07}$
NE006A*	50	2.1	App 5	–3.017	0.003104	$1.1 \cdot 10^{-05}$
NE008A	39	3.9	R22	–4.157	0.00255	$1.1 \cdot 10^{-06}$
NE010A	34	3.4	R22	–4.157	0.00255	$1.3 \cdot 10^{-06}$
NE011A	50	10.5	R22	–4.157	0.00255	$9.0 \cdot 10^{-07}$
NE012A	50	5.6	App 5	–3.673	0.002209	$2.9 \cdot 10^{-06}$
NE015A	10	1.9	R21	–5.137	0.00219	$5.0 \cdot 10^{-07}$
NE018A	50	1.3	R21	–5.137	0.00219	$1.0 \cdot 10^{-07}$
NE019A	20	3.7	R22	–4.157	0.00255	$2.2 \cdot 10^{-06}$
NE021A	40	4.7	R22	–4.157	0.00255	$1.1 \cdot 10^{-06}$
NE022A	28	2.8	R22	–4.157	0.00255	$1.6 \cdot 10^{-06}$
NE024A	50	15.0	App 5	–2.234	0.007197	$3.4 \cdot 10^{-05}$
NE024B	16	1.6	App 5	–2.234	0.007197	$1.1 \cdot 10^{-04}$
NE031A	15	4.2	R22	–4.157	0.00255	$3.0 \cdot 10^{-06}$
NE031B	19	1.9	R21	–5.137	0.00219	$2.6 \cdot 10^{-07}$
NE032A	26	2.6	R22	–4.157	0.00255	$1.7 \cdot 10^{-06}$
NE033A	30	3.0	R22	–4.157	0.00255	$1.5 \cdot 10^{-06}$
NE034A	29	2.9	R22	–4.157	0.00255	$1.5 \cdot 10^{-06}$
NE036A	23	2.3	R22	–4.157	0.00255	$1.9 \cdot 10^{-06}$
NE040A	20	1.6	R21	–5.137	0.00219	$2.5 \cdot 10^{-07}$
NE062A	17	1.7	R21	–5.137	0.00219	$3.0 \cdot 10^{-07}$
NE063A	10	1.1	R21	–5.137	0.00219	$5.0 \cdot 10^{-07}$
NE065A	10	1.4	R21	–5.137	0.00219	$5.0 \cdot 10^{-07}$
NE073A	36	3.6	R22	–4.157	0.00255	$1.2 \cdot 10^{-06}$
NE079A	10	2.7	R22	–4.157	0.00255	$4.5 \cdot 10^{-06}$
NE081A	21	2.1	R22	–4.157	0.00255	$2.2 \cdot 10^{-06}$
NE095A	23	2.3	R22	–4.157	0.00255	$2.0 \cdot 10^{-06}$

HCD (prefixed ZSM)	Thickness in the flow model (m)	Trace Length (km)	Category	a	B	Equivalent K > –150 m (m/s)
NE096A	17	1.7	R21	–5.137	0.00219	$2.9 \cdot 10^{-07}$
NE107A	35	3.1	R22	–4.157	0.00255	$1.3 \cdot 10^{-06}$
NE108A	10	1.8	R21	–5.137	0.00219	$5.0 \cdot 10^{-07}$
NE132A	28	2.8	R22	–4.157	0.00255	$1.6 \cdot 10^{-06}$
NE133A	24	2.4	R22	–4.157	0.00255	$1.8 \cdot 10^{-06}$
NE185A	24	2.4	R22	–4.157	0.00255	$1.9 \cdot 10^{-06}$
NE210A	21	2.1	R22	–4.157	0.00255	$2.1 \cdot 10^{-06}$
NE210B	28	2.8	R22	–4.157	0.00255	$1.6 \cdot 10^{-06}$
NE218A	50	6.5	R22	–4.157	0.00255	$9.0 \cdot 10^{-07}$
NE229A	20	2.0	R22	–4.157	0.00255	$2.2 \cdot 10^{-06}$
NE257A	27	2.7	R22	–4.157	0.00255	$1.7 \cdot 10^{-06}$
NE258A	26	2.6	R22	–4.157	0.00255	$1.7 \cdot 10^{-06}$
NE259A	28	2.8	R22	–4.157	0.00255	$1.6 \cdot 10^{-06}$
NE267A	23	2.3	R22	–4.157	0.00255	$2.0 \cdot 10^{-06}$
NE286A	27	2.7	R22	–4.157	0.00255	$1.7 \cdot 10^{-06}$
NE289A	21	2.1	R22	–4.157	0.00255	$2.1 \cdot 10^{-06}$
NE295A	31	3.1	R22	–4.157	0.00255	$1.4 \cdot 10^{-06}$
NE302A	24	2.4	R22	–4.157	0.00255	$1.8 \cdot 10^{-06}$
NE307A	18	1.8	R21	–5.137	0.00219	$2.8 \cdot 10^{-07}$
NE308A	24	2.4	R22	–4.157	0.00255	$1.9 \cdot 10^{-06}$
NE313A	50	9.0	R22	–4.157	0.00255	$9.0 \cdot 10^{-07}$
NE901A	25	2.5	R22	–4.157	0.00255	$1.8 \cdot 10^{-06}$
NE903A	25	2.5	R22	–4.157	0.00255	$1.8 \cdot 10^{-06}$
NE909A	17	1.7	R21	–5.137	0.00219	$2.9 \cdot 10^{-07}$
NE910A	22	2.2	R22	–4.157	0.00255	$2.1 \cdot 10^{-06}$
NE911A	50	5.5	R22	–4.157	0.00255	$9.0 \cdot 10^{-07}$
NE912A	31	3.1	R22	–4.157	0.00255	$1.5 \cdot 10^{-06}$
NE913A	50	5.9	R22	–4.157	0.00255	$9.0 \cdot 10^{-07}$
NE914A	50	5.7	R22	–4.157	0.00255	$9.0 \cdot 10^{-07}$
NE915A	20	1.9	R21	–5.137	0.00219	$2.6 \cdot 10^{-07}$
NE930A	5	4.2	R22	–4.157	0.00255	$9.0 \cdot 10^{-06}$
NE940A	16	1.6	R21	–5.137	0.00219	$3.1 \cdot 10^{-07}$
NE941A	22	2.2	R22	–4.157	0.00255	$2.1 \cdot 10^{-06}$
NE942A	15	2.5	App 5	–4.559	0.002405	$1.2 \cdot 10^{-06}$
NS001A*	50	3.4	App 5	–3.680	0.002405	$2.8 \cdot 10^{-06}$
NS001B*	50	1.1	App 5	–3.680	0.002405	$2.8 \cdot 10^{-06}$
NS001C*	50	1.9	App 5	–3.680	0.002405	$2.8 \cdot 10^{-06}$
NS001D*	50	0.2	App 5	–3.680	0.002405	$2.8 \cdot 10^{-06}$
NS001E*	50	4.3	App 5	–3.680	0.002405	$2.8 \cdot 10^{-06}$
NS009A	25	9.8	R22	–4.157	0.00255	$1.8 \cdot 10^{-06}$
NS017A	21	2.1	R22	–4.157	0.00255	$2.2 \cdot 10^{-06}$
NS017B	20	2.1	App 5	–3.240	0.002405	$1.9 \cdot 10^{-05}$
NS046A	20	2.1	R22	–4.157	0.00255	$2.2 \cdot 10^{-06}$
NS057A	20	5.0	R22	–4.157	0.00255	$2.2 \cdot 10^{-06}$
NS059A*	50	4.8	App 5	–3.652	0.002405	$2.9 \cdot 10^{-06}$
NS064A	50	5.5	R22	–4.157	0.00255	$9.0 \cdot 10^{-07}$
NS071A	18	1.8	R21	–5.137	0.00219	$2.7 \cdot 10^{-07}$
NS084A	32	3.2	R22	–4.157	0.00255	$1.4 \cdot 10^{-06}$
NS085A	37	3.7	R22	–4.157	0.00255	$1.2 \cdot 10^{-06}$
NS117A	17	1.7	R21	–5.137	0.00219	$3.0 \cdot 10^{-07}$
NS141A	20	2.5	R22	–4.157	0.00255	$2.2 \cdot 10^{-06}$
NS165A	18	1.8	R21	–5.137	0.00219	$2.8 \cdot 10^{-07}$
NS182A	30	3.0	R22	–4.157	0.00255	$1.5 \cdot 10^{-06}$
NS182B	30	3.0	R22	–4.157	0.00255	$1.5 \cdot 10^{-06}$
NS215A	16	1.6	R21	–5.137	0.00219	$3.1 \cdot 10^{-07}$
NS221A	22	2.2	R22	–4.157	0.00255	$2.0 \cdot 10^{-06}$

HCD (prefixed ZSM)	Thickness in the flow model (m)	Trace Length (km)	Category	a	B	Equivalent K > –150 m (m/s)
NS287A	34	3.4	R22	–4.157	0.00255	$1.3 \cdot 10^{-06}$
NS291A	19	1.9	R21	–5.137	0.00219	$2.6 \cdot 10^{-07}$
NS301A	19	1.9	R21	–5.137	0.00219	$2.7 \cdot 10^{-07}$
NS916A	44	4.4	R22	–4.157	0.00255	$1.0 \cdot 10^{-06}$
NS917A	50	5.3	R22	–4.157	0.00255	$9.0 \cdot 10^{-07}$
NS918A	29	2.9	R22	–4.157	0.00255	$1.6 \cdot 10^{-06}$
NS919A	50	8.0	R22	–4.157	0.00255	$9.0 \cdot 10^{-07}$
NS920A	31	3.1	R22	–4.157	0.00255	$1.5 \cdot 10^{-06}$
NS945A	10	2.0	R22	–4.157	0.00255	$4.5 \cdot 10^{-06}$
NS947A	20	1.8	R21	–5.137	0.00219	$2.5 \cdot 10^{-07}$
NW025A	10	1.9	R21	–5.137	0.00219	$5.0 \cdot 10^{-07}$
NW027A	34	3.4	R22	–4.157	0.00255	$1.3 \cdot 10^{-06}$
NW042A-EAST	50	8.3	R22	–4.157	0.00255	$9.0 \cdot 10^{-07}$
NW042A-WEST*	50	8.3	R22	–4.157	0.00255	$9.0 \cdot 10^{-07}$
NW060A	32	3.2	R22	–4.157	0.00255	$1.4 \cdot 10^{-06}$
NW066A	50	5.1	R22	–4.157	0.00255	$9.0 \cdot 10^{-07}$
NW067A	50	7.9	R22	–4.157	0.00255	$9.0 \cdot 10^{-07}$
NW068A	18	1.8	R21	–5.137	0.00219	$2.8 \cdot 10^{-07}$
NW068B	22	2.2	R22	–4.157	0.00255	$2.0 \cdot 10^{-06}$
NW068C	4	0.4	R21	–5.137	0.00219	$1.1 \cdot 10^{-06}$
NW074A	33	3.3	R22	–4.157	0.00255	$1.4 \cdot 10^{-06}$
NW075A	38	3.8	R22	–4.157	0.00255	$1.2 \cdot 10^{-06}$
NW083A	17	1.6	R21	–5.137	0.00219	$3.0 \cdot 10^{-07}$
NW086A	22	2.2	R22	–4.157	0.00255	$2.0 \cdot 10^{-06}$
NW088A	20	3.2	R22	–4.157	0.00255	$2.2 \cdot 10^{-06}$
NW089A	21	2.1	R22	–4.157	0.00255	$2.1 \cdot 10^{-06}$
NW106A	17	1.7	R21	–5.137	0.00219	$2.9 \cdot 10^{-07}$
NW113A	31	3.0	R22	–4.157	0.00255	$1.5 \cdot 10^{-06}$
NW119A	10	2.0	R22	–4.157	0.00255	$4.5 \cdot 10^{-06}$
NW123A	32	3.2	R22	–4.157	0.00255	$1.4 \cdot 10^{-06}$
NW126A	37	3.7	R22	–4.157	0.00255	$1.2 \cdot 10^{-06}$
NW126B	36	3.6	R22	–4.157	0.00255	$1.3 \cdot 10^{-06}$
NW131A	50	5.2	R22	–4.157	0.00255	$9.0 \cdot 10^{-07}$
NW173A	21	2.1	R22	–4.157	0.00255	$2.1 \cdot 10^{-06}$
NW178A	41	4.1	R22	–4.157	0.00255	$1.1 \cdot 10^{-06}$
NW184A	17	1.6	R21	–5.137	0.00219	$3.0 \cdot 10^{-07}$
NW202A	16	1.6	R21	–5.137	0.00219	$3.1 \cdot 10^{-07}$
NW206A	19	1.9	R21	–5.137	0.00219	$2.7 \cdot 10^{-07}$
NW222A	27	2.7	R22	–4.157	0.00255	$1.7 \cdot 10^{-06}$
NW233A	19	1.9	R21	–5.137	0.00219	$2.6 \cdot 10^{-07}$
NW235A	20	2.0	R22	–4.157	0.00255	$2.2 \cdot 10^{-06}$
NW245A	23	2.3	R22	–4.157	0.00255	$1.9 \cdot 10^{-06}$
NW247A	16	1.6	R21	–5.137	0.00219	$3.1 \cdot 10^{-07}$
NW251A	20	2.0	R21	–5.137	0.00219	$2.5 \cdot 10^{-07}$
NW254A	49	4.9	R22	–4.157	0.00255	$9.1 \cdot 10^{-07}$
NW261A	22	2.2	R22	–4.157	0.00255	$2.0 \cdot 10^{-06}$
NW263A	16	1.6	R21	–5.137	0.00219	$3.1 \cdot 10^{-07}$
NW269A	21	2.1	R22	–4.157	0.00255	$2.1 \cdot 10^{-06}$
NW280A	20	2.0	R22	–4.157	0.00255	$2.2 \cdot 10^{-06}$
NW294A	23	2.3	R22	–4.157	0.00255	$2.0 \cdot 10^{-06}$
NW312A	50	5.0	R22	–4.157	0.00255	$9.0 \cdot 10^{-07}$
NW312B	12	1.2	R21	–5.137	0.00219	$4.0 \cdot 10^{-07}$
NW312C	17	1.7	R21	–5.137	0.00219	$3.0 \cdot 10^{-07}$
NW321A	21	2.1	R22	–4.157	0.00255	$2.2 \cdot 10^{-06}$
NW322A	50	6.9	R22	–4.157	0.00255	$9.0 \cdot 10^{-07}$
NW921A	25	2.5	R22	–4.157	0.00255	$1.8 \cdot 10^{-06}$

HCD (prefixed ZSM)	Thickness in the flow model (m)	Trace Length (km)	Category	a	B	Equivalent K > –150 m (m/s)
NW922A	18	1.8	R21	–5.137	0.00219	$2.8 \cdot 10^{-07}$
NW923A	38	3.7	R22	–4.157	0.00255	$1.2 \cdot 10^{-06}$
NW925A	28	2.8	R22	–4.157	0.00255	$1.6 \cdot 10^{-06}$
NW928A	10	1.5	R21	–5.137	0.00219	$5.0 \cdot 10^{-07}$
NW929A	20	1.6	R22	–4.157	0.00255	$2.2 \cdot 10^{-06}$
NW931A	50	3.8	R22	–4.157	0.00255	$9.0 \cdot 10^{-07}$
NW931B	38	3.8	R22	–4.157	0.00255	$1.2 \cdot 10^{-06}$
NW933A	22	2.2	R22	–4.157	0.00255	$2.0 \cdot 10^{-06}$
NW937A	17	1.7	R21	–5.137	0.00219	$2.9 \cdot 10^{-07}$
NW943A	17	1.7	R21	–5.137	0.00219	$2.9 \cdot 10^{-07}$
NE944A	10	1.2	R21	–5.137	0.00219	$5.0 \cdot 10^{-07}$
EW946A	10	1.5	App 5	–4.210	0.004638	$2.8 \cdot 10^{-06}$
EW900A	25	0.9	R21	–5.137	0.00219	$2.0 \cdot 10^{-07}$
NW047A	25	1.3	R21	–5.137	0.00219	$2.0 \cdot 10^{-07}$
NW052A	15	1.1	R21	–5.137	0.00219	$3.3 \cdot 10^{-07}$
EW014A	10	1.2	R21	–5.137	0.00219	$5.0 \cdot 10^{-07}$
EW900B	25	0.69	R21	–5.137	0.00219	$2.0 \cdot 10^{-07}$
HLX28_DZ1	10	1.0	R21	–5.137	0.00219	$5.0 \cdot 10^{-07}$
KLX03_DZ1B	10	1.0	R21	–5.137	0.00219	$5.0 \cdot 10^{-07}$
KLX03_DZ1C	10	1.0	R21	–5.137	0.00219	$5.0 \cdot 10^{-07}$
KLX04_DZ6B	14	1.0	R21	–5.137	0.00219	$3.6 \cdot 10^{-07}$
KLX04_DZ6C	30	1.0	R21	–5.137	0.00219	$1.7 \cdot 10^{-07}$
KLX07_DZ10	10	1.0	R21	–5.137	0.00219	$5.0 \cdot 10^{-07}$
KLX07_DZ11	30	1.0	R21	–5.137	0.00219	$1.7 \cdot 10^{-07}$
KLX07_DZ12	47	1.0	R21	–5.137	0.00219	$1.1 \cdot 10^{-07}$
KLX07_DZ13	10	1.0	R21	–5.137	0.00219	$5.0 \cdot 10^{-07}$
KLX07_DZ7	30	1.0	R21	–5.137	0.00219	$1.7 \cdot 10^{-07}$
KLX07_DZ9	10	1.0	R21	–5.137	0.00219	$5.0 \cdot 10^{-07}$
KLX08_DZ1	27	1.0	R21	–5.137	0.00219	$1.9 \cdot 10^{-07}$
KLX08_DZ10	11	1.0	R21	–5.137	0.00219	$4.5 \cdot 10^{-07}$
KLX08_DZ6	10	1.0	R21	–5.137	0.00219	$5.0 \cdot 10^{-07}$
KLX09_DZ10	25	1.0	R21	–5.137	0.00219	$2.0 \cdot 10^{-07}$
KLX09E_DZ2	22	1.0	R21	–5.137	0.00219	$2.3 \cdot 10^{-07}$
KLX09F_DZ1	14	1.0	R21	–5.137	0.00219	$3.6 \cdot 10^{-07}$
KLX10C_DZ3	10	1.0	R21	–5.137	0.00219	$5.0 \cdot 10^{-07}$
KLX10C_DZ7	10	1.0	R21	–5.137	0.00219	$5.0 \cdot 10^{-07}$
KLX11_DZ11	20	1.0	R21	–5.137	0.00219	$2.5 \cdot 10^{-07}$
KLX18_DZ9	10	1.0	R21	–5.137	0.00219	$5.0 \cdot 10^{-07}$
KLX19_DZ5-8_ DOLERITE*	45	1.0	R21†	–4.183	0.00219	$1.0 \cdot 10^{-06}$
KLX21B_DZ10-12	10	1.0	R21	–5.137	0.00219	$5.0 \cdot 10^{-07}$
KLX28_DZ1	13	1.0	R21	–5.137	0.00219	$3.8 \cdot 10^{-07}$
KLX09_DZ9	6	1.0	R21†	–3.201	0.00219	$5.4 \cdot 10^{-06}$
KLX09_DZ14	9	1.0	R21†	–3.448	0.00219	$6.0 \cdot 10^{-07}$
KLX16_DZ6	1	1.0	R21†	–3.797	0.00219	$5.4 \cdot 10^{-05}$
KLX19_DZ2	4	1.0	R21†	–3.397	0.00219	$1.4 \cdot 10^{-05}$

† Based on R21 but adjusted to match measured T value.

*** Anisotropic HCD:**

HCD	Anisotropic ratio ($K_{Transverse}$: $K_{Longitudinal}$)
EW002A	1:100
NE006A	1:100
NS001A-E	1:10000
NS059A	1:10000
NW042A-WEST (part west of NS059A)	1:1000
KLX19_DZ5-8_DOLERITE	1:10000

Table 7-2. Default multiplication factors applied to the HCD in the base case flow model.

Elevation (m)	Factor
100 to –150	1.00
–150 to –400	0.30
–400 to –650	0.30
Below –650	0.10

Table 7-3. Exceptions to the multiplication factors specified in Table 7-2 for particular HCD in the base case flow model.

HCD (prefixed ZSM) and Elevation (m)	Factor	Adjustment	Borehole providing calibration results indicating that properties should change. (approximate elevation for intersection)
EW007A		Increase	
100 to –150	50.0		KLX07A (–70 m), KLX07B (–150 m), KLX08 (–170, –250 m) HLX33 interference test
–150 to –400	10.0		KLX04 (–250 to –350 m) HLX33 interference test
NE107A		Increase	
100 to –150	10		KLX15A (–300 m)
–150 to –400	10		KLX16A (–200 to –400 m)
NS001C		Increase	
100 to –150	3		KLX20A (–50 to –200 m)
–150 to –400	3		
NE944A		Lower	
Below –400	0.1		KLX18A (–250 m)

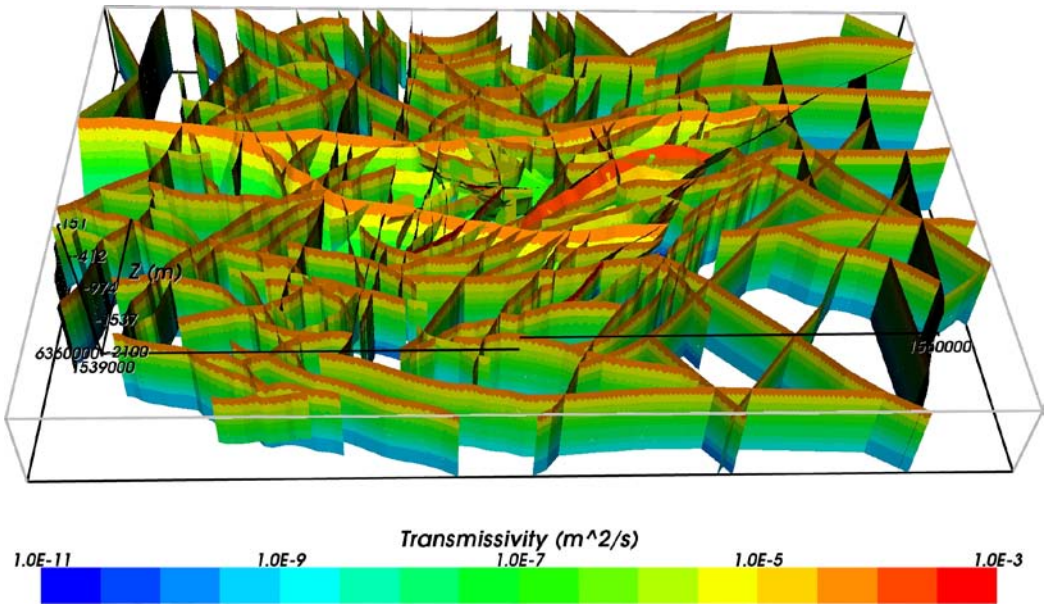

Figure 7-3. *All HCD and their inferred depth dependent transmissivity for the deterministic base case model (cf Figures 3-7 and 3-8). Here from an oblique view looking from the south.*

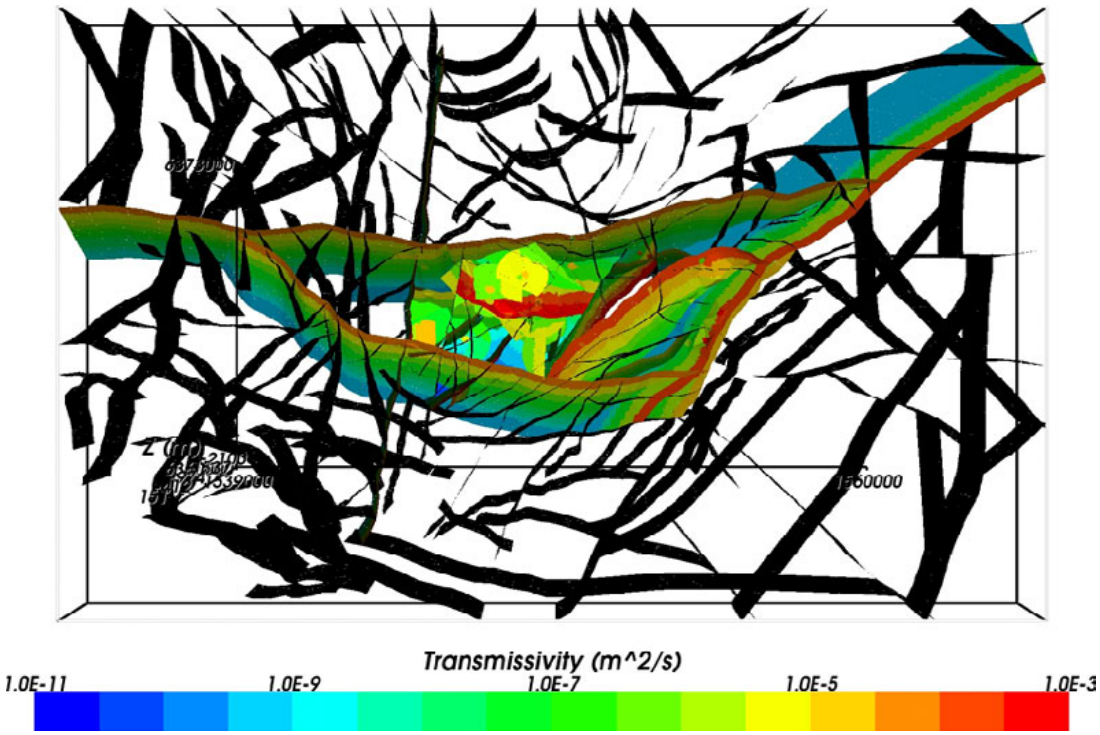

Figure 7-4. *All HCD and their inferred depth dependent transmissivity for the deterministic base case model (cf Figures 3-7 and 3-8). Here shown in map view.*

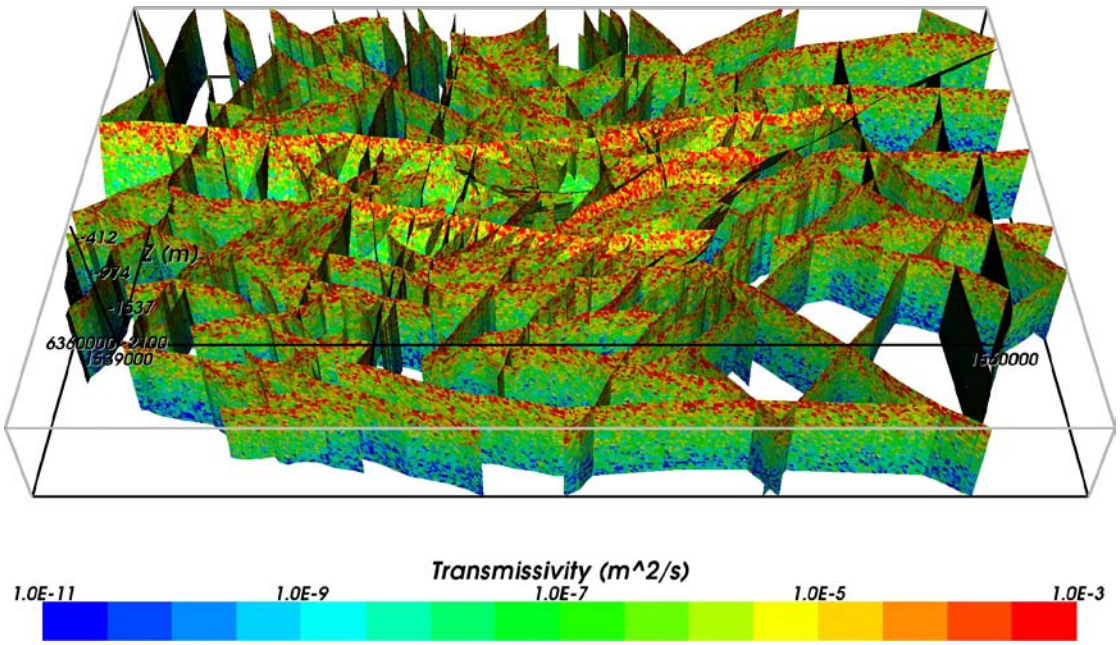

Figure 7-5. *All HCD and their inferred depth dependent transmissivity for a case with spatial heterogeneity and a standard deviation in Log(T) of 1.4. Here from an oblique view looking from the south (cf Figures 3-7 and 3-8).*

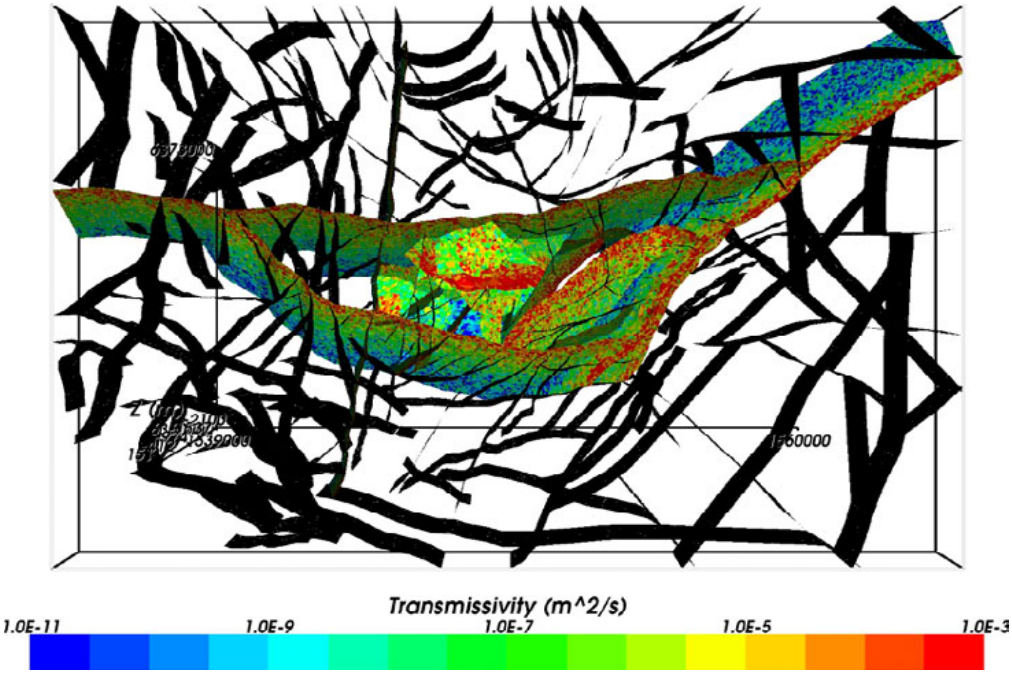

Figure 7-6. *All HCD and their inferred depth dependent transmissivity for a case with spatial heterogeneity and a standard deviation in Log(T) of 1.4. Here shown in map view (cf Figures 3-7 and 3-8).*

7.4.1 Transport properties

The transport properties required for palaeohydrogeological modelling relating to the fracture system are the kinematic porosity and the flow-wetted surface. The kinematic porosity (n_e) is used in the transport equation for reference waters (Equation 7-8) and affects the rate of change of concentration in the fractures; it also used in particle tracking calculations to determine advective travel time. The flow-wetted surface is also used in two places, but in this case it is implemented as two independent parameters in ConnectFlow. Firstly, a flow-wetted surface parameter, σ, is used in the transport equation for reference waters (Equation 7-8) to scale the flux of diffusive exchange between fractures and matrix per unit volume of bedrock. In ConnectFlow, this parameter is assigned as a property of a rock type rather than on each finite-element for reasons of numerical efficiency. A second flow-wetted surface parameter, a_r, is defined solely for estimating the flow related transport resistance, F, in Equation (7-1) for particles released in the repository volume, which is not reported here. These two parameters, σ and a_r are in principle the same, but for modelling convenience are defined independently. The values of σ are used as calibration parameters in the palaeohydrogeological modelling and for simplicity are defined as uniform within a given HRD and depth zone. The values used are estimated from measured average (within a HRD and depth zone) Terzaghi corrected intensity, $P_{10,corr}$, of conductive fractures detected by the PFL-f method as, $2 \cdot P_{10,corr}$(PFL). The values used for a_r, are assigned individually to each finite-element according to the connected open fracture area having been generated within each element for a particular realisation of the hydrogeological DFN and to the additional fracture area associated with any HCD that cross the element.

For the HCD, the kinematic porosities, and flow-wetted surface parameters have been inferred as depth dependent properties as shown in Table 7-4. There are measurements of intensity of conductive fractures (based on PFL-f data) in some HCD that could be used to estimate flow-wetted surface for individual deformation zones and depth intervals with such measurements. The uncertainty in the kinematic porosity is probably even greater. For the majority of HCD, measurements are not available, and it is necessary to describe the transport properties in terms of appropriate average values with depth trends. Even where there are measurements available in a HCD it is not clear if it is more representative to use local estimates or the overall average values. The sensitivity of the palaeohydrogeology to the σ assigned to HCD is discussed in Section 9.1.4.

Table 7-4. Depth dependent kinematic porosity and flow-wetted surface values used for all deformation zones in the base case HCD model.

Elevation (m)	Kinematic Porosity	Flow-wetted surface		
	(–)	σ (m^2/m^3) Base case	σ (m^2/m^3) Variant (See Table 9–1)	a_r (m^2/m^3)
100 to –150	$6.0 \cdot 10^{-3}$	1.00	3.00	1.86
–150 to –400	$6.0 \cdot 10^{-3}$	0.40	1.20	1.70
–400 to –650	$3.0 \cdot 10^{-3}$	0.22	0.66	0.82
Below –650	$2.0 \cdot 10^{-3}$	0.02	0.06	0.60

Initially, the kinematic porosities, n_e, were calculated from $n_e = e_T/b_T$, using an interpreted HCD thickness b_T and transport aperture e_t estimated from an empirical relationship with transmissivity, $e_T = a\ T^b$, where the constants a and b are obtained by fitting compiled results of tracer tests in crystalline rock /Rhén et al. 2008/ and /Hjerne et al. 2009/. In the hydrogeological modelling, a preliminary relation was used: $e_T = 0.705\ T^{0.404}$, which compares with $e_T = 0.46\ T^{0.5}$ /Dershowitz et al. 2003/ used in SDM-Site Forsmark. Typical transmissivities in the range 10^{-9} to 10^{-6} m^2/s suggest the values of transport aperture used in the hydrogeological modelling are 3–5 times higher than suggested by the formula used for Forsmark. This formulation for kinematic porosity is highly dependent on the interpreted transmissivity and thickness of zones. For the HRD, kinematic porosity was calculated based on the integrated fracture volume within a grid cell, and can be approximated by $n_e = e_t\ P_{10,corr,PFL}$, using the same relation between transport aperture and transmissivity for individual stochastic fractures. With this dependence on water-conducting fracture intensity used for the HRD, it was found that higher kinematic porosities were derived for the HRD than for the HCD, which is counter-intuitive. Since palaeohydrogeological simulations gave best results for higher kinematic porosities, the approach based on fracture intensity was used for both HCD and HRD. Since the corrected P_{10} values within HCD are about 3 times larger than HRD, then kinematic porosities for the HCD were based on typical kinematic porosities calculated for the HRD, multiplied by 3 giving a depth dependent kinematic porosity, see Table 7-8 and Table 7-9).

The values of flow-wetted surface area were based on Terzaghi corrected P_{10} values obtained from PFL measurements /Rhén et al., 2008/, calculated as $a_r = 2 \cdot P_{10,corr}$(PFL-f). In the majority of simulations, including the base case, the same values of σ were used for finite-elements within both HRD and HCD, and hence the values given in Table 7-4 are the same as those for HRD_C given in Table 7-9. A variant was considered where σ was enhanced by a factor of 3 in HCD relative to HRD_C (see section 9.1.4) based on open fracture intensity being on average about 3 times higher. The values of a_r used to estimate F were based on average intensity of PFL-f features observed in borehole sections in HCD.

7.5 Hydraulic rock domain (HRD) model

Based on borehole core-, image-logging and PFL-f hydraulic testing, hydrogeological DFN models have been developed for HRD_C, HRD_W, HRD_EW007 and HRD_N /Rhén et al. 2008/. Each hydrogeological DFN model is defined in terms of a statistical parameterisation of fracture orientation probability distribution functions (PDFs) and fracture length PDFs, fracture intensity, fracture spatial arrangement and relationships between transmissivity and fracture size. The lengths of borehole logged for constructing these models was 5,230 m for HRD_C, 3,135 m for HRD_W, 2,337 m for HRD_EW007 and 2,160 m for HRD_N. These HRD are based on the fracture domains (FSM), which are only defined within the local scale geological model. Specific hydrogeological DFN descriptions of the regions outside were not developed. Instead they followed the recom-

mendations made in /Rhén et al. 2008/ of six additional HRD (see Figure 7-7) defined for the larger regional-scale model based on the RSM rock domains (see Figure 3-7):

- HRD_A – corresponds to RSMA01, RSMA02 and RSMBA03 with HRD_A2 excluded (see below).
- HRD_A2 – a sub-domain of RSMA01 and RSMA02 within a rhombus corresponding to the Äspö shear zone.
- HRD_D-E-M – corresponds to RSMD01-07, RSME01-18 and RSMM01.
- HRD_B-C – corresponds to RSMB01-06 and RSMC01-02.
- HRD_F-G – corresponds to RSMF01-03 and RSMG01-02.
- HRD_P – corresponds to RSMP01 and RSMP02.

Based on analogy between borehole fracture data from Laxemar, Äspö, Ävrö and Simpevarp, hydrogeological DFN properties for these extra HRD are proposed in Table 7-5. The three-dimensional definition of rock domains and fracture domains are available from the geological modelling as files of voxels that describe the spatial extent of each subdomain. The FSM voxels are available on a scale of 20 m resolution, while the RSM are given on a coarser 100 m scale.

Using the hydrogeological DFN model for the four local-scale HRD and 6 regional-scale HRD, realisations of the regional scale DFN model were generated for the purpose of deriving equivalent hydraulic and transport properties for an ECPM. The hydrogeological DFN model assumes statistical homogeneity within each HRD and depth zone and is based on a Poisson point process spatial model, but the particular locations, lengths, orientations and transmissivities of fractures vary between realisations. Since each ECPM model is derived based on an underlying DFN realisation, the ECPM approach is also inherently stochastic. However, for the base case calibration, only a single realisation was considered. Sensitivities to stochastic variability are considered as part of the uncertainty analysis.

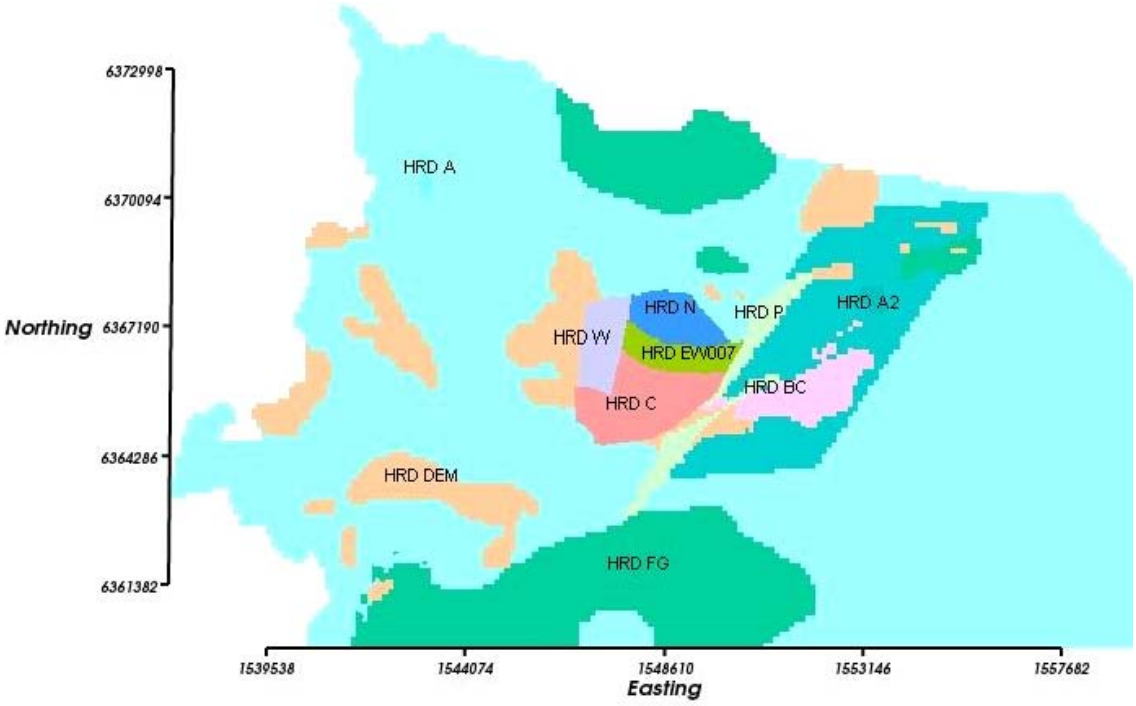

Figure 7-7. *Hydraulic rock domains on the top surface of the bedrock in the regional scale hydrogeological model (cf Figure 3-7).*

Table 7-5. Proposed hydrogeological property assignment of the regional-scale hydraulic rock domains to be used in SDM-Site Laxemar regional groundwater flow modelling. /Rhén et al. 2008/.

Regional hydraulic rock domain	Suggested hydraulic properties based on hydrogeological DFN
HRD_A	HRD_N
HRD_A2	HRD_N, but rock below –650 m is the same as –400 m to –650 m
HRD_D-E-M	HRD_C
HRD_B-C	HRD_C
HRD_F-G	HRD_N, but 10 times higher T
HRD_P	HRD_N

A key assumption of the hydrogeological DFN model is the relationship between fracture transmissivity and size. Three alternative relationships were considered from a direct correlation between transmissivity and size to no correlation as expressed in Table 7-6, and for each assumed relationship, the independent parameters were calibrated to achieve a match between simulated and measured flow-rates to boreholes, as quantified by several objective measures, cf /Rhén et al. 2008/. An example of the statistical parameterisation of the hydrogeological DFN model for HRD_C is given in Table 7-7. A depth trend in the hydrogeological DFN is defined in terms of four depth zones such that parameters vary in a step-wise manner. Four orientation sets are defined for each depth zone. The parameterisation for each set involves a definition of the orientations in terms of a Univariate Fisher distribution, a fracture intensity, a power-law size distribution given by the parameters (r_0, k_r), and distribution for transmissivity. Equivalent tables for the other HRD are given in /Rhén et al. 2008/. For the regional scale modelling reported here, the *base case model* assumed the semi-correlated model between fracture transmissivity and size; this being considered the most realistic. The hydrogeological DFN modelling also considered other uncertainties associated with:

- whether all open and partly open (OPO) fractures were considered as possible advective flowing features, or only the open fractures characterised as such with high confidence (categorised as certain or probable, and hence denoted OPO-CP), and
- how the fracture size parameters (k_r, r_0) for a power-law size model were determined.

Table 7-6. The three fracture transmissivity-size relationships considered as alternative parameterisations of flow in the hydrogeological DFN model.

Type	Description	Relationship	Parameters
Semi-correlated (SC)	Log-normal distribution about a correlated mean	$Log_{10}T = Log_{10}(a \times r^b) + \sigma N(0,1)$	(a, b, σ)
Uncorrelated (UC)	Log-normal distribution about a specified mean	$Log_{10}T = \mu + \sigma N(0,1)$	(μ, σ)
Correlated (C)	Power-law relationship	$T = a \times r^b$	(a, b)

Table 7-7. Description of the calibrated hydrogeological DFN input parameters for HRD_C with fixed r_0 = 0.038 m and intensity of open fractures based on open and partly open fractures (OPO) /Rhén et al. 2008/.

Elev. zone (m.a.s.l.)	Set	Fisher orientations pole: (trend, plunge), conc.	Fracture radius modelpower-law (k_r, r_0)	Intensity P_{32} (m^2/m^3) of open fractures	Transmissivity model T (m^2/s) See Table 7-6
–150 to 0	ENE	(155.1,3.4), 9.6	(2.6, 0.04)	0.52	SC: ($6\cdot10^{-8}$, 0.5, 0.4) UC: ($2\cdot10^{-7}$, 0.6) C: ($2\cdot10^{-8}$, 0.9)
	WNW	(204,1.6), 12	(2.5, 0.04)	0.95	SC: ($2\cdot10^{-7}$, 0.6, 0.7) UC: ($1\cdot10^{-5}$, 0.9) C: ($5\cdot10^{-8}$, 1.1)
	N-S	(270.2,8.4), 7.8	(2.7, 0.04)	0.54	SC: ($2\cdot10^{-7}$, 0.6, 0.5) UC: ($1\cdot10^{-7}$, 0.7) C: ($6\cdot10^{-8}$, 1.2)
	SubH	(46.3,84.7), 12	(2.7, 0.04)	1.20	SC: ($1.5\cdot10^{-7}$,0.7, 0.7) UC: ($3\cdot10^{-7}$, 0.8) C: ($6\cdot10^{-8}$, 1.0)
–400 to –150	ENE	(155.1,3.4), 9.6	(2.85, 0.04)	0.47	SC: ($1\cdot10^{-6}$, 0.7, 0.7) UC: ($2\cdot10^{-7}$, 0.7) C: ($5\cdot10^{-8}$, 1.4)
	WNW	(204,1.6), 12	(2.45, 0.04)	0.55	SC: ($8\cdot10^{-8}$, 0.3, 0.1) UC: ($3\cdot10^{-7}$, 0.6) C: ($2\cdot10^{-9}$, 1.3)
	N-S	(270.2,8.4), 7.8	(2.85, 0.04)	0.63	SC: ($1\cdot10^{-7}$, 0.7, 0.7) UC: ($2\cdot10^{-7}$, 0.4) C: ($3\cdot10^{-8}$, 1.0)
	SubH	(46.3,84.7), 12	(2.85, 0.04)	0.71	SC: ($1.5\cdot10^{-7}$,0.8, 0.9) UC: ($8\cdot10^{-7}$, 1.4) C: ($3\cdot10^{8}$, 1.1)
–650 to –400	ENE	(155.1,3.4), 9.6	(2.8, 0.04)	0.38	SC: ($5\cdot10^{-7}$, 0.5, 0.5) UC: ($2\cdot10^{-6}$, 0.8) C: ($3\cdot10^{-8}$, 0.7)
	WNW	(204,1.6), 12	(2.5, 0.04)	0.74	SC: ($2\cdot10^{-8}$, 0.6, 0.4) UC: ($1\cdot10^{-7}$, 0.9) C: ($3\cdot10^{-9}$, 0.9)
	N-S	(270.2,8.4), 7.8	(2.9, 0.04)	0.47	SC: ($1\cdot10^{-8}$, 0.4, 0.4) UC: ($8\cdot10^{-8}$, 0.4) C: ($1\cdot10^{-8}$, 0.5)
	SubH	(46.3,84.7), 12	(2.9, 0.04)	0.58	SC: ($3\cdot10^{-7}$, 0.6, 0.6) UC: ($2\cdot10^{-6}$, 0.9) C: ($1.5\cdot10^{-7}$, 0.9)
–1,000 to –650	ENE	(155.1,3.4), 9.6	(2.9, 0.04)	0.46	SC: ($5\cdot10^{-9}$, 0.6, 0.4) UC: ($1\cdot10^{-8}$, 0.4) C: ($5\cdot10^{-9}$, 0.6)
	WNW	(204,1.6), 12	(2.8, 0.04)	0.73	SC: ($5\cdot10^{-8}$, 0.6, 0.4) UC: ($5\cdot10^{-7}$, 0.4) C: ($5\cdot10^{-8}$, 0.6)
	N-S	(270.2,8.4), 7.8	(2.95, 0.04)	0.25	SC: ($5\cdot10^{-9}$, 0.6, 0.4) UC: ($1\cdot10^{-8}$, 0.4) C: ($5\cdot10^{-9}$, 0.6)
	SubH	(46.3,84.7), 12	(2.95, 0.04)	0.35	SC: ($1\cdot10^{-7}$, 0.6, 0.4) UC: ($2\cdot10^{-7}$, 0.4) C: ($1\cdot10^{-7}$, 0.6)

For the base case hydrogeological DFN model, the open fracture intensity was based on all open (OPO) fractures observed in boreholes, the semi-correlated transmissivity versus size relationship, and the location parameter, r_0, was based on the radius of the borehole. In the hydrogeological DFN modelling (OPO-CP, fracture size model (r_0, k_r), and transmissivity model) each variant was calibrated to the same PFL-f flow measurements, using the same objective measures of the quality of match, which included measures of the distribution of borehole inflows as well as statistics of total flows to 100 m borehole intervals. In consequence, the hydrogeological DFN variants were found to all predict similar hydraulic block properties on the 100 m scale, which is a demonstration that the conditioning process placed strong constraints on the flow characteristics of the alternative models considered. The difference in hydraulic block properties on the 100 m scale between hydrogeological DFN variants was about half an order of magnitude. Some more significant variations between cases were seen on the 5 m and 20 m scale hydraulic block properties for the uncorrelated transmissivity variant, for example. However, in terms of regional-scale flow and solute transport, the main focus here, it is expected that findings made on the basis of the hydrogeological DFN base case will be equally applicable to the hydrogeological DFN variants. Therefore, only the base case hydrogeological DFN model is considered in the regional modelling reported here. The uncertainties in the scale behaviour of the hydraulic properties resulting from the non-uniqueness in the hydrogeological DFN parameterisation may have more significance to the flow and transport in the immediate vicinity of the repository, and hence such uncertainties may need further attention in future modelling work.

The methodology to obtain a realisation of ECPM parameters for the HRD starts by generating a hydrogeological DFN realisation using the same grid as used in the ECPM model. A connectivity analysis is then made to identify the parts of the network that have a connection to the top surface of the model, and so all isolated fractures and isolated clusters of fractures are removed, as are dead-end fractures that only have one intersection. The fracture generation takes account of the spatial variations in fracture statistical properties according to HRD and depth zone. Fractures may extend in to neighbouring elements depending on the fracture size value sampled. For practical reasons, only fractures with radii between 5.6–564 m were generated within the local scale model volume where a 40 m grid is used, and between 16.8–564 m on the wider regional scale where a 120 m grid is used. This truncation keeps the number of fractures generated down to a manageable size, about 7 million. Since large fractures tend to be responsible for the large scale connections for sparse networks, it is considered that this truncation is acceptable when modelling regional-scale flow. However, it is noted that smaller scale fractures need to be considered in future safety assessment calculations at least around the repository tunnels where flows on smaller scales have to be considered around the deposition holes. Small open connected fractures may also have a large effect on kinematic porosity and flow wetted surface, even if they do not form part of the main regional advective flow system. This is because they under natural flow conditions contribute a large additional volume available for slow advection and free-water diffusion, as well as enhancing the area of fracture/matrix contact surface area. Therefore, it is necessary to correct for the effects of the truncation on kinematic porosity and flow wetted surface. The final stage is to apply an upscaling algorithm that loops over each grid element and calculates equivalent hydraulic and solute transport properties for each element.

Some examples of the regional hydrogeological DFN model are shown in Figure 7-8 through Figure 7-11 on slices through the model by drawing fractures as traces where they intersect horizontal slices. The horizontal slices are taken through each of the HRD depth zones colouring fractures according to which HRD they belong. In these figures only connected fractures are shown. A fracture is defined as being connected if it is connected via a network of fractures to the top surface boundary. For sparse networks, e.g. below –650 m in Laxemar, it tends to be only the large fractures that are connected. The effect of removing isolated fractures gradually increases with depth, so that below –650 m, it is seen that connected fractures are very sparse indeed (as shown in the slice at –800 m in Figure 7-11). The methodology used to generate the ECPM model is to:

- generate open fractures according to the hydrogeological DFN parameters,
- perform a connectivity analysis on the regional scale to identify the fracture network connected to any part of the top surface of the model,
- remove all isolated clusters that have no connection to the top surface, as well as dead-end fractures (ones that only have one fracture intersection) as these do not contribute advective flow,
- derive ECPM properties for each grid element for the remaining fractures.

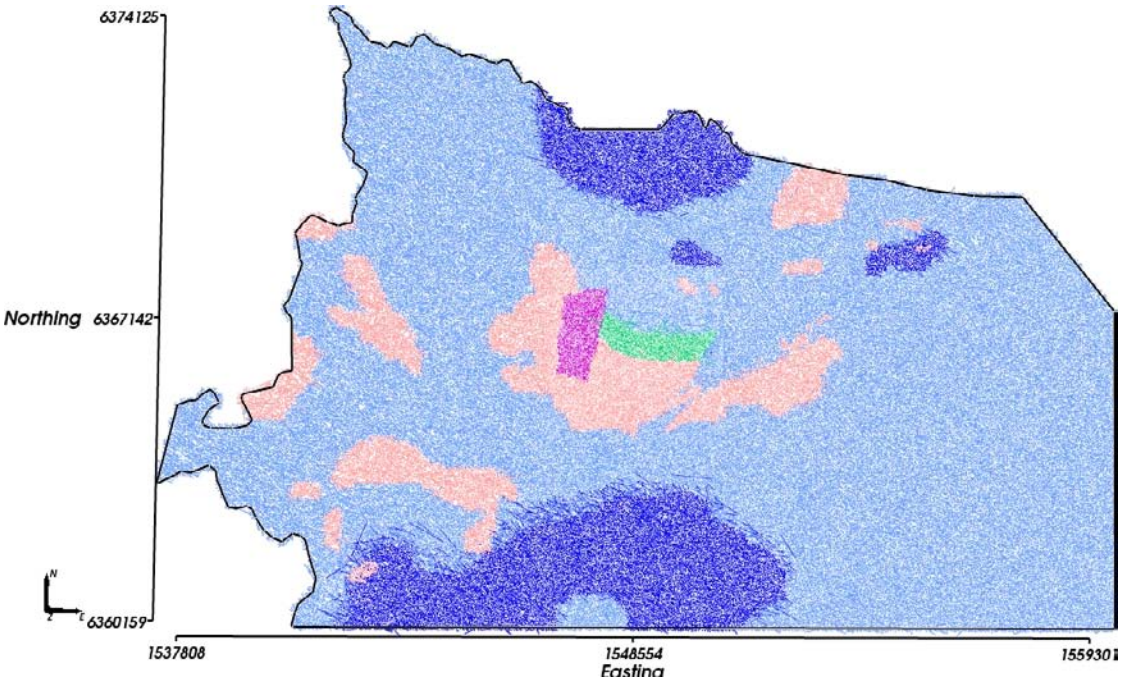

Figure 7-8. *A horizontal slice through the regional hydrogeological DFN model at –100 m elevation with fractures coloured by HRD: HRD_W (purple), HRD_EW007 (green), HRD_C/HRD_B-C/HRD_D-E-M (pink), HRD_N/HRD_A/HRD_A2 (blue), HRD_F-G (dark blue).*

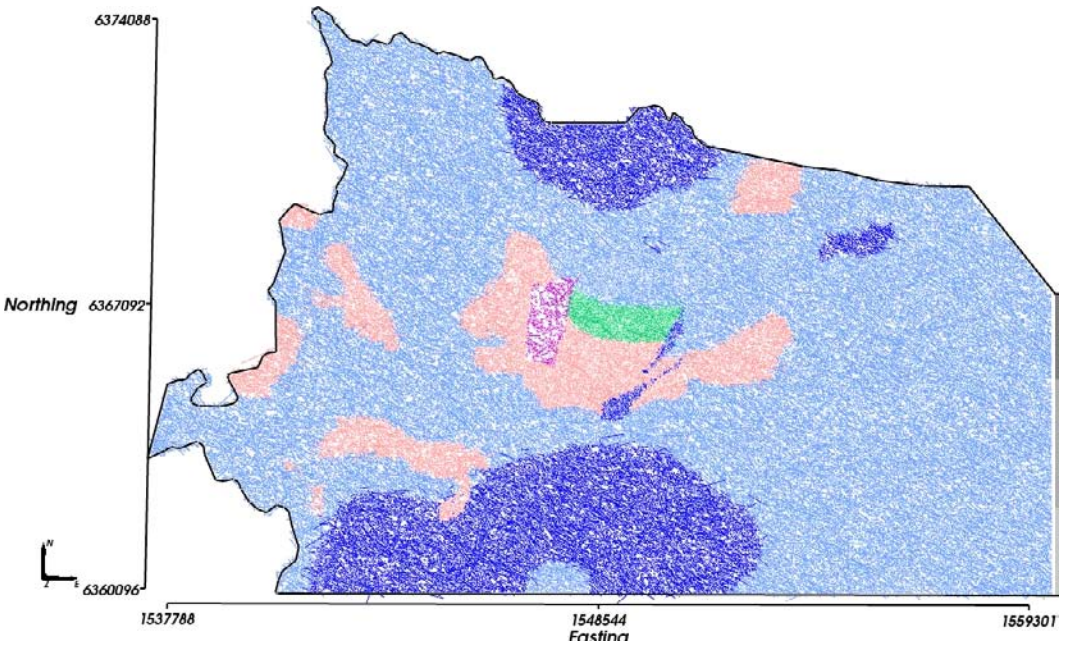

Figure 7-9. *A horizontal slice through the regional hydrogeological DFN model at –300 m elevation with fractures coloured by HRD: HRD_W (purple), HRD_EW007 (green), HRD_C/HRD_B-C/HRD_D-E-M (pink), HRD_N/HRD_A/HRD_A2 (blue), HRD_F-G (dark blue).*

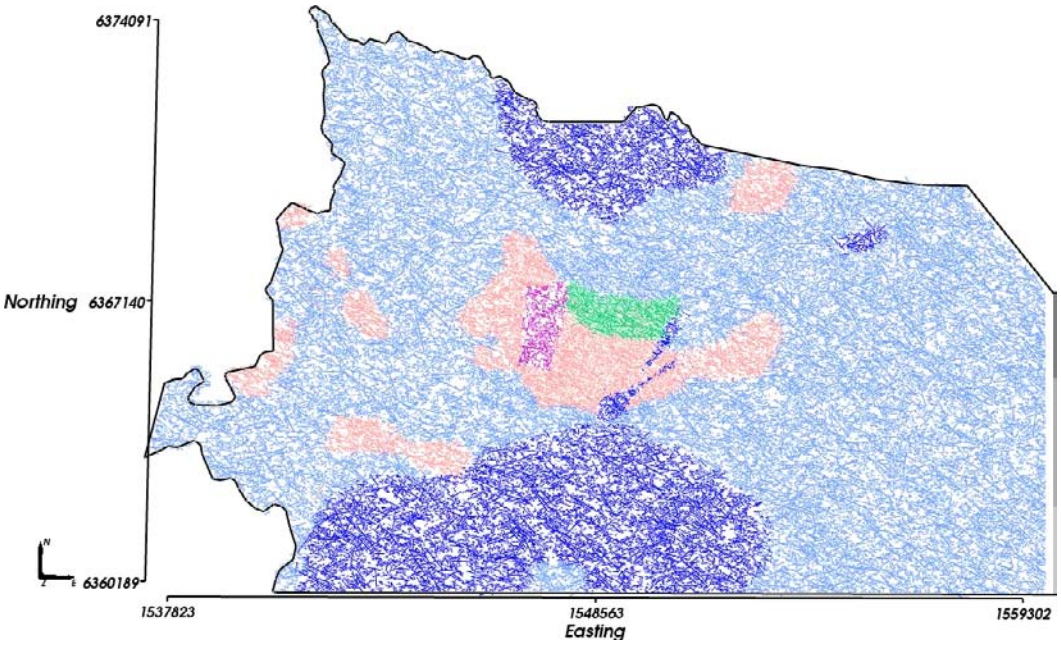

Figure 7-10. *A horizontal slice through the regional hydrogeological DFN model at –500 m elevation with fractures coloured by HRD: HRD_W (purple), HRD_EW007 (green), HRD_C/HRD_B-C/HRD_D-E-M (pink), HRD_N/HRD_A/HRD_A2 (blue), HRD_F-G (dark blue).*

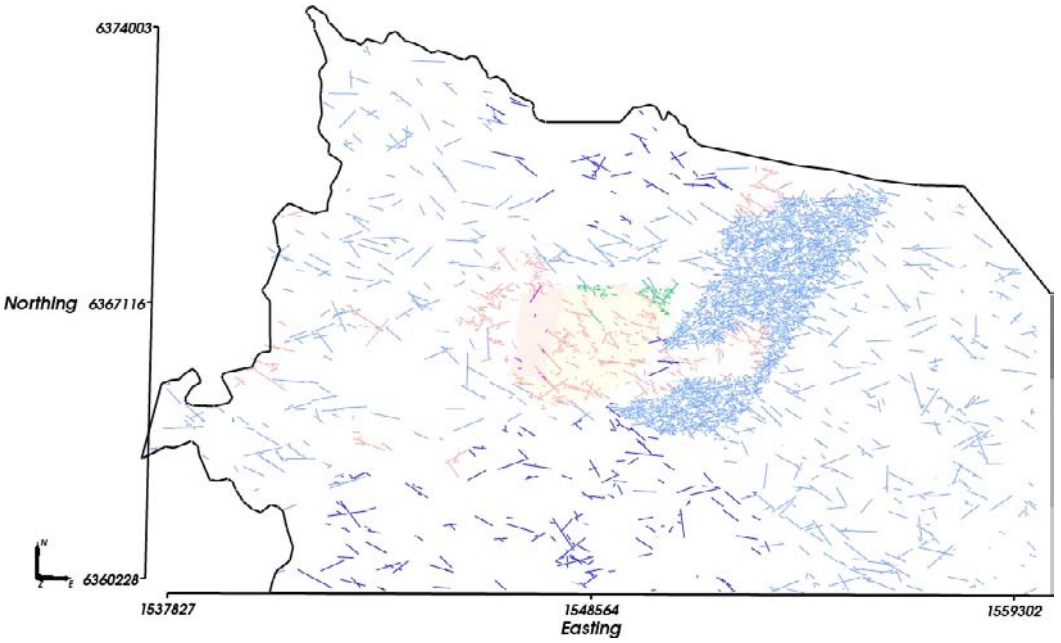

Figure 7-11. *A horizontal slice through the regional hydrogeological DFN model at –800 m elevation with fractures coloured by HRD: HRD_W (purple), HRD_EW007 (green), HRD_C/HRD_B-C/HRD_D-E-M (pink), HRD_N/HRD_A/HRD_A2 (blue), HRD_F-G (dark blue).*

The isolated fractures are removed based on a regional scale connectivity analysis so that ECPM properties are derived only for the network of fractures that contributes to regional scale flow. Another issue is whether the flow through an element is limited by the connectivity and transmissivity of fractures in the surrounding volume. If hydraulic conductivity is calculated for an element where the flux through the element is calculated on the scale of the element, then a higher hydraulic conductivity may result than if the flux is calculated through the same element, but within the context of flow through a larger surrounding volume, as will be discussed below.

The removal of isolated fracture clusters reduces the fracture count from about 7 million to about 4 million, and the total connected fracture porosity, averaged over the entire flow model domain, reduces marginally from $1.1 \cdot 10^{-4}$ to $1.0 \cdot 10^{-4}$ for the fracture size truncated model (with r = 5.6 m), cf Table 7.8.

As part of the hydrogeological DFN modelling /Rhén et al. 2008/, statistics of effective hydraulic block properties were calculated for cubes of 5 m, 20 m and 100 m side to evaluate the scale dependence of the hydraulic conductivity and kinematic porosity, as well as considering methodology issues such as the sensitivity to truncation of the fracture size distribution and to the use of 'guard zones' in upscaling /Jackson et al. 2000/. The idea of a guard zone is simple – instead of simulating flow through a network in a domain of the same size as the scale of interest, a larger model domain is considered and only the flux through the central portion of the model of the required scale is used in calculating the effective hydraulic block property in terms of flow-rate. By increasing the simulation volume, the flow through the required block volume is calculated in the context of its neighbourhood of fracture network, as it was *in situ*, rather than in isolation. The "shell" of extra volume around the central block is called the guard zone. Typically, the use of a guard zone decreases the hydraulic block conductivity due to 'bottlenecking' of flow when long, high transmissivity fractures are relatively rare. Sensitivity studies of the Laxemar hydrogeological DFN found that hydraulic conductivity of a 40 m block could be reduced by half to one order of magnitude when a 40 m guard zone was used, especially in elevations between –150 m and –650 m where the number of fractures cross-cutting a 40 m block was typically around 1. Due to this sensitivity, a guard zone was introduced in the regional upscaling process to yield equivalent hydraulic conductivities representative of *in situ* conditions. For practical reasons, a guard zone of 20 m was used, making a flow domain of size 80 m for each element in the embedded fine-scale grid. A sensitivity study of the effect of using a guard zone on hydraulic conductivity statistics is given in Appendix 7. Appendix 7 also presents an illustration of how sensitive the Forsmark hydrogeological DFN /Follin et al. 2007b/ is to using a guard zone for upscaling, there on a 20 m block, since a guard zone had not been used in SDM-Site Forsmark.

Statistics for the upscaled hydraulic conductivity for each HRD within the fine-scale 40 m grid part of the ECPM model are given in Table 7-8. The equivalent hydraulic conductivity is defined as the geometric mean and the standard deviation of the 3 axial components of the equivalent hydraulic conductivity tensor. The mean, standard deviation and percentage of elements that are hydraulically active, i.e. excluding those that do not have flow a 3D flow-field (i.e. excluding cells with only planar flow, which are not quantified here) is also listed (The mean and standard deviation are calculated with the non-active elements excluded so as not to distort the statistics by essentially zero values). Generally, the number of hydraulically active elements drops dramatically below –650 m to less than about 20%, and hence there will only be localised percolation of groundwater deep into the bedrock. The part of HRD_W below –400 m also has low percolation. For the hydraulically active elements, the hydraulic conductivities fall from around 10^{-7} m/s at the top to 10^{-9} m/s at the bottom. Mean kinematic porosities for the 40 m elements are also given in Table 7-8 based on statistics for the regional scale hydrogeological DFN. These are based on the connected open fracture volume within each element and using a minimum fracture size of $r = 5.6$ m for the 40 m elements. These modelled porosities are compared with the equivalent results for generic 5 m block property results using radius $r = 0.28$ m fracture size truncation from /Rhén et al. 2008/ in the far right column in Table 7-8. This reveals that using a fracture truncation $r = 5.6$ m leads to about a factor 5 reduction in kinematic porosity given by the regional scale hydrogeological DFN compared to the equivalent results were it possible to model all fractures down to the scales considered in the hydrogeological DFN flow calibrations. Therefore, the elementwise values of kinematic porosity calculated by upscaling the regional hydrogeological DFN model were multiplied by a factor 5.0 before use in the ECPM model. This resulted in average values for HRD as given in the 6th column of Table 7-9.

Table 7-8. Statistics of upscaled hydraulic conductivities and kinematic porosities by HRD and depth zone for the 40 m local-scale grid embedded within the ECPM model (HCDs not included). Results represent a guard zone of 20 m, i.e. 80 m hexahedral flow domain.

	Log_{10} Hydraulic conductivity (m/s)			Mean (Log_{10} Kin. Porosity) (–)	
	Mean Log10(*Keff*)	Std Log10(*Keff*)	% Active	Truncated (*r* = 5.6 m)	Untruncated (*r* = 0.28 m)
HRD_C					
0 to –150 m	–7.32	0.59	100.0%	–3.38	–2.59
–150 to –400 m	–8.18	0.94	89.1%	–3.77	–2.87
–400 to –650 m	–8.58	0.90	80.1%	–4.03	–3.01
–650 to –1,000 m	–8.16	1.16	17.5%	–4.45	–4.00
HRD_EW007					
0 to –150 m	–7.08	0.38	100.0%	–3.22	–2.58
–150 to –400 m	–7.34	0.49	100.0%	–3.36	–2.87
–400 to –650 m	–8.09	0.67	98.7%	–3.68	–2.82
–650 to –1,000 m	–8.77	0.93	14.4%	–4.63	–4.00
HRD_W					
0 to –150 m	–6.94	0.61	100.0%	–3.24	–2.72
–150 to –400 m	–7.92	0.97	83.3%	–3.76	–3.08
–400 to –650 m	–8.51	0.97	65.9%	–4.24	–3.15
–650 to –1,000 m	–8.29	1.05	10.1%	–4.61	–4.00
HRD_N					
0 to –150 m	–6.49	0.43	100.0%	–3.01	–2.57
–150 to –400 m	–7.19	0.75	99.5%	–3.35	–2.75
–400 to –650 m	–8.33	0.80	86.3%	–3.90	–3.23
–650 to –1,000 m	–8.70	0.83	21.0%	–4.74	–4.00

For the *base case model* a slight reduction (by a multiplication factor of 1/3) in hydraulic conductivity (horizontal and vertical) of the HRD below –150 m elevation was implemented, compared to what is shown in Table 7-8, since it improved the palaeohydrogeological calibration, cf Chapter 9. The resulting hydrogeological property assignment for the ECPM model is illustrated by Figure 7-12 through Figure 7-14, which show the distribution of East-West horizontal hydraulic conductivity on three different horizontal slices chosen to cut through the three upper HRD depth zones. These figures show the results of the combined HRD and HCD features. The slices show the clear reduction in hydraulic conductivity with depth in both the HCD and the HRD in between. They also show that the finer grid discretisation within the 40 m scale embedded grid leads to a more heterogeneous spatial distribution since it is able to resolve many individual features, while the coarser grid tends to give more homogenised fracture network properties on the scale of the 120 m elements. One can see that the hydraulic conductivity is generally lower in HRD_C, HRD_W and HRD_B-C. The kinematic porosity used in the ECPM model is shown in Figure 7-15 and Figure 7-16.

The other parameters used in the advection-dispersion transport equations with rock matrix diffusion (RMD) are given in Table 7-9 and Table 7-10. The flow-wetted surface is the amount of open connected fracture surface area per unit volume of rock. The values are estimated from measured average (within a HRD and depth zone) Terzaghi corrected intensity, $P_{10,corr}$, of conductive fractures detected by the PFL-f method as, $2 \cdot P_{10,corr}$(PFL). The values of both PFL feature intensity and the resulting flow-wetted surface are given in Table 7-9. The matrix diffusion length is the maximum penetration of the solute into the matrix. This is specified as min(1/flow-wetted surface, 6 m), with 6 m being used as an appropriate maximum as the time taken to diffuse 6 m into the matrix is larger than the 10,000 years duration simulated.

Table 7-9. Properties used in the reference-water transport modelling (PFL-f intensities are reproduced from /Rhén et al. 2008/ as they form the basis for setting the flow wetted surface ≈2·$P_{10,corr}$(PFL-f)).

Domain	Depth zone (m)	PFL-f $P_{10,corr}$ (m^{-1})	Flow wetted surface, σ, (m^2/m^3)	Matrix diffusion length (m)	Mean kinematic porosity (–)	Matrix porosity (–)
HRD_C,	50 to –150	0.564	1.00	1.00	$2.1\cdot10^{-3}$	$8.0\cdot10^{-3}$
HRD_B-C,	–150 to –400	0.164	0.40	2.50	$8.5\cdot10^{-4}$	$8.0\cdot10^{-3}$
HRD_D-E-M	–400 to –650	0.107	0.22	4.50	$4.7\cdot10^{-4}$	$8.0\cdot10^{-3}$
	–650 to –1,000	0.008	0.02	7.00	$3.5\cdot10^{-5}$	$8.0\cdot10^{-3}$
HRD_EW007	50 to –150	0.816	1.50	0.66	$3.0\cdot10^{-3}$	$8.0\cdot10^{-3}$
	–150 to –400	0.550	1.00	1.00	$2.2\cdot10^{-3}$	$8.0\cdot10^{-3}$
	–400 to –650	0.225	0.40	2.50	$1.0\cdot10^{-3}$	$8.0\cdot10^{-3}$
	–650 to –1,000	N/A	0.04	7.00	$1.2\cdot10^{-4}$	$8.0\cdot10^{-3}$
HRD_W	50 to –150	0.499	1.00	1.00	$2.9\cdot10^{-3}$	$8.0\cdot10^{-3}$
	–150 to –400	0.078	0.40	2.50	$5.8\cdot10^{-4}$	$8.0\cdot10^{-3}$
	–400 to –650	0.060	0.12	7.00	$2.9\cdot10^{-4}$	$8.0\cdot10^{-3}$
	–650 to –1,000	N/A	0.02	7.00	$1.2\cdot10^{-4}$	$8.0\cdot10^{-3}$
HRD_N, HRD_A,	50 to –150	0.773	1.50	0.66	$4.9\cdot10^{-3}$	$8.0\cdot10^{-3}$
HRD_A2,	–150 to –400	0.339	0.67	1.50	$2.2\cdot10^{-3}$	$8.0\cdot10^{-3}$
HRD_F-G,_P	–400 to –650	0.115	0.33	3.00	$6.3\cdot10^{-4}$	$8.0\cdot10^{-3}$
HRD	–650 to –1,000	0.082	0.16	6.00	$1.8\cdot10^{-5}$	$8.0\cdot10^{-3}$

Table 7-10. Other transport parameters assigned uniformly throughout the model (dispersion lengths only vary according to the grid scale used).

Entity	Value
Effective diffusivity (m^2/s)	$1.5\cdot10^{-13}$
Local-scale longitudinal dispersion length (m)	30
Local-scale transverse dispersion length (m)	10
Regional-scale longitudinal dispersion length (m)	60
Regional-scale transverse dispersion length (m)	20

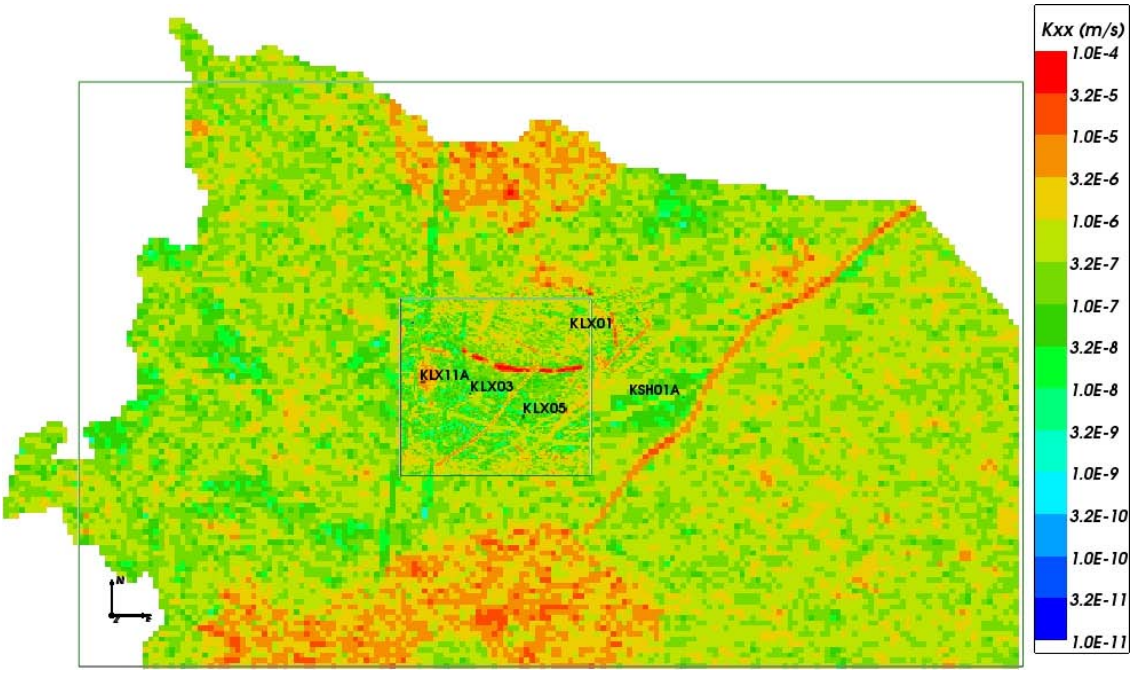

Figure 7-12. *Resulting effective horizontal (E-W) hydraulic conductivity for the combined HRD and HCD at –50 m elevation (depth zone 1) on the regional scale. The Laxemar-Simpevarp regional and Laxemar local scale model areas are superimposed.*

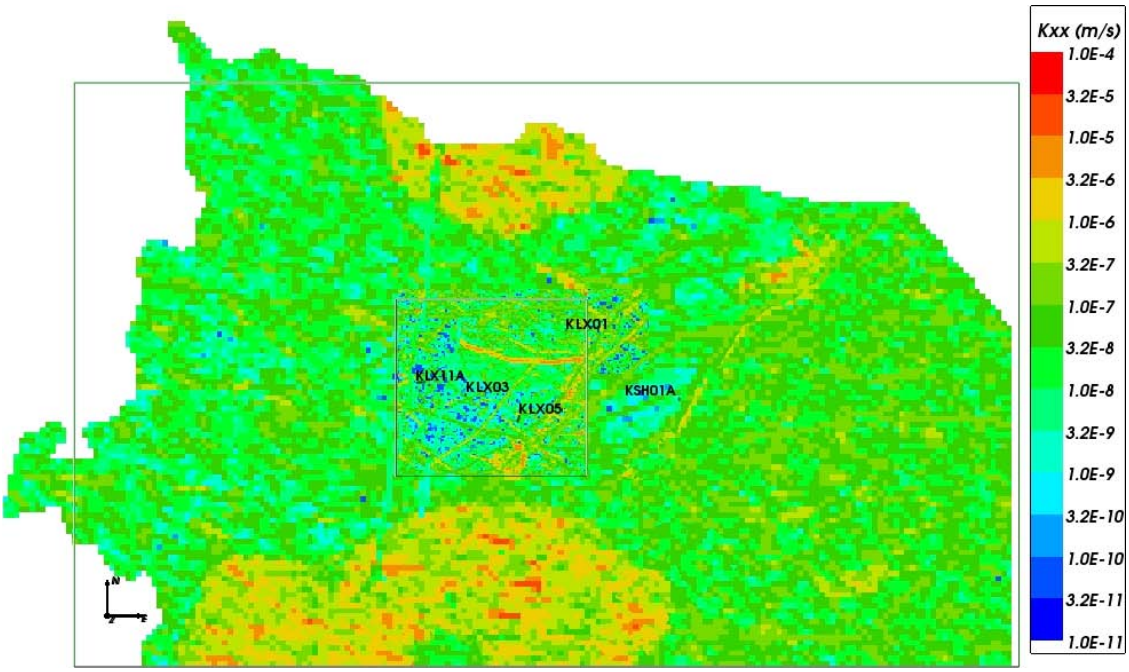

Figure 7-13. *Resulting effective horizontal (E-W) hydraulic conductivity for the combined HRD and HCD at –250 m elevation (depth zone 2) on the regional scale. The Laxemar-Simpevarp regional and Laxemar local scale model areas are superimposed.*

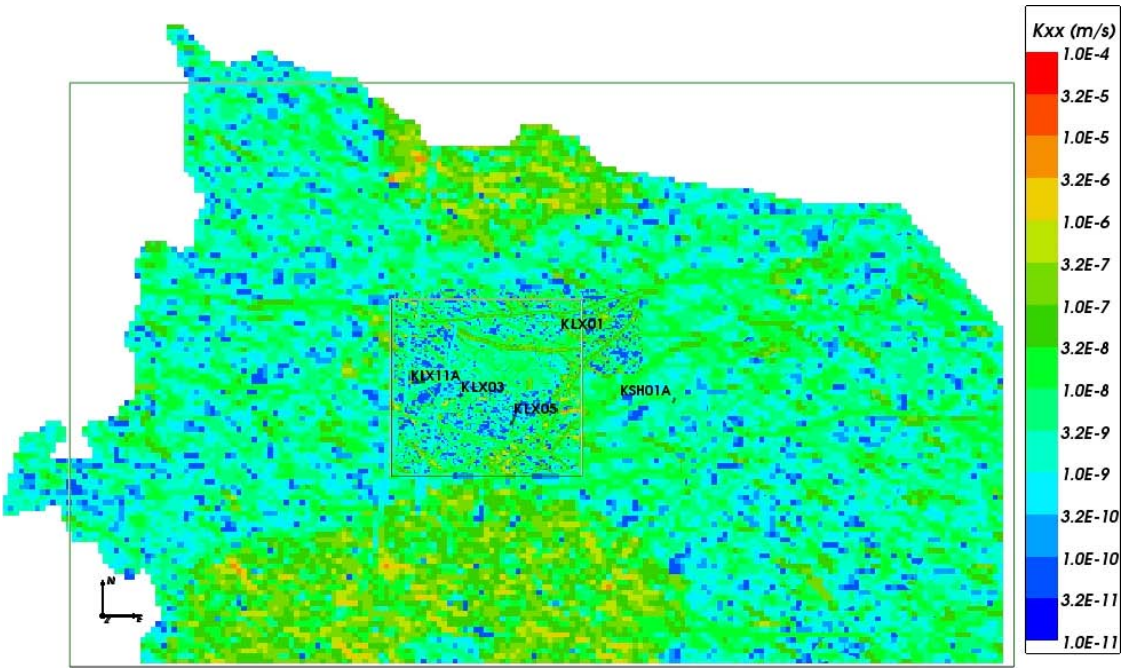

Figure 7-14. *Resulting effective horizontal (E-W) hydraulic conductivity for the combined HRD and HCD at –500 m elevation (depth zone 3) on the regional scale. The Laxemar-Simpevarp regional and Laxemar local scale model areas are superimposed.*

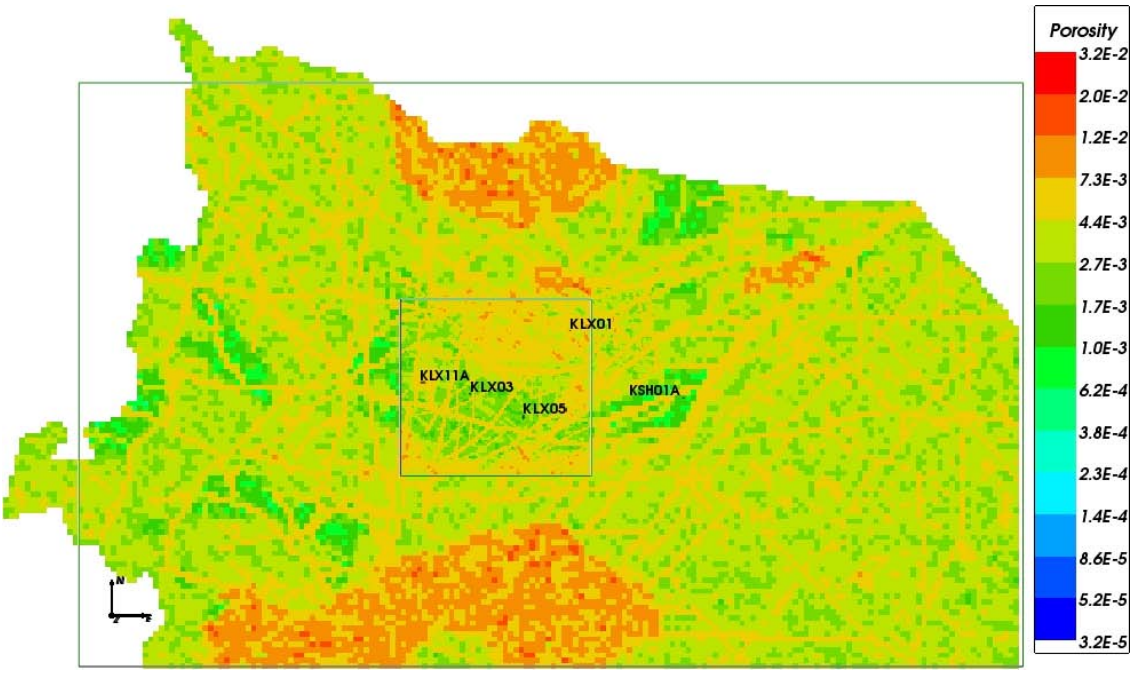

Figure 7-15. *Resulting kinematic porosity for the combined HRD and HCD at –50 m elevation (depth zone 1) on the regional scale. The Laxemar-Simpevarp regional and Laxemar local scale model areas are superimposed.*

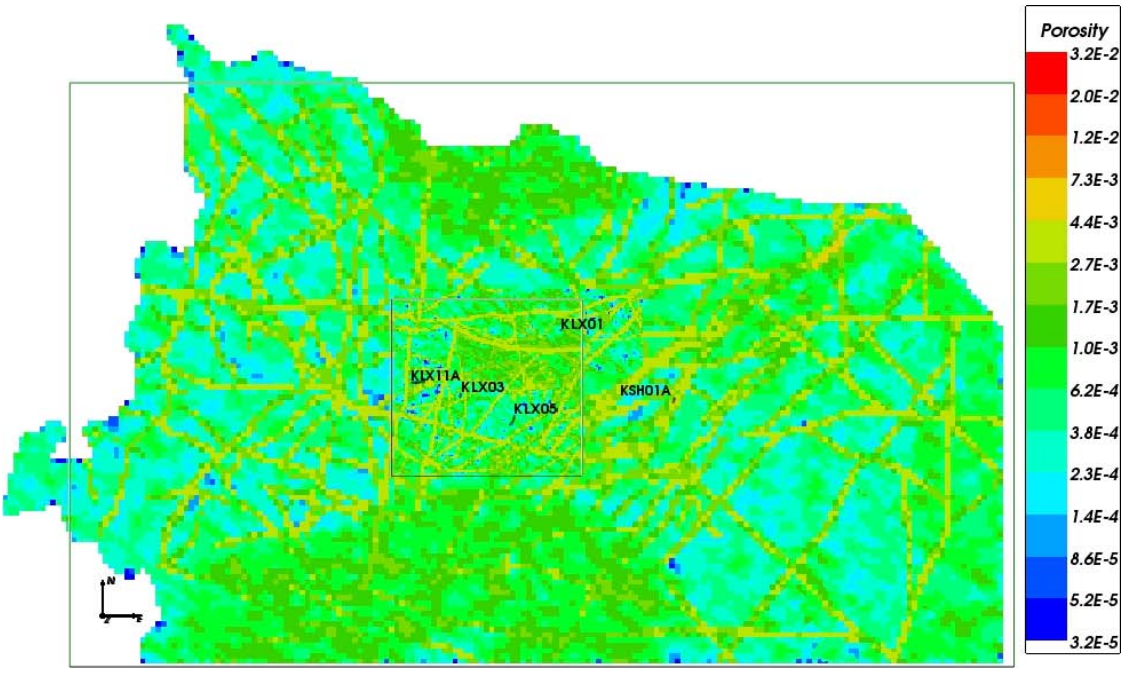

Figure 7-16. *Resulting kinematic porosity for the combined HRD and HCD at –500 m elevation (depth zone 3) on the regional scale. The Laxemar-Simpevarp regional and Laxemar local scale model areas are superimposed.*

For the purposes of informing the SDM of bedrock transport properties, some limited calculations of flow related transport resistance, F, were made by calculating flow-paths in the regional-scale groundwater flow model for a release at 2000 AD. This by computing the sum

$$F = \sum_{l} \frac{a_r \delta l}{q} \tag{7-1}$$

over the elements, the total path length l, through which the path passes, where a_r is the specific flow-wetted surface, δl is the path length through the element and q is the magnitude of Darcy velocity. For this calculation, a_r is calculated element-wise directly from the regional-scale hydro-geological DFN based on $2 \cdot P_{32}$(simulated connected open fractures). The values calculated in this way vary within each HRD and are considered more appropriate for the fracture surface area seen by advective transport (see Figure 7-17 and Figure 7-18). In subsequent safety assessments F may be calculated more directly and in more detail using flows calculated through a hydrogeological DFN model of the site.

7.6 Hydraulic soil domain (HSD) model

For the hydrogeological modelling for model version Laxemar 1.2 /Hartley et al. 2006a/, the *base case model* represented the HSD simply as a uniform 3 m thick layer of silty till. As a variant, a heterogeneous HSD was implemented based on a three layer model of varying vertical thickness and spatial variations in the soil types within each layer based on the Quaternary deposits (QD) model of /Nyman et al. 2008/. This more realistic HSD model was developed further in modelling stage Laxemar 2.1 for modelling the distribution of drawdowns in observation holes around the Äspö HRL /Hartley et al. 2007/. In the latter case it was found that the observed drawdowns on the mainland could only be reproduced if the Quaternary deposits in the bays around Äspö are of relatively low hydraulic conductivity in the range 10^{-8} to 10^{-7} m/s, i.e. similar to that of Gyttja clay. However, modelling the spatial variations of the soil thickness explicitly for each layer that varies from a few centimetres to over 30 m created issues for the numerical grid, such as high aspect ratios of the finite-elements representing the soil and difficulties of interpolation when not using the 20 m grid on which the model of the Quaternary deposits was provided.

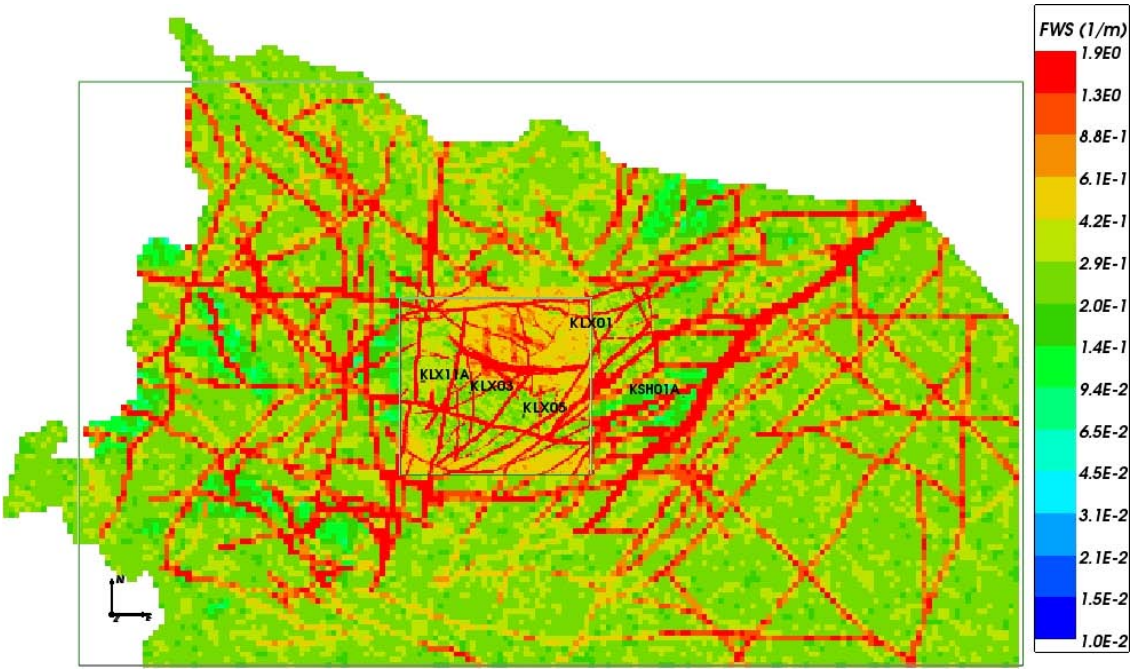

Figure 7-17. *Resulting flow wetted surface for the combined HRD and HCD at –50 m elevation (depth zone 1) on the regional scale. The Laxemar-Simpevarp regional and Laxemar local scale model areas are superimposed.*

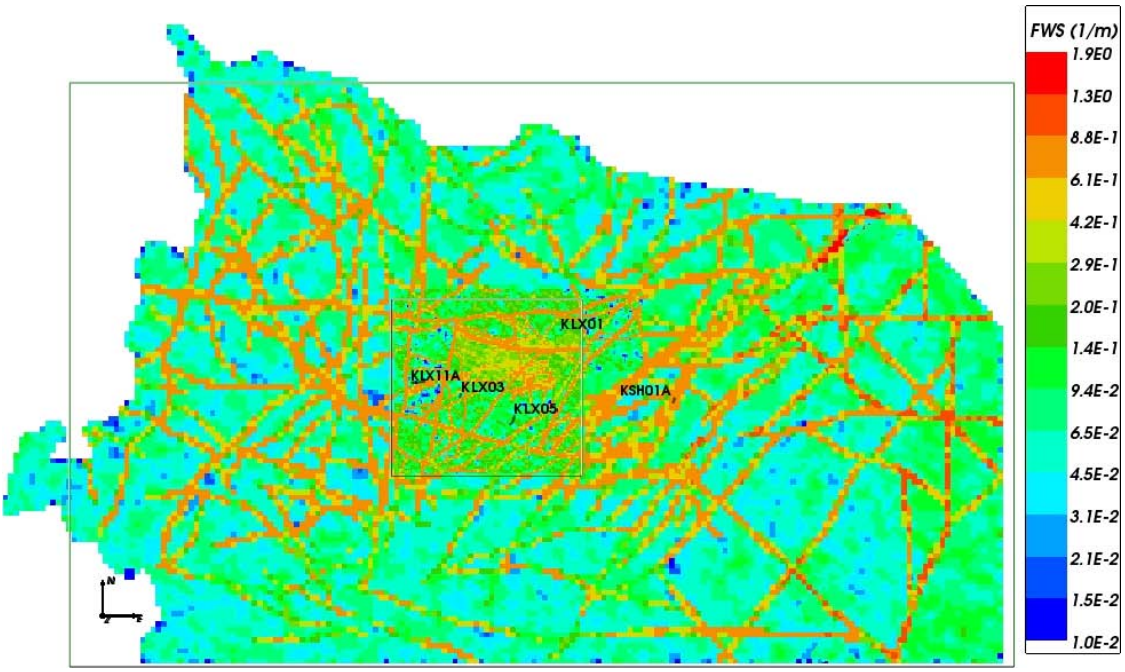

Figure 7-18. *Resulting flow wetted surface for the combined HRD and HCD at –500 m elevation (depth zone 3) on the regional scale. The Laxemar-Simpevarp regional and Laxemar local scale model areas are superimposed.*

As a result of the Laxemar 2.1 modelling, an approach was developed for the Forsmark 2.2 hydrogeological models /Follin et al. 2007c/ in which the soil layers were modelled as being uniform in thickness, but for each finite-element representing the HSD, an effective hydraulic conductivity tensor for the soil package was calculated according to the actual modelled thickness of the layers of the Quaternary deposits and the hydraulic conductivities of the soil types at that location. The same approach was subsequently used for the SDM-Site Laxemar modelling since it honours the spatial variability and anisotropy of the model of Quaternary deposits, as specified in /Werner et al. 2008/, cf Section 3.6 and 4.1.4, without heavily distorting the finite-element grid.

7.6.1 Conceptual model

The Quaternary deposits (QD) model consisting of 6 layers (Z1–Z6) were provided as horizons for the base of each soil layer along with a total thickness. The grid refinement of the data was 20×20 m. The spatial location of the layers in concept, cf Figure 3-12, along with their definition is given in Section 3.6. The QD model was developed for the area shown in Figure 3-16, which covers most of the regional model area. However, it is truncated in the south slightly more than in the regional-scale hydrogeological model.

7.6.2 Numerical implementation

An effective treatment of the hydrogeology of the QD model is adopted. In the hydrogeological model the QD sequence is modelled by four finite-element layers each of a constant 1 m thickness to represent the HSD. The same effective hydraulic conductivity tensor is specified for each vertical stack of four finite-elements, but varies horizontally from element-to-element, and is anisotropic with regard to horizontal and vertical components. If the hydrogeological model uses the same 20 m horizontal grid as the QD model, the approach is simply to calculate the horizontal effective hydraulic conductivity as the arithmetic average of the transmissivities of the QD layers for the corresponding QD data cell divided by the 4 m thickness, while the vertical effective hydraulic conductivity is based on the harmonic average. In areas of very thin QD (exposed bedrock) the top 4 m of elements of the hydrogeological model has relatively high vertical effective hydraulic conductivity (a maximum of 10^{-1} m/s was used), because any resistance of the thin QD package

is stretched over 4 m of elements, and relatively low horizontal conductivity because the effective transmissivity of the QD package is averaged over 4 m. For areas of thick QD (there are areas with 15 m or more), the vertical effective hydraulic conductivity is decreased relative to the soil properties because the representation of soil is compressed to 4 m of elements, while the horizontal effective hydraulic conductivity is increased.

The actual hydrogeological model uses elements of 40 m horizontal side in the embedded grid within Laxemar local model area, so there are 2-by-2 QD model cells for each hydrogeological grid element, and hence some averaging of the QD model is required. For the coarser hydrogeological grid further afield, a 120 m grid is used, so there are 6-by-6 QD model cells per hydrogeological grid element, and hence a greater degree of averaging has to be performed. The approach is to first calculate the effective horizontal and vertical hydraulic conductivity for the QD package associated with each 20 m cell within the finite-element using arithmetic and harmonic averages, as described above. Then, the effective vertical hydraulic conductivity is calculated as the arithmetic mean of vertical hydraulic conductivities for the 20 m QD packages within the element. The method for calculating the effective horizontal hydraulic conductivity where there are several 20 m QD cells within the horizontal extent of the hydrogeological grid element is illustrated in Figure 7-19 for the example of hydraulic conductivity in the E-W direction. Using the effective hydraulic conductivity of the 20 m QD cells, the harmonic average of each E-W row of blocks is first calculated, and then the arithmetic average of these values is taken in the N-S direction. Therefore, the hydraulic conductivity can differ in all three directions according to the spatial distribution of the QD layering.

The hydrological parameterisation of the QD model /Werner et al. 2008/ was defined in terms of 27 QD types each having a description of properties suggested for one or more of the 6 layers, Z1–Z6. Many of the QD types share layers of the same sort of soils and corresponding properties. Hence, for the hydrogeological modelling, properties were defined according to the distinct soil properties listed in Table 7-11. The approach for obtaining the HSD properties at a particular location was to:

1. Determine the QD type defined in the model of Quaternary deposits at that point.
2. Look-up which of the hydraulic soil property domains is appropriate to each layer in that QD type.
3. Obtain the thicknesses of the layers at the point
4. Calculate the effective horizontal and vertical hydraulic conductivity for the corresponding QD 20 m data cell.
5. Perform any necessary upscaling, as described above, for the larger finite-elements used in the hydrogeological grid (40–120 m).

An example of the resulting hydraulic conductivity distribution is illustrated in Figure 7-20 for the E-W horizontal and vertical hydraulic conductivity after upscaling the HSD to the regional-scale hydrogeological grid.

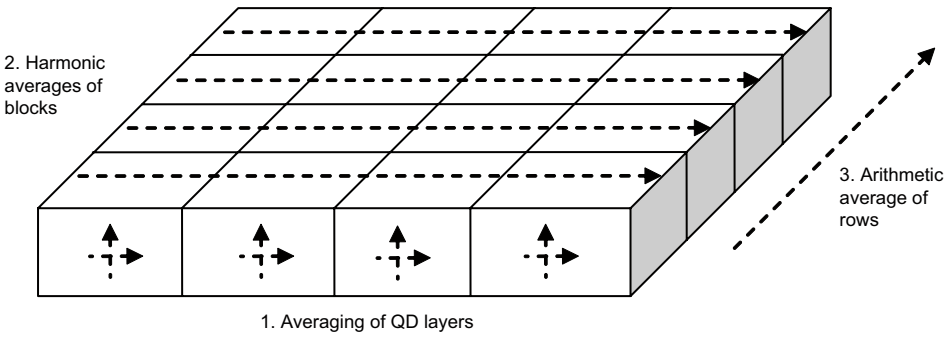

Figure 7-19. *Steps in averaging of the layers of the Quaternary deposits (QD) to calculate the effective E-W component (left to right here) of hydraulic conductivity of the HSD where the hydrogeological grid elements are larger than the QD data (here 4 to 1 for illustration).*

Table 7-11. Prescription for hydrogeological properties of soil property domains used in the hydrogeological modelling. The relation to the model and description of the Quaternary deposits /Nyman et al. 2008, Sohlenius and Hedenström 2008, Werner et al. 2008/ is given in the second column. The modifications relative to the initial HSD assignments are highlighted in bold font, with main change to introduce anisotropy. Porosity is derived from specific yield /Werner et al. 2008/.

Hydraulic soil property domain	QD type and layer applied to	*K* (m/s)	Porosity
Surface affected layer	Soil > 5 m thick: QD type: 1, 2, 5, 6, 7, 9, 13, 16, 17, 18, 20, 22, 24, 25, 26, 27 Layer Z1 Domain 2–24 Layer Z6	**K_h = 8·10^{-4}** **K_h/K_v = 10:1** Original: 4·10^{-4}	0.15
Peat	QD type: 11, 12 Layer Z2	K_h = 3·10^{-6} **K_h/K_v = 10:1**	0.24
Glacial clay	QD type: 6, 8, 9, 10, 12 Layer Z3	K_h = 1·10^{-7} **K_h/K_v = 10:1**	0.03
Postglacial sand/gravel	QD type: 6, 7, 8, 9, 10, 12 13, 14, 15, 16, 20, 23, 24, 25, 26 Layer Z4	K_h = 5·10^{-3} **K_h/K_v = 10:1**	0.25
Glacial clay	QD type: 6, 8, 9, 10, 12, 13, 14, 15, 16, 17, 18, 19, 20, 21, 22, 23, 24 Layer Z5	K_h = 1·10^{-8} **K_h/K_v = 2:1**	0.03
Till	Soil < 5 m thick: QD type: 1, 2, 5, 6, 7, 9, 13, 16, 17, 18, 20, 22, 24, 25, 26, 27 Layer Z1 Domain 2–24 Layer Z6	K_h = 4·10^{-5} **K_h/K_v = 10:1**	0.05
Surface affected peat	QD type: 3,8, 21, 23 Layer Z1	K_h = 3·10^{-6} **K_h/K_v = 10:1**	0.24
Surface affected shingle	QD type: 4 Layer Z1	K_h = 1·10^{-2} **K_h/K_v = 10:1**	0.25
Surface affected sand	QD type: 10, 15 Layer Z1	K_h = 1·10^{-2} **K_h/K_v = 10:1**	0.25
Gyttja	QD type: 7 Layer Z3	K_h = 1·10^{-8} **K_h/K_v = 2:1**	0.03
Postglacial fine sand	QD type: 17 Layer Z4	K_h = 5·10^{-4} **K_h/K_v = 10:1**	0.25
Postglacial sand	Domain 18, 19 Layer Z4	K_h = 1·10^{-3} **K_{hh}/K_v = 10:1**	0.25
Postglacial gravel	QD type: 21, 22 Layer Z4	K_h = 1·10^{-2} **K_h/K_v = 10:1**	0.25
Artifical fill	QD type: 27 Layer Z4	K_h = 4·10^{-5} **K_h/K_v = 10:1**	0.05

7.6.3 Uncertainties

One objective of the hydrogeological flow modelling was to consider how pointwater head data for percussion holes and groundwater monitoring wells could be used to calibrate the properties of the HSD. Considering the amount of head measurements available for calibrating the HSD in Table 7-11, one percussion hole is drilled through Peat soil type, one is through Gyttja soil type, while the rest of the percussion holes are drilled through either Till or exposed bedrock. For the groundwater monitoring wells, there are more than 10 pipes in each of Till, Gyttja clay, and Peat; and only a few holes in postglacial gravel, postglacial sands. Therefore, a meaningful calibration can only be considered for Till, Gyttja clay and Peat. The other factor considered in the calibration was the anisotropy of the HSD. The starting position for the calibration was K_h/K_v = 1, i.e. isotropy. The values given in Table 7-11 are those arrived at after calibration.

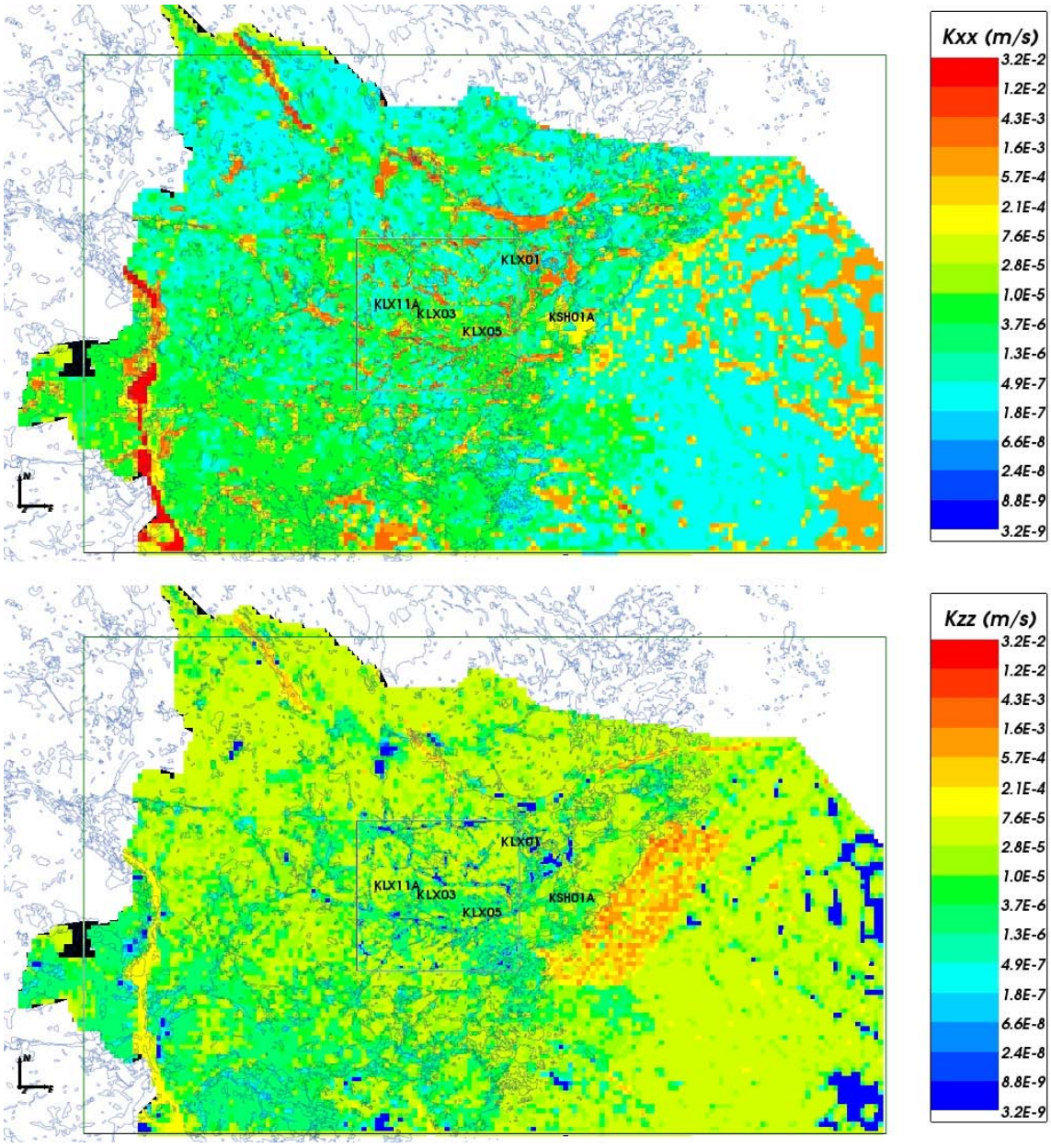

Figure 7-20. *Resulting effective hydraulic conductivity for HSD top layer based on layer thicknesses and hydraulic properties of the Quaternary deposits. Top: E-W horizontal component; Bottom: vertical component.*

7.7 Groundwater flow boundary conditions

For flow, there are two main possible boundary conditions that could be applied onshore: either specified head, or a flux type boundary condition. Typically, when specifying the head, the model is assumed to be fully saturated, and hence head is equal to the height of the topographic surface or some interpolated groundwater surface. Specified head boundary conditions are straightforward to implement numerically by setting the value at nodes on the surface to the required head. For the flux type boundary condition, it is more complicated because in reality, the flux through the top surface will vary spatially, both in magnitude and direction since in some areas groundwater is recharging and in others it is discharging. This distribution of flux varies according to the amount of potential groundwater recharge, the amount of surface run-off, and the hydraulic properties. Measurements of pointwater head within the Laxemar local model area suggest a watertable often near to or a few metres below the topographic surface, cf Chapter 4, and hence a fixed head boundary conditions is

unrealistic in areas of higher topography. /Hartley et al. 2007/ tested a flux boundary condition on the top surface, and found that the head distribution on the top surface was similar to the interpolated watertable used in model version Laxemar 1.2 when the recharge to the saturated zone was set to about 180 mm/year. This type of boundary condition is essential when modelling situations such as the impact of the Äspö HRL or the interference response to abstraction at boreholes after many days of pumping since the groundwater head will be reduced at least near the abstraction borehole.

For the area under the sea, it is most natural to use a specified head type boundary condition, where the head is equal to the depth of the sea multiplied by ρ_s/ρ_0, where ρ_s is density of the Baltic Sea and ρ_0 is fresh water density.

7.7.1 Specified infiltration

The standard approach in ConnectFlow for specifying an infiltration type condition is to define the recharge flux, R, into or out of the model as a function of the current head, h, in the model, the topographic surface elevation, z, and the maximum potential groundwater recharge, R_p. The potential groundwater recharge to the saturated zone is equal to the precipitation minus evapo-transpiration (P–E) and minus overland flow and flow through the unsaturated zone ($R_p = P–E–Q_s$). Overland flow and flow through the unsaturated zone is subtracted since only the potential recharge to the saturated zone is of interest (Such detailed processes of near-surface hydrogeology are the subject of /Werner et al. 2008/). Appropriate functions for the flux, R, must have certain characteristics. For recharge areas, the head, h, or watertable, is below ground surface and so the recharge must be equal to the full recharge, R_p. In discharge areas, the watertable is just above ground surface and so head is just above ground surface, which can be achieved by taking a suitably large flux out of the model, i.e. a negative value of R, whenever the head goes above ground surface. The standard function used in ConnectFlow is:

$$R = \begin{cases} R_p & h \le z - \varepsilon, z > z_0 \\ -R_p(h-z)/\varepsilon & h > z - \varepsilon, z > z_0 \\ -R_p(h-z_0)/\delta & z \le z_0 \end{cases} \qquad (7\text{-}2)$$

where ε and δ are small numbers (0.01 and 0.005, respectively), and z_0 is the elevation of the shoreline. This function implies that if the watertable is more than ε below the topographic surface then recharge equals the full potential groundwater recharge. Above that, the recharge reduces until the watertable is at the surface. If the watertable is above the topographic surface, then recharge becomes negative, i.e. discharge, and an appropriate flux of groundwater is taken from the model to reduce the head until the watertable is restored to just above topographic height. Hence, this boundary condition is a non-linear equation (the flux depends on the free-variable head) that ensures a specified flux if the watertable is low and a specified head where the watertable is at or above ground surface. The non-linearity requires that multiple iterations of the groundwater flow equations be performed at each time-step to reach convergence, which implies longer run times for this boundary condition. The topographic surface is not constant in time due to post-glacial seashore displacement, and hence $z = z(t)$. Newton-Raphson iteration was used to achieve convergence of the non-linear equations at each time-step. This technique works best for systems with smooth gradients. The standard function given above for flux has a discontinuous derivative at $h = z–\varepsilon$ and this can lead to a slow rate of convergence; typically three to five Newton-Raphson iterations were required at each time-step. Hence, an alternative smooth function for recharge was used:

$$R = \begin{cases} R_p \times \left(\exp\left(\dfrac{h-z}{0.15} \right) - 1 \right) & z > z_0 \\ -R_p(h-z_0)/0.005 & z \le z_0 \end{cases} \qquad (7\text{-}3)$$

The definition for the onshore part has similar characteristics to the standard function, but has smooth derivatives around $h = z$. This often gives convergence in two Newton-Raphson iterations, and hence gives quicker and more robust solutions. There are other candidates for this function, such as a modification to the standard function using a hyperbola to give a smooth transition around $h = z$.

It should be noted that in this model any groundwater that discharges through the top surface exits the model and does not enter a separate surface model that allows recharge downstream. Alternative approaches are to couple the groundwater model to a surface hydrology model, such as MIKE-SHE /Bosson et al. 2008/, or to add a surface layer with very high hydraulic conductivity to model the surface flow explicitly. In the second of these approaches, a flux is specified over the onshore region not covered by lakes, a head is specified in the sea and lakes, and the unsaturated flow equations should be solved in the near-surface layers. In this case, the flux should be set to precipitation minus evapo-transpiration, and these in principle can vary spatially.

When simulating the palaeohydrogeology over the last 10,000 years, transient variations in surface boundary conditions have to be considered both due to changes in the shoreline and the salinity of the Littorina/Baltic sea. The approach used is to apply the same definition of the boundary conditions as detailed above, but to calculate heads and elevations relative to a sea-level datum that evolves in time. ConnectFlow uses residual pressure, P^R, as the independent flow variable which is related to total pressure, P^T, by

$$P^R = P^T + \rho_0 g(z - z_0) \tag{7-4}$$

where ρ_0 is the density of freshwater, g is acceleration due to gravity, and z is the elevation of the point. Hydraulic head scales with residual pressure as

$$h = P^R/\rho_0 g \tag{7-5}$$

For transients, the datum, $z_0 = z_0(t)$, varies in time according to the shoreline curve, $z_0(t)$, see Section 4.2.

7.8 Palaeohydrogeology and hydrogeochemistry

The transient evolution of the chemical composition of surface waters infiltrating the bedrock over approximately the last 10,000 years offers a series of natural tracers that have entered the groundwater system and are mixed with the pre-existing groundwater. A conceptual model for the evolution of the chemistry of surface waters and groundwaters has been developed by the ChemNet group /Laaksoharju et al. 2009/ in terms of the chemical composition and mixing of different reference waters (see also Section 5.6.3). This is implemented in a 3D transient coupled groundwater flow and solute transport model to simulate the mixing of the different reference waters to give a prediction of the present-day distribution of groundwater chemistry for calibration against analysed groundwater samples from packed-off borehole sections.

7.8.1 Concepts for reference water transport

The representation of coupled groundwater flow and solute transport that gives rise to variations in salinity and hence fluid density can be handled in several ways in ConnectFlow. Generally, salinity is modelled in terms of a number of groundwater constituents. This can be modelled either in terms of transport of concentrations of each of the basic hydrogeochemical constituents (such as chloride, sodium, oxygen isotope ratio), which are taken to be conservative, or in terms of transport of mass fractions of selected reference waters. Either way, the transport equations are coupled with the overall mass conservation equation for groundwater.

The first approach involves solving transport equations for each of the major ions and isotopic ratios with the transient groundwater flow, including a coupling back to flow via spatial variations in groundwater density due to its varying composition. Since the raw hydrogeochemistry is analysed in terms of concentrations of major ions, then this option is attractive as it models directly what is measured. However, the number of transport equations that need to be solved is as large as the number of ions and isotope ratios that are required for the calibration, around 10. The second approach, i.e. to simulate the transport of mass fractions of reference waters, requires the solution of fewer transport equations, equal to the number of reference waters minus one, as the mass fractions muss sum to one, and so four solute transport equations are solved in this case. Hence, the second method is significantly more computationally efficient, but relies on the approximation

that the geochemical composition of a mixture of reference waters can be related linearly to the compositions of the individual reference waters, which, in the absence of chemical reactions requires that the transport properties of the major ions (only the diffusivities are of relevance in the equations consider here) are similar. Considering that the diffusivities of the major ions Na, K, Ca, Mg, HCO_3, SO_4 and Br differ from that of Cl by a few tens of percent /Li and Gregory 1974/, this appears to be a reasonable approximation relative to other uncertainties. Hence, with this assumption and neglecting chemical reactions, the two approaches can be considered inter-changeable, i.e. they would predict the same concentrations for the major ions.

The advantage of the reference water approach, and reasons why it was used in this study, is its computational efficiency and its convenience in terms of relating the model to the hydrogeochemical conceptual model. For example, the boundary and initial conditions, and alternatives, can be easily posed in terms of mixtures of reference waters, whereas the equivalent for ion concentrations one has to first work out the appropriate mixing fractions for that time, and then multiply these by the chemical compositions to get the concentrations of the individual components. Further, although simulating the evolution of ion concentration makes it easy to compare with borehole measurements, it can be difficult to interpret the overall 3D spatial distribution of ions and relate this to the hydrogeological and hydrogeochemical conceptual models. If it was considered necessary to include reactions in the timescale of last 10,000 years, then clearly it would be necessary to solve a modified equation for each major ion.

In summary, by simulating solute transport in terms of the transport of reference waters it is straightforward to implement the hydrogeochemical conceptual model and for example to illustrate how the mixing of the reference waters evolves in time on appropriate slices through the model. At the borehole locations, the calculated reference water fractions can either be converted to concentrations and isotope ratios using the compositions given in Section 5.6.3 and compared with the measured concentrations, or the reference water fractions can be compared directly with the mixing fractions calculated using Mixing and mass-balance modelling (M3) and the geochemical analysis presented by /Laaksoharju et al. 1999/.

The transport of the reference waters, or constituents, is described by equations representing advection, hydrodynamic dispersion and diffusion. The model of diffusion includes both diffusion within the water flowing within the fractures as well as the diffusive transfer between groundwater flowing in fractures and immobile water in the rock matrix between the fractures (Rock Matrix Diffusion or RMD). The numerical approach used for RMD /Hoch and Jackson 2004/ is based on a method developed by /Carrera et al. 1998/, enhanced to enable potentially larger time steps to be employed. The approach combines an approximation that is accurate for small times with one that is accurate for long times, to give a representation of the diffusion into the rock matrix that is accurate for all times. At early times, the diffusion is represented in terms of the inverse of the square root of time, and at long times it is represented as a series of decaying exponentials. The approach is very efficient computationally, although it is necessary to make the assumption that the groundwater density does not vary in the rock matrix at each location.

In the modelling, the groundwater density and viscosity vary spatially in three dimensions based on equations of state that are a function of total groundwater salinity, total pressure, and temperature. The salinity for a given water composition is simply the sum over reference waters of the product of the reference water fraction and the salinity of that reference water. The salinities for the reference waters were calculated from the Total Dissolved Solids (TDS, g L^{-1}) using:

$$\text{Salinity} = \text{TDS}/\text{density}, \qquad (7\text{-}6)$$

where density is a function of salinity (and temperature, and total pressure). It was assumed that the data given in Section 5.6 were obtained under laboratory conditions. Therefore, it was assumed that the data correspond to a temperature of 20°C and pressure of one atmosphere. The density and viscosity were obtained using empirical correlations for NaCl brines (see /SKB 2004a/ and /Kestin et al. 1981/). This corresponds to representing transport of equivalent NaCl for each water. The approximation made is reasonable, but will lead to the density and salinity being slightly underestimated for a Ca-rich solution such as the Brine reference water.

Assuming a down-hole pressure profile (surface ~0.1 MPa to ~25 MPa at depth), a salinity profile (surface 0‰ to 72.3‰ (brine) at depth), and a temperature range (7.2°C at the surface; geothermal gradient 0.015°C m^{-1}; i.e. ~40°C at bottom of the model), the groundwater density (ρ) can be calculated from the equation of state. At the surface, the fluid density is around 1,000 kg m^{-3}; and at depth the density is around 1,053 kg m^{-3} (i.e. 8.25%, 82,500 TDS mg/l, the bottom of the model is at an elevation of –2,164 m). The groundwater viscosity (μ) can be calculated in a similar fashion. At the surface, the viscosity is around 1.4 10^{-3} Pa s^{-1} and at depth, the viscosity at depth is around $0.8 \cdot 10^{-3}$ Pa s^{-1}.

The equations used to represent the transport of fractions of reference waters, with rock-matrix diffusion, are:

Mass conservation for groundwater: $$\frac{\partial(n_e \rho)}{\partial t} + \nabla \cdot (\rho \mathbf{q}) = 0 \quad (7\text{-}7)$$

Transport of reference waters: $$\frac{\partial(n_e \rho c_i)}{\partial t} + \nabla \cdot (\rho c_i \mathbf{q}) = \nabla \cdot (n_e \rho \mathbf{D} \cdot \nabla c_i) + \sigma \rho D_e \left.\frac{\partial c_i'}{\partial w}\right|_{w=0} \quad (7\text{-}8)$$

Rock-matrix diffusion: $$\alpha_i \frac{\partial c_i}{\partial t} = D_e \frac{\partial^2 c_i'}{\partial w^2} \quad (7\text{-}9)$$

where c_i is the mass fraction of reference water i in the water in the fracture system (mobile water); c'_i is the mass fraction of reference water i in the water in the matrix (immobile water); $\boldsymbol{q}$ is the Darcy velocity:

$$\mathbf{q} = -\frac{k}{\mu}\left(\nabla P^R - \rho \mathbf{g}\right) \quad (7\text{-}10)$$

$\boldsymbol{D}$ is the dispersion tensor; n_e is the kinematic porosity, ρ is the groundwater density, σ is the specific surface area per unit volume of the fractures, and D^e is the effective diffusion coefficient, α_i is the capacity factor for the rock matrix (or matrix porosity), w is a coordinate into the rock matrix from the fracture surface, k is the permeability, μ is the fluid viscosity, P^R is residual pressure, t is time, and $\boldsymbol{g}$ is acceleration due to gravity. All parameters use SI units.

In fact, the transport equations for the fractions of reference waters are not all independent. Since the sum of the reference water fractions must be equal to one, then it is not necessary to solve explicitly the transport equation for the final reference water. It can simply be evaluated as the remaining water fraction once the other reference water fractions have been computed at each time-step.

7.8.2 Solute boundary conditions

The boundary conditions for solutes, here formulated in terms of mass fractions of reference waters, must represent the evolution of groundwater composition on the upper surface of the model, which mainly vary as a consequence of changes in shoreline displacement due to post-glacial rebound and the variations in the salinity of the Baltic Sea.

The evolution of shoreline displacement and salinity of the Baltic Sea are discussed in Section 4.2 (cf Figures 4-25; Base cases are the SDM-Site model alt 1, and 4-26; SDM-Site Laxemar, Alt. 1). From these it is inferred that prior to 6500 BC the western part of the Laxemar focused area, corresponding to HRD_W, will be close to the shoreline of a freshwater lake, while the eastern part, corresponding to HRD_C will be mostly covered by the lake. After 6500 BC, the lake gradually evolves into the Littorina Sea, and hence in the surface depressions corresponding to the major deformation zones ZSMEW002A (Mederhult zone), ZSMEW007A and ZSMNW042A there is denser, saline, surface water that will sink into the bedrock until it encounters groundwater of similar or higher density, i.e. *Deep Saline Water*. Salinity and density of the sea continue to increase, so the buoyancy force will increase until the Littorina maximum at about 4500 to 3000 BC. Later the *Littorina Sea Water* slowly dilutes with *Altered Meteoric Water* toward the composition of the modern Baltic. During

this period, surface water will continue to infiltrate the bedrock depending on whether water from the maximum salinity period formed a continuous vertical column down to the *Deep Saline Water*, or whether water corresponding to the Littorina phase only forms a 'slug' sinking slowly down toward the dense *Deep Saline Water*. This will depend on the vertical hydraulic conductivity and transport properties of the fractures and matrix, and should be apparent from the chloride data for the fracture groundwater and matrix porewater samples. In the far western part of the flow model, groundsurface is above the shore level from that start of the simulation at 8000 BC, whereas in the east, the Äspö, Ävrö and Simpevarp areas have only been land for a thousand years, or so. Hence, the hydrogeochemical sampling in the core-drilled boreholes from west to east and from the low hills to the valleys capture a range of different states in the hydrogeochemical evolution of the site.

One uncertainty in prescribing the hydrogeochemical boundary condition is what reference water composition was appropriate for the dilute water when sea water salinity was less than 100% of the Littorina reference water. After 4500 BC, *Littorina Sea Water* was diluted with *Altered Meteoric Water*. Before the Littorina maximum (4500 BC), the precursors to the Baltic Sea were a series of ice lakes, and so the dilute sea water was in the base case assumed to be *Glacial Melt Water* in origin. For simplicity in the numerical implementation of the boundary conditions, the same dilute groundwater composition was used above the shore level also prior to 4500 BC in the base case. A variant calculation was also considered where the dilute water prior to 4500 BC was *Altered Meteoric Water* instead. In which case, *Glacial Melt Water* was introduced into the palaeohydrogeological model only via the initial condition. The time variation in the mass fractions of reference waters specified for recharge areas at the top surface of the model for both off-shore and on-shore areas is illustrated in Figure 7-21 for the base case. (It should be noted that areas of recharge and areas above the shoreline are re-calculated at each timestep).

In order to implement this evolution in a numerical model, a time varying specified value boundary condition is used on the top surface where there is an advective flow into the model (recharge area), or an outflow condition where there is flow out (discharge). Because the flows are transient, the areas of recharge and discharge evolve in time, and hence it is important to have an automatic way

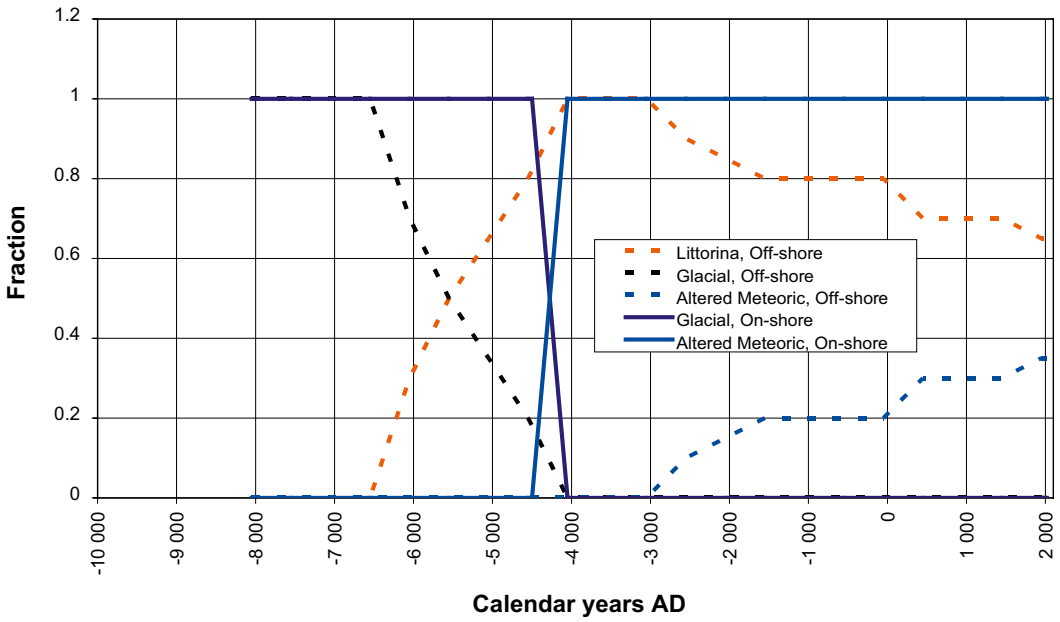

Figure 7-21. *A sketch of the transient hydrogeochemical boundary conditions on the top surface of the hydrogeological model. For off-shore parts of the model, i.e. below the shoreline $z < z_0(t)$, the dashed curves show the mixture of Glacial Melt Water, Littorina Sea Water and Altered Meteoric Water assumed. For the on-shore parts of the model, i.e. above the shoreline z > z0(t), the solid curves show the mixture of Glacial Melt Water and Altered Meteoric Water assumed.*

of determining the recharge and discharge areas. The difficulty in achieving this is that it requires mixing a Neumann (flux) type boundary condition on outflow with a Dirichlet (head) type boundary condition on inflow; and since the recharge/discharge areas change in time, the type of boundary condition has to be changed in time. Our solution is to specify a flux of solute through the top surface that changes depending on the direction of flow across the surface. Where an inflow of groundwater at a specified input mass fraction is required (i.e. a Dirichlet condition), flux is equated to a penalty weight function based on the difference between solute mass fraction in the model and the required input mass fraction. Therefore, the flux of solute out of the model, F_c, is then given by the equation:

$$F_c = \begin{cases} (\underline{q} \bullet \underline{n})c & q \cdot n \geq 0 \\ (c - c_0)/\delta & q \cdot n < 0 \end{cases} \qquad (7\text{-}11)$$

where $\underline{q} \bullet n$ is the advective flux out of the model, i.e. the groundwater flow, $\underline{q}$, in the direction parallel to the outward normal to the surface, $\underline{n}$, c is the mass fraction of a particular reference water, and δ is a small number ($5\ 10^{-5}$ was used). For $\underline{q} \bullet \underline{n} \geq 0$ the flux corresponds to an outflow condition, for $\underline{q} \bullet \underline{n} < 0$ a specified value condition, $c = c_0(z,t)$, is implemented as a penalty function such that solute is removed if $c > c_0(z,t)$, and injected if $c < c_0(z,t)$. This effectively ensures that $c \approx c_0(z,t)$. As indicated the mass fraction of each reference water is specified as a function of time t and elevation z.

The boundary condition on the vertical sides is assumed to be zero flux of solutes. On the base of the model at –2,164 m elevation, the mixture of reference waters is held constant in time (i.e. equal to the initial condition) since it is expected that groundwater below 2 km depth is mostly ancient high salinity stable water subject to very little advective flow below this elevation.

7.8.3 Initial conditions

The initial hydrochemical condition at 8000 BC is by its nature uncertain. Nevertheless in order to perform numerical modelling it is necessary to make an informed guess of appropriate initial hydrochemical conditions, and consider suitable variants to quantify the sensitivity to our speculation. Some useful clues for the initial conditions can be obtained by combining our knowledge of the bedrock hydrogeology and the present-day hydrochemistry. In the deep bedrock below c. –650 m fracture transmissivities as well as the conductive fracture intensity are low, implying very long advective transport times, and the timescales for diffusion to penetrate fully into the matrix blocks between the conductive fractures are far longer than the current Holocene. The presence of *Deep Saline Water* and *Glacial Melt Water* in the fractures also suggests that the hydrochemical conditions at such depths have changed very little during the Holocene. Hence, the hydrochemical samples below c. –650 m can be used as indicators of appropriate initial conditions at depth, which can be extrapolated to higher elevations where post-glacial mixing may have taken place. Still, there are brackish-glacial groundwater samples collected at elevations down to c. –200 m, which suggest a persistence of hydrochemical composition over the timescale of interest. Above c. –150 m, appropriate initial conditions are very uncertain since a younger post-glacial age is suggested by groundwater samples, but these also imply that the initial conditions are largely irrelevant at such shallow depth as the groundwater will in any case be replaced by later surface waters infiltrating according to the defined hydraulic boundary conditions. Hence, the approach used here is to consider the present-day groundwater samples below –650 m as being predominantly stable during the Holocene, and to use them to infer an initial hydrochemical composition and extrapolate this to shallower depths. Simple piecewise linear depth trends in the initial chemical composition are assumed.

In the wider perspective, the initial conditions at 8000 BC are the result of a palaeohydrogeological evolution over several glacial cycles which are even more uncertain to predict. Hence, the approach here is to consider relatively simple initial conditions at 8000 BC consistent with the data and physical processes such as rock matrix diffusion, and then quantify the sensitivity of palaeohydrogeological simulations to these assumptions. How hydrochemical conditions may evolve during a glacial event are the subject of future studies.

In order to estimate the initial groundwater composition at 8000 BC, the fracture water is first assumed to be predominantly a mixture of *Deep Saline Water* and *Glacial Melt Water*. Considering the composition of saline waters first (Cl > 200 mg/L), an initial fraction of *Deep Saline Water* is guessed. Two alternative cases are considered:

1. A line that approximates the Cl data below c. –200 m. This essentially assumes all present-day salinity is of *Deep Saline Water* origin and a remnant from the initial condition. This requires the mass fraction of *Deep Saline Water* to start at –150 m and become 1 at –2,100 m (used as base case).
2. A steeper line that is based solely on the data below c. –650 m. This would require later Littorina infiltration to provide the present-day salinity in the shallow bedrock above c. –400 m. This requires the mass fraction of *Deep Saline Water* to start at –400 m and become 1 at –1,800 m.

These two alternative guesses for the initial linear trend of *Deep Saline Water* are illustrated in Figure 7-22 on the basis of Cl concentrations compared with the hydrochemical sampling data (see Section 5.6).

Within the Laxemar subarea there is little evidence of any Littorina signature remaining. Figure 7-23 shows the levels of magnesium measured in groundwater samples from the Laxemar subarea and the corresponding mixing fractions of *Littorina Sea Water* interpreted by M3. These indicate no more than about 10–20% *Littorina Sea Water*, even accepting the uncertainty of the interpretation. Given this lack of marine-derived salinity, the Case 1 interpretation of chloride data seems the more likely scenario for the initial condition. Possible mechanisms for elevated *Deep Saline Water* in the past are up-coning of salinity during the retreat of the ice sheet causing discharge of saline groundwater due to the high groundwater pressure behind the ice sheet /Jaquet and Siegel 2006; Vidstrand et al. 2009/. Still, it is considered useful to consider both scenarios to quantify the sensitivity to the initial *Deep Saline Water* profile.

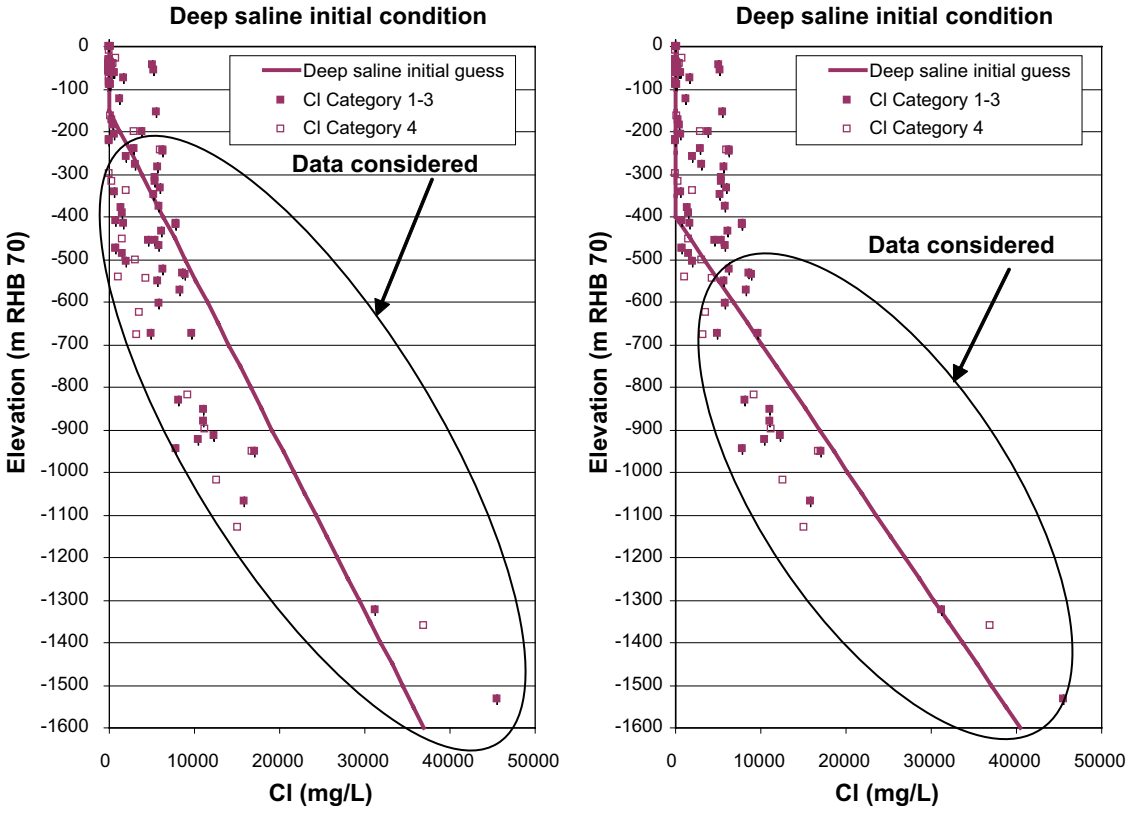

Figure 7-22. *Illustration of assumed initial condition for Cl in fracture groundwater at 8000 BC for two alternative interpretations compared with measured groundwater concentrations. Two alternative fits are considered: Case 1 (left) assumes the majority of present-day salinity results from the initial condition; Case 2 (right) assumes only the salinity at depth originates from Deep Saline Water, the salinity at shallow depth arising from Littorina infiltration.*

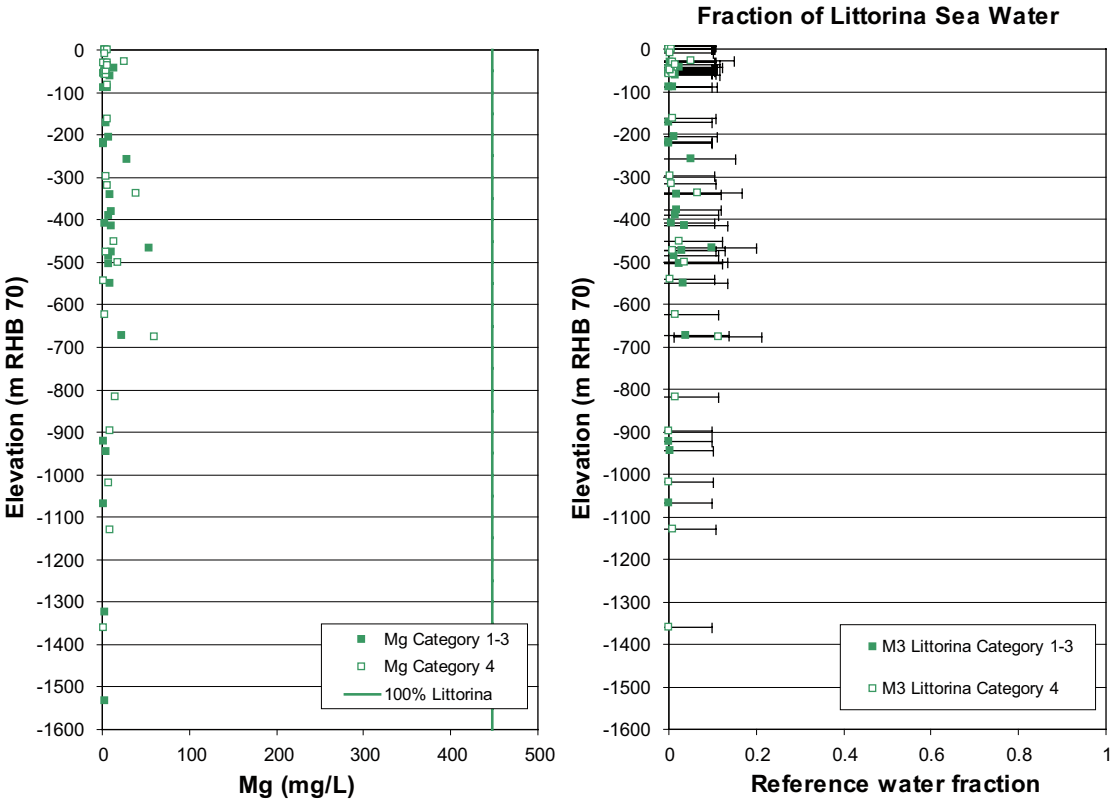

Figure 7-23. *Measured magnesium concentrations (left) for groundwater samples within the Laxemar local model area compared with the concentration of Littorina Sea Water (vertical line). On the right is the mixing fractions of Littorina Sea water from interpreted by M3 for these data points.*

The remaining fraction of water in fractures is necessarily more dilute (Cl < 200 mg/L) and is assumed initially to be mostly *Glacial Melt Water*, which is consistent with an injection of *Glacial Melt Water* under high pressure during either the retreat of the ice sheet or earlier. A similar approach to the above was used for defining the appropriate initial mass fractions for *Glacial Melt Water*, but was based on interpreting measurements of $\delta^{18}O$. These interpretations of $\delta^{18}O$ have to factor in the mass fractions already assigned to *Deep Saline Water,* and the results are shown in Figure 7-24 for the alternative interpretations corresponding to Cases 1 and 2 from Figure 7-22.

If one assumes all the non-*Deep Saline Water* is *Glacial Melt Water* (i.e. if one were to assume the two mass fractions summed to unity) then the levels of $\delta^{18}O$ are too depleted. Hence, the initial conditions need a third component, otherwise using mixtures of only *Deep Saline Water* and *Glacial Melt Water* results in either too much chloride or water that is too depleted in $\delta^{18}O$. The mass fractions not accounted for (i.e. a third component) after fitting to the chloride and $\delta^{18}O$ data are about 10–30%. This can be compared qualitatively with the fraction of meteoric water in groundwater sampled below –650 m interpreted by M3 analysis, which are about 20–40% in the deeper groundwater samples. The M3 analysis does not differentiate between post-glacial meteoric water and earlier meteoric water. Conceptually, any meteoric water in the initial condition is considered to be of *Inter-glacial Porewater* origin, and could be interpreted as the result of diffusive exchange with the porewater at such depths which is generally enriched in $\delta^{18}O$. Figure 7-25 compares the mass fractions of the 3rd component of initial condition, assumed to be *Inter-glacial Porewater* for the 2 alternative cases with the mixing fractions of meteoric water interpreted by M3.

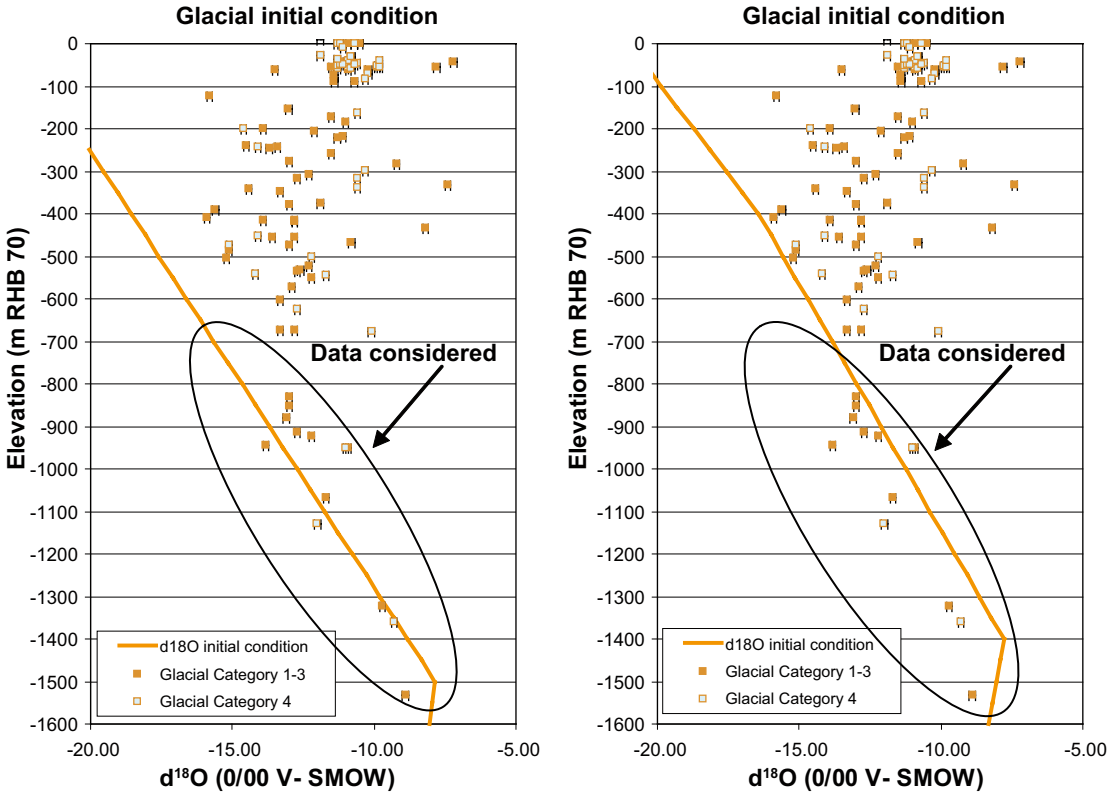

Figure 7-24. *Two alternative interpretations of the initial profiles of $\delta^{18}O$ used to indicate appropriate initial conditions of Glacial Meltwater for Case 1 (left), Case 2 (right) corresponding to the interpretations of Cl illustrated in Figure 7-22. Only the data below –650 m (shown by the ellipse) are considered in these interpretations.*

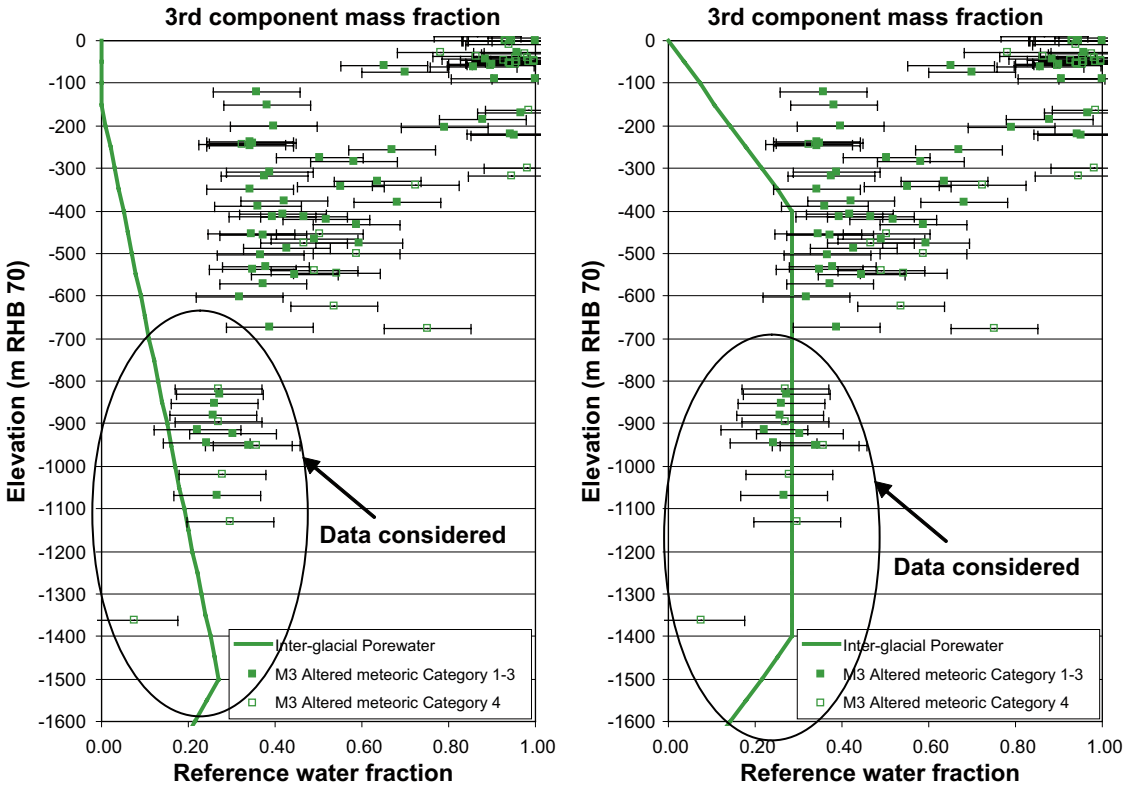

Figure 7-25. *Comparison of remaining mass fractions for a third component of the initial condition for fracture groundwater at 8000 BC for Case 1 (left) and Case 2 (right) with the mixing fractions of meteoric water interpreted by M3 (squares with error bars showing ~10% uncertainty in the M3 interpretation). Only the data below –650 m (shown by the ellipse) are relevant.*

A summary of the compositions of initial conditions in the fracture water at 8000 BC for the two alternative cases tested in the modelling is illustrated in Figure 7-26.

The initial chemistry in the matrix is more difficult to define since there are relatively few porewater samples and conditions depend strongly on the distance of the samples to the nearest conductive fracture. Hence, the initial conditions are strongly dependent on the local hydraulic properties, mainly the fracture surface area per unit volume. The data for both δ^2H and $\delta^{18}O$ below –650 m suggest differences between the matrix porewater and fracture groundwater in at least the freshwater composition at depth, tending toward enriched $\delta^{18}O$ away from the conductive fractures. Simulations showed that if one simply assumes different initial conditions in the fractures and matrix, then very soon the back-diffusion from the matrix porewater into the fracture water entirely dilutes the composition of the fracture water with whatever is assumed in the porewater due to the high ratio between matrix and fracture porosities. Therefore, it is necessary to have an initial condition in the rock matrix that varies according to the distance of the matrix porewater sample from the nearest conductive fracture that is consistent with the process of rock matrix diffusion. In this way differences between in initial concentrations in the fracture water and porewater far from the conductive fractures can be maintained over long time periods. The way this was implemented was to hold the initial guess for the fracture water according to the distributions shown in Figure 7-26, but allow a diffusive exchange (or equilibration) with the adjoining porewater for 5,000 years. The starting condition in the porewater was assumed to have the same mass fraction of *Deep Saline Water*, but the remaining water is all *Inter-glacial Porewater* prior to allowing for diffusion. Therefore, the

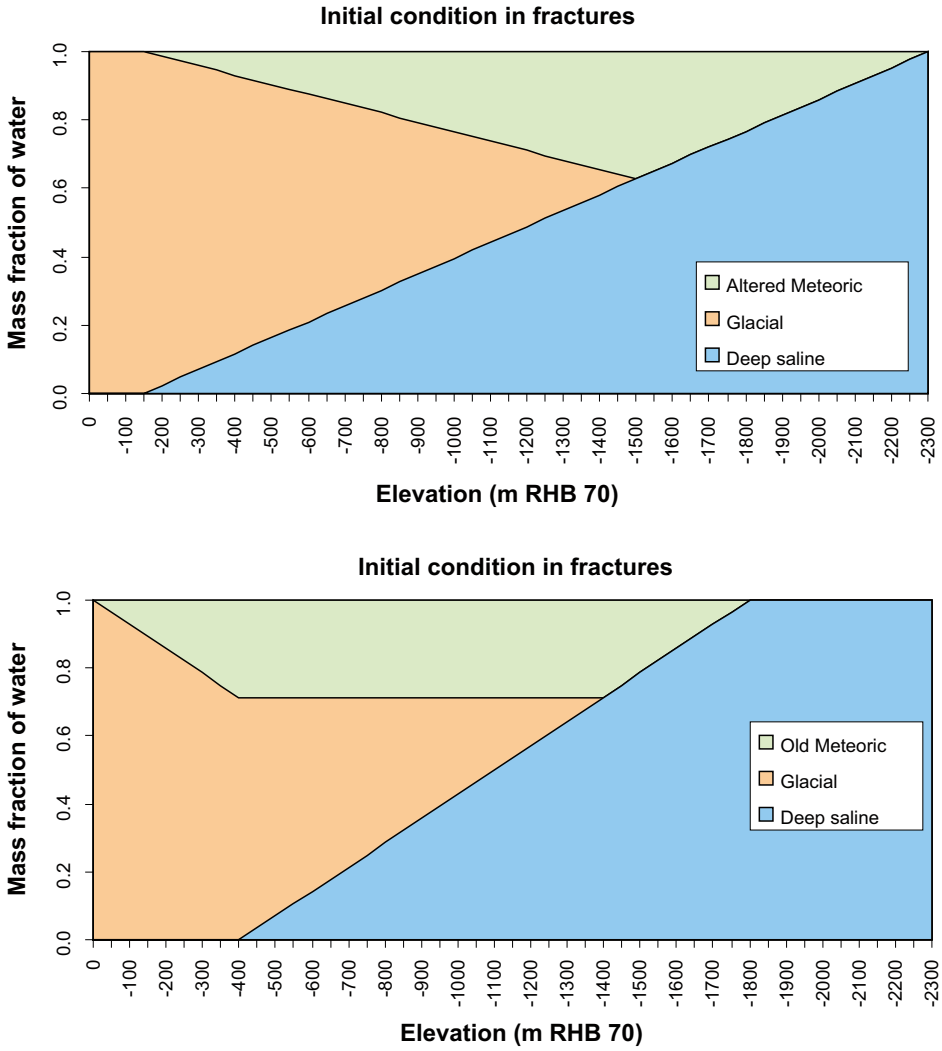

Figure 7-26. *The 2 alternative initial conditions at 8000 BC tested for the fracture water: Case 1 (top) (used as base case), Case 2 (bottom).*

diffusive exchange just considers the in-diffusion of *Glacial Melt Water* replacing older *Inter-glacial Porewater*. The physical interpretation is that during the Weichselian glaciation and subsequent melting, *Glacial Melt Water* will have infiltrated the fractures under high pressures and in-diffused into the matrix, but did not have had time to diffuse into the large matrix blocks (10–100 m in size) between conductive fractures at depth. The profile of the initial condition in the matrix porewater therefore varies both with depth and distance from the nearest conductive fracture, i.e. distance in the matrix block. This is illustrated for four different depths in HRD_C and initial condition Case 1 in Figure 7-27 and Figure 7-28. The matrix length range shown varies according to the average half size of the matrix blocks within each depth zone, since the spacing between conductive fractures decreases with depth.

In summary, these two alternative initial conditions tested in the modelling are consistent with the conceptual model that has very slow advective mixing at depth and hence is based on the measured Cl and $\delta^{18}O$ below c. –650 m, as well as account for the role of rock matrix diffusion. The two cases allow uncertainty in the origins of salinity, key to groundwater flow, to be assessed.

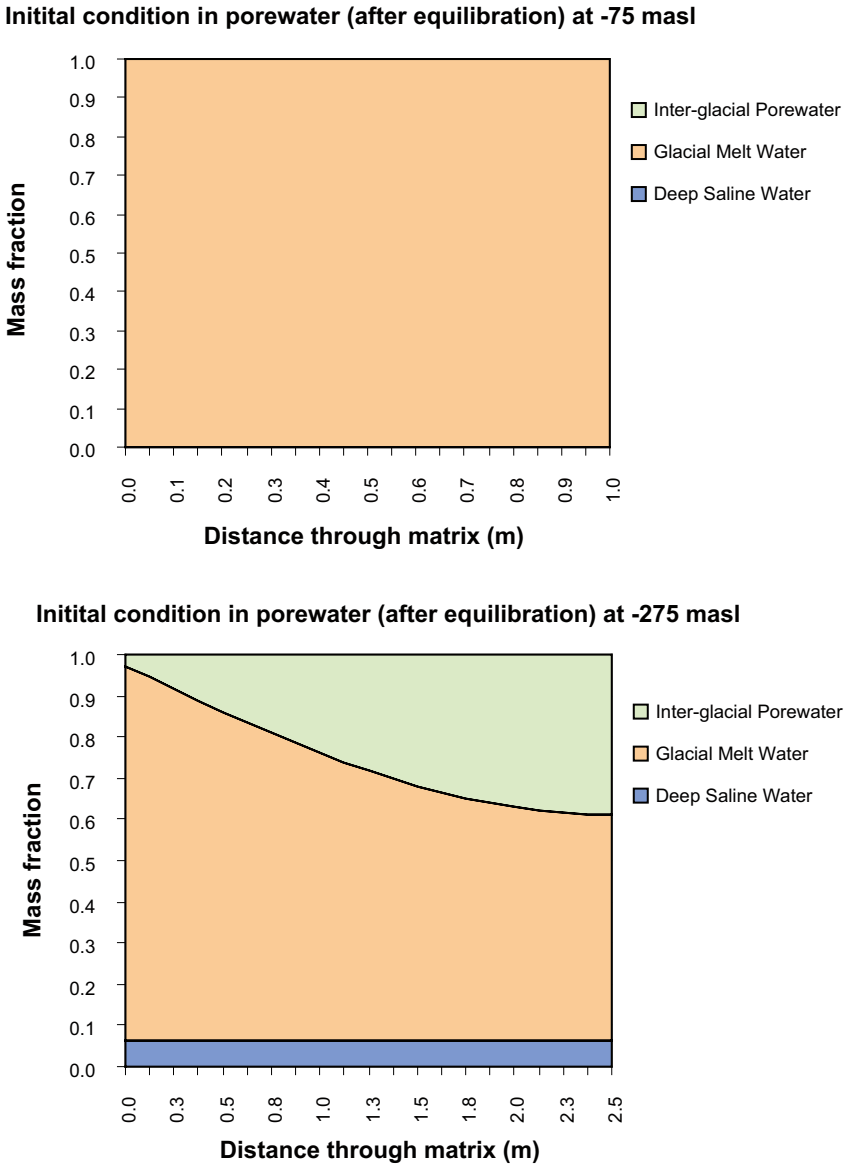

Figure 7-27. *Examples of initial conditions in the matrix at two different depths (in the two upper depth zones) for HRD_C based on initial condition Case 1. Profiles are shown as a function of distance from a water conducting fracture surface, so that 0 m is the equal to the initial condition in the fracture, and the right hand distance is the initial condition at the centre of a matrix block, the distance increasing with depth as conductive fracture intensity decreases.*

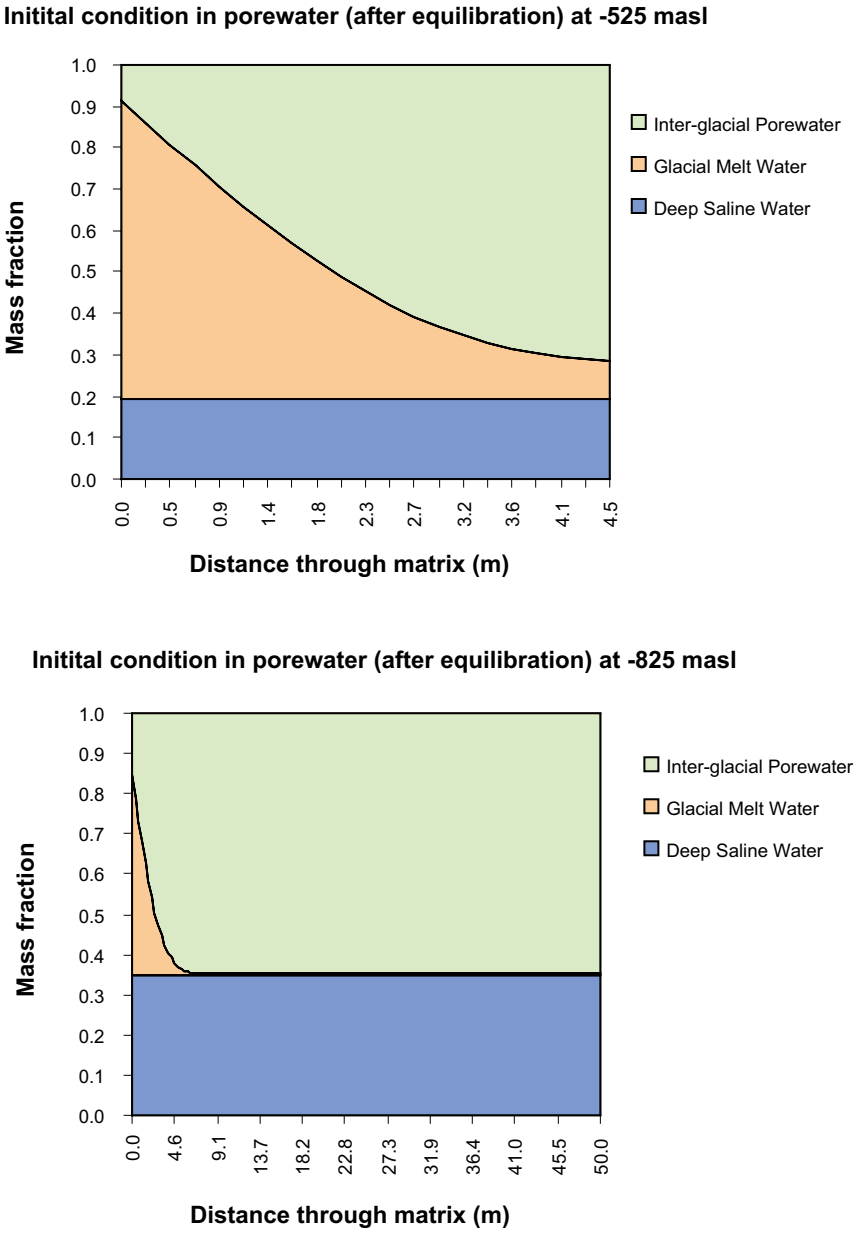

Figure 7-28. *Examples of initial conditions in the matrix at two different depths (in the lower two depth zones) for HRD_C based on initial condition Case 1. Profiles are shown as a function of distance from a water conducting fracture surface, so that 0 m is the equal to the initial condition in the fracture, and the right hand distance is the initial condition at the centre of a matrix block, the distance increasing with depth as the conductive fracture intensity decreases*

8 Regional model – calibration on hydraulic tests and monitoring data

This chapter presents the results of confirmatory tests of the groundwater flow model against measurements of groundwater levels, pressures and drawdowns from a variety of different hydraulic tests as described in Chapters 5 and 6. The comparisons made are based on the results of simulations performed using the calibrated *base case model* as specified in Chapter 7 along with a series of variants used to illustrate some of steps made in the calibration and quantify the sensitivity to some remaining uncertainties.

8.1 Natural groundwater heads

Groundwater levels measured in open boreholes are available for the upper bedrock and Quaternary deposits to help confirm appropriate boundary conditions and hydraulic properties for the near-surface hydrogeology. This situation is comparable to that for SDM-Site Forsmark /Follin et al. 2007c/. Important issues such as the direction and magnitude of the hydraulic gradient between the bedrock and soil can be simulated and compared to such data. In addition, groundwater levels in deep, core-drilled boreholes are also available for comparisons. Since, salinity increases with depth, so does the groundwater density. The groundwater levels measured in deep boreholes are therefore conceived to represent pointwater heads. Such information can be used to confirm the predicted pointwater heads in the deeper bedrock, as well directions and magnitudes of vertical head gradients at depth. However, in order to understand vertical head gradients in a variable-density groundwater flow system, measured groundwater levels (pointwater heads) must be transformed to environmental heads, i.e. the buoyancy term due to groundwater density variations is removed, so that vertical flows are linearly proportional to the environmental head gradient.

As discussed in Sections 5.5.3 and 6.6, there are some uncertainties as to whether the correct density adjustments have been made to the data transformation from pointwater heads to environmental water heads, and hence the simulated pointwater head is plotted in addition to the environmental head to quantify the likely maximum possible error in calculating the measured environmental heads. This uncertainty is mainly present below about –400 m, and becomes very significant below about –800 m, and therefore the comparisons are truncated at this lowermost depth.

8.1.1 Methodology

Since the simulated environmental heads in the deep core drilled boreholes are affected by salinity below –400 m, the calibration on head data needs to be made with a realistic groundwater density distribution in the simulations. Hence, the head comparison is made on the basis of the palaeohydrogeology simulations of the evolution of fluid pressure and density over time, using the predictions at 2000 AD to calculate environmental and pointwater heads. The top surface boundary condition is based on the estimated average annual precipitation minus evapotranspiration (often denoted as P-E) and specific-discharge of 180 mm/year /Werner et al. 2008/. Therefore, the head calculations are based on simulation of the very long-term transient processes. A time-step of 20 years is used, though shorter seasonal or diurnal transient processes are ignored, essentially predicting only the time-averaged head distribution in the HRD and HSD. The effects of specific storage on these long timescales are assumed to be negligible.

To compare simulation results with measurements, the following results were calculated.

- A plot of the simulated and time-averaged measured heads in all HLX boreholes.
- A plot of the simulated and time-averaged measured heads in all SSM holes.
- A plot of the simulated and time-averaged measured heads in each core drilled KLX borehole.
- Objective functions comparing the average difference and average absolute difference between simulated and measured heads over the HLX boreholes, SSM holes, and the KLX packer intervals.

The three plots provide details of matches and/or discrepancies at individual locations or depths that can be used to calibrate particular features of the model such as changing the transmissivity of a particular HCD or HRD, whereas the objective functions provide an overall scalar measure of how good a match is achieved.

As illustrated in Section 6.6, the measured heads are averaged over time and the seasonal variation was shown, in the HLX and SSM comparison plots, to indicate the uncertainties in the measurements. For the simulations, the head at the very top of the HLX boreholes was plotted as well as at the mid elevation of the borehole to indicate the predicted direction of vertical flow, i.e. recharge or discharge. A good match was judged to have been achieved where the general pattern of heads within the Laxemar local model area, as quantified by the three plots, was reproduced and when the mean discrepancy was less than the mean seasonal variation in the measurements.

For the calibration on near-surface heads using HLX and SSM data, the quality of the fit was judged mainly on the defined objective functions augmented by scanning the comparison plots for any notable trends or sensitivities between model variants. Hence, calibration steps were made where a parameter change resulted in a reduction in the average head difference between simulations and measurements. As well as calculating the head difference over all available boreholes, the average differences were also calculated for each HRD and soil type to identify the sensitivity to parameters of individual HRD and HSD, thereby determining which parameters were most important for the calibration. For the KLX boreholes, a log of the HRD and HCD in each borehole was included in the head comparison plots to guide which hydraulic features might be controlling the simulated head in each borehole.

8.1.2 Calibration steps

Initial simulations used the parameterisation of HCDs and HRDs suggested in /Rhén et al. 2008/ although gradually adjusted toward the base case described in Chapter 7. Since the heads in the deep boreholes are dependent on the salinity distribution, the calibration on heads and palaeohydrogeology (see Chapter 9) were largely performed in parallel, although it was possible to make some scoping calculations of effects of the HSD without performing repetitive palaeohydrogeological simulations. The main changes made to the hydrogeological model guided by the head data were to:

1. Increase the transmissivity of ZSMEW007A.
2. Introduce anisotropy 1:0.01 (longitudinal: transverse) in ZSMEW002A.
3. Use anisotropy of 1:0.0001 (longitudinal:transverse) in the dolerite dykes associated with ZSMNS001A-E, ZSMNS059A and KLX19DZ5-8.
4. Introduce anisotropy of 1:0.1 (horizontal: vertical) in the HSD (except Gyttja clay, which uses 1:0.5).

Change 1) was necessary to lower predicted heads in and around ZSMEW007A. Change 2) was necessary to produce the large drop in head at around –300 m across ZSMEW002A. Change 3) was made to sustain elevated heads in the south of HRD_W around HLX28. Change 4) was made to bring groundwater levels close to the topographic surface in the HSD as generally indicated by the data.

8.1.3 Resulting calibration

An example of the matching of the point water heads is shown here for HLX boreholes in Figure 8-1 and for SSM boreholes in Figure 8-2 for the *base case model*. Lines indicating the elevation of the topographic surface and the elevation of the soil/bedrock contact are shown for reference.

The simulations predict a distribution of heads for HLX boreholes that is in reasonable agreement with the distribution in the data, i.e. predicted heads are generally within the measured seasonal variations. The general pattern of behaviours is consistent. For example, for about half the boreholes the measured head is below the bedrock surface (green line) and this occurs in the simulations for largely the same boreholes. The same is true for the boreholes where the measured head is around the bedrock surface, and also the boreholes where the measured head is close to ground surface.

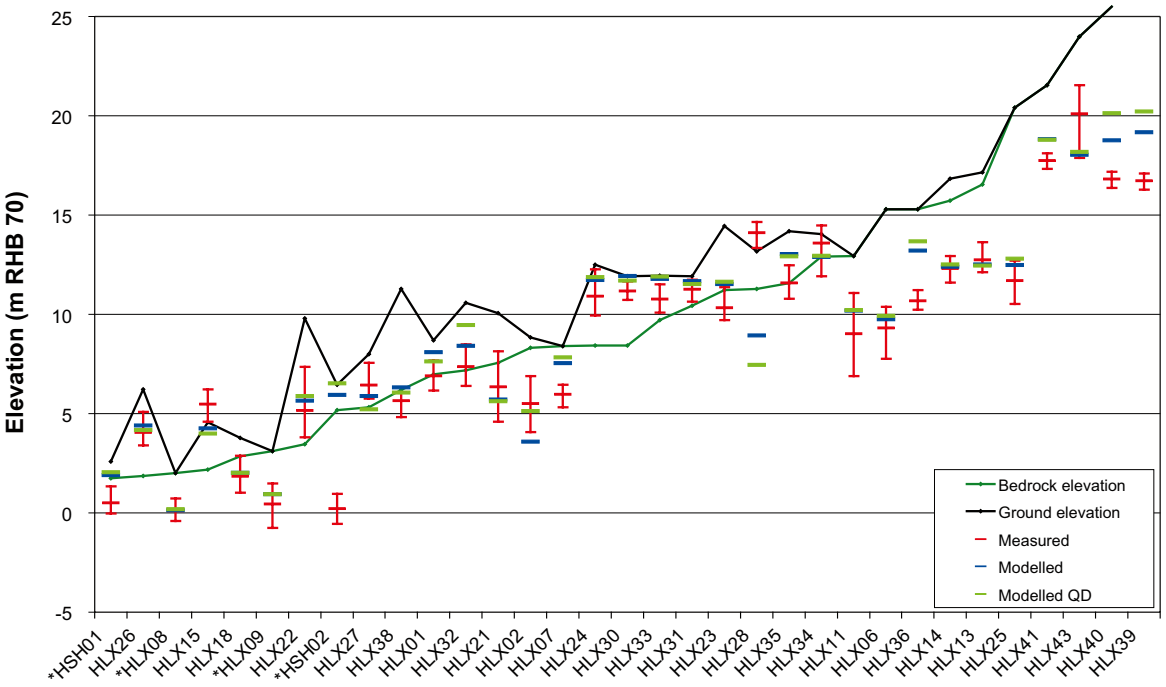

Figure 8-1. *Comparison of measured heads in percussion drilled boreholes (HLX) with results of the base case model. For the model, values are given for the QD and at the mid elevation of the borehole section in the bedrock. The field data are plotted as mean point water heads in the bedrock with error bars to show the range of values at different measurement times. Boreholes marked by a * are outside the local model area.*

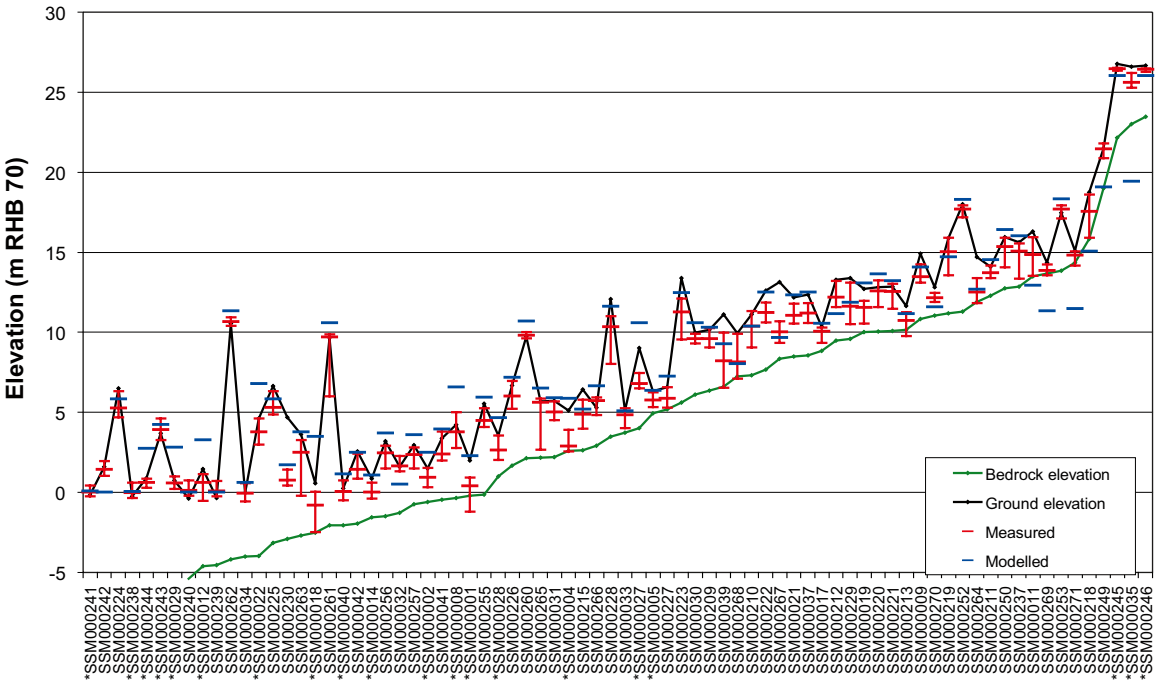

Figure 8-2. *Comparison of measured heads in groundwater monitoring wells (SSM) with the results of the base case model. For the model, values are given for the QD only. The field data are plotted as mean point water heads in the soil with error bars to show the range of values at different measurement times. Boreholes are ordered by bedrock elevation at the borehole collar. Boreholes marked by a * are outside the Laxemar local model area.*

One problematic borehole is percussion borehole HSH02 where the head measurement appears anomalously low and may be affected by the nearby Clab facility and possibly by drainage to shafts of limited depth extent associated with the foundations of the nuclear power plants. Another is percussion borehole HLX28 where head is under-predicted by about 4 m. This borehole is located in a complex area near the Laxemarån river valley with relatively steep topographic gradients, and hence there may be interpolation issues involved using a 40 m grid, as well as there being several local-scale deformation zones and dolerite dykes nearby.

The head in the Quaternary deposits is higher than in the bedrock for the majority of boreholes, suggesting recharge conditions, although there are discharge areas indicated also at lower elevations. For the *base case model*, the average head difference for HLX boreholes is 0.32 m within the Laxemar local scale model area, implying a slight overall over-prediction of the head, and the average absolute difference is 1.17 m. This should be compared with the average seasonal variation of 1.85 m (i.e. average max-min measured head) for the HLX measurements.

For the SSM groundwater monitoring wells the predicted heads largely follow topography as for the measurements. For the *base case model*, the average head difference for SSM holes is 0.35 m within the Laxemar local scale model area, implying a slight overall over-prediction of the head, and the average absolute difference is 0.98 m. This should be compared with the average seasonal variations of 1.57 m (i.e. average max-min measured head) for the SSM measurements. It may be seen that the head exceeds the topographic height of the ground surface at some locations. This highlights the issue of grid resolution. The simulation grid uses a 40 m grid and the digital elevation map (DEM) provided uses a 20 m grid. Depending on undulations in ground surface on scales less than 20 m, then there are inevitably going to be discrepancies in the modelled heads in relation to the magnitude of these local scale undulations. The over-predictions are concentrated to HSD types of Peat (QD type 11) and Gyttja clay (QD type 6), and so this could imply a higher horizontal conductivity for these layers, probably associated with postglacial sediments layers and lower till layers, respectively.

Some examples of comparisons between simulated and measured environmental heads in core-drilled boreholes are given in Figure 8-3 through Figure 8-5 for the *base case model*. A full set of KLX borehole comparisons is included in Appendix 8 for the base case. KLX04 starts in HRD_N, passes through ZSMEW007A at around –300 m, and then enters HRD_EW007. The magnitude of environmental head is about right and the gradual decrease in environmental head with depth is reproduced well. Cored borehole KLX06, entirely within HRD_N, intersects ZSMEW002A at around –300 m where there is a sharp drop in head of about 5 m. This is too shallow to be explained by uncertainties in groundwater density, and is interpreted to be an indication that ZSMEW002A acts as barrier to transverse flow due to fault gouge or clayey material. This motivated introduction of anisotropy in HCD ZSMEW002A as part of the calibration process in order to reproduce this ‘jump’ in environmental head as seen in Figure 8-3.

Most of the core drilled boreholes in the Laxemar subarea display a gradual decrease in environmental head with depth, i.e. recharge conditions, as illustrated by the data and simulations of KLX10 and KLX12A in Figure 8-4. These boreholes are situated in the Laxemar focused area, involving HRD_C and HRD_EW007. The measurements of lower environmental head in KLX10 illustrate the occasional sudden drop in measured environmental head at about –650 m associated with uncertainty in correcting the data for measured groundwater density. The magnitude of uncertainty is consistent with the difference between the simulated environmental and pointwater heads. Figure 8-5 gives examples of the environmental heads in KLX11A and KLX21B, both within HRD_W and the focused area. The gradual decrease in environmental head with depth is reproduced; although with a higher gradient around –100 m in KLX11A, probably associated with the subhorizontal HLX28_DZ1 minor deformation, is slightly under-predicted by the model. The environmental head predicted in the upper 400 m of KLX21B seems acceptable, and the sudden drop in environmental head below –400 m may result from the density correction, as is predicted by the pointwater head deviation. The mean difference between modelled and measured environmental head over all borehole packer intervals is calculated as 0.41 m and a mean absolute difference of 2.04 m, compared with an average seasonal variation of 1.21 m (i.e. average max-min measured head). It should be noted that these objective measures were calculated for all boreholes intervals above an elevation of –800 m, and hence includes intervals between –400 m and –800 m that may be subject to density correction errors.

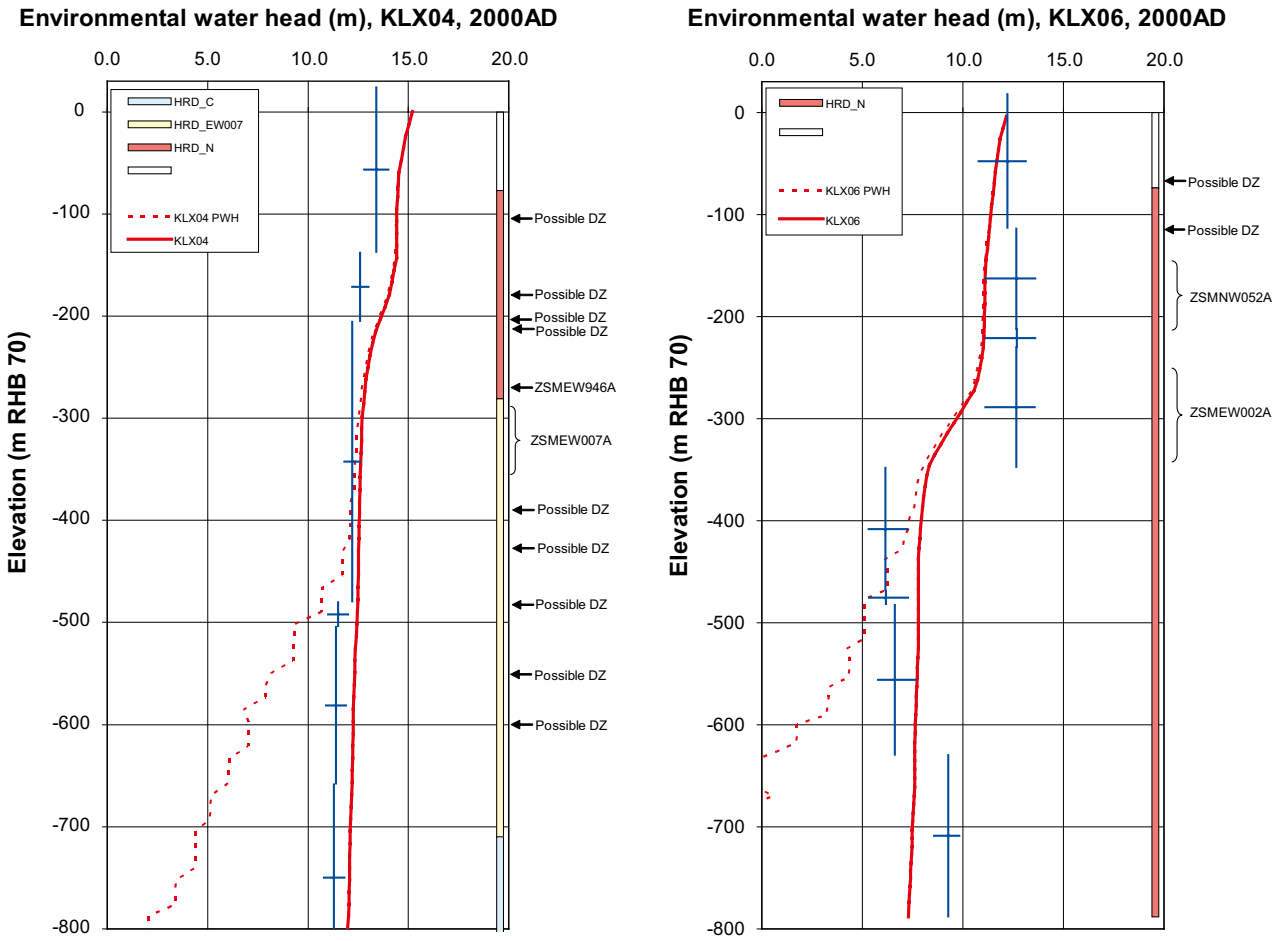

Figure 8-3. *Examples of modelled environmental-water head (solid red line) and point-water head (dotted red line) in KLX04 and KLX06 for the base case compared with environmental-water heads (blue crossed lines, centre showing midpoint of the section, vertical line showing the extent of the section and horizontal line showing the temporal variation of the measured head) calculated from measured point-water head data in sections along the borehole. At the right hand side, the prevailing hydraulic rock domains are shown as coloured bars along the borehole. Detected deformation zones are indicated at the intersection depth in the borehole.*

The simulated distribution of pointwater head on the top surface of the model is shown in Figure 8-6 for the base case. Plots are shown for the full regional model and in and around the Laxemar local model area. Heads are highest in the west, but there are number of low hills within the Laxemar local model area and two WNW-ESE valleys to the south (Laxemarån river valley) and north (along the Mederult zone) of the Laxemar focused area, along with the topographic depression coinciding with ZSMEW0007A.

By plotting the total pressure (residual pressure + hydrostatic pressure, See Equation 7-4) on the surface of the model in Figure 8-7, areas of predicted recharge and discharge can be identified. Total pressure scales in proportion to the elevation of the watertable relative to ground surface. Hence, positive values of total pressure indicate discharge areas (shown in dark blue), whereas negative values indicate the distance (divide by $9.8 \cdot 10^3$ to convert pressure to a distance) to the watertable, and so a total pressure of $-1.0 \cdot 10^5$ Pa indicates that the watertable is 10 m below ground surface. The predicted discharge areas coincide well with the surface waterbodies shown from GIS data. These figures also demonstrate that there are many potential discharge areas, at least for shallow groundwater, within the Laxemar local model area. Another way of visualising the recharge/discharge pattern is to shown the vertical velocity as in Figure 8-8. This shows that the full available recharge is applied over majority of recharge areas, and confirms the discharge areas suggested by Figure 8-7.

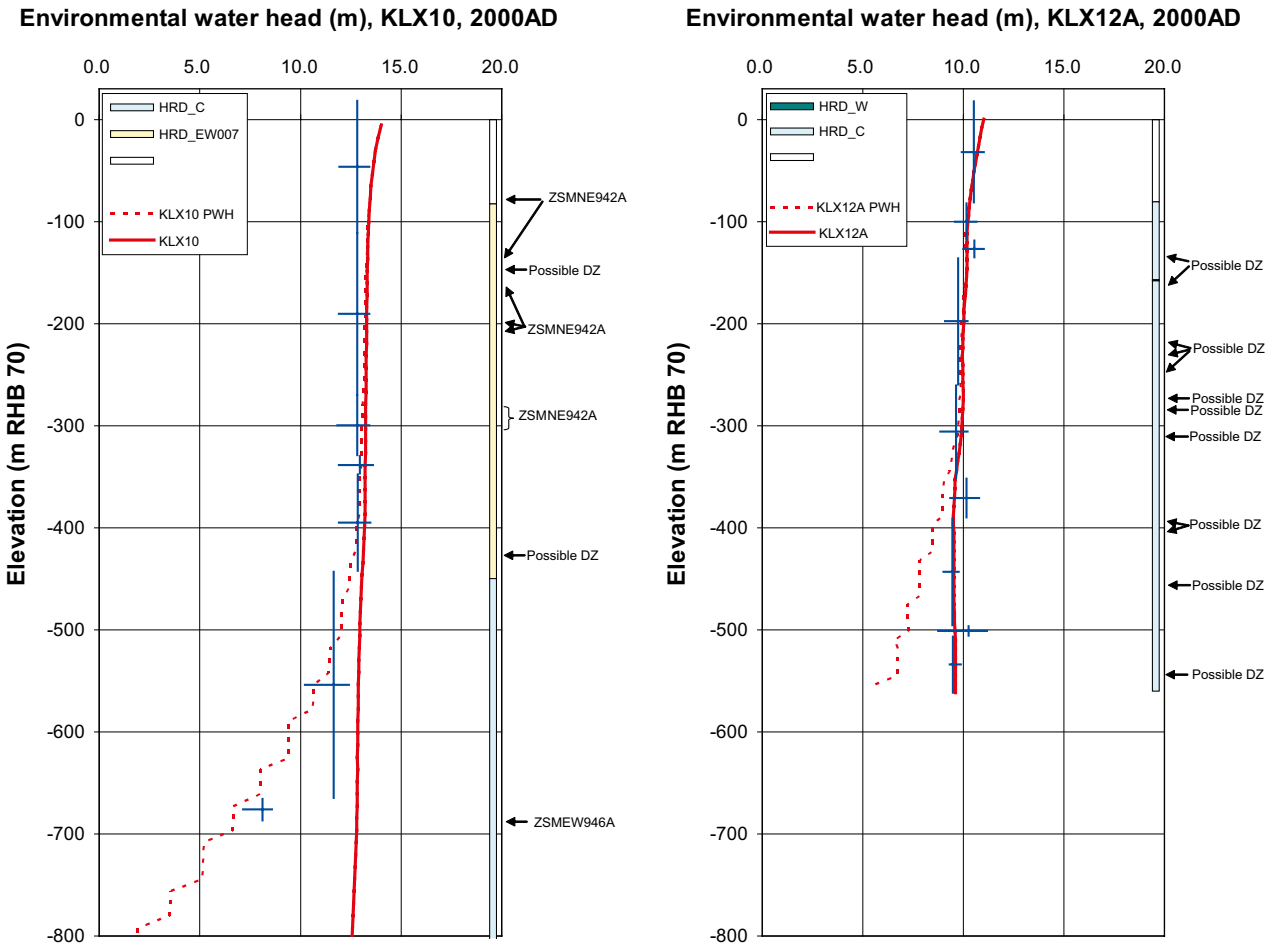

Figure 8-4. *Examples of modelled environmental-water head (solid red line) and point-water head (dotted red line) in KLX10 and KLX12A in HRD_C for the base case compared with environmental-water heads (blue crossed lines, centre showing midpoint of the section, vertical line showing the extent of the section and horizontal line showing the temporal variation of the measured head) calculated from measured point-water head data in sections along the borehole. At the right hand side, the prevailing hydraulic rock domains are shown as coloured bars along the borehole. Detected deformation zones are indicated at the intersection depth in the borehole.*

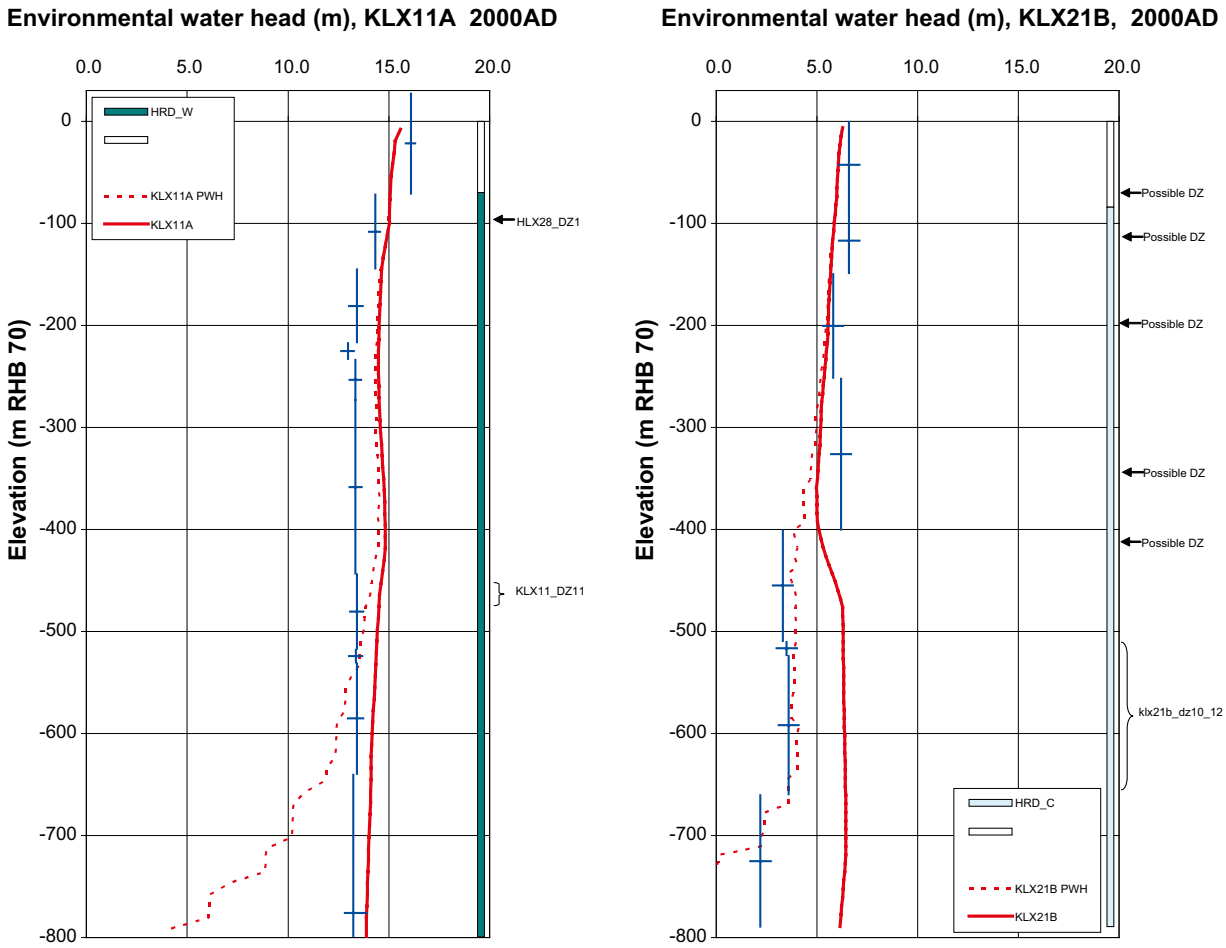

Figure 8-5. *Examples of modelled environmental-water head (solid red line) and point-water head (dotted red line) in KLX11A and KLX21B in HRD_W for the base case compared with environmental-water heads (blue crossed lines, centre showing midpoint of the section, vertical line showing the extent of the section and horizontal line showing the temporal variation of the measured head) calculated from measured point-water head data in sections along the borehole. At the right hand side, the prevailing hydraulic rock domains are shown as coloured bars along the borehole. Detected deformation zones are indicated at the intersection depth in the borehole.*

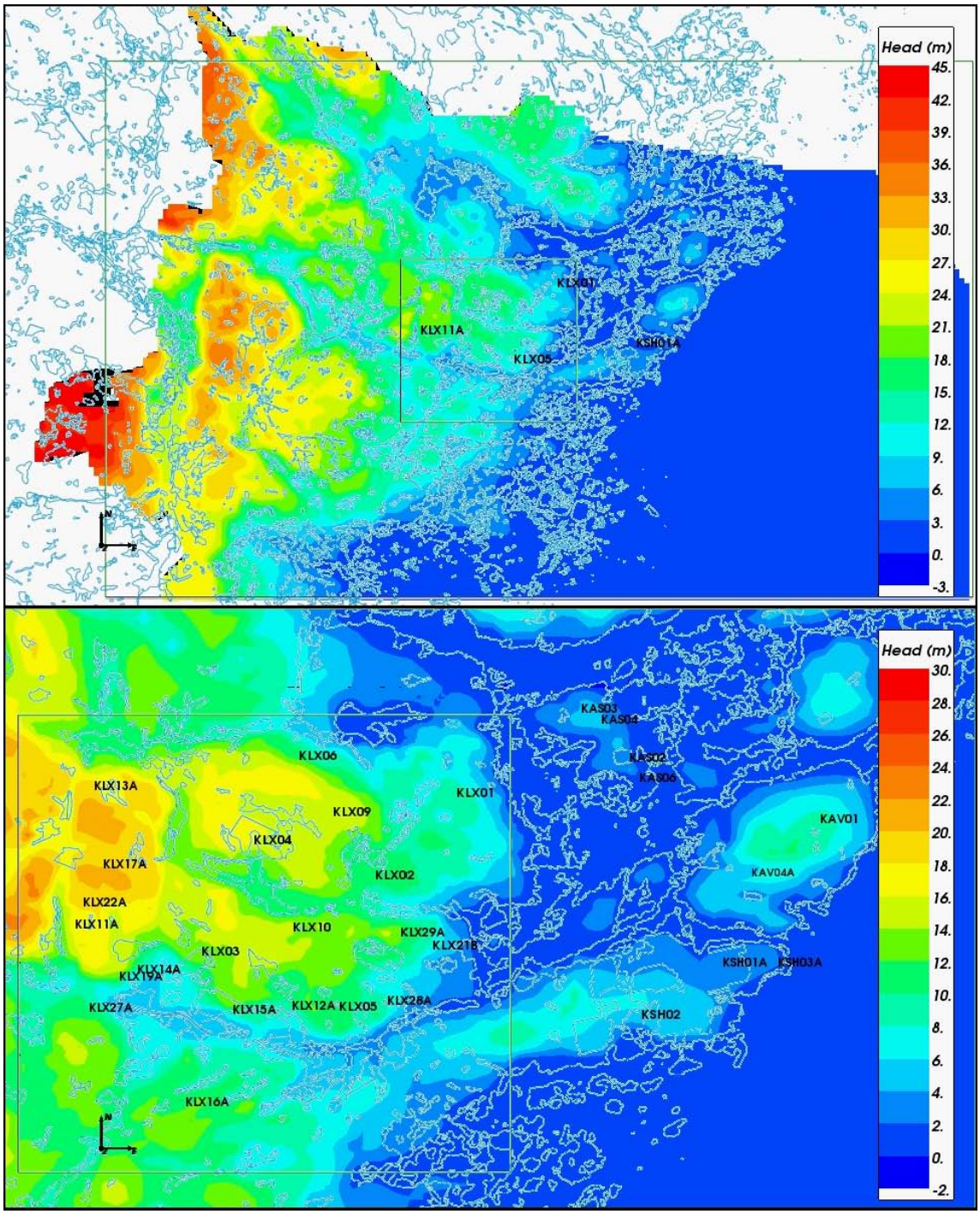

Figure 8-6. *Pointwater head distribution on the top surface of the base case model on the regional scale (top) and in the Laxemar local model area (bottom). The outlines of surface waterbodies (including shoreline) and local model area (square) are superimposed.*

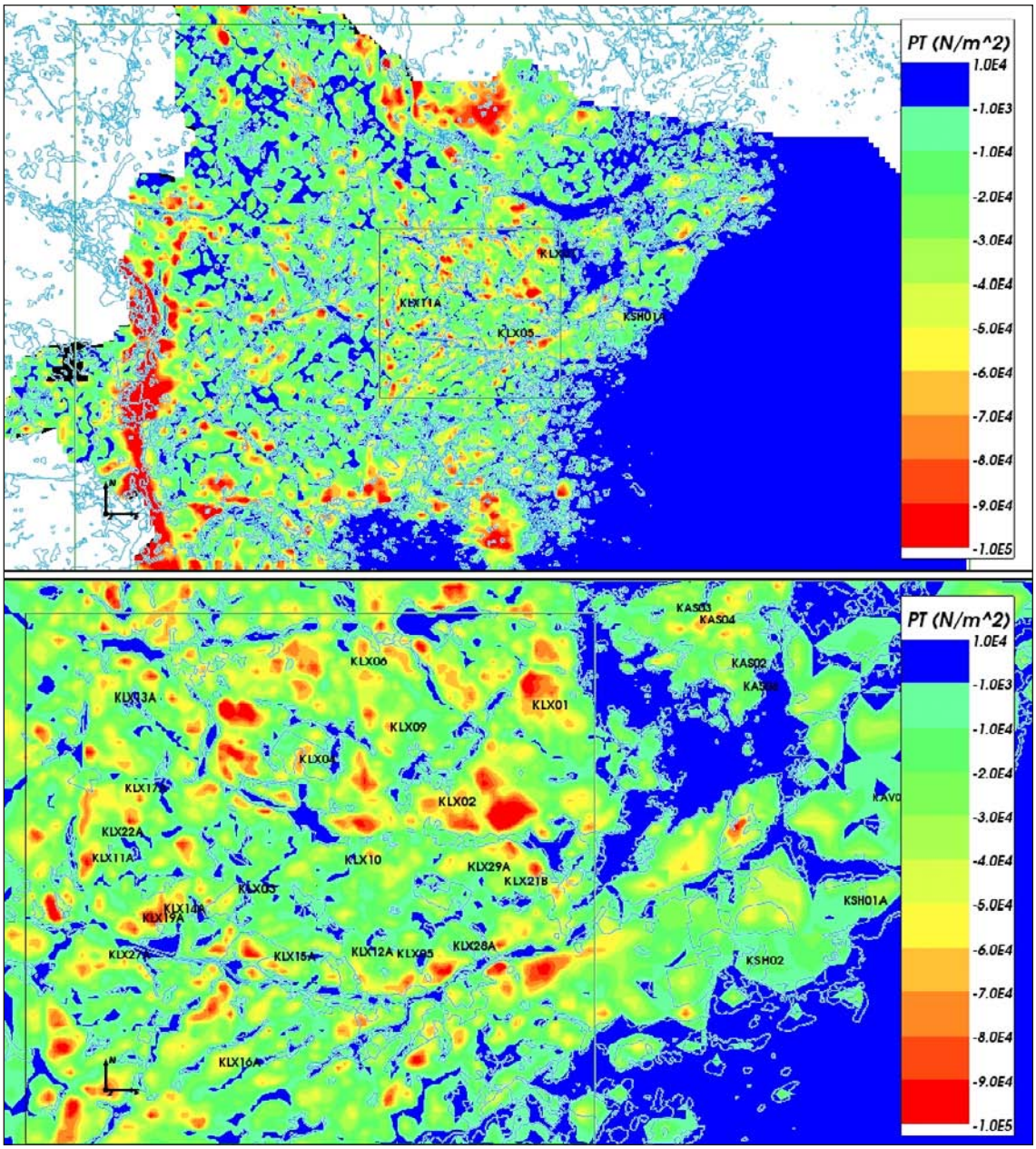

Figure 8-7. *Total pressure (Pa) distribution on the top surface of the base case model on the regional scale (top) and in the Laxemar local model area (bottom) to show the distribution of recharge (red to green) and discharge (dark blue). The outlines of surface waterbodies (including shoreline) and Laxemar local model area (square) are superimposed.*

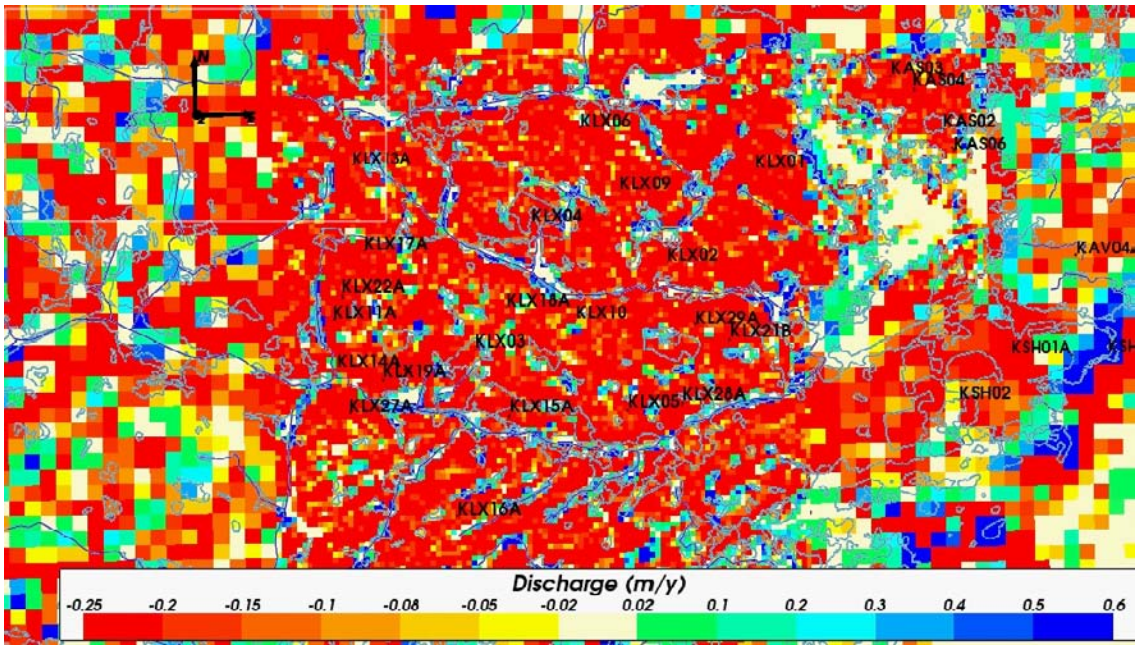

Figure 8-8. *The distribution of upward vertical Darcy velocity, recharge, on the top surface of the base case model in the Laxemar local model area to show the distribution of recharge (red to yellow) and discharge (green to blue). The outlines of surface waterbodies (including shoreline) and core-drilled borehole locations are superimposed.*

Table 8-1 is included to give an indication of the distribution of flows, or water balance, at different depths and in different components of the hydraulic system. The first row is in the HSD showing that over most of the area there is full recharge ~180 mm/year and this gets largely converted to horizontal flows through the soil layers, which have an average thickness of around 4 m. The recharge to the upper bedrock is about 46 mm/year, and discharge nearly balances recharge at this depth. By repository depth at –500 m, recharge is about 0.3 mm/year, and the geometric mean Darcy velocity is about four times higher in HCD than HRD.

Table 8-1. Summary of arithmetic average discharge and recharge through a series of depth-distributed surfaces corresponding to the ground surface topography in the Laxemar 1.2 local model area, cf Figure 1-1, as extracted from the SDM-Site Laxemar *base case model* groundwater flow simulation. The geometric means of the magnitude of the Darcy velocity vector for points in each plane are given for the entire bedrock, outside of the deformation zones, and inside the deformation zones.

Vertical depth below ground surface [m]	Average discharge in discharge areas [m/year]	Average recharge in recharge areas [m/year]	Geometric mean Darcy velocity [m/year]	Geometric mean Darcy velocity outside deformation zones [m/year]	Geometric mean Darcy velocity in deformation zones [m/year]
–1	$4.96 \cdot 10^{-2}$	$1.86 \cdot 10^{-1}$	$1.3 \cdot 10^{0}$	$9.7 \cdot 10^{-1}$	N/A
–20	$4.38 \cdot 10^{-2}$	$4.57 \cdot 10^{-2}$	$6.6 \cdot 10^{-2}$	$5.8 \cdot 10^{-2}$	$8.8 \cdot 10^{-2}$
–100	$2.21 \cdot 10^{-2}$	$2.35 \cdot 10^{-2}$	$4.5 \cdot 10^{-2}$	$3.7 \cdot 10^{-2}$	$6.2 \cdot 10^{-2}$
–180	$6.93 \cdot 10^{-3}$	$6.52 \cdot 10^{-3}$	$6.1 \cdot 10^{-3}$	$4.2 \cdot 10^{-3}$	$1.2 \cdot 10^{-2}$
–340	$1.82 \cdot 10^{-3}$	$1.95 \cdot 10^{-3}$	$1.7 \cdot 10^{-3}$	$1.0 \cdot 10^{-3}$	$4.0 \cdot 10^{-3}$
–500	$3.21 \cdot 10^{-4}$	$3.15 \cdot 10^{-4}$	$2.9 \cdot 10^{-4}$	$1.6 \cdot 10^{-4}$	$6.4 \cdot 10^{-4}$
–660	$8.36 \cdot 10^{-5}$	$9.37 \cdot 10^{-5}$	$5.5 \cdot 10^{-5}$	$2.6 \cdot 10^{-5}$	$1.5 \cdot 10^{-4}$
–780	$4.10 \cdot 10^{-5}$	$4.02 \cdot 10^{-5}$	$1.4 \cdot 10^{-5}$	$8.5 \cdot 10^{-6}$	$2.8 \cdot 10^{-5}$

8.1.4 Illustration of sensitivities considered during calibration

The interpretation of both HCD and HRD indicated significant spatial heterogeneity. Therefore, one important factor to be quantified in the simulations is how sensitive is the calibration to the effects of spatial variability, which can be estimated by generating several realisations of the hydrogeological model including lateral heterogeneity in the property assignment to HCD. For the HRD, 10 realisations of the hydrogeological DFN model were generated and each upscaled to give an ECPM model. Each of these was combined with one of 10 stochastic realisations of the HCD model with transmissivity sampled on a 200 m triangulated grid of each HCD (with local conditioning to measured transmissivities), see Section 7.4. A standard deviation of Log(transmissivity) equal to 1.4 was used in the HCD based on data (see Section 4.1.2). Since this gives large variability over nearly 6 orders of magnitude within the same deformation zone and depth zone, 10 realisations with standard deviation 0.7 were also run to give a comparison. The same set of realisations was used to predict both environmental heads and palaeohydrogeology, as presented in Chapter 9.

Figure 8-9 and Figure 8-10 illustrate the variability in predicted pointwater heads for the percussion drilled holes and the groundwater monitoring wells by plotting the minimum, mean, and maximum modelled pointwater head for the variant with a standard deviation of 1.4 in Log(T) in HCD. This indicates which borehole measurements are most subject to spatial heterogeneity, e.g. percussion boreholes HLX06 and HLX36. The span of simulated pointwater heads and measured variations overlap for many of the boreholes. Some that do not overlap, such as HLX02 and HSH02 are indications that these boreholes are affected by pumping at Äspö HRL and (possibly) Clab, respectively. The variability in the near-surface pointwater heads in SSM holes appears to be small. SSM holes are biased towards lower elevations, i.e. discharge areas, while HLX boreholes are typically in more elevated areas. Groundwater levels in recharge areas are generally more sensitive to variations in recharge and hydraulic properties; whereas levels in discharge areas tend to follow topography, and hence a lower sensitivity in SSM holes is expected.

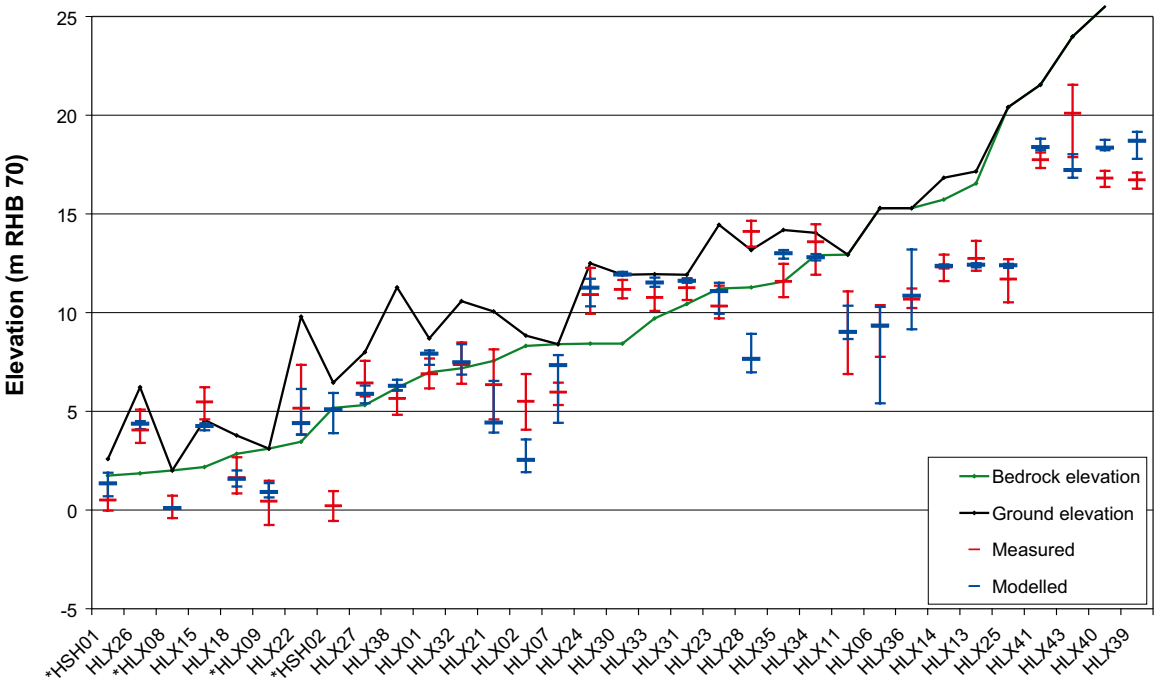

Figure 8-9. *Comparison of measured heads in percussion drilled boreholes (HLX) for 10 stochastic realisations of HCD and HRD. For the model, the minimum, maximum and median value in the bedrock is shown in blue. The field data are plotted as mean point water heads in the bedrock with error bars to show the range of values at different measurement times. Boreholes marked by a * are outside the local model area.*

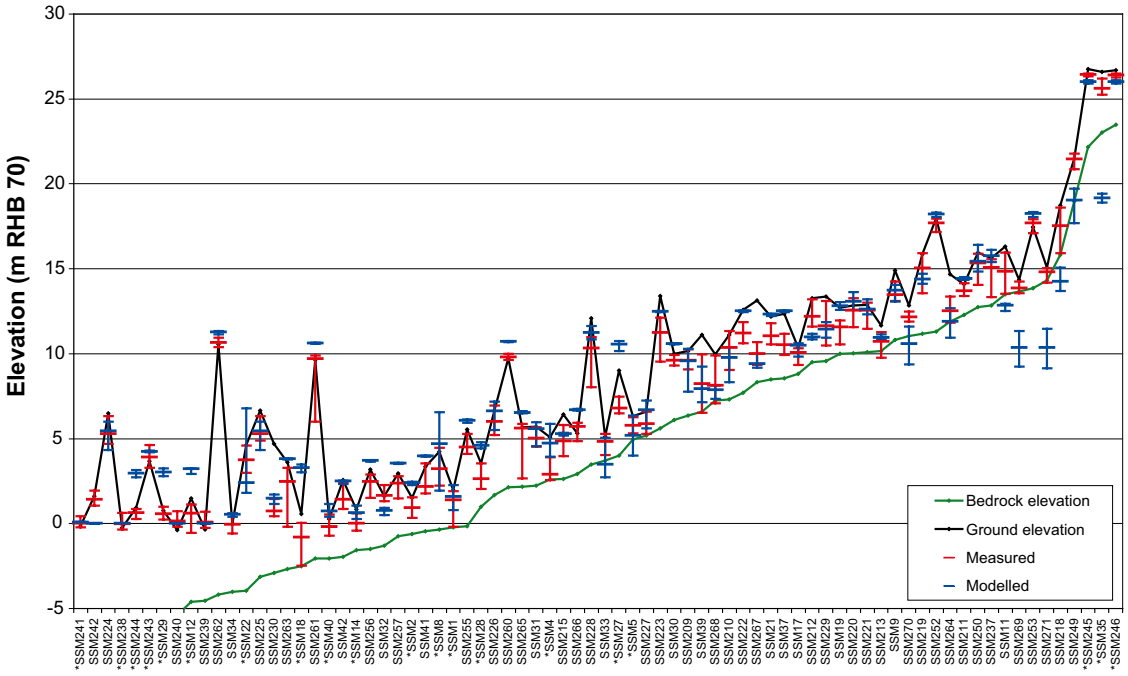

Figure 8-10. *Comparison of measured heads in groundwater monitoring wells (SSM) for 10 stochastic realisations of HCD and HRD. For the model, the minimum, maximum and median value in the bedrock is shown in blue. The field data are plotted as mean point water heads in the soil with error bars to show the range of measurements at different times. Boreholes marked by a * are outside the Laxemar local model area.*

Figure 8-11 and Figure 8-12 show examples of the variability in the profiles of environmental head in core drilled boreholes due to spatial heterogeneity. The variations are generally 1–2 m on either side of the mean value and span nearly all measured data, indicating that the deviations of the measurements from the *base case model* predictions can be explained by the combined spatial heterogeneity of the HCD and HRD. As mentioned in Section 8.1.2, a limited number of adjustments of model parameters were made in order to obtain a reasonable match to the head data. Two variants are used here to illustrate why such changes were considered necessary. The first is based on the original prescription for HCD transmissivities defined in /Rhén et al. 2008/. This generally over-predicted heads in the boreholes, see Figure 8-13 for KLX04 and KLX10, suggesting the transmissivity of ZSMEW007A should be increased to reduce heads. This lead to some of the HCD property re-assignments recommended in Table 7-3. The average difference between modelled and measured environmental heads in KLX boreholes for this variant was 0.74 m, with a mean absolute difference of 2.29 m. In the HLX boreholes the mean difference was 0.79 m, with mean absolute difference of 1.55 m. Another important ingredient in the HCD property description was strong anisotropy in the dolerite dykes (associated with ZSMNS001C and ZSMNS059A, KLX19DZ5-8) as well as ZSMEW002A and ZSMNW042A-west that are thought to have some fault gouge (see Section 4.1.2) creating a hydraulic barrier effect in the core of the zone. Hence, as a second illustration, these HCD were made isotropic, and the resulting environmental heads are shown in Figure 8-14. The result is that the simulated sharp drop in head near ZSMEW002A shown in KLX06 Figure 8-3 disappears, and environmental head increases in the lower part of KLX19A rather than having a sharp drop across the dolerite dyke in DZ5-8. The effects of the dolerite dykes ZSMNS001A-C and ZSMNS059A, KLX19DZ5-8 in HRD_W on pointwater head contours and Darcy velocity for a horizontal slice at –120 m are exemplified in Figure 8-15. Head contours tend to run mainly perpendicular to the dolerite dykes and flow is forced to run parallel to the HCD within and around them. It results in large gradients in groundwater head toward the Laxemarån river valley in the south, which is confirmed by data in HLX28 and KLX19A, for example.

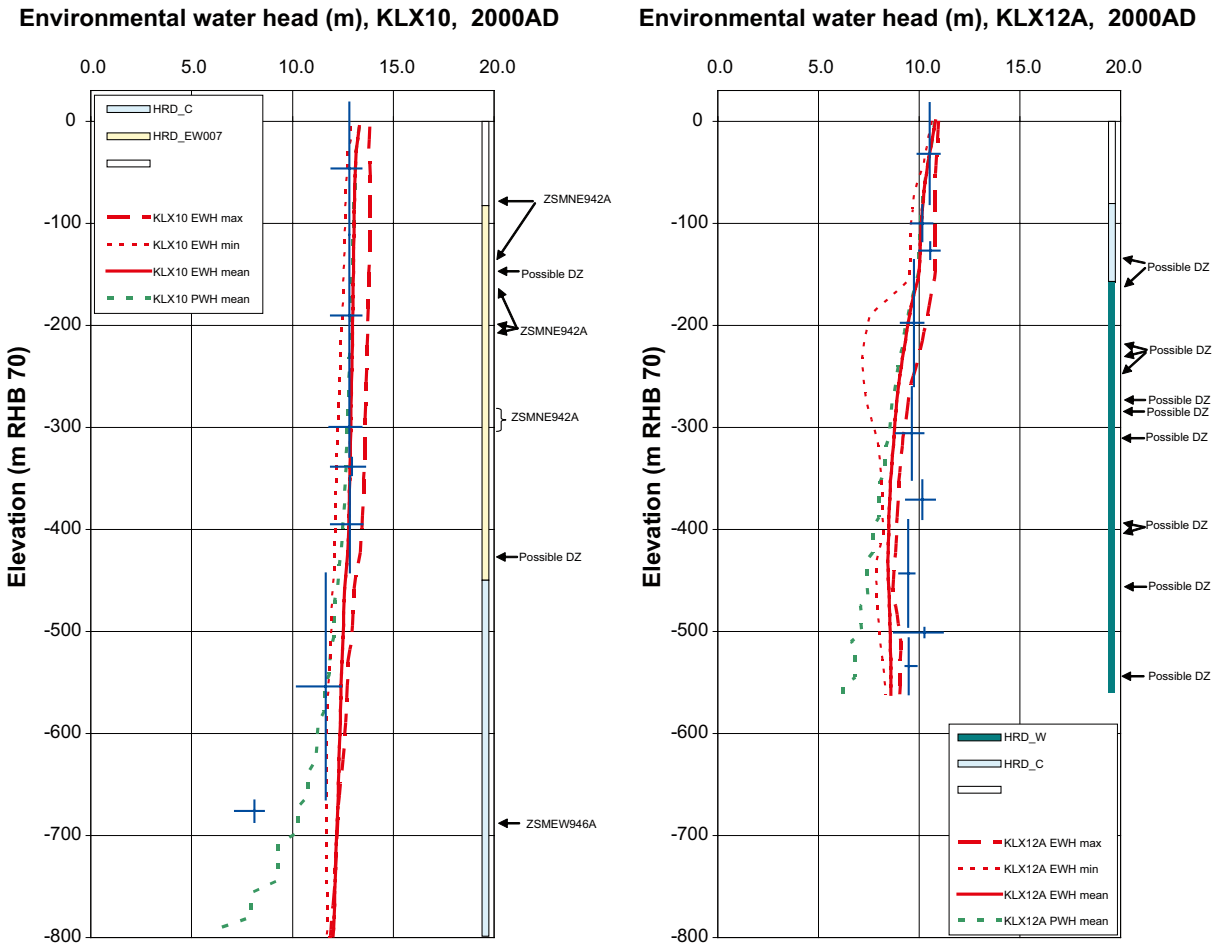

Figure 8-11. *Examples of stochastic variability of modelled environmental-water head for 10 realisations of HCD and HRD (mean: solid red line; min:dotted red line; max:dashed red line) and point-water head (mean: dotted green line) in KLX10 and KLX12A in HRD_C compared with environmental-water heads (blue crossed lines, centre showing midpoint of the section, vertical line showing the extent of the section and horizontal line showing the temporal variation of the measured head) calculated from measured point-water head data in sections along the borehole. At the right hand side, the prevailing hydraulic rock domains are shown as coloured bars along the borehole. Detected deformation zones are indicated at the intersection depth in the borehole.*

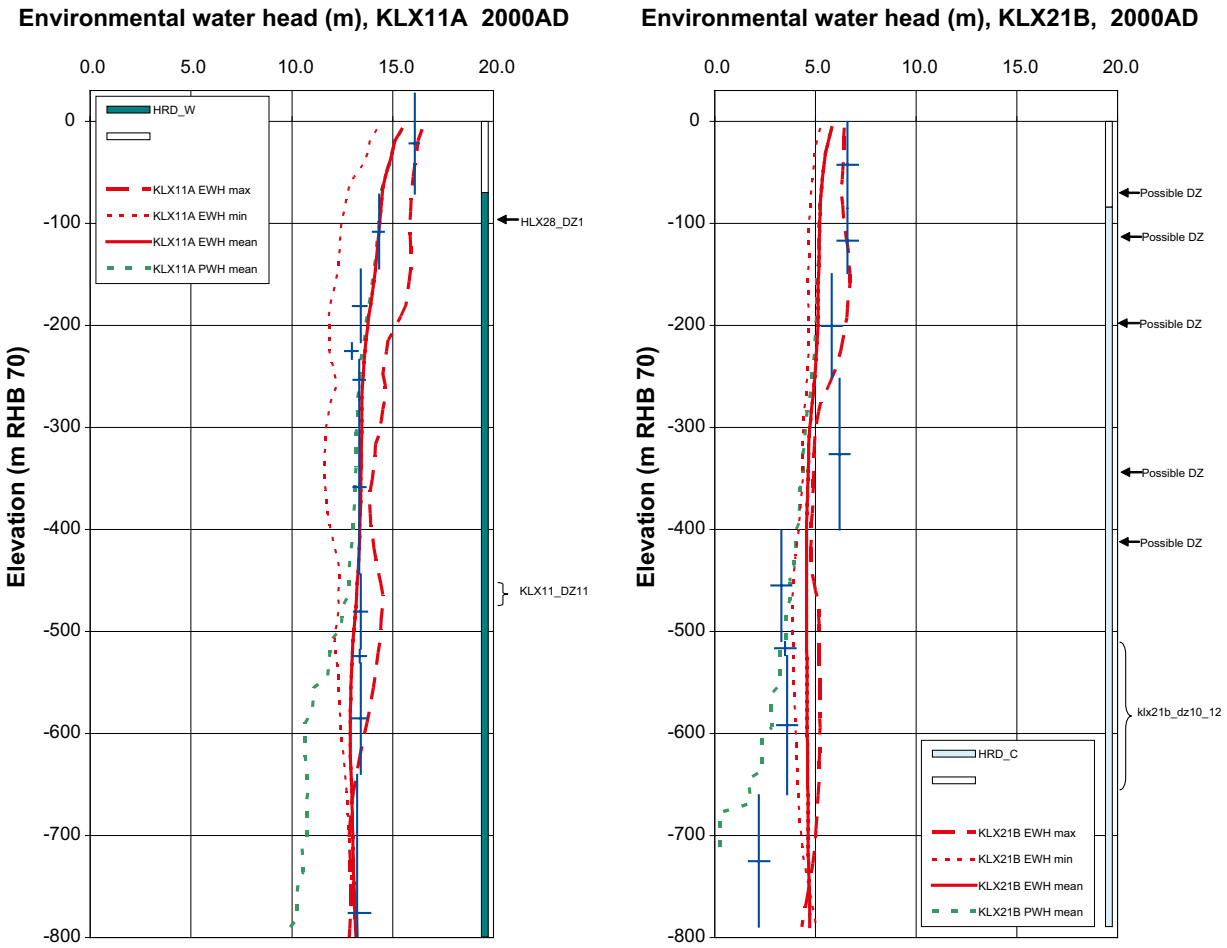

Figure 8-12. *Examples of stochastic variability of modelled environmental-water head for 10 realisations of HCD and HRD (mean: solid red line; min:dotted red line; max:dashed red line) and point-water head (mean: dotted green line) in KLX11A in HRD W and KLX21B in HRD_C compared with environmental-water heads (blue crossed lines, centre showing midpoint of the section, vertical line showing the extent of the section and horizontal line showing the temporal variation of the measured head) calculated from measured point-water head data in sections along the borehole. At the right hand side, the prevailing hydraulic rock domains are shown as coloured bars along the borehole. Detected deformation zones are indicated at the intersection depth in the borehole.*

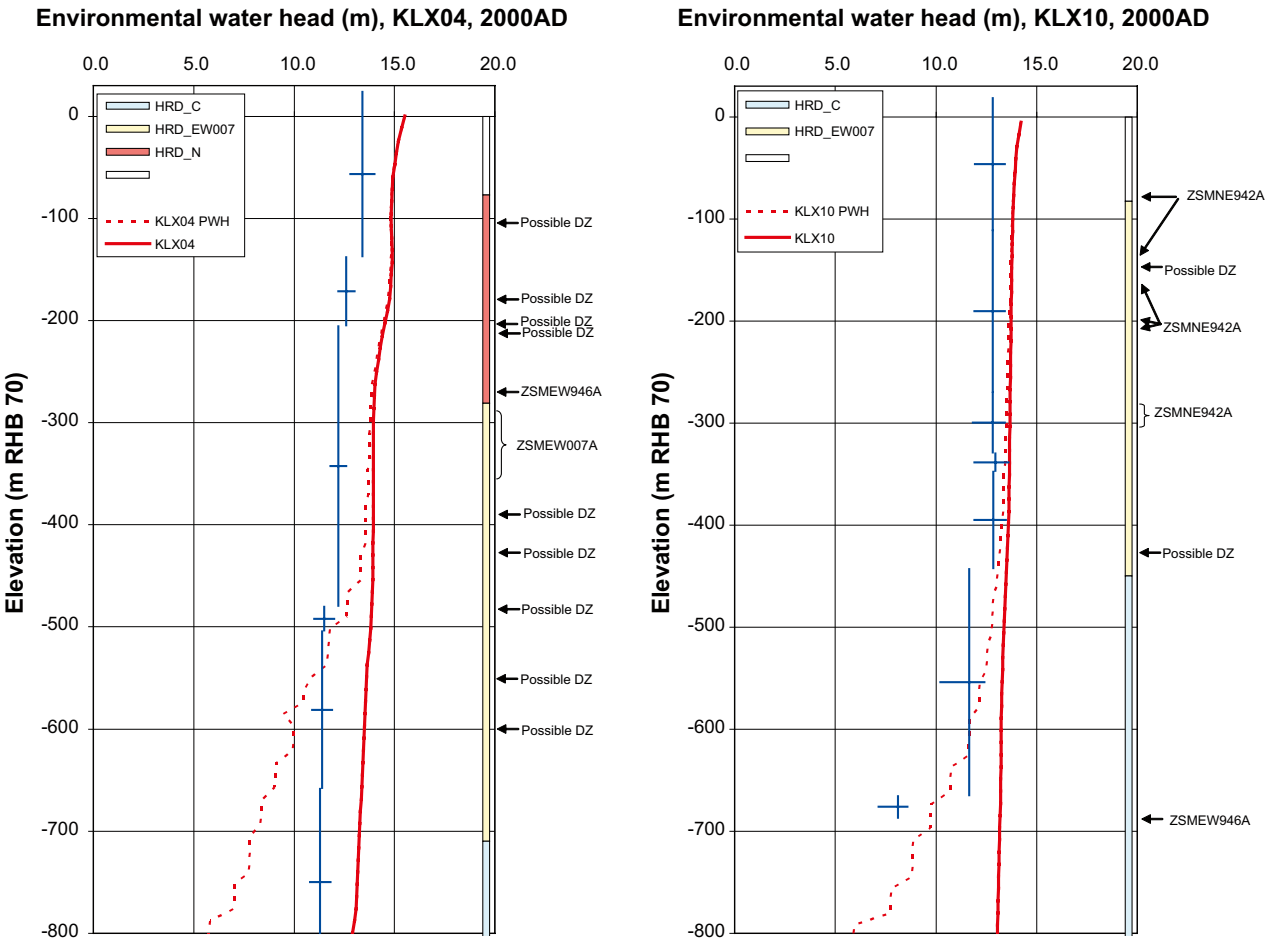

Figure 8-13. *Examples of modelled environmental-water head (solid red line) and point-water head (dotted red line) in KLX04 and KLX10 for the initial HCD model compared with environmental-water heads (blue crossed lines, centre showing midpoint of the section, vertical line showing the extent of the section and horizontal line showing the temporal variation of the measured head) calculated from measured point-water head data in sections along the borehole. At the right hand side, the prevailing hydraulic rock domains are shown as coloured bars along the borehole. Detected deformation zones are indicated at the intersection depth in the borehole.*

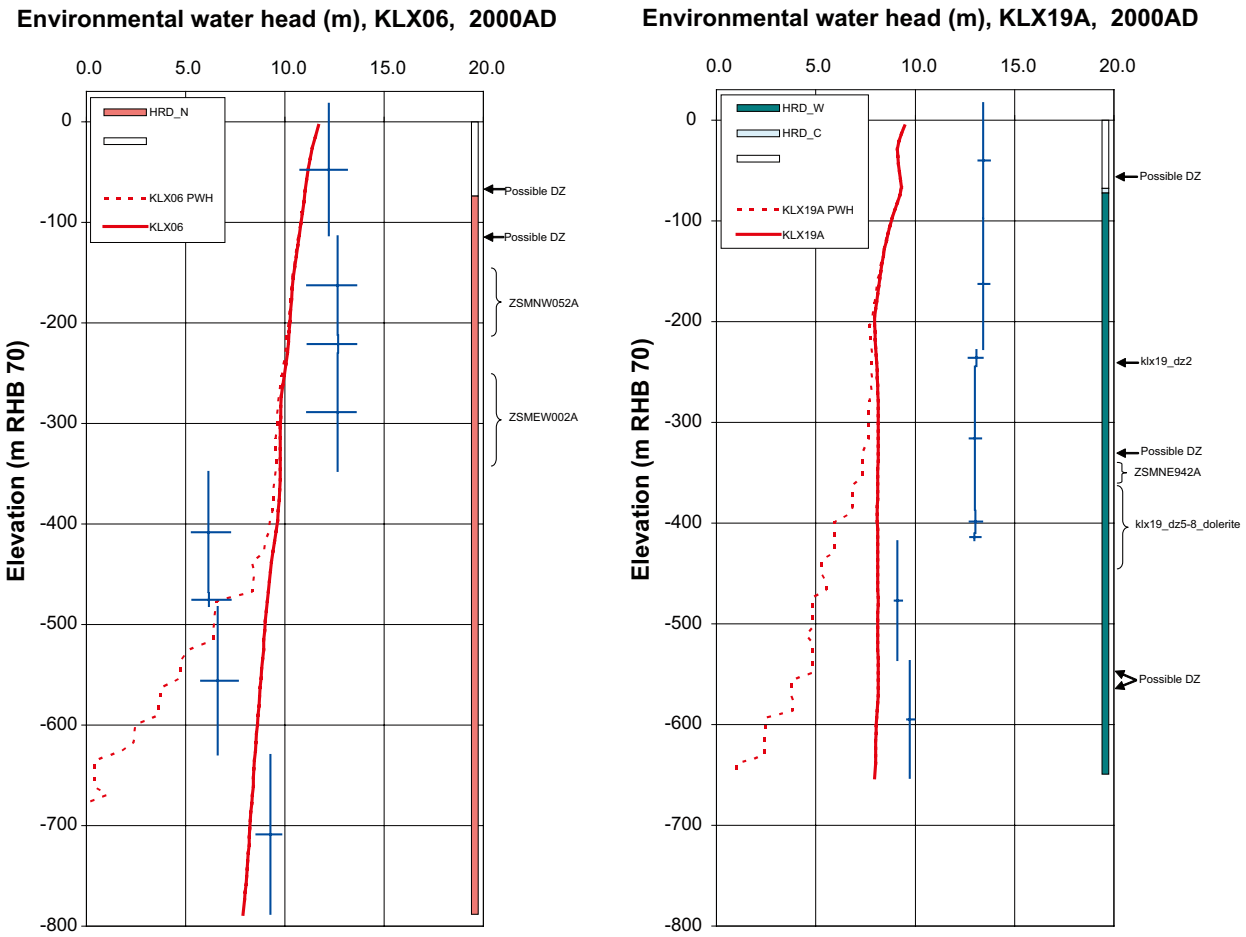

Figure 8-14. *Examples of modelled environmental-water head (solid red line) and point-water head (dotted red line) in KLX06 and KLX19A for the model without any anisotropy in HCD compared with measurements (blue crossed lines, centre showing midpoint of the section, vertical line showing the extent of the section and horizontal line showing the temporal variation of the measured head) calculated from measured point-water head data in sections along the borehole. At the right hand side, the prevailing hydraulic rock domains are shown as coloured bars along the borehole. Detected deformation zones are indicated at the intersection depth in the borehole.*

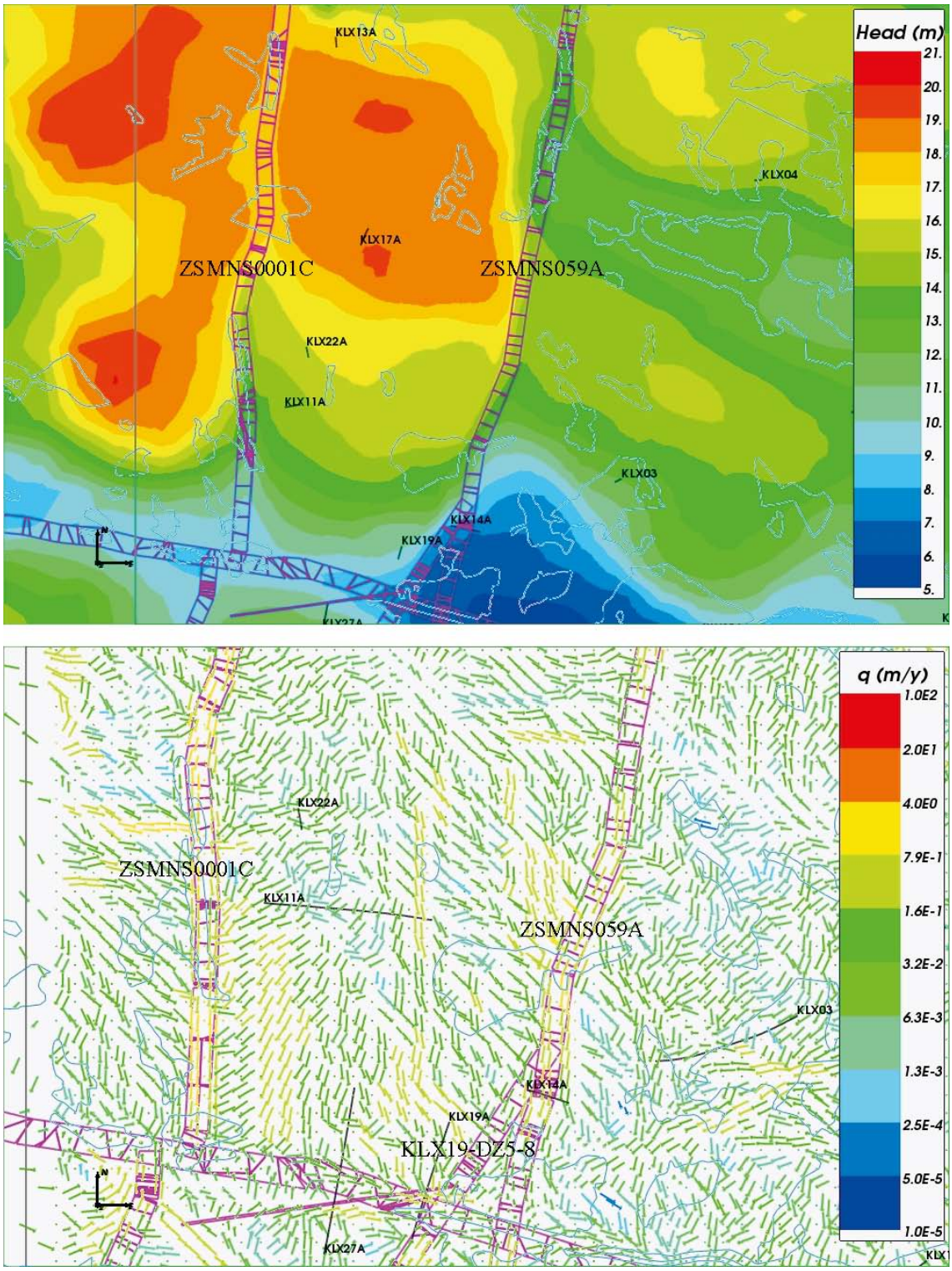

Figure 8-15. *Effects of dyke structures in HRD_W. Top: head contours at –120 m bending around ZSMNS001C, ZSMN059A. Bottom: velocity arrows at –120 m parallel to the dolerite dykes in ZSMNS001C, ZSMNS059A, and KLX19-DZ5-8.*

Other main calibration variants and the resulting objective functions for comparing simulated and measured heads in the three different types of boreholes are summarised in Table 8-2. All variants in Table 8-2 have all the same parameters and settings apart from the changes specified in the left hand column. These first four variants are centred on the base case and have been constructed *a posteriori* to quantify how sensitive the overall head agreement is to the changes made to HCD, HRD and HSD, respectively. Hence, the '*Initial uncalibrated HCD + HRD*' variant is identical to the base case apart from properties for the HCD and HRD were reverted to those used prior to any calibration, i.e. as recommended in /Rhén et al. 2008/. The last two variants represent increases in the hydraulic conductivity of the HRD above –150 m by factors 3 or 10 that were considered as possibilities for further improving the calibration. A factor 10 is more than what is supported by the limited hydraulic data available for the superficial bedrock, but it was thought useful as a trial in understanding how hydraulic contrasts between the shallow and deep bedrock affect the calibration. This confirms that using a general increase of a factor of around 3 in the top 150 m of bedrock is about optimal for improving the head match. The sensitivities to the other variants were low apart from the changes made in calibrating the HCD. The changes made to the HRD properties, reducing hydraulic conductivity by a factor 1/3 below –150 m, made very little difference to environmental and pointwater heads, as did the changes to the HSD in calibrating on the drawdown due to the Äspö HRL. The only other significant sensitivity of the environmental and pointwater heads was to the calibration of the HCD properties.

8.2 Äspö HRL drawdown

The calibration of the flow model, against the measured drawdowns in percussion-drilled monitoring boreholes surrounding the Äspö HRL and the flow rates into the tunnels and shafts is largely a repeat of one of pre-modelling exercises reported in /Hartley et al. 2007/. There it was concluded that the measured drawdowns could be reproduced provided the Quaternary deposits in the bays around Äspö were of gyttja clay type so as to reduce recharge from the sea bed since this would otherwise restrict the zone of influence of pumping on the Laxemar-Simpevarp mainland. Another significant finding was that the operation of the Äspö HRL facility has had little effect on the natural hydrochemistry measured in the Laxemar subarea, and hence it was not necessary to include pumping at the Äspö HRL in the palaeohydrogeology simulations reported in Chapter 9.

The methodology for these simulations was to import the reference water and pressure distributions from the palaeohydrogeology simulations predicted at 1980, and then restart the simulations with a 1 year time-step and a time dependent pump-rate specified in the HRL (distributed in the finite-elements along the HRL as a function of hydraulic conductivity in the orthogonal to the tunnels).

Table 8-2. Comparison of objective functions used to measure the quality of match between the simulated mean environmental head, h_m, in the model variants and the observed mean environmental head, h_o, (KLX holes) and pointwater heads (HLX and SSM holes).

Variant	KLX holes		HLX holes		SSM holes	
Measured mean temporal range (h_{max}–h_{min}) (m)	1.21		1.89		1.57	
	Mean (h_m–h_o) (m)	Mean $\lvert h_m–h_o \rvert$ (m)	Mean (h_m–h_o) (m)	Mean $\lvert h_m–h_o \rvert$ (m)	Mean (h_m–h_o) (m)	Mean $\lvert h_m–h_o \rvert$ (m)
Base case	0.41	2.04	0.32	1.17	0.35	0.98
Initial uncalibrated HCD + HRD	0.75	2.27	0.76	1.52	0.46	0.99
Initial uncalibrated HCD	0.74	2.29	0.79	1.55	0.84	1.26
Initial uncalibrated HRD	0.42	2.01	0.29	1.15	0.33	0.98
Initial uncalibrated HSD	0.46	2.05	0.33	1.17	0.38	0.99
HRD variant with higher K_h (×3) above –150 m	0.08	1.90	0.22	1.10	0.20	1.01
HRD variant with higher K_h (×10) above –150 m	–0.42	1.85	0.03	1.02	–0.14	1.11

Details of the numerical implementation of the extraction boundary condition are given in /Hartley et al. 2007/. The SDM-Site Laxemar model of the HSD has largely gyttja clay type sediments in the bays around Äspö, but there are a few gaps. It was found necessary to modify all the remaining HSD on the seabed to use gyttja clay type in the bays around the Äspö HRL to confine the upper bedrock for sea water infiltration. This was done in a square of side 2 km centred on the bay south of Äspö. Possibly this is just a consequence of using a coarser grid, 40 m, rather than the 20 m grid used to define the Quaternary deposits model. A vertical hydraulic conductivity of $5 \cdot 10^{-9}$ m/s for gyttja clay was chosen for the *base case model*. A comparison of the simulated and measured drawdowns in 1996 AD is presented in Table 8-4 for the base case and sensitivity variants. The comparison is broadly consistent in that small drawdowns are predicted in the boreholes where no response was seen in the measurements, and responses in the Laxemar local model area are predicted to occur at HLX08 and HLX09. The sensitivity study is discussed below. The effect of the Äspö HRL on head and groundwater velocities at 2004 AD is demonstrated on horizontal slices at –20 m and –450 m in Figure 8-16 through Figure 8-19. At depth the changes in Darcy velocity are highest in the HCD. At shallower depths effects on Darcy velocity only extend as far as HLX08 and HLX09 in the Laxemar local model area apart from the eastern end of HCD ZSMEW007A (see Figure 8-17).

In order to quantify sensitivities of the drawdowns, 6 variants were constructed as described in Table 8-3. The drawdown in the tunnel reported in Table 8-4 for the base case is very high, which is also the case for the shaft. This would suggest the hydraulic conductivity is too low in the rock surrounding the HRL, which belongs to HRD_A2. Hence, the first variant (V1) considered increasing the hydraulic conductivity in HRD_A2 by restoring it to the uncalibrated values (only for this rock domain) below –150 m, and increasing the horizontal conductivity by a factor 3 above –150 m. This gave a reasonable agreement for the tunnel and shafts and improved the match at some HAV and HMJ01 boreholes to the east of Äspö. Using uncalibrated HRD values for all the bedrock was considered in V2, which gave similar results, confirming that the drawdown is only sensitive to the properties of the immediate bedrock, HRD_A2.

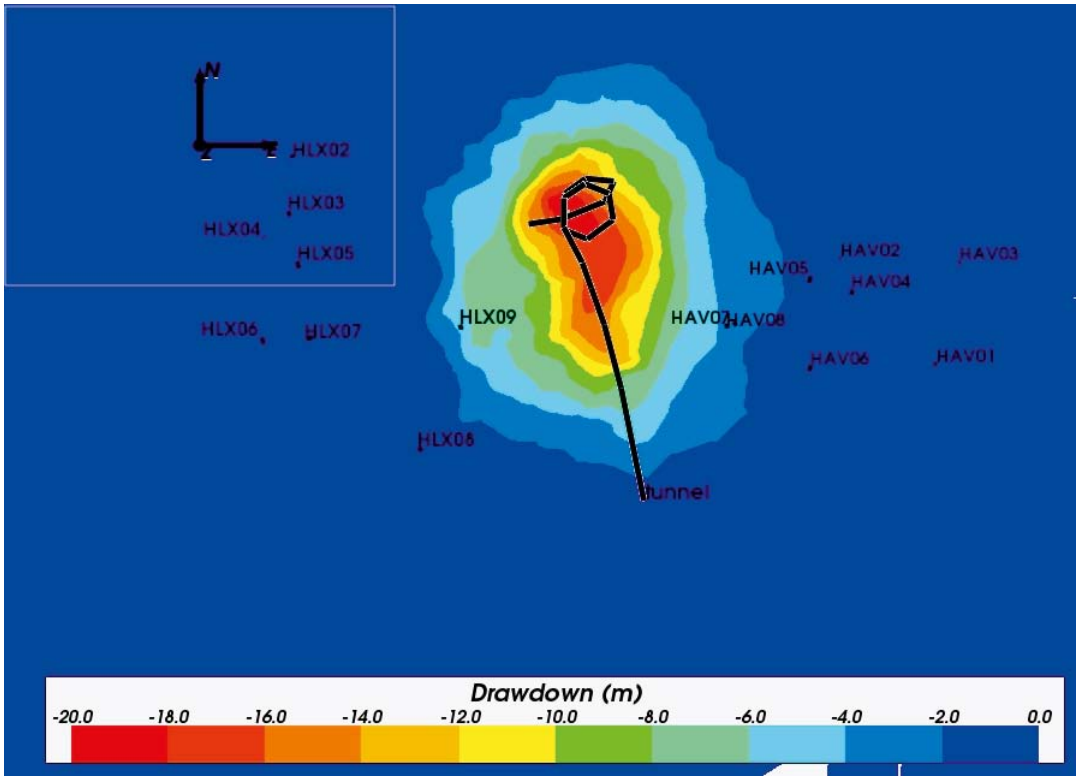

Figure 8-16. *The simulated drawdown resulting from groundwater extraction in the sp HRL for the base case model. The slice is shown for 2004 AD at –20 m elevation.*

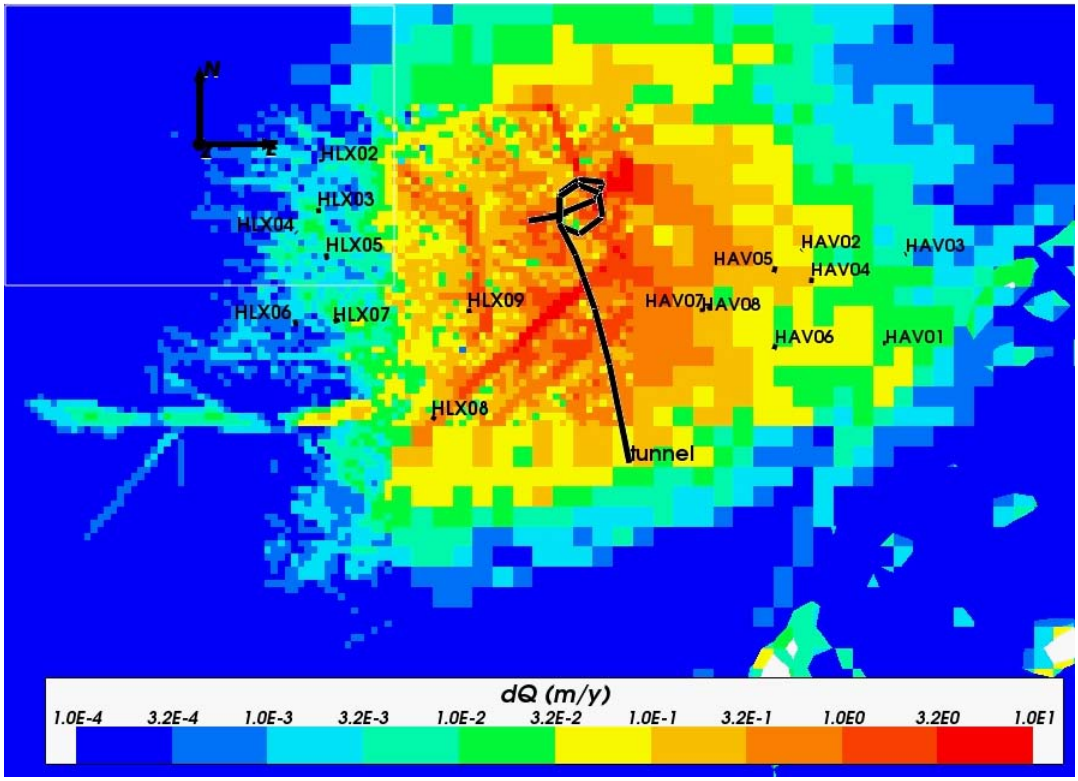

Figure 8-17. *The magnitude of difference in Darcy velocity between simulations with and without groundwater extraction in the Äspö HRL for the base case model. The slice is shown for 2004 AD at –20 m elevation.*

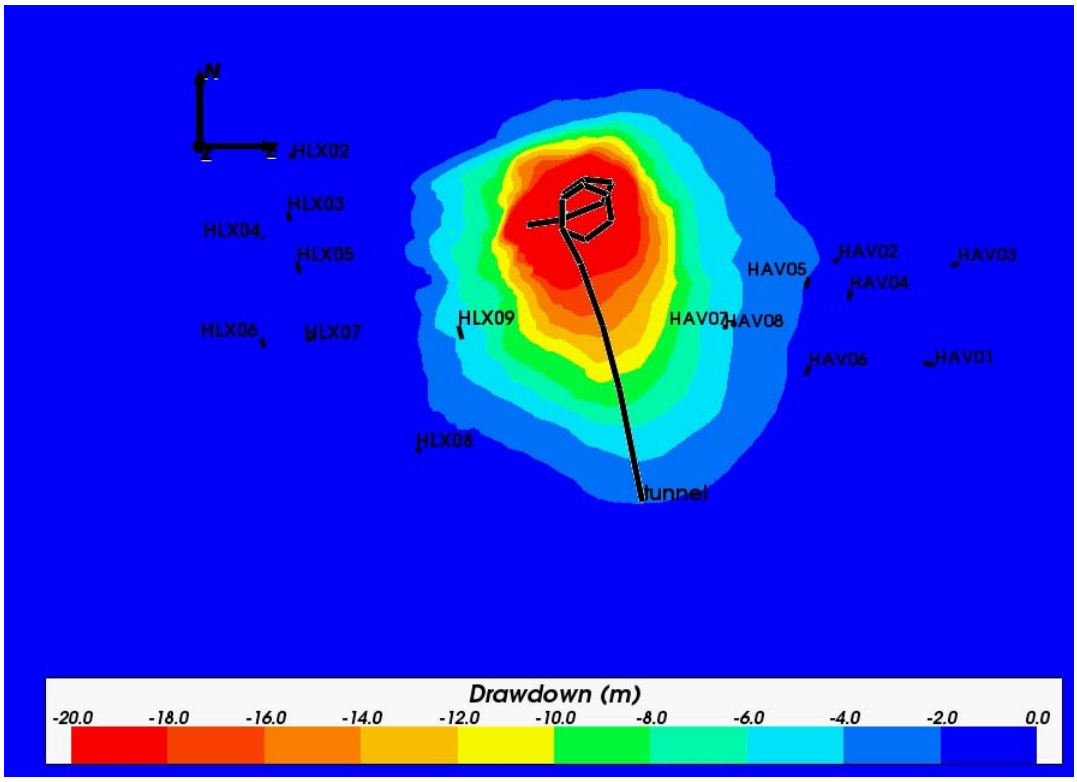

Figure 8-18. *The simulated drawdown resulting from groundwater extraction in the Äspö HRL for the base case model. The slice is shown for 2004 AD at –450 m elevation.*

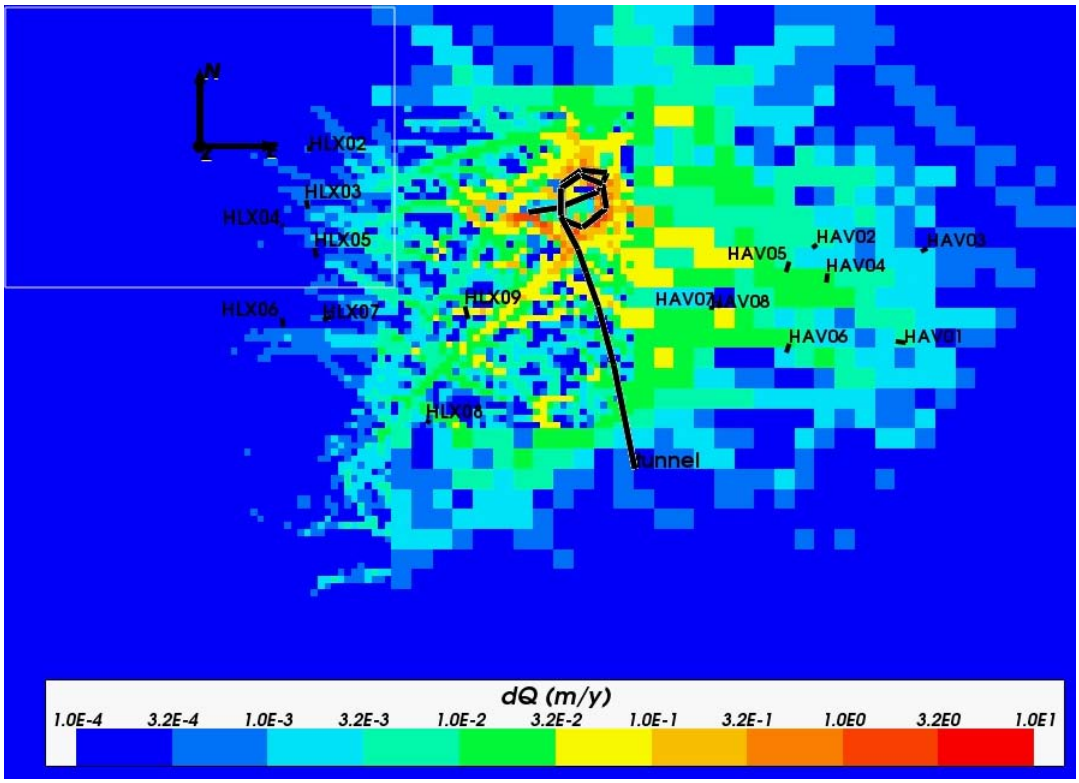

Figure 8-19. *The magnitude of difference in Darcy velocity between simulations with and without groundwater extraction in the Äspö HRL for the base case model. The slice is shown for 2004 AD at –450 m elevation.*

Given the significant improvement in the drawdown predicted in the tunnels and shaft, the remaining variants were centred on variant V1. Variant V3 reverted to the uncalibrated HCD model using values of transmissivities as recommended in /Rhén et al. 2008/. This gave similar results to variant V1 for the boreholes in the upper bedrock, although it did reduce the drawdowns at depth in the tunnels and shaft. Hence, it is concluded that the drawdowns in the percussion drilled holes are more sensitive to the hydraulic properties of the HRD than the HCD.

The last 3 variants all considered sensitivities to the hydraulic properties of the HSD. Variant V4 was introduced to demonstrate the effects of not modifying the soil type in the bays around Äspö to gyttja clay. The result is virtually no drawdown in any of the precussion drilled boreholes since in that case the recharge that supplies the inflow to the tunnel comes from the sea immediately above the tunnels rather than the surrounding islands and mainland where the boreholes are situated. Variant V5 uses the same horizontal hydraulic conductivities in the HSD as in the base case, but increases the vertical hydraulic conductivity of all HSD such that they are isotropic. This reduced the drawdown in the precussion drilled boreholes to roughly half of that in variant V1, on which V5 is centred. Variant V6 considered the effects of reducing the vertical hydraulic conductivity of gyttja clay to 10^{-9} m/s, a reduction of a multiplication factor of 1/2. This increased drawdowns to most percussion drilled boreholes by about a factor of 3. Hence, the simulated drawdowns of the percussion drilled boreholes are most sensitive to the properties of the HSD. In fact, the variants explored for the HSD give results that span the observations, and hence one could imagine obtaining a perfect match to the observations by better representation of HSD model in terms of heterogeneity and spatial discretisation.

Table 8-3. A description of the sensitivity variants considered in the simulations of drawdowns resulting from the operation of the Äspö HRL.

Variant	Changes relative to the base case
V1	HRD hydraulic conductivities modified for HRD_A2. $K_h = 3 \times K_h$ above –150 m in HRD_A2, and K restored to uncalibrated values below –150 m.
V2	Uncalibrated HRD hydraulic conductivities for all HRD.
V3	As V1 combined with uncalibrated HCD transmissivities.
V4	As V1 combined without all subsea HSD changed to gyttja clay in the bays around Äspö.
V5	As V1 combined with isotropic HSD hydraulic conductivities.
V6	As V1 combined with $K_v = 10^{-9}$ m/s for Gyttja clay.

Table 8-4. A comparison of modelled and measured drawdowns (m) for 1995AD in percussion drilled boreholes. The drawdown is given for the base case and variants based on the difference predicted heads at 1996 AD with pumping in the Äspö HRL and in 1990 before pumping.

Borehole	Measured drawdown	Response?	Modelled drawdown for variants						
			Base case	V1	V2	V3	V4	V5	V6
HAV01	0.3	possibly small	0.0	0.2	0.1	0.3	0.0	0.1	0.7
HAV02	1.5	yes	0.4	1.1	0.6	1.2	0.0	0.5	3.2
HAV03	0.0	no	0.0	0.1	0.1	0.1	0.0	0.1	0.3
HAV04	0.2	possibly small	0.3	1.1	0.4	1.4	0.0	0.5	3.7
HAV05	2.4	yes	1.4	2.7	1.8	2.8	0.1	1.4	7.7
HAV06	3.2	yes	0.1	1.6	0.6	1.6	0.1	0.8	5.6
HAV07	?	?	3.7	5.6	4.0	5.4	0.1	3.0	14.7
HAV08	4.5	yes	4.6	6.4	4.8	6.1	0.1	3.6	16.1
HMJ01	8.5	yes	6.8	7.4	6.8	7.1	0.1	4.4	16.8
HLX01	0.0	no	0.0	0.0	0.0	0.0	0.0	0.0	0.0
HLX02	0.5	possibly	0.0	0.0	0.1	0.1	0.0	0.0	0.1
HLX03	0.0	no	0.1	0.1	0.1	0.1	0.0	0.0	0.2
HLX04	0.0	no	0.1	0.1	0.1	0.1	0.0	0.0	0.1
HLX05	0.0	no	0.1	0.1	0.2	0.2	0.0	0.1	0.3
HLX06	0.0	no	0.0	0.0	0.1	0.1	0.0	0.0	0.1
HLX07	0.0	no	0.0	0.1	0.1	0.1	0.0	0.0	0.1
HLX08	1.0	possibly	1.4	1.4	1.4	1.5	0.0	0.6	4.0
HLX09	1.7	yes	7.4	7.7	7.6	7.7	0.1	4.3	18.3
Tunnel	70	yes	99	60	65	47	40	55	71
Shaft	70	yes	224	103	110	82	83	99	115

In summary, the following conclusions are drawn:

- A reasonable match to the observed drawdowns resulting from the Äspö HRL can be obtained by modifying the HSD on the seabed in the bays around Äspö to be of gyttja clay type with vertical hydraulic conductivity in the range 10^{-9} to 10^{-8} m/s, centred on $5 \cdot 10^{-9}$ m/s, and uncalibrated hydraulic conductivities for HRD_A2 (i.e. 3 times higher than the *base case model*).
- The drawdowns at depth are mainly controlled by the hydraulic conductivities of HRD_A2. They have a lesser but significant dependence HCD and HSD.
- The drawdowns in the percussion boreholes are mostly sensitive to the hydraulic conductivity of the HSD below the sea around Äspö.

8.3 Interference tests at HLX33

As described in Section 5.3 the interference test in HLX33 is dominated by responses in HCD ZSMNEW007A. The configuration is shown in Figure 5-2. It confirms the adjustments described in Table 7-3 to the transmissivity of this zone, but introduces a strong constraint on the hydraulic properties of the HRD. Even without pumping, groundwater levels were falling gradually during the test period 28th June 2006 to 7th August 2006, and hence some correction to the measured drawdowns was necessary in order to estimate the drawdown resulting from pumping alone. The correction procedure is explained in detail in /Morosini et al. 2009/. An example is shown in Figure 8-20 for KLX02A. This demonstrates that some intervals show a clear response to pumping (here in intervals above 494 m borehole length), others only suggest possible responses (e.g. interval 495 to 717 m borehole length), and others are very uncertain (e.g. below 717 m borehole length).

The simulation of the HLX33 interference test was performed with a lowered infiltration rate (1 mm/year) on top surface of the model since there was little recharge during the test, and an internal flux condition was set in all finite-elements lying along the trajectory of HLX33 with the total abstraction distributed according to the geometric mean horizontal conductivity of each element. The drawdown was calculated as the difference between a transient simulation with pumping and a steady-state solution without pumping. Any changes in salinity due to pumping were neglected.

Simulation results for the base case are compared with corrected drawdowns in monitoring intervals at the end of pumping after 40 days in Figure 8-21. This shows the predicted distribution of drawdown compared to measurements (blue bars correspond to the certain responses where the head recovered once pumping stopped, orange bars correspond to intervals which did not recover once pumping stopped, which indicate intervals where it is uncertain if pumping HLX33 resulted in a drawdown). The results are compared with the Theim radial flow solution based on the pump-rate, an assumed constant transmissivity in HCD ZSMNEW007A and the distance from HLX33 as measured in 3D. The comparison is made difficult by the uncertainty in the interpretation of the measured drawdowns.

The responses in thee core drilled boreholes that have multiple packer sections are shown in Figure 8-22 through Figure 8-24 for the *base case model*.

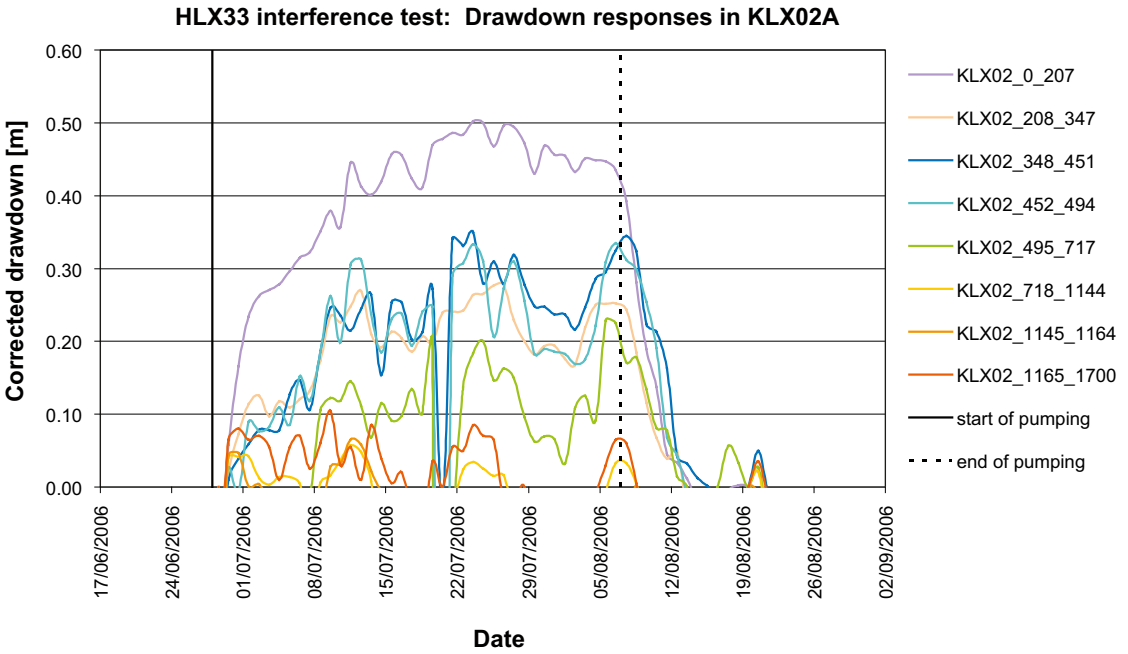

Figure 8-20. *An example of the corrected responses to pumping in HLX33 measured in KL02A packer sections. It is not clear if drawdowns seen below 717 m borehole length are a consequence of pumping in HLX33. Borehole sections listed in the legend are labelled according to borehole length from the top of borehole.*

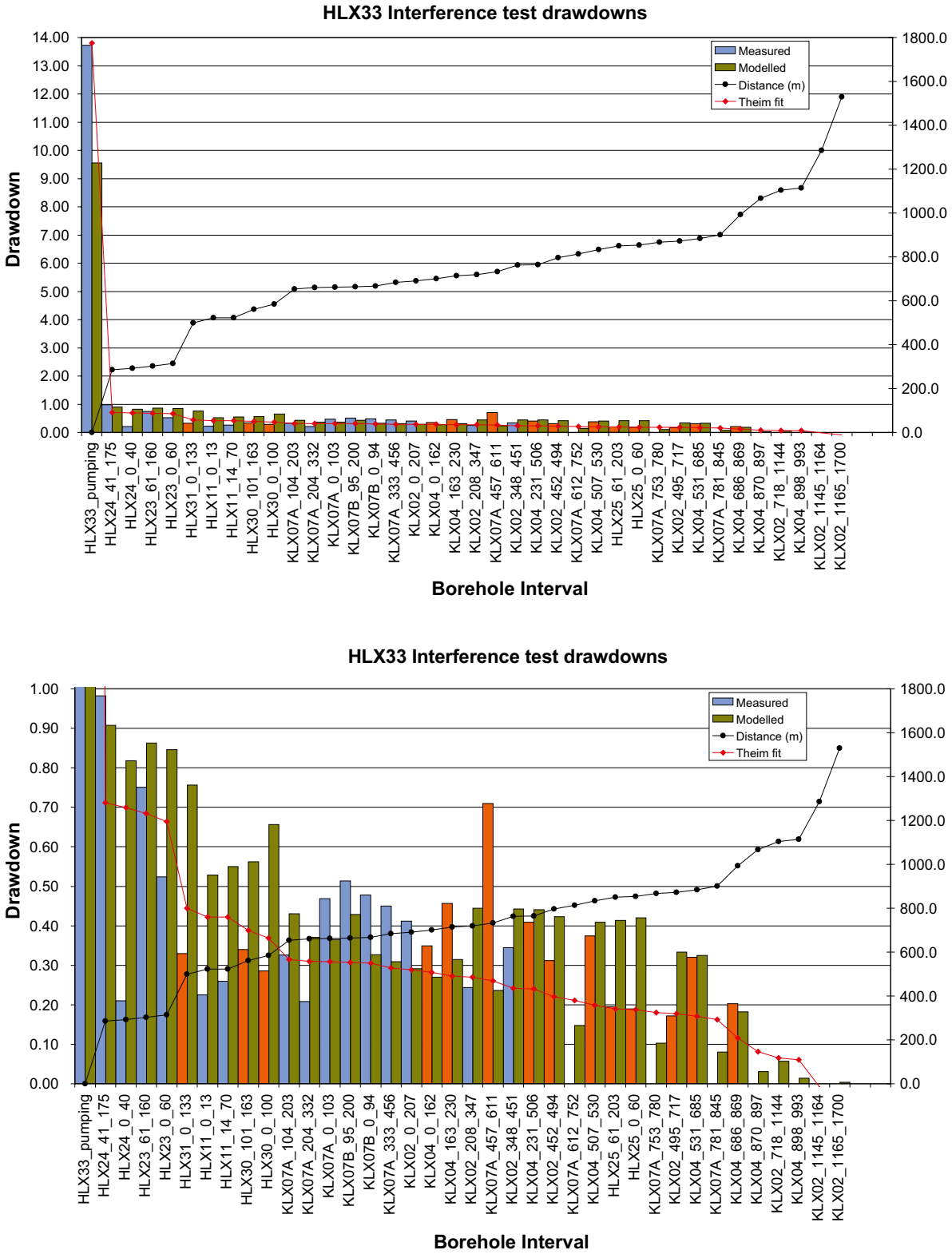

Figure 8-21. *Comparison of measured (blue for certain response, orange for less certain) and modelled (green) drawdown at the end of pumping (40 days) for all monitored borehole intervals for the base case model. The borehole intervals are ordered according to the Eucludian distance (the right axis) of the monitoring intervals to the abstraction at HLX33. The plot is shown on 2 scales: top shows includes the drawdown at HLX33, bottom shows drawdowns up to 1 m. The Theim solution based on Euclidian distances is given by the red line.*

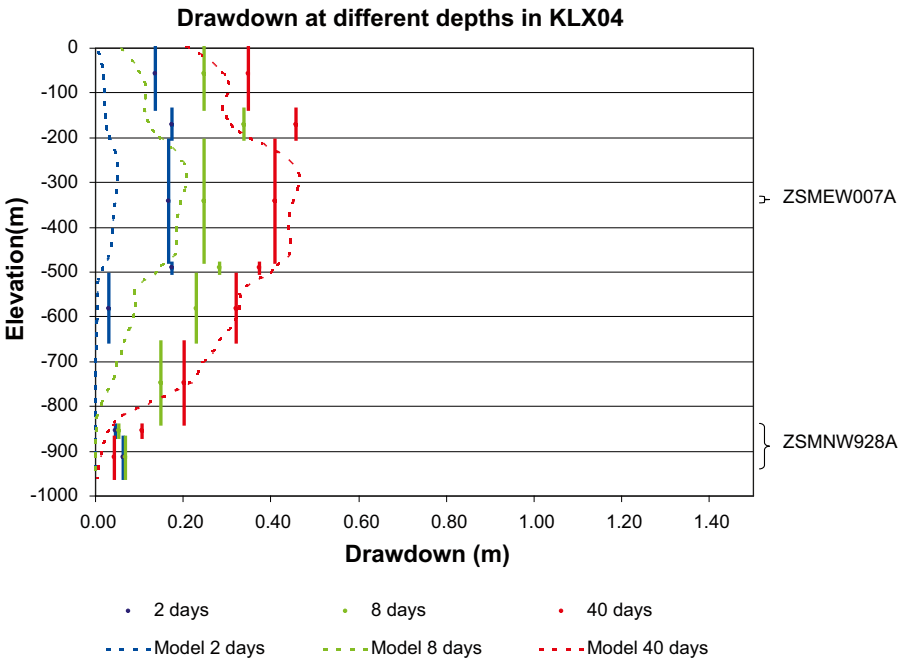

Figure 8-22. *Comparison of measured (solid) and base case model (dashed) drawdown at three times for the KLX04 monitoring hole in response to pumping in HLX33. For the data, a vertical line shows the extent of the monitoring section with the drawdown representing an average within the interval, while the simulated spatial variation in drawdown in the borehole is shown for the model.*

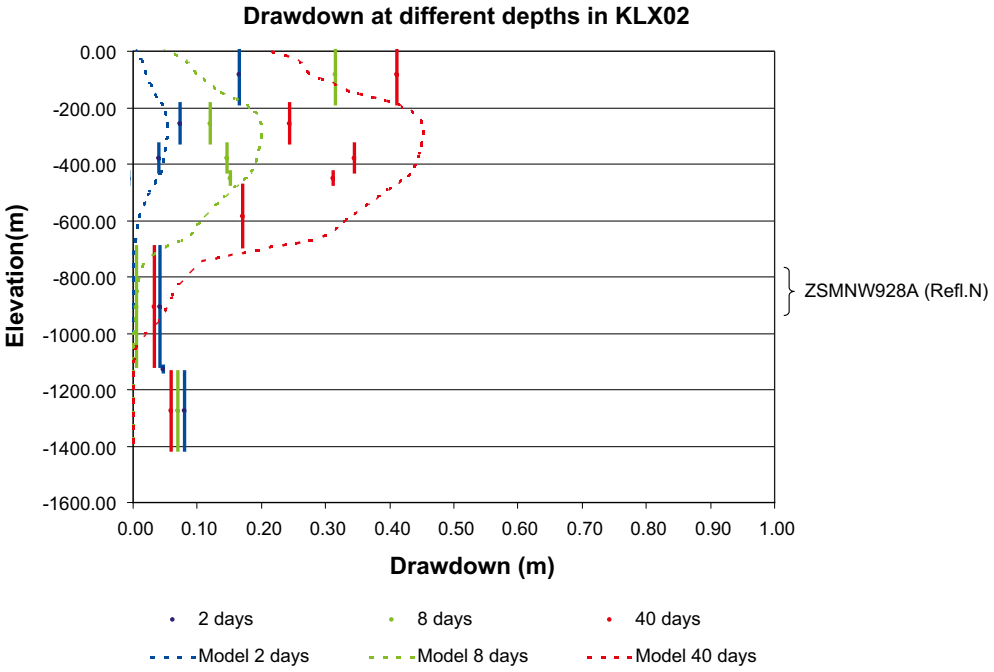

Figure 8-23. *Comparison of measured (solid) and base case model (dashed) drawdown at three times for the KLX02 monitoring hole in response to pumping in HLX33. For the data, a vertical line shows the extent of the monitoring section with the drawdown representing an average within the interval, while the simulated spatial variation in drawdown in the borehole is shown for the model.*

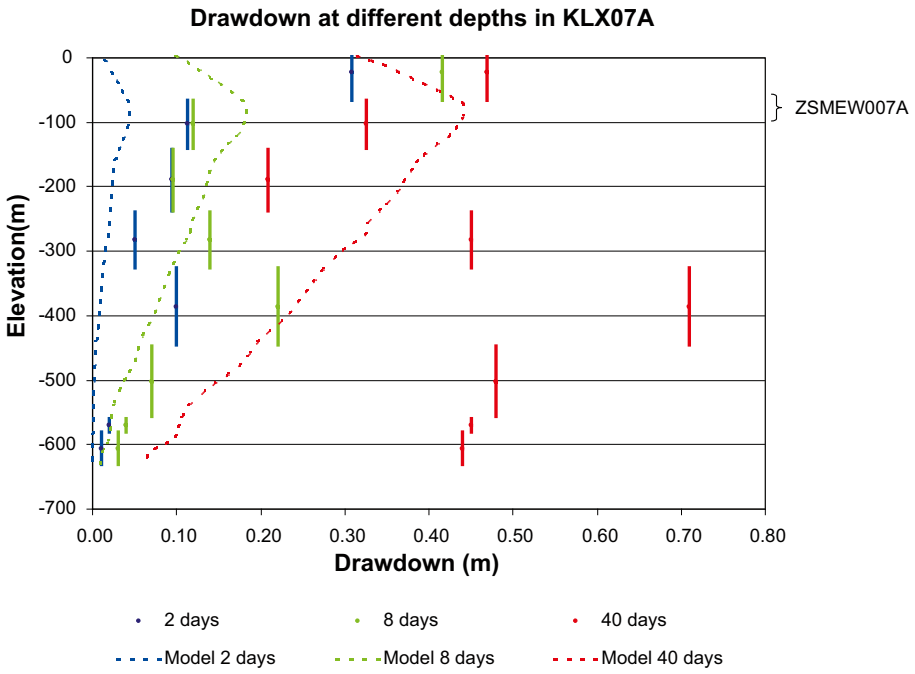

Figure 8-24. *Comparison of measured (solid) and base case model (dashed) drawdown at three times for the KLX07A monitoring hole in response to pumping in HLX33. For the data, a vertical line shows the extent of the monitoring section with the drawdown representing an average within the interval, while the simulated spatial variation in drawdown in the borehole is shown for the model. (The measured drawdowns in the lowermost four intervals after 40 days are considered to be erroneous, and these intervals did not show a recovery after the end of pumping).*

The results shown are for the calibrated *base case model* specified in Chapter 7. The drawdown responses to pumping in HLX33 are modest (up to a maximum of 1 m) and appear to vary fairly predictably with distance from HLX33 since assignment of an appropriate value to the transmissivity of ZSMEW007A and assuming radial flow within this HCD seems sufficient to gain a qualitative understanding of the hydraulic test. The main changes made in calibrating the *base case model* (i.e.the changes already included in the model specified in Chapter 7) to match the HLX33 test were:

- An increase in the transmissivity of HCD ZSMEW007A in the top 2 depth zones by factors of 50 and 10 (see Table 7-3), respectively, was required to obtain the right magnitude of drawdown in HLX33 and responses c. –300 m elevation observed in KLX04 and KLX02.
- Low specific storage coefficients of around 10^{-7} m^{-1} for the bedrock and 10^{-3} m^{-1} for the soil were required to obtain the correct timescales for transmitting the responses.

The storage coefficient above suggests a storativity of about 10^{-5} for ZSMEW007A, which is at the low end of values suggested by /Rhén et al. 2008, cf Chapter 7 therein/, but within the range of values interpreted for HCD at Laxemar and Äspö.

The lowering of the hydraulic conductivity of HRD_EW007 by a factor 0.3 below –150 m used in the calibrated base case to match pointwater heads resulted in a significantly increased drawdown which improved the calibration boreholes KLX04 and KLX07A/B, while other increases were less beneficial at boreholes such as HLX25 and HLX30. Hence, the tightening of HRD_EW007 suggested by pointwater heads and palaeohydrogeology is only partially confirmed by the HLX33 interference test.

8.4 Interference test at HLX28

The interference test in HLX28 is again dominated mainly by the HCD model (The configuration is shown in Figure 5-5). In this case, mainly the minor deformation zone HLX28_DZ1 is responsible for transmitting the response, while KLX19_DZ5-8 ZSMNS059A, ZSMNS001C and ZSMNW042A-west act to transmit the response longitudinally and inhibit it transversely. This confirms the barrier effect of these zones. Some response in the HRD is seen in this test, but these are generally in the close vicinity of the HCD. That is, the HCD are responsible for the primary response, and the background fractures distribute these responses slightly further. If the HRD were too hydraulically conductive, then the responses in the HCD would be reduced since the background rock would provide additional water flux to replenish that pumped. Preliminary tests suggest the hydraulic conductivity in the immediate vicinity of HLX28 is perhaps lower than interpreted in the hydrogeological DFN model for HRD_W.

It was not considered necessary to correct the drawdowns for the HLX28 test for any natural fall in water levels because pumping was only performed for 5 days. Unlike HLX33 the measured responses cannot be approximated by a simple radial flow fit as shown in Figure 8-25, since the responses are governed by a complex network of HCD and barrier effects of the dolerite dykes.

Because of the very discrete nature of the responses seen in this test two simulation approaches were tried. The first was essentially the same as employed for HLX33 using an ECPM model for the calibrated base case. The second was to use the underlying DFN model directly to simulate the test. For this second approach, the full regional HCD model was used, but only the stochastic fractures in a region about 1.5 km by 1.5 km centred on HLX28 were considered to make the simulations tractable. The results for the calibrated base case ECPM model are shown in Figure 8-26 for distribution of drawdowns in monitoring intervals at the end of pumping compared to measurements, while Figure 8-27 shows the predicted drawdowns in KLX19A. As can be seen in Figure 8-26 the responses in the closer monitoring boreholes were reasonably well reproduced, but further away the magnitudes of responses could not be reproduced by the ECPM model for a number of variants. The problem was considered to be a result of the limitations of using a relatively coarse grid, 40 m, and the continuum method that tends to allow a hydraulic signal to diffuse outside of the network of HCD.

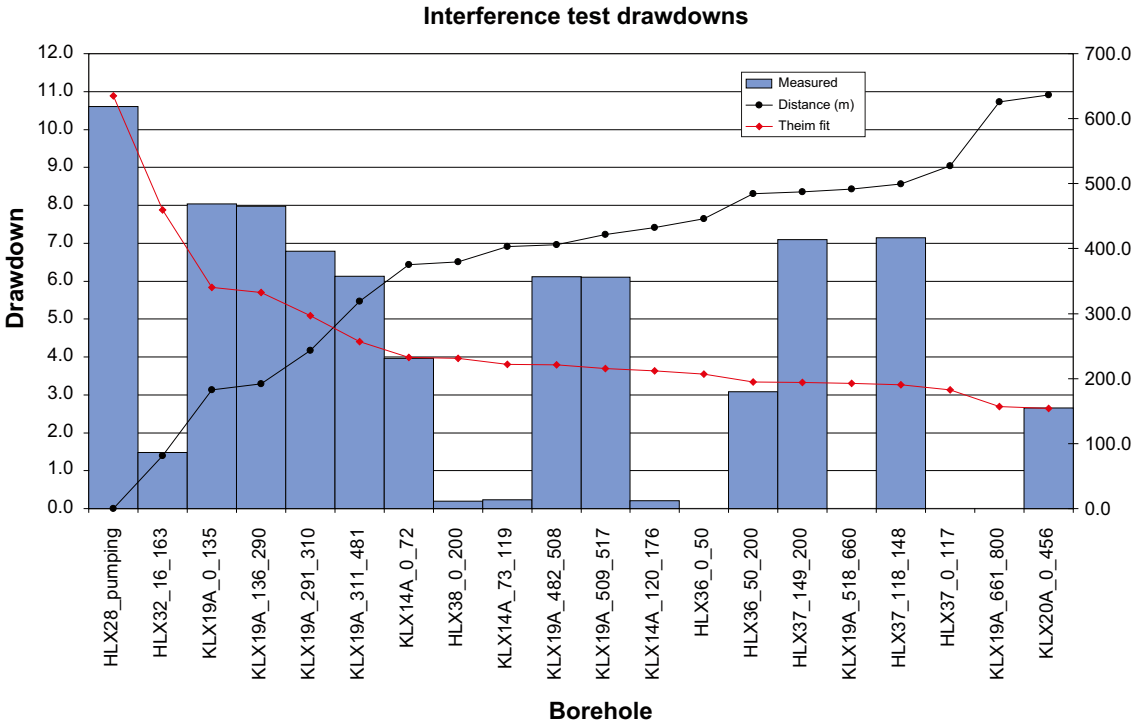

Figure 8-25. *Measured drawdown at the end of pumping (5 days) for all monitored borehole. The borehole intervals are ordered according to the 3-dimensional distance (the right axis) of the monitoring intervals to the abstraction at HLX28. The Theim solution for radial flow based on the 3D distance from the pumping borehole is plotted for comparison.*

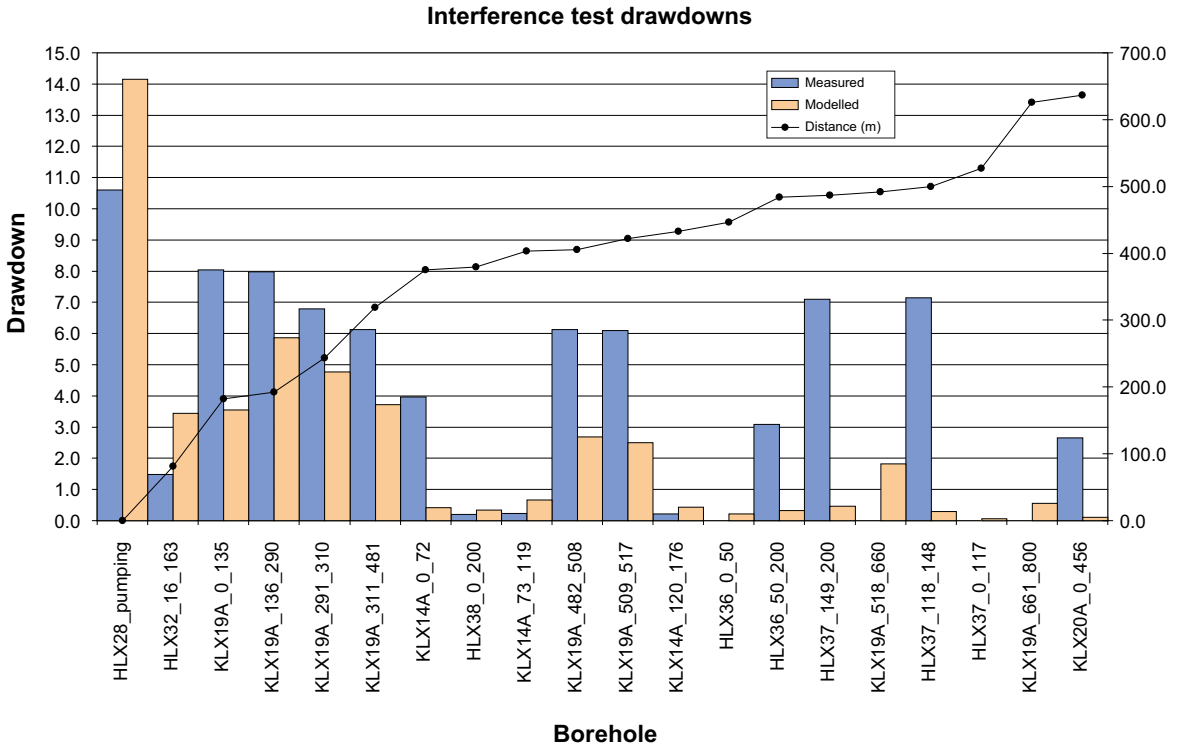

Figure 8-26. *Comparison of measured (blue) and modelled (orange) drawdown at the end of pumping (5 days) for all monitored borehole intervals for the base case ECPM model. The borehole intervals are ordered according to the Euclidian distance (the right axis) of the monitoring intervals to the abstraction at HLX28.*

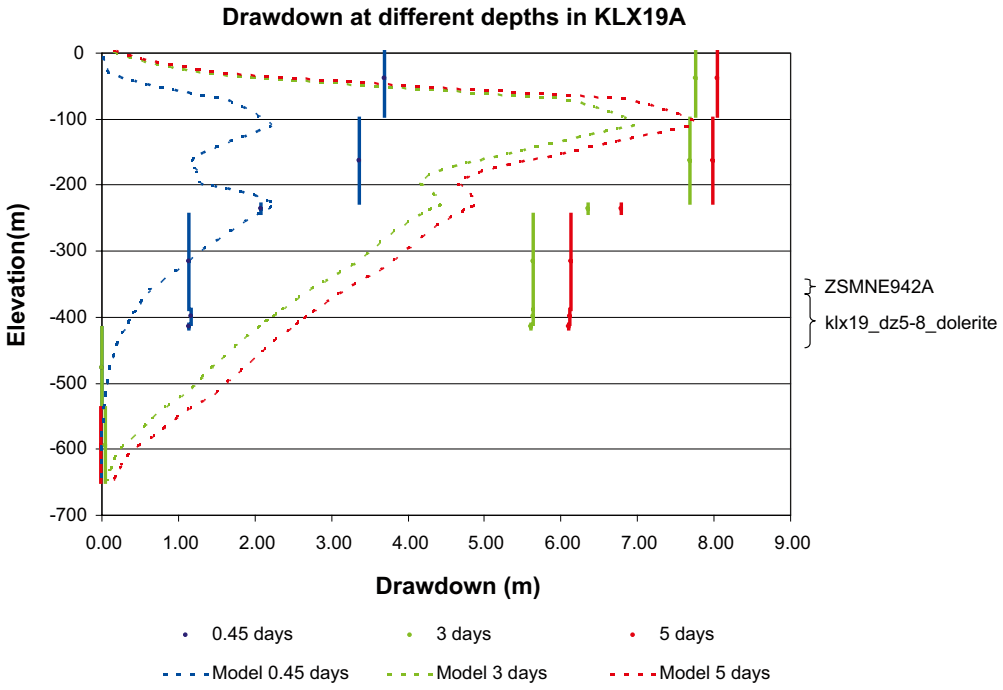

Figure 8-27. *Comparison of measured (solid) and calibrated base case ECPM model (dashed) drawdown at three times for the KLX19A monitoring hole in response to pumping in HLX28. For the data, a vertical line shows the extent of the monitoring section with the drawdown representing an average within the interval, while the simulated spatial variation in drawdown in the borehole is shown for the model.*

Therefore, the underlying DFN model, without upscaling, was used directly to simulate the transient pumping in HLX28. It should be noted however that anisotropy of the dolerite dykes could not implemented in the DFN model. As a result the model tends to predict some responses propagating across ZSMNS001C and ZSMNS0059A via stochastic fractures crossing these two dolerite dykes, cf Figure 8-26 and Figure 8-27. Still, by using a DFN model it was possible to simulate the correct levels of drawdown in the system even at large distance from HLX28. To achieve this it was necessary to modify the properties of 3 HCD from those used in the calibrated base case ECPM model as specified in Chapter 7. The changes were:

- A factor 4 increase in transmissivity of HCD HLX28_DZ1.
- A factor 3 in the transmissivity of HCD ZSMNW042A-west.
- A factor 3 in the transmissivity of HCD ZSMNS059A.

These changes gave the best case DFN model whose results are given in Figure 8-28 through Figure 8-31.

The storativity model used in these transient DFN calculations was based on a preliminary relationship $S = aT^b$, with $a = 0.001$, and $b = 0.5$. The relationship recommended in Section 7 of /Rhén et al. 2008/ has $a = 0.01$ and $b = 0.71$, which gives similar storativities for transmissivities around 10^{-5} m^2/s that are characteristic of the HCD in the superficial bedrock.

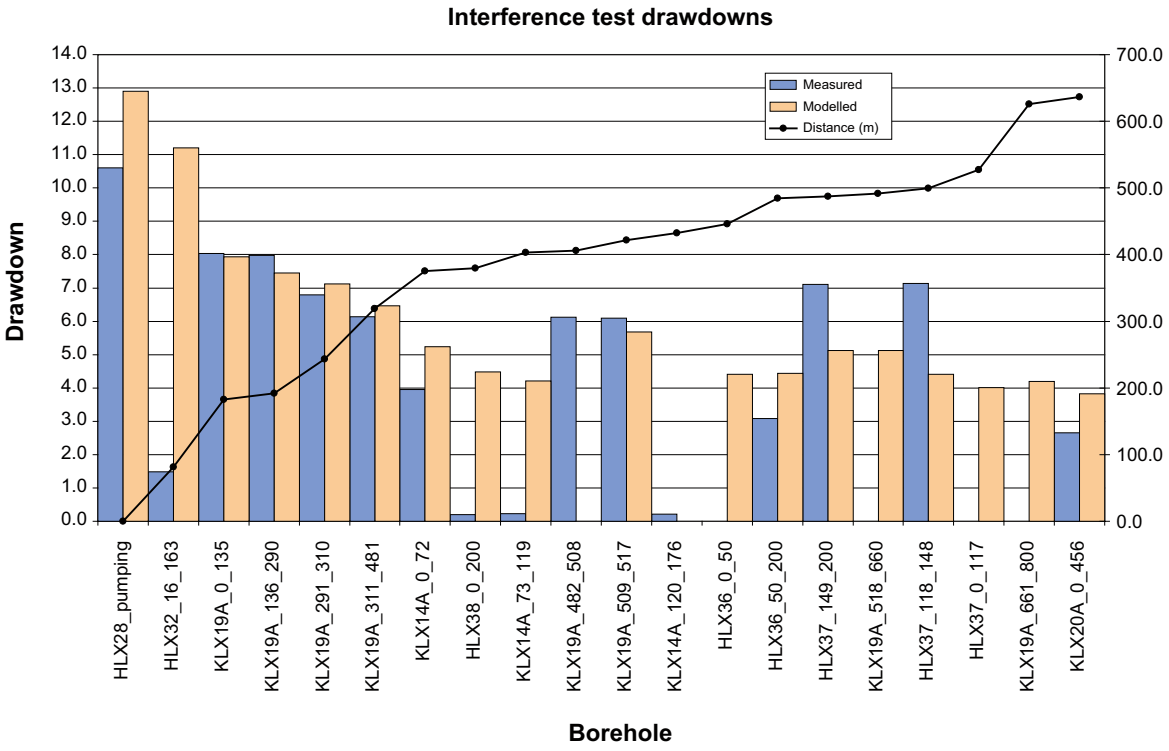

Figure 8-28. *Comparison of measured (blue) and modelled (orange) drawdown at the end of pumping (5 days) for all monitored borehole intervals for the best case DFN model. The borehole intervals are ordered according to the Euclidian distance (the right axis) of the monitoring intervals to the abstraction at HLX28.*

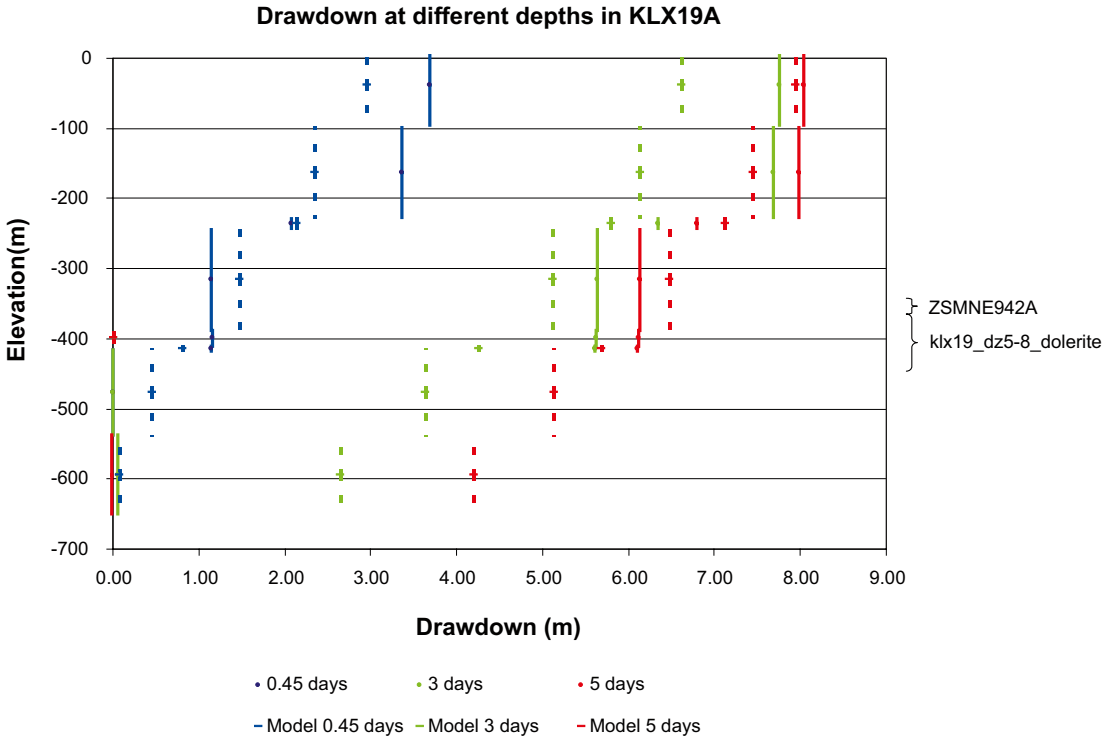

Figure 8-29. *Comparison of measured (solid) and best case DFN model (dashed) drawdown at three times for the KLX19A monitoring hole in response to pumping in HLX28. For the data, a vertical line shows the extent of the monitoring section with the drawdown representing an average within the interval, while the simulated average drawdown in fractures intersecting the borehole interval is shown for the model.*

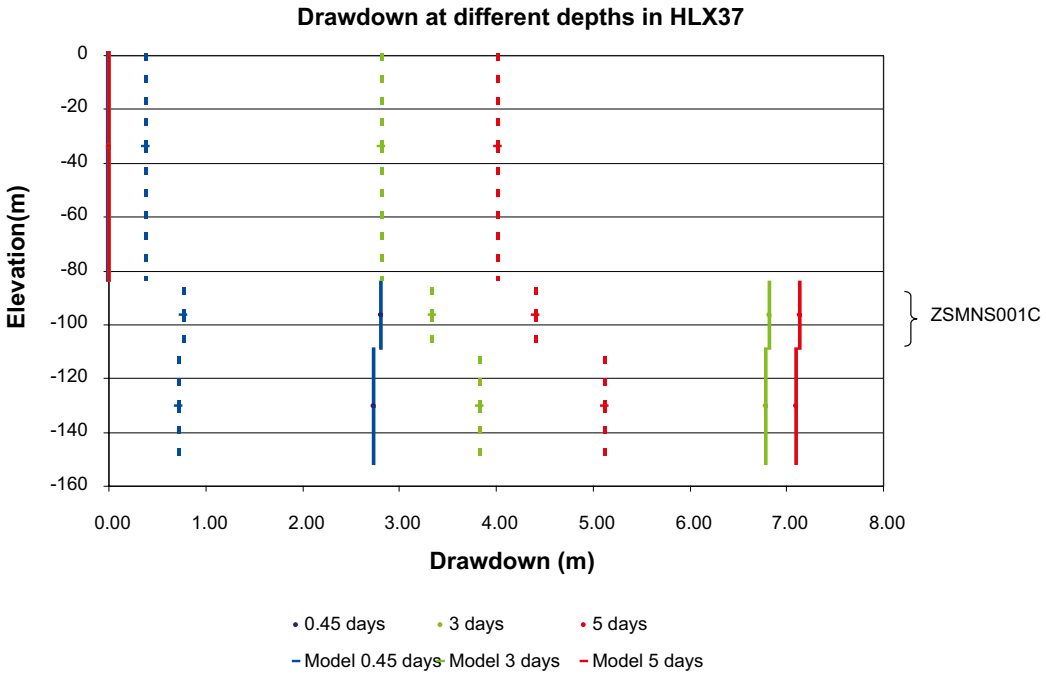

Figure 8-30. *Comparison of measured (solid) and best case DFN model (dashed) drawdown at three times for the HLX37 monitoring hole in response to pumping in HLX28. For the data, a vertical line shows the extent of the monitoring section with the drawdown representing an average within the interval, while the simulated average drawdown in fractures intersecting the borehole interval is shown for the model.*

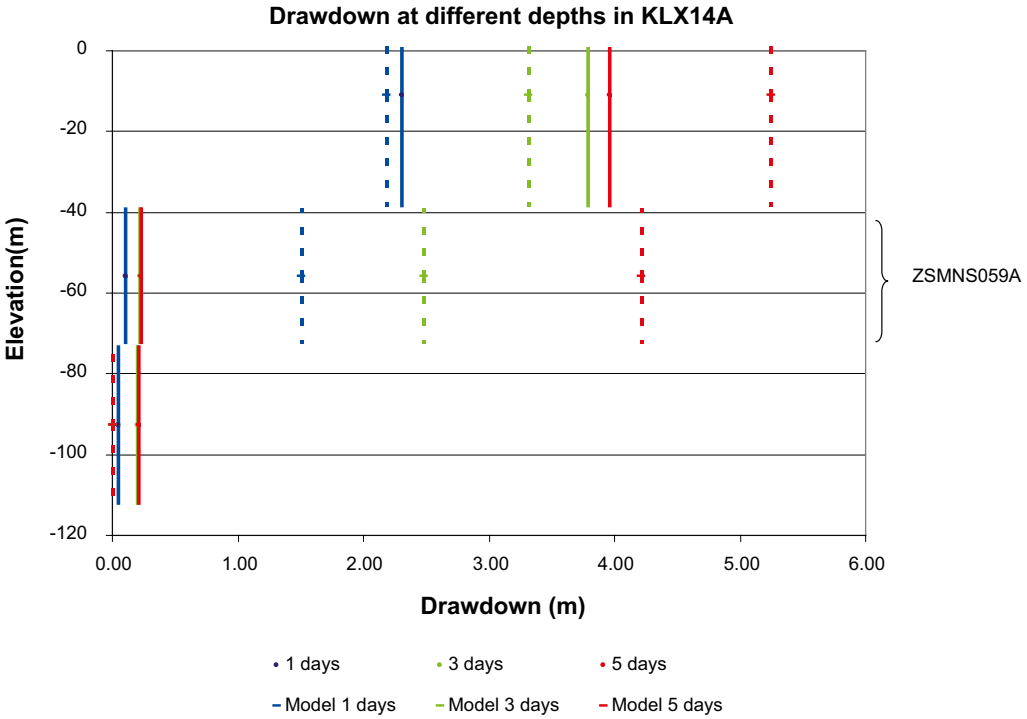

Figure 8-31. *Comparison of measured (solid) and best case DFN model (dashed) drawdown at three times for the KLX14A monitoring hole in response to pumping in HLX28. For the data, a vertical line shows the extent of the monitoring section with the drawdown representing an average within the interval, while the simulated average drawdown in fractures intersecting the borehole interval is shown for the model.*

8.5 Conclusions

A reasonable match has been achieved between simulated and measured natural pointwater heads in the Quaternary deposits and percussion boreholes with the discrepancy between the steady-state model results and the average measurements less than the measured seasonal variations. Likewise, the match of environmental heads in the core-drilled boreholes is also acceptable, following the general trends seen between the different boreholes and within the boreholes. In some boreholes a possible error in the correction of the environmental head according to measured density prevented a confident appraisal of the match. The following remarks are made focussing on specific components of the hydrogeological model.

HCD

- The main change to the calibration made on natural heads was to make the changes listed in Table 7-3, of these increasing the transmissivity of ZSMEW007A had the largest impact. This change was also of key importance to the HLX33 interference test.
- Simulations of the natural heads and HLX28 interference tests demonstrate the need for anisotropy in the hydraulic properties of the dolerite dykes ZSMNS001C and ZSMNS0059A and in the HCD ZSMNW042A-west and ZSMEW002A, which are interpreted as being rendered anisotropic by the effects of fault gouge.
- The hydraulic interference test in HLX28 suggests a possible increase by a factor 3-4 in the transmissivity (in plane) of the upper sections of HCD HLX28_DZ1, HCD ZSMNW042A-west and ZSMNS059A.
- The introduction of spatial heterogeneity in the HCD demonstrated that many of the discrepancies in the core-drilled boreholes could be explained by spatial heterogeneity.

- A low specific storage coefficient around 10^{-7} m^{-1} for the bedrock and 10^{-3} m^{-1} for the soil gave the correct timescales for the transient evolution seen in the HLX33 interference test. This implies a storativity for HCD ZSMEW007 around 10^{-5} which dominates this test. For the transient DFN simulations of the HLX28 interference test, a relationship between storativity and transmissivity for fractures, $S = 0.001T^{0.5}$ was used, which predicts storativities for the HCD in the upper bedrock around 10^{-6} to 10^{-4}.

HRD

- The hydraulic properties of the HRD were confirmed by the natural head measurements. Scaling the hydraulic conductivity of the HRD by a factor 3 up or down gives a similar quality of fit (i.e. the changes to the predictions are within the variability in the data), but larger changes affect the match adversely.
- An increase in hydraulic conductivity in the top –150 m by a factor of about 3 would benefit the head match. A larger increase would reduce the heads too much, and is not supported by hydraulic test data.
- The HLX28 interference test may suggest a lowering of hydraulic conductivity in the upper bedrock, but this may just reflect localised conditions in the southern part of HRD_W.
- The drawdowns in the tunnels and shafts resulting from the Äspö HRL suggest the hydraulic conductivity of HRD_A2 should be 3 times higher than in the base case. This essentially implies that the hydraulic conductivity of HRD_A2 should be based directly on the upscaled Hydro-DFN without adjustment. The hydraulic conductivity of HRD_A2 had been reduced by a factor 3 below –150 m in the base case due to its analogy with HRD_N (See Table 7-5), which had been reduced for the calibration on pointwater heads.

HSD

- The drawdowns in the percussion drilled boreholes resulting from the Äspö HRL are predominantly sensitive to the hydraulic properties of the HSD. The sediments on the seabed in the bays around Äspö need to be relatively tight, with a vertical hydraulic conductivity generally less than 10^{-8} m/s.

The simulations of the drawdown resulting from the Äspö HRL suggest that measurements of pointwater heads and hydrochemistry will not have been significantly affected by the facility apart from the far eastern part of Laxemar local model area.

9 Palaeohydrogeology

This chapter presents the results of confirmatory tests of the groundwater flow and solute transport model based on the concepts described in Chapter 5 against measurements of hydrogeochemistry data as described in Chapter 6. The comparisons made are based on the calibrated *base case model* described in Chapter 7 along with a series of variants used to illustrate some of steps made in the calibration and quantify the sensitivity to some remaining uncertainties.

9.1 Matching hydrochemistry profiles in boreholes

The hydraulic parameters described in Chapter 7 were arrived at based on the calibration on hydraulic tests as described in Chapter 8. Hydrochemical data was then used as a series of natural tracer tests to check the consistency of the hydraulic parameters and for examining the description of transport parameters and concepts for the palaeohydrogeological evolution.

9.1.1 Methodology

As described in Section 7.8, the calibration against hydrogeochemistry measurements involves the simulation of palaeohydrogeology in terms of the evolution of coupled solute transport and groundwater flow from 8000 BC to the present-day. The transport of solutes is modelled in terms of the infiltration and mixing of several different reference waters that are assumed to be transported conservatively, i.e. without reaction, but subject to advection, dispersion, and diffusive exchange between the fracture- and pore-waters (i.e. rock matrix diffusion). Groundwater flow is subject to buoyancy forces that arise due to variations in fluid density according to salinity, temperature (a fixed geothermal gradient is assumed between 7.2°C at the surface and an increase of 0.015°C/m with depth), and total pressure. Variations in fluid viscosity with temperature, salinity and total pressure are also considered. The boundary conditions evolve in time according to both seashore displacement and variations in marine salinity. The chemical compositions of the reference waters are fixed. Therefore, given the simulated mixture of references waters (defined by the mass fraction) at any point in space and time, the concentration of the major ions or environmental isotope ratios can be calculated by multiplying the reference water fraction by the concentration of the component in that reference water and then summing over the reference waters. The predicted concentrations, or isotope ratios, can then be compared with the data. The chemical composition is calculated both for the mobile water in the fractures and the immobile (no advection) porewater in the matrix. For simplicity, the simulated values for the porewater used for comparison purposes are essentially an average within the matrix blocks. The change in average matrix concentration is calculated as an integral of the fluxes in/out of the matrix during the simulated time divided by the volume of the matrix blocks. Since ConnectFlow stores internally the spatial variation of reference water fractions within the matrix blocks, this could in principle be analysed in more detail to consider the variability of porewater concentration as a function of the distance to a conductive fracture. The spatial variations of hydrochemistry within the porewater are likely to be large where the spacing between water conducting fractures becomes larger than about 10 m (i.e. when PFL-f intensity is below about 0.1 m^2/m^3) since the timescales for rock matrix diffusion into the matrix blocks are long, 10,000s years, compared to the timescales for changes in chemistry of infiltrating groundwater at the surface. In Laxemar this occurs in HRD_C below –400 m and in HRD_W below –150 m. Hence, it should be borne in mind that there may be trends within the porewater data according to where a sample was taken relative to water-bearing fractures that are as important as trends with respect to the absolute elevation of the sample, for example.

9.1.2 Calibration steps

The calibration is assessed by comparing the predicted and measured profiles of major ions and environmental isotope ratios in the core-drilled boreholes grouped together according to HRD and general flow conditions (recharge or discharge areas) as described in Section 5.6.1, Table 5-6. Primarily, the predicted and measured profiles in the fracture system are compared, although comparisons are

also made with the porewater data in the three boreholes (KLX03, KLX08 and KLX17A) where this information is available to better understand the role of RMD on solute transport. Due to time constraints the calibration process was based primarily on one single realisation of the HRD ECPM properties and deterministic properties for the HCD. Only once a satisfactory base case had been identified, the sensitivity of the calibration to the HRD realisation and spatial heterogeneity in the HCD were quantified. This sensitivity proves to be significant, as is demonstrated in Section 9.1.4, and so it is not appropriate to expect any single simulation to match all the data points. Instead, the ideal goal is to obtain a base case that approximates the data to within a margin that is consistent with variability between realisations of the HRD and HCD. Also, because of grid resolution the representation of hydraulic conditions near a borehole will be smeared out according to the grid size used, and so zones not seen in the actual borehole may affect the simulated borehole, and the effects of individual hydraulic features may be more discrete in reality than is possible to reproduce in the model. Therefore, it is important to look at the profiles of chemical constituents on vertical and horizontal sections as well as along borehole profiles to obtain an impression of the predicted groundwater chemistry in the neighbourhood of a calibration borehole in case the borehole just misses a simulated lens of glacial or brackish water, for example. Hence, the calibration process is a mixture of quantitative and qualitative comparisons.

The key calibration steps in matching the hydrochemical data were:

- Reducing the transmissivity of each HCD by the factors specified in Table 7-2.
- Increasing the kinematic porosity of HCD.
- Reducing the hydraulic conductivity of the HRD below –150 m by a multiplication factor 1/3.
- Increasing the kinematic porosity of the HRD by a multiplication factor 5 to compensate for the effects of truncating the size distribution.
- To use a physically based initial condition in the matrix porewater that varies according distance from a flowing feature and allows for difference composition, mainly $\delta^{18}O$, in the porewater far from a flowing feature to that in fracture water.
- Use low values of the flow-wetted surface area per unit volume of rock, so as to maintain the difference in Cl and $\delta^{18}O$ between matrix and fracture water seen at some places in the bedrock. Modelling suggests values of $a_r < 0.2$ m^2/m^3, consistent with values suggested by the intensity of fractures detected by the PFL method, see Table 7-9.

Once a satisfactory calibration had been achieved based on comparison against major ions and environmental isotopes, extra consistency checks were made by using the derived model to simulate tritium migration considering the enrichment of tritium in the atmosphere resulting from bomb-tests performed in the 1950s–1960s as a tracer for modern meteoric water.

9.1.3 Resulting calibration

The quality of the calibration for the *base case model* is indicated in this subsection. It should be noted that the base case does not necessarily represent the best match to the hydrogeochemistry data that can be achieved. More it is a model that yields an acceptable match to data. Section 9.1.4 considers sensitivities of the palaeo-hydrogeological simulations and identifies changes that improve the match. However, it was considered that such changes would need further investigation and integration with other information before they could become definite modifications to the site-descriptive hydrogeological model.

Figure 9-1 and Figure 9-2 show the match between the simulated base case and measured salinity in the fracture system for eight groups of boreholes associated with different HRD and/or hydrological conditions. The agreement is reasonably good with salinity (> 200 mg/l) starting to occur from –200 m to –400 m depending on borehole and gradually increasing with depth. The initial condition at 8000 BC is largely preserved below –600 m to –800 m, and hence the match could be improved simply by devising a more complex initial condition than the simple linear initial Deep saline distribution described in Section 7.8.3. The salinity in most boreholes seems acceptable, although the measured salinity is lower in some boreholes than simulated, but again this is a direct result of using a simple initial condition that does not account for local heterogeneity.

Further, Figure 9-3 through Figure 9-11 show the comparison of the simulations with data for selected major ions and environmental isotopes for the core-drilled borehole grouped according to HRD and hydrogeological conditions. The chemical indicators used in these plots are, as also pointed out in Section 5.6.3:

- Cl - since it is conservative and indicates the locations of *Littorina Sea Water* and *Deep Saline Water*.
- Br/Cl ratio – since both are conservative and their ratio can be used to determine where the origin of saline water changes from a *Littorina Sea Water* to *Deep Saline Water* when the ratio increases from around 0.004 to 0.007, or more.
- $\delta^{18}O$ – since this is conservative over the timescales considered in the simulations and indicates any remnants of *Glacial Melt Water* when $\delta^{18}O < -13$ /Laaksoharju et al. 2009/.
- HCO_3 – because we model the infiltration of an *Altered Meteoric Water* into the bedrock. The HCO_3 is used as a signature for infiltrating post-glacial meteoric water (although it is a non-conservative species), this signature can also be traced by the low Cl content.

Cf Section 5.6.3 for more details about the reference waters.

Figure 9-3 for Cl in the fracture water HRD_C shows reasonable results, and the inclusion of porewater data for KLX03 suggests less saline water in the matrix. This not reproduced in the model since the model assumes an equality of Deep saline water in the initial fracture and matrix water. Better results could be obtained by simply reducing the proportion of *Deep saline water* in the initial condition for the matrix rock. The initial condition used in the base case assumes that *Deep saline water* is relatively shallow, starting from –150 m. Qualitatively this seems consistent with the Br/Cl ratios, although the sparsity of data means that probably any initial condition for *Deep saline water* starting between –150 m and –400 m might be consistent with the data. The penetration of post-glacial meteoric water suggested by HCO_3 is well predicted by the model, perhaps somewhat too deep in the simulations. The general absence of glacial water in HRD_C, apart from one measurement in KLX03 around –380 m, is reproduced by the model, which also matches the higher levels of $\delta^{18}O$ in the porewater below –650 m associated with *Inter-glacial Porewater*.

In the case of recharge areas of HRD_W, cf Figure 9-4, the model predicts flushing of the fracture water by altered meteoric water to almost the bottom of these boreholes at about –600 m, whereas data suggests –500 m. The likely cause is thought to be the model underestimating the effects of RMD in KLX13A and KLX17A which intersect many minor deformation zones between –200 m and –400 m that would result in a higher fracture surface area per unit and more retardation by RMD than what is present in the flow model. The model does, however, predict the retention of a *Deep saline water* in the porewater in these boreholes and a lower salinity in the fracture water as measured in the boreholes.

Figure 9-5, for the discharge areas of HRD_W, shows the brackish water below about –400 m is predicted by the *base case model* and that this is largely of high Br/Cl ratio, i.e. Deep saline water origin. Again, post-glacial meteoric flushing is well predicted based on HCO_3, including the prediction of some glacial water below –400 m which is consistent with data.

Figure 9-6 for HRD_EW007 suggests consistent predictions of Cl in the fracture system, although KLX08 data would again suggest less salinity in the matrix than is assumed in the initial condition. The transition from salinity of deep origin rather than marine at depths between –400 m to –500 m is consistent with available data. Post-glacial meteoric flushing is perhaps 50 m deeper in the model than suggested by measured data. Similarly, $\delta^{18}O$ would suggest slightly less flushing by recent surface water to preserve glacial lenses higher up. The transition to *Inter-glacial Porewater* in the porewater below –650 m is consistent between the model and data.

Figure 9-7 through Figure 9-11 correspond to boreholes outside the Laxemar focused area. Model predictions for boreholes in HRD_N in the northern part of the Laxemar local model area are consistent with data, as are the predictions for boreholes in HRD_A situated farther to the east on Ävrö. Predictions for the HRD_A2 boreholes located on Äspö are generally reasonable, although the model predicts flushing by Altered meteoric water in the last few thousand years down to nearly –350 m, while data would suggest an elevation closer to –200 m. However, Äspö chemical data appears to show an uncharacteristically low depth trend in salinity and $\delta^{18}O$ below –200 m, which may be a result of some vertical averaging of chemical composition during the data acquisition or other disturbances. As in the case of KLX13A and KLX17A, a slight increase in fracture surface area per unit volume linked

to higher fracture intensity in the depth zone –200 m to –400 m would improve the results here. The prediction applicable to boreholes in HRD_BC of the Simpevarp subarea is also reasonable.

Another way of presenting the palaeohydrogeological conceptual model of the mixing of different reference waters is to plot the predicted mass fractions of reference waters as a function of elevation in boreholes, i.e. show the composition of groundwater relative to the 5 reference waters modelled. This is done for KLX03, KLX04, KLX05 and KLX08, all within the Laxemar focused area, in Figure 9-12. These are included to illustrate in a compact way the composition of the fracture water and average matrix porewater in terms of mixes of reference waters. Such plots provide useful insights into the mixing of reference waters and the influence of structures observed in the single-hole interpretations indicated on the right hand side of the graphs. They are not used as a calibration target in the same way as the major ions, but still comparisons are made to the fractions computed by the M3 method /Laaksoharju et al. 2009/ to aid conceptual discussions. It should be noted that the M3 analysis was based on four reference waters (*Inter-galcial Porewater* excluded), and hence the sum of the two simulated fractions for Altered meteoric water (orange line) and *Inter-glacial Porewater* (green line) should be compared with the M3-interpreted Altered meteoric results (orange squares). The mass fractions predicted for the fracture system are shown as solid lines, while those predicted for the matrix are plotted as dashed lines. Deep saline water follows a consistent profile and there is very little Littorina sea water (2–3%) in any borehole as interpreted by M3. Altered meteoric water circulates perhaps a little too deep in the model flushing, considering Glacial water in KLX03 and KLX05, cf Figure 9-12 and Appendix 9. It is interesting to see that in these boreholes, the prediction for matrix water fractions is closer to the interpreted fractions, which would suggest that slightly enhanced RMD in the depth zone –150 m and –400 m would improve the simulation results. The comparison is better in KLX04 and KLX08. Plots of this type for other boreholes are included in Appendix 9, where it is seen than the Littorina content increases to 10–20% in the east, as seen in the data.

Examples of the palaeohydrogeological cross-section information used qualitatively in the calibration are shown in Figure 9-13 and Figure 9-14 for Cl and $\delta^{18}O$ on horizontal sections at –300 m and –500 m, respectively. It can be seen that continuous lenses of Cl exist along the low-lying E-W valleys associated with the Laxemarån river valley in the south, the Mederhult zone to the north, and ZSMEW007A in the centre of the Laxemar local model area. There are more localised lenses of brackish-glacial water within HRD_C associated with regions of lower hydraulic conductivity. At –300 m it can be seen that KLX05, KLX08 and KLX15A (of the boreholes with chemical data) are predicted to intersect brackish water at this quite shallow depth, which is consistent with data. KLX05, KLX08 and KLX15A are also predicted to be close to lenses of glacial water, although it is not actually seen at the borehole in either the simulations or in data. At repository depth, –500 m, brackish water is much more common with large lenses of brackish-glacial water beneath low lying areas and also beneath ZSMEW007A that dips towards north. There are also smaller localised lenses of glacial-brackish water throughout the focused area that are the result of spatial heterogeneity, and hence may vary in position and magnitude according to the particular realisation of HRD and HCD hydraulic properties. The model predicts that KLX01, KLX02, KLX03, KLX04, KLX05, KLX08 all either intersect, or are very close to, lenses of brackish water at this depth. There are areas of non-saline water predicted in the centre of HRD_C and HRD_W which are not intersected by any boreholes with chemical sampling.

Similar plots of simulated chemical constituents, reference water mass fractions and Darcy velocities on several vertical and horizontal cross-sections through the *base case model* are presented in Appendix 9.

As an example of simulated hydrochemistry on a vertical slice, Figure 9-15 shows Cl, $\delta^{18}O$ and Altered meteoric water mass fraction on a WNW-ESE section (see Appendix 9 for details). This shows that the saline transition zone is generally located between –200 m to –500 m in the Laxemar local model area, at little deeper in the west, and a continuous Glacial pocket exists in HRD_EW007 centred on repository depth, –500 m.

Additional confirmatory tests were made of the palaeohydrogeological model by simulating the migration of tritium over the last 120 years using the derived calibrated *base case model* and selected variants. These calculations are presented in Appendix 10 where it is concluded that the developed palaeohydrogeological models are consistent with the interpretation of hydrogeochemistry /Laaksoharju et al. 2009, Section 7.2.2/ that modern meteoric recharge from the last 50–60 years has penetrated the groundwater system to a depth of approximately 150 to 200 m.

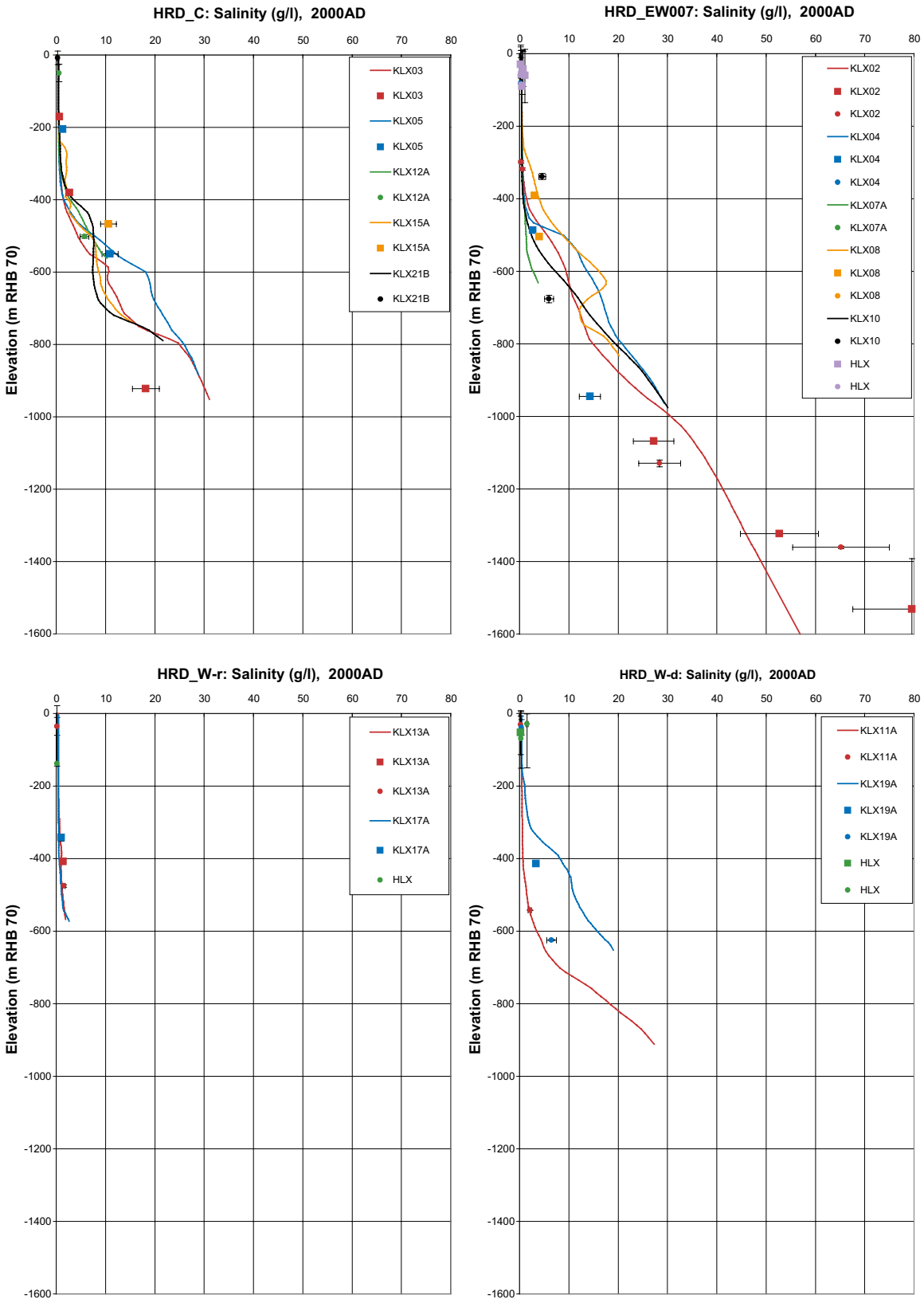

Figure 9-1. *Comparison of the modelled and measured distributions of salinity (TDS) in the fracture system for different groups of calibration boreholes. Square symbols are used for Category 1–3 data, and small diamond symbols for the Category 4 data. The error bars on the data indicate the laboratory analytical error. The solid lines show the complete distribution in the borehole simulated in the fracture system.*

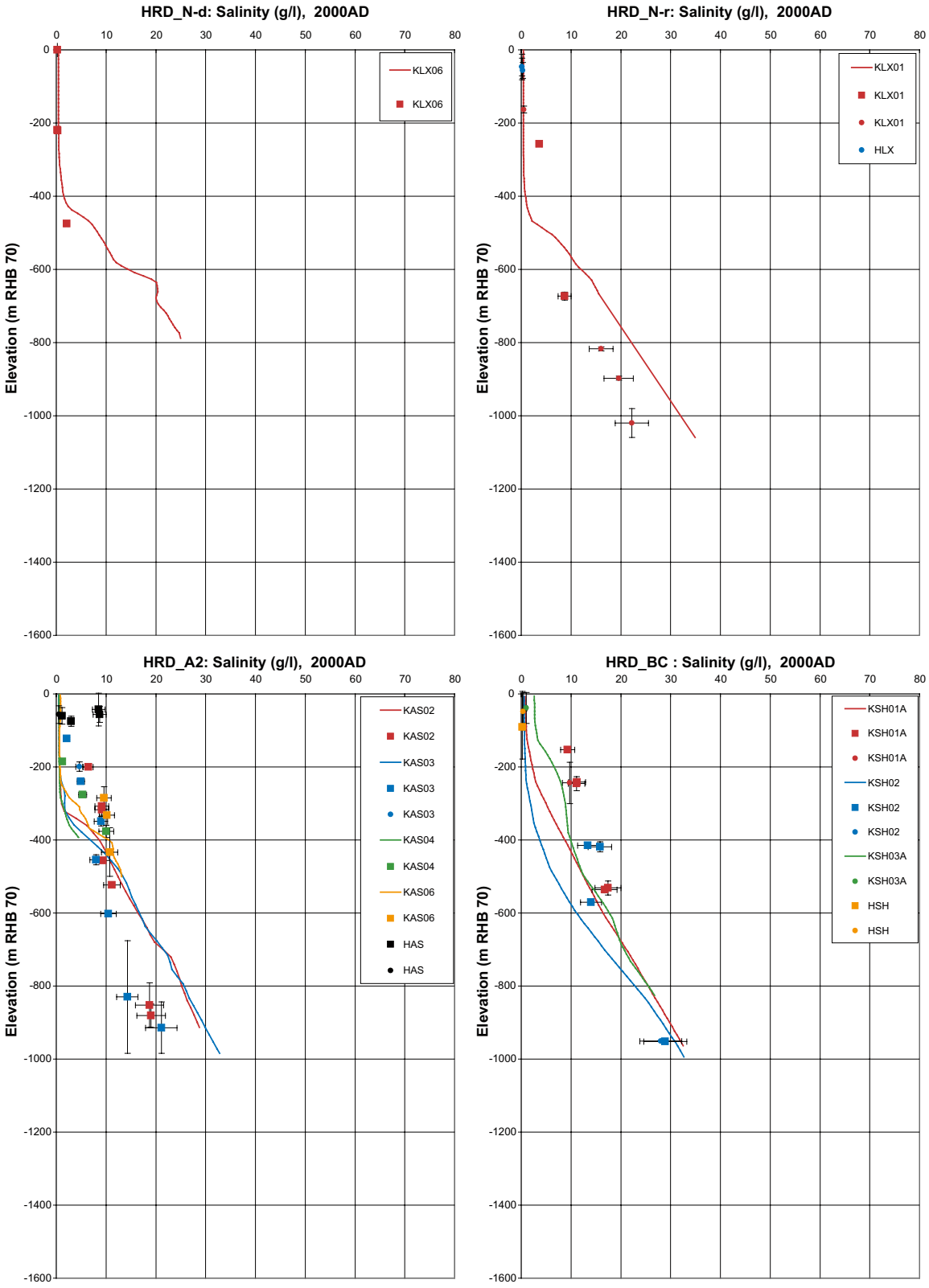

Figure 9-2. *Comparison of the modelled and measured distributions of salinity (TDS) in the fracture system for different groups of calibration boreholes. Square symbols are used for Category 1–3 data, and small diamond symbols for the Category 4 data. The error bars on the data indicate the laboratory analytical error. The solid lines show the complete distribution in the borehole simulated in the fracture system.*

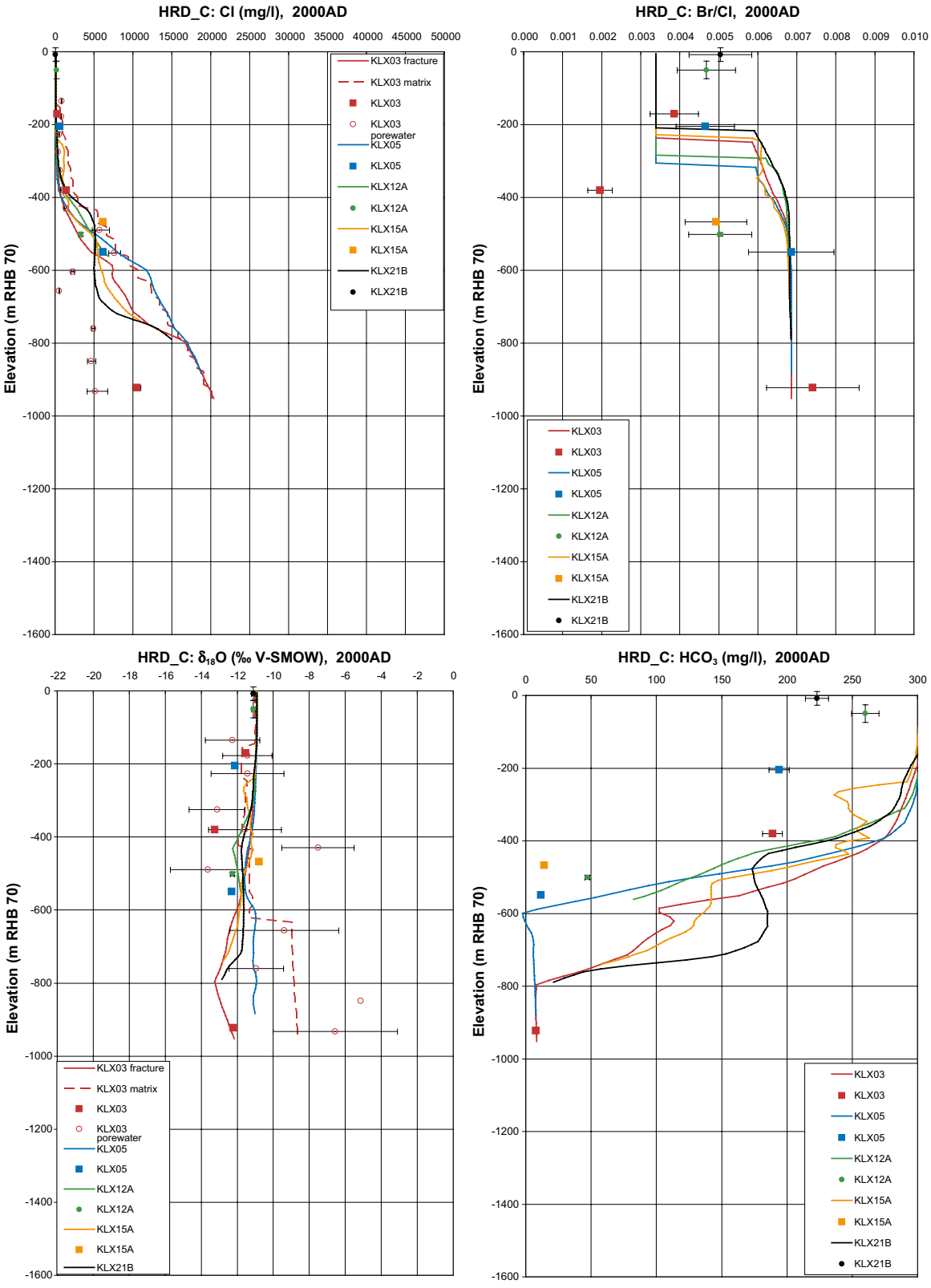

Figure 9-3. *Comparison of the modelled and measured Cl, Br/Cl, $\delta^{18}O$ and HCO_3 in the fracture system for boreholes in HRD_C. Square symbols are used for Category 1–3 data, circles are used for the pore-water data, and small diamond symbols for the Category 4 data. The error bars on the data indicate the laboratory analytical error. The solid lines show the complete distribution in the borehole simulated in the fracture system, and the dashed lines are for the matrix.*

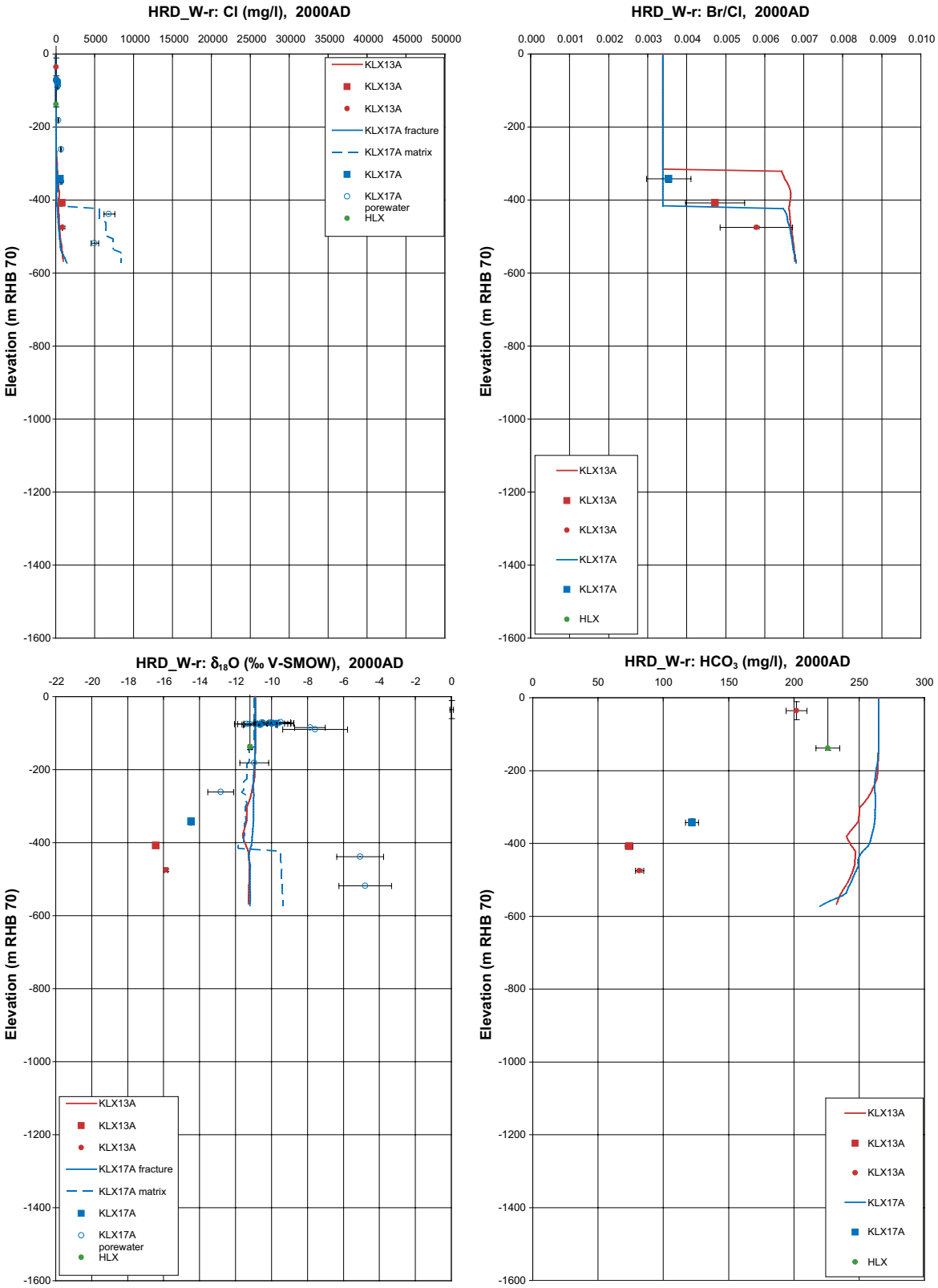

Figure 9-4. *Comparison of the modelled and measured Cl, Br/Cl, $\delta^{18}O$ and HCO_3 in the fracture system for boreholes in HRD_W-recharge. Square symbols are used for Category 1–3 data, circles are used for the porewater data, and small diamond symbols for the Category 4 data. The error bars on the data indicate the laboratory analytical error. The solid lines show the complete distribution in the borehole simulated in the fracture system, and the dashed lines are for the matrix.*

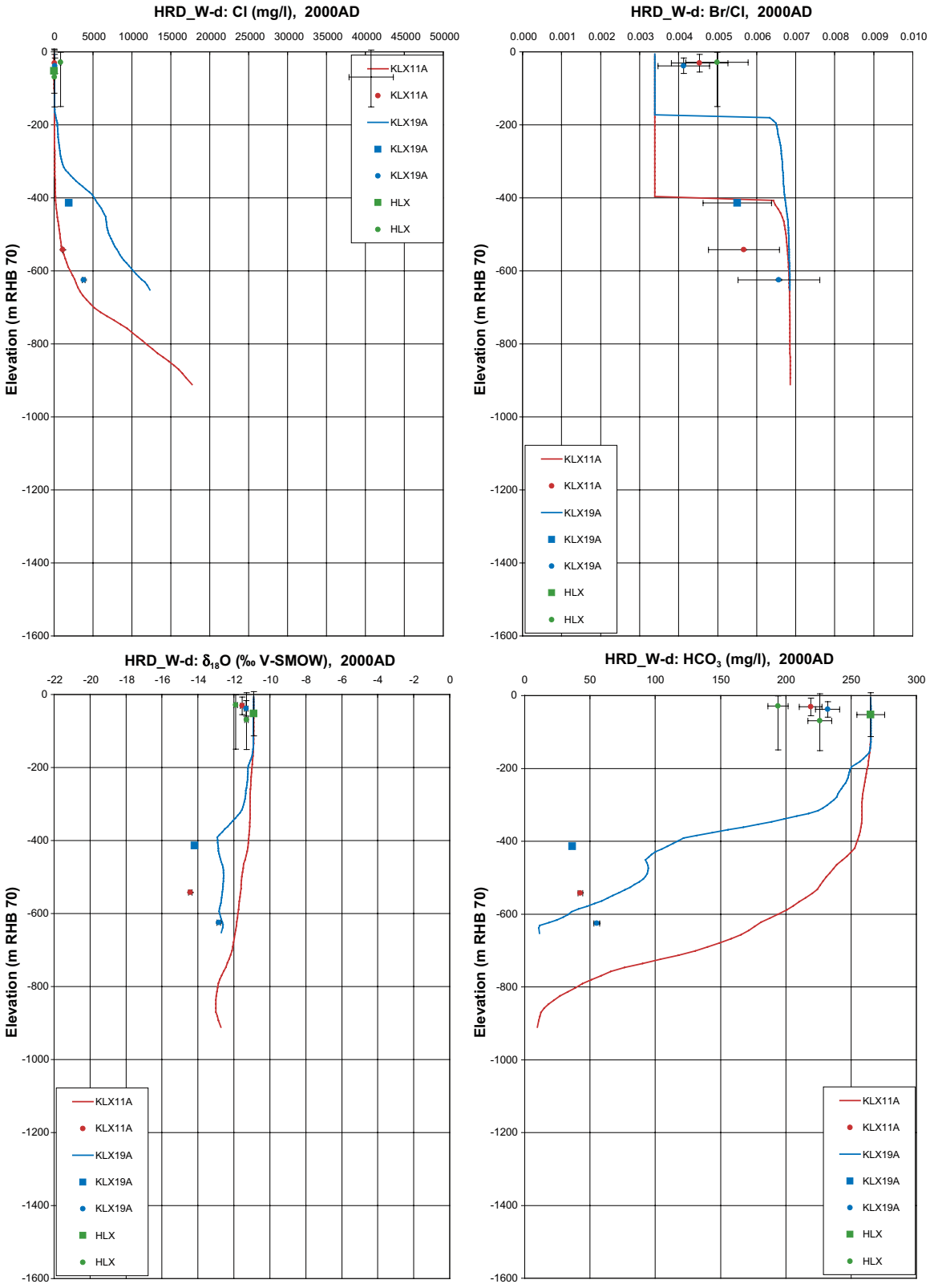

Figure 9-5. *Comparison of the modelled and measured Cl, Br/Cl, $\delta^{18}O$ and HCO_3 in the fracture system for boreholes in HRD_W-discharge. Square symbols are used for Category 1–3 data, and small diamond symbols for the Category 4 data. The error bars on the data indicate the laboratory analytical error. The solid lines show the complete distribution in the borehole simulated in the fracture system, and the dashed lines are for the matrix.*

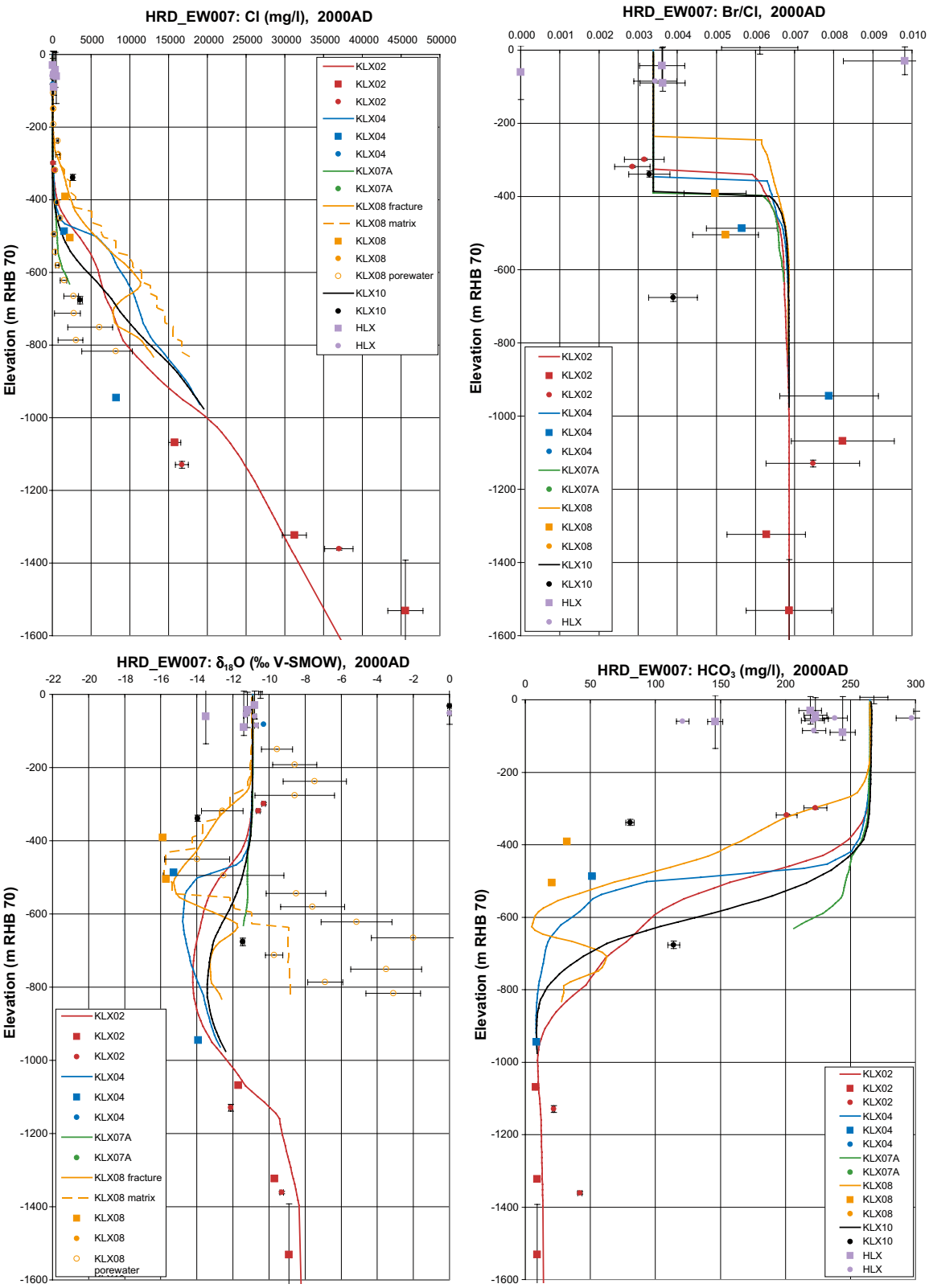

Figure 9-6. *Comparison of the modelled and measured Cl, Br/Cl, $\delta^{18}O$ and HCO_3 in the fracture system for boreholes in HRD_EW007. Square symbols are used for Category 1–3 data, circles are used for the porewater data, and small diamond symbols for the Category 4 data. The error bars on the data indicate the laboratory analytical error. The solid lines show the complete distribution in the borehole simulated in the fracture system, and the dashed lines are for the matrix.*

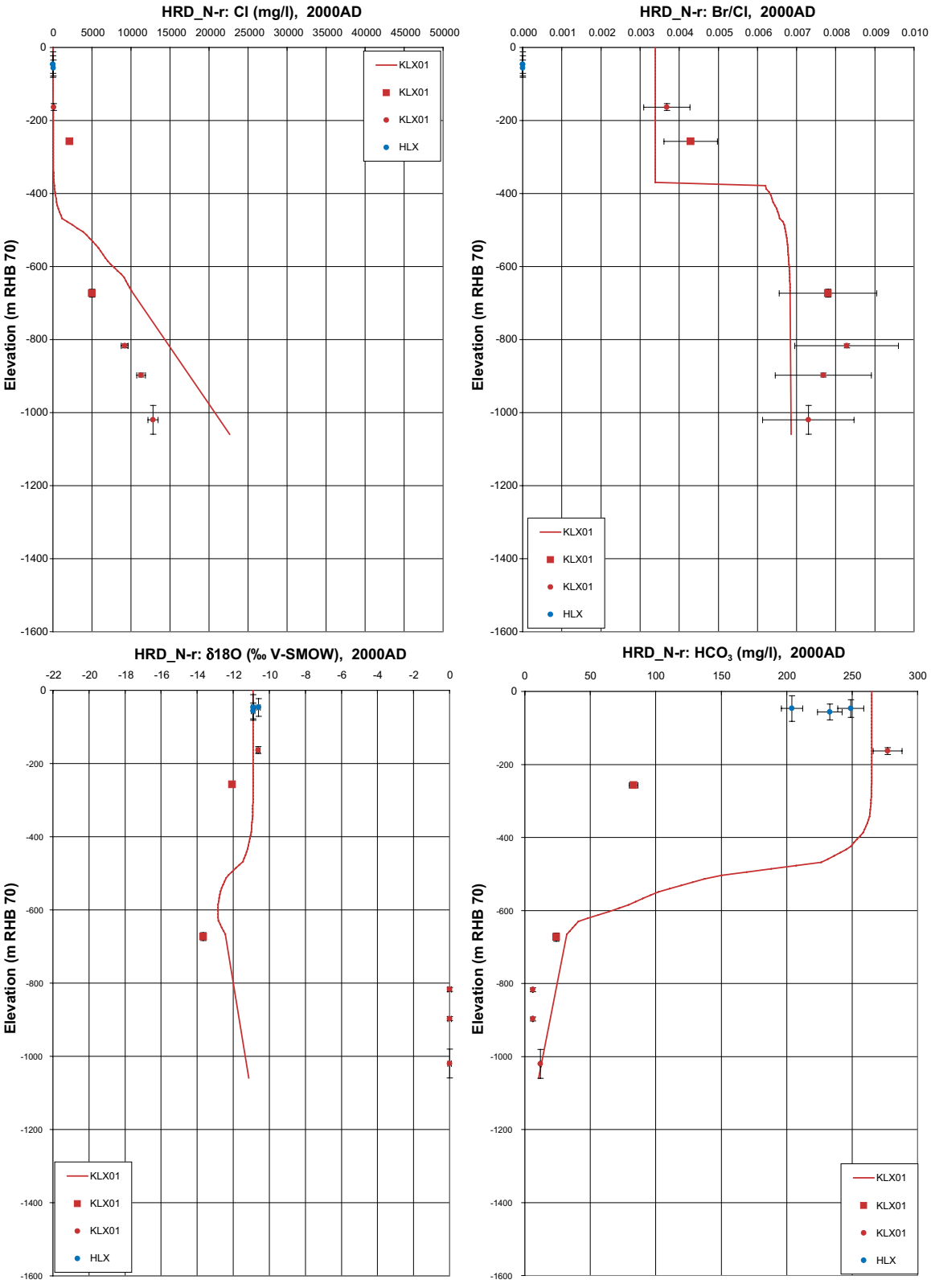

Figure 9-7. *Comparison of the modelled and measured Cl, Br/Cl, $\delta^{18}O$ and HCO3 in the fracture system for boreholes in HRD_N-recharge. Square symbols are used for Category 1–3 data, and small diamond symbols for the Category 4 data. The error bars on the data indicate the laboratory analytical error. The solid lines show the complete distribution in the borehole simulated in the fracture system, and the dashed lines are for the matrix.*

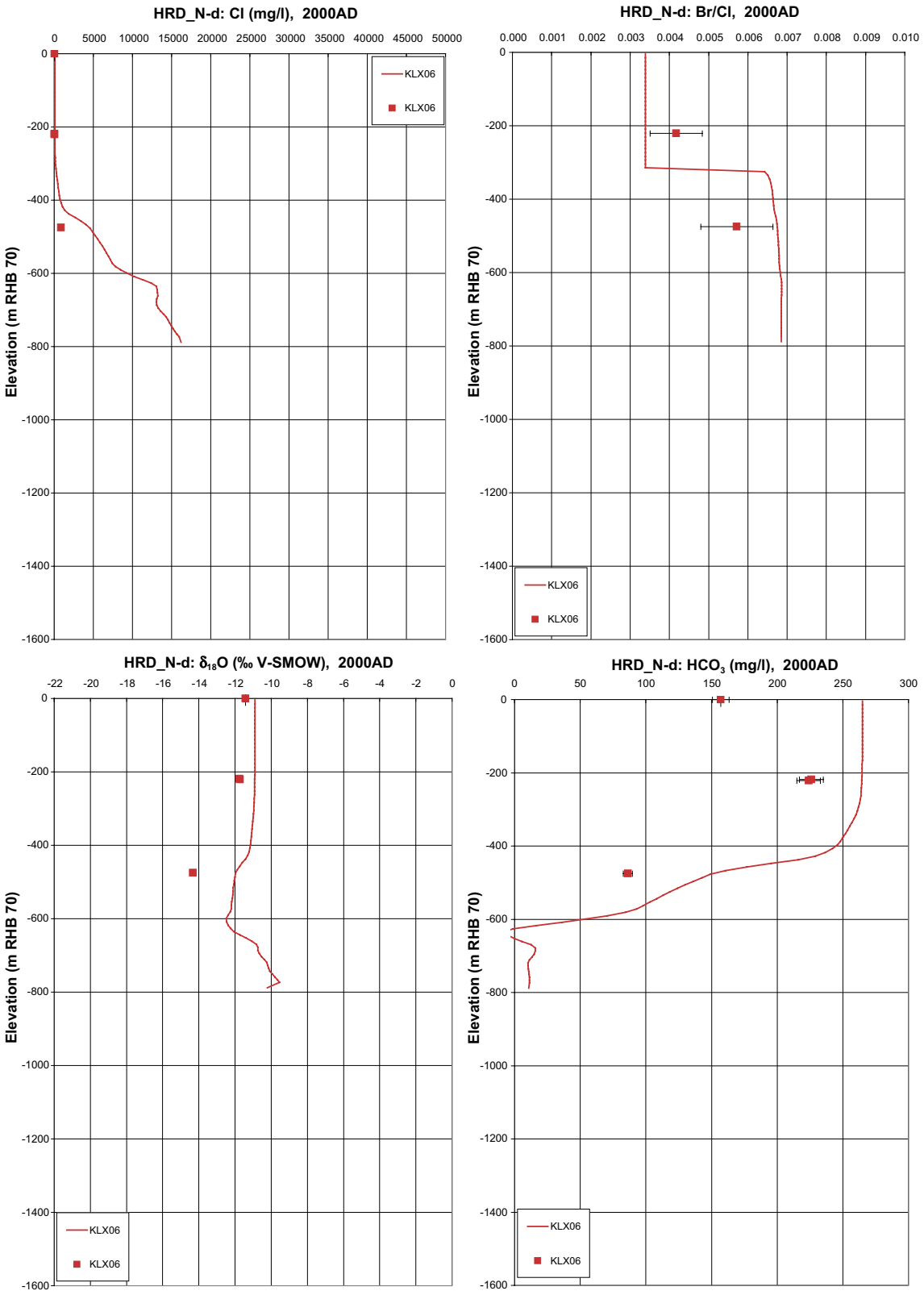

Figure 9-8. *Comparison of the modelled and measured Cl, Br/Cl, $\delta^{18}O$ and HCO_3 in the fracture system for boreholes in HRD_N-discharge. Square symbols are used for Category 1–3 data, and small diamond symbols for the Category 4 data. The error bars on the data indicate the laboratory analytical error. The solid lines show the complete distribution in the borehole simulated in the fracture system, and the dashed lines are for the matrix.*

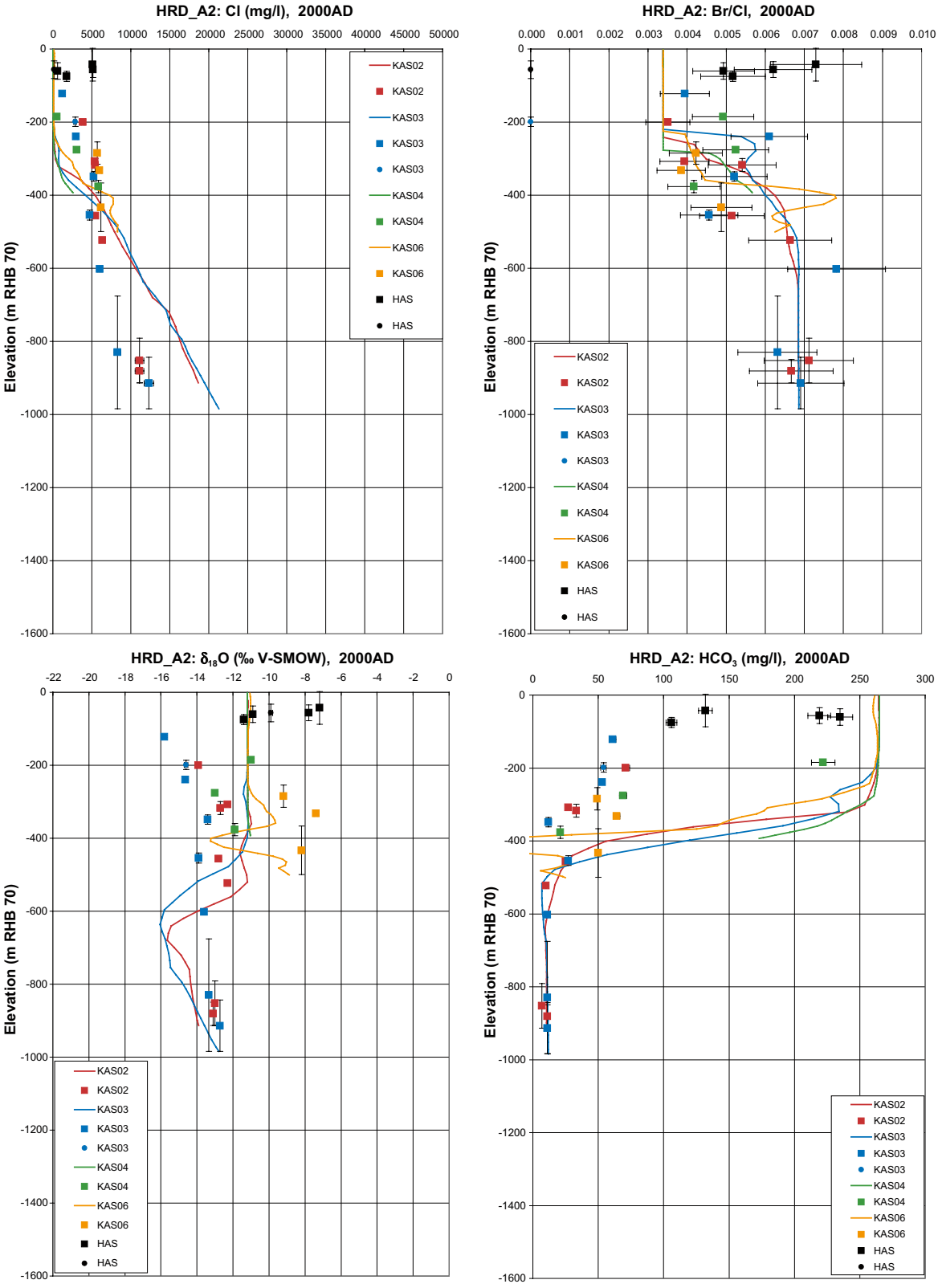

Figure 9-9. *Comparison of the modelled and measured Cl, Br/Cl, $\delta^{18}O$ and HCO_3 in the fracture system for boreholes in HRD_A2. Square symbols are used for Category 1–3 data, and small diamond symbols for the Category 4 data. The error bars on the data indicate the laboratory analytical error. The solid lines show the complete distribution in the borehole simulated in the fracture system, and the dashed lines are for the matrix.*

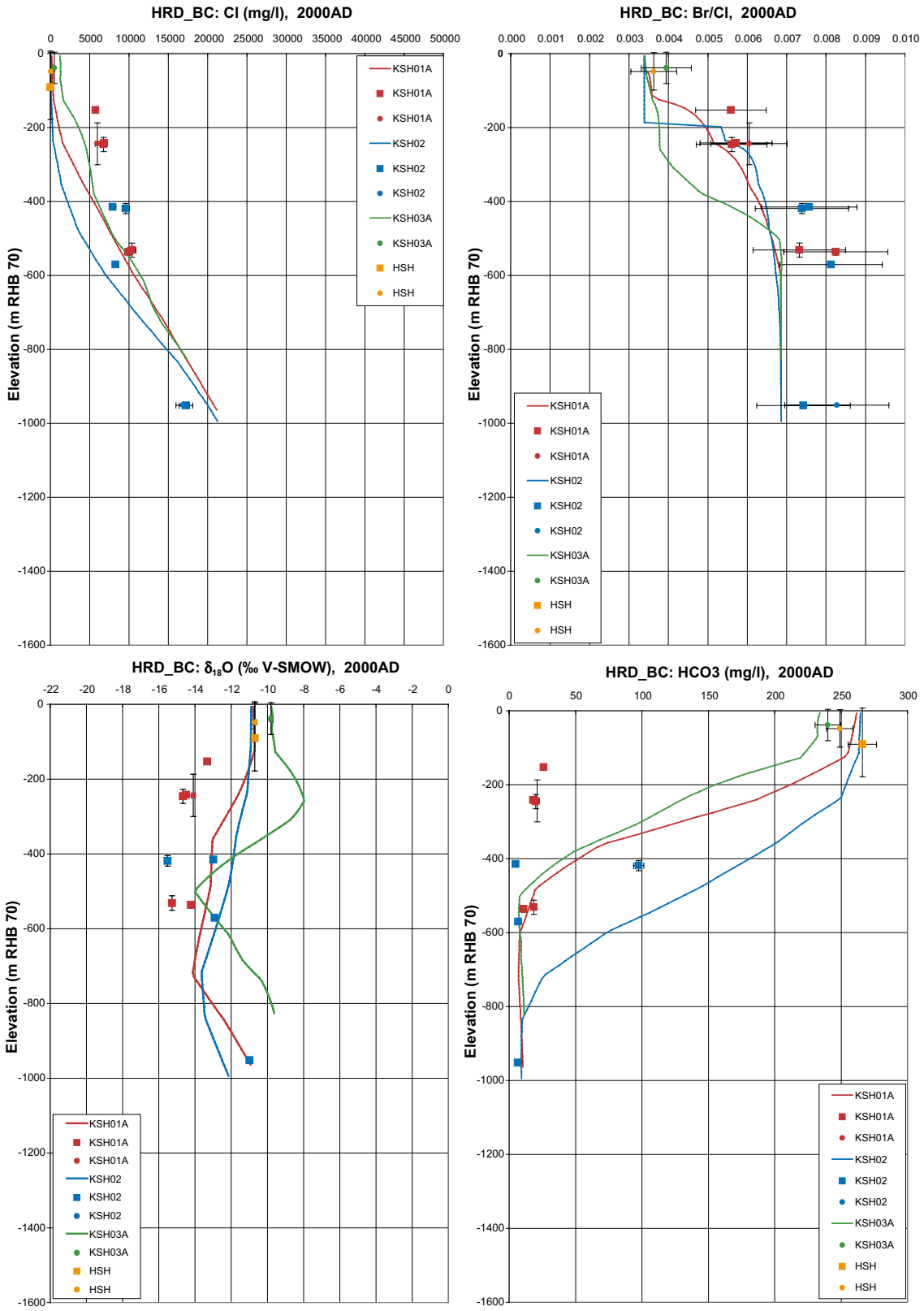

Figure 9-10. *Comparison of the modelled and measured Cl, Br/Cl, $\delta^{18}O$ and HCO_3 in the fracture system for boreholes in HRD_BC. Square symbols are used for Category 1–3 data, and small diamond symbols for the Category 4 data. The error bars on the data indicate the laboratory analytical error. The solid lines show the complete distribution in the borehole simulated in the fracture system, and the dashed lines are for the matrix.*

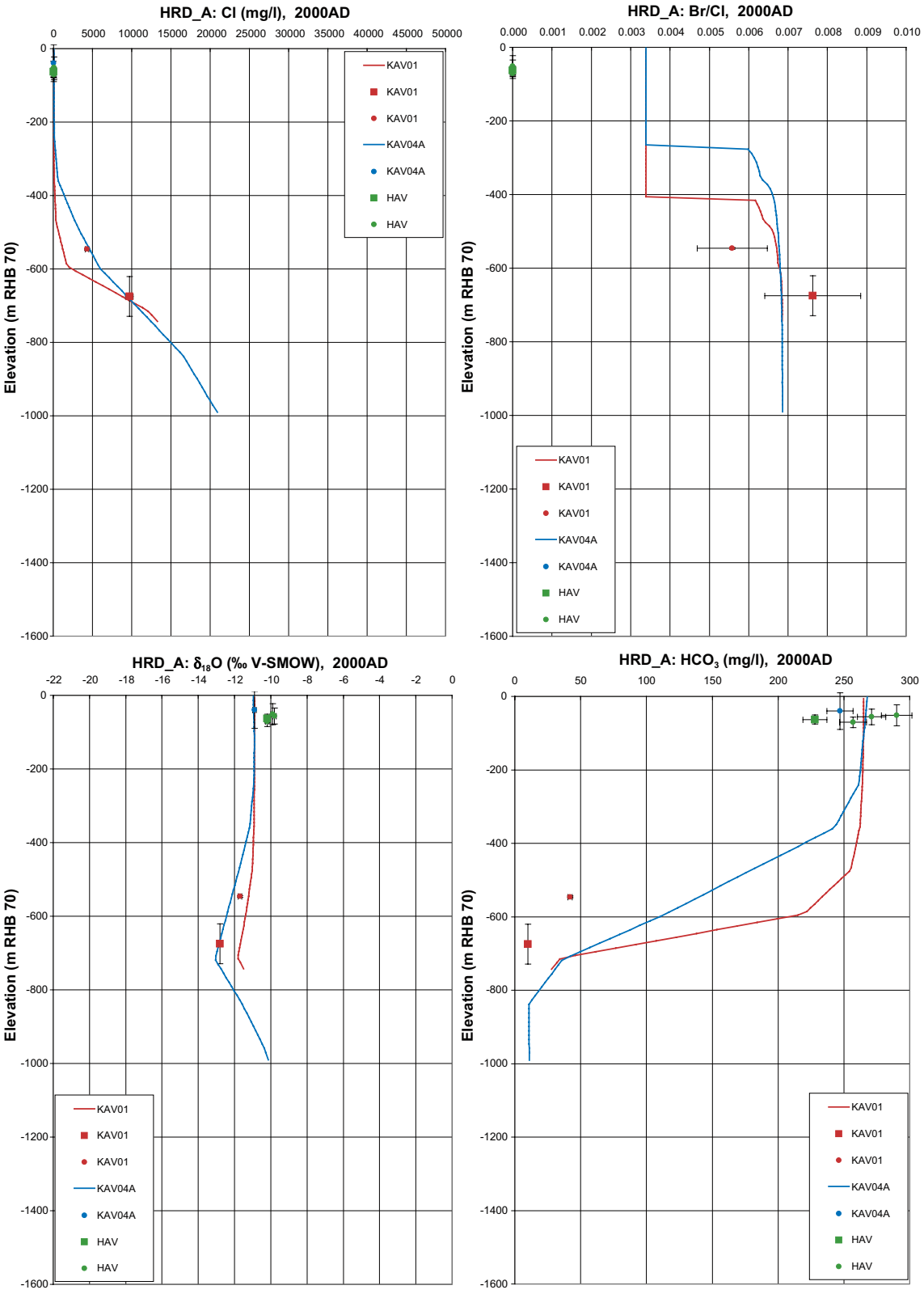

Figure 9-11. *Comparison of the modelled and measured Cl, Br/Cl, $\delta^{18}O$ and HCO_3 in the fracture system for boreholes in HRD_A. Square symbols are used for Category 1–3 data, and small diamond symbols for the Category 4 data. The error bars on the data indicate the laboratory analytical error. The solid lines show the complete distribution in the borehole simulated in the fracture system, and the dashed lines are for the matrix.*

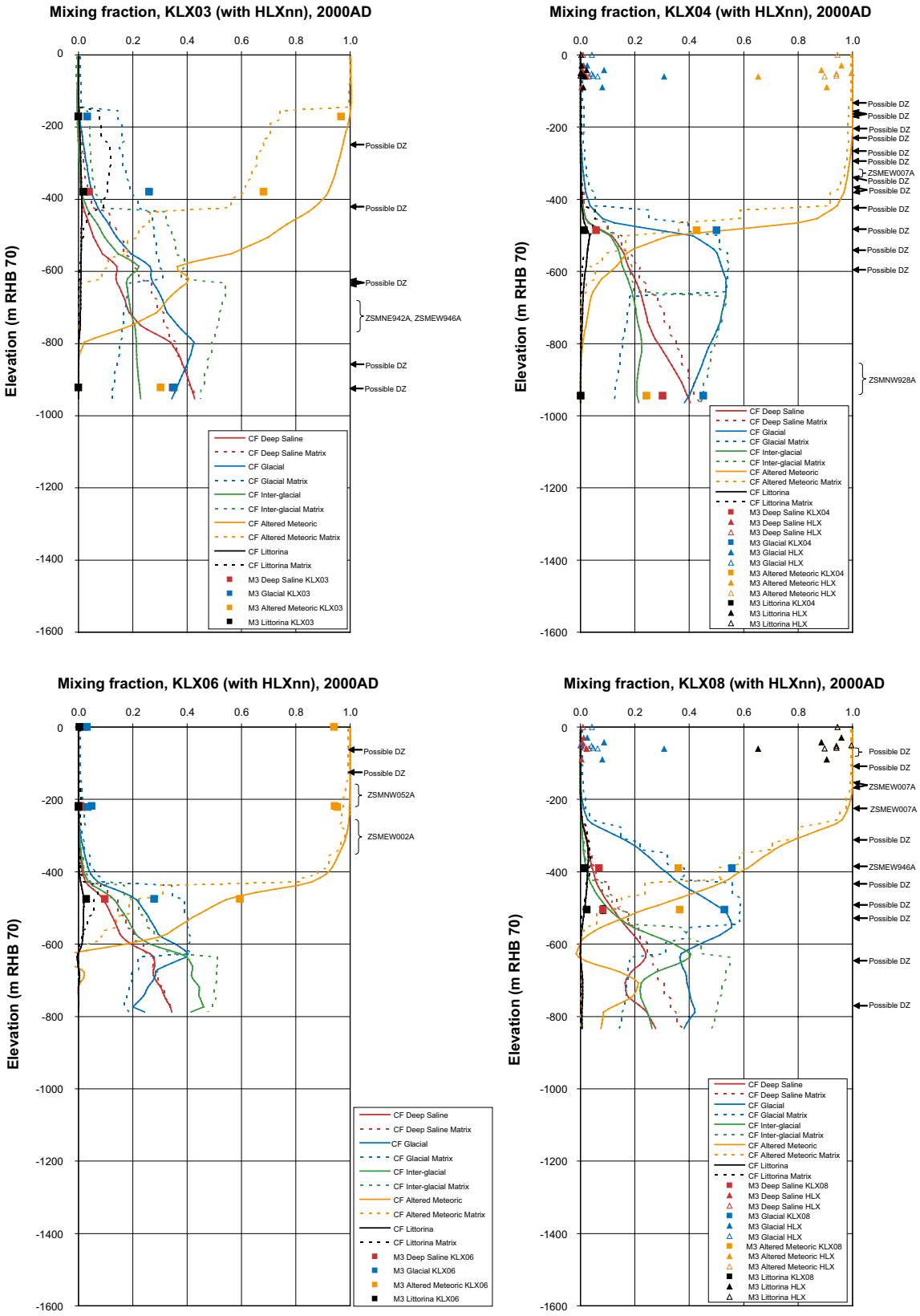

Figure 9-12. *Illustration of simulated mixtures of reference water mass fractions in boreholes KLX03, KLX04, KLX05 and KLX08. Solid lines show simulated reference water mass fractions for Deep Saline, Littorina, Altered Meteoric, Glacial and Inter-glacial porewater in the fracture system; dashed correspond to the reference water mass fractions in the matrix. The points show the mixture of four reference waters (Deep Saline, Littorina, Altered Meteoric, Glacial and Inter-glacial porewater) interpreted from ground-water samples by the M3 method.*

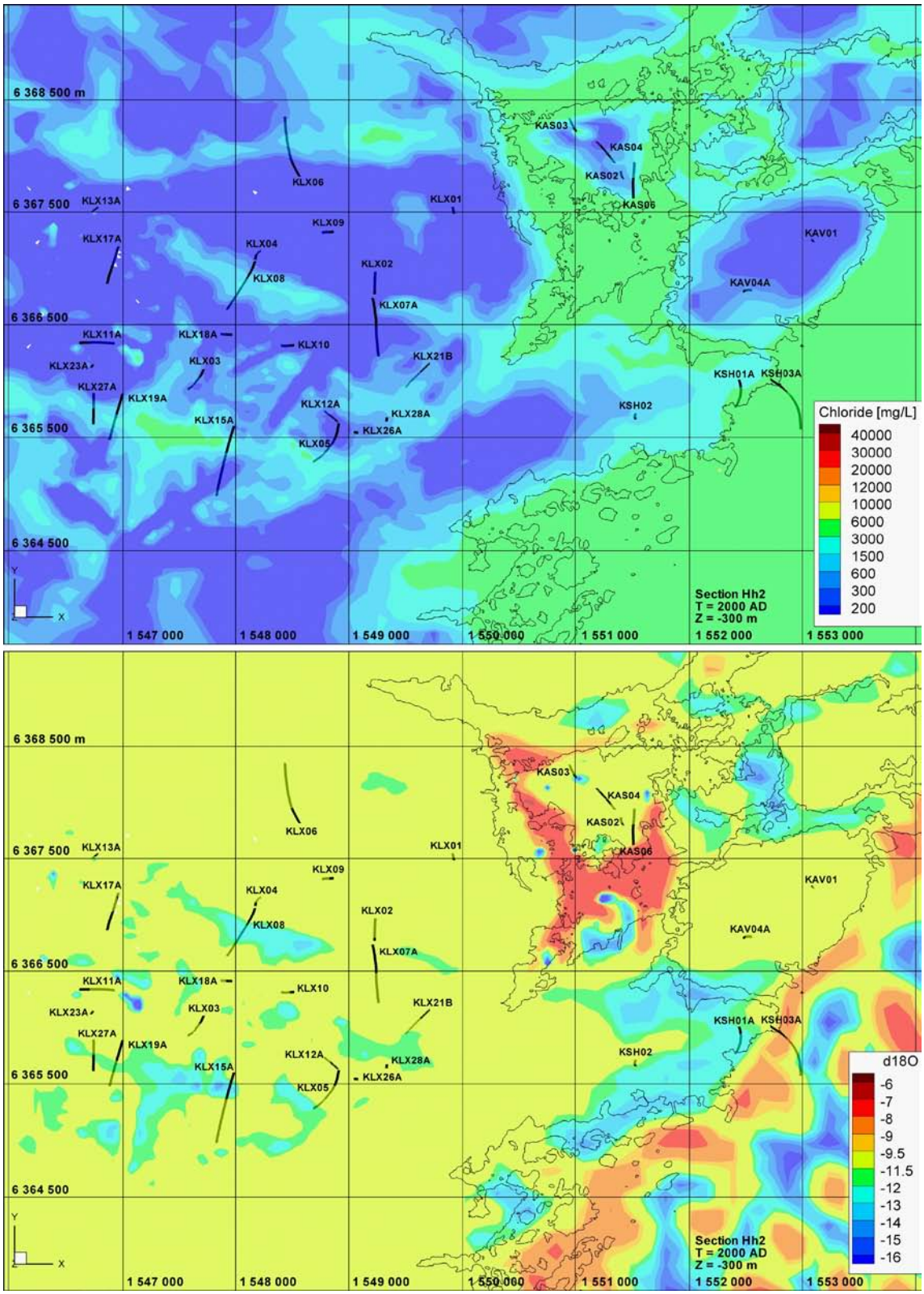

Figure 9-13. *Distribution of Cl (top) and $\delta^{18}O$ (bottom) predicted on a horizontal slice at –300 m covering the Laxemar-Simpevarp area through the base case model.*

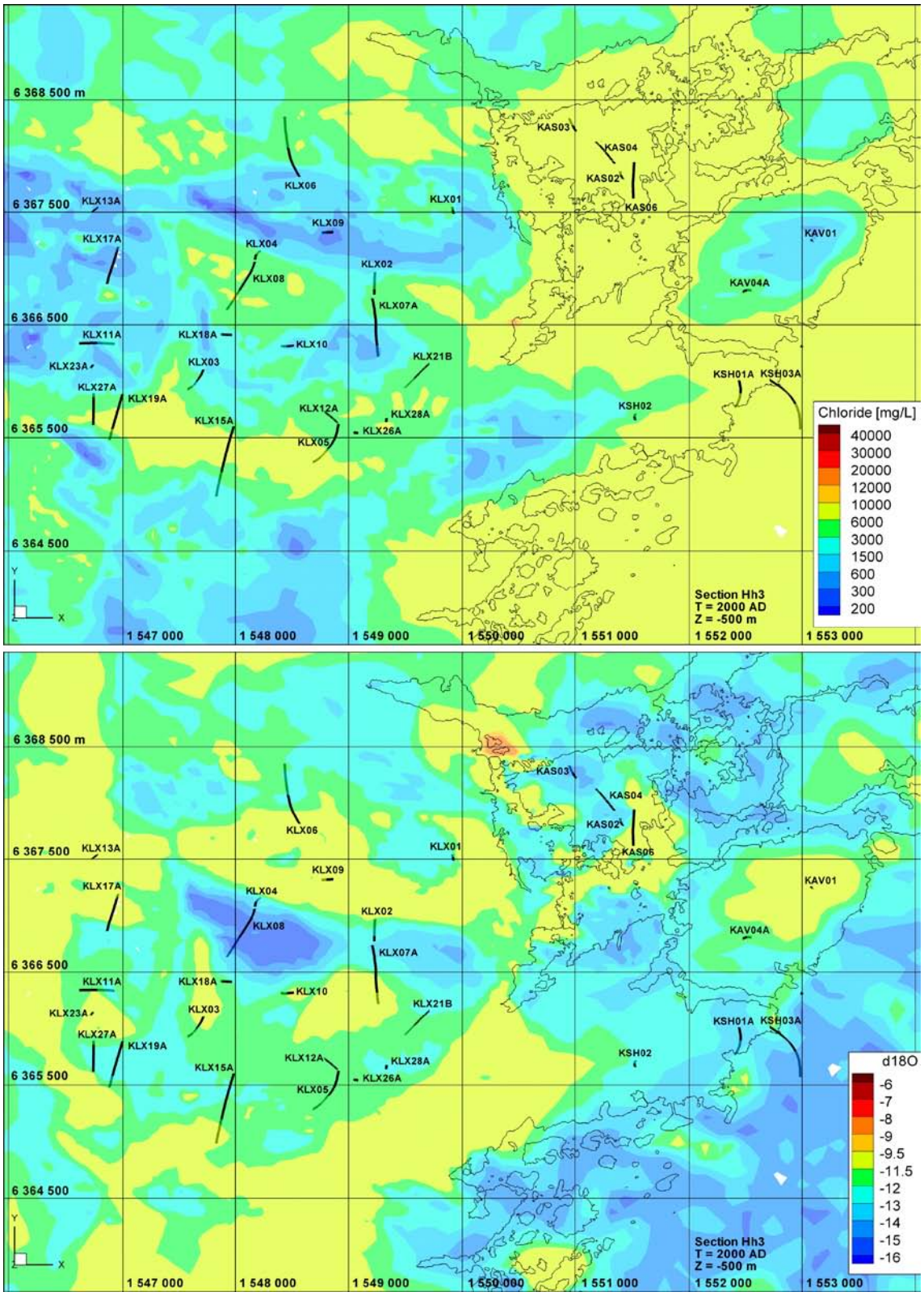

Figure 9-14. *Distribution of Cl (top) and $\delta^{18}O$ (bottom) predicted on a horizontal slice at –500 m covering the Laxemar-Simpevarp area through the base case model.*

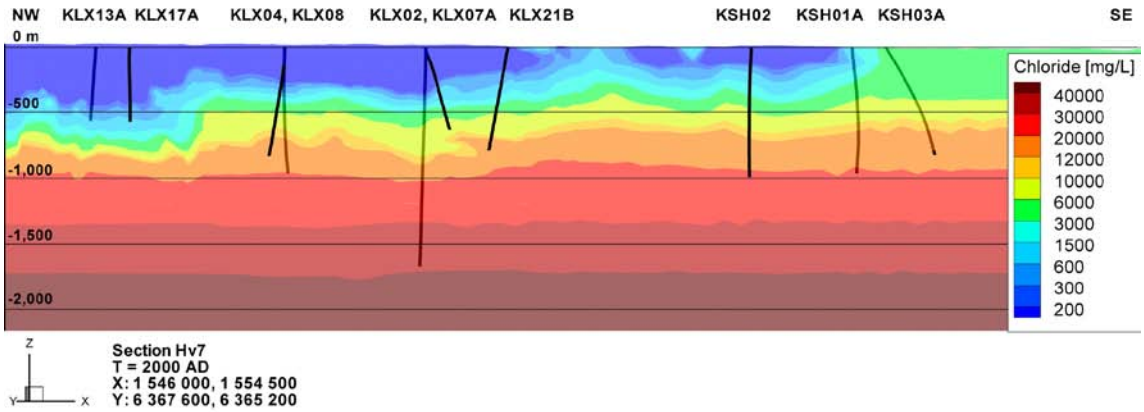

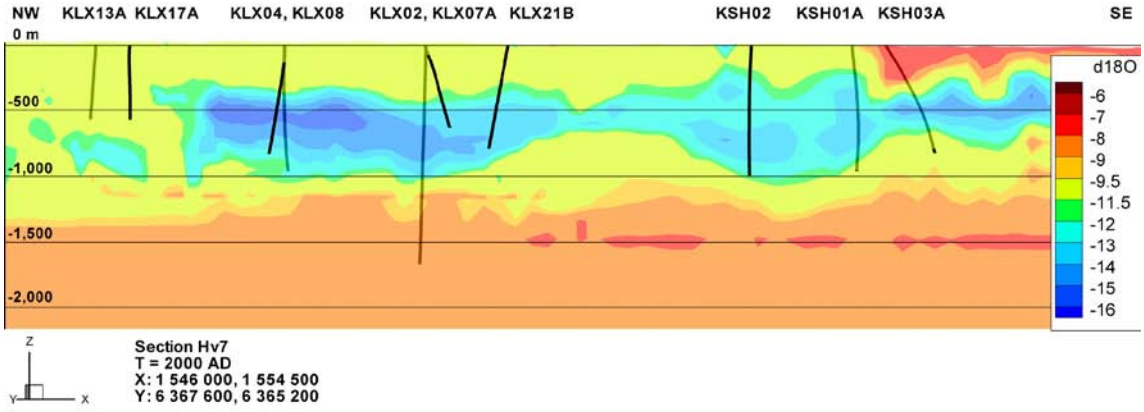

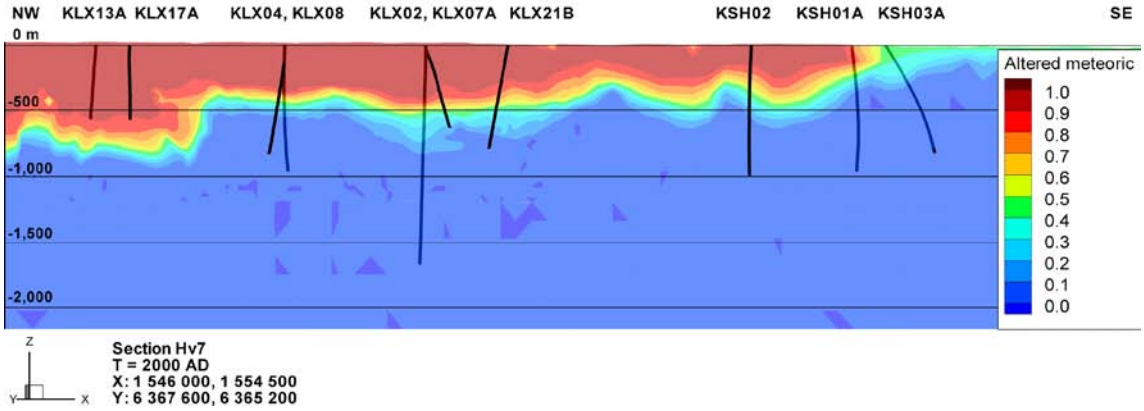

Figure 9-15. *Distribution of Cl (top) and $\delta^{18}O$ (middle) and Altered meteoric (bottom) predicted by the base case on vertical slice (7: see Appendix 9 for details) covering the Laxemar-Simpevarp area.*

9.1.4 Illustration of sensitivities considered in the calibration

Around 30 variant simulations were performed to quantify the sensitivity of the palaeo-hydrogeology calibration to the hydraulic properties of the HRD and HCD, as well as initial and boundary conditions. These are summarised in Table 9-1 along with brief comments on the effects on the simulated present-day hydrogeochemistry resulting from each variant relative to the base case. Detailed illustrations of the results for these sensitivity variants that may be compared with the base case results in Figure 9-1 to Figure 9-11 are included in Appendix 9.

The effects of spatial heterogeneity in the HCD and HRD are illustrated in more detail in Figure 9-16 through Figure 9-19 for the case with std.(Log(T)) = 1.4 in the HCD. The plots compare the minimum, mean and maximum of chosen chemical constituents across 10 realisations for KLX03, LX04, KLX05 and KLX08 with the base case.

Several variants were made to illustrate why changes were made in the calibration using uncalibrated HCD, or uncalibrated HRD, or both, or a variant without anisotropy in the HCD, all demonstrate a significant deterioration in the match to hydrogeochemistry data. The case with both uncalibrated HCD and HRD is based directly on the transmissivities and Hydro-DFN specified in /Rhén et al. 2008/, which gave a very poor match to the hydrogeochemistry data since it predicted virtually no *Glacial Water* remaining, for example. Changes to HSD made little difference.

The variant based on a change to the hydrochemical boundary conditions to assume the freshwater specified on the top surface to be *Altered Meteoric Water* prior to 4500 BC rather than *Glacial Melt Water* made little difference to the simulated present-day hydrogeochemistry.

Three variants on the initial condition were considered. The first had an alternative initial mixture of reference waters in the fractures and porewater corresponding to Case 2 in Section 7.8.3. This case predicted saline groundwater to be slightly deeper, and to have a *Littorina Water* component about 2–3 times higher than the base case. The second variant allowed more time for diffusive exchange (i.e longer equilibration time) between the initial condition in the fracture and matrix porewater (see Section 7.8.3), which only affects the levels of $\delta^{18}O$ in the fractures and matrix resulting in less *Glacial Melt Water* in the fracture water. Shorter equilibration times tend to improve the match for the fracture water, but degrade the match to the porewater for $\delta^{18}O$. The third variant uses the composition of *Inter-glacial Water* endorsed by the ChemNet Group referred to as 'Case 2' in Table 5-8 (Note: the initial amount of *Deep Saline* water in the matrix was reduced for this variant since *Inter-glacial porewater* is brackish in this case). This gave very similar results apart from predicting slightly lower salinity in the porewater below –500 m which is more consistent with the data.

Two further variants were considered as possible ways of improving the palaeohydrogeological calibration beyond that achieved for the base case. The first was to implement an enhanced fracture surface area per unit volume for rock matrix diffusion of solutes (σ in Equation 7-8) in the HCD based on the values suggested in Table 7-4 for the flow-wetted surface parameter, a_r, used in particle tracking. ConnectFlow treats σ as a property of the hydrogeological rock units rather than as a function associated with each finite-element, and hence modifying σ for the finite-elements intersected by each HCD required modifications to ConnectFlow. Such code changes were not available in time to be included the base case. This variant gave the best results overall, especially for boreholes intersecting major HCD, since the increased fracture surface area in the HCD retarded the mixing from where advection was greatest and suggests a methodology improvement to correlate σ with hydraulic conductivity, since both correlate strongly to connected open fracture intensity. The second variant considered a higher hydraulic conductivity in the top 150 m of bedrock. This variant also gave a significant improvement to the match, one affecting more boreholes than the first variant, but to a lesser degree overall.

Table 9-1. Variants considered in the palaeohydrogeology calibration and sensitivity studies. The effects on simulated borehole chemistry profiles are commented relative to the *base case model*.

Variant	Summary of effects on palaeohydrogeology
HCD/HRD: 10 realisations of HRD and HCD (std.(Log(*T*)) = 1.4)	Mean salinity curve, meteoric flushing and glacial water generally 50–100 m (more in KLX03) deeper than in the base case. Variability in depth to brackish water between realisations is 50–100 m. $\delta^{18}O$ and HCO_3 are the most sensitive to spatial heterogeneity.
HCD/HRD: 10 realisations of HRD and HCD (std.(Log(*T*)) = 0.7)	Mean salinity curve, meteoric flushing and glacial water often 50 m deeper than in the base case (i.e. worse). Variability in depth to brackish water between realisations is 50–100 m. $\delta^{18}O$ and HCO_3 are the most sensitive to spatial heterogeneity.
HCD/HRD: Initial uncalibrated model	Salinity and meteoric flushing generally about 200 m deeper than the base case. Very little remnant of glacial water in any borehole. A poor match.
HCD: Initial uncalibrated model	Salinity and meteoric flushing often about 50–200 m deeper than the base case. Lens of glacial water ~50 m shallower and very small in magnitude. A worse match.
HCD: no transverse anisotropy	Salinity and meteoric flushing 200 m deeper in KLX19A: not consistent with data. A worse match.
HCD: enhanced fracture surface area: σ (×3) relative to adjacent HRD	*Deep Saline* retained 50–100 m shallower in some boreholes. Meteoric flushing penetration 200 m shallower in KLX03 and KLX15A, 50–100 m less in other boreholes intersected by HCD; less meteoric water in KLX13A and KLX17A. *Littorina water* retained in KLX15A. Improved match to $\delta^{18}O$ in HRD_EW007 (KLX08, KLX10), HRD_W (KLX11A, KLX19A), and HRD_C (KLX03). An improvement on the base case.
HRD: Initial uncalibrated model	Salinity and meteoric flushing often about 50–100 m deeper than base case, and salinity weaker in magnitude (i.e. worse). Lens of glacial water ~50 m shallower and very small in magnitude.
HRD: higher K_h (×3) above –150 m	Salinity and meteoric flushing often about 20–50 m shallower than base case. $\delta^{18}O$ slightly elevated. An improvement relative to the base case.
HSD: Initial uncalibrated model	Very little difference.
BC: meteoric surface water before 4500 BC	Little difference. Cl 10 m deeper in matrix. meteoric flushing 20 m deeper in HRD_W, 10 m deeper in HRD_C.
IC: equilibration time = 20,000 years	Mainly affect $\delta^{18}O$ giving more *Inter-glacial Porewater* than *Glacial Melt Water* in the fracture water (i.e. slightly worse).
IC: *Deep saline Water* initially deeper	Salinity in fractures and matrix 100 m deeper. *Deep Saline* 100–150 m deeper. 2–3 higher Mg concentration (still < 40 mg/L in Laxemar local model area). Meteoric flushing about 20 m deeper (i.e. slightly worse).
IC: Alternative composition for inter-glacial porewater (“case 2”)	Very similar results to base case. Slightly improved match to salinity in pore-water and $\delta^{18}O$ in fractures.

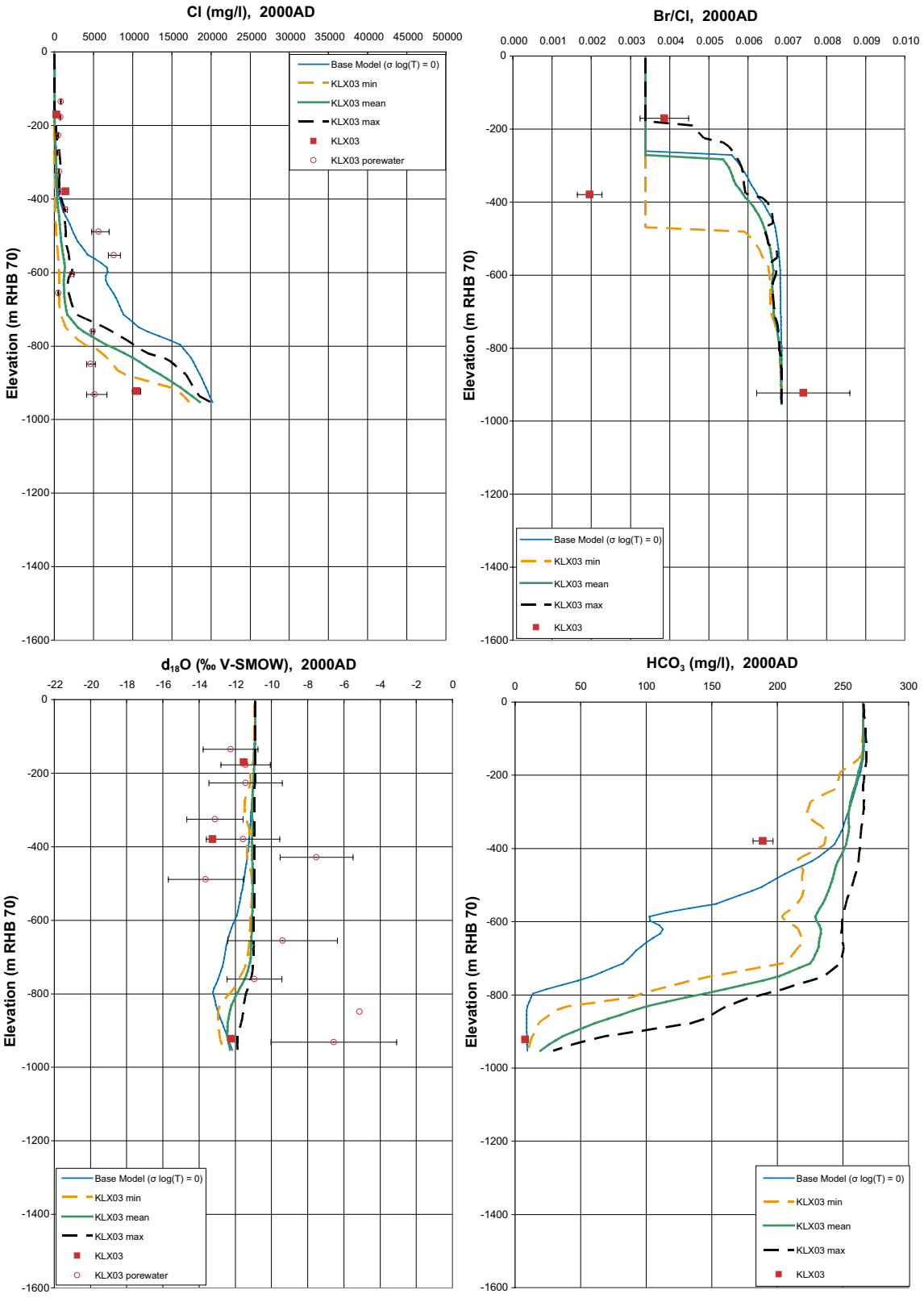

Figure 9-16. *Examples of stochastic variability of Cl, Br/Cl, $\delta^{18}O$ and HCO_3 in the fracture system for 10 realisations of HCD and HRD (mean: solid green line; min: dashed orange; max: dashed black; base case: solid blue) compared to data in KLX03. Square symbols are used for Category 1–3 data, circles are used for the porewater data, and small diamond symbols for the Category 4 data. The error bars on the data indicate the laboratory analytical error.*

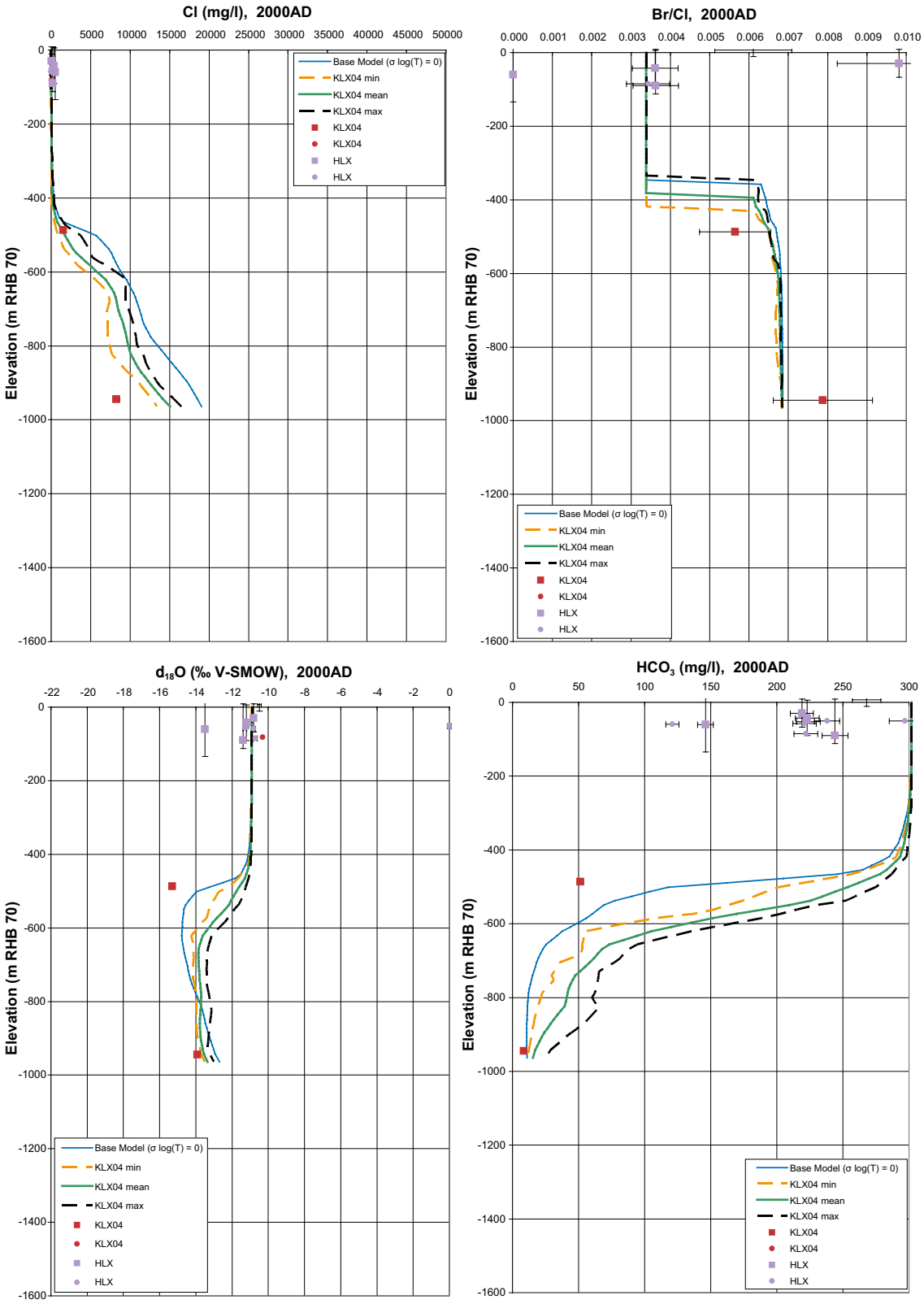

Figure 9-17. *Examples of stochastic variability of Cl, Br/Cl, $\delta^{18}O$ and HCO_3 in the fracture system for 10 realisations of HCD and HRD (mean: solid green line; min: dashed orange; max: dashed black; base case: solid blue) compared to data in KLX04. Square symbols are used for Category 1–3 data, and small diamond symbols for the Category 4 data. The error bars on the data indicate the laboratory analytical error.*

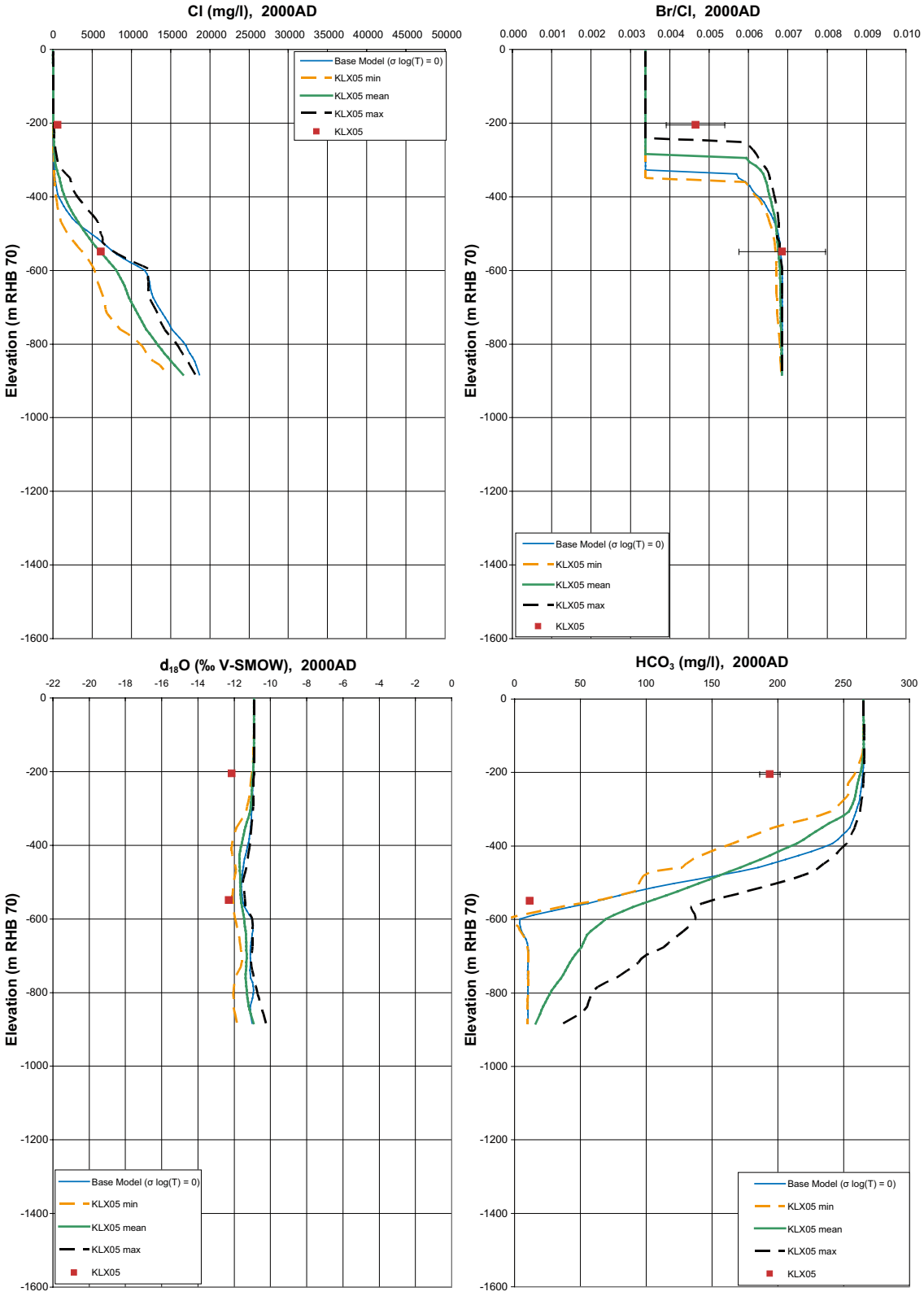

Figure 9-18. *Examples of stochastic variability of Cl, Br/Cl, $\delta^{18}O$ and HCO_3 in the fracture system for 10 realisations of HCD and HRD (mean: solid green line; min: dashed orange; max: dashed black; base case: solid blue) compared to data in KLX05. Square symbols are used for Category 1–3 data, and small diamond symbols for the Category 4 data. The error bars on the data indicate the laboratory analytical error.*

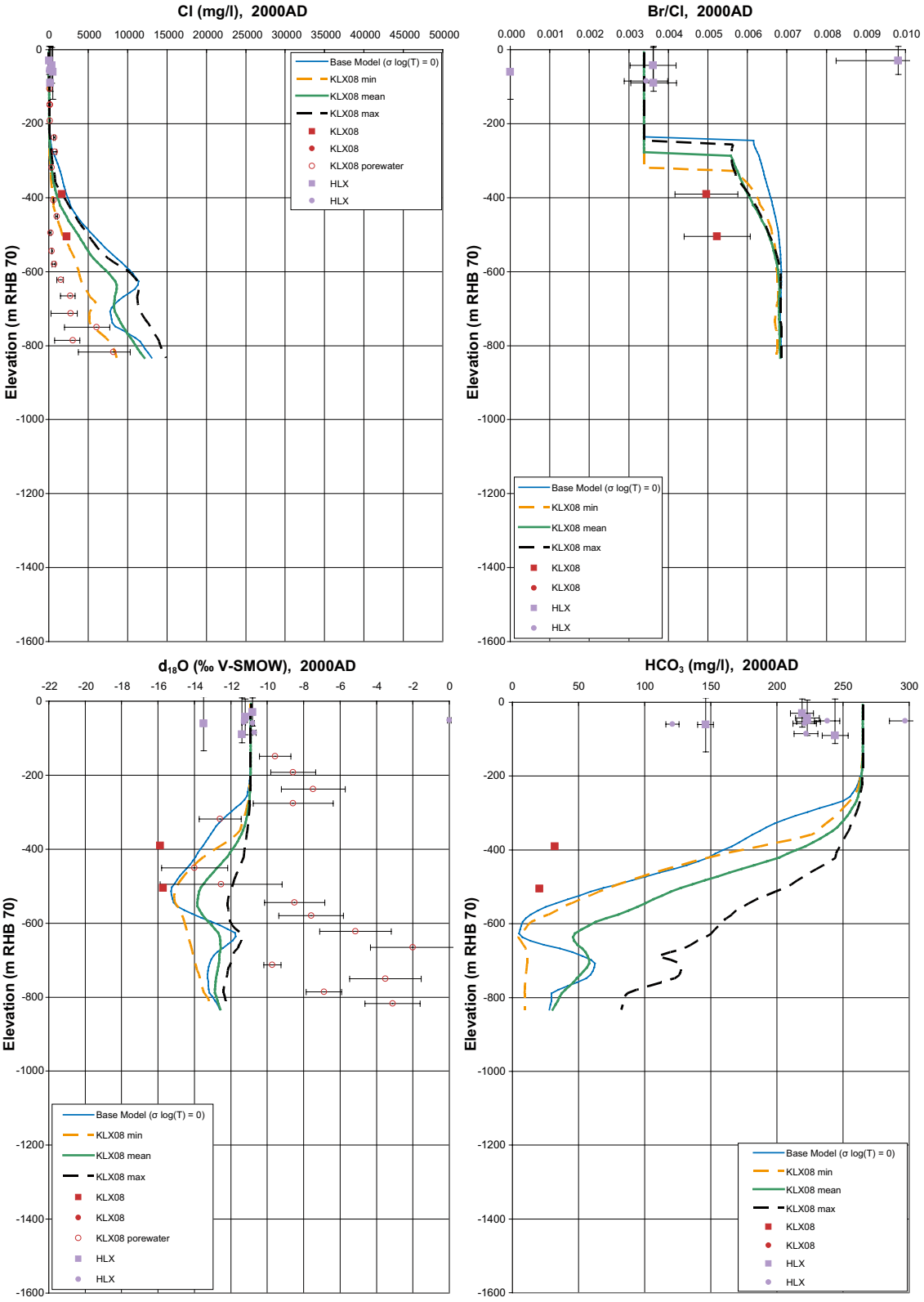

Figure 9-19. *Examples of stochastic variability of Cl, Br/Cl, $\delta^{18}O$ and HCO_3 in the fracture system for 10 realisations of HCD and HRD (mean: solid green line; min: dashed orange; max: dashed black; base case: solid blue) compared to data in KLX08. Square symbols are used for Category 1–3 data, circles are used for the porewater data, and small diamond symbols for the Category 4 data. The error bars on the data indicate the laboratory analytical error.*

9.2 Conclusions

9.2.1 Hydrochemical conceptual model

Combining the interpretation of hydraulic characteristics of the bedrock from /Rhén et al. 2008/ with the understanding gained from simulating the palaeohydrogeological evolution, the hydrogeological situation in terms of groundwater flow and solute transport is summarised in Table 9-2. This description focuses on the balance between advective solute transport and the effect of rock matrix diffusion RMD, as suggested by the measured hydrochemical data. This balance will be affected by the natural hydraulic gradients present during the current climate period, and is subject to change during periods of elevated gradient, e.g. during deglaciation.

Other remarks on the Palaeohydrogeological conceptual model are as follows:

- The boundary conditions assessed on the top surface, covered by the Baltic Sea and its precursors, require that a shore displacement curve slightly higher than suggested for SDM-Site Laxemar be used in the base case palaeohydrogeological model in order to reproduce some small (< 10%) localised remnants of *Littorina Sea Water* as suggested by Br/Cl and Mg in samples (e.g. KLX01, KLX08 and KLX15A).
- The results are not very sensitive to the boundary conditions applied on land before the start of the Littorina period (6500 BC), as it mainly affects the top –150 m, which is later replaced by still more modern meteoric water.
- The initial conditions for fracture groundwater below c. –650 m can be defended as being similar to the present values due to the low frequency of conductive fractures and the increasing salinity both of which limit the groundwater flow rate in the perspective of c. 10,000 years. The properties of porewater below this depth is uncertain due to the few samples and the hydrochemistry in the matrix being a result of processes that act on timescales far longer than the Holocene considered here. In order to reproduce the difference in $\delta^{18}O$ in porewater and fracture water suggested by measured data, then the addition of the Inter-glacial Porewater reference is required. The difference in $\delta^{18}O$ can then be described in terms of the distance of a porewater sample from a flowing feature since the time for diffusive exchange scales quadratically with this distance, and typical matrix blocks sizes increase dramatically with depth. However, the composition and origin of this water is of course uncertain and non-distinct.
- Above c. –150 m the evolution of hydrochemistry is sufficiently rapid such that the results are not sensitive to the initial condition. The relatively rapid mixing in this depth zone is confirmed by simulations of tritium migration using the tritium arising from bomb-tests during the last 60 years as a tracer.
- In the interval –150 to –600 m the palaeohydrogeology results are however dependent on the hydraulic parameters, solute transport parameters (fracture surface area in particular) and initial conditions. However, the data suggest the hydrochemical situation in this depth range being relatively consistent between boreholes throughout Laxemar, despite there being large differences in heterogeneity of hydraulic properties between boreholes. This seemingly stable of hydrochemistry is thought to result from a balance between advective flow and RMD, both of which governed by fracture intensity, i.e. the two effects are correlated. Hence, when fracture intensity is low, advective transport is reduced, but when fracture intensity is increased, then exchange with the matrix is increased, and so is the penetration of the solute mixing front is retarded more by RMD. Such a correlation needs to be further developed in the conceptual and numerical models.
- The assessed variants for salinity in the initial conditions at different elevations have limited effect. When the initial *Deep Saline Water* composition was generally at a higher elevation than at present, the remaining Littorina fraction in the Laxemar local model area was about 2–3%. When the Deep saline water composition assumed similar to today, then slightly more Littorina water persisted, around 5–6% in the Laxemar local model area. It is difficult to say which of these alternatives is the more plausible.
- A variant that used the final composition of Inter-glacial Porewater (essentially the composition of Porewater below –600 m, cf case 2 in Table 5-8) endorsed by the ChemNet Group gave very similar results apart from predicting slightly lower salinity in the porewater below –500 m which is more consistent with the data.

Table 9-2. Schematic summary of groundwater flow and solute transport characteristic under the current temperate climate conditions.

Depth zone	General characteristics
dZ1: > –150 m	Advection dominated – high groundwater flow rates with sub-horizontal fracturing giving $K_h > K_v$ in many areas. Flushed by post-glacial meteoric water. High fracture intensity implies matrix blocks 1–2 m in size, which gives equilibrium between fracture and matrix on timescales of ~1,000 years.
dZ2: –150 m to –400 m	Some advection, but rock matrix diffusion (RMD) retards post-glacial meteoric penetration. Fracture intensity is generally much lower, reducing groundwater flux and increasing matrix blocks to typically ~5 m in size, such that porewater chemistry lags behind that of the fracture water by 1,000 s years. In more fractured areas, RMD is more effective, and consequently slows down mixing.
dZ3: –400 m to –650 m	Low advection. RMD important because advective flow rates are small. Fracture intensity lower still, with typical matrix blocks ~10 m in size, such that porewater chemistry lags behind that of fracture water ~10,000 years. Expect some difference between fracture and porewater chemistries.
dZ4: < –650 m	Very low advection. RMD dominates. Fracture intensity very low, with typical matrix blocks ~100 m in size, such that porewater chemistry lags behind that of fracture water ~100,000 years. Difference between fracture and porewater chemistries are to be expected.

9.2.2 HCD

- A slight reduction, by a multiplication factor of 1/3 below –150 m, in the interpreted HCD transmissivity was found beneficial to the palaeohydrogeology calibration.
- Since conductive fracture intensity is higher in the deformation zones it implies that the fracture surface area available for diffusive exchange of solute with the matrix, i.e. RMD, should be higher than in the HRD. This is currently difficult to implement in ConnectFlow for solute transport, and was not included in the base case. However, a variant that included a three times higher fracture surface area in the HCD gave a marked improvement to the palaeohydrogeology calibration for several boreholes. It implies that enhancing fracture surface area outside of the HCD, such as in minor deformation zones, might also improve palaeohydrogeology simulations. Consequently, a more general correlation between surface area and hydraulic conductivity would be the best representation of the coupled groundwater flow and solute transport.
- The calibration also benefitted from deriving kinematic porosity based on fracture intensity of the deformation zone rather than using as an empirical relationship to interpreted transmissivity.
- Introducing lateral and vertical heterogeneity (stochastic variation) in the HCDs, which is considered more realistic than the base case, generally caused more flushing of the system and in some cases pushes the post-glacial meteoric flushing well below the measurement values.

9.2.3 HRD

- Introducing several realisation of the hydrogeological DFN provides a means to study the variability which one has to accept when comparing with measurements. The results indicate that a vertical variation of 50 to 100 m between realisations of the fracture groundwater is expected (though also incorporating the effect of the variation generated by the stochastic variation of HCDs).
- The mean intensity of conductive fracture intensity within the depth zones as described by the hydrogeological DFN model compares well with the expected time ranges for equilibration between fracture groundwater and porewater discussed in Section 9.2.1. One can also conclude from the expected variation of intensity of conductive fracture frequency within the depth zones, as described by the hydrogeological DFN, model that there should be some near-surface rock where the fracture groundwater and porewater is not in equilibrium.

- Increasing the horizontal conductivity of HRD in the top –150 m reduces post-glacial meteoric flushing at greater depths and hence improves the match. Such a scenario is within the uncertainty in interpreting the measured data, which is sparse in the top 100 m of bedrock. Comparing with Chapter 8, if such a change were made to the base case it would improve the match to both natural groundwater heads and hydrochemistry.
- The values of kinematic porosity used based on the fracture volume of connected open fractures seem appropriate and range from about 10^{-4} at depth to about $2 \cdot 10^{-3}$ in the upper bedrock.
- Fracture surface area per unit volume (σ in Equation 7-8) has particular importance since it controls the importance of RMD. Using $\sigma = 2 \times P_{10,corr}$(PFL-f) seems to give appropriate levels of RMD. In the base case this formula was used to estimate average values of σ for each HRD and depth zone for use in the solute transport equations. It would be more realistic to calculate σ based on upscaling the connected open fracture intensity based on the underlying hydrogeological DFN model. There are however practical problems in doing this for regional scale DFN models since it is usually necessary to truncate the fracture size distribution. Although flow through a rock block may not be sensitive to removing the smallest fractures, σ and kinematic porosity are likely to be more sensitive, and one would need to compensate for the truncation in some way. The expected result would be a correlation between σ and kinematic porosity and equivalent hydraulic conductivity since all depend strongly on the intensity of open connected fractures, which would enhance RMD where fracture intensity is highest in a particular realisation.

9.2.4 HSD

The results are not very sensitive to the HSD properties. The base case includes anisotropy such that the vertical hydraulic conductivity is 10 times lower than the horizontal. Anisotropy was introduced to improve simulations of the drawdown resulting from Äspö HRL, but this made very little difference to the simulations of palaeohydrogeology. The limited thickness of the Quaternary deposits and the relatively high hydraulic conductivity (compared to the bedrock) do not in a significant way effect the recharge of different reference water. It should be remembered that Altered Meteoric reference water is used in the simulation that has undergone major reactions (Calcite dissolution) in the Quaternary deposits and the very upper most part of bedrock.

10 Analysis of groundwater flow-paths

10.1 Flow-paths from a tentative repository layout

Following the calibration exercises, flow-paths from a tentative repository layout have been simulated for the base case and a limited number of key variants. The pathlines calculations are performed in the groundwater flow-field simulated for year 2000 AD (i.e. based on a snapshot in time, and not considering the future evolution of groundwater flow as the particles move in that flow). The flow-paths are simulated by releasing particles in relevant parts of HRD_C, HRD_EW007 and HRD_W with the approximate repository footprint positioned at –500 m. Initially, particle starting positions were considered within the Laxemar focused area on a 40 m by 40 m mesh, but those starting positions within the same element as a HCD are removed, leaving a total of 2,142 particles traced. This is illustrated in Figure 10-1 and Figure 10-2.

Figure 10-3 and Figure 10-4 show particle exit locations on the top surface of the model for pathlines released in the base case. Exit locations for a release from HRD_W are mostly localised to ZSMNW042A-west and ZSMNS059A; for HRD_C, their destinations are grouped around ZSMNW042A-east or ZSMNE005A; for HRD_EW007, the exit locations are associated with ZSMNE006A or ZSMNE012A.

10.1.1 Pathlines

As well as considering the discharge points it is interesting to consider the sub-surface paths taken by particles. Here, the pathlines followed by each particle are plotted, sorted according to the HRD that they start in, and identifying which HCD transport the most particles. Figure 10-5, Figure 10-6 and Figure 10-7 show the paths followed by particles starting in HRD_C, HRD_W and HRD_EW007, respectively. The pathlines are necessarily 3D, but are here shown in map view.

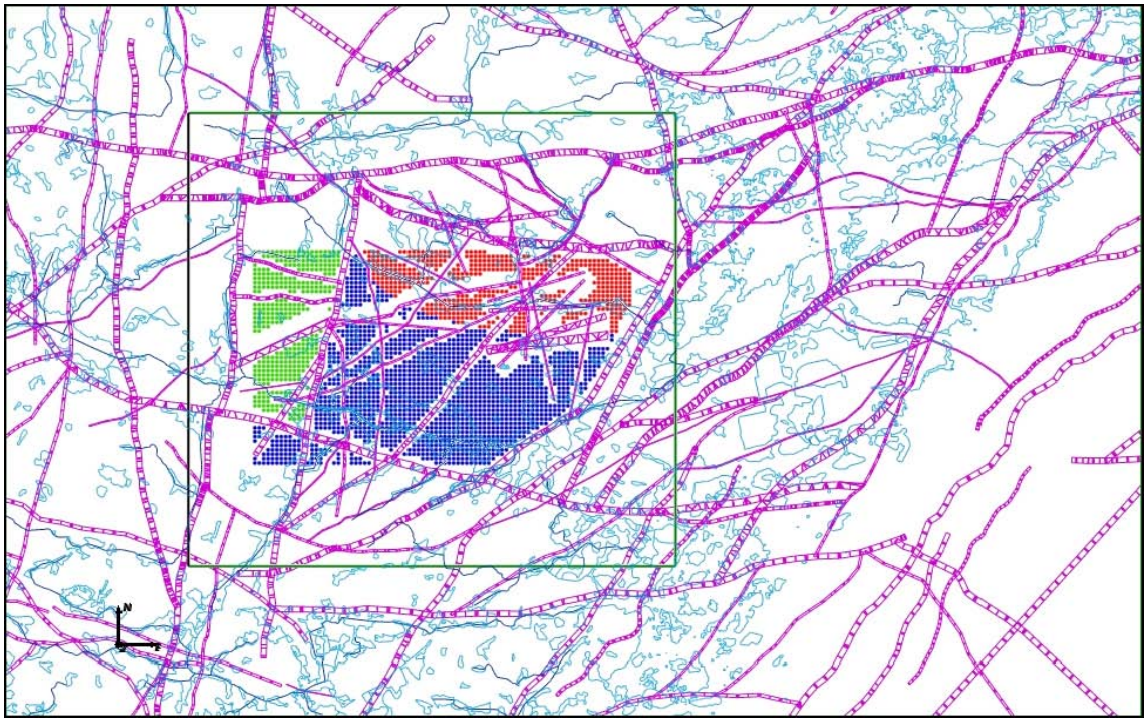

Figure 10-1. *Particle starting positions representing a tentative repository area in map view of a slice centred at –500 m. The green particles are starting in HRD_W, the red particles are starting in HRD_EW007 and the blue particles are starting in HRD_C. The particles are initially located in a 40 m by 40 m mesh at –500 m, but positions within HCD are omitted. HCDs are sliced at –500 m (purple), surface waterbodies (cyan), streams (blue), and the Laxemar local model area (green box) are indicated.*

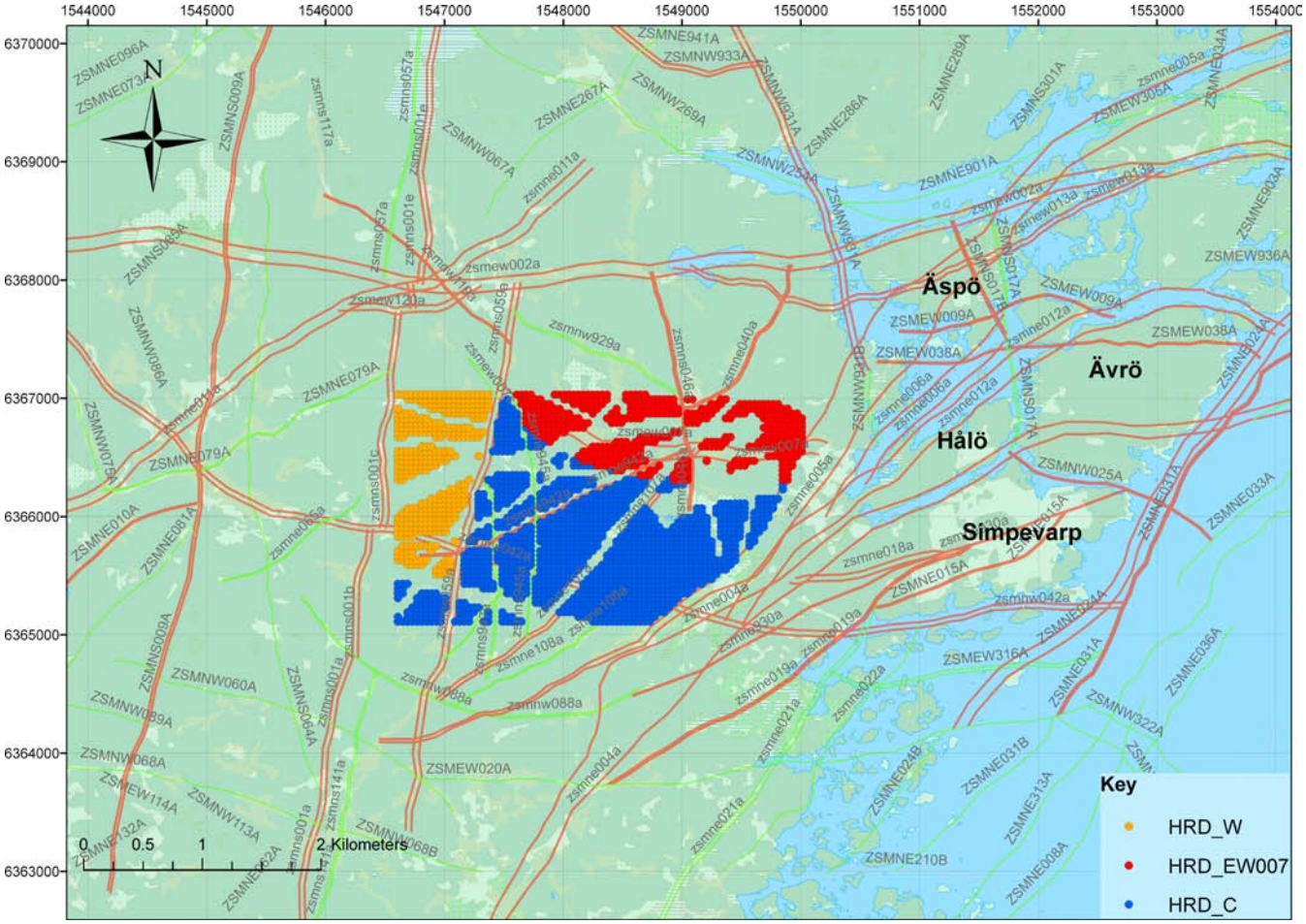

Figure 10-2. *Particle starting positions representing a tentative repository area in map view projected on the surface. The yellow particles are starting in HRD_W, the red particles are starting in HRD EW007 and the blue particles are starting in HRD_C. The particles are initially located at–500 m depth in a 40 m by 40 m mesh, but positions within HCD are omitted. The positions of HCD on the surface are indicated.*

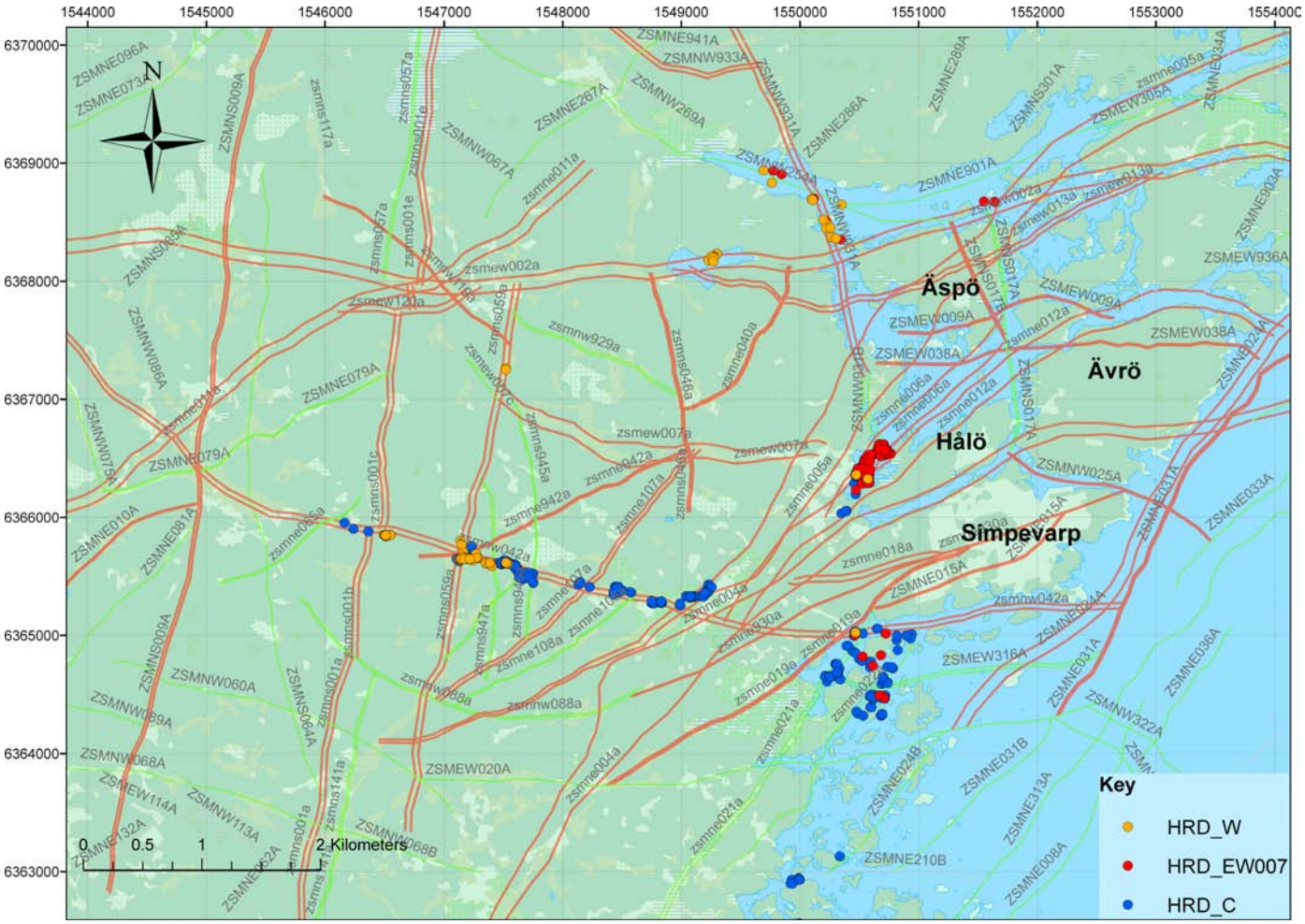

Figure 10-3. *Particle exit locations of pathlines released in HRD_C, HRD_EW007 and HRD_W for the base case and are coloured by the HRD they start in. The positions of HCD on the surface are indicated.*

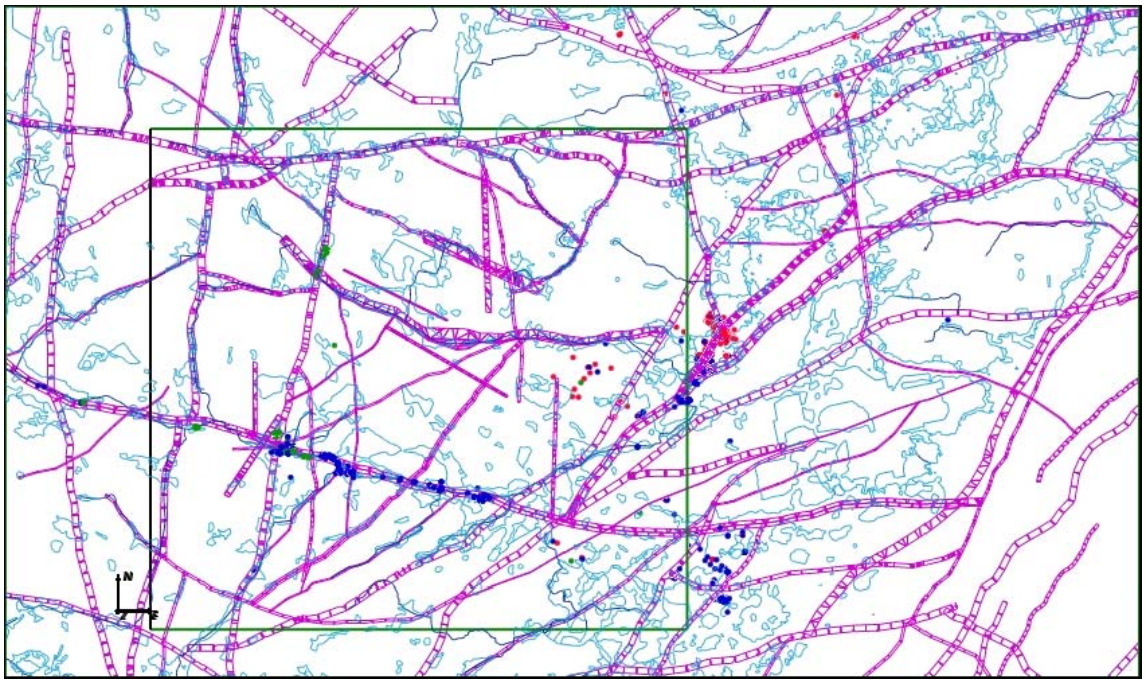

Figure 10-4. *Particle exit locations of pathlines released in HRD_C (blue), HRD_EW007 (red) and HRD_W (green) for the base case. HCDs on a slice at 0 m (purple), surface waterbodies (cyan), streams (blue), and the Laxemar local model area (green box) are superimposed. The start positions for these points are shown in Figure 10-1 with same corresponding colours.*

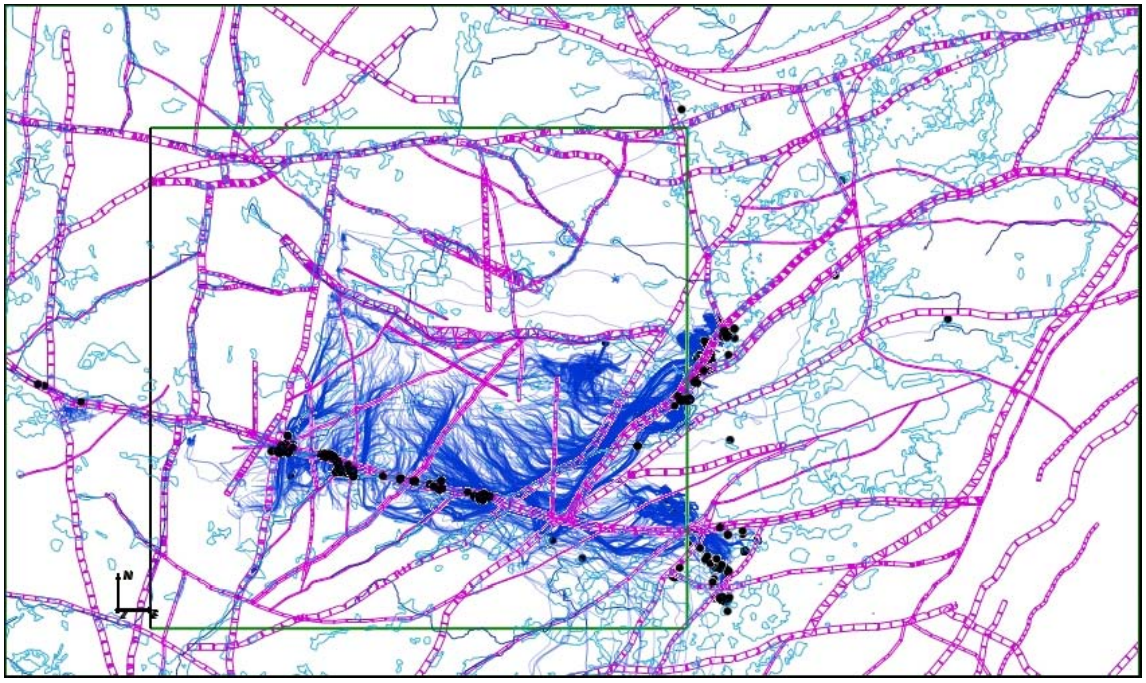

Figure 10-5. *Pathlines for the base case model. Pathlines starting in HRD_C are shown in blue with the exit locations (discharge) in black. HCDs at 0 m (purple), surface waterbodies (cyan), streams (blue), and the Laxemar local model area (green box) are superimposed. The start positions for these pathlines are the blue ones shown in Figure 10-1.*

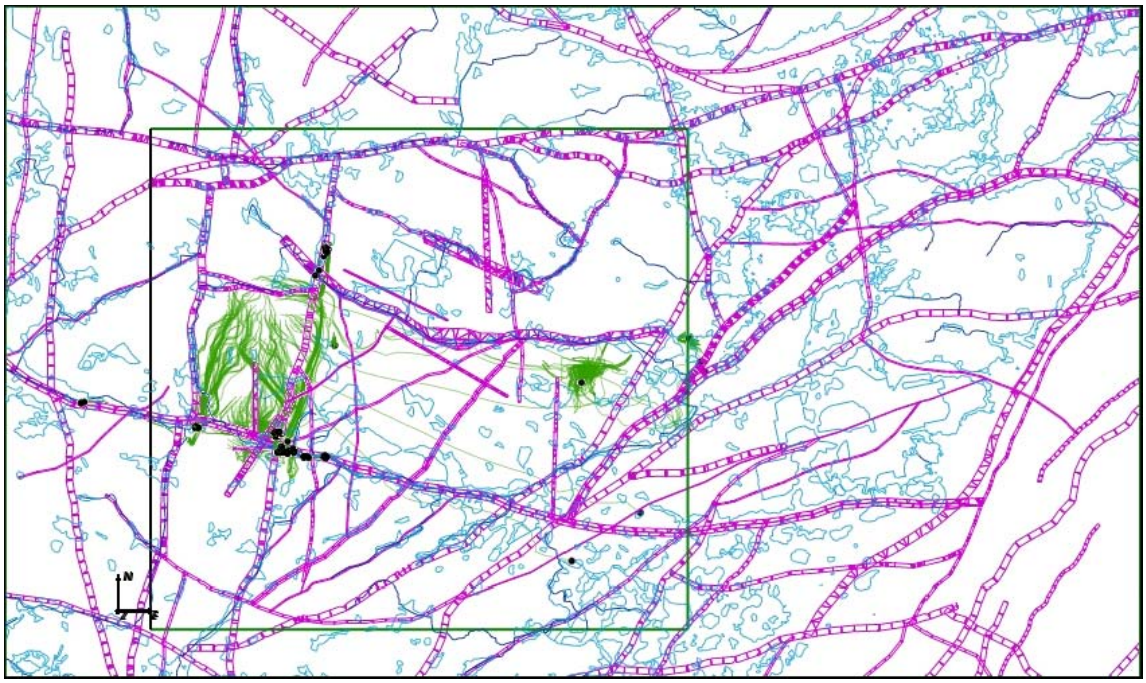

Figure 10-6. *Pathlines for the base case model. Pathlines starting in HRD_W are shown in green with the exit locations (discharge) in black. HCDs at 0 m (purple), surface waterbodies (cyan), streams (blue), and the Laxemar local model area (green box) are superimposed. The start positions for these pathlines are the green ones shown in Figure 10-1.*

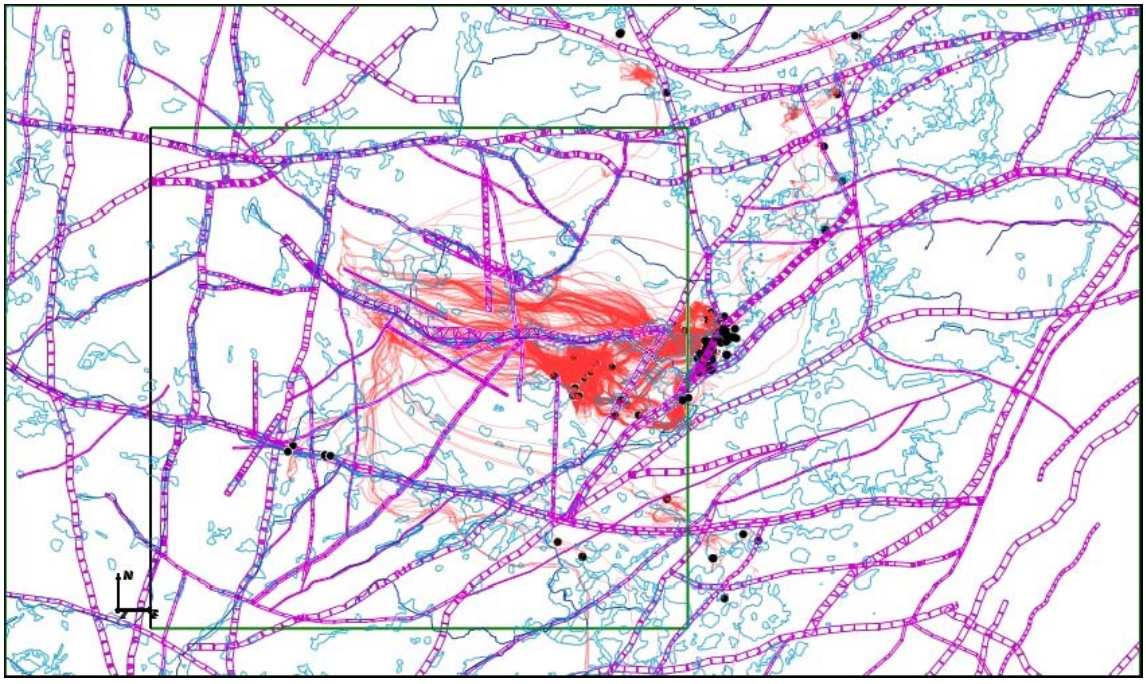

Figure 10-7. *Pathlines for the base case model. Pathlines starting in HRD_EW007 are shown in red with the exit locations (discharge) in black. HCDs at 0 m (purple), surface waterbodies (cyan), streams (blue), and the Laxemar local model area (green box) are superimposed. The start positions for these pathlines are the red ones shown in Figure 10-1.*

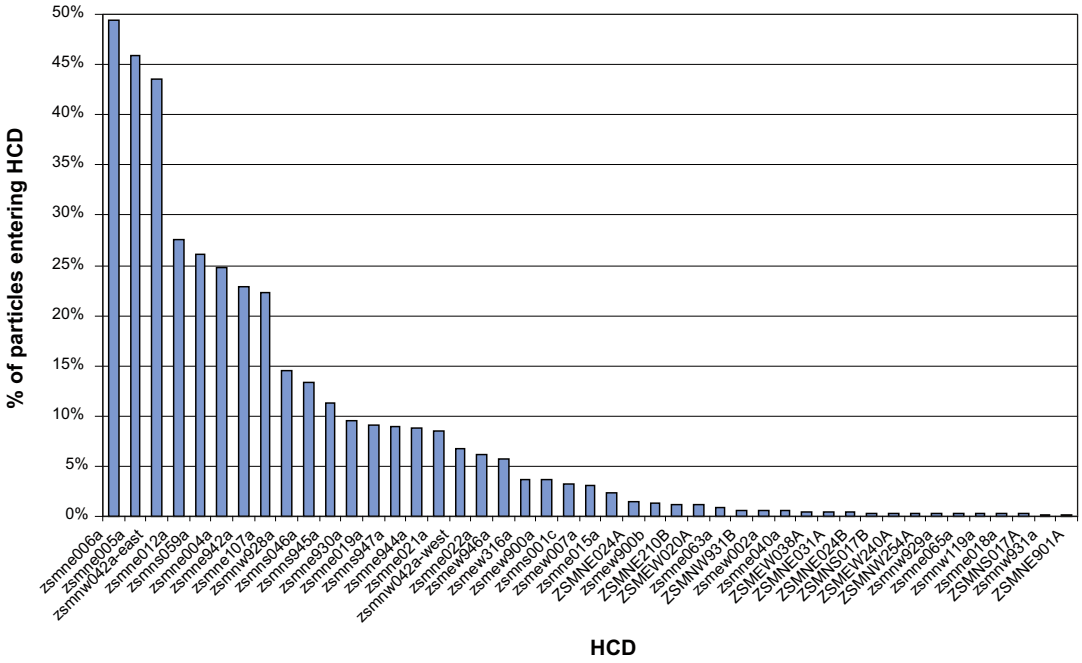

Figure 10-8. *Histogram showing the percentage of particles that enter each HCD along pathlines started at the 2,142 locations shown in Figure 10-1 for the base case. The HCD are ordered accordingly. Thus, almost 50% of particles enter ZSMNE006A. A particle may enter several HCD, and so the percentages add to > 100%.*

In HRD_C the particles generally head south toward ZSMNW042A or east toward ZSMNE005A and ZSMNE006A where they reach the bay near Äspö, with a few particles continuing further south-east to the Baltic south of the Simpevarp peninsula. For HRD_W, the flow-paths are hemmed in by the dolerite dykes associated with ZSMNS001C and ZSMNS059, and hence most discharge to the south in ZSMNW042A. For HRD_EW007, most particles follow ZSMEW007A eastward to discharge either in ZSMNE005A or in ZSMNE006A, where they reach the bay near Äspö.

In order to identify which HCD are most important for transport, the number of particles that enter each HCD is recorded, and then the HCD are ranked according to how many particles pass through them. This shows that ZSMNE005A, ZSMNW04A-east and ZSMNE006A form the downstream path for 40–50% of particles. ZSMNE012A, ZSMNE004A, ZSMNE107A, ZSMNS059A and ZSMNE942A all encounter about 20–30% of the particles.

10.2 Flow-paths indicating present-day recharge areas relevant to the repository volume

In addition to following flow-paths downstream with the advective velocity from the repository, it also informative to track particles upstream, reversing the Darcy velocity vector to trace back flow-paths from the repository to where the surface recharge comes from, and hence locate the origin of surface water that reaches the focused volume. The particles are tracked upstream until they reach the top surface based on the flow-field calculated at 2000 AD. This approach is deterministic since it identifies the unique flow-path that links a point in the focused volume to a point on the surface. It does not consider the divergence or convergence of flow near to this path, or how groundwater flow may have changed during the time it takes for a particle released at the surface to reach repository depth (backward pathlines suggest timescales of 10,000s years).

The backward pathlines for the base case are illustrated for HRD_C, HRD_W and HRD_EW007 in Figure 10-9, Figure 10-10 and Figure 10-11, respectively. The main recharge area for HRD_C is the low hills south of HRD_EW007 within the HRD_C area. South of ZSMNW042A, the recharge areas are some low hills further south, again very localised. For HRD_W, the recharge area is also

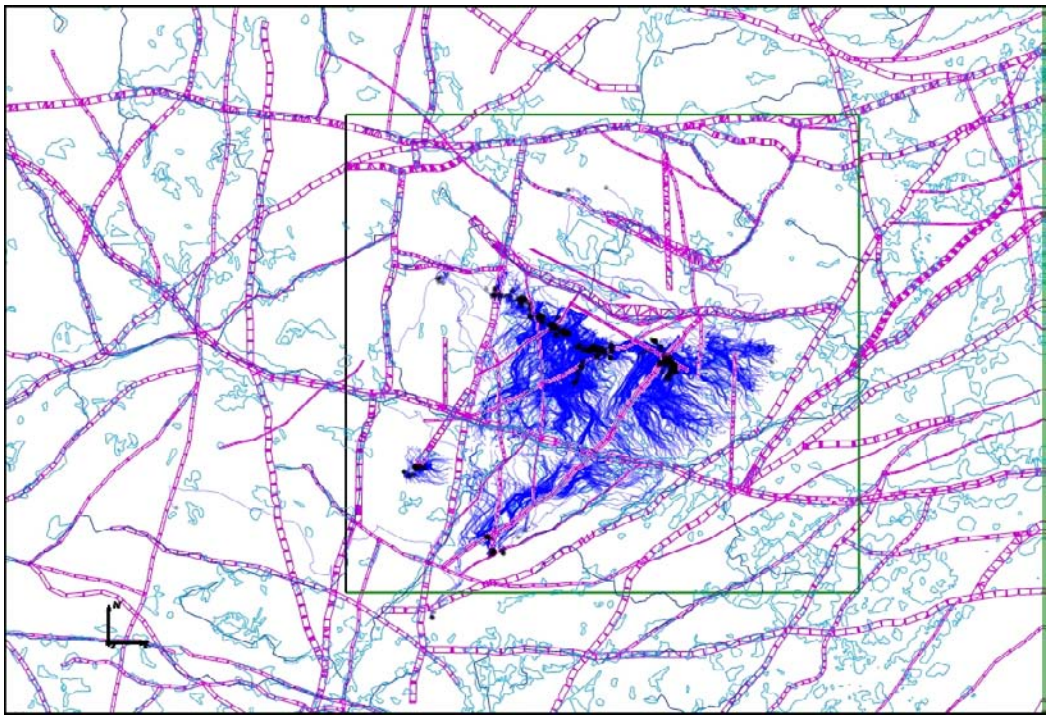

Figure 10-9. *Backward pathlines for the base case model. Pathlines starting in HRD_C are shown in blue with the exit locations (recharge) in black. HCDs on a slice at 0 m (purple), surface waterbodies (cyan), streams (blue), and the Laxemar local model area (green box) are shown. The start points for the paths are the blue points in Figure 10-1.*

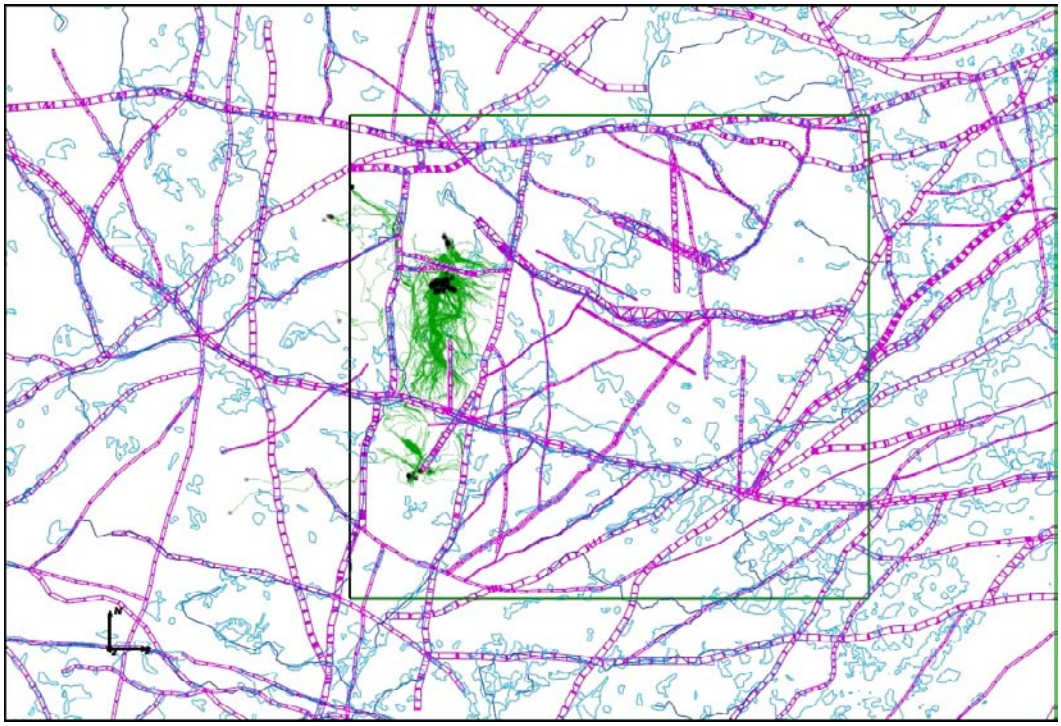

Figure 10-10. *Backward pathlines for the base case model. Pathlines starting in HRD_W are shown in green with the exit locations (recharge) in black. HCDs on a slice at 0 m (purple), surface waterbodies (cyan), streams (blue), and the Laxemar local model area (green box) are superimposed. The start locations for these paths are the green points shown in Figure 10-1.*

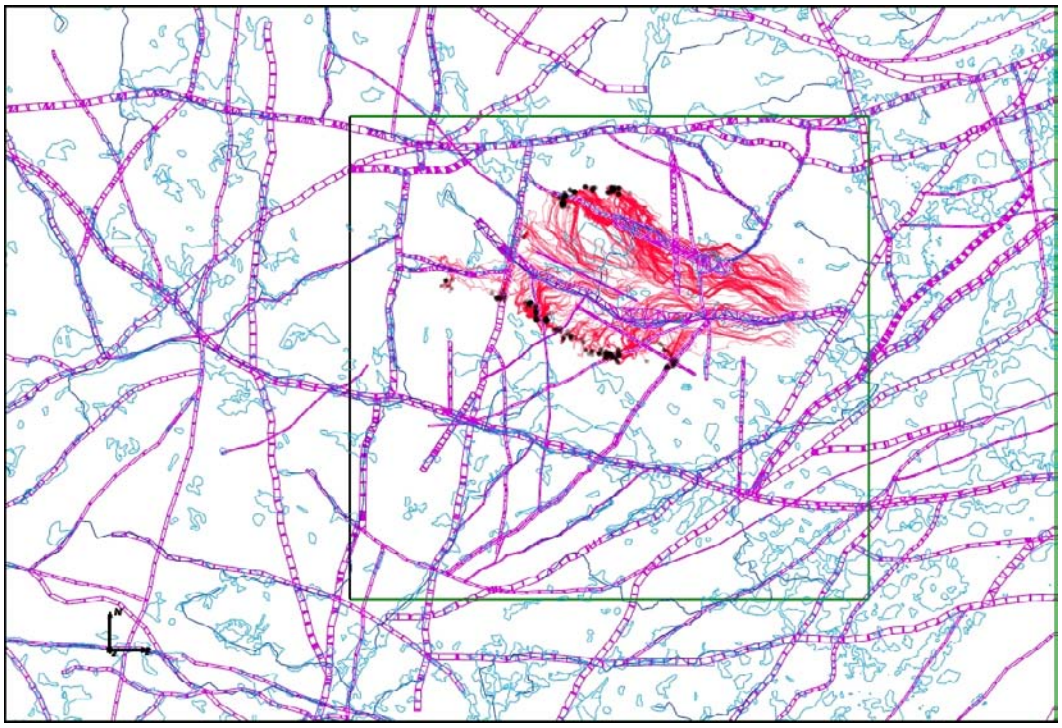

Figure 10-11. *Backward pathlines for the base case model. Pathlines starting in HRD_EW007 are shown in red with the exit locations (recharge) in black. HCDs on a slice at 0 m (purple), surface waterbodies (cyan), streams (blue), and the Laxemar local model area (green box) are superimposed. The start locations for these paths are the red points shown in Figure 10-1.*

within the HRD lying toward the north, near high topography around ZSMEW900A. HRD_EW007 receives recharge from the same low hills near the northern part of HRD_C south of ZSMEW007A, and from some hills slightly to the north. In summary, all recharge areas affecting the focused volume at 2000 AD are localised, predominantly within the Laxemar local model area. Hence, flow and chemistry boundary conditions far west of the Laxemar local model area have limited influence on hydrogeological conditions in the focused volume, although this depends on whether the ZSMNS001 acts as a barrier along its length within the Laxemar local model area.

10.3 Flow-path sensitivities

The two most important sensitivities considered relevant to flow-paths are those relating to spatial heterogeneity and the influence of hydraulic anisotropy, especially that seen in the dolerite dykes ZSMNS059A and ZSMNS001. To quantify the effects of anisotropy, exit locations were calculated for the variant without any anisotropy in the HCD as shown in Figure 10-12. The main difference is that particles starting in HRD_W generally exit further to the east. Figure 10-13 shows the pathlines for particles starting in HRD_W. The particles starting in the southern part of HRD_W still exit fairly close by in ZSMNW042A-east, though a little further east than before. Particles starting in the northern part of HRD_W around ZSMEW900A seem to enter ZSMEW007 and discharge many kilometres further east. Backward pathlines for this case are shown in Figure 10-14. Comparing with Figure 10-9 through Figure 10-11 more recharge to the HRD_C part of the focused volume comes from west of ZSMNS059A, and more recharge to HRD_W comes from west of ZSMNS001C. Some particles reaching HRD_C and HRD_W originate from a considerable distance to the west southwest of the site. The base case also has anisotropy included in ZSMEW002A and the part of ZSMNW042A between ZSMNS059A and ZSMNS001. ZSMEW002A is too far north to have an effect. The changes in exit locations for HRD_W are attributed to the isotropy in ZSMNS059A rather than ZSMNW042A-west. These results demonstrate the strong influence of the dolerite dykes on HRD_W for the base case.

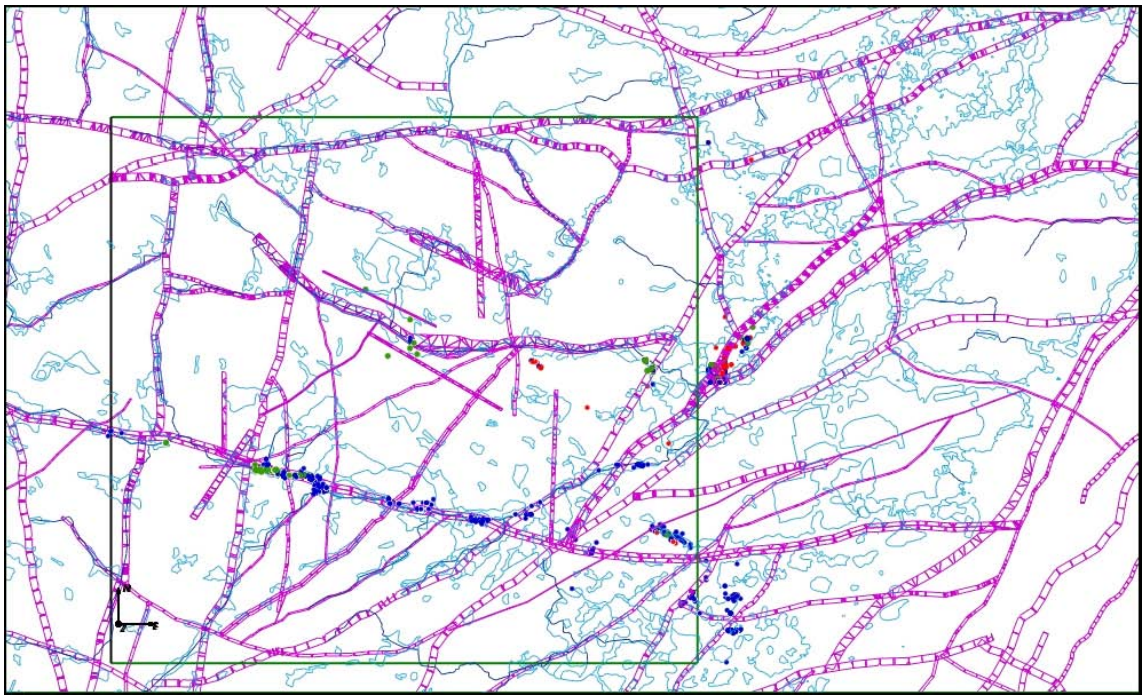

Figure 10-12. *Particle exit locations of pathlines released in HRD_C (blue), HRD_EW007(red) and HRD_W (green) for the variant without anisotropy in HCD. HCDs on a slice at 0 m (purple), surface waterbodies (cyan), streams (blue), and the Laxemar local model area (green box) are indicated.*

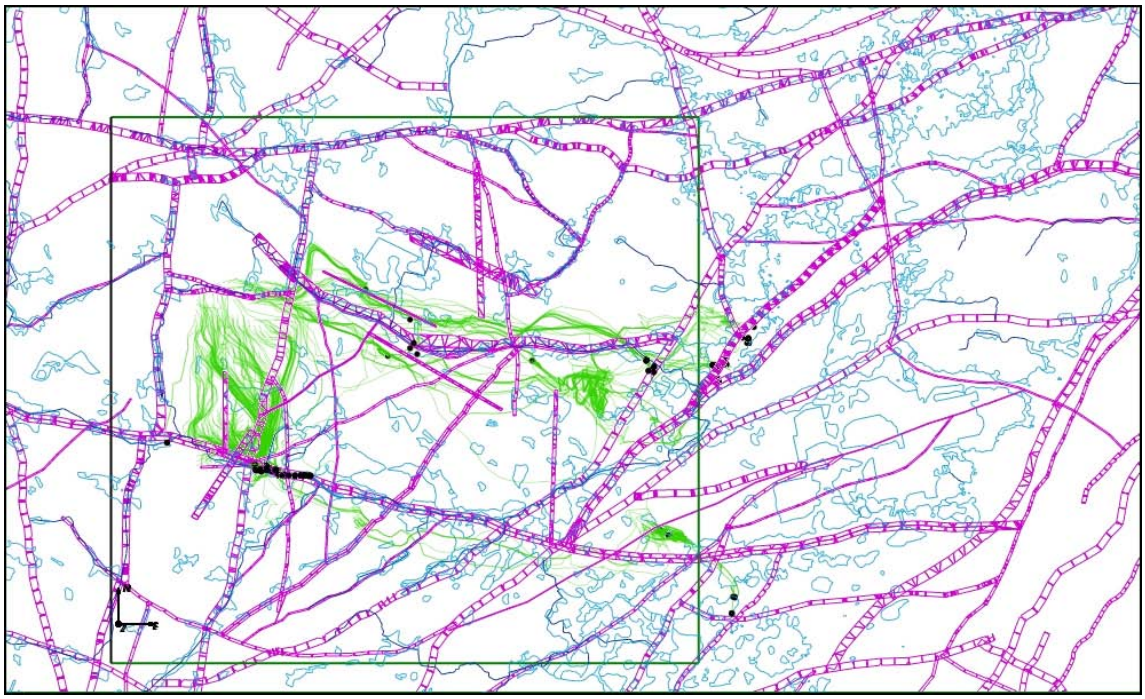

Figure 10-13. *Pathlines for the variant without anisotropy in HCD. Pathlines starting in HRD_W are shown in green with the exit locations in black. HCDs at 0 m (purple), surface waterbodies (cyan), streams (blue), and the Laxemar local scale model area (green box) are indicated.*

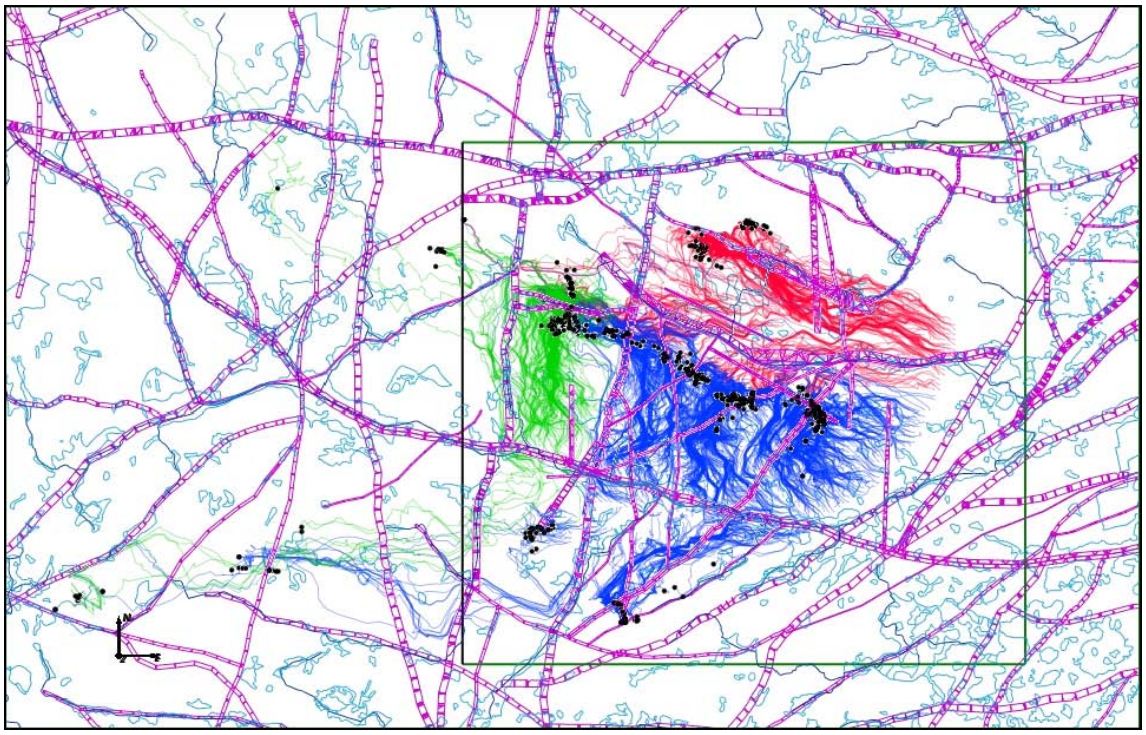

Figure 10-14. *Backward pathlines for the variant without anisotropy in HCD. Pathlines starting in HRD_C (blue), in HRD_EW007 (red), and in HRD_W (green) with the exit locations (recharge) in black. HCDs on a slice at 0 m (purple), surface waterbodies (cyan), streams (blue), and the laxemar local scale model area (green box) are indicated.*

For spatial heterogeneity, the variability of exit locations for the 10 realisations of HCD/HRD were considered with a standard deviation in Log(T) of 1.4 in the HCD. The results are presented in Figure 10-15 and indicate the same key areas of discharge, but there are also quite a lot of additional minor discharge areas that occur when spatial heterogeneity is considered. Discharge associated with ZSMNS001D, ZSMEW002A, ZSMNW254A, ZSMNE021A all appear as being possible discharge areas when a stochastic representation of HCD/HRD is used. Hence, it is recommended that multiple realisations also be considered in future modelling work.

10.4 Conclusions

Flow-paths from tentative repository deposition volumes have been simulated for the base case and a limited number of key variants to inform our understanding of advective groundwater circulation relevant to this volume. Particle tracking has been performed for both forward (downstream) and backward (upstream) flow-paths using the groundwater flow-field corresponding to 2000 AD. The start locations have been sub-divided according to HRD to discern potential differences between the relevant HRD.

For HRD_W, the flow-paths are hemmed in by the dolerite dykes associated with ZSMNS001C and ZSMNS059A, and hence most discharge to the south in ZSMNW042A-west is around its intersection with ZSMNS059A. In HRD_C, the particles generally move south toward ZSMNW042A-east or east toward ZSMNE005A and ZSMNE006A where they reach the bay north-west of the island of Hålö, with a few particles continuing further south-east to the Baltic south of the Simpevarp peninsula. For HRD_EW007, most particles follow ZSMEW007A eastward to discharge either in ZSMNE005A, ZSMNE006A or ZSMNE012A where they reach the bay north-west of Hålö (see Figure 10-3).

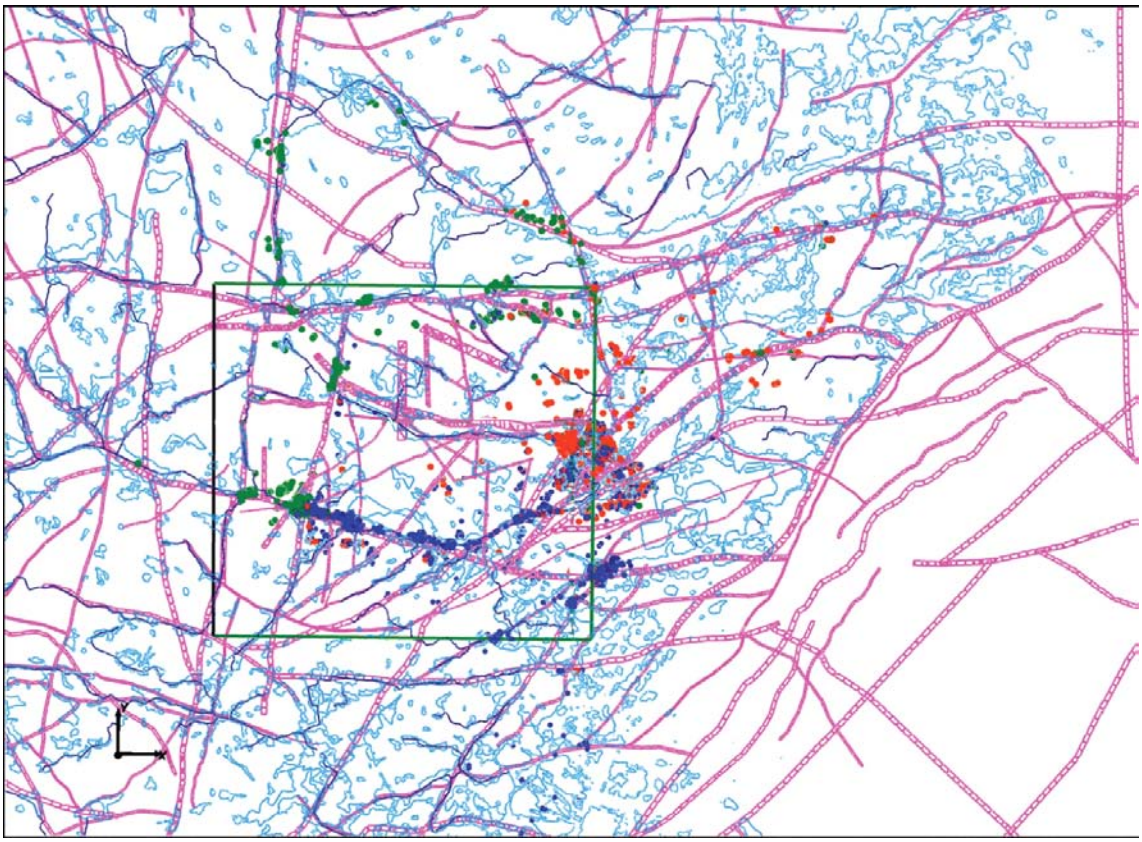

Figure 10-15. *Particle exit locations of pathlines released in HRD_C (blue), HRD_EW007(red) and HRD_W (green) for 10 realisations of the HRD and HCD. HCDs on a slice at 0 m (purple), surface waterbodies (cyan), streams (blue), and the Laxemar local scale model area (green box) are superimposed.*

The actual sub-surface flow-paths were considered in more detail to identify which HCD formed part of the pathway for the most particles. This showed that ZSMNE005A, ZSMNW042A-east and ZSMNE006A form the downstream path for 40–50% of the released particles. ZSMNE012A, ZSMNE004A, ZSMNE107A, ZSMNS059A and ZSMNE942A all encounter about 20–30% of the particles.

The backward pathline simulations show the possible recharge areas for the water that reaches the approximated repository volume based on the present-day simulated flow-field. In this type of simulation the particles are transported using the reversed Darcy velocity vector. For deposition volume in HRD_C the recharge areas are a ridge south of ZSMEW007A, a ridge south of ZSMEW900A and some areas south of ZSMNW042A. For deposition volumes in HRD_EW007, the recharge area seems to be located near ZSMNW929A to the north and some low hills south of ZSMEW007A; and for HRD_W, the recharge areas seem to be mainly located near ZSMEW900A. All these discharge areas lie with the Laxemar local scale model area. This is in part likely to be a result of the strong anisotropy interpreted in the major N-S dolerite dykes forming a barrier to recharge coming from the higher ground further west. Although the heterogeneity and strong depth trends in hydraulic properties are also thought to make a significant contribution to this effect.

A sensitivity case without anisotropy in the HCD confirms the strong influence of the dolerite dykes on flow and transport in HRD_W mainly. Without the introduced hydraulic anisotropy, paths starting beneath the lower lying areas in HRD_W tend to head (exit) eastwards rather than south and are longer and deeper.

When stochastic spatial heterogeneity in both HRD and HCD was considered it resulted in considerable spatial variations in the locations of the discharge areas, although the key areas identified by the base case remain relevant. On the basis of this result it is recommended that multiple realisations of spatial heterogeneity should be assessed in any future modelling considering far-field flow and release to the Biosphere.

11 Conclusions

11.1 Hydrogeological conceptual model

11.1.1 The main findings of the data interpretation and confirmatory testing

HCD model:

- The key interpreted characteristics are:
  - A clear trend of decreasing transmissivity with depth.
  - A positive correlation between interpreted "size" and transmissivity. Size here corresponds to interpreted trace length on the surface.
  - Indications that the transmissivity of HCDs is dependent on the orientations of deformation zones. E-W zones appear more conductive to zones of other orientations.
  - Significant lateral heterogeneity with a suggested standard deviation of Log(T) of 1.4.
- The confirmatory testing with the regional groundwater flow model has shown that in general the primary assessed transmissivity models for the HCD (based on the hydraulic test results) complies with the confirmatory model testing performed, however with a general slightly lower transmissivity. (Multiplication factors of 1.0, 0.3 and 0.1 of original values were assessed between ground surface down to –150 m, between –150 to –650 m and below –650 m, respectively.)
- In a few HCDs larger corrections of the transmissivities were applied. In three HCD, ZSMEW007A, ZSMNE107A and ZSMNS001C, the longitudinal transmissivity was increased significantly (a factor 3–50) above –400 m elevation, while the transmissivity of ZSMNE944A was reduced slightly below –400 m.
- The hydraulic interference test in HLX28 suggests a possible increase by a factor 3–4 higher than in the base case for the transmissivity (in plane) of the upper sections of HCD HLX28_DZ1, HCD ZSMNW042A-west and ZSMNS059A. (This has not been implemented in the *base case model*.[3])
- The palaeohydrogeological calibration suggested use of a methodology for deriving kinematic porosity and fracture surface area per unit volume based on the intensity of conductive fractures within the HCD rather than using a scaling relationship with transmissivity. It implies that conductive fracture intensity is a more reliable indicator of solute transport parameters than the interpreted transport aperture as function of transmissivity of the HCD.
- In fact, some of the most significant improvements were seen in the palaeohydrogeological calibration when the fracture surface area per unit volume was enhanced in the HCD relative to the HRD three times. It is considered that this may have wider implications in that the most representative model would have a correlation between hydraulic conductivity and fracture surface area whether in HCD or HRD (This has not been implemented in the *base case model*.).
- The role of N-S dolerite dykes associated with ZSMNS001A-C and ZSMNS059A (along with some other dolerite effected minor HCD) as flow barriers appears confirmed by discontinuities in natural head measurement in core drilled boreholes. A similar effect arising from clayey fracture fills or fault gouge in ZSMEW002A and ZSMNW042A-west also seems to be confirmed in the natural heads. This behaviour is confirmed by modelling these structures as strongly anisotropic, i.e. large contrast between longitudinal (in plane) hydraulic conductivity and transverse hydraulic conductivity. Particle tracking has shown that this has significant impact on groundwater flow patterns in at least the western part of the Laxemar local model area.

[3] "Base case", in this report accounting for the SDM-Site Laxemar modelling, corresponds to "Deterministic base model simulation" in the SDM-Site Forsmark modelling /Follin 2008/.

HRD model:

- Regional scale groundwater flow and solute transport simulation tests of palaeohydrogeology, natural head measurements and hydraulic interference test data have confirmed that hydrogeological properties implied by the hydrogeological DFN model base case /Rhén et al. 2008/ (based on all open and partly open fractures and semi-correlated transmissivity model) provide an appropriate description of the hydrogeological situation in the bedrock. Only relatively minor modifications were considered necessary to obtain acceptable comparisons between the flow model results and field data.
- For the *base case model* a slight reduction (a multiplication amounting to a factor of 1/3 relative to the originally assessed values) in hydraulic conductivity (horizontal and vertical) of the HRD below –150 m elevation was implemented since it improved the palaeohydrogeological calibration.
- The modelling of the drawdown around the Äspö HRL indicated that HRD_A2 should be based on intial values for hydraulic conductivity rather than the reduction by a multiplication factor 1/3 of the hydraulic conductivity found relavant for the regional model area based on the palaeohydrogeological calibration. (This has not been implemented in the *base case model*.)
- Basing kinematic porosity on conductive fracture intensity and transport aperture as calculated by the hydrogeological DFN model was confirmed as being appropriate for the palaeohydrogeological simulations, although it was necessary to include the contribution to kinematic porosity from small fractures down to the $r = 0.28$ m scale.
- Fracture surface area per unit volume used in parameterising rock matrix diffusion (RMD) of solute transport based on the average intensity of conductive fractures detected by the PFL method proved appropriate in the palaeohydrogeological calibration. This confirms the decreasing intensity of flowing features with depth as indicated by the hydrogeological DFN model.

HSD model:

- The applied hydraulic conductivities based on hydraulic tests complies with the confirmatory testing but it was considered appropriate to generally decrease the vertical hydraulic conductivities to 1/10 of the originally suggested values (isotropic), to be able to reproduce the head difference between the soil and the near-surface bedrock.
- To reproduce the drawdowns on mainland Laxemar-Simpevarp resulting from pumping in the Äspö HRL facility, it was necessary to use Gyttja clay soil type in the bays around Äspö HRL with vertical hydraulic conductivity $5 \cdot 10^{-9}$ m/s.

Hydrogeological boundary condition model (i.e. groundwater-level, -recharge and -discharge):

- The natural (undisturbed) groundwater levels generally follow the topography. In the Quaternary deposits, the depth to the groundwater table is expected to be within a few metres of ground surface, with maximum depth at topographic highs and minimum depth in the valleys, as shown by measurements. The natural (undisturbed) groundwater level in the upper bedrock behaves similarly, but there is a noticeable downward gradient in the upper 200 m of bedrock for around half the core drilled boreholes, the rest showing low vertical hydraulic gradients.
- According to the regional groundwater flow modelling discharge takes place in the larger valleys and towards the sea. This is consistent with measured heads in groundwater monitoring wells, which suggest that groundwater levels are at ground surface throughout the seasonal cycle in low lying areas (see Figure 8-2), and with the locations of mapped surface water (see Figure 8-7).
- Use of backwards advective particle tracking suggest the recharge areas relevant to the focused volume are localised mainly within the Laxemar local model area. This is a result of the strong depth trend in hydraulic conductivity, increasing salinity with depth and the compartmentalisation of flow created by the dolerite dykes.

Palaeohydrogeological model:

- Combining the interpretation of hydraulic characteristics of the bedrock from /Rhén et al. 2008/ with the understanding gained from simulating the palaeohydrogeological evolution, the hydrogeological situation for groundwater flow and solute transport is summarised in Figure 11-1 which is a schematic representation of Table 9-2.
- The presence of brackish-glacial water at relatively shallow depths, c. –200 to –600 m, in several groundwater samples suggest the persistence of pre-Holocene water in the fractures implying low rates of mixing in the fracture system.
- The description in Figure 11-1 focuses on the balance between advective solute transport and the effect of rock matrix diffusion (RMD) suggested by the measured hydrochemical data. However, this balance will be affected by the natural hydraulic gradients present during the current climatic period, and changes imposed during periods of elevated gradient, e.g. during deglaciation.
- There are some minor hydrochemical indications of older water in the upper 200 m of bedrock with glacial signature. However, this can be explained by the large heterogeneity one should expect in fractured crystalline bedrock, creating some larger matrix blocks and volumes with fairly low permeability not reproduced by the present ECPM.
- Simulations of tritium migration have confirmed that the developed palaeohydrogeological models are generally consistent with the interpretation of hydrogeochemistry /Laaksoharju et al. 2009, cf Section 7.2.2 therein/ that modern meteoric recharge from the last 50–60 years has penetrated the groundwater system to a depth of approximately 150 to 200 m.
- In the elevation range of c. –200 to –600 m, the hydrogeological and hydrochemical system is in a transient state. There is evidence from several hydrochemical samples that where the intensity of conductive fractures is low, one can find a difference in water composition between fracture groundwater and matrix porewater. In this elevation range the intensity of conductive fractures decreases successively also leading to a slower circulation of water. Generally, one finds fracture groundwater with cold signature, which indicates that parts of the fracture water are at least more than 10,000 years old. There are also fracture groundwaters believed to have some small (3–10%) *Littorina sea Water* in their composition, which indicate water of ages 4,000 to 6,000 years old within the Laxemar local model area. These traces of Littorina are uncertain within the Laxemar local model area but are well sustained in the lowing lying areas near Äspö and Ävrö.
- At elevations below –650 m, the circulation of water is slow and the conductive network is sparse. At this depth the salinity starts to increase by depth. Hydrochemical data in the fracture groundwater indicate that the age may be several hundred thousands years below some –900 to –1,000 m elevation. Probably there exists an equilibrium between the fracture groundwater and the immediate matrix porewater adjacent to the fractures (several metres), due to the low permeability of the system and low diffusion gradients.

11.1.2 Base case main components

The base case properties are summarised in the following tables:

- HCD: Tables 7-1 to 7-4.
- HRD Tables 7-5 to 7-10 and that the hydraulic conductivity (horizontal and vertical) of the ECPM below –150 m elevation of the HRDs were reduced to 1/3 of initial estimate from the upscaled hydrogeological DFN.
- HSD: Table 7-11.

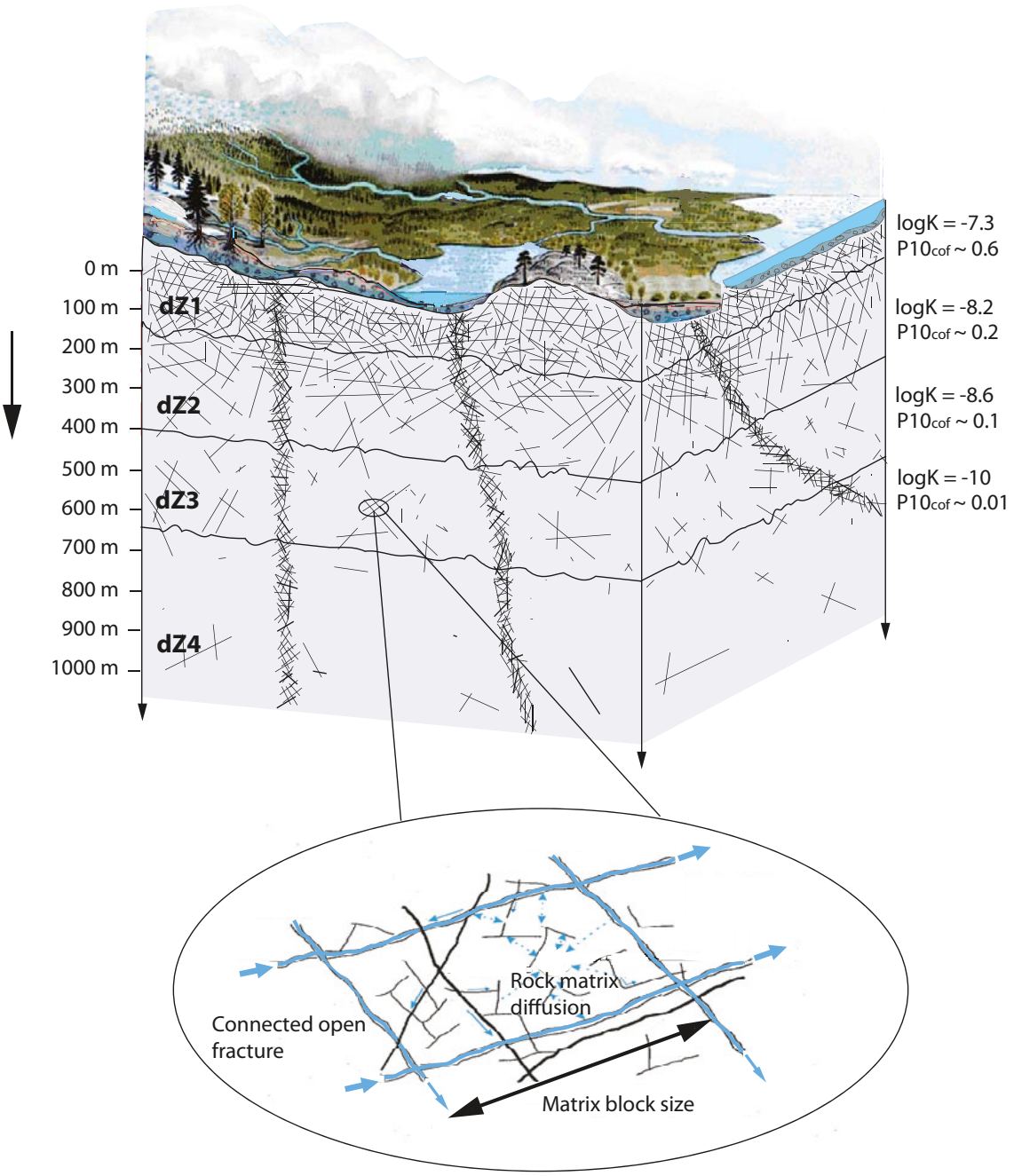

Figure 11-1. *Schematic 3D cross-section summarising the hydrogeological conceptual model of the bedrock within the focused volume in Laxemar. Flow in the upper most depth zone* **dZ1** *is dominated by subhorizontal and WNW fracturing. Solute transport is advection dominated with matrix block sizes of about 2 m, and about 1,000 years for hydrochemical equilibrium between fractures and matrix. WNW fractures dominate flow in* **dZ2**–**dZ4**. *In* **dZ2,** *advective solute transport is retarded significantly by RMD with matrix block sizes of about 5 m and chemical signatures in the matrix lagging 1,000 s of years behind the fractures. RMD dominates solute transport in* **dZ3** *with a few sparse areas of significant advection. Matrix block sizes are around 10 m, and matrix hydrochemistry lags 10,000 s of years behind fractures. There is very little advection in* **dZ4** *with matrix block sizes of about 100 m and 100,000 s of years lag between matrix and fracture hydrochemistry. (K: hydraulic conductivity, m/s. $P10_{cof}$ (Corrected intensity) of connected open fractures with a tramsmissivty > c. 10^{-9} m^2/s.)*

11.2 Solute transport model

Hydrochemical boundary condition model:

- The boundary conditions assessed on the top surface, covered by the Baltic Sea and its precursors, considers shoreline displacement and salinity development of the Baltic. The shoreline displacement curve "SDM-Site Laxemar Alt1, slightly higher in the past compared to that is suggested for SDM-Site Laxemar, cf Figure 4-26, was considered most realistic based on the calibrations. The salinity curve for the Baltic "SDM-Site Model Alt1, cf Figure 4-25, was considered most realistic based on the calibrations. The base case included these boundary conditions. This was necessary to allow *Littorina Sea Water* to infiltrate during the Littorina salinity maximum and be retained at the level of a few percent in the Laxemar local model area at the present-day.
- The results are not very sensitive to the boundary conditions applied on land before the start of the Littorina period (6500 BC), as it mainly affects groundwater in the top –150 m, which is later replaced by still more modern meteoric water.

Hydrochemical initial condition model:

- The initial conditions for fracture groundwater below c. 650 m can be considered to be similar to the present-day values due to the low frequency of conductive fractures and the increasing salinity, both of which limit the groundwater flow rate in the perspective of c. 10,000 years The base case for fracture groundwater is case 1, cf Figure 7-26. The properties of porewater below this depth are uncertain due to the few samples and the chemistry in the matrix being a result of processes that act on timescales far longer than the Holocene considered here. However, the composition and origin of this water is of course uncertain. The difference in $\delta^{18}O$ suggested by data, is reproduced in the modelling by assuming the porewater is mostly *Inter-glacial Porewater*, which is enriched in $\delta^{18}O$, while the fracture water is more of *Glacial Melt Water* in composition, which is depleted in $\delta^{18}O$. An interpretation of porewater data is that it has a composition similar to that defined for the case 1 *Inter-glacial Porewater* in Table 5-8 (essentially *Altered Meteoric water* with enriched $d_{18}O$) in the bedrock above 500 m depth, but is comparable to case 2 *Inter-glacial Porewater* in Table 5-8 in the bedrock below c. 500–600 m depth. The base case initial condition assumes *Inter-glacial Porewater* case 1 for the entire rockmass, cf Figures 7-27 and 7-28. A more realistic initial condition could be to consider porewater that is more *Altered Meteoric water* in the upper bedrock trending toward case 2 *Inter-glacial Porewater* at depth.
- Above c. –150 m the evolution of hydrochemistry is sufficiently rapid that the results are non-sensitive to the initial condition.
- In the interval –150 to –600 m the palaeohydrogeology results are however dependent on the hydraulic parameters, solute transport parameters (fracture surface area in particular) and initial conditions. However, the data suggest the hydrochemical situation in this depth range being relatively consistent between boreholes throughout Laxemar, despite there being large differences in heterogeneity of hydraulic properties between boreholes. This seemingly stable hydrochemistry is thought to result from a balance between advective flow and RMD, both of which are governed by fracture intensity, i.e. the two effects are correlated. Hence, when fracture intensity is low, advective transport is reduced, but when fracture intensity is increased, then both advection and exchange with the matrix are increased with the matrix is increased, and so is the penetration of the solute mixing front is retarded more by RMD. Such a correlation needs to be further developed in the conceptual and numerical models.
- The assessed variants for salinity in the initial conditions at different elevations have limited effect. When the initial *Deep Saline Water* composition was generally at a higher elevation than at present, the remaining Littorina fraction in the Laxemar local model area was about 2–3%. When the Deep saline water composition was assumed similar to today, then slightly more Littorina water persisted, around 5–6% in the Laxemar local model area. It is difficult to say which of these alternatives is the more plausible.

11.3 Uncertainty analysis

As part of the groundwater flow and solute transport modelling, several variants about the *base case model* were considered to both illustrate the development of the base case and to quantify uncertainties in the flow model description.

Sensitivities to assigned parameters in the HCD model:

- Strong hydraulic anisotropy in ZSMNS001A-C, ZSMNS059A, and KLX19_DZ5-8, which are associated with interpreted dolerite dykes, is essential to reproduce the interference test in HLX28 and 'jumps' in natural heads in the southern part of HRD_W.
- Anisotropy in ZSMNW042A-west and ZSMEW002A is also required for similar reasons, although attributed to fault gouge.
- Varying the HCD transmissivity half an order of magnitude has some noticeable effect on both hydrochemistry and natural heads.
- The palaeohydrogeological calibration was found to improve significantly in several boreholes when an enhanced fracture surface area for diffusive exchange with the matrix was implemented. This implies that a correlation between hydraulic conductivity and fracture surface area per unit volume, as is apparent from site data, should be implemented in the numerical modelling. It seems to be a key characteristic for coupled groundwater flow and solute transport in Laxemar. It is recommended that this should receive further attention in the further development of the conceptual model and numerical modelling methodology.
- The HLX33 interference test is dominated by the hydraulic characteristics of ZSMEW007A. Modelling of the natural head measurements suggest that they are sensitive to the transmissivity in the upper 400 m of this zone.
- Modelling of the HLX28 interference test suggests suggest that they are sensitive to the transmissivity in the following HCD: HLX28_DZ1, ZSMNW042A and ZSMNS059C.
- Introduction of lateral heterogeneity (stochastic variation) in the HCDs, which is considered more realistic than the base case, generally caused more flushing of the system and in some cases pushes the post-glacial meteoric flushing well below the measured hydrochemical concentrations. The discharge areas for particle releases in the Laxemar focused volume are dispersed considerably more for the ten realisations of the HCD and HRD than for the base case.
- A sensitivity case without anisotropy in the HCD confirms the strong influence of the dolerite dykes on the flow conditions and transport in HRD_W mainly. Without hydraulic anisotropy, paths starting beneath the lower lying areas in HRD_W tend to move eastwards rather than south, and they are longer and go deeper.

Sensitivities to assigned parameters in the HRD model:

- Increasing the hydraulic conductivity of the HRD below –150 m, gave little change in natural groundwater heads, but produced a worse match with hydrogeochemistry data.
- In contrast, increasing the horizontal conductivity of HRD in the top –150 m by a factor 3 gives some improvements to the matches to both natural groundwater heads and the hydrogeochemistry data by reducing post-glacial meteoric water at greater depths. Such a scenario is within the uncertainty in interpreting the measured data, which is sparse in the top 100 m of bedrock. (This has not been implemented in the *base case model*). However, the HLX28 interference test suggested, if anything, the contrast between HCD should be higher by a factor 3, suggesting one should consider increasing transmissivity of HCD in the top 150 m rather than in the HRD. Given this uncertainty, such a change was not included in the *base case model*.
- Introducing several realisations of the hydrogeological DFN provides a means to study the variability which one has to take into account when comparing with measurements. The results indicate that a vertical variation in the depth of post-glacial meteoric flushing of the fracture groundwater of about 50 to 100 m is to be expected between realisations (here also incorporating the effect of the variation generated by the stochastic variation of HCDs).

- The effects of heterogeneity on groundwater chemistry are most evident in the depth zones –150 m to –400 m where pockets of brackish-glacial water tend to occur in areas of relatively low hydraulic conductivity. In reality, such areas are likely to occur also higher up given the expected variation in intensity of conductive fractures.
- The values of kinematic porosity (based on the fracture volume of connected open fractures) seem appropriate and range from about 10^{-4} at depth to about $2 \cdot 10^{-3}$ in the upper bedrock. The upscaled kinematic porosity in the ECPM is sensitive to truncation of fracture size in the hydrogeological DFN model. Ideally the truncation used in the hydrogeological DFN calibration, $r = 0.28$ m should be used.
- The mean intensity of conductive fractures within the depth zones as described by the hydrogeological DFN model compares well with the expected time ranges for equilibration between fracture groundwater and matrix porewater as discussed in Section 9.2.1.
- Fracture surface area per unit volume (σ in Equation 7-8) has particular importance since it controls the importance of RMD. Using $\sigma = 2 \cdot P_{10,corr}$(PFL-f) seems to give appropriate levels of RMD. In the base case this formula was used to estimate average values of σ for each HRD and depth zone for use in the solute transport equations. It would be more realistic to calculate σ based on upscaling the connected open fracture intensity based on the underlying hydrogeological DFN model. However, it is necessary to correct for the effects of any truncation of fracture size distribution that is often inevitable with regional-scale DFN models. Still, if such corrections are made, then realistic correlations between σ, kinematic porosity and equivalent hydraulic conductivity might be expected to result since all depend strongly on the intensity of open connected fractures. The expected consequence would be to enhance RMD where fracture intensity is highest in a particular stochastic realisation.

Sensitivities to assigned parameters in the HSD model:

- The assigned hydraulic conductivities affect the modelled head in the Quaternary deposits on land but do not affect the calibration in other ways. However, the hydraulic conductivity of the sea sediments is important for the description of how bedrock volumes are coupled to the sea.
- The modelled chemistry during the Holocene is quite insensitive to the applied hydraulic properties of the Quaternary deposits, due to the overburden being generally thin and mostly having a higher hydraulic conductivity compared to the near-surface bedrock.

Sensitivities to the conceptual model for palaeohydrogeology:

- Sensitivities to the considered variants in boundary and initial conditions were relatively small compared to changes in hydraulic or transport properties. Hence, it is concluded that although these conditions are quite uncertain, as long as they are defined based on careful conceptual considerations, the simulation results are not overshadowed by their uncertainty.
- Likewise, the hydrogeochemical composition of the porewater at depth is uncertain, but plausible alternatives can be accommodated within the conceptual model without large implications for the results.

11.4 Unresolved issues

Dolerite dykes:

- It has been shown that the deformation zones associated with dolerite dykes locally act as flow barriers, in the south-western part of the Laxemar local model area. However, it is not known if the dolerite dykes within the two large deformation zones ZSMNS001C and ZSMNS059A are continuous along the extents of these zones. According to the geological model there may also be other, probably small, dolerite dykes within the local model domain. These possible smaller dolerite dykes are not believed to have any significant effect on the flow field, but this has not been tested in the flow model.

Alternative hydrogeological DFN models:

- The hydrogeological DFN models used are based on the assumption that all mapped open fractures are possible flowing features, the so called OPO case (All mapped Open and Partly Open fractures, including mapping classes; certain, probable and possible). Hydrogeological DFN models based on the assumption that mapped open fractures, classified as certain or probable, are possible flowing features, the so called OPO-CP case (All mapped Open and Partly Open fractures) have not been tested in the regional groundwater flow modelling and the difference in relation to the OPO case can therefore not be judged.
- Hydrogeological DFN models were also developed for different transmissivity models for the conductive fractures with a positive correlation to fractures size or being not correlated to fracture size. In this report, the case with a semi-correlated model was used, in which fracture transmissivity is correlated to size, but with significant degree of variability within any size range. The developed correlated and un-correlated transmissivity models, so called C and UC models have not been tested in the regional groundwater flow modelling. Both alternative models predict similar upscaled hydraulic conductivities on the 100 m scale (see /Rhén et al. 2008/) since they were conditioned on the same PFL-f and PSS 100 m interval data, similar regional flows are to be expected. For the correlated model, flow is concentrated in the larger fractures and kinematic porosity is a bit lower, which is likely to result in slightly faster mixing in the palaeohydrogeology simulations, and are therefore expected to perform less well than the semi-correlated case. The uncorrelated variant tends to give a higher kinematic porosity and distribute the bulk flow over more fractures, which could be expected to give similar results for the palaeohydrogeology simulations as the SC case, but possibly worse results for the interference test simulations since the hydraulic responses would be expected to be less discrete than for the semi-correlated case.
- The dominant fracture set for flow is the subvertical, steeply dipping WNW set. Since boreholes are either vertical or steeply dipping, the intensity and transmissivity of fractures of this set are more uncertain than the subhorizontal set. Efforts have been made in the hydrogeological DFN modelling (see /Rhén et al. 2008/) to compensate for this bias, but the resulting interpretation is still more sensitive to the methodology than to the subhorizontal set itself.

Transport properties:

- It is recommended that future attention be given to how best to characterise and model numerically the correlation between the equivalent hydraulic conductivity of a volume and the connected open fracture surface area within that volume. It appears from limited model variants that representing the enhanced fracture surface area in HCD, minor deformation zones and other volumes of relative high fracture intensity would provide more realistic models of solute transport. Similarly, of lesser importance, the correlation between kinematic porosity and hydraulic conductivity for an upscaled hydrogeological DFN model could be further developed.

References

Almén K-E, Stenberg L, 2005. Äspö Hard Rock Laboratory. Characterisation methods and instruments. Experiences from the construction phase. SKB TR-05-11, Svensk Kärnbränslehantering AB.

Andersson J, Ström A, Almén K-E, Ericsson L O, 2000. Vilka krav ställer djupförvaret på berget? Geovetenskapliga lämplighetsindikationer och kriterier för lokalisering och platsutvärdering. SKB R-00-15, Svensk Kärnbränslehantering AB.

Andersson J, Berglund J, Follin S, Hakami E, Halvarson J, Hermanson J, Laaksoharju M, Rhén I, Wahlgren C-H, 2002. Testing the methodology for site descriptive modelling. Application for the Laxemar area. SKB TR-02-19, Svensk Kärnbränslehantering AB.

Andersson J, 2003. Site descriptive modelling – strategy for integrated evaluation. SKB R-03-05, Svensk Kärnbränslehantering AB.

Auqué L F, Gimeno M J, Gómez J, Puigdoménech I, Smellie J, Tullborg E-L, 2006. Groundwater chemistry around a repository for spent nuclear fuel over a glacial cycle. Evaluation for SR-Can. SKB TR-06-31, Svensk Kärnbränslehantering AB.

Björck S, 1995. A review of the history of the Baltic Sea 13-8 ka. Quaternary International 27, 19–40.

Bosson E, 2006. Near-surface hydrogeological model of Laxemar, Open repository – Laxemar 1.2. SKB R-06-66, Svensk Kärnbränslehantering AB.

Bosson E, Sassner M, Gustafsson L-G, 2008. Numerical modelling of hydrology and near-surface hydrogeology at Laxemar-Simpevarp. Site descriptive modelling, SDM-Site Laxemar. SKB R-08-72, Svensk Kärnbränslehantering AB.

Carrera J, Sanchez-Vila X, Benet I, Medina A, Galarza G, Guimera J, 1998. On Matrix Diffusion: Formulations, Solution Methods and Quantitative Effects, Hydrogeology Journal, 6, No. 1, 178–190.

Dershowitz W, Winberg A, Hermanson J, Byegård J, Tullborg E-L, Andersson P, Mazurek M, 2003. Äspö Hard Rock Laboratory. Äspö Task Force on modelling of groundwater flow and transport of solutes – Task 6C – A semi-synthetic model of block scale conductive structures at the Äspö HRL. SKB IPR-03-13, Svensk Kärnbränslehantering AB.

Ekman L, 2001. Project deep drilling KLX02 – Phase 2, Methods, scope of activities and results. Summary report. SKB TR-01-11, Svensk Kärnbränslehantering AB.

Enachescu C, Böhner J, Rohs S, 2006a. Hydraulic interference tests, pumping borehole KLX07A, Subarea Laxemar. Oskarshamn site investigation. SKB P-06-145, Svensk Kärnbränslehantering AB.

Enachescu C, Rohs S, Wolf P, 2006b. Hydraulic injection tests in borehole KLX11A, Subarea Laxemar. Oskarshamn site investigation. SKB P-06-201, Svensk Kärnbränslehantering AB.

Enachescu C, Roh S, Wolf P, 2007a. Hydraulic interference tests, pumping borehole KLX20A, Subarea Laxemar. Oskarshamn site investigation. SKB P-07-39, Svensk Kärnbränslehantering AB.

Enachescu C, Wolf P, Rohs S, van der Wall R, 2007b. Hydraulic interference tests, pumping borehole KLX08, Subarea Laxemar. Oskarshamn site investigation. SKB P-07-18, Svensk Kärnbränslehantering AB.

Enachescu C, Rohs S, van der Wall R, 2008a. Evaluation of hydraulic interference tests, pumping borehole KLX19A, Subarea Laxemar. Oskarshamn site investigation. SKB P-08-15, Svensk Kärnbränslehantering AB.

Enachescu C, Rohs S, van der Wall R, Wolf P, Morosini M, 2008b. Evaluation of hydraulic interference tests, pumping borehole KLX27A, Subarea Laxemar. Oskarshamn site investigation. SKB P-08-16, Svensk Kärnbränslehantering AB.

Enachescu C, Wolf P, Rohs S, van der Wall R, 2008c. Hydraulic injection tests in borehole KLX27A, Subarea Laxemar. Oskarshamn site investigation. SKB P-08-27, Svensk Kärnbränslehantering AB.

Ericsson L, Holmén J, Rhén I, Blomquist N, 2006. Storregional grundvattenmodellering – fördjupad analys av flödesförhållanden i östra Småland. Jämförelse av olika konceptuella beskrivningar. SKB R-06-64, Svensk Kärmbränslehantering AB.

Fairbanks R, 1989. A 17,000-year glacio-eustatic sea level record: influence of glacial melting rates on the Younger Dryas event and deep-ocean circulation. Nature 342, 637–642.

Follin S, Johansson P-O, Levén J, Hartley L, Holton D, McCarthy R, Roberts D, 2007a. Updated strategy and test of new concepts for groundwater flow modelling in Forsmark in preparation of site descriptive modelling stage 2.2. SKB R-07-20, Svensk Kärnbränslehantering AB.

Follin S, Levén J, Hartley L, Jackson P, Joyce J, Roberts D, Swift B, 2007b. Hydrogeological characterisation and modelling of deformation zones and fracture domains, Forsmark modelling stage 2.2. SKB R-07-48, Svensk Kärnbränslehantering AB.

Follin S, Johansson P-O, Hartley L, Jackson P, Roberts D, Marsic N, 2007c. Hydrogeological conceptual model development and numerical modelling using CONNECTFLOW. Forsmark modelling stage 2.2. SKB R-07-49, Svensk Kärnbränslehantering AB.

Follin S, 2008. Bedrock hydrogeology Forsmark, Site descriptive modelling, SDM-Site Forsmark. SKB R-08-95, Svensk Kärnbränslehantering AB.

Follin S, Hartley L, Jackson P, Roberts D, Marsic N, 2008. Hydrogeological conceptual model development and numerical modelling using CONNECTFLOW, Forsmark modelling stage 2.3. SKB R-08-23, Svensk Kärnbränslehantering AB.

Fredén C (ed.), 2002. Berg och jord. Sveriges nationalatlas. Tredje upplagan.

Gokall-Norman K, Ludvigson J, 2007. Hydraulic pumping- and interference tests in soil monitoring wells on Laxema, spring of 2007. Oskarshamn site investigation. SKB P-07-173, Svensk Kärnbränslehantering AB.

Gustafsson E, Ludvigson J, 2005. Combined interference test and tracer test between KLX02 and HLX10. Oskarshamn site investigation. SKB P-05-20, Svensk Kärnbränslehantering AB.

Hakami E, Fredriksson A, Lanaro F, 2008. Rock mechanics Laxemar, Site descriptive modelling, SDM-Site Laxemar. SKB R-08-57, Svensk Kärnbränsle hantering AB.

Hartley L, Hoch A, Hunter F, Jackson P, Marsic N, 2005. Regional hydrogeological Simulations – Numerical modelling using CONNECTFLOW. Preliminary site description. Simpevarp subarea – version 1.2. SKB R-05-12, Svensk Kärnbränslehantering AB.

Hartley L, Hunter F, Jackson P, McCarthy R, Gylling B, Marsic N, 2006a. Regional hydrogeological simulations using CONNECTFLOW. Preliminary site description Laxemar subarea – version 1.2. SKB R-06-23, Svensk Kärnbränslehantering AB.

Hartley L, Hoch A, Jackson P, Joyce S, McCarthy R, Swift B, Gylling B, Marsic N, 2006b. Groundwater flow and transport modelling during the temperate period for the SR-Can assessment. Laxemar subarea - version 1.2, SKB R-06-99, Svensk Kärnbränslehantering AB.

Hartley L, Jackson P, Joyce S, Roberts D, Shevelan J, Swift B, Gylling B, Marsic N, Hermanson J, Öhman J, 2007. Hydrogeological Pre-Modelling Exercises: Assessment of impact of the Äspö Hard Rock Laboratory; Sensitivities of Palaeo-Hydrogeology; Development of a Local Near-Surface Hydro-DFN for KLX09B-F. Site descriptive modelling, SDM-Site Laxemar. SKB R-07-57, Svensk Kärnbränslehantering AB.

Harrström J, Walger E, Ludvigson J, Morosini M, 2007. Hydraulic interference tests HLX27, HLX28 and HLX32, Subarea Laxemar. Oskarshamn site investigation, SKB P-07-186, Svensk Kärnbränslehantering AB.

Hermanson J, Fox A, Öhman J, Rhén I, 2008. Compilation of data used for the analysis of the geological and hydrogeological DFN models. Site Descriptive Modelling, SDM-Site Laxemar. SKB R-08-56. Svensk Kärnbränslehantering AB.

Hjerne C, Nordqvist R, Harrström J, 2009 (in prep). Compilation and analyses of results from cross-hole tracer tests with conservative tracers. SKB R-09-28. Svensk Kärnbränslehantering AB.

Hoch A R, Jackson C P, 2004. Rock-matrix Diffusion in Transport of Salinity. Implementation in CONNECTFLOW. SKB R-04-78, Svensk Kärnbränslehantering AB.

Holmén J G, 2008. Premodelling of the importance of the location of the upstream hydraulic boundary of a regional flow model of the Laxemar-Simpevarp area. Site descriptive modelling, SDM-Site Laxemar. SKB R-08-60, Svensk Kärnbränslehantering AB.

Holzbecher E, 1998. Modeling density-driven flow in porous media. Principles, numerics, software. Springer, Berlin.

Jaquet O, Siegel P, 2006. Regional groundwater flow model for a glaciation scenario. Simpevarp subarea – version 1.2. SKB R-06-100, Svensk Kärnbränslehantering AB.

Jackson C P, Hoch A R, Todman S, 2000. Self-consistency of a heterogeneous continuum porous medium representation of a fractured medium. Water Resourc. Res., 36(1), 189–202.

Kestin J, Khalifa H E, Correia R J, 1981. Tables of dynamic and kinematic viscosity of aqueous NaCl solutions in the temperature range 20–150°C and the pressure range 0.1–35 MPa, J.Phys. Chem. Ref. Data Vol 10, No 1.

Kloppmann W, Matray J M, Aranyossy J F, 2001. Contamination of deep formation waters by drilling fluids: correction of the chemical and isotopic composition and evaluation of errors. Applied Geochemistry, 16(2001), pp 1083–1096.

Konikow L, Bredehoeft J D, 1992. Ground-water models cannot be validated, Advances in Water Resources, 15(1), 1992, 75–83.

La Pointe P, 1995. Estimation of undiscovered hydrocarbon potential through fractal geometry. Chap. 3, Fractals in Petroleum Geology and Earth Processes, Plenum Press, New York. 35–57.

La Pointe P, Fox A, Hermanson J, Öhman J, 2008. Geological discrete fracture network model for the Laxemar site, Site Descriptive Modelling, SDM-Site Laxemar. SKB R-08-55, Svensk Kärnbränslehantering AB.

Laaksoharju M, Skårman C, Skårman E, 1999. Multivariate Mixing and Mass-balance (M3) calculations, a new tool for decoding hydrogeochemical information. Applied Geochemistry Vol. 14, #7, 1999, Elsevier Science Ltd., pp 861–871.

Laaksoharju M, Smellie J, Tullborg E-L, Wallin B, Drake H, Gimeno M, Hallbeck L, Molinero J, Waber N, 2009. Bedrock hydrogeochemistry Laxemar, Site descriptive modelling, SDM-Site Laxemar. SKB R-08-93, Svensk Kärnbränslehantering AB.

Larsson-McCann S, Karlsson A, Nord M, Sjögren J, Johansson L, Ivarsson M, Kindell S, 2002. Meteorological, hydrological and oceanographical data for the site investigation program in the community of Oskarshamn. SKB TR-02-03, Svensk Kärnbränslehantering AB.

Li Y-H, Gregory S, 1974. Diffusion of ions in sea water and in seep-dea sediments. Geochimia et Cosmochimica Acta, Vol. 38, pp 703–714.

Lusczynski N J, 1961. Head and flow of ground water of variable density. Journal of Geophysical Research, 66(12), pp 4247–4256.

Marsic N, Hartley L, Jackson P, Poole M, Morvik A, 2001. Development of hydrogeological modelling tools based on NAMMU. SKB R-01-49, Svensk Kärnbränslehantering AB.

Molinero J, Salas J, Arcos D, Duro L, 2009. Integrated hydrogeological and geochemical modelling of the Laxemar-Simpevarp area during the recent Holocene (last 8000 years). In: Kalinowski, B. (ed.), Background complementary hydrogeochemical studies. SKB R-08-111, Svensk Kärnbränslehantering AB.

Morén L, Påsse T, 2001. Climate and shoreline in Sweden during Weichsel and the next 150,000 years. SKB TR-01-19, Svensk Kärnbränslehantering AB.

Morosini M, Wass E, 2006. Hydraulic interference and tracer testing of a rock-soil aquifer system between HLX35 and HLX34, SSM000037, SSM000222 and SSM000223, Subarea Laxemar. Oskarshamn site investigation. SKB P-06-151, Svensk Kärnbränslehantering AB.

Morosini M, Jönsson S, 2007. Pump- and interference testing of percussion drilled section of cored boreholes KLX09, KLX11A, KLX12A, KLX13A, KLX18A, KLX19A and KLX39, Subarea Laxemar. Oskarshamn site investigation. SKB P-07-182, Svensk Kärnbränslehantering AB.

Morosini M, Ludvigson J-E, Walger E, 2009. Hydraulic characterisation of deformation zone EW007, Subarea Laxemar. Oskarshamn site investigation. SKB P-05-193, Svensk Kärnbränslehantering AB.

Nilsson A-C, 2009. Quality of hydrochemical analyses in data freeze Laxemar 2.3. In: B. Kalinowski (ed) 2009. Background complementary hydrogeochemical studies Model, Site descriptive modelling, SDM-Site Laxemar. SKB R-08-111, Svensk Kärnbränslehantering AB.

Nyberg G, Wass E, 2005. Oskarshamn site investigation. Groundwater monitoring program. Report for November 2004–June 2005. SKB P-05-282, Svensk Kärnbränslehantering AB.

Nyberg G, Wass E, Askling P, 2005. Oskarshamn site investigation. Groundwater monitoring program. Report for December 2002–October 2004. SKB P-05-205, Svensk Kärnbränslehantering AB.

Nyberg G, Wass E, 2007a. Oskarshamn site investigation. Groundwater monitoring program. Report for July 2005–December 2006. SKB P-07-219, Svensk Kärnbränslehantering AB.

Nyberg G, Wass E, 2007b. Oskarshamn site investigation. Groundwater monitoring program. Report for January–August 2007. SKB P-08-28, Svensk Kärnbränslehantering AB.

Nyberg G, Wass E, 2008. Oskarshamn site investigation. Groundwater monitoring program. Report for September 2007 – September 2008. SKB P-08-88, Svensk Kärnbränslehantering AB.

Nyman H, Sohlenius G, Strömgren M, Brydsten L, 2008. Depth and stratigraphy of regolith. Site descriptive modelling, SDM-Site Laxemar. SKB R-08-06, Svensk Kärnbränslehantering AB.

Påsse T, 1996. A mathematical model of the shore level displacement in Fennoscandia. SKB TR 96–24, Svensk Kärnbränslehantering AB.

Påsse T, 1997. A mathematical model of past, present and future shore level displacement in Fennoscandia. SKB TR-97-28, Svensk Kärnbränslehantering AB.

Påsse T, 2001. An empirical model of glacio-isostatic movements and shore-level displacement in Fennoscandia. SKB R-01-41, Svensk Kärnbränslehantering AB.

Pöllänen J, Sokolnicki M, Väisäsvaara J, 2007. Oskarshamn site investigation. Difference flow logging of borehole KLX15A, Sub-area Laxemar. SKB P-07-176, Svensk Kärnbränslehantering AB.

Pöllänen J, Pekkanen J, Väisäsvaara J, 2008. Oskarshamn site investigation. Difference flow logging of borehole, KLX27A, Sub-area Laxemar. SKB P-08-22, Svensk Kärnbränslehantering AB.

Rahm N, Enachescu C, 2004. Oskarshamn site investigation, Hydraulic testing of percussion drilled lineament boreholes on Ävrö and Simpevarp. Sub-area Simpevarp. SKB P-04-287, Svensk Kärnbränslehantering AB.

Rhén I (ed.), Gustafson G, Stanfors R, Wikberg P, 1997. Äspö HRL – Geoscientific evaluation 1997/5. Models based on site characterization 1986–1995. SKB TR 97-06, Svensk Kärnbränslehantering AB.

Rhén I, Forsmark T, 2001. Äspo Hard Rock Laboratory, Prototype repository, Hydrogeology, Summary report of investigations before the operation phase. SKB IPR-01-65, Svensk Kärnbränslehantering AB.

Rhén I, Smellie J, 2003. Task force on modelling of groundwater flow and transport of solutes, Task 5 Summary report. SKB TR-03-01, Svensk Kärnbränslehantering AB**.**

Rhén I, Follin S, Hermanson J, 2003. Hydrological Site Descriptive Model – a strategy for its development during Site Investigations. SKB R-03-08, Svensk Kärnbränslehantering AB.

Rhén I, Forsmark T, Forsman I, Zetterlund M, 2006. Evaluation of hydrogeological properties for Hydraulic Conductor Domains (HCD) and Hydraulic Rock Domains (HRD), Laxemar subarea – version 1.2, SKB R-06-22, Svensk Kärnbränslehantering AB.

Rhén I, Forsmark T, Hartley L, Jackson C P, Roberts D, Swan D, Gylling B, 2008. Hydrogeological conceptualisation and parameterisation, Site descriptive modelling, SDM-Site Laxemar. SKB R-08-78, Svensk Kärnbränslehantering AB.

Rhén I, Hartley L, 2009 (in prep). Bedrock hydrogeology Laxemar, Site descriptive modelling, SDM-Site Laxemar. SKB R-08-92, Svensk Kärnbränslehantering AB.

Serco, 2009a. CONNECTFLOW Release 9.7 Technical Summary Document, Serco Technical and Assurance Services report SA/ENV/CONNECTFLOW/15.

Serco, 2009b. NAMMU Release 9.7 Technical Summary Document, Serco Technical and Assurance Services report SA/ENV/CONNECTFLOW/8.

Serco, 2009c. NAPSAC Release 9.7 Technical Summary Document, Serco Technical and Assurance Services report SA/ENV/CONNECTFLOW/12.

SKB, 2002. Simpevarp – site descriptive model version 0. SKB R-02-35, Svensk Kärnbränslehantering AB.

SKB, 2004a. Hydrogeochemical evaluation for Simpevarp model version 1.2. Preliminary site description of the Simpevarp area. SKB R-04-74, Svensk Kärnbränslehantering AB.

SKB, 2004b. Preliminary site description Simpevarp area – version 1.1. SKB R-04-25, Svensk Kärnbränslehantering AB.

SKB, 2005a. Preliminary site description. Simpevarp subarea – version 1.2. SKB R-05-08, Svensk Kärnbränslehantering AB.

SKB 2005b. Preliminary safety evaluation for the Simpevarp subarea. Based on data and site descriptions after the initial site investigation stage. SKB TR-05-12, Svensk Kärnbränslehantering AB.

SKB, 2006a. Slutförvar för använt kärnbränsle. Preliminär anläggningsbeskrivning – layout D. Oskarshamn, delområde Simpevarp. SKB R-06-31, Svensk Kärnbränslehantering AB.

SKB, 2006b. Preliminary site description. Laxemar subarea – version 1.2. SKB R-06-10, Svensk Kärnbränslehantering AB.

SKB 2006c. Preliminary safety evaluation for the Laxemar subarea. Based on data and site descriptions after the initial site investigation stage. SKB TR-06-06, Svensk Kärnbränslehantering AB.

SKB, 2006d. Slutförvar för använt kärnbränsle. Preliminär anläggningsbeskrivning – layout D. Oskarshamn, delområde Laxemar. SKB R-06-32, Svensk Kärnbränslehantering AB.

SKB, 2006e. Long-term safety for KBS-3 repositories at Forsmark and Laxemar – a first evaluation. Main Report of the SR-Can project. SKB TR-06-09, Svensk Kärnbränslehantering AB.

SKB, 2006f. Programme for further investigations of bedrock, soil, water and environment in Laxemar subarea. Oskarshamn site investigation. SKB R-06-29, Svensk Kärnbränslehantering AB.

SKB, 2006g. Preliminary site description Laxemar stage 2.1. Feedback for completion of the site investigation including input from safety assessment and repository engineering. SKB R-06-110, Svensk Kärnbränslehantering AB.

SKB, 2007a. Prioritering av platsen för ett slutförvar i Oskarshamn. SKB R-07-21, Svensk Kärnbränslehantering AB

SKI, 2005. Need for Confirmatory Testing of Upscaled Flow and Transport Models, INSITE Report TRD-05-08, Statens Kärnkraftsinspektion.

Sohlenius G, Hedenström A 2008. Description of regolith at Laxemar-Simpevarp. Site descriptive modelling, SDM-Site Laxemar. SKB R-08-05, Svensk Kärnbränslehantering AB.

Streltsova T D, 1988. Well testing in heterogeneous formations. Exxon, Monograph. John Wiley and sons.

Sundberg J, Wrafter J, Back P-E, Rosén L, 2008. Thermal properties Laxemar Site descriptive modelling, SDM-Site Laxemar. SKB R-08-61, Svensk Kärnbränslehantering AB.

Svensson T, Ludvisgsson J-E, Walger E, Thur P, Gokall-Norman K, Wass Morosini M, 2007. Combined interference- and tracer test in HLX33, SSM000228 and SSM000229, Subarea Laxemar. Oskarshamn site investigation. SKB P-07-187, Svensk Kärnbränslehantering AB.

Söderbäck B (ed.), 2008. Geological evolution, palaeoclimate and historic development of the Forsmark and Laxemar-Simpevarp areas. Site descriptive modelling, SDM-Site. SKB R-08-19, Svensk Kärnbränslehantering AB.

Söderbäck B, Lindborg T, (eds.), 2009. Surface system Laxemar-Simpevarp. Site descriptive modelling, SDM-Site Laxemar. SKB R-09-01, Svensk Kärnbränslehantering AB.

Thur P, Walger E, Ludvigson J-E, 2007. Hydraulic interference in HLX34, HLX27, and HLX42 in the Laxemar subarea. Oskarshamn site investigation, SKB P-07-185, Svensk Kärnbränslehantering AB.

Triumf C-A, 2007. Oskarshamn site investigation, Assessment of probable and possible dolerite dykes in the Laxemar subarea from magnetic total field data and digital elevation models. SKB P-07-223, Svensk Kärnbränslehantering AB.

Tröjbom M, Söderbäck B, Kalinowski B, 2008. Hydrochemistry of surface water and shallow groundwater. Site descriptive modelling, SDM-Site Laxemar, SKB R-08-46, Svensk Kärnbränslehantering AB.

Vidstrand P, 2003. Äspö Hard Rock Laboratory, Update of the Hydrogeological model 2002. SKB IPR-03-35, Svensk Kärnbränslehantering AB.

Vidstrand P, Follin S, Zugec N, 2009 (in prep). Groundwater flow modelling of the glacial and permafrost periods – SR-Site. SKB R-09-25, Svensk Kärnbränslehantering AB.

Waber H N, Smellie J A T, 2006a. Borehole KLX03: Characterisation of pore water Part 1: Methodology and analytical data. Oskarshamn site investigation, SKB P-06-12, Svensk Kärnbränslehantering AB.

Waber H N, Smellie J A T, 2006b. Borehole KLX03: Characterisation of pore water. Part 2: Rock properties and diffusion experiments. Oskarshamn site investigation, SKB P-06-77, Svensk Kärnbränslehantering AB.

Waber H N, Smellie J A T, 2006c. Borehole KLX08. Characterisation of pore water. Part 1: Methodology and analytical data. Oskarshamn site investigation. SKB P-06-163, Svensk Kärnbränslehantering AB.

Waber H N, Smellie J A T, 2008b. Borehole KLX17A: Characterisation of pore water, Part 1: Methodology and analytical data, SKB P-08-43, Svensk Kärnbränslehantering AB.

Waber H N, Smellie J A T, 2008a. Characterisation of porewater in crystalline rocks. Applied Geochemistry 23, 1834–1861.

Waber H N, Gimmi T, de Haller A, Smellie J A T, 2009. Pore water in the rock matrix, Site descriptive modelling, SDM-Site Laxemar, SKB R-08-112, Svensk Kärnbränslehantering AB.

Wahlgren C-H, Hermanson J, Curtis P, Forssberg O, Triumf C-A, Drake H, Tullborg E-L, 2005. Geological description of rock domains and deformation zones in the Simpevarp and Laxemar subareas. Preliminary site description, Laxemar subarea, version 1.2. SKB P-05-69, Svensk Kärnbränslehantering AB.

Wahlgren C-H, Curtis P, Hermanson J, Forssberg O, Öhman J, Fox A, La Pointe P, Drake H, Triumf C-A, Mattsson H, Thunehed H, Juhlin C, 2008. Geology Laxemar. Site descriptive modelling, SDM-Site Laxemar. SKB R-08-54, Svensk Kärnbränslehantering AB.

Walger E, Ludvigson J-E, Svensson T, Thur P, Harrström J, 2007. Hydraulic interference in KLX06, KLX14A, KLX15A, KLX16A, KLX17A, KLX18A, KLX19A, KLX21B, KLX22A, KLX22B, KLX23A, KLX23B, KLX26A and KLX26B, Laxemar subarea. Oskarshamn site investigation. SKB P-07-183, Svensk Kärnbränslehantering AB.

Werner K, Öhman J, Holgersson B, Rönnback K, Marelius F, 2008. Meteorological, hydrological and hydrogeological monitoring data and near-surface hydrogeological properties data from Laxemar-Simpevarp. Site descriptive modelling, SDM-Site Laxemar. SKB R-08-73, Svensk Kärnbränslehantering AB.

Westman P, Wastegård S, Schoning K, Gustafsson B, Omstedt A, 1999. Salinity change in the Baltic Sea during the last 8,500 years: evidence, causes and models. SKB TR-99-38, Svensk Kärnbränslehantering AB.

Wijnbladh E, Aquilonius K, Floderus S, 2008. The marine ecosystems at Forsmark and Laxemar-Simpevarp. Site descriptive modelling, SDM-Site. SKB R-08-03, Svensk Kärnbränslehantering AB.

Appendix 1

A1 Interference tests

Interference tests have been performed in a number of boreholes and are reported in /Enachescu et al. 2006a, Enachescu et al. 2007a, b, Enachescu et al. 2008a, Gokall-Norman and Ludvigson 2007, Gustafsson and Ludvigson 2005, Harrström et al. 2007, Morosini and Wass 2006, Morosini and Jönsson 2007, Morosini et al. 2009, Rahm and Enachescu 2004, Svensson et al. 2007, Thur et al. 2007, Walger et al. 2007/. Interference test data involving observations in KLX27A /Enachescu et al. 2008b/ were not available for the evaluation.

In this appendix some of the interference tests made during the Site Investigations are analysed and discussed mainly in relation to the geological structural model. Some of these tests have been of fairly short duration and involving only a few observation sections, but some tests have both a long duration and several observation sections, which make their results more interesting for comparison with the structural model and form calibration cases for the numerical groundwater flow model. These later tests are commented in this appendix.

A1.1 Interference tests – response indicators for interpretation

For the overall interpretation of mainly hydraulic connectivity, distance drawdown-plots and response index plots are used.

In the distance-drawdown plots the skin factor of the pumped section to estimate the effective borehole radius. The distance between the pumped section and the observed section is the spherical distance (r_s) between the point of application in the pumped section and the observed section. Generally it is just the mid point of the sections that is used but it may also be based on the point of balance for the hydraulic conductivity distribution along a borehole section.

Three response indexes are estimated as:

Index 1:

$\mathbf{r_s^2/dt_L}$(s = 0.1 m) = normalised squared spherical distance r_s with respect to the response time lag dt_L at the observation section, for the drawdown s = 0.1 m or if possible s = 0.01 m (m^2/s). This index is proportional to the expected hydraulic diffusivity.

Index 2:

$\mathbf{s_p/Q_p}$ = specific drawdown, normalised drawdown s_p with respect to the pumping rate Q_p at the end of the pumping period (s/m^2). The spatial distribution of the drawdown is illustrated by this index. A response that was smaller than 0.1 m in an observation section was generally regarded as no response.

Index 2 new:

$\mathbf{(s_p/Q_p)*ln(r_s/r_0)}$ distance weight specific drawdown, assuming $r_0 = 1$. For the pumped borehole $r_s = e^1$ (i.e. a fictive borehole radius of 2.718 m). The spatial distribution of the drawdown is normalized, assuming radial flow, for (mostly) a more clear indication of the hydraulic connections than by Index 2.

The larger the index value is, the better hydraulic contact can be assumed. In figures with deformation zones and boreholes the size of the disc indicates the magnitude of the index and no-response is indicated with a grey sphere. The Pumped borehole is also indicated by a disc, which is black if the response index 2 or index 2 new is not plotted. The colours on index 1/2/2 new: blue/light green/ dark green. Generally plots with index 2 new are shown.

In distance-drawdown plots no responses are also indicated in the plots with assigned value of $s_p = 0.01$ m to be able to plot them in the diagrams with log-log representation on the axis. If no time-lag dt_L has been evaluated, generally no drawdown response is seen but occasionally no time-lag has been possible to evaluate even though a drawdown at pumping stop has been evaluated. For such observations with no time-lag estimate, nothing is plotted in the response index diagrams except for the active observation section label in the legend.

The hydraulic diffusivity can be estimated, either based on T/S for the observation borehole or based on radial flow and the time lag dt_L and pumping time t_p according to /Streltsova 1988/:

$$T/S = r_s^2 / [4 \cdot dt_L \cdot (1 + dt_L / t_p) \cdot \ln (1 + t_p / dt_L)]$$

A1.2 Interference test; HLX27, May–June 2007

The HLX27 interference test was performed between 2007-05-30 and 2007-06-02 (c. 3 days or 72.75 h) with HLX27 as pumping hole Observations were made in boreholes (No of sections within parenthesis): KLX03 (10), KLX05A (10), KLX15A (3), KLX19A (1), HLX26 (1), HLX38 (1) and HLX42 (2), as observation boreholes. The test is reported in /Harrström et al. 2007/.

Test description

The pumping was performed in an open borehole in the borehole interval 6.03–164.7 m with final pumping rate $Q_p = 0.001517$ m³/s and arithmetic mean pumping rate $Q_m = 0.00152$ m³/s. The pump time was $t_p = 4{,}365$ min (3.03 days) with a draw at pump-stop of $s_p = 23.6$ m. In Figure A1-1 the pumped borehole and the observation boreholes are shown.

Responses

The responses are shown as final drawdown at pumping stop in Figure A1-2, using the skin factor of the pumped section to estimate the effective borehole radius. The response indexes for the observation boreholes are presented in Figure A1-3 and mapped on the structural model in Figure A1-4 and Figure A1-5.

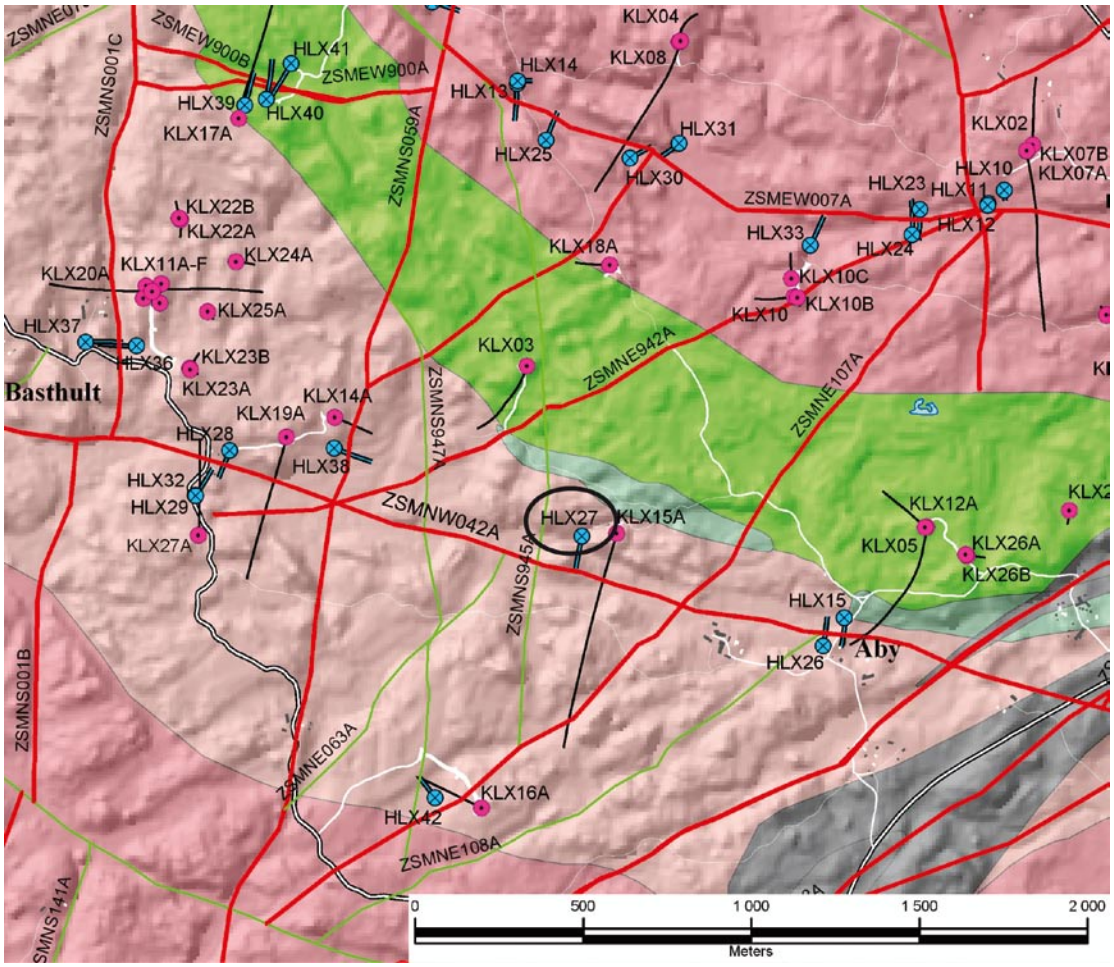

Figure A1-1. *Borehole map. Test in May–June 2007 with HLX27 as pumping borehole.*

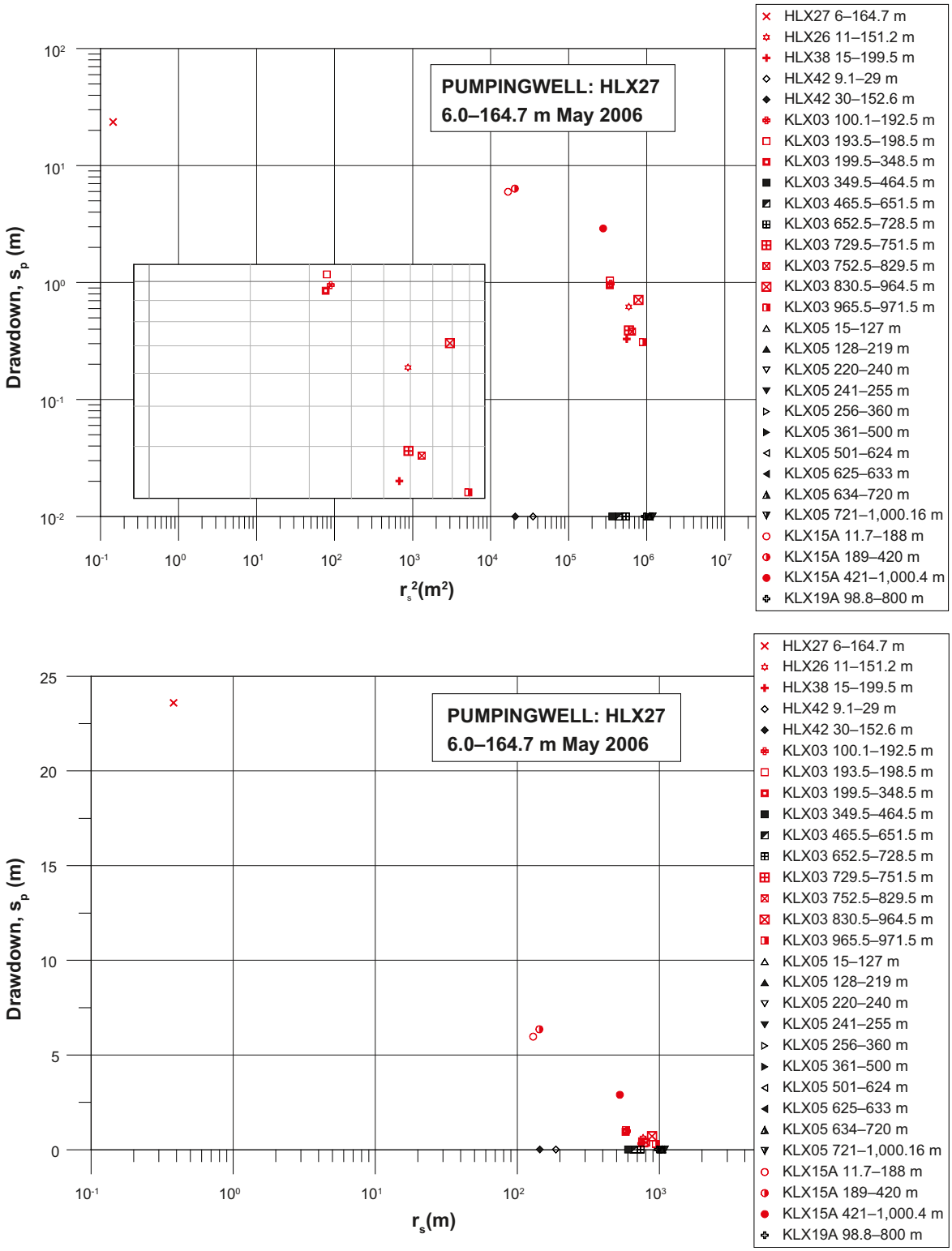

Figure A1-2. *Distance-drawdown plots. Test in May–June 2007 with HLX27 as pumping borehole.*

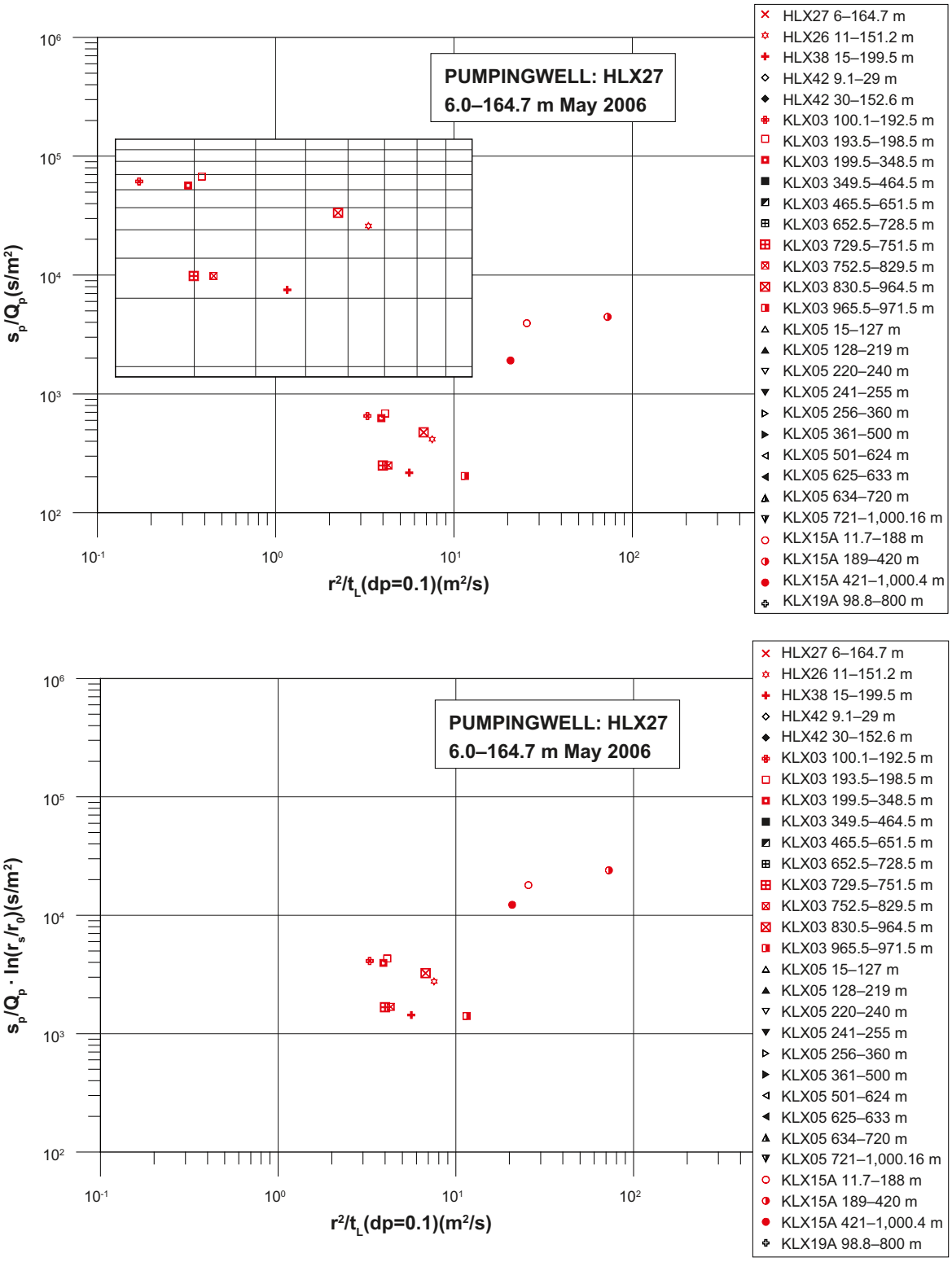

Figure A1-3. *Response- index plots. Test in May–June 2007 with HLX27 as pumping borehole.*

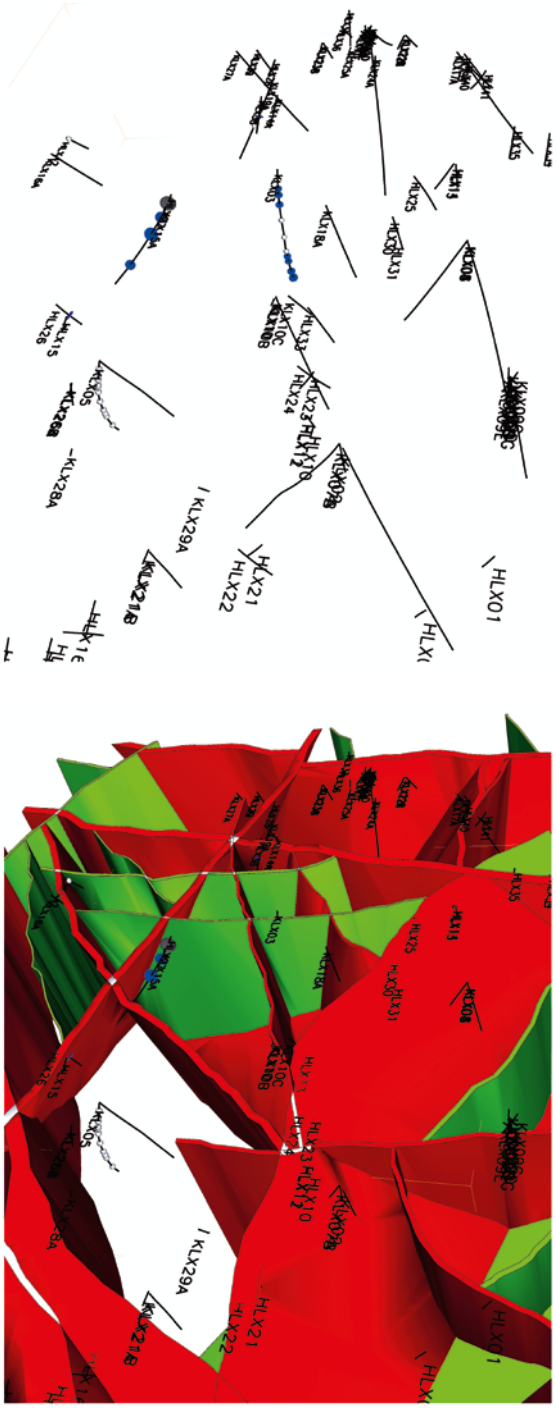

Figure A1-4. *Test in May–June 2007 with HLX27 as pumping borehole. Top of figures: western part of local model area. Response indexes are mapped on the boreholes. Pumping hole plotted as a black disc. The larger the disc (green or blue) for a response index is, the better hydraulic contact with pumped borehole section can be assumed. No-response is indicated with a grey sphere. Boreholes without discs or spheres have not been measured.*

Figure A1-5. *Test in May–June 2007 with HLX27 as pumping borehole. Top of figures: western part of local model area. Deformation zones ZSMEW946A and ZSMNS945A are removed in the figure to better show responses. Response indexes are mapped on the boreholes. Pumping hole plotted as a black disc. The larger the disc (green or blue) for a response index is, the better hydraulic contact with pumped borehole section can be assumed. No-response is indicated with a grey sphere. Boreholes without discs or spheres have not been measured.*

There are clear responses in KLX15A, HLX26, HLX38 and in KLX03 (borehole sections 100.1–340.5 m and 729.5–971.5 m). The responses in KLX15 sections 193.5–198.5 and 199.5–348.5 m are underestimated due to that the pressure transducer were placed to high up. No responses in KLX05, KLX19 and HLX46 and mid part of KLX03.

Conclusions

There were significant responses along KLX15A supporting that ZSMNW042 is conductive and dipping south. A response in HLX26 confirms also hydraulic connection along ZSMNW042. There were responses in HLX38 but not KLX19A supporting that ZSMNS059 might be a hydraulic barrier. The leaky character of the late response in HLX27 indicates that it is not only the planar feature ZSMNW042A that is dominating the flow, it should be significant conductive features intersecting ZSMNW042A causing this leaky behaviour.

The clear responses in parts of KLX03: 729.5–971.5 m can possibly be explained by hydraulic connection between ZSMNW042A and the subhorizontal structure ZSMEW946A and the response in KLX03: 100.1–340.5 m and 729.5–971.5 m with hydraulic connection between ZSMNW042A and the top part of steep structure ZSMNS945A. The lacking responses in KLX03: 341.5–728.5 m indicate that the deeper part of ZSMNS945A is less transmissive, if now the structure exists at depth.

There are no responses in KLX05 indication at least low hydraulic contact with ZSMNW042A, however with the reservation that the pumping time was fairly short.

A longer pumping test in HLX27A spring–summer 2008, not yet (summer 2009) reported, indicate that there are also hydraulic connection with KLX16A and HLX42. This indicates that ZSMNW042A does not act as a hydraulic barrier in this part of the zone, or possibly that ZSMNE107A is able to transmit the responses through ZSMNW042A.

A1.3 Interference test; HLX28, April 2007

The interference test was performed between 2007-04-05 and 2007-04-10 with HLX28 as pumping hole. Observations were made in boreholes (No of sections within parenthesis): KLX19A (8), KLX20A (1), KLX14A (3), HLX32 (1), HLX36 (2), HLX37 (3) and HLX38 (1) as observation boreholes. The test is reported in /Harrström et al. 2007/.

Test description

The pumping was performed in an open borehole within borehole length 6.03–154.2 m with final pumping rate Q_p = 0.0016 m^3/s and arithmetic mean pumping rate Qm = 0.00161 m^3/s. The pump time was t_p = 6,839 min (4.75 days) with a drawdown at pump-stop of s_p = 11.1 m. In Figure A1-6 the pumped borehole and the observation boreholes are shown.

HLX28 is a borehole with high transmissivity and is assumed to be well connected to the deformation zone ZSM042A but not directly intersecting the zone.

Responses

The responses are shown as final drawdown at pumping stop in Figure A1-7, using the skin factor of the pumped section to estimate the effective borehole radius. The response indexes for the observation boreholes are presented in Figure A1-8 and mapped on the structural model in Figure A1-9 and Figure A1-10.

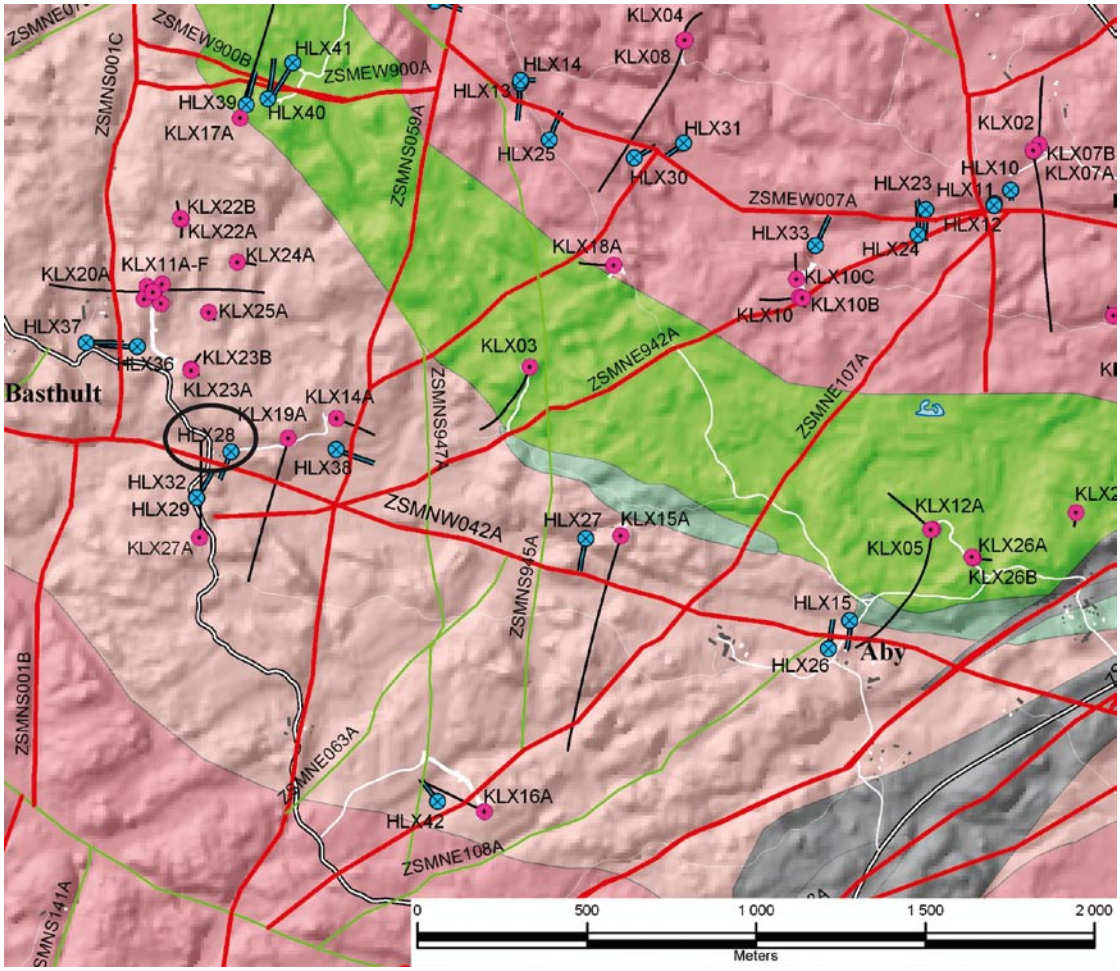

Figure A1-6. *Borehole map. Test in April 2007 with HLX28 as pumping borehole. KLX20A intersects ZSMNS01, KLX14A intersects ZSM059A and KLX19A, HLX27A and others intersects ZSMNW042A.*

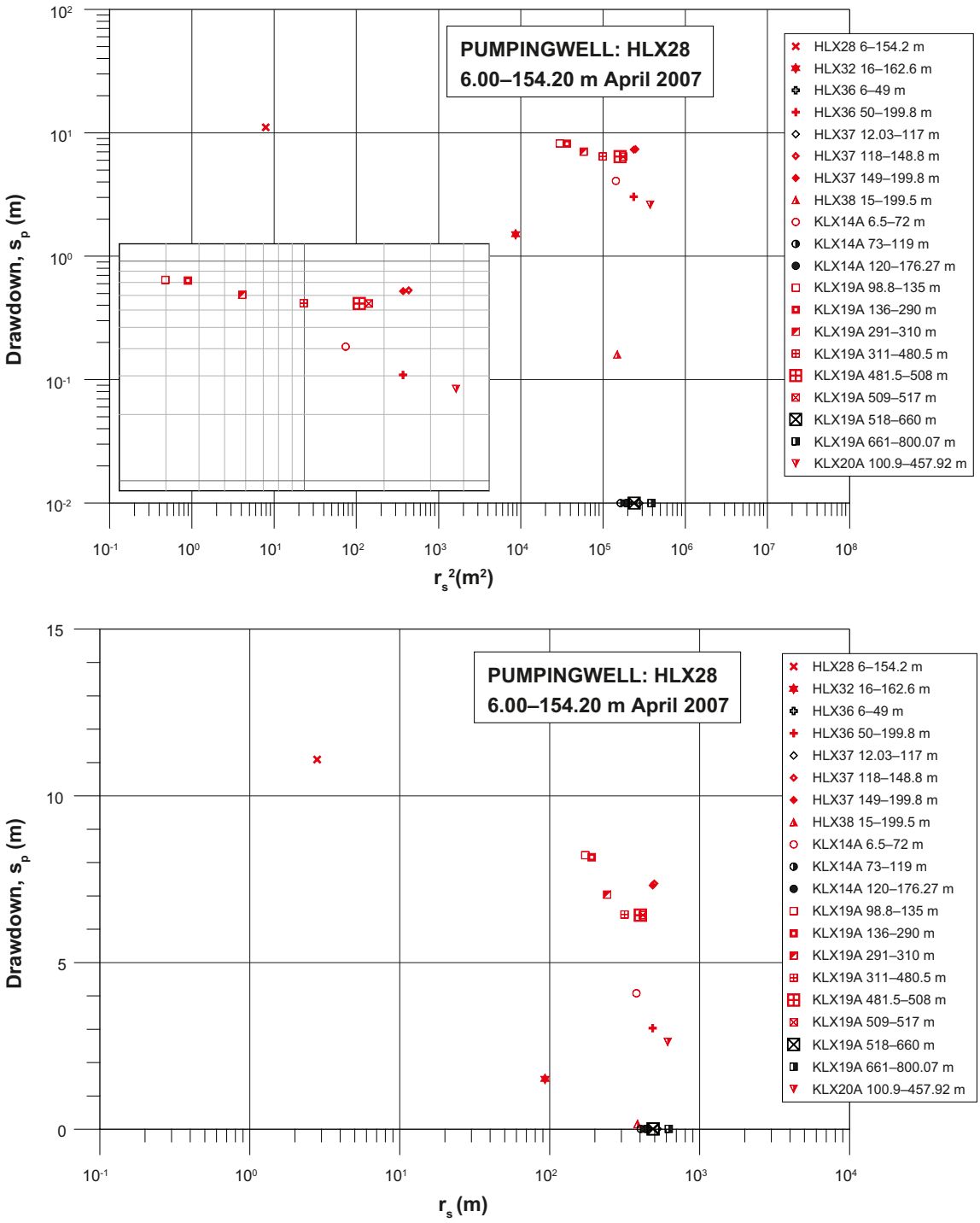

Figure A1-7. *Distance-drawdown plots. Test in April 2007 with HLX28 as pumping borehole.*

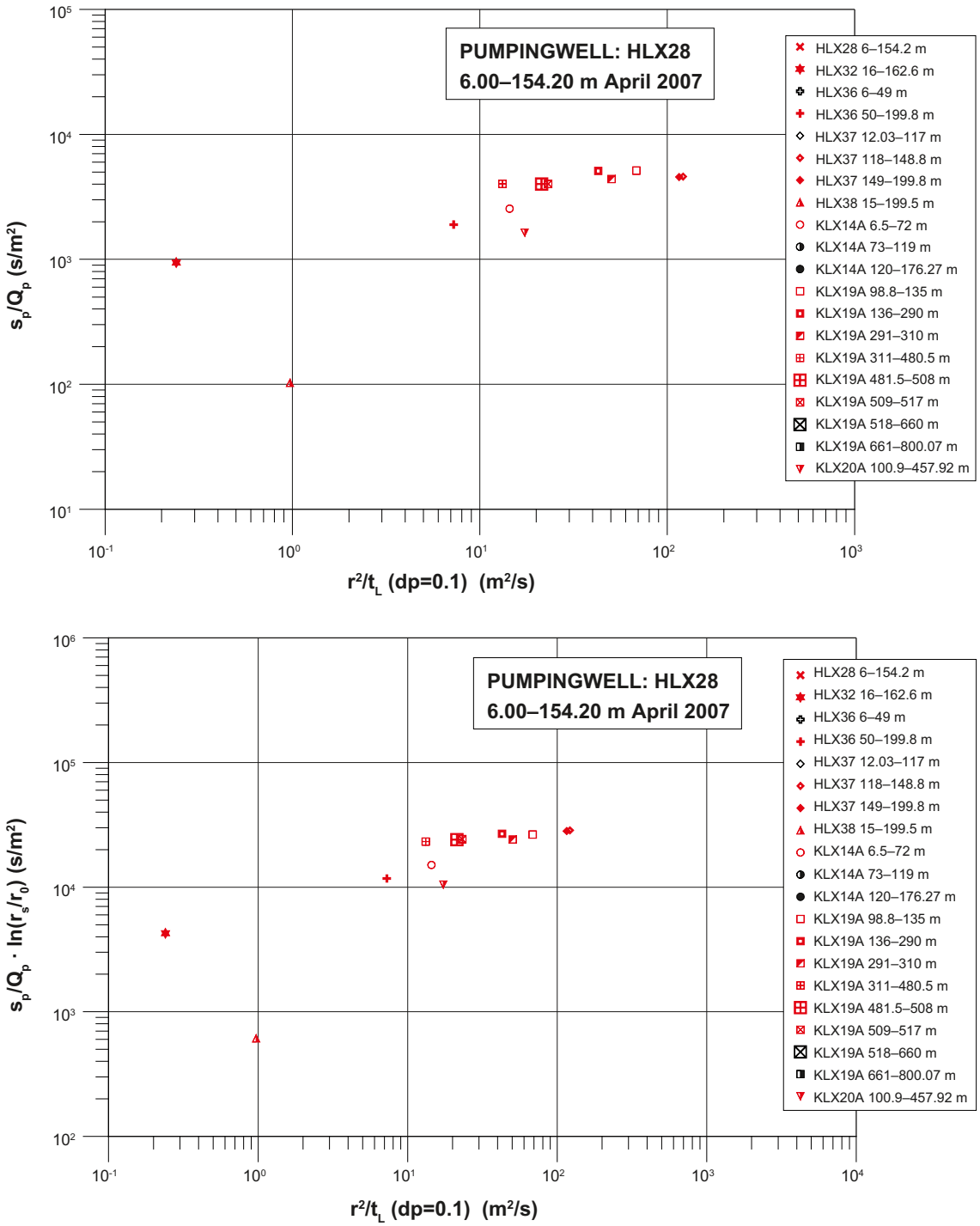

Figure A1-8. *Response- index plots. Test in April 2007 with HLX28 as pumping borehole.*

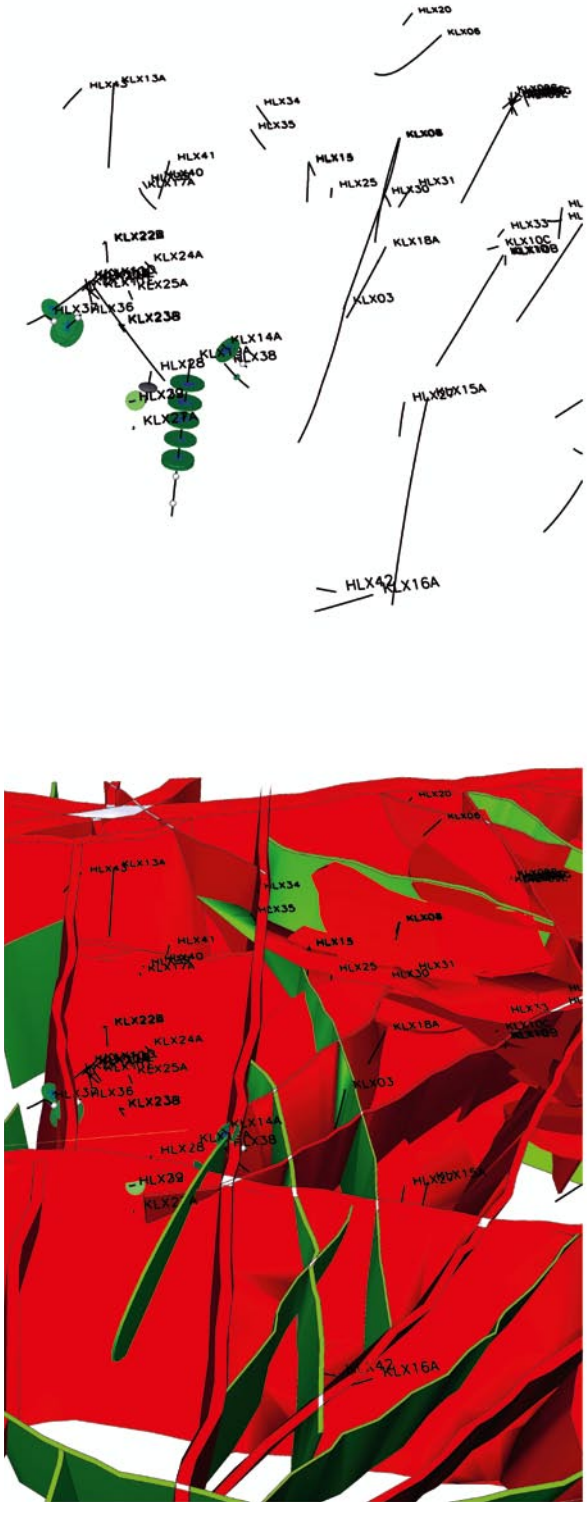

Figure A1-9. *Test in April 2007 with HLX28 as pumping borehole. Top of figures: north part of local model area. A steeply dipping dolerite dyke striking NNE intersects KLX19A below the responses in the borehole. Response indexes are mapped on the boreholes. Pumping hole plotted as a black disc. The larger the disc (green or blue) for a response index is, the better hydraulic contact with pumped borehole section can be assumed. No-response is indicated with a grey sphere. A borehole without discs or spheres have not been measured.*

Figure A1-10. *Test in April 2007 with HLX28 as pumping borehole. Top of figures: north part of local model area. Deformation zone ZSMNW042A and hlx28_dz1 (a subhorizontal disc intersection HLX28) are removed in the figure to better show responses. A steeply dipping dolerite dyke striking NNE intersects KLX19A, KLX19_DZ5-8_DOLORITE, below the responses in the borehole. Response indexes are mapped on the boreholes. Pumping hole plotted as a black disc. The larger the disc (green or blue) for a response index is, the better hydraulic contact with pumped borehole section can be assumed. No-response is indicated with a grey sphere. A borehole without discs or spheres have not been measured.*

There are clear responses in the uppermost section in KLX14A, KLX19A sections between 98.8 to 517 m borehole length and KLX20A (open borehole conditions), HLX37 two bottom section and HLX36 sections and in HLX28. There are small responses in HLX32 and HLX38, but no responses in KLX14A two lowest sections, KLX19A two lowest sections and HLX37 uppermost section.

The pumping borehole HLX28 shows a early response rather typical for a dual porosity system or layered system or delayed yield, indicating that the first part represents a high transmissive feature of limited extension. The early response indication of a layered system character can also be seen in the three uppermost sections in KLX19A. By the end of the flow period there is a weak indication in HLX28 that spherical flow is beginning to develop, which indicates that probably several intersecting structures interact. This weak tendency for a "leaky" character for late times, or pseudo-spherical flow regime, can also be seen in several of the observations sections.

Conclusions

ZSMNS059A acts as an barrier, as can be seen by the responses in KLX14A. ZSMNW942A or a modelled dolerite dyke, KLX19_DZ5-8_DOLERITE, seems to act as a hydraulic barrier considering responses in KLX19A. However, it seems that test section 3 (509.0–517.0 m) in KLX19A is situated above the hydraulic barrier. This means that the flow anomalies between the two dolerite dykes in KLX19A (modelled as KLX19_DZ5-8_dolerite) are coupled to the rock above the uppermost dolerite dyke, that then seem to be leaking, but the lower dolerite dyke acts more like a hydraulic barrier.

The responses in HLX32 and HLX37:3 (12.03–117 m) are rather small. The responses are not significant in HLX36:2 and HLX37:3. HLX32 response may indicate that ZSMNW042A transmits most of the hydraulic signal from HLX28 along the zone and not across. As the responses in HLX37:1 and: 2 are clear and HLX37:3 is insignificant, the character of ZSMNS001 as a hydraulic barrier is demonstrated. There are clear responses in HLX36:1 but as this section cover the dolerite dyke and rock east of the dyke, the responses are consistent with HLX37 responses. The deformation zone HLX28_DZ1 is probably not intersecting ZSMNS001 as there are no responses in HLX37:3.

The non-responses in the upper most section in HLX36 may just be due to tight rock. KLX20A (north of HLX36 and HLX37) was an open borehole without packer during the test and drilled through the dolerite dyke but seem not have affected the test acting as a hydraulic short-cut.

Possibly both HLX28_DZ1 and ZSMNW042A structures transmit the hydraulic response to the eastern part of ZSMNS001, part C.

A1.4 Interference test; KLX19 and KLX20A

Deformation zone ZSMNS001 is of particular interest as it is a dolerite dyke, and as such, a potential hydraulic barrier as thicker dolerite dykes is expected to be low-conductive.

Two pumping tests were conducted during the same period in KLX20A and KLX19A, due to some practical reasons. Observations were made in boreholes (No of sections within parenthesis): HLX36 (2), HLX37 (3), HLX43 (2), KLX11A (1), KLX11B (1) and KLX20A (3) /Walger et al. 2007, Enachescu et al. 2007a/.

Test description

The interference tests were performed as flows:

KLX20A:1 (pumped borehole section 250.2–306.2 m), 2006-11-15 to 2001-11-20. (RVS_INFO 13144401).

KLX20A:2 (pumped borehole section 99.5–180 m), 2006-11-21 to 2001-11-25. (RVS_INFO 13144402).

KLX19A (pumped borehole section 92.75–800.07 m), 2006-11-12 to 2001-11-18. (RVS_INFO 13143474).

In Figure A1-11 the pumped borehole and the observation boreholes are shown.

The pumping 1 in KLX20A was performed in a packed-off borehole within borehole length 250.2–306.2 m with final pumping rate $Q_p = 4.87 \cdot 10^{-5}$ m^3/s and arithmetic mean pumping rate $Q_m = 4.83 \cdot 10^{-5}$ m^3/s. The pump time was t_p = 2,880 min (2 days) with a draw at pump-stop of s_p = 25.58 m.

The pumping 2 in KLX20A was performed in a packed-off borehole within borehole length 99.5–180 m with final pumping rate $Q_p = 2.55 \cdot 10^{-4}$ m^3/s and arithmetic mean pumping rate $Q_m = 2.57 \cdot 10^{-4}$ m^3/s. The pump time was t_p = 2,880 min (2 days) with a draw at pump-stop of s_p = 40.05 m.

The pumping in KLX19A was performed in an open borehole within borehole length 98.8–800.1 m with final pumping rate c. $Q_p = 9.68 \cdot 10^{-4}$ m^3/s. The pump time was t_p = 8,281 (5.75 days) with a draw at pump-stop of c. s_p = 9.7 m.

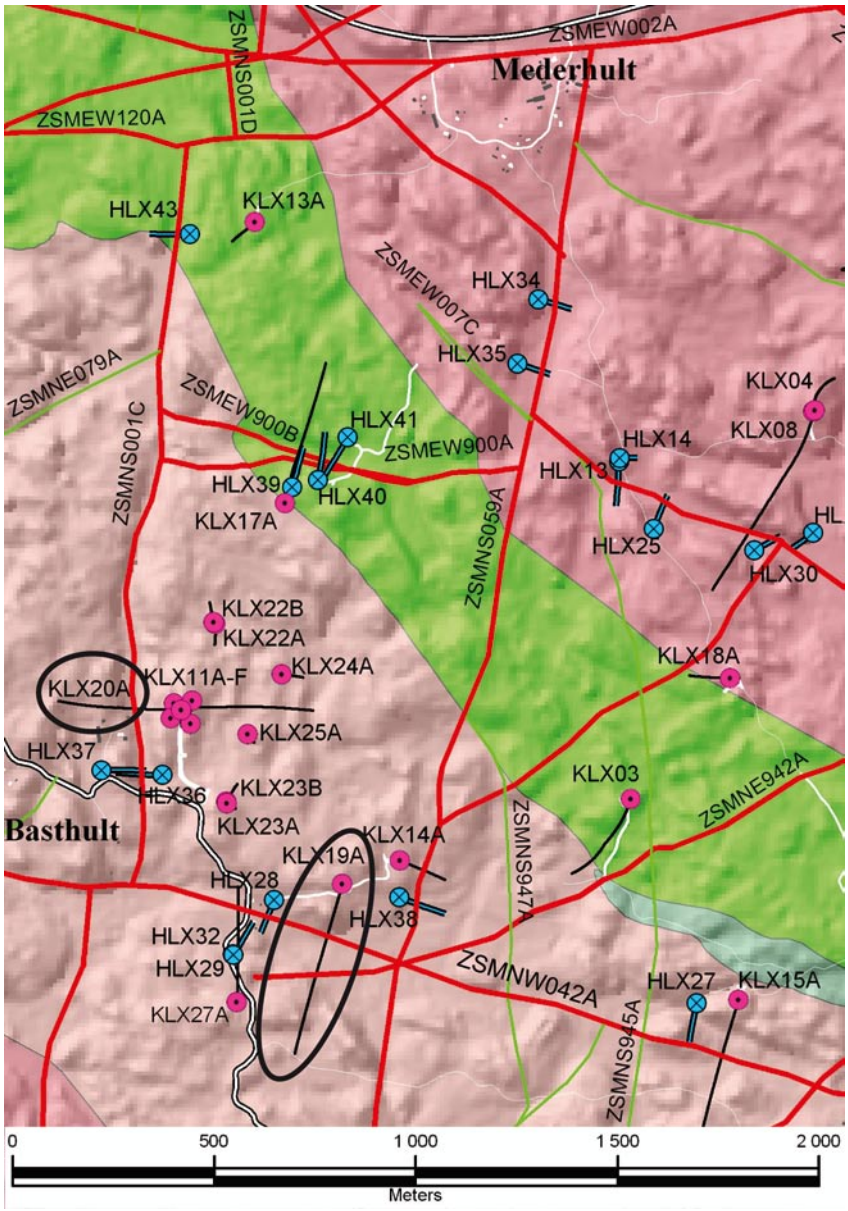

Figure A1-11. *Borehole map. Test in November 2006 with KLX20 and KLX19 as pumping boreholes.*

Responses

The responses from these three hydraulic disturbances in HLX37 can be seen in Figure A1-12.

Test in November 2006 with KLX20:1 (250.2–306.2 m) as pumping borehole: The responses are shown as final drawdown at pumping stop in Figure A1-13, using the skin factor of the pumped section to estimate the effective borehole radius. The response indexes for the observation boreholes are presented in Figure A1-14 and mapped on the structural model in Figure A1-15.

Test in November 2006 with KLX20:2 (99.5–180 m) as pumping borehole: The responses are shown as final drawdown at pumping stop in Figure A1-16, using the skin factor of the pumped section to estimate the effective borehole radius. The response indexes for the observation boreholes are presented in Figure A1-17 and mapped on the structural model in Figure A1-18.

Conclusions

It is concluded from the responses that ZSMNS001 must have a tight core but permeable wall rock, at least in the southern part of ZSMNS001 near KLX20A, see Figure A1-19 for the interpreted hydraulic communication paths:

- Pumping in KLX20A on the west side of the dolerite dyke in ZSMNS001 generates responses in borehole HLX37 west of the dolerite dyke in ZSMNS001 and no responses east of the dolerite dyke (**Test 1**).
- When pumping in KLX20A on the east side of the dolerite dyke in ZSMNS001 generates responses in borehole HLX37 east of the dolerite dyke in ZSMNS001 and no responses west of the dolerite dyke (**Test 2**).
- Pumping in KLX19A gives clear responses East of dyke but NOT west of dyke.

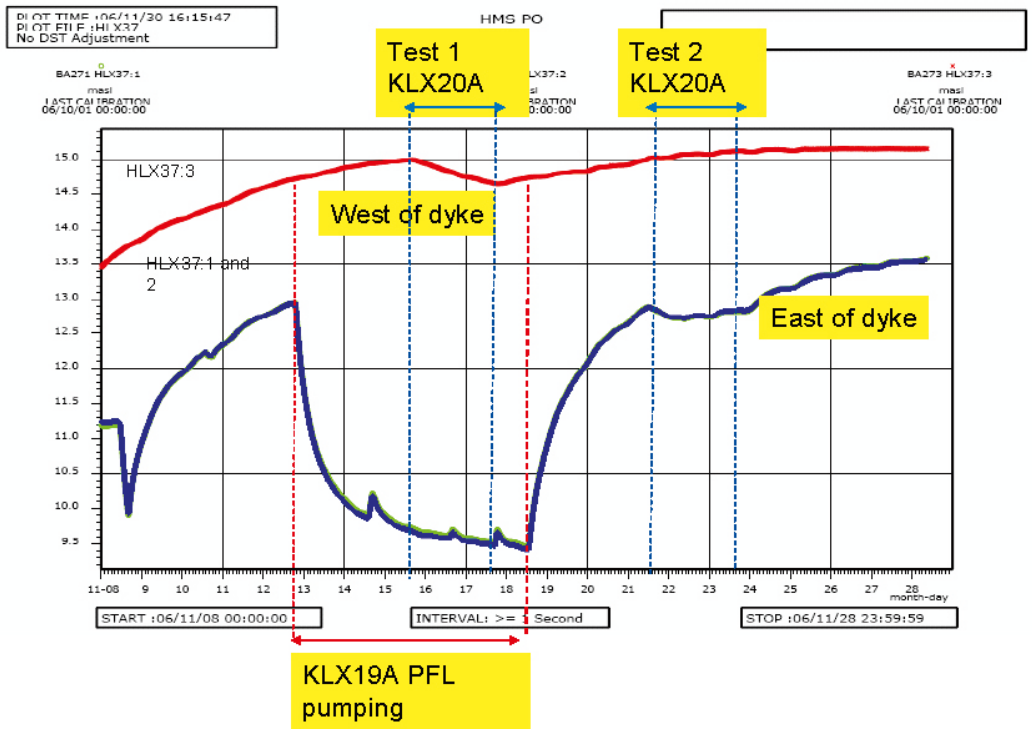

Figure A1-12. *Hydraulic head plots. Test in November 2006 with KLX20 and KLX19 as pumping boreholes.*

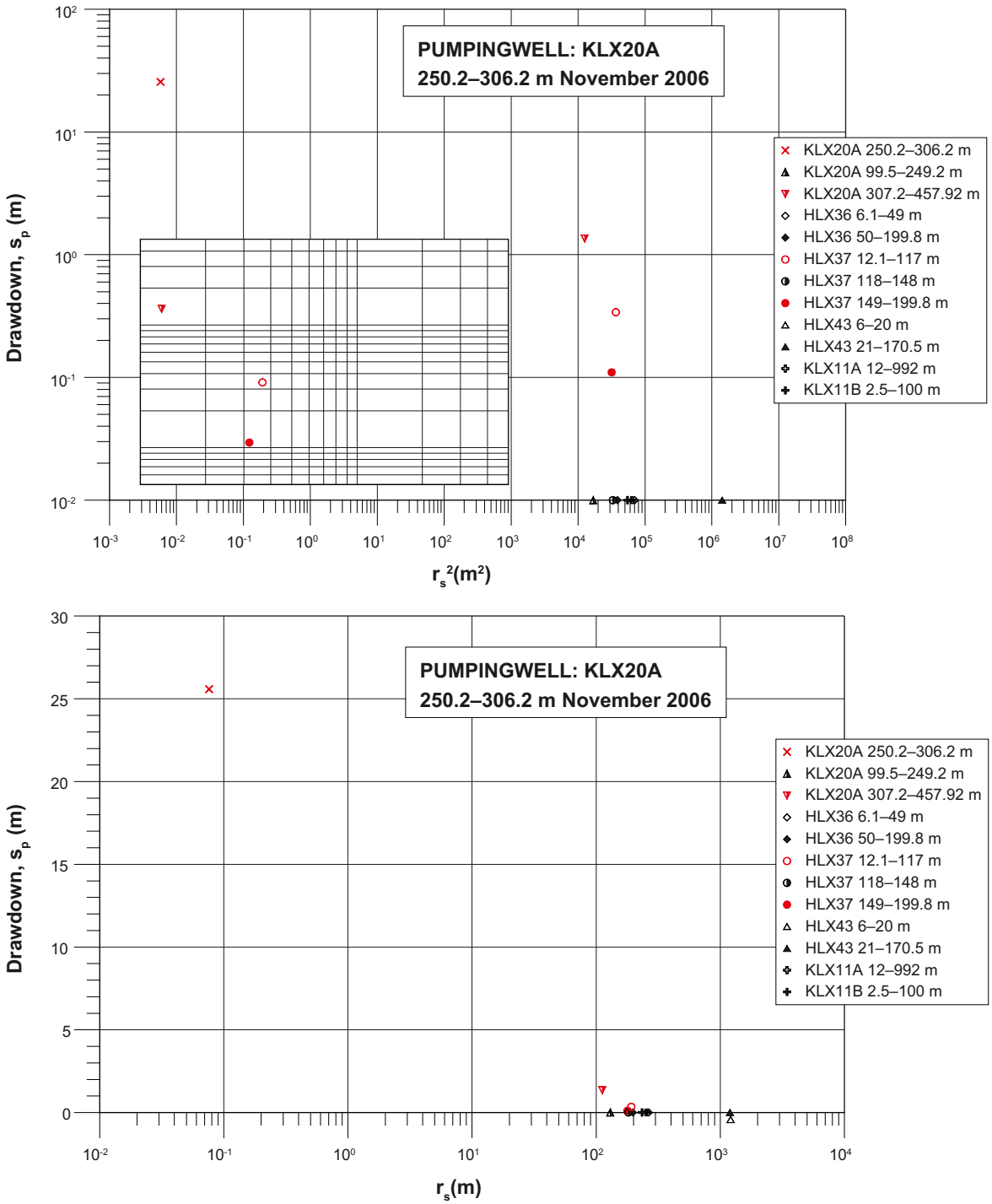

Figure A1-13. *Distance-drawdown plots. Test in November 2006 with KLX20:1 (250.2–306.2 m) as pumping borehole.*

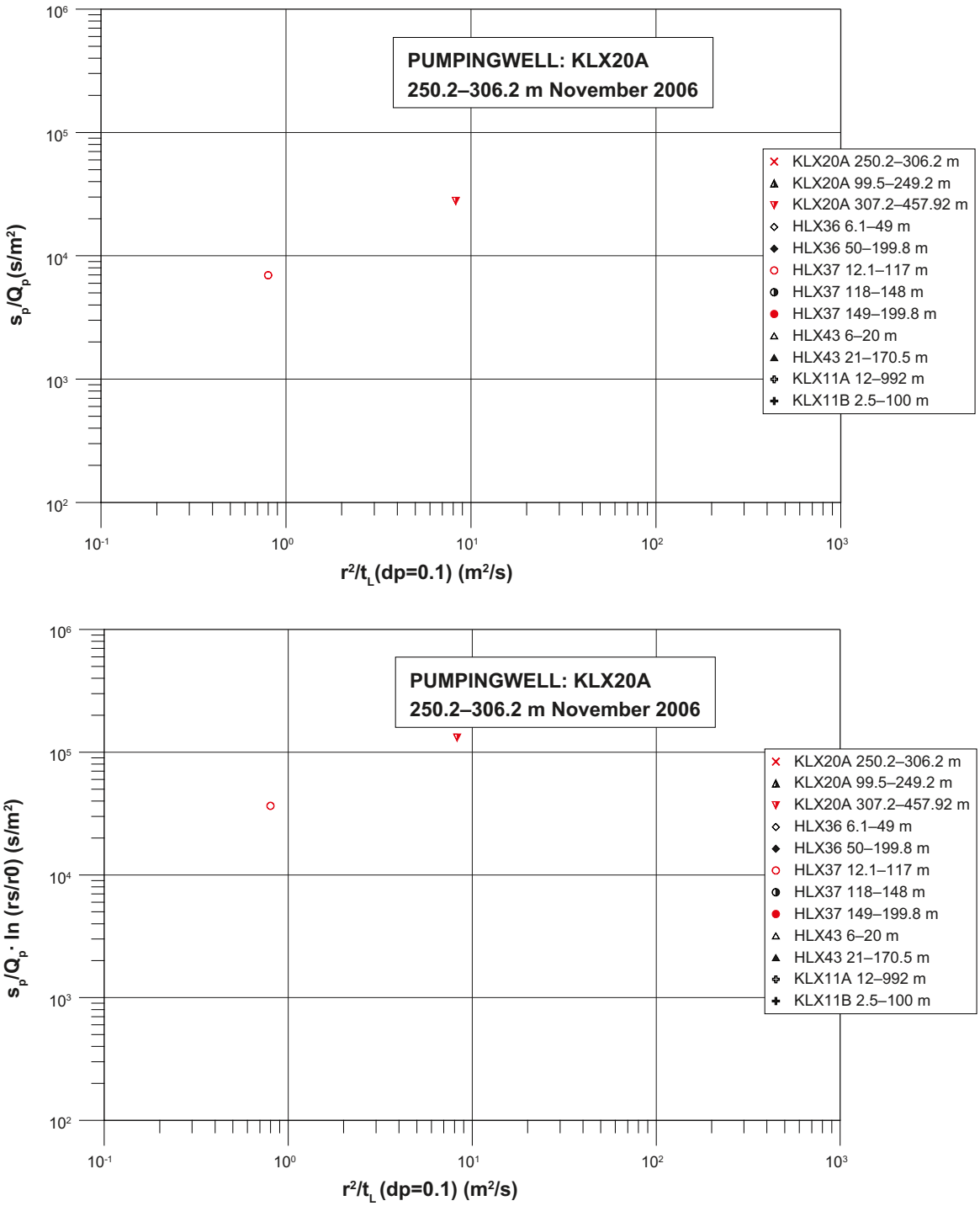

Figure A1-14. *Response- index plots. Test in November 2006 with KLX20:1 (250.2–306.2 m) as pumping borehole.*

Figure A1-15. *Test in November 2006 with KLX20:1 (250.2–306.2 m) as pumping borehole. Top of figures: north part of local model area. Response indexes are mapped on the boreholes. Pumping hole plotted as a black disc. The larger the disc (green or blue) for a response index is, the better hydraulic contact with pumped borehole section can be assumed. No-response is indicated with a grey sphere. A borehole without discs or spheres have not been measured. (RVS_INFO 13144401).*

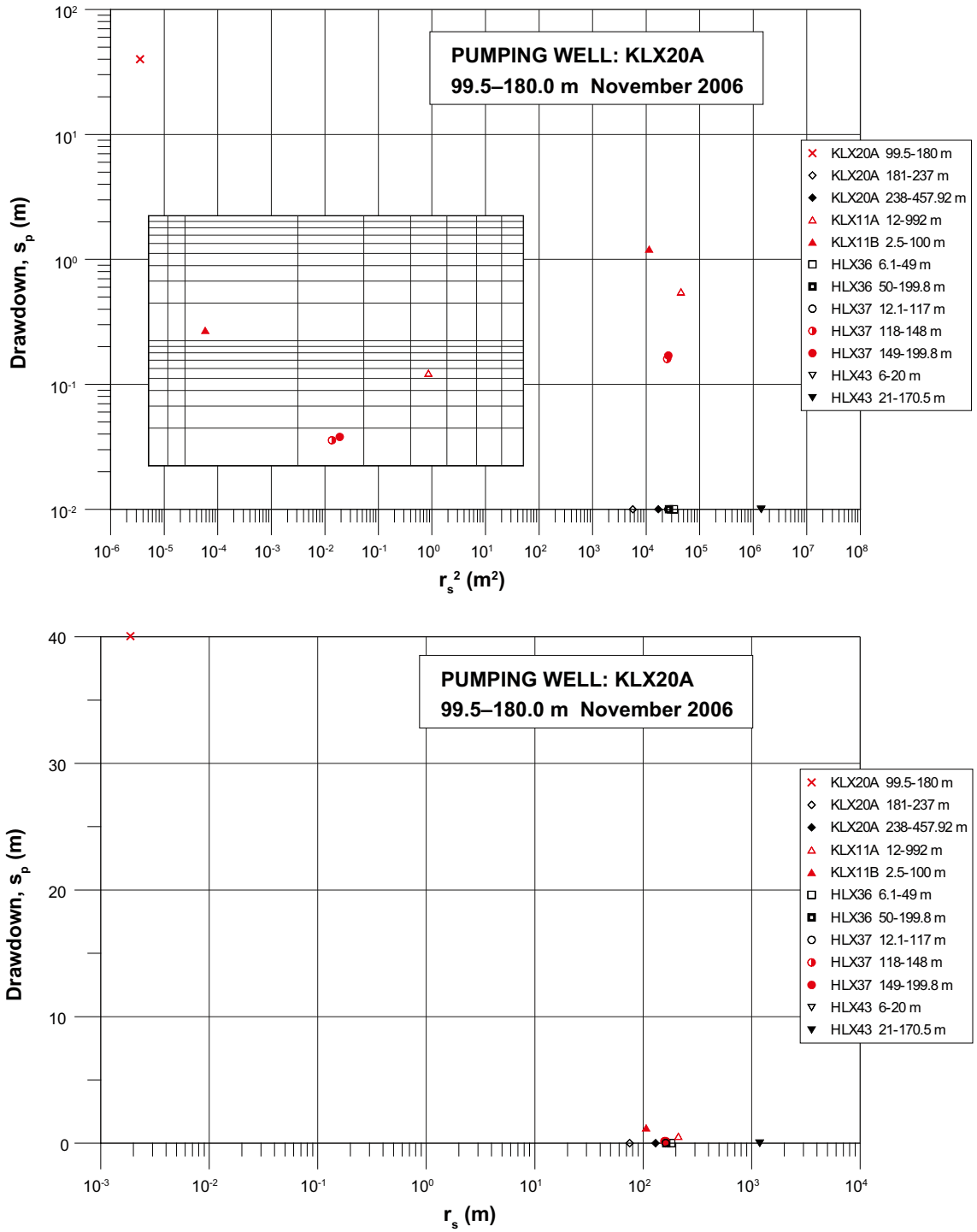

Figure A1-16. *Distance-drawdown plots. Test in November 2006 with KLX20:2 (99.5–180 m) as pumping borehole.*

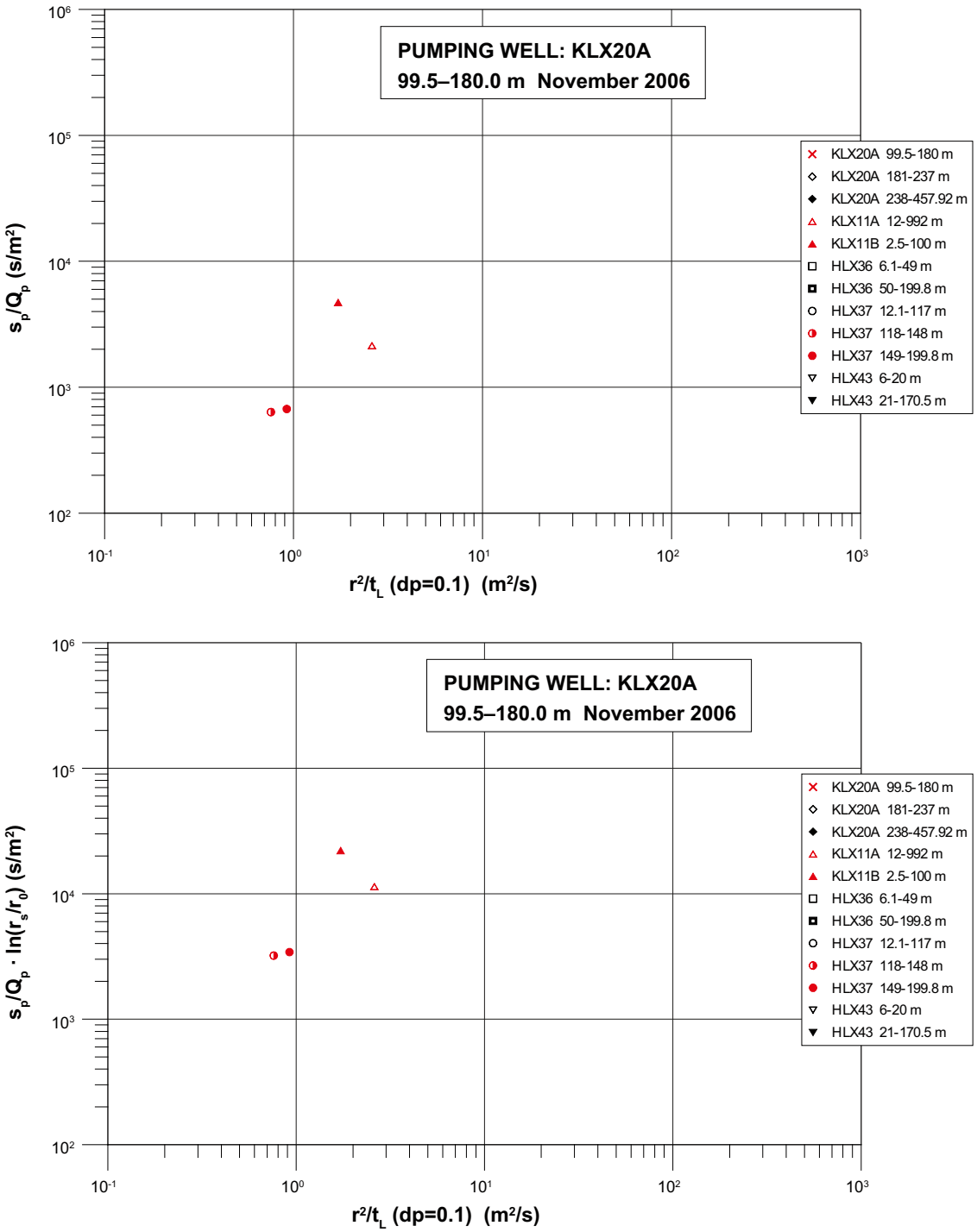

Figure A1-17. *Response- index plots. Test in November 2006 with KLX20:2 (99.5–180 m) as pumping borehole.*

Figure A1-18. *Test in November 2006 with KLX20:2 (99.5–180 m as pumping borehole. Top of figures: north part of local model area. Response indexes are mapped on the boreholes. Pumping hole plotted as a black disc. The larger the disc (green or blue) for a response index is, the better hydraulic contact with pumped borehole section can be assumed. No-response is indicated with a grey sphere. A borehole without discs or spheres have not been measured. (RVS_INFO 13144402).*

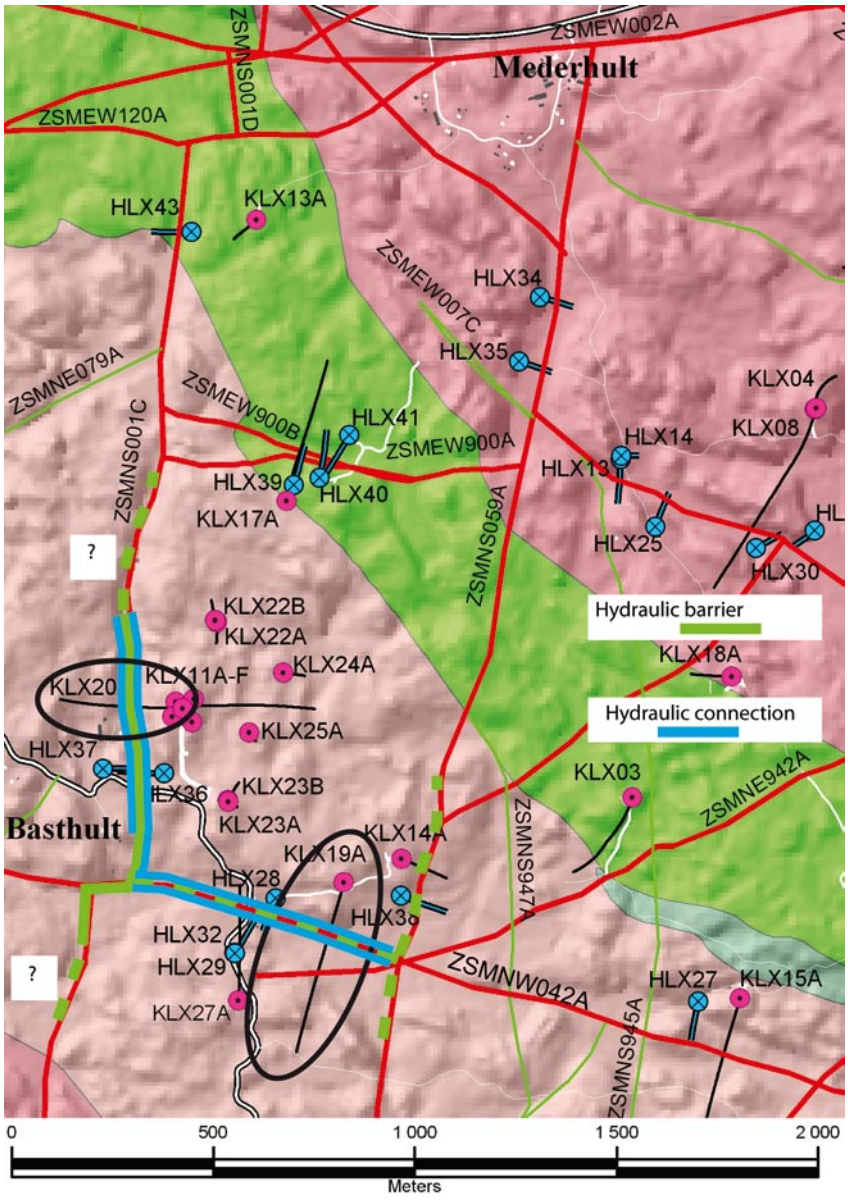

Figure A1-19. *Interpreted hydraulic connections. Test in November 2006 with KLX20 and KLX19 as pumping boreholes.*

A1.5 Interference test; KLX27A

The interference test was performed between 2008-01-03 to 2008-01-16 with KLX27A as pumping hole (entire borehole). Observations were made in boreholes (No of sections within parenthesis): KLX11A (10), KLX11E (1), KLX14A (3), KLX19A (8), KLX20A (6), KLX23A (2), KLX24A(3), HLX36 (2), HLX37 (3) and HLX38 (1) as observation boreholes. The test is not reported as an interference test but responses are available in the database and the pumping during PFL-logging and single hole evaluations are reported in /Pöllänen et al. 2008, Enachescu et al. 2008c/.

Test description

The pumping was performed in an open borehole within borehole length 14.76–650.56 m with final pumping rate c. $Q_p = 2.32 \cdot 10^{-4}$ m^3/s. The pump time was c. $t_p = 13$ days with a draw at pump-stop of c. $s_p = 10.0$ m. In Figure A1-20 the pumped borehole and the observation boreholes are shown.

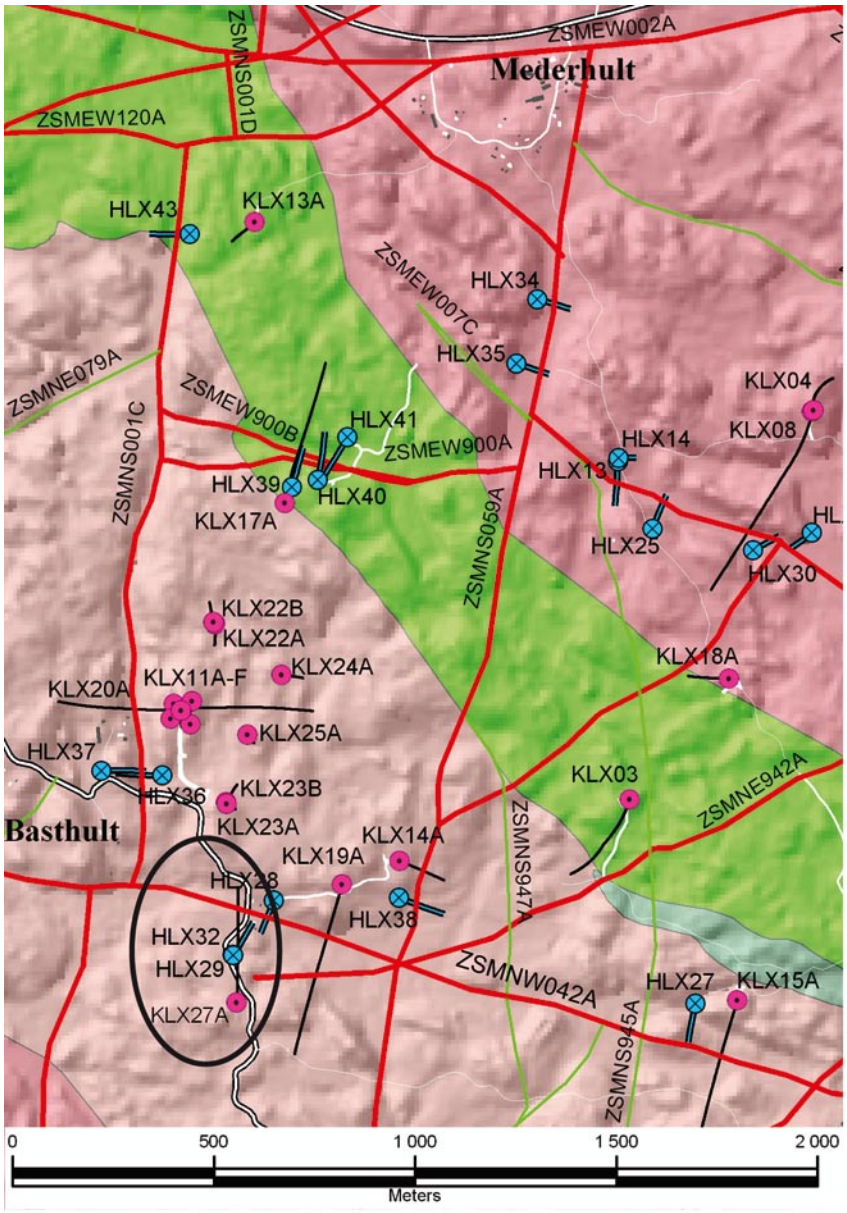

Figure A1-20. *Borehole map. Test in January 2008 with KLX27A as pumping borehole.*

Responses

The pumping in KLX27A 2008-01-03 to 2008-01-09 caused some response (a few dm) in the nearby KLX19A (sections 3–8, 0–509 m borehole length) and clear responses in the more distant KLX11A (sections 2–7, 180–702 m borehole length), see Figure A1-21. Other wise hardy any response could be seen.

Conclusions

Deformation zone KLX11_DZ11

Looking at the PFL logging in KLX27A ca 70% of the pumped flow should come from bh section 580–650 m and the rest from borehole section 70–250 m (ZSMNW0042 position in the bh) /Pöllänen et al. 2008/.

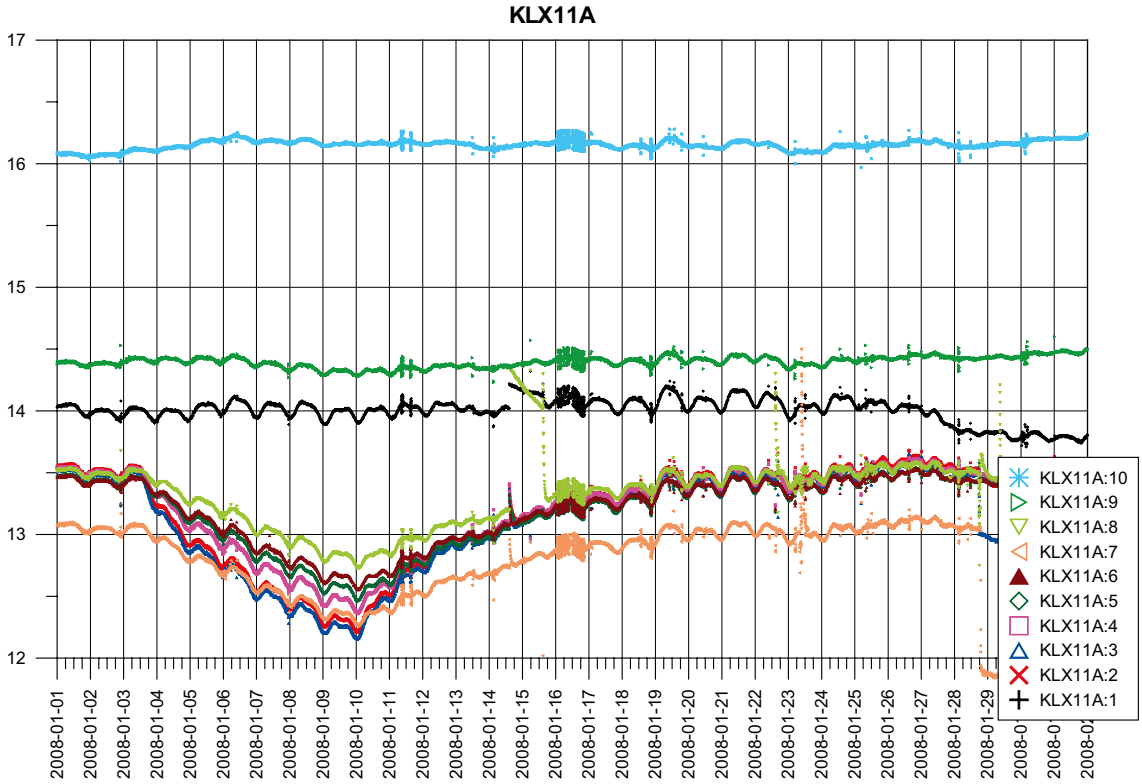

Figure A1-21. *Groundwater levels plot. Test in January2008 with KLX27A as pumping borehole.*

Pumping in HLX28 and KLX19A have indicated that responses probably transmits along ZSMNW042A, HLX28_DZ1 and ZSMNS001, see previous sections, and reaches HLX36, HLX37 and KLX20A and KLX11A boreholes in the near surface part. It was only open bh conditions in KLX11A during tests in KLX20A and KLX19A, but responses could be seen in KLX11A, KLX11B and KLX11E. Reponses in KLX11B and KLX11E clearly demonstrate the hydraulic barrier effect in ZSMNS001 during the two pumpings in KLX20A. Based on the tests in KLX20A, KLX19A and HLX28A it can be concluded that it is only the top part of KLX11A (0–179 m) that is in some way connected to ZSMNS001s eastern contact zone.

This suggests that one or possibly two hydraulic structures making a significant contact between lower part of KLX27A and “mid part” of KLX11A. The responses in KLX11A are quite uniform; that rather should indicate that a feature in running more or less parallel with KLX11A. However, looking in more detail the largest drawdown is in section 3 followed by, in decreasing order: 4, 5, 6, 7, 8 (visual check). It seems that section 2 has a drawdown rather similar as 3. This means that the possible hydraulic feature is closest at bh length ca 573–586 m, where we have significant geological and hydrogeological indications and KLX11_DZ11 defined. Hydraulically and geologically one should say that probably responses in section 2 come from the location with borehole length ca 600 m! Comparing with dip and strike of KLX11_DZ11 (strike/dip: 065/20) it seems right tendency knowing the bh-orientation. The responses in KLX11A is considered most likely to be associated with subvertical N-S striking fractures that maybe associated with one or more steeply dipping to vertical MDZs. Support for this interpretation comes generally from the predominance of N-S steeply dipping fractures and major deformation zones in this area (the western DFN fracture domain, ZSMNS001, ZSMNS059A etc) More specifically N-S brittle-ductile indicators have been identified along the KLX11_DZ11 drillcore interval as well as characteristic N-S trending epidote filled fractures (see the property tables for KLX11_DZ11 in /Wahlgren et al. 2008/. Thus, a hydraulic conducting feature, steeply dipping to subvertical could very reasonably be added to the KLX11_DZ11 interval. As discussed above, a set of steep vertical N-S fractures connected to KLX11_DZ11 can explain the responses in KLX11A.

If it is KLX11_DZ11 that connects to lower part of KLX27A it does not seem to connect to ZSMNS001 and ZSMNW0042 and is not in contact with KLX19A and KLX20A (Geometrically KLX11_DZ11 is below the bottom of KLX20 and KLX19). It does not seem to be in contact with a possible conductive part of ZSMNS059A. One can hardly see any responses in KLX14A during the pumping in KLX27A, but there are other the dolerite dyke KLX19_DZ5-8_DOLERITE that probably also plays a role.

Deformation zone HLX28_DZ1

When pumping in the upper part of KLX27A (during the drilling) it was rather good contact with HLX32 (both boreholes intercept ZSMNW042A) and just small response in HLX28A and ZSMNW042A (HLX28 is parallel but slightly to the north of ZSMNW042A. Probably HLX28_DZ1 do not extend through and south of NW042. This is supported by the fracture orientation evidence from HLX32 and KLX27 – see property table for HLX28_DZ1 in /Wahlgren et al. 2008/. HLX28_DZ1 is interpreted to intercept HLX28 (target 75–89 m), with modelled thickness of only 10 m i.e it is at the lower size limit for deterministic modelling. Although has a ductile origin very open fractures are noted in the HLX28 DZ section. When looking at the potential intercepts in KLX11A, two sections are noted 142–143 m and 162–163 m i.e two very thin features. They have the same character and orientation as the HLX28_DZ1.

Pumping in HLX28 and KLX19 have indicated good contact with borehole sections east of ZSMNS001 in KLX20A and HLX36 and 37 as well as KLX11B and KLX11E. HLX28_DZ1 as well as hydraulic contacts along ZSMNW042A and ZSMNS001 can possible both explain the responses from interference tests. A problem here is that responses are within near-surface rock that we know generally is more permeable. Known is that there is a fairly good contact between KLX20A and KLX11 B–F, but they are also close. The natural head difference between HLX32 and HLX28 (7 m) is large also indicate that HLX28_DZ1 does probably not intercept ZSMNW042A. HLX32 is tighter than HLX28, but not very tight; so it is likely to connect to a wider rock volume.

Summary of some observations

Deformation zone KLX11_DZ11

This feature has its original orientation intersecting KLX11A (borehole-length: 486–513 m) and it goes ca 15 m below bottom of KLX27A (KLX11_DZ11 elevation c. –567 m). The conductive section in KLX27A below bh length 496 m consist of nearly just steep fractures with strike ca E-W, providing a possible hydraulic connection between bottom of KLX27A and KLX11A via KLX11_DZ11, explaining the responses in KLX11 when KLX27A was pumped. (Looking at the PFL logging ca 70% of the pumped flow should come from borehole section 580–650 m and the rest from 70–250 m (ZSMNW042A position in the borehole) in this pumping test). As KLX11_DZ11 is just 48 m below KL20A (KLX11_DZ11 there has the elevation c. –311 m) and the interference tests in KL20A shows zero response on the side of ZSMNS001 not pumped it seem likely that KLX11_DZ11 does not intersect NS001.

HLX28_DZ1

HLX28_DZ1 is interpreted to intersect KLX11A (target 142–163 m) and HLX28 (target 75–89 m) but does probably not cross ZSMNW042A and ZSMNS001.

Deformation zone ZSMNW042SA

There is a pressure drop in KLX27 during natural conditions (ca 2.5 m: ca +12 to 12.5 m north of NW002 and ca +9 to +9.5 m south of ZSMNW042) that probably can be explained by having fault-gauge in ZSMNW042 between ZSMNS001 and ZSMNS0059A. It is unlikely that we have fault-gauge continuously along the ZSMNW042A (test summer 2008, not reported yet, in HLX27 indicate this). So ZSMNW042A should be modelled as a semi-permeable barrier between ZSMNS001 and ZSMNS059A.

KLX19_DZ5-8_DOLERITE

This feature that acts as a hydraulic barrier is needed to describe the pressure jumps in KLX19A and also hydraulic responses from tests east of this borehole.

A1.6 Interference test; HLX33, June–August 2006

The interference test was performed between 2006-06-28 and 2006-08-07 (c. 40 days; 960.7 hrs) with HLX33 as the pumping well. Hydraulic observations were made in boreholes (the number of sections is show within parenthesis): HLX11 (2), HLX23 (2), HLX24 (2), HLX25 (2), HLX30 (2), HLX31 (1), HLX33 (1), KLX02 (8), KLX04 (8), KLX07A (8) and KLX07B (2). Unfortunately no responses are available for boreholes KLX01, KLX10, KLX10B, KLX10C and KLX08A. The test is reported in /Morosini et al. 2009/.

Test description

The pumping was performed in an open borehole within borehole length 9.0–202.1 m with final pumping rate Q_p = 0.00162 m^3/s. The pump-test started 2006-06-28. The pump time was t_p = 960.7 h (40.0 days) with a draw at pump-stop of s_p = 13.46 m. In Figure A1-22 the pumped borehole and the observation boreholes are shown.

The test is also influenced by pumping in HLX14 (that was used for drilling water). The pumping in HLX14 started 2006-05-22, i.e. c. 40 days (54,000 min) before pump-start in HLX33 with a flow rate of c. 0.00082 m^3/s (49 L/min) and with a sudden increase to 0.00092 m^3/s (55 L/min) 2006-06-27 and a pump-stop 2006-10-27.

HLX33 is a borehole with high transmissivity and is judged to be well connected to the deformation zone ZSMEW007.

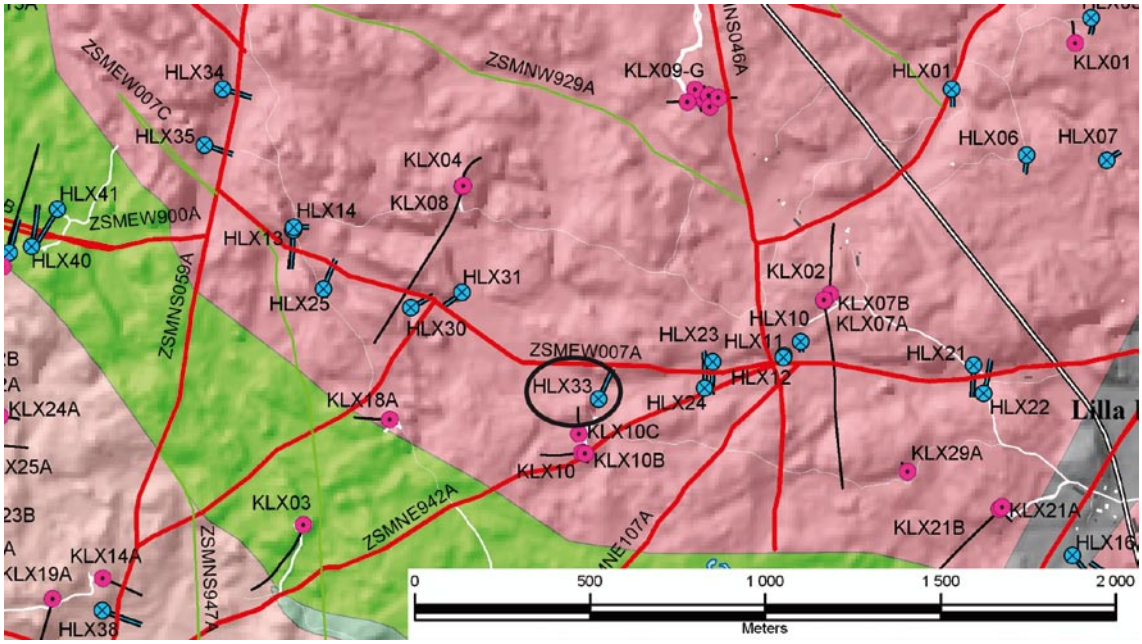

Figure A1-22. *Borehole map. Test in June–August 2006 with HLX33 as pumping borehole.*

Responses

The responses are shown as final drawdown at pumping stop in Figure A1-23 using the skin factor of the pumped section to estimate the effective borehole radius. The response indexes for the observation boreholes are presented in Figure A1-24 and mapped on the structural model in Figure A1-25 and Figure A1-26. All data was trend corrected for a decreasing trend during the entire period. Heavy rainfall at the end of the recovery period disturbed the last part of the pressure recovery.

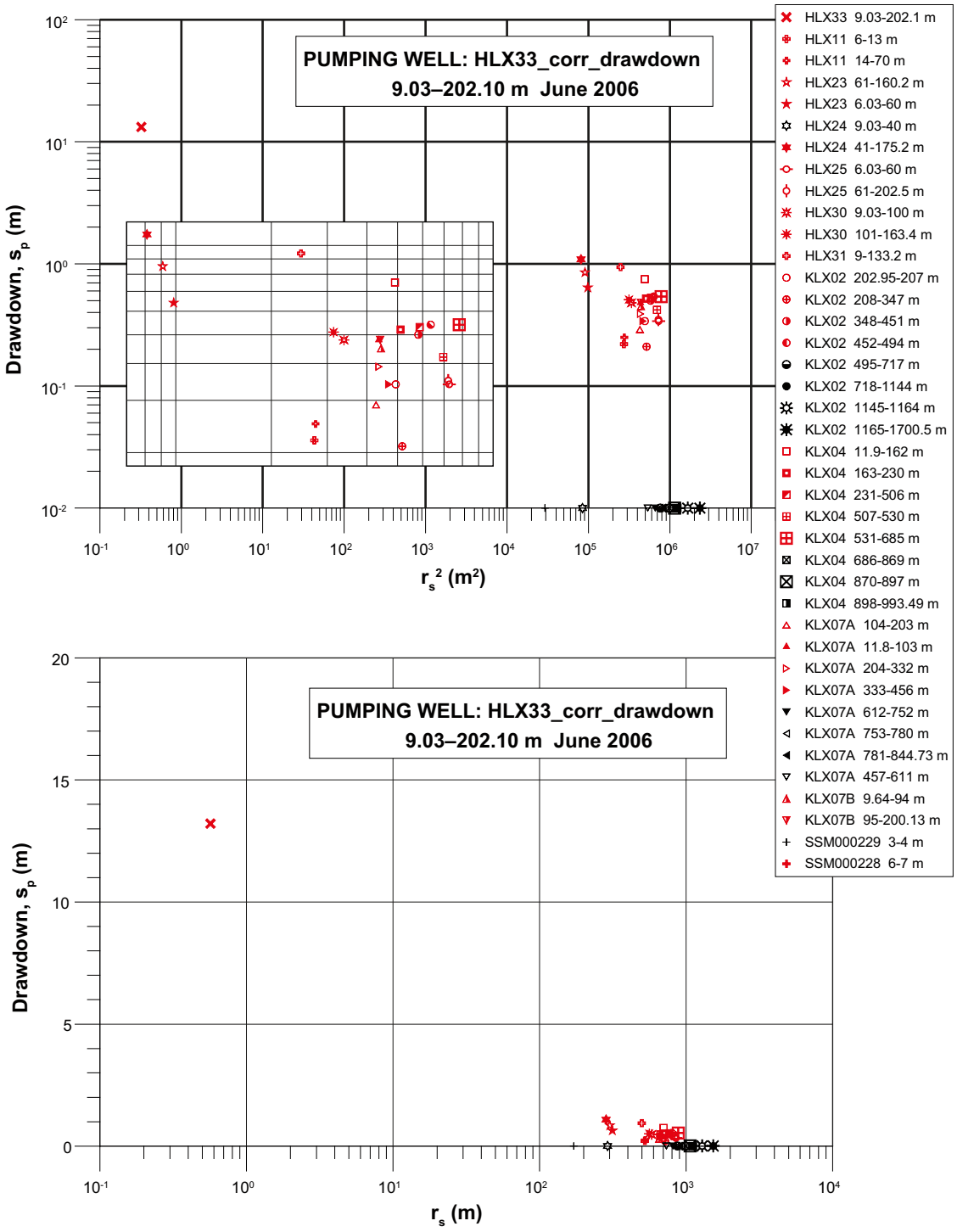

Figure A1-23. *Distance-drawdown plots (including blow-up) related to June–August 2006 interference test with HLX33 as pumping borehole. Drawdown at pump stop is shown. No response is plotted as a 0.02 m drawdown with black symbols, cf lower right of main plot).*

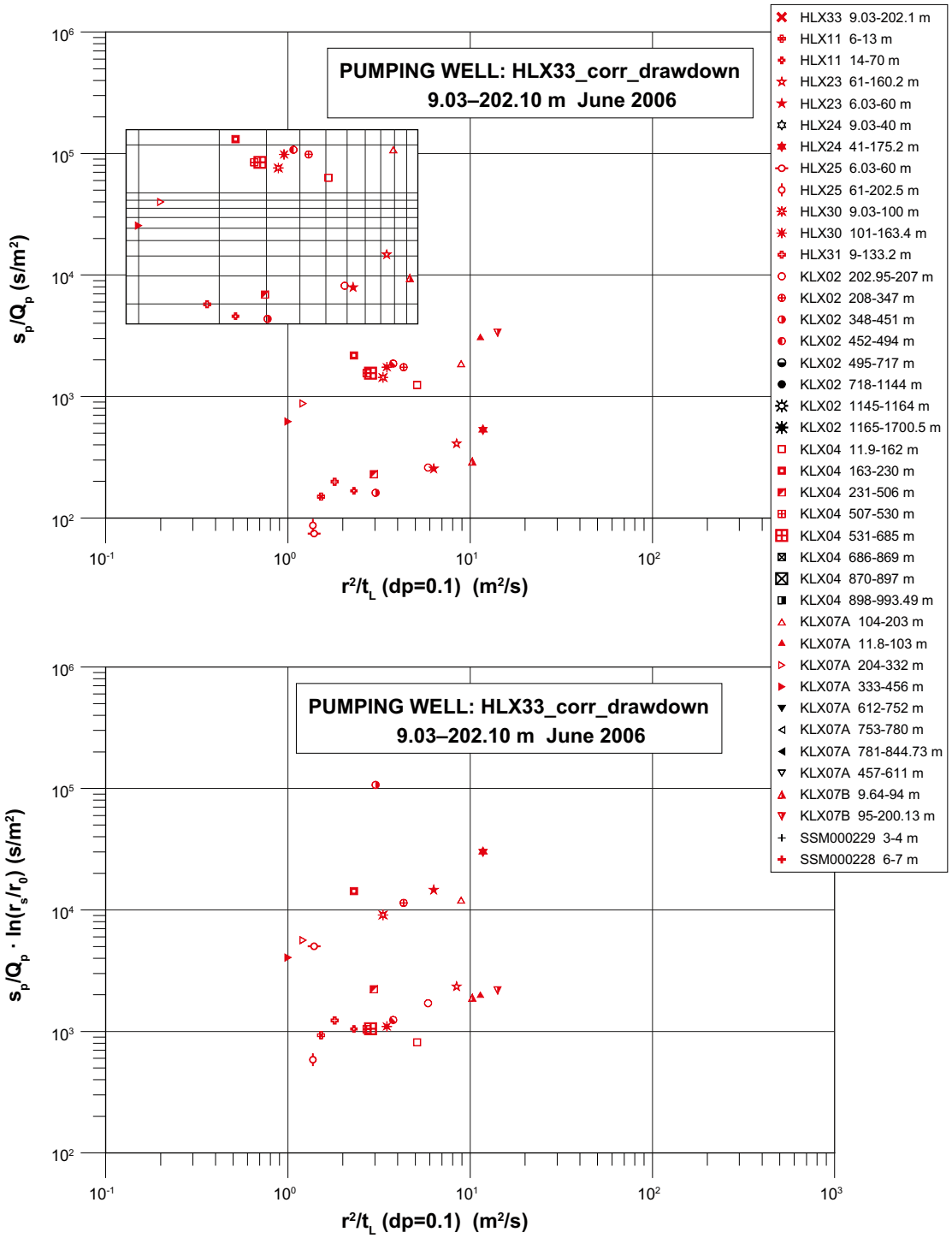

Figure A1-24. *Response- index plots. Test in June–August 2006 with HLX33 as pumping borehole.*

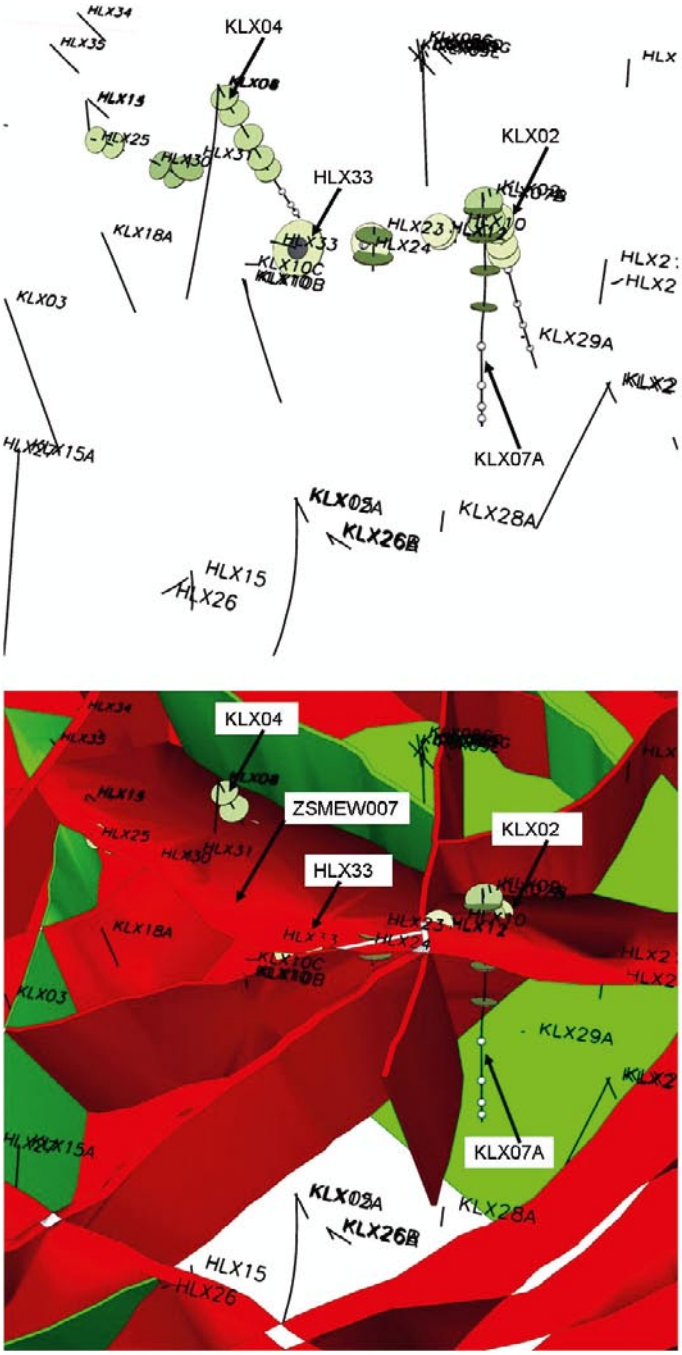

Figure A1-25. *Test in June–August 2006 with HLX33 as pumping borehole. Top of figures: north part of local model area, view from SSE. Response indexes are mapped on the boreholes. Pumping hole plotted as a black disc. The larger the disc (green or blue) for a response index is, the better hydraulic contact with pumped borehole section can be assumed. No response is indicated by a grey sphere. A borehole without discs or spheres have not been measured. (RVS_info: HLX33–13178725).*

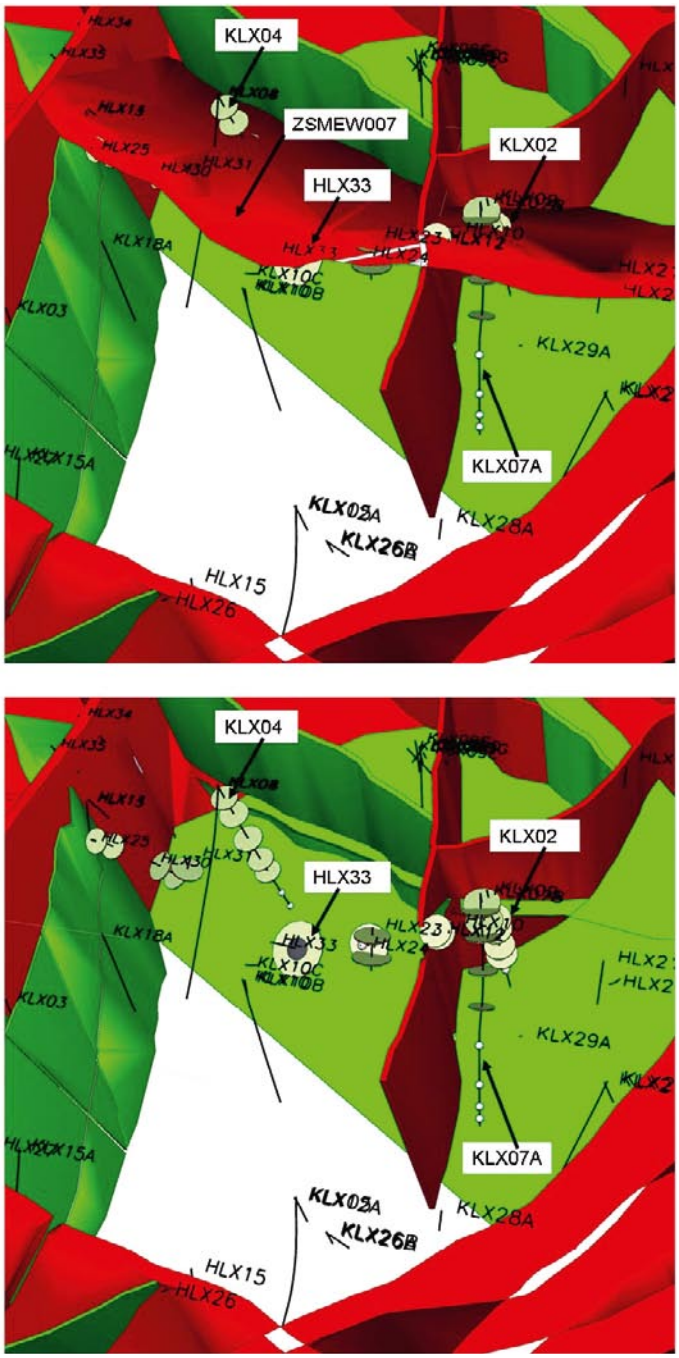

Figure A1-26. *Test in June–August 2006 with HLX33 as pumping borehole. Deformation zones ZSMNE107A, ZSMNE942A, ZSMNE944A and ZSMNE946A(refl M) removed in both figures and also ZSMEW007 in lower figure to display responses. Top of figures: north part of local model area. Response indexes are mapped on the boreholes. Response indexes mapped on the structural model. Pumping hole plotted as a black disc. The larger the disc (green or blue) for a response index is, the better hydraulic contact with pumped borehole section can be assumed. No-response is indicated with a grey sphere. A borehole without discs or spheres have not been measured. (RVS-info: HLX33–13178725)*

Responses are seen in the upper parts of KLX02 and KLX07A and in several short boreholes along the deformation zone ZSMEW007; KLX07B, HLX11, HLX23, HLX24, HLX25, HLX30, HLX31 and HLX33. Responses were also seen in five borehole sections in the upper part of KLX04 (11.9–685 m) that are very uniform.

Conclusions

The fast responses in KLX02 at depths where ZSMEW007 intercepts (modelled intercept 180–200 m), the only responses in the upper part of KLX07A (modelled intercept 105–168 m) as well as clear responses in several percussion boreholes along ZSM007 indicate that the deformation zone dips to the north as geologically modelled.

The response in the upper part of KLX07 is clear down to borehole section 456 m and below that no responses are seen. This is interpreted as responses within HRD_EW007, which is more conductive than other HRD:s and also with a more pronounced anisotropy in the E-W direction. HRD_EW007 is interpreted to be within KLX07A borehole sections: 102–737.9 m.

There are also clear responses in the upper part of KLX04 (above borehole length 685 m) and in KLX04 the deformation zone ZSMEW007 modelled intercept is 310–385 m.The target intersection in KLX04 for the geological modelling of ZSMEW007 is 310–385 m, which is within borehole section 3. Borehole section 3 shows slightly faster response than the other four sections. Otherwise, both the maximum drawdown and the time-lag are rather similar for the five borehole sections indication that there is significant number of subvertical conductive fractures within what is interpreted to be within HRD_EW007 causing the hydraulic responses. HRD_EW007 is interpreted to be within KLX04 borehole sections: 306.6–737.7 m.

The tests support the geological interpretation of the structure dipping towards the north, as described in /Rhén et al. 2008/. For instance, the pumping test in HLX10 in section A1.7 show a very clear responses in one of the monitoring sections in KLX02 (borehole length c. 200–300 m). This fits well with the geologically interpreted geometry of the zone ZSMEW007A /Wahlgren et al. 2008/, as the zone ZSMEW007A is interpreted to be a feature more conductive than the surrounding rock.

Some of the interference tests performed between 1992–1995 pumping the entire KLX02 (201–1,700 m) indicated hydraulic responses in KLX01 (mainly below 700 m borehole length) /Ekman 2001/. A closer look at KLX02 /Andersson et al. 2002/ indicated that in KLX02 borehole section 200–400 m the flowing features were oriented in WNW-NW and that the transmissivity in the upper 500 m of KLX02 was considerably higher than below 500 m. These observations indicate that ZSMEW007A may be one of the important structures causing hydraulic connection between KLX02 and the lower part of KLX01. Also, the geological model /Wahlgren et al. 2008/ projects that ZSMEW007A should intercept KLX01 between 1,000–1,020 m borehole length.

A1.7 Interference test; HLX10, January–February 2005

The interference test was performed between 2004-12-29 and 2005-02-10 with HLX10 as pumping hole Observations were made in boreholes (No of sections within parenthesis): HLX11 (2), HLX13 (1), HLX14 (1), HLX18 (1), HLX21 (2), HLX22 (2), HLX23 (2), HLX24 (2), HLX25 (2), HLX30 (2), HLX31 (2), HLX33 (2) and KLX02 (8) as observation boreholes. The test is reported in /Morosini et al. 2009/.

Test description

The pumping was performed in an open borehole within borehole length 3–85 m with final pumping rate $Q_p = 0.00155$ m^3/s. The pump time was $t_p = 42$ days with a draw at pump-stop of $s_p = 5.3$ m. In Figure A1-27 the pumped borehole and the observation boreholes are shown.

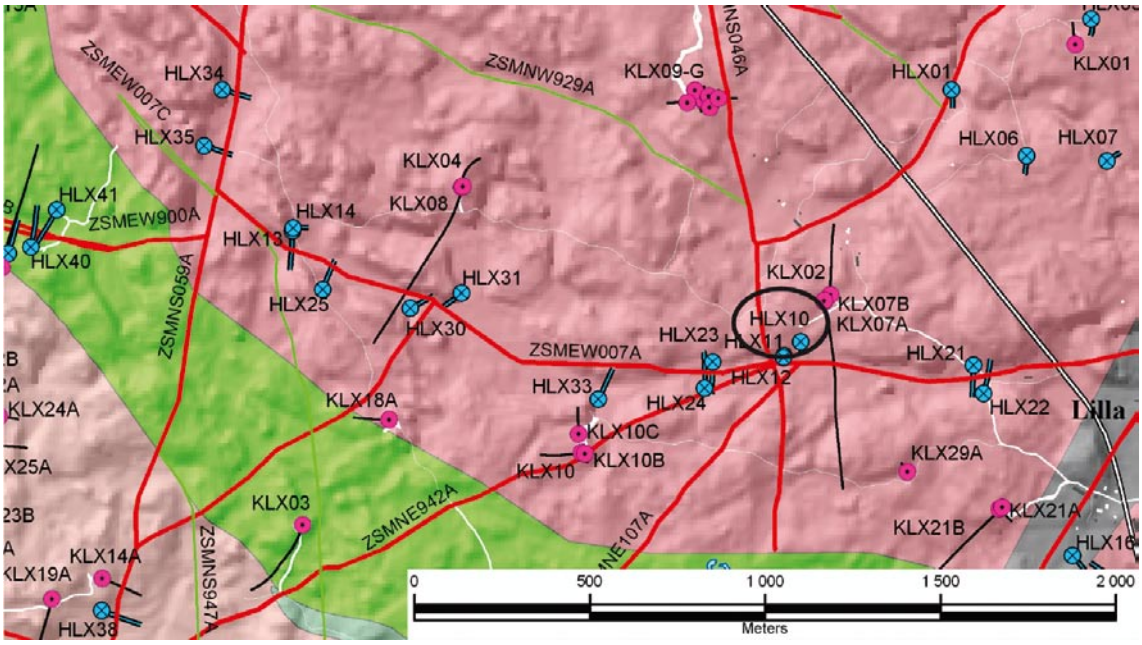

Figure A1-27. *Borehole map. Test in January–February 2005 with HLX10 as pumping borehole.*

Responses

The responses are shown as final drawdown at pumping stop in figure Figure A1-28 using the skin factor of the pumped section to estimate the effective borehole radius. The response indexes for the observation boreholes are presented in Figure A1-29 and mapped on the structural model in Figure A1-30 and Figure A1-31.

Conclusions

The fast responses in KLX02 at depths where ZSMEW007 intercepts (modelled intercept 180–200 m), the only responses in the upper part of KLX07A (modelled intercept 105–168 m) as well as clear responses in several percussion boreholes along ZSM007 indicate that the deformation zone dips to the north as geologically modelled.

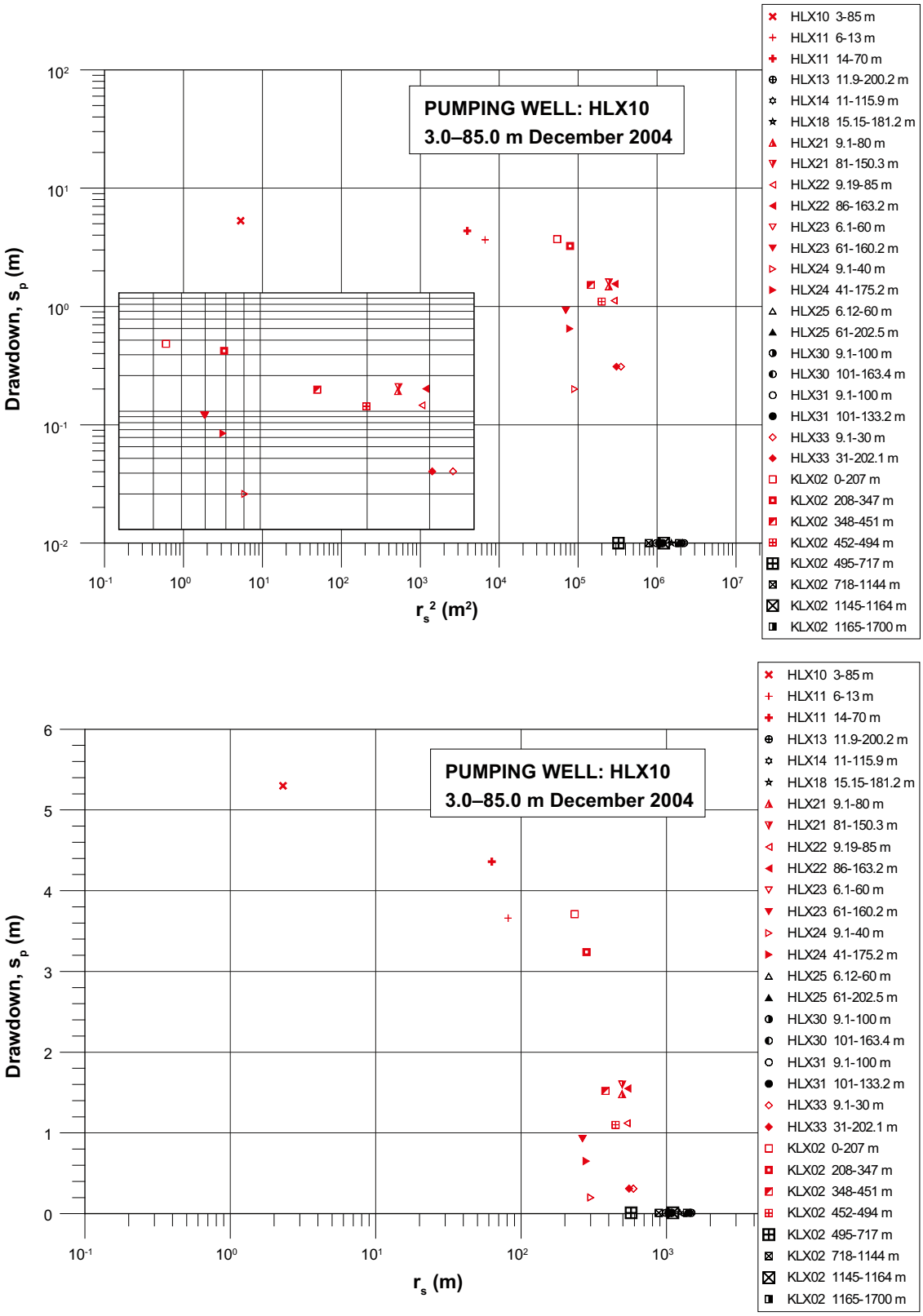

Figure A1-28. *Distance-drawdown plots. Test in January–February 2005 with HLX10 as pumping borehole.*

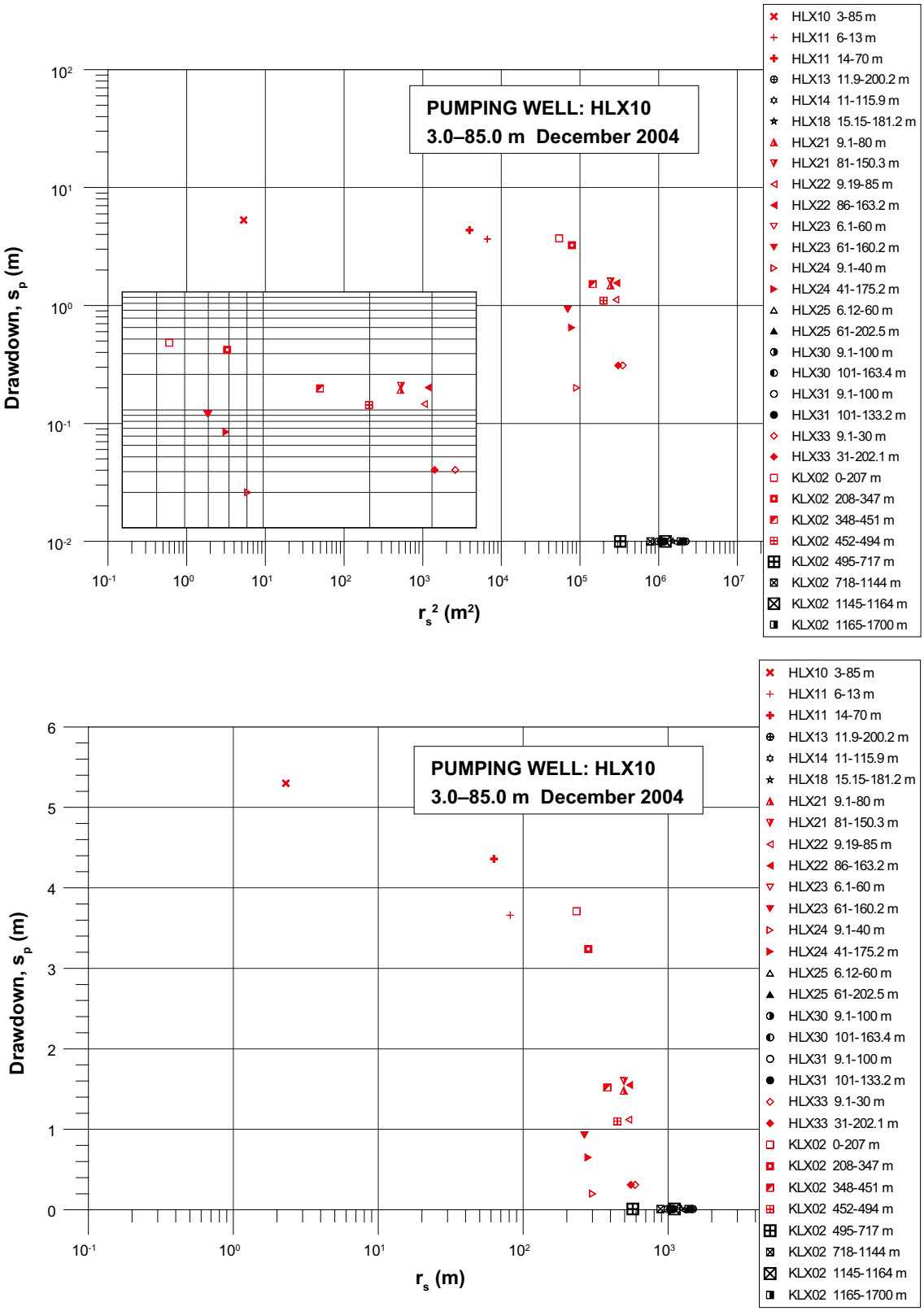

Figure A1-29. *Response- index plots. Test in January–February 2005 with HLX10 as pumping borehole.*

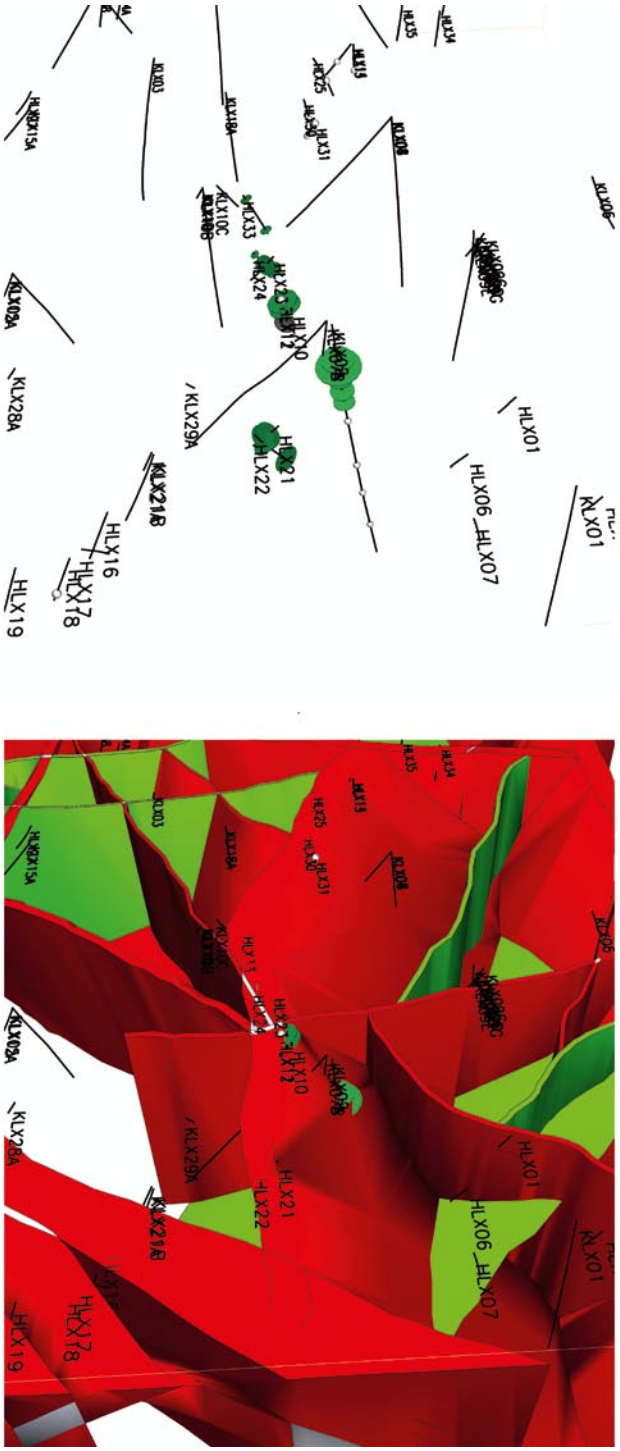

Figure A1-30. *Test in January–February 2005 with HLX10 as pumping borehole. A few deformation zones south of ZSMEW007A, ZSMNW928, ZSMNE012A and ZSMNE107A removed to show responses. Top of figures: west part of the local model area. Response indexes are mapped on the boreholes. Pumping hole plotted as a black disc. The larger the disc (green or blue) for a response index is, the better hydraulic contact with pumped borehole section can be assumed. No-response is indicated with a grey sphere. A borehole without discs or spheres have not been measured.*

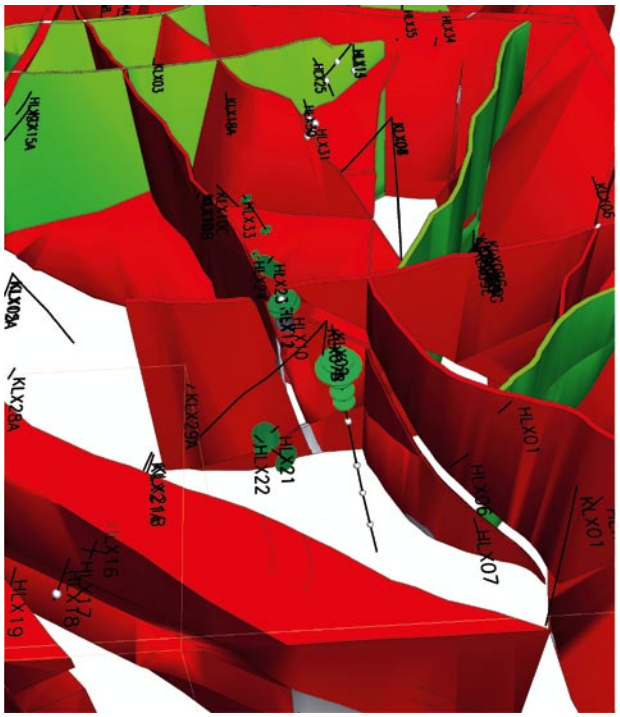

Figure A1-31. *Test in January–February 2005 with HLX10 as pumping borehole. A few deformation zones south of ZSMEW007A, ZSMNW928, ZSMNE012A and ZSMNE107A removed to show responses. Top of figure: west part of the local model area. Response indexes are mapped on the boreholes. Pumping hole plotted as a black disc. The larger the disc (green or blue) for a response index is, the better hydraulic contact with pumped borehole section can be assumed. No-response is indicated with a grey sphere. A borehole without discs or spheres have not been measured.*

A1.8 Interference test; KLX08A:3 September 2006

The interference test was performed between 2006-09-11 and 2006-09-18 with KLX08 as pumping hole. Observations were made in boreholes (No of sections within parenthesis): KLX02 (8), KLX03 (10), KLX04 (8), KLX06 (8), KLX07A (8), KLX07B (2), KLX10 (8), KLX18A (3), HLX11 (2), HLX13 (1), HLX14 (1), HLX23 (2), HLX24 (2), HLX25 (2), HLX30 (2), HLX31 (1), HLX33 (2), HLX34 (1) and HLX35 (2) as observation boreholes. The test is reported in /Enachescu et al. 2007b/.

Test description

The pumping was performed in a packed-off section 357.0–497.0 m with mean pumping rate $Q_m = 5.17 \cdot 10^{-4}$ m^3/s. The pump time was $t_p = 72$ h (3.0 days) with a draw at pump-stop of $s_p = 4.48$ m. In Figure A1-32 the pumped borehole and the observation boreholes are shown.

Responses

The responses are shown as final drawdown at pumping stop in figure Figure A1-33, using the skin factor of the pumped section to estimate the effective borehole radius. The response indexes for the observation boreholes are presented in Figure A1-34 and mapped on the structural model in Figure A1-35 and Figure A1-37.

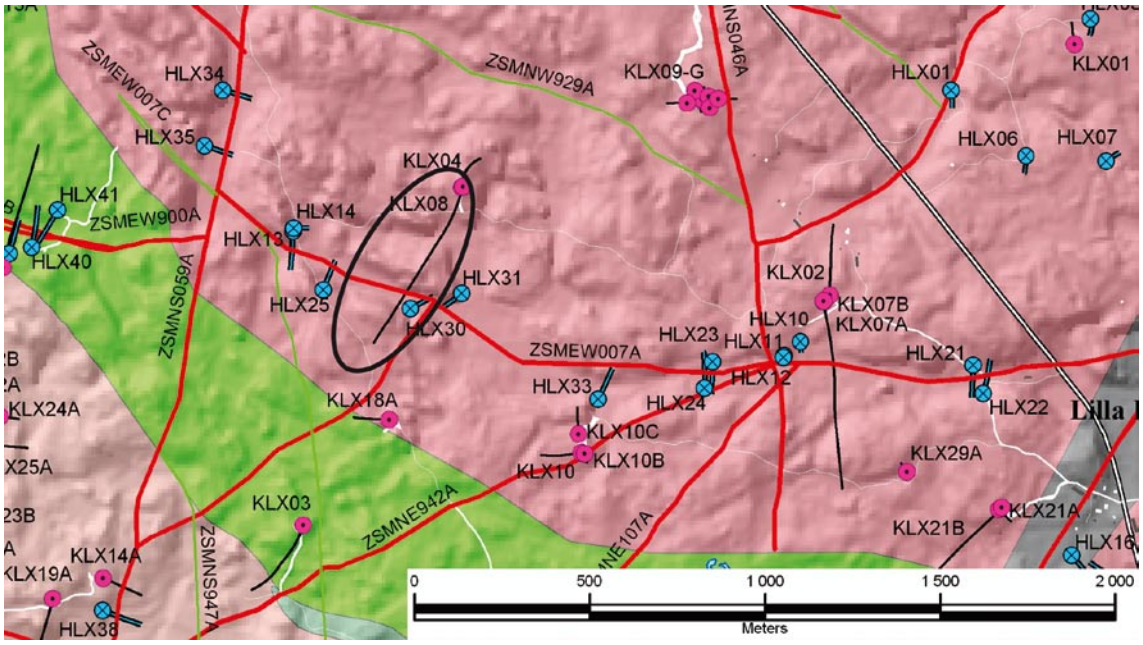

Figure A1-32. *Borehole map. Test in September 2006 with KLX08A:3 (357–497 m) as pumping borehole.*

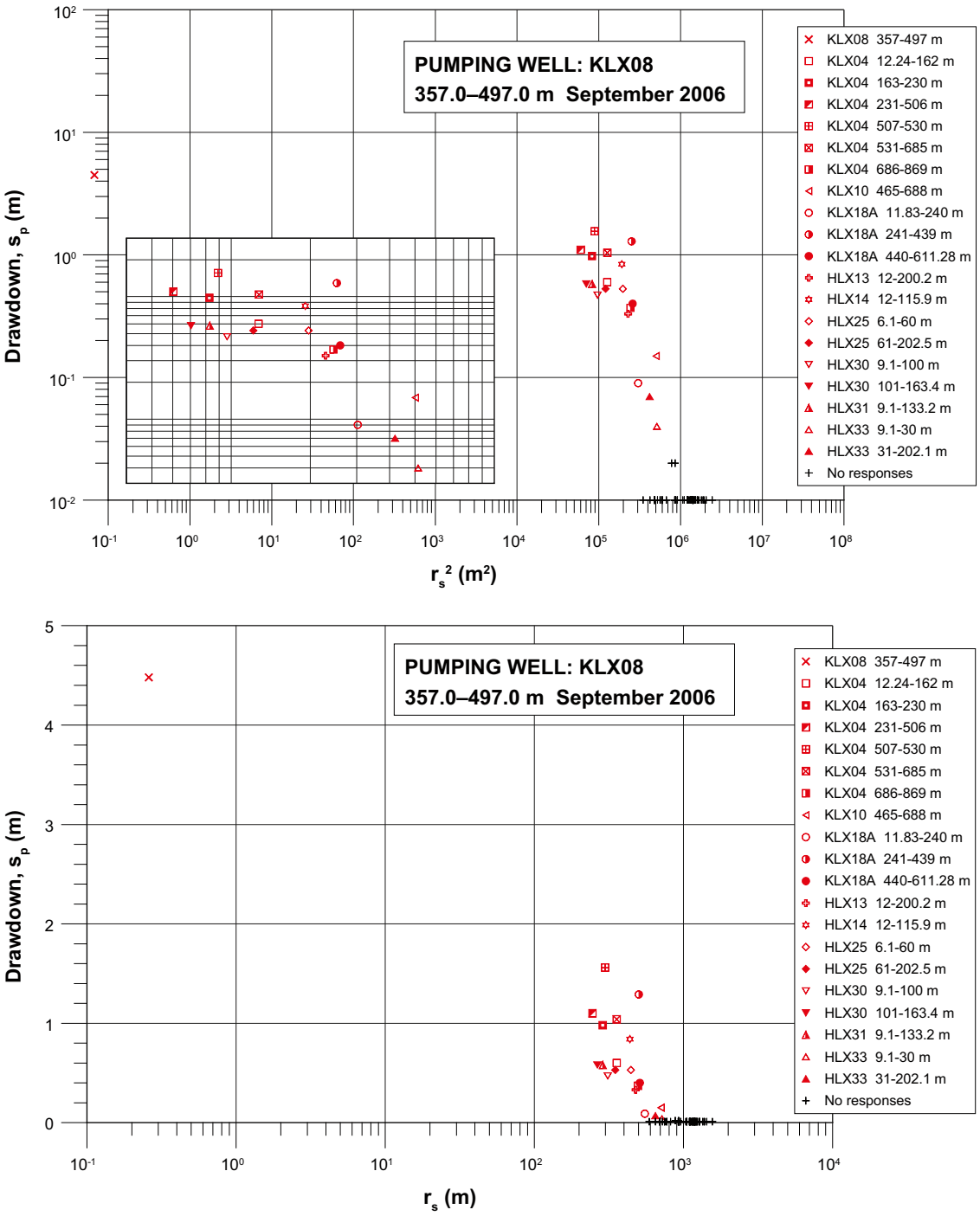

Figure A1-33. *Distance-drawdown plots. Test in September 2006 with KLX08A:3 (357–497 m) as pumping borehole.*

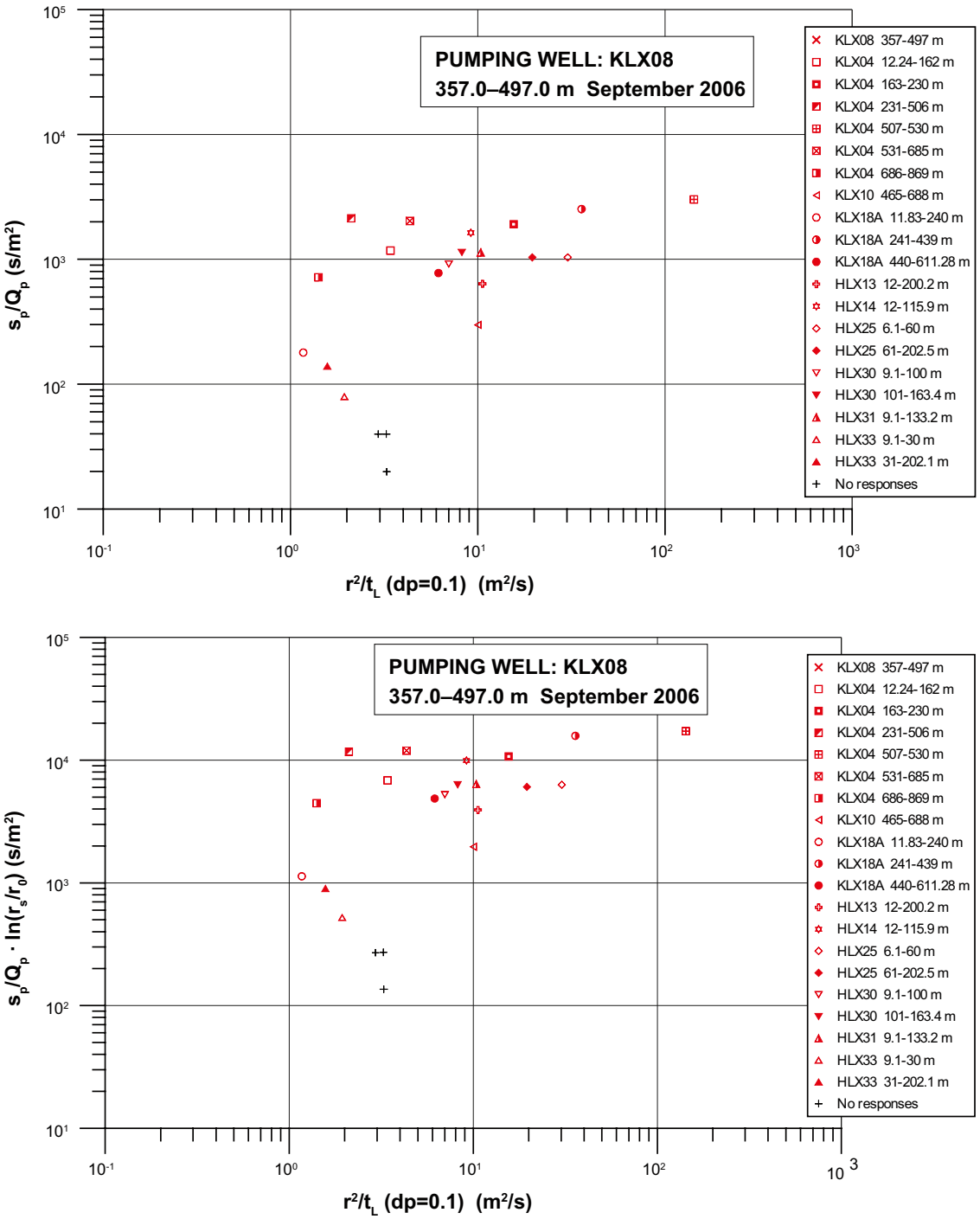

Figure A1-34. *Response- index plots. Test in September 2006 with KLX08A:3 (357–497 m) as pumping borehole.*

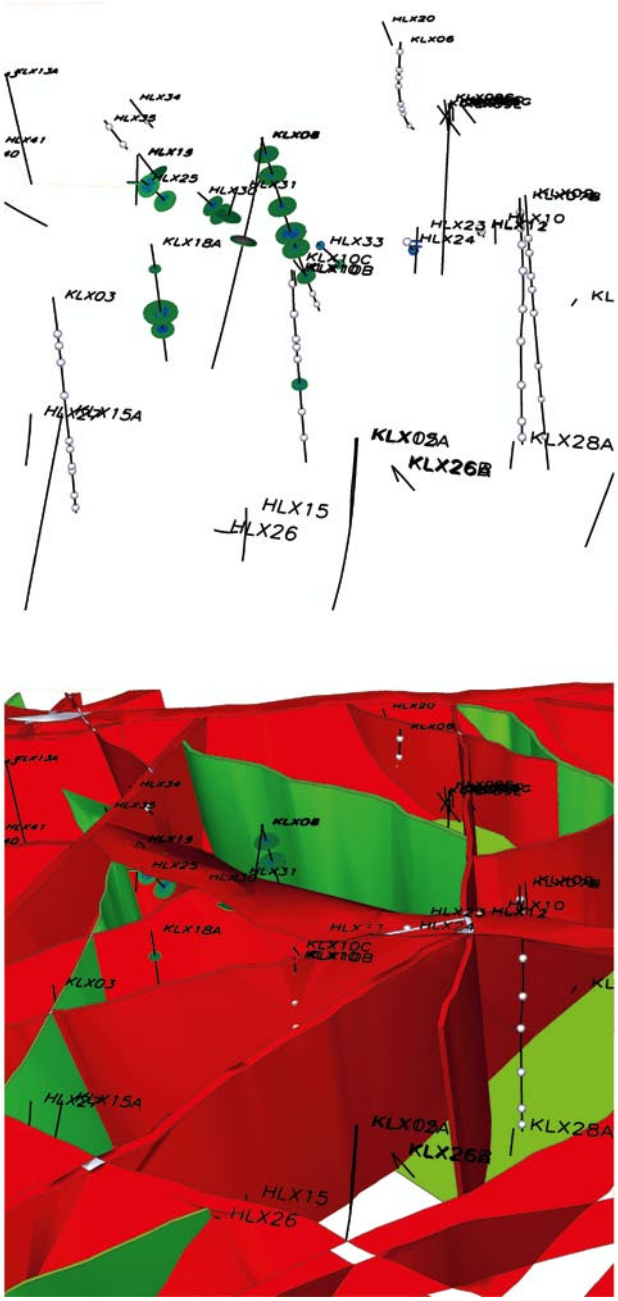

Figure A1-35. *Test in September 2006 with KLX08A:3 (357–497 m) as pumping borehole. Top of figures: north-west part of local model area (DZ modelled as discs around boreholes are not shown). Response indexes are mapped on the boreholes. Pumping hole plotted as a black disc. The larger the disc (green or blue) for a response index is, the better hydraulic contact with pumped borehole section can be assumed. No-response is indicated with a grey sphere. A borehole without discs or spheres have not been measured (RVS_info: KLX08–13140113).*

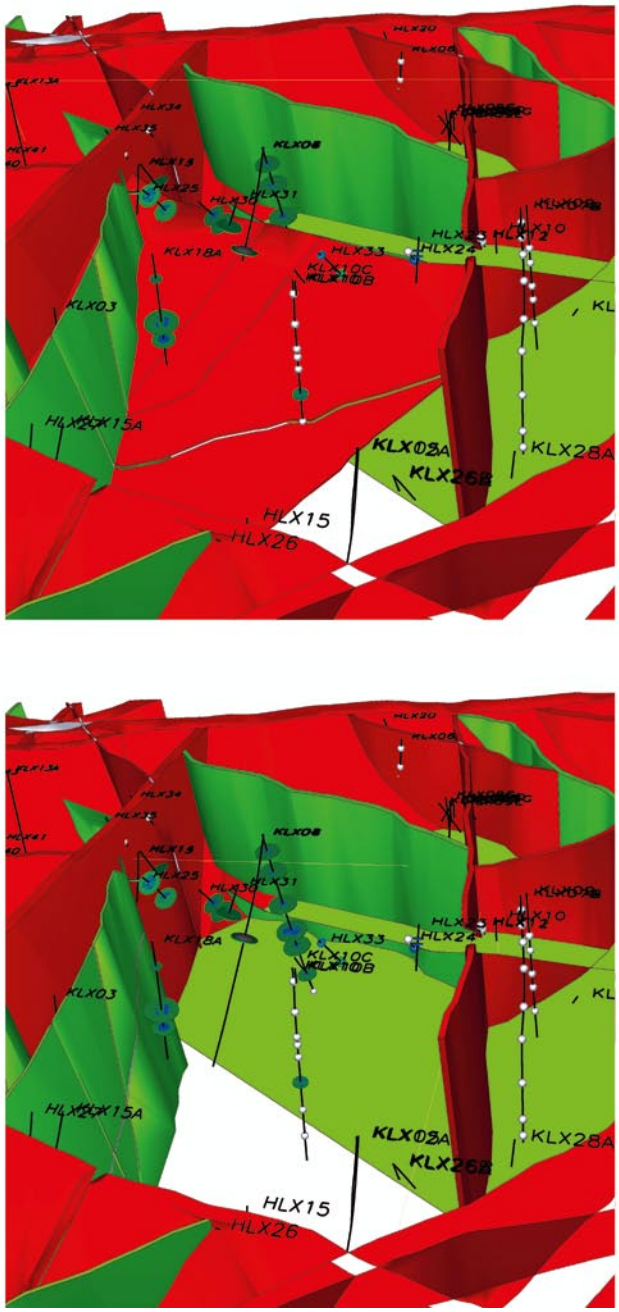

Figure A1-36. *Test in September 2006 with KLX08A:3 (357–497 m) as pumping borehole. Top of figures: north-west part of local model area (DZ modelled as discs around boreholes are not shown). Top: Deformation zones ZSMEW007, ZSMNE942A, ZSMNE944A and ZSMNE107A removed to show responses. Bottom: Deformation zones ZSMEW007, ZSMNE942A, ZSMNE944A,ZSMNE107A and ZSMNE946A removed to show responses. Response indexes are mapped on the boreholes. Response indexes mapped on the structural model. Pumping hole plotted as a black disc. The larger the disc (green or blue) for a response index is, the better hydraulic contact with pumped borehole section can be assumed. No-response is indicated with a grey sphere. A borehole without discs or spheres have not been measured (RVS_info: KLX08–13140113).*

Figure A1-37. *Test in September 2006 with KLX08A:3 (357–497 m) as pumping borehole. Top of figures: north-west part of local model area (DZ modelled as discs around boreholes are shown). Deformation zones ZSMEW007, ZSMNE942A, ZSMNE944A,ZSMNE107A and ZSMNE946A removed to show responses. Response indexes are mapped on the boreholes. Response indexes mapped on the structural model. Pumping hole plotted as a black disc. The larger the disc (green or blue) for a response index is, the better hydraulic contact with pumped borehole section can be assumed. No-response is indicated with a grey sphere. A borehole without discs or spheres have not been measured (RVS_info: KLX08–13140113).*

Conclusions

ZSMNE944A probably can explain the responses in KLX18, if ZSMEW946 that intersects KLX08 transmits the signal to ZSMNE944A. Figure A1-37 indicates that there are several deformation zones modelled as discs (with radius c. 560 m) around the boreholes near deformation zone ZSMEW007A, that makes the interpretation of possible hydraulic connections difficult. It seems likely that KLX08_DZ1, KLX10C_DZ3 and KLX18_DZ9 may also be part of the explanation of responses seen in upper part of KLX18.

ZSMEW946A target intercept in KLX10 is 698–706 m and pumped section in KLX08 and can possibly transmit signal to lower parts of KLX10 through some discrete single fractures near KLX10 as the only response in KLX10 is in section 465–688 m. ZSMNE946A is more or less parallel to KLX10 and does not seem to be very conductive or quite heterogeneous as it does not transmit signals along KLX10. KLX10 down to ca 430 m borehole length is interpreted as belonging to ZSMNE942A /Wahlgren et al. 2008/.

A1.9 Interference test; KLX21B, March 2007

The interference test was performed between 2007-03-11 and 2007-03-18 with KLX21B as pumping hole. Observations were made in boreholes (No of sections within parenthesis): KLX07A (8), KLX07B (2), KLX12 (9), KLX05 (10), HLX18 (2), HLX22 (1), HLX23 (2) as observation boreholes. The test is reported in /Walger et al. 2007/.

Test description

The pumping was performed in an open borehole within borehole length 11.9–858.8 m with final pumping rate $Q_p = 0.000908$ m^3/s and arithmetic mean pumping rate $Q_m = 0.000908$ m^3/s. The pump time was $t_p = 10{,}366$ min (c. 7.2 days) with a drawdown at pump-stop of $s_p = 3.51$ m. In Figure A1-38 the pumped borehole and the observation boreholes are shown.

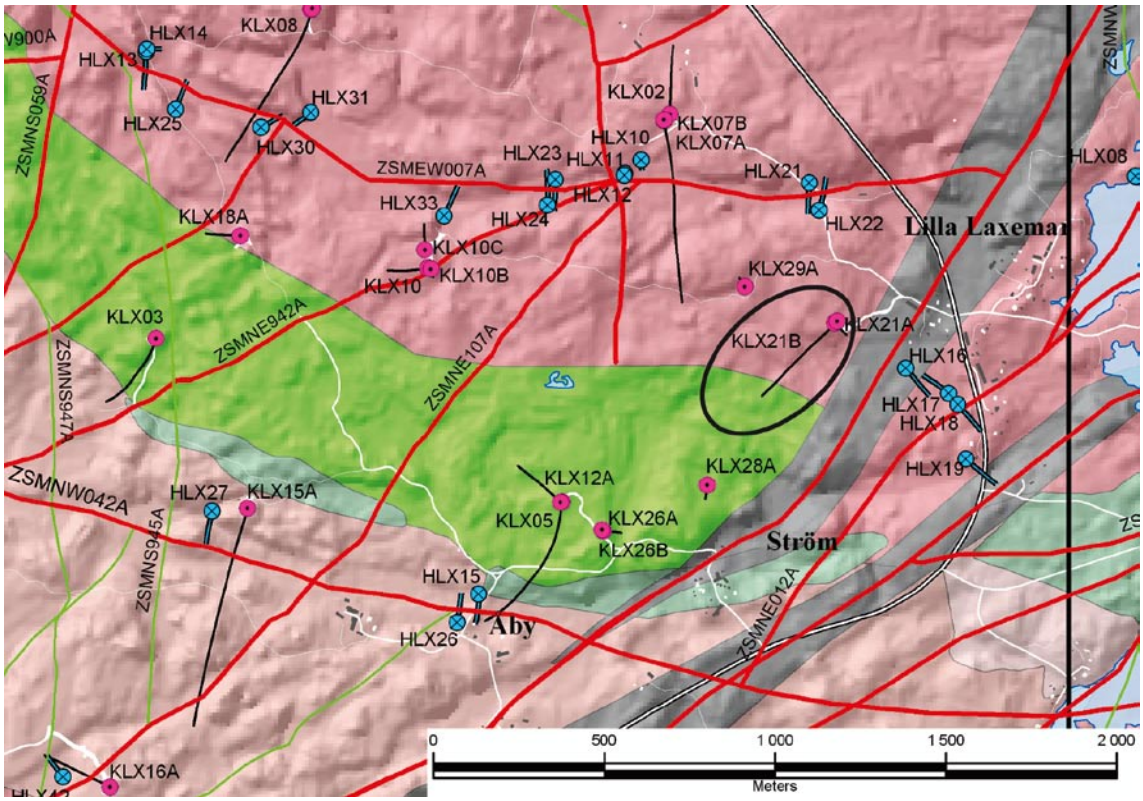

Figure A1-38. *Borehole map. Test in March 2007 with KLX21B (11.9–858.8 m) as pumping borehole.*

The pressure observations during the test in KLX21B are considered uncertain due to effects from a precipitation period before the start of the test and due to earth-tidal effects.

Responses

The responses are shown as final drawdown at pumping stop in figure Figure A1-39, using the skin factor of the pumped section to estimate the effective borehole radius. The response indexes for the observation boreholes are presented in Figure A1-40 and mapped on the structural model in Figure A1-41 and Figure A1-42.

Conclusions

There are responses in all KLX07A borehole sections but the greatest and most distinct responses are in sections 5 and 4 (333–456 m and 457–611 m) followed by HLX22 and KLX07 sections 3 to 1 (612–752 m, 753–780 m and 781–844.7 m). Probably deformation zones KLX07_DZ9 and KLX07_DZ10 are the primary conductors transmitting the response to KLX07A sections 5 and 4, but probably ZSMNE107A is transmitting the response to the upper part of KLX07A. Possibly ZSMNS046A contributes to responses in the lower part of KLX07A.

The response in HLX22 can possibly be explained by KLX21B_DZ10–12 but also responses via ZSMNE005A and ZSMEW007.

It is more difficult to explain the response in upper parts of KLX05A and KLX12A. Possibly the response is transmitted via ZSMNE005A and through deformation zone KLX28_DZ1 and a hydraulically connected fracture network around the KLX05A and KLX12A down to a depth of c. 500 m.

The responses are difficult to interpret but indicates that it must be several structures interacting to create a so spatially distributed response.

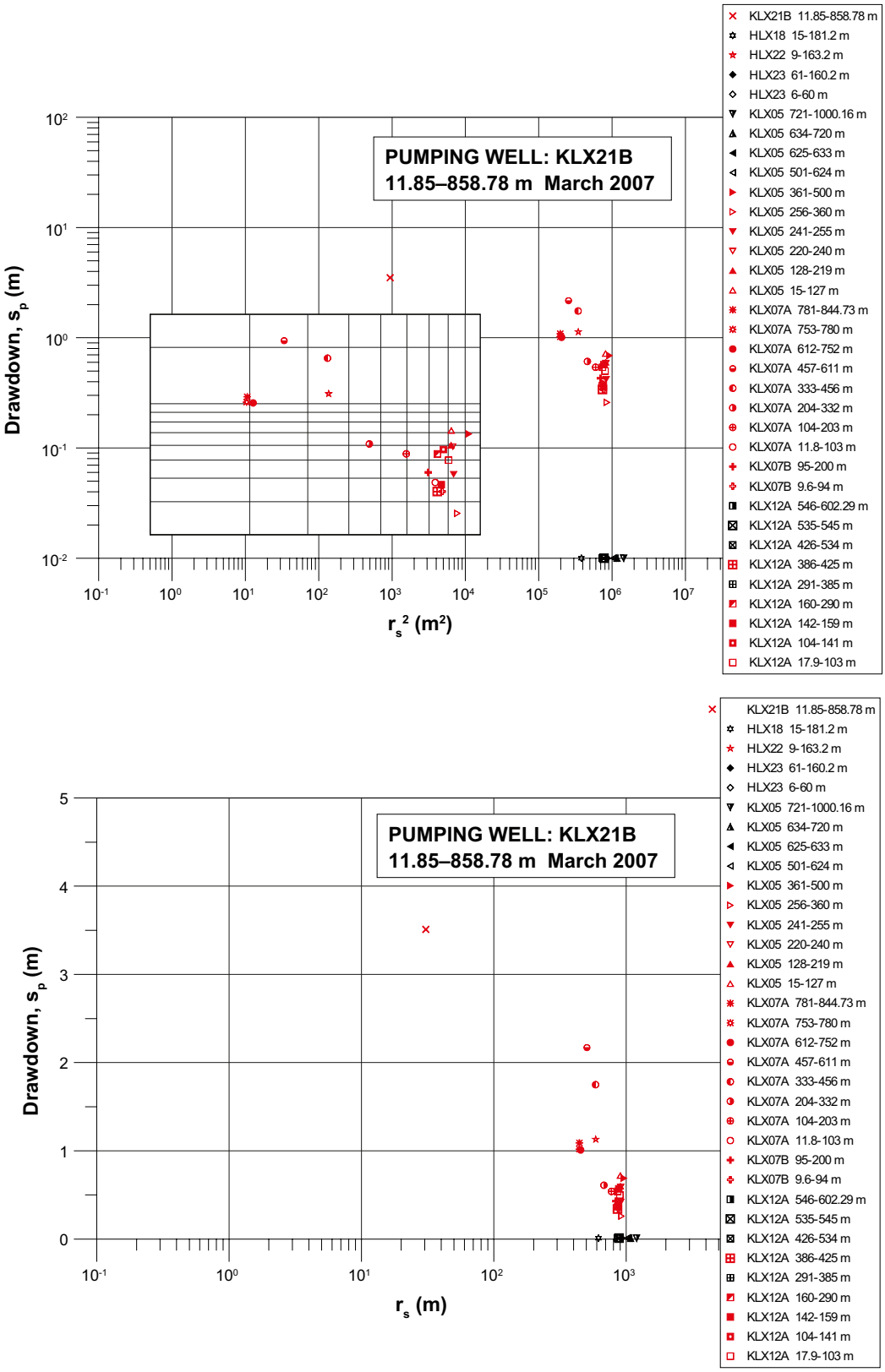

Figure A1-39. *Distance-drawdown plots. Test in March 2007 with KLX21B (11.9–858.8 m) as pumping borehole.*

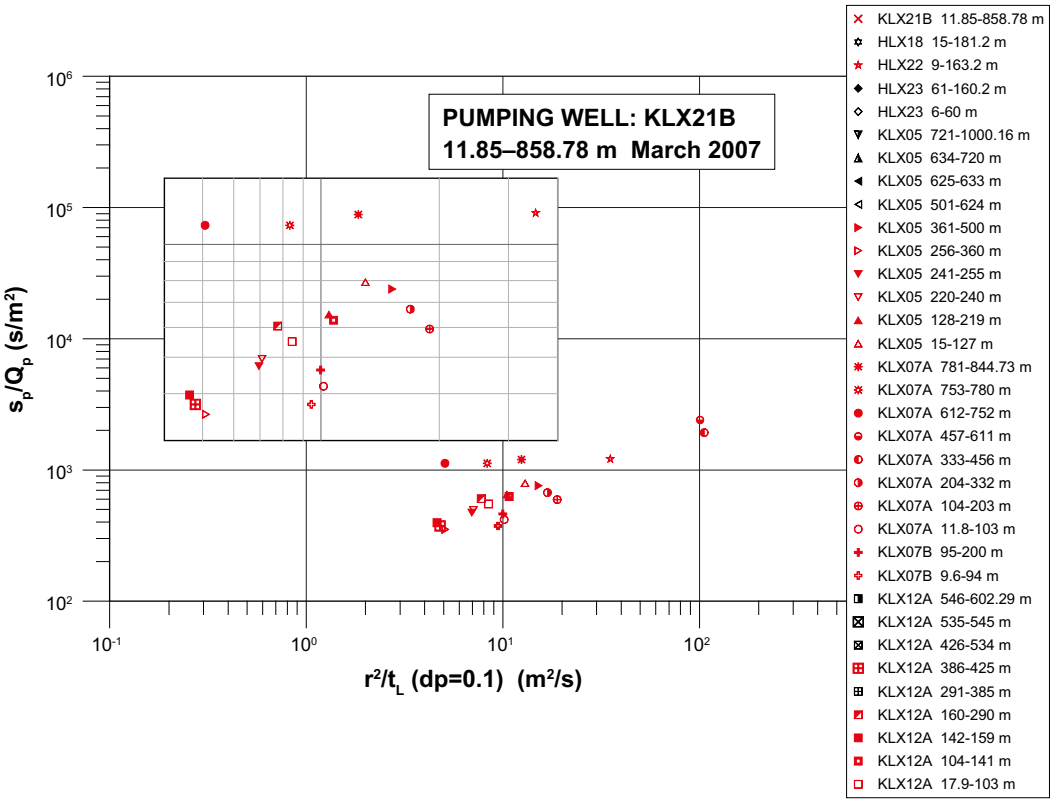

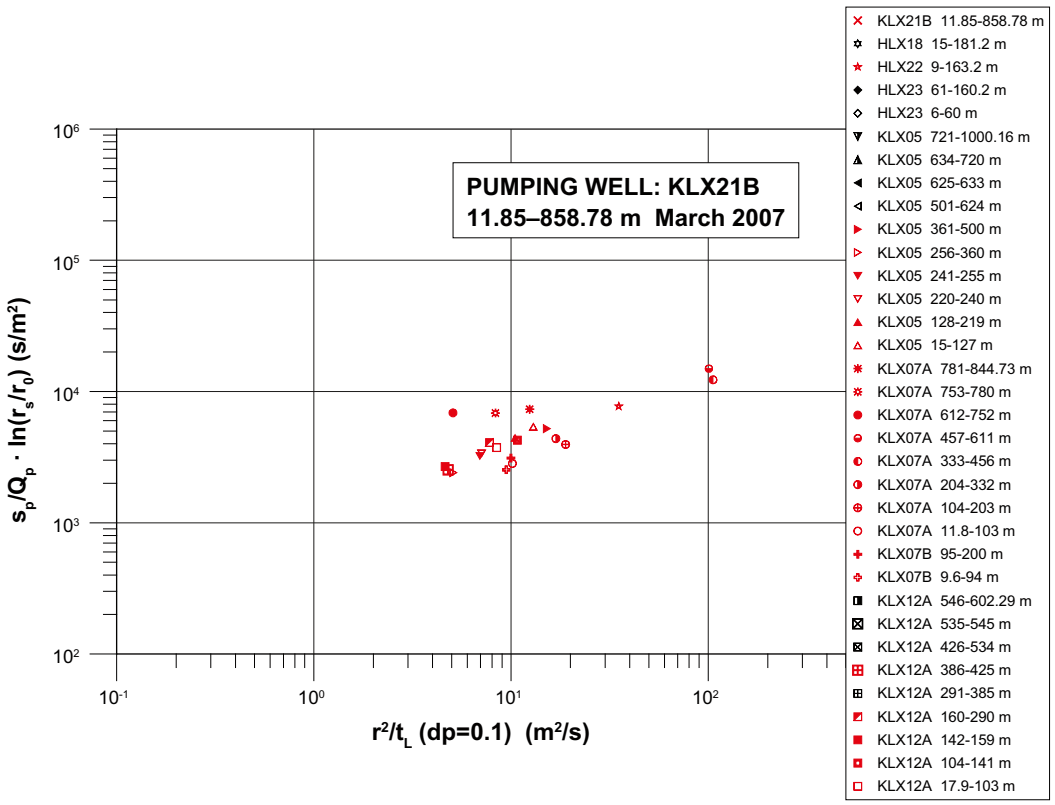

Figure A1-40. *Response- index plots. Test in March 2007 with KLX21B (11.9–858.8 m) as pumping borehole.*

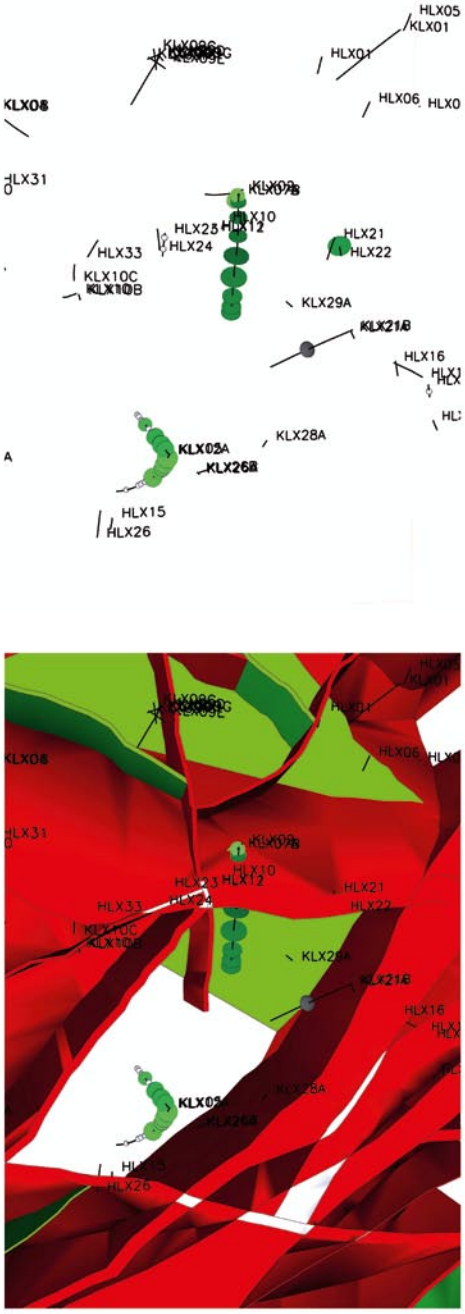

Figure A1-41. *Test in March 2007 with KLX21B (11.9–858.8 m) as pumping borehole. Top of figures: north part of local model area (DZ modelled as discs around boreholes are* ***not*** *shown). Response indexes are mapped on the boreholes. Response indexes mapped on the structural model. Pumping hole plotted as a black disc. The larger the disc (green or blue) for a response index is, the better hydraulic contact with pumped borehole section can be assumed. No-response is indicated with a grey sphere. A borehole without discs or spheres have not been measured.*

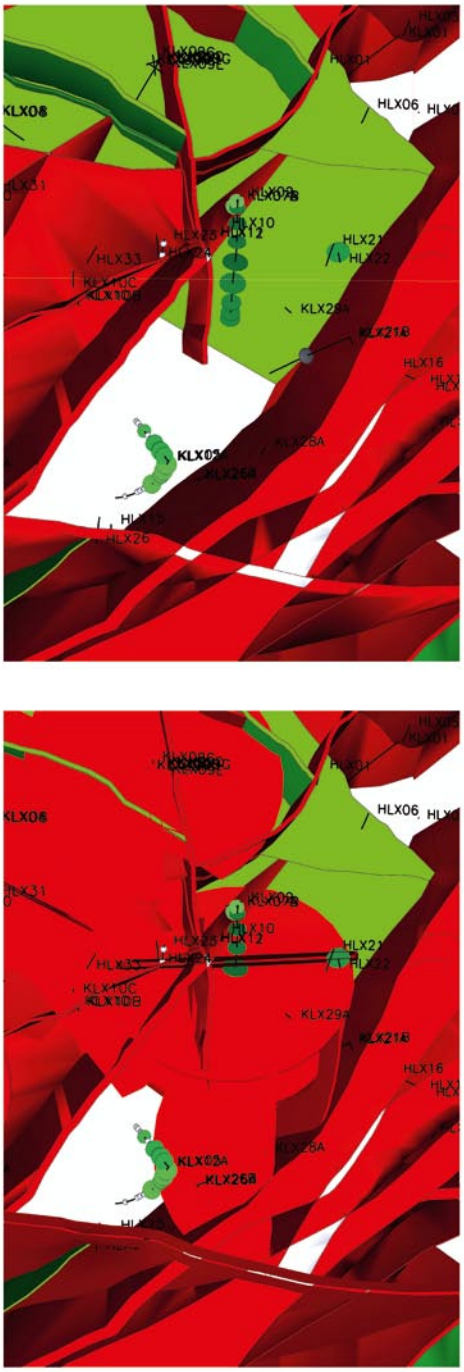

Figure A1-42. *Test in March 2007 with KLX21B (11.9–858.8 m) as pumping borehole. Top of figures: north part of local model area (DZ modelled as discs around boreholes are not shown in uppermost figure but in the lower figure). Deformation zones ZSMEW007A is removed in the figures. Response indexes are mapped on the boreholes. Response indexes mapped on the structural model. Pumping hole plotted as a black disc. The larger the disc (green or blue) for a response index is, the better hydraulic contact with pumped borehole section can be assumed. No-response is indicated with a grey sphere. A borehole without discs or spheres have not been measured.*

Appendix 2

A2 Additional information and data used in the HRL study

This section gives additional information and references to data sources. An attempt is made to record the data that has been used. File names refer to the files in the directory that was created for this pre-modelling exercise on the Project Place. (A similar appendix was also presented in /Hartley et al. 2007/).

A2.1 Tunnel geometry

In the delivered data set, the geometry of the tunnels and shafts are given. The names of the different Äspö HRL tunnel objects are given in Table A2-1 and Table A2-2. The location of the Äspö HRL is illustrated Figure A2-1 and Figure A2-2.

Table A2-1. The main tunnel objects that are included in the model.

Name	Object
TASA	The main tunnel, A.
TASH	Elevator shaft, H
TASV	Ventilation-in shaft, V
TASW	Ventilation-out shaft, W

Table A2-2. The diameters of the drilled parts.

Object	Diameter
TBM tunnel	5.0 m
Elevator shaft, H	3.8 m
Ventilation-in shaft, V	1.5 m
Ventilation-out shaft, W	1.5 m

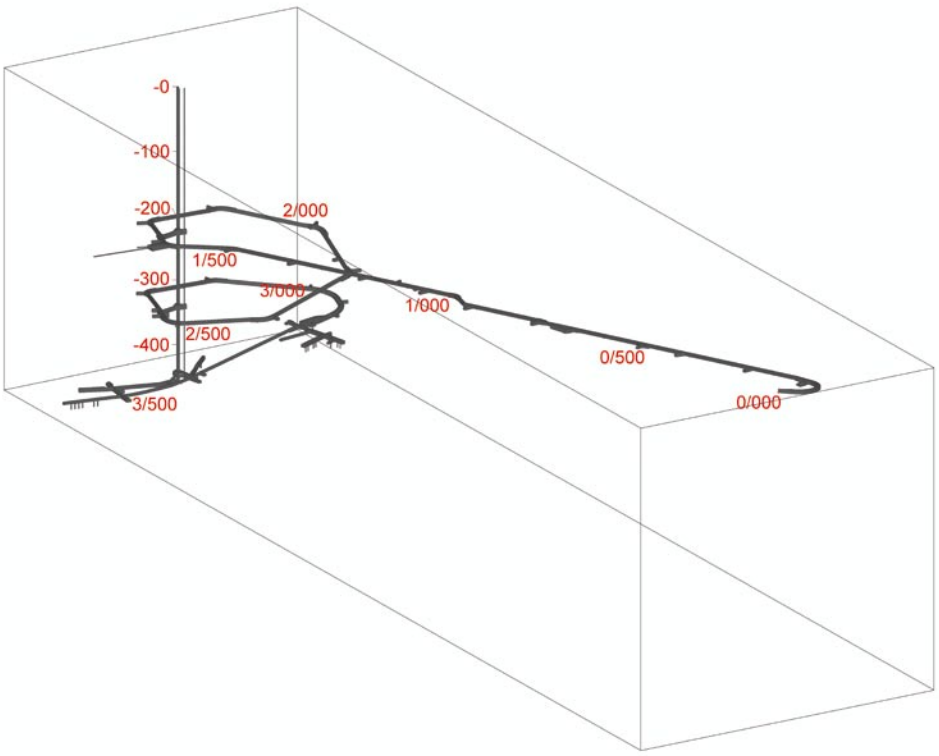

Figure A2-1. *An illustration of the tunnels and shafts at the Äspö HRL.*

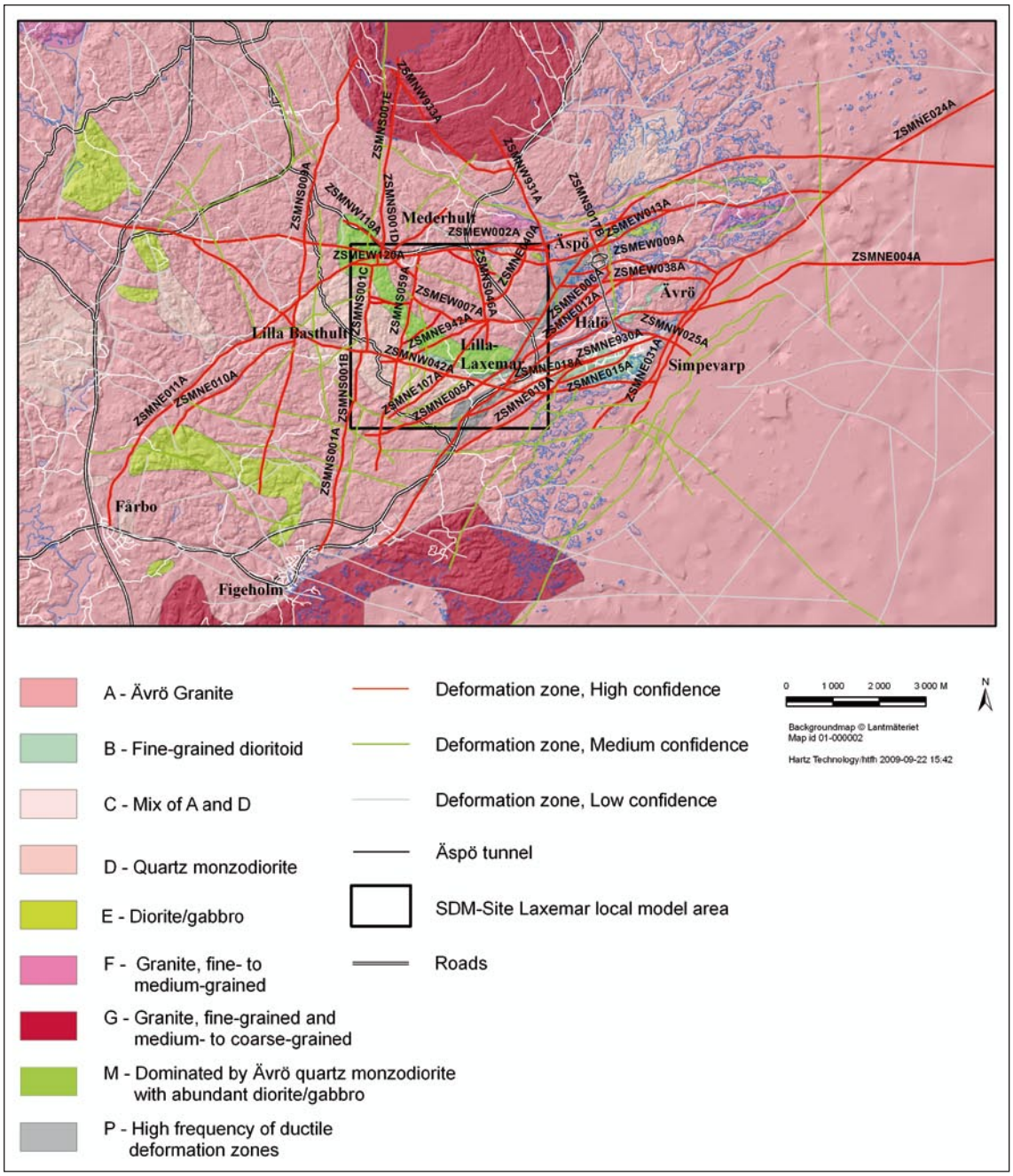

Figure A2-2. *Modelling areas from SDM-Site modelling showing rock domains, deformation zones and the Äspö HRL tunnel. The black box is the local-scale modelling area /Wahlgren et al. 2008/.*

The influences of the ventilation shafts are included into the elevator shaft. The inflows to Tunnel G and F, which run parallel and close to Tunnel A (approximately at section 3,400–3,510 m and 3,510–3,600 m) are added to the last part of tunnel A (TASA), and thus tunnels G and F are not modelled geometrically. All other short tunnels are excluded in the modelling. The coordinates for the tunnel line for tunnel A is 0.25 m above the tunnel floor in the drill and blasted tunnel (tunnel section 0–3,191 m) and 0.8 m above the tunnel floor in the TBM tunnel (tunnel section 3,191–3,600 m). An observation or measurement in the tunnel is linked to a ”Tunnel section”. ”Tunnel section” is defined as the length of the projection of the tunnel line on a horizontal plane, called SECTION in the tables for tunnel A and other tunnel parts. All flow rates are related to SECTION for the tunnels. The cross-section area of the drill and blasted tunnel is about 25 m^2 in the straight parts of the tunnel and about 43 m^2 in the bends. In the TBM assembly hall, the cross-sectional area is about 100 m^2.

File Tunnel-geometry.doc is basically the same as Tunnel-geometry_Aspo-HRL.doc. The files tunnel_surveying.xls and object_location.xls contain data of the geometry of the tunnel line of Äspö HRL. File Official_tunnel_IR-image3b.gif shows the tunnel and using a CAD system, and the tunnel can be visualized using Official_tunnel_V3(MS_V8_cd).dwg.

The influences of the ventilation shafts are included into the elevator shaft. Inflow to Tunnel G and F are added to the last part of tunnel TASA, and thus tunnels G and F are not modelled geometrically. All other short tunnels are excluded in the modelling.

The coordinates for the tunnel line for tunnel A is 0.25 m above the tunnel floor in the drill and blasted tunnel (tunnel section 0–3,191 m) and 0.8 m above the tunnel floor in the TBM tunnel (tunnel section 3,191–3,600 m).

An observation or measurement in the tunnel is linked to a “Tunnel section”. “Tunnel section” is defined as the length of the projection of the tunnel line on a horizontal plane, called SECTION in the tables for tunnel A and other tunnel parts. All flow rates are related to SECTION for the tunnels.

The cross-section area of the drill and blasted tunnel is about 25 m^2 in the straight parts of the tunnel and about 43 m^2 in the bends. In the TBM assembly hall the cross-section area is about 100 m^2.

A2.2 DZ – tunnel intersections

The file DZ_AHRL-tunnel.xls gives information on intersections between deformation zones and the HRL tunnel.

A2.3 Flow into the Äspö HRL

Data on the measured flow rates at a number of weir positions are available along the tunnel. This gives information on the total inflow, and inflow at different sections of the HRL as monthly averaged values. Data are available at the weirs along the Äspö tunnel during the excavation of the Äspö Hard Rock Laboratory (HRL) and operation of the Äspö HRL, for the time period May 1991 until December 2004.

Tunnel F and G are parallel and close to tunnel A, approximately section 3,400–3,510 m and 3,510–3,600 m. Hence, the flow rates in tunnels F and G are included in the main tunnel. Data from May 1991 to January 1994 are from the Task 5 modelling exercise with the Äspö HRL Task Force /Rhén and Smellie 2003/. Data from later periods are monthly mean values, calculated from SICADA data. Some spikes of inflow rates, with short duration, have been removed, as generally they can be assumed to be related to drill water when excavating new tunnels. However, it is possible that some of these spikes, totally or partly, can be related to true inflow from the rock, due e.g. hydraulic tests. No attempt has been made to sort this out as it was judged that it would only result in smaller changes of the total flow rate. At some occasions data are missing after 1995 or there is an indication that a weir has been clogged and linear interpolation has been used to estimate flow rates for months with missing or erroneous data. Flow rates are missing for 2005, but can be assumed to be more or less as December 2004.

Table A2-3. Examples of intersections of fracture zones intersecting the main Äspö HRL tunnel A.

DZ	Start-A (m)	End-A (m)	Comment – Eng
ZSMNE004A	276	378	
ZSMNW025A	286	301	
ZSMNS017A	327	*	Corner of the DZ touches the tunnel at 327 m
ZSMNE012A	706	858	
ZSMEW038A	1,164	1,173	
ZSMNE006A	1,169	1,341	
ZSMEW009A	1,403	1,414	
ZSMNS017B	1,998	2,036	Local DZ, not implemented in the L 1.2 model
–"–	2,095	2,142	–"–
–"–	2,908	2,935	–"–
–"–	3,132	3,152	–"–
ZSMNE005A	3,600	*	The DZ touches the corner of the tunnel at end of tunnel

Weir flow – Äspö HRL
File: Weir-flow_Aspo-HRL.doc

Weir flow rate tot ver 3.xls contains data for the water flow into the Äspö HRL tunnel. The flow rates in the xls-file are plotted in Weir-flow_Aspo-HRL.doc. This file contain data of the monthly mean flow rates measured at the weirs along the Äspö tunnel during the excavation of Äspö Hard Rock Laboratory (HRL) and operation of Äspö HRL, for period: May 1991–Dec 2004.

Details about the flow measurements are found in SKB PR 25-95-28, App. 2:4. The flow rates have also been presented in SKB TR 97-06, App. 2. However minor adjustments of the flow rates reported in SKB TR 97-06 and in SKB PR 25-95-28 have been made for some of the monthly mean flow rates after August 1995. A few corrections of the measured flow rates have been made according to SKB PR 25-95-28:

Table A2-4. Explanations to the inflow data set.

Column:	Unit:	Description:
Month	MMYY	Period for the estimated monthly mean flow rate.
MA682G etc	l/min	IDCODE for the weir. The figure (in this case 682) is the position in the tunnel A for the ditch (dam) that is collecting the water.
		Figures in the column show the estimated or mean value of the measured flow rate.
Total inflow	l/min	Sum of all measurements of the flow into the tunnel.

Table A2-5. Definition of measurement sections.

ROW:	Unit:	Description:
SECUP	m	Upper measurement section along the tunnel line or depth in the shafts, which were defined in TUNNGEOM.zip.
SECLOW	m	Lower measurement section along the tunnel line or depth in the shafts, which were defined in TUNNGEOM.zip.
Tunnel part	–	IDCODE for tunnel or "shafts"

A complete set of plots of the weir flow rates is given in Figure A2-3 through Figure A2-5.

The pump pit PG2 is losing water by leakage, which January 1994 was estimated to 42 L/min. The monthly mean flow rate measured at MA1030G has been reduced with this amount when PG2 was in operation.

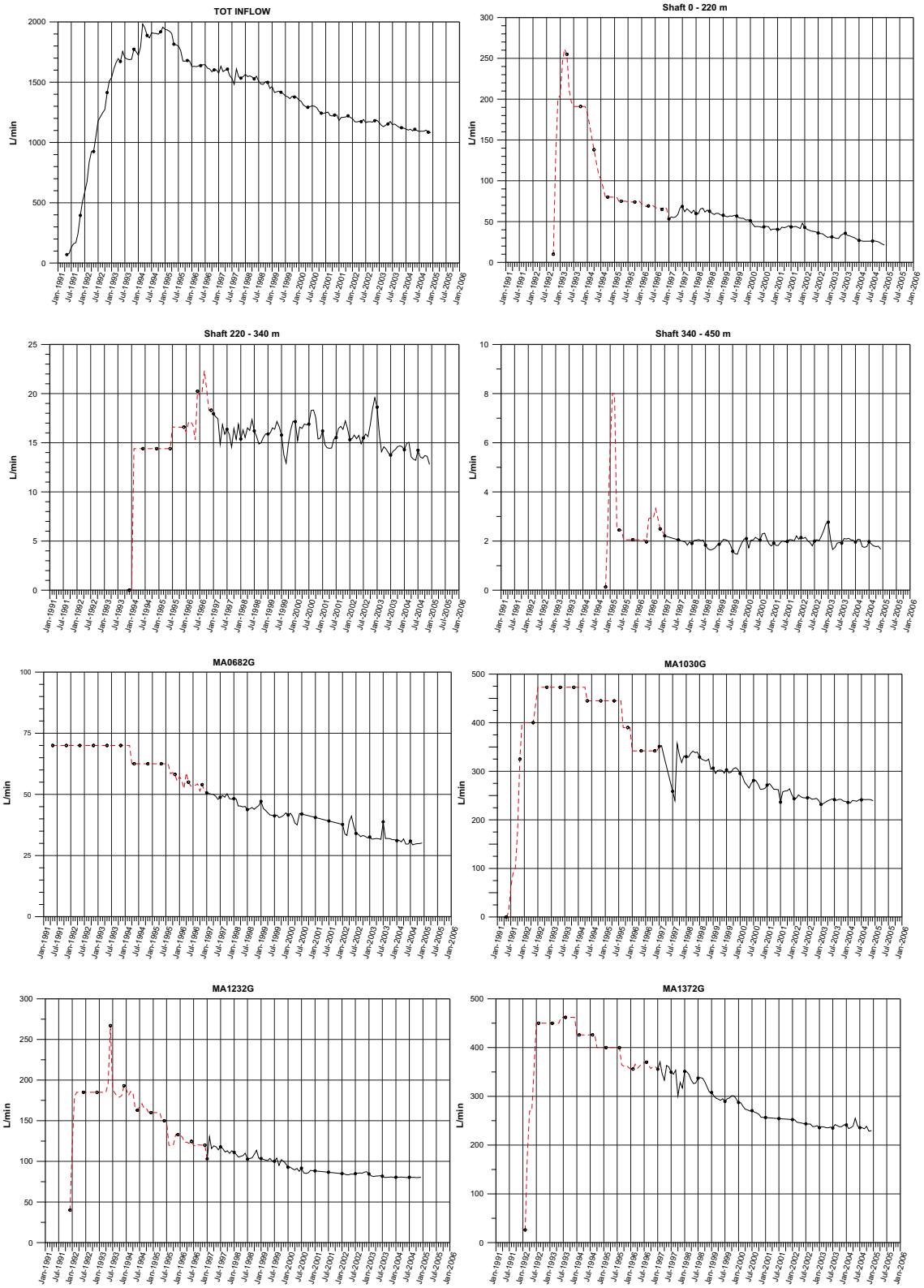

Figure A2-3. *Complete set of weir measurements. The red dashed lines are Äspö Task Force, Task 5 data /Rhén and Smellie 2003/.*

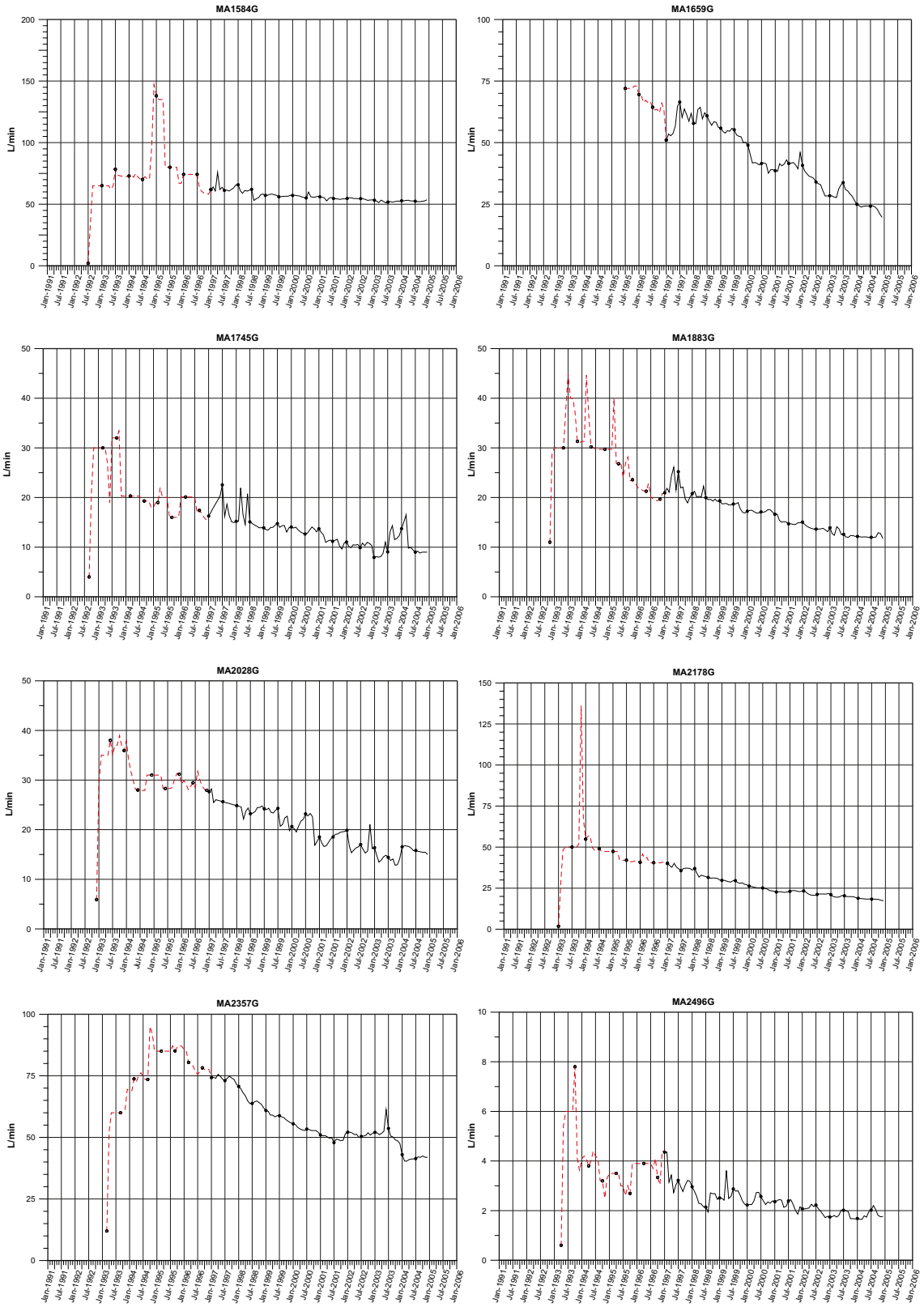

Figure A2-4. *Complete set of weir measurements. The red dashed lines are Äspö Task Force, Task 5 data /Rhén and Smellie 2003/.*

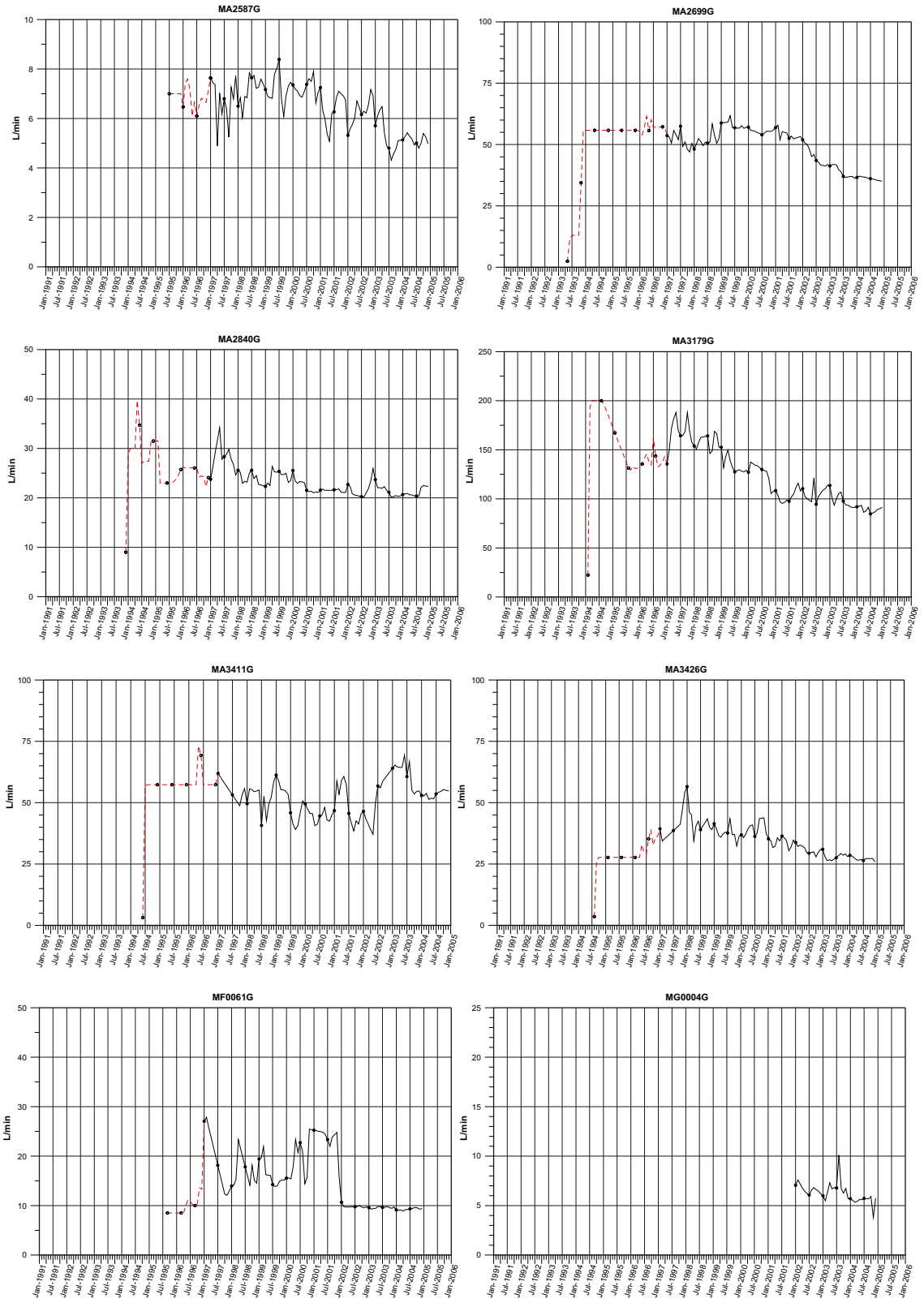

Figure A2-5. *Complete set of weir measurements. The red dashed lines are Äspö Task Force, Task 5 data /Rhén and Smellie 2003/.*

The pump pit PG3 is probably losing water by leakage, which has been estimated to 5 L/min. The monthly mean flow rate measured at MA1745G has been reduced with this amount when PG3 was in operation.

The pump pit PG4 is possibly losing water by leakage when the water level is high in the pump pit. The leakage has been estimated to 10 L/min. The monthly mean flow rate measured at MA2699G has been reduced with this amount when PG4 was used for a drilling operation 22 November 1994–24 January 1995. When the water level is low in the pump pit, during normal operation, the leakage is probably small and no corrections have been made for other periods.

Water is flowing into the pump pit P5 which is not measured by MF0061G (down-stream the ditch (dam), the deepest part of tunnel F). Autumn 1995 this flow rate was estimated to 6 L/min. 6 L/min has been added to the monthly mean flow rate measured at MF0061G.

The columns SHAFT220, SHAFT340, SHAFT450 represent the estimated flow rates for –z = 0–220 m, 220–340 m and 340–450 m respectively. In May 1995 the measurements with weirs started. Unfortunately not all shafts were equipped with water collecting devices at levels –220 m, –340 m and –450 m. Therefore must the measurements after May 1995 for the shafts be adjusted to depth levels. In SKB PR 25-95-28, App. 2:4 and in SKB TR 97-06, App. 2 a suggestion was made of how to make these adjustments. These calculations have been made in the file for Columns SHAFT220, SHAFT3340, SHAFT 450 for data collected after July 1995.The actual measurements at MA1659G, MA2587G and MA3384G are just provided to show the measured value AND SHALL NOT BE USED IN THE MODELLING.

MA3411G collects water from tunnel section 3,179–3,426 m in tunnel A.

MA3426G collects water from tunnel section 3,426–3,600 m in tunnel A.

Tunnel F and G are parallel and close to tunnel A, approximately section 3,400–3,510 m and 3,510–3,600 m. The flow rate shown in column MF0061G and MG0045 should be added to A3411G (50%) and MA3426G (50%) if tunnels F and G are not modelled. (For a short period, ca 2 month, the flow from tunnel G was measured by MF0061G before MG0045 was in operation).

Data from May 1991 to Jan 1994 are from the Task 5 modelling exercise with the Äspö HRL Task Force. These data are used here. Data from later period are monthly mean values, calculated from SICADA data. Some spikes of inflow rates, with short duration, have been removed, as generally they can be assumed to be related to drill water when excavation new tunnels. It is possible that some of these spikes, totally or partly, can be related to true inflow from the rock, due e.g. hydraulic tests. No attempt has been made to sort this out as it was judged that it would only result in smaller changes of the total flow rate. At some occasions data are missing after 1995 or there is an indication that a weir has been clogged. Linear interpolation has been used to estimate flow rates for moths with missing or erroneous data. Flow rates are missing for 2005, but can be assumed to be more or less as Dec 2004.

Table A2-6. Explantions to the hydrochemistry data.

Column:	Unit: :	Description
START_DATE	YYYYMMDD	Date for sampling
TIME	hhmmss	Hours,minutes, seconds for sampling
IDCODE	–	Code for measurement point
SECUP	m	Upper measurement section in the tunnel
SECLOW	m	Lower measurement section in the tunnel
SAMPLE_NO		The No of the sample
CL	mg/l	Cloride
PH	–	Ph
COND	mS/m	Electrical conductivity
TDS(COND)	g/L	Estimate of TDS based on COND
TDS(Cl)	g/L	Estimate of TDS based on Cl

A2.4 Weir and Chemistry data

File: WEIRCHEM.doc

Weirch02 bearb.xls contains hydochemistry data for the water flow into the Äspo HRL tunnel. This file contains data of Chloride, pH and electrical conductivity measured at the weirs along the Äspö tunnel during the excavation of Äspö Hard Rock Laboratory for period.

ÄspoHRL, for period: May 1991–ca 2003. Based on Cl and electrical conductivity (Cond) measured, TDS has been calculated based on relations:

TDS(Cl) = Cl*1.7

TDS(COND) = Cond*0.00467/0.741 (ref: TR-97-06)

TDS: g/L

Cl: g/L

Cond: mS/m

A2.5 Water table at Äspö

The estimated mean water levels in percussion boreholes based on data from HMS and soundings for three time periods, and calculated drawdowns in relation to the undisturbed conditions are shown in Table A2-7 .The estimated water levels are approximate, since other activities may have influenced the water levels as well.

Table A2-7. Estimated mean water levels in percussion boreholes based on data from HMS and for three time periods, and calculated drawdowns in relation to the undisturbed conditions. Yellow indicates a significant drawdown. Note, that other activities may have influenced the water levels as well.

Borehole information			Undisturbed conditions 1989–1991		Max inflow conditions 1993–1995			Recent conditions 2000–2004			SKB Reference 910601–930521
BH-ID	Bh length Secup	Bh length Seclow	Water level (m.a.s.l.)	Comment	Water level (m.a.s.l.)	Drawdown	Comment	Water level (m.a.s.l.)	Drawdown	Comment	
HAV01	0	175	1.7		1.4	0.3		1.5	0.2	Uncertain	
HAV02	0	93	1		–0.3	1.3					PR 25-94-16
HAV02	94	163	1.7		–0.1	1.8					PR 25-94-16
HAV02	0	163						0.2	1.5	Uncertain	
HAV03	0	100	0.5	Uncertain			Uncertain				
HAV03	101	134	0.1	Uncertain							
HAV03	0	134			0.4		Uncertain	0.3		Uncertain	
HAV04	0	32	4.6	???							
HAV04	33	100	4.4		4.2						
HAV04	0	100						4.1		Uncertain	
HAV05	0	50	3.5	Uncertain							
HAV05	51	100	3.4		1	2.4					
HAV05	0	100						1.7	1.7		
HAV06	0	100	5.3		2.1	3.2		2.1	3.2	Uncertain	
HAV07	0	70	0.9								
HAV07	71	100	0.9								
HAV08	0	28	0.5								
HAV08	29	63	0.5								
HAV08	0	63			–4	4.5		–2.5	3		PR 25-94-16
HMJ01	0	33	0	Unknown, but should be close to +1 or 0	–8.5	8.5		–7	7		PR 25-94-16
HMJ01	34	46	0	Unknown, but should be close to +1 or 1	–8.5	8.5		–7	7		PR 25-94-16
HLX01	0	55	6.8		6.8						
HLX01	56	100	7		7						
HLX01	0	100						6.8			
HLX02	0	15	5		5		Uncertain				

Borehole information			Undisturbed conditions 1989–1991		Max inflow conditions 1993–1995			Recent conditions 2000–2004			SKB Reference 910601–930521
BH-ID	Bh length Secup	Bh length Seclow	Water level (m.a.s.l.)	Comment	Water level (m.a.s.l.)	Drawdown	Comment	Water level (m.a.s.l.)	Drawdown	Comment	
HLX02	26	132	2.3		1.8	0.5	Possibly a drawdown				
HLX02	0	132						5.5		Uncertain	
HLX03	0	10	7		7						
HLX03	11	100	8.2		8.2						
HLX03	0	100						7.5			
HLX04	0	10	8		8.2						
HLX04	11	125	7.5		7.5						
HLX04	0	125						8			
HLX05	1	10	14.3		14.3						
HLX05	11	100	14		14						
HLX05	0	100						14			
HLX06	0	44	9		10						PR 25-94-16
HLX06	45	100	8		8						PR 25-94-16
HLX06	0	100						9			
HLX07	0	15	6.5		6.5						
HLX07	16	100	6.2		6.2						
HLX07	0	100						6.2		Uncertain	
HLX08	0	10	1	Unknown, but should be close to +1 or 0	0						
HLX08	11	40	1	Unknown, but should be close to +1 or 1	0						
HLX09	0	50	1	Uncertain	–0.5	1.5					PR 25-94-16
HLX09	51	151	0.5	Uncertain	–1.4	1.9					PR 25-94-16

Appendix 3

A3 Pointwater head and environmental head

A3.1 Background

The groundwater level measurements in the Laxemar-Simepvarp regional model area are presented in detail in /Werner et al. 2008/ and briefly in Section 5.5. As discussed in this report and this section, the density of water increases with depth due to an increased salinity. Interpretation of the prevailing horizontal and vertical head gradients in a variable-density groundwater flow system requires transformation of measured pointwater heads (H_{ip}) to fresh-water heads (H_{if}) and environmental-water heads (or just environment head) (H_{in}), respectively /Lusczynski 1961/. According to /Werner et al. 2008/ the measured pointwater heads were transformed to environmental head for the deep cored borehole data. /Werner et al. 2008/ describes the procedure used for the Laxemar-Simpevarp groundwater level data and in /Follin et al. 2007c/ the principles for transforming pointwater heads to environmental heads are discussed. In the text below these principles are outlined.

A3.2 Groundwater level and pointwater head

The groundwater levels (GWL in the Laxemar-Simepvarp regional model area are calculated from pressures measured with pressure transducers connected to a logger system and data are stored in SKB's hydrologic monitoring system (HMS). The pressure transducers are calibrated once a month using a manually operated water level measurement device (tape).

The groundwater levels recorded in the field are so called pointwater heads. The illustration in Figure A3-1 shows how they are measured. The borehole in Figure A3-1 is intersected by a flowing fracture at point *i* and is completely filled with groundwater of density ρ_i. The fluid pressure p_i reflects the weight of the fluid $g\,\rho_i$ in the borehole above the point i. Figure A3-2 shows the principle of pointwater head measurements with a multipacker system. The different straddle intervals can have different fluid densities.

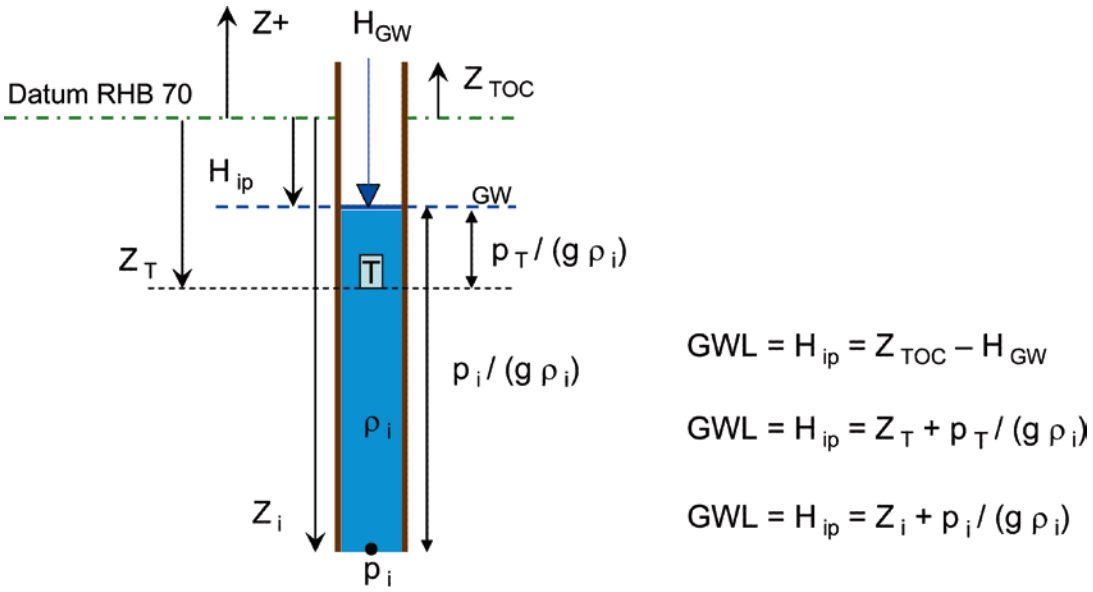

Figure A3-1. *The definition of the groundwater level (GWL) in a borehole filled with a fluid of density ρ_i. The HMS uses programmed pressure transducers which are calibrated against the levels recorded with a manually operated water level device (tape). TOC = top of casing, GW = groundwater. /Follin et al. 2007c/.*

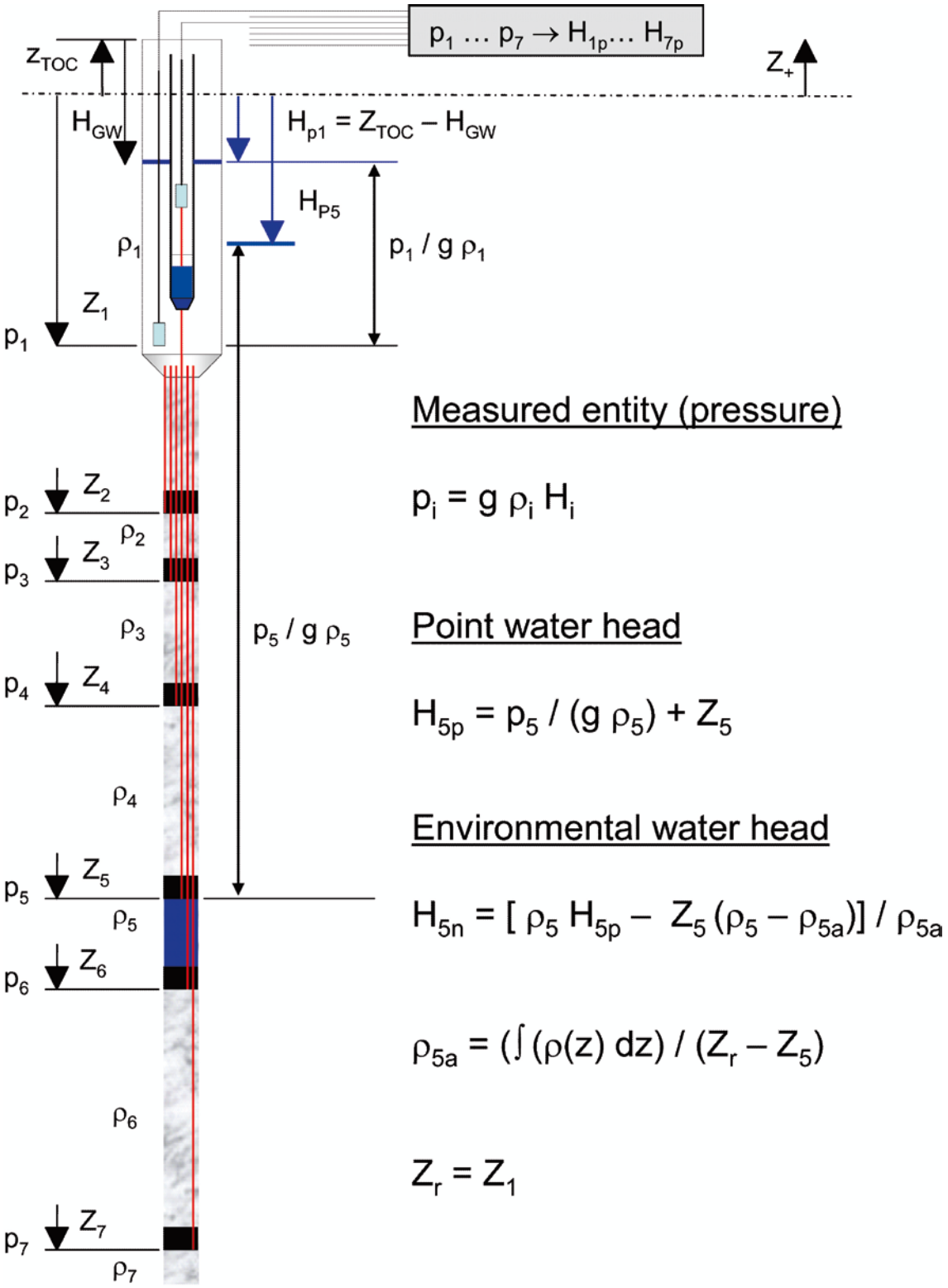

Figure A3-2. *Principle for point-water head measurements in a borehole equipped with a multipacker system. /Lusczynski 1961/ is the key reference used in this report for transferring pointwater heads H_{ip} to environmental heads H_{in}. /Follin et al. 2007c/.*

Pointwater head and environmental head

The interpretation of flow gradients from pointwater head data in fractured crystalline rock can be quite misleading unless care is taken with regard to uncertainties in the fluid density measurements, geometrical positions of the packers and the structural geology. If a *porous medium* with a continuous density profile in the vertical direction $\rho(z)$ is assumed, the average fluid density ρ_a between the two elevations Z_i and Z_r can be written as /Lusczynski 1961/:

$$\rho_a = \frac{1}{Z_r - Z_i} \int_{Z_i}^{Z_r} \rho(z)\, dz$$

where

Z_i = elevation of point i; elevation measured positively upwards.

Z_r = elevation of a reference point from which the average density of water to point i is determined and above which water is constant (e.g. fresh water).

From Figure A3-1 we conclude that the pressure p_i is given by $g\,\rho_i\,(H_{ip} - Z_i)$ when the borehole is filled with groundwater of density ρ_i. By the same token, it is given by $g\,\rho_a\,(H_{in} - Z_i)$ when it is filled with groundwater of average density ρ_a. From this equality, the environmental head H_{in} may be expressed in terms of the pointwater head as:

$$H_{in} = \rho_i\, H_{ip} - Z_i\, (\rho_i - \rho_a) / \rho_a$$

In a *porous medium* the environmental head can be used to interpret the vertical gradients.

Moreover, fresh-water heads h_{if} (used to interpret horizontal head gradients) are calculated from measured point-water heads H_{ip} according to the expression.

$$H_{if} = \frac{\rho_i H_{ip} - Z_i(\rho_i - \rho_f)}{\rho_f}$$

Appendix 4

A4 Hydrogeochemistry

This appendix provides a few details of the hydrochemical data used in the SDM-Site Laxemar groundwater flow modelling.

A4.1 Available chemical data for flow modelling

In Table A4-1 and Table A4-2, a summary of the constituents and boreholes considered in the model calibration for SDM-Site Laxemar is shown for core-drilled and percussion-drilled boreholes, respectively, cf Chapter 3 (Figures 3-3- and 3-4) for borehole locations. A full list of the constituents encompassed by the hydrochemical programme providing data for SDM-Site Laxemar is given in /Laaksoharju et al. 2009/.

Table A4-3 and Table A4-4 present the criteria used for categorisation for core-drilled and percussion-drilled boreholes. (The various categories are colour-coded; orange (Category 1), yellow (Category 2), green (Category 3), grey (Category 4) and uncoloured (Category 5).

Table A4-1. Coverage of hydrochemistry data in the core-drilled boreholes used as calibration targets in SDM-Site Laxemar. Table A4-3 contains a detailed specification of the quality classification system used for the data samples.

Name	Salinity	Major ions	Isotopes	Water types	Pore water	No. of samples [Cat. 1+2+3 / Cat. 4 / Cat. 5 (not used)]	Highest elevation of used data (m RHB 70)	Lowest elevation of used data (m RHB 70)
KLX01	yes	yes	yes	yes	–	[2 / 4 / 12]	–163	–1,020
KLX02	yes	yes	yes	yes	–	[3 / 4 / 61]	–299	–1,531
KLX03	yes	yes	yes	yes	yes	[3 / 0 / 21]	–171	–922
KLX04	yes	yes	yes	yes	–	[3 / 1 / 12]	7	–944
KLX05	yes	yes	yes	yes	–	[2 / 0 / 11]	–205	–550
KLX06	yes	yes	yes	yes	–	[4 / 0 / 14]	0	–475
KLX07A	yes	yes	–	–	–	[0 / 1 / 17]	6	6
KLX08	yes	yes	yes	yes	yes	[2 / 1 / 29]	7	–505
KLX10	yes	yes	yes	yes	–	[0 / 3 / 1]	–32	–676
KLX11A	yes	yes	yes	yes	–	[0 / 2 / 12]	–31	–542
KLX12A	yes	yes	yes	yes	–	[0 / 2 / 5]	–50	–501
KLX13A	yes	yes	yes	yes	–	[1 / 2 / 6]	–35	–475
KLX15A	yes	yes	yes	yes	–	[1 / 0 / 0]	–467	–467
KLX17A	yes	yes	yes	yes	yes	[1 / 0 / 8]	–342	–342
KLX18A	yes	yes	yes	yes	–	[0 / 1 / 0]	–453	–453
KLX19A	yes	yes	yes	yes	–	[1 / 2 / 7]	–38	–414
KLX20A	yes	yes	yes	yes	–	[0 / 1 / 4]	8	8
KLX21B	yes	yes	yes	yes	–	[0 / 1 / 8]	–8	–8
KAS02	yes	yes	yes	yes	–	[7 / 0 / 0]	–200	–881
KAS03	yes	yes	yes	yes	–	[7 / 1 / 0]	–122	–914
KAS04	yes	yes	yes	yes	–	[3 / 0 / 4]	–185	–377
KAS06	yes	yes	yes	yes	–	[3 / 0 / 4]	–284	–433
KAV01	yes	yes	yes	yes	–	[1 / 1 / 18]	–546	–675
KAV04A	yes	yes	yes	yes	–	[0 / 1 / 13]	–40	–40
KSH01A	yes	yes	yes	yes	–	[5 / 1 / 12]	–153	–536
KSH02	yes	yes	yes	yes	–	[4 / 1 / 10]	–415	–952
KSH03A	yes	yes	yes	yes	–	[0 / 1 / 11]	–39	–39

Table A4-2. Coverage of hydrochemistry data in the percussion-drilled boreholes used as calibration targets in SDM-Site Laxemar. Table A4-4 contains a detailed specification of the quality classification system used for the data samples.

Name	Salinity	Major ions	Isotopes	Water types	Pore water	No. of samples [Cat. 1+2+3 / Cat. 4 / Cat. 5 (not used)]	Highest elevation of used data (m RHB 70)	Lowest elevation of used data (m RHB 70)
HLX01	yes	yes	yes	yes	–	[0 / 1 / 0]	–56	–56
HLX03	yes	yes	yes	yes	–	[0 / 1 / 0]	–47	–47
HLX06	yes	yes	yes	yes	–	[0 / 1 / 0]	–46	–46
HLX10	yes	yes	yes	yes	–	[1 / 0 / 0]	–10	–10
HLX14	yes	yes	yes	yes	–	[1 / 0 / 0]	–42	–42
HLX20	yes	yes	yes	yes	–	[1 / 0 / 1]	–54	–54
HLX21	yes	yes	–	–	–	[0 / 1 / 0]	–51	–51
HLX22	yes	yes	yes	yes	–	[0 / 1 / 0]	–57	–57
HLX23	yes	yes	yes	yes	–	[0 / 1 / 0]	–52	–52
HLX24	yes	yes	yes	yes	–	[0 / 1 / 0]	–60	–60
HLX28	yes	yes	yes	yes	–	[1 / 0 / 0]	–53	–53
HLX30	yes	yes	yes	yes	–	[1 / 0 / 0]	–60	–60
HLX33	yes	yes	yes	yes	–	[0 / 1 / 0]	–65	–65
HLX34	yes	yes	yes	yes	–	[0 / 1 / 0]	–50	–50
HLX35	yes	yes	yes	yes	–	[1 / 0 / 0]	–90	–90
HLX38	yes	yes	yes	yes	–	[0 / 1 / 0]	–29	–29
HLX39	yes	yes	yes	yes	–	[0 / 1 / 0]	–138	–138
HAS02	yes	yes	yes	–	–	[1 / 0 / 0]	–56	–56
HAS03	yes	yes	yes	yes	–	[1 / 0 / 0]	–60	–60
HAS05	yes	yes	yes	–	–	[0 / 1 / 0]	–56	–56
HAS07	yes	yes	yes	yes	–	[1 / 0 / 0]	–75	–75
HAS13	yes	yes	yes	–	–	[1 / 0 / 0]	–43	–43
HAV04	yes	yes	yes	–	–	[0 / 1 / 0]	–51	–51
HAV05	yes	yes	yes	–	–	[0 / 1 / 0]	–56	–56
HAV06	yes	yes	yes	–	–	[1 / 0 / 0]	–63	–63
HAV07	yes	yes	yes	–	–	[0 / 1 / 0]	–70	–70
HSH02	yes	yes	yes	yes	–	[1 / 0 / 0]	–91	–91
HSH03	yes	yes	yes	yes	–	[0 / 1 / 4]	–48	–48

Table A4-3. Colour coding with respect to quality of the used data from core-drilled boreholes in the extended hydrochemistry data freeze Laxemar 2.3.

Category	Specification for KBH samples
Category 1	**Considered to be of High quality.** Characterised by good time-series data accompanied by complete analytical data (particularly all major ions and environmental isotopes when available). A charge balance of ±5%. Less than or close to 1% drilling water.
Category 2	**Considered to be of High quality.** Of quality similar to Category 1 but marked by incomplete analytical data (no implications for the hydrogeological modelling). A charge balance of ±5%. Less than or close to 5% drilling water.
Category 3	**Considered to be of Intermediate quality.** These differ significantly in quality from Categories 1 and 2 in terms of: inadequate time-series data. Time-series data that indicate instability during sampling. Incomplete analytical data (no implications for the hydrogeological modelling). Elevated drilling water contents (5–10%).
Category 4	**Considered to be of Intermediate to low quality.** Samples largely similar in quality to Category 3 but mostly restricted to Br, Ca, Cl, HCO_3, Mg, Na, SO_4 and $\delta^{18}O$. Type samples are of an exploratory one-off nature, i.e. mostly taken to see if there is adequate water volume and to check strategic indicators such as drilling water content, salinity (El conductivity), pH, major ions (Br, Cl, HCO_3, SO_4,) and $\delta^{18}O$. Some samples taken during drilling also fall within this category. Absent or very incomplete time-series data. Elevated drilling water contents (> 10%)
Category 5	**Considered to be of Intermediate to low quality. Not used.** Type samples in this category include those collected during drilling and during hydraulic pump tests. Samples of Tube Sample origin also fall within this category because of unacceptable open hole mixing effects. Samples with some major ions and/or $\delta^{18}O$ missing. Absent or very incomplete time-series data. No charge balance values. Elevated drilling water contents (> 10%).

Table A4-4. Colour coding with respect to quality of the used data from percussion-drilled boreholes in the extended hydrochemistry data freeze Laxemar 2.3.

Category	Specification for HBH samples
Category 1	**Considered to be of High quality.** Borehole sections where Flow Log data are available to demarcate more specifically the major groundwater input section along the open borehole. These input locations are indicated in a special column. Isolated borehole sections < 50 m long where the groundwater data can be related approximately (or precisely) to constrained bedrock levels characterised by dominant water-conducting fracture(s). Both a) and b) cases should be characterised by good time-series data and be accompanied by complete analytical data (i.e. particularly all major ions and environmental isotopes; in most cases a good trace element coverage.
Category 2	**Considered to be of High quality.** Of similar quality to Category 1 but marked by incomplete analytical data (no implications for the hydrogeological modelling).
Category 3	**Considered to be of Intermediate quality.** Borehole sections were Flow Log data are available to demarcate more specifically the major groundwater input section (s) along the open borehole. These input locations are indicated in a special column. Isolated borehole sections ≤ 50 m long were the groundwater data can be related approximately (or precisely) to constrained bedrock levels characterised by dominant water-conducting fracture (s). Samples differ significantly in quality from Category 1 and 2 in terms of inadequate time-series data, time-series data that indicate instability during sampling and incomplete analytical data (i.e. mostly absence of some isotopic and trace element data).
Category 4	**Considered to be of Intermediate to Low quality.** Sampling is restricted to ≤ 150 m open borehole sections. No Flow Log data available. Samples largely similar in quality to Category 3 but restricted to Br, Ca, Cl, HCO_3, Mg, Na, SO_4, $\delta^{18}O$. Absent or very incomplete time-series data, often an absence of trace element data.
Category 5	**Considered to be of Intermediate to Low quality. Not used.** Open boreholes lacking Flow Log data such that there is a long section (≥ 200 m) characterised by groundwater mixing. Samples with some major ions and/or $\delta^{18}O$ missing. Often absence of trace element data. No charge balance. Absent or very incomplete time-series data.

A4.2 Drilling water source and composition

Of great concern for the interpretation of the hydrochemical data is the contamination by drilling water in the groundwater samples. The dye uranine is used to trace the drilling water. Factors such as reliability of the uranine analyses, the size of the analytical errors, the stability of uranine concentration in the automatically injected drilling water and inadequate mixing of uranine in drilling water affect the confidence in the drilling water budget calculations as well as in drilling water contents in water samples. Indirectly it also affects the judgement of sample quality and representativity discussed above. An attempt is made here to correct the sampled data for Cl, Br, $\delta^{18}O$ and TDS with respect to the drilling water residues. This was made possible using the delivered data for drilling water source. The drilling water compositions that were used for correction calculations for the core-drilled boreholes are shown in Table A4-5. The correction for contamination due to mixing with drilling water was calculated according to /Kloppmann et al. 2001/:

$$C_{i,corr} = \frac{C_{i,mix} - x_{dw} \cdot C_{i,dw}}{1 - x_{dw}} \qquad \text{A4-1}$$

where $C_{i,corr}$ is the corrected concentration of component i, $C_{i,mix}$ is the concentration of component i in the contaminated sample, x_{dw} is the drilling water residue (fraction of drilling water) in the contaminated sample and $C_{i,dw}$ is the concentration of component i in the drilling water.

Table A4-5. Drilling water source and composition used for the core-drilled boreholes.

Core-drilled borehole	Drilling water source	Cl (mg/L)	Br (mg/L)	$\delta^{18}O$ (‰)
KLX01	HLX05	–	–	–
KLX02	HLX10	6.3	–0.200	–10.9
KLX03	HLX14	–	–	–
KLX04	HLX10	6.3	–0.200	–10.9
KLX05	HLX10	6.3	–0.200	–10.9
KLX06	HLX29	–	–	–
KLX07	HLX10	6.3	–0.200	–10.9
KLX08	HLX10	6.3	–0.200	–10.9
KLX09	HLX20	23.0	–0.200	–10.9
KLX10	HLX27 (first10 days) HLX10 (next 4 months)	6.3	–0.200	–10.9
KLX11	HLX28	23.0	–0.200	–10.9
KLX12	HLX10	6.3	–0.200	–10.9
KLX13	HLX14	357.0	1.290	–11.2
KLX14	HLX28	23.0	–0.200	–10.9
KLX15	HLX14	357.0	1.290	–11.2
KLX16	HLX10	6.3	–0.200	–10.9
KLX17	HLX14	357.0	1.290	–11.2
KLX18	HLX14	357.0	1.290	–11.2
KLX19	HLX28	23.0	–0.200	–10.9
KLX21	HLX10	6.3	–0.200	–10.9
KLX27	HLX10	6.3	–0.200	–10.9

A4.3 Measured concentrations and analytical uncertainties for Cl, δ^2H and $\delta^{18}O$ in pore water samples

In Table A4-6 through Table A4-8, the measured concentrations and analytical uncertainties for Cl, δ^2H and $\delta^{18}O$ in pore water samples from boreholes KLX03, KLX08 and KLX17A respectively, for the Extended data freeze Laxemar 2.3 are shown (Similar tables for most data can be found in /Waber and Smellie 2006a, b, c, 2008b/). The analytical uncertainties for the pore water samples are given as absolute uncertainties. Elevations where no data were present for any component have been removed from the tables.

Table A4-6. Measured concentrations and analytical uncertainties for Cl, δ^2H and $\delta^{18}O$ in pore water samples from KLX03.

Sample No	Elevation (m.a.s.l.)	Cl (mg/L)	Cl (+) error	Cl (–) error	$\delta^{18}O$ (‰)	$\delta^{18}O$ (±) error	δ^2H (‰)	δ^2H (±) error
KLX03-1	–135.35	819.20	55.62	48.86	–12.26	1.51	–90.13	23.98
KLX03-2	–177.32	765.21	15.79	15.15	–11.44	1.37	–92.46	15.25
KLX03-3	–226.70	501.99	41.15	35.21	–11.43	2.03	–116.83	27.33
KLX03-4	–274.47	373.91	43.94	35.32	–	–	–	–
KLX03-5	–325.37	618.66	49.55	42.58	–13.12	1.55	–78.20	22.31
KLX03-6	–379.66	729.95	22.14	20.84	–11.58	2.02	–161.20	
KLX03-7	–429.20	1,374.58	304.33	209.24	–7.51	2.01	–83.87	14.82
KLX03-8	–489.29	5,674.30	1,333.60	897.33	–13.64	2.08	–54.87	17.15
KLX03-9	–552.84	7,600.83	830.75	679.71	–	–	–	–
KLX03-10	–604.34	2,260.39	249.48	204.12	–	–	–	–
KLX03-11	–655.67	511.40	27.98	25.19	–9.38	3.02	–28.32	33.13
KLX03-12	–760.02	4,895.58	184.97	171.66	–10.94	1.52	–58.58	13.70
KLX03-14	–848.97	4,631.50	616.82	486.27	–5.14	–	–	–
KLX03-16	–932.01	5,122.58	1,619.09	988.69	–6.56	3.46	–28.72	37.94

Table A4-7. Measured concentrations and analytical uncertainties for Cl, δ^2H and $\delta^{18}O$ in pore water samples from KLX08.

Sample No	Elevation (m.a.s.l.)	Cl (mg/L)	Cl (+) error	Cl (–) error	$\delta^{18}O$ (‰)	$\delta^{18}O$ (±) error	δ^2H (‰)	δ^2H (±) error
KLX08-1	–105.83	98.63	24.23	49.32	–	–	–	–
KLX08-2	–148.57	138.42	28.57	49.83	–	–	–	–
KLX08-3	–149.28	126.56	21.78	33.69	–9.56	0.86	–83.45	0.93
KLX08-4	–192.59	117.02	15.30	20.93	–8.58	1.23	–81.32	10.11
KLX08-5	–237.67	705.13	90.32	122.17	–7.47	1.75	–76.66	1.40
KLX08-6	–276.22	772.16	179.41	340.36	–8.58	2.20	–95.07	16.41
KLX08-7	–318.00	364.31	71.15	118.14	–12.59	1.16	–105.60	1.20
KLX08-9	–407.36	612.94	56.12	69.34	–	–	–	–
KLX08-10	–450.54	997.37	99.00	99.00	–13.99	1.81	–101.59	16.38
KLX08-11	–494.50	239.61	61.39	128.97	–12.53	3.35	–100.80	27.71
KLX08-12	–544.29	387.69	26.83	31.22	–8.50	1.66	–89.44	1.66
KLX08-13	–580.10	686.67	150.16	270.09	–7.59	1.78	–83.91	14.73
KLX08-14	–621.58	1,532.41	301.83	505.35	–5.15	1.97	–71.33	1.49
KLX08-15	–665.23	2,720.64	636.38	1,220.34	–2.00	2.33	–54.36	17.16
KLX08-16	–712.37	2,761.01	871.97	2,501.15	–9.72	0.47	–72.12	0.42
KLX08-17	–750.44	6,053.95	1,707.46	4,044.41	–3.51	1.97	–53.14	14.94
KLX08-18	–785.95	3,037.77	907.74	2,316.63	–6.89	0.97	–59.45	0.86
KLX08-19	–817.15	8,214.69	2,108.99	4,440.81	–3.11	1.51	–43.00	11.03

Table A4-8. Measured concentrations and analytical uncertainties for Cl, δ^2H and $\delta^{18}O$ in pore water samples from KLX17A.

Sample No	Elevation (m.a.s.l.)	Cl (mg/L)	Cl (+) error	Cl (–) error	$\delta^{18}O$ (‰)	$\delta^{18}O$ (±) error	δ^2H (‰)	δ^2H (±) error
KLX17A-1B	–70.42	91.00	10.00	8.00	–9.49	0.55	–74.30	4.70
KLX17A-2B	–70.75	81.00	9.00	7.00	–10.53	0.38	–79.90	3.30
KLX17A-3A	–71.44	70.00	7.00	6.00	–10.46	0.46	–79.60	4.10
KLX17A-4	–71.99	77.00	8.00	7.00	–10.10	0.43	–79.10	3.90
KLX17A-5B	–72.35	107.00	12.00	9.00	–9.92	1.01	–75.30	8.70
KLX17A-6	–72.68	143.00	15.00	13.00	–9.74	0.47	–75.30	3.90
KLX17A-7	–72.94	161.00	18.00	14.00	–9.76	1.01	–75.10	9.70
KLX17A-8B	–73.29	253.00	28.00	23.00	–9.62	0.85	–76.60	7.10
KLX17A-9	–73.67	215.00	23.00	19.00	–9.97	1.04	–80.60	8.90
KLX17A-10	–73.99	180.00	20.00	16.00	–10.00	0.91	–82.40	7.60
KLX17A-11	–74.25	188.00	20.00	17.00	–10.90	0.65	–83.40	5.40
KLX17A-12B	–74.57	161.00	17.00	14.00	–11.38	0.69	–86.80	6.00
KLX17A-13	–74.87	151.00	16.00	13.00	–	–	–	–
KLX17A-14B	–75.32	204.00	22.00	18.00	–11.22	0.67	–74.80	5.60
KLX17A-15B	–75.77	278.00	30.00	25.00	–10.64	0.87	–89.00	7.90
KLX17A-16B	–76.22	275.00	30.00	25.00	–10.68	0.96	–90.10	7.50
KLX17A-17	–78.09	287.00	31.00	25.00	–10.62	0.94	–89.80	8.00
KLX17A-18	–80.49	252.00	27.00	22.00	–	–	–	–
KLX17A-19	–84.99	310.00	34.00	28.00	–7.86	0.85	–82.20	6.60
KLX17A-20	–89.33	235.00	26.00	21.00	–7.58	1.80	–84.10	12.70
KLX17A-21	–181.10	315.00	34.00	28.00	–10.96	0.80	–96.50	6.70
KLX17A-22	–261.36	680.00	74.00	61.00	–12.82	0.72	–97.80	5.90
KLX17A-23	–349.97	709.00	78.00	64.00	–	–	–	–
KLX17A-24	–438.65	6,823.00	748.00	612.00	–5.07	1.30	–34.50	9.90
KLX17A-25	–518.18	4,960.00	544.00	445.00	–4.79	1.47	–37.60	15.80

Appendix 5

A5 HCD, HRD and HSD primary assessment of parameters before calibration

A5.1 HCD

Trend functions for individual HCDs.

In the modelling of Laxemar it was suggested that 5 main categories are used to infer the depth dependency for the hydraulic conductor domain /Rhén et al. 2008/. One category contains the zones with several hydraulic measurements within an individual HCD and the other four are less known but divided according strike and trace length. However, the zones where rather few hydraulic tests have been made are still deemed as uncertain are classified based on strike and trace length as for the less known deformation zones. The zones where hydraulic tests have been performed are listed in Table A5-1.

For the less known deformation zones, there are two groups for the strike, East-West and Other. Each group is sub-sequentially divided based on the trace length being shorter or longer than 2 km. For all categories the transmissivity is expressed as $T = 10^{(a+BZ)}$ where a and B are constants, and Z is the elevation, cf Table A5-2.

Table A5-1. Deformation zones where several hydraulic measurements have been performed in individual HCDs /Rhén et al. 2008/. The depth dependency is inferred as $T = 10^{(a+BZ)}$ where a and B are constants, and Z is the elevation. /Rhén et al. 2008/.

Zone	a	B	Comment
HLX28_DZ1	–4.578	0.002405	Uncertain
ZSMEW002A	–4.848	0.002405	Uncertain
ZSMEW007A	–3.996	0.002158	Suggested to be used
ZSMEW009A	–4.852	0.002405	Uncertain
ZSMEW013A	–6.230	0.002405	Uncertain
ZSMEW038A	–2.808	0.002405	Uncertain
ZSMEW900	–4.093	0.002405	Uncertain
ZSMEW946	–4.210	0.004638	Suggested to be used
ZSMNE004A	–5.789	0.002405	Uncertain
ZSMNE005A	–5.267	0.002120	Uncertain
ZSMNE006A	–3.017	0.003104	Suggested to be used
ZSMNE012A	–3.673	0.002209	Suggested to be used
ZSMNE024A	–2.234	0.007197	Suggested to be used
ZSMNE031A	–1.409	0.009965	Uncertain
ZSMNE040A	–6.038	0.002405	Uncertain
ZSMNE107A	–4.095	0.003426	Uncertain
ZSMNE942A	–4.559	0.002405	Suggested to be used
ZSMNE944A	–5.760	0.002405	Uncertain
ZSMNS001	–4.203	0.002405	Uncertain
ZSMNS017B	–3.240	0.002405	Suggested to be used
ZSMNS059A	–3.698	0.002405	Uncertain
ZSMNW025A	–4.527	0.002405	Uncertain
ZSMNW042A	–6.227	0.002405	Alt 1, Uncertain
ZSMNW042A	–6.398	0.000973	Alt 2 ,Uncertain
ZSMNW928A	–4.900	0.002405	Uncertain

Table A5-2. Inferred depth dependency for deformation zones where no hydraulic measurements have been performed /Rhén et al. 2008/. The depth dependency is inferred as $T = 10^{(a+BZ)}$ where a and B are constants, and Z is the elevation. /Rhén et al. 2008/.

Category	a	B	Strike, Trace Length
R19	–4.665	0.00263	EW, < 2 km
R20	–4.091	0.00187	EW, > = 2 km
R21	–4.997	0.00250	Other, < 2 km
R22	–4.070	0.00274	Other, > = 2 km

Transmissivities within HCDs with several borehole intercepts

A number of HCDs have several borehole intercepts and then generally also hydraulic tests that can be used to estimate several transmissivity estimates for a single HCD. The HCDs that have more than 2 borehole intercepts with hydraulic tests are plotted in Figure A5-1 and Figure A5-2.

Storage coefficiet as function of transmissivities

In Figure A5-3 and Table A5-3 the correlation between T and S is shown. The data covers roughly tests performed down to ca 500 m depth. As indicated, also a few minor deformation zones (MDZ) are included, /Rhén et al. 2008/.

A5.2 HRD

In /Rhén et al. 2006/ the hydraulic properties of the geologically defined rock domains were discussed. As no new data are available for the area outside the Laxemar local model area, the conclusion made in /Rhén et al. 2006/ is used for assessment of the hydraulic properties outside the domains defined by the fracture domains /La Pointe et al. 2008/. Below is the discussion in /Rhén et al. 2006/ compiled.

Hydraulic properties outside the local model volume.

Based on PFL (5 m scale) measurements, the fine-grained granite bodies (Sicada rock type code 511058) are an order of magnitude more conductive than the dominant rock type in the regional modelling area (Sicada code 501044, Ävrö granite), which is the main rock type in the geological Rock domain A. Possibly the fine-grained granite bodies modelled in the RVS can be assumed to be as conductive as the smaller fine-grained granites intersecting the boreholes.

Hydraulic properties of geological Rock domain A differs between the Laxemar subarea and the Äspö and Ävrö areas; the Laxemar area appearing to be less permeable. A reason for this may be that the rock mass east of the Äspö shear zone, including the southern part of Äspö and Ävrö as well as the Simpevarp peninsula, see the rhombohedral area indicated in Figure A5-4**,** may be part of a largescale shear belt, cf /Wahlgren et al. 2005/, that can explain the observed difference in hydraulic properties. The geological rock domain A is therefore suggested to be divided into two HRDs as defined below.

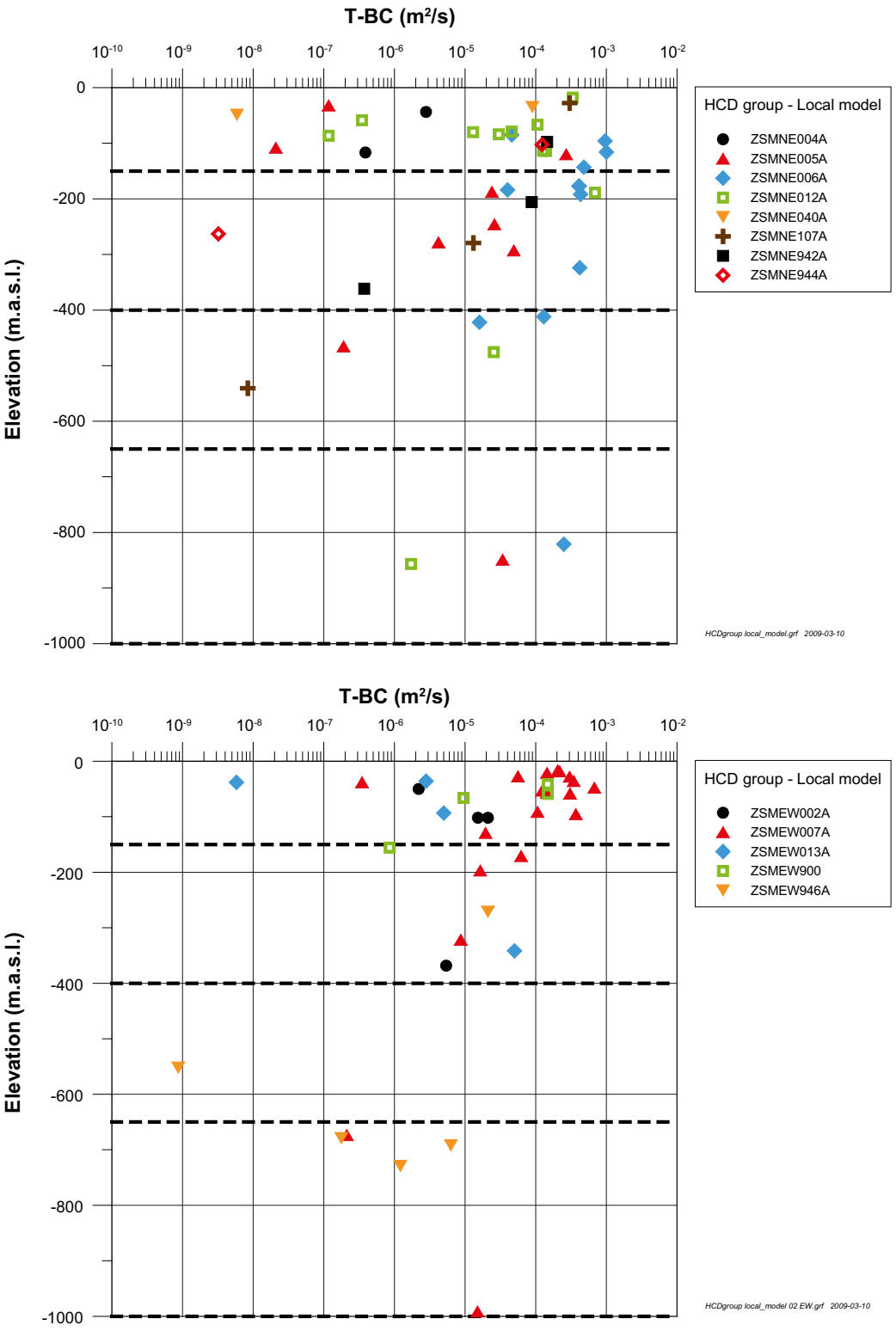

Figure A5-1. *Transmissivity of individual borehole intercepts with HCDs for HCDs with 2 or more borehole intercepts with hydraulic test data. NE and EW HCDs, local model area. /Rhén et al. 2008/.*

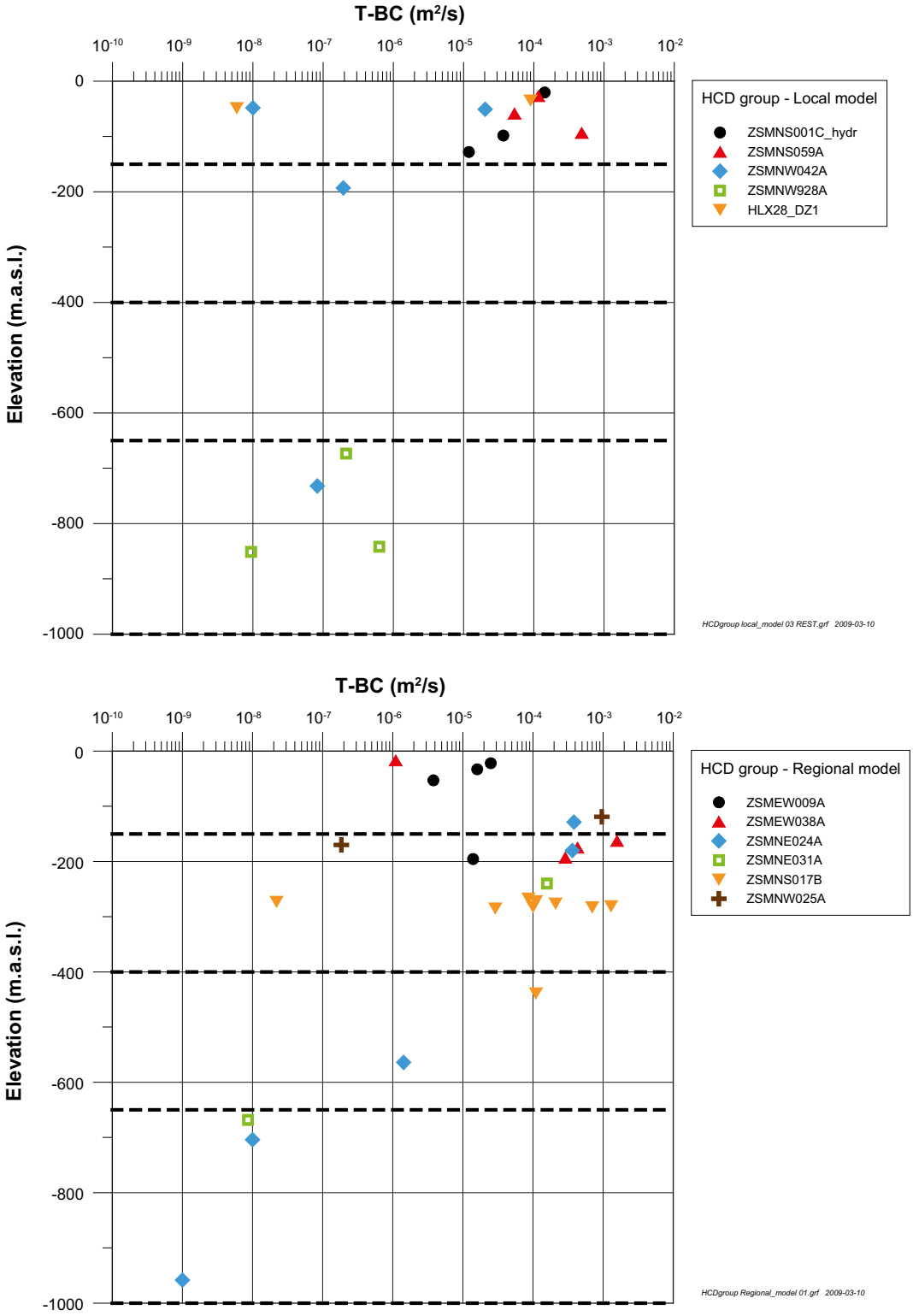

Figure A5-2. *Transmissivity of individual borehole intercepts with HCDs for HCDs with 2 or more borehole intercepts with hydraulic test data. Top: NS, NW and a disc in local model area. Bottom: HCDs with more than 2 bh intercepts outside the local model volume. /Rhén et al. 2008/.*

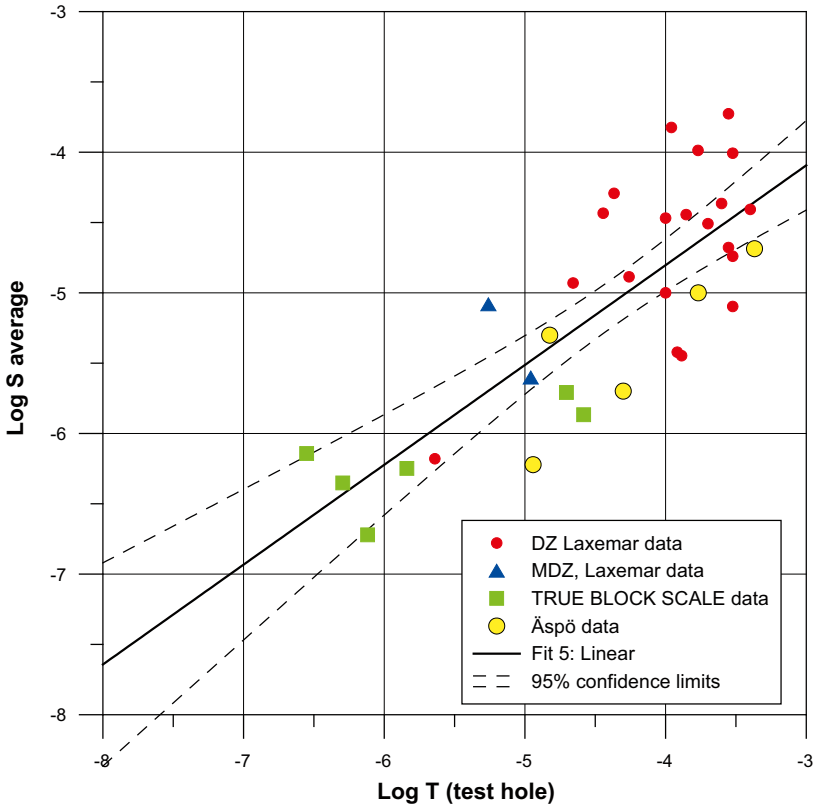

Figure A5-3. *Correlation between T and S for deformation zones. /Rhén et al. 2008/.*

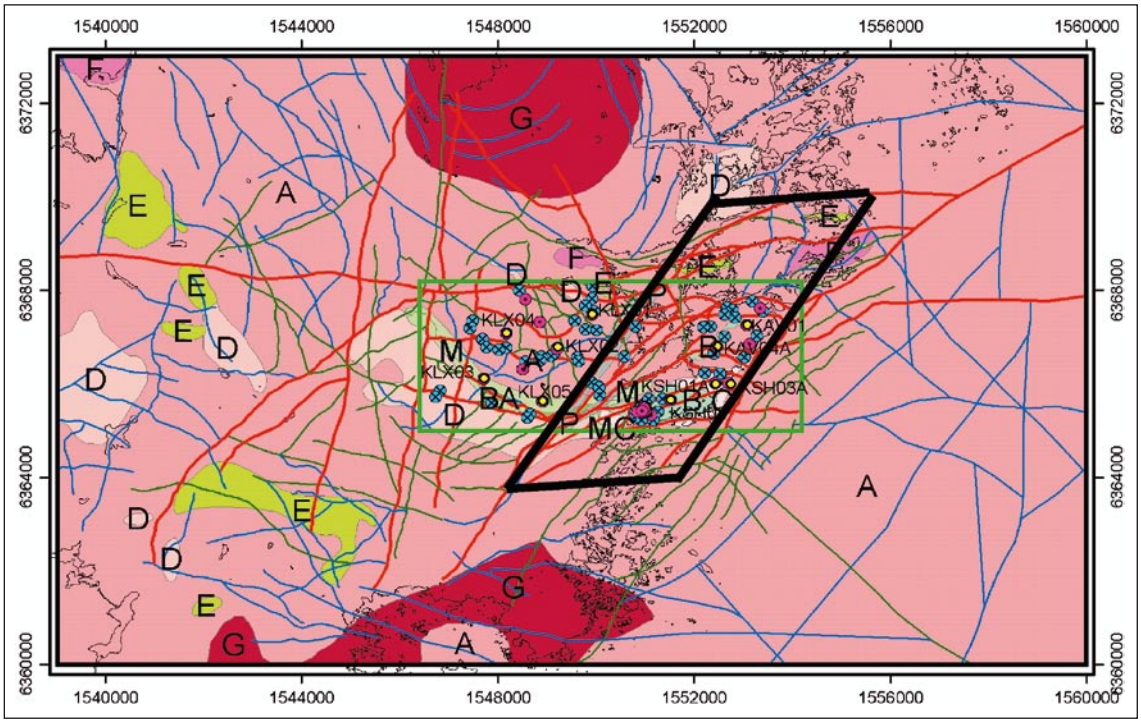

Figure A5-4. *Rock domain model for Laxemar model version 1.2. The rhombohedral area indicates the area of HRD(A2), interpreted more strongly affected by low-grade ductile shear zones than the corresponding HRD(A) in the Laxemar subarea, see /Wahlgren et al. 2005/.*

Table A5-3. Correlation between T and S for deformation zones. $S = a \cdot T^B$ /Rhén et al. 2008/.

Model ID	Object	Data type	Coeff. a	Coeff. B	Corr, coeff. r^2
DZ-TS1	DZ, MDZ	Storage coefficient as function of Transmissivity in deformation zones	0.0109	0.71	0.62

The following hydraulic rock domains (HRDs) are proposed, based on grouping of geological rock domains as defined in /Wahlgren et al. 2005/ (letters given within parentheses indicate the underlying geological rock domains):

- **HRD(F,G):** (G01, (Götemar granite), G02 (Uthammar granites)). The most conductive domain. Assume 10* HRD(A) properties. (F) (Granite, Fine- to medium-grained). One of the most conductive rock types. Assume 10* HRD(A) properties. The bodies are small and may probably be neglected in the regional model, but have been implemented.
- **HRD(A):** (A+BA), Part of rock domain A outside rhombohedral area shown in Figure A5-4). It is motivated due to the higher hydraulic conductivity in domain A in boreholes on Ävrö and southern Äspö compared to the Laxemar subarea.
- **HRD(A2):** (A), Part of rock domain A within rhombohedral area shown in Figure A5-4). See comment on HRD (A) above.
- **HRD(B,C):** (B+C). Low conductive domain.
- **HRD(D,E,M):** (M(A)+M(D)+D+E). The least conductive domain. Data corresponding to rock domains D and M(D) constitute small samples. M(A) is included in HRD(D, M) as it has a low hydraulic conductivity and is fairly small in size and is part of the M domain. There are no hydraulic data for rock domain E (diorite to gabbro), but as it is a basic rock type, the hydraulic conductivity is probably small according to the text above.

(The rhomboid in *Figure A5-4* is defined by the following 4 planes.

Ax+By+Cz+D = 0

A	B	C	D
–1.20739E-8	1.60076E-7	0.0	–1.0
–3.61952E-7	2.45391E-7	0.0	–1.0
1.20629E-8	–1.59930E-7	0.0	1.0
3.61503E-7	–2.45087E-7	0.0	1.0

A5.3 HSD

In order to enable the construction of the regolith depth model (RDM). /Nyman et al. 2008/ divided the area into 3 type areas (denoted I–III) and 9 domains, cf figures in Chapter 3. Table A5-4 summarises the QD layer structure of the RDM, including notations on which layers that are present "locally", given different types of QD on the QD map. In addition, the table presents average thicknesses of the individual layers.

Based on the available hydrogeological properties data presented in /Werner et al. 2008/, the assignment follows the geometrical representation of the QD according to the RDM /Nyman et al. 2008/. It should be noted that the hydrogeological properties assignment below is preliminary, and it should be considered as a starting point for the quantitative water-flow modelling. Parameter values could be changed as a result of the quantitative modelling, e.g. for purposes of flow model calibration.

Table A5-5 presents a preliminary assignment of hydrogeological properties (hydraulic conductivity and storage parameters) to each layer defined in the RDM.

Table A5-4. Summary of the layer definitions according to the regolith depth and stratigraphy model. /Werner et al. 2008/.

Domain no. (type area no.) and QD on QD map	Average total QD depth (m)	Z1 – Surface-affected layer (average layer depth, m)	Z2 – Peat	Z3 – Clay gyttja, gyttja or recent fluvial sediments	Z4 – Post-glacial sand/ gravel, glacio-fluvial sediments and/or artificial fill	Z5 – Glacial clay	Z6 – Till
1 (I)							
Rock outcrops	0.1	Surface-affected layer (0.1)	–	–	–	–	–
2 (I)							
Till	2.1	Surface-affected layer (0.6)	–	–	–	–	Till (2.0–2.3 m on land, 3.6 m in clay-covered valleys below the sea)
Till with a thin surface layer of peat	2.1	Surface-affected layer (0.6)	–	–	–	–	Till (2 m)
Postglacial shingle	2.1	Surface-affected layer (0.6)	–	–	–	–	Till (2 m)
Boulder deposit	2.1	Surface-affected layer (0.6)	–	–	–	–	Till (2 m)
3 (II)							
Gyttja clay/clay gyttja	5.7 (only terrestrial)	Surface-affected layer (0.6)	–	Gyttja clay/ clay gyttja (1.6 m land, 1.7 m sea)	Postglacial sand/gravel (0.7 m land, 0.8 m sea)	Glacial clay (1.3 m land, 2.6 m sea)	Till (2 m)
Gyttja	5.7 m (terrestrial) 8.7 m (sea)	Surface-affected layer (0.6)	–	Gyttja (1.6 m land, 1.7 m sea)	Postglacial sand/gravel (0.7 m land, 0.8 m sea)	Glacial clay (1.3 m land, 2.6 m sea)	Till (2 m)
Gyttja clay/clay gyttja with a thin surface layer of peat	5.7 m (only terrestrial)	Surface-affected layer (0.6)	–	Gyttja clay/ clay gyttja (1.6 m land, 1.7 m sea)	Postglacial sand/gravel (0.7 m land, 0.8 m sea)	Glacial clay (1.3 m land, 2.6 m sea)	Till (2 m)
Recent fluvial sediments	5.7 m (only terrestrial)	Surface-affected layer (0.6)	–	Gyttja clay/ clay gyttja (1.6 m land, 1.7 m sea)	Postglacial sand/gravel (0.7 m land, 0.8 m sea)	Glacial clay (1.3 m land, 2.6 m sea)	Till (2 m)
Gyttja clay with a thin surface layer of sand-gravel	8.7 (only below sea)	Surface-affected layer (medium sand-gravel)	–	Gyttja clay/ clay gyttja (1.6 m land, 1.7 m sea)	Postglacial sand/gravel (0.7 m land, 0.8 m sea)	Glacial clay (1.3 m land, 2.6 m sea)	Till (2 m)
4 (I)							
Peat, shallow (fen peat, bog peat, and unspecified peat)	3 m (only terrestrial)	–	Peat (0.85 m)	–	–	–	Till (2 m)
5 (II)							
Peat, deep (fen peat, bog peat, and unspecified peat)	6.6 m (only terrestrial)	–	Peat (0.85 m)	Gyttja clay/ clay gyttja (1.6 m land, 1.7 m sea)	Postglacial sand/gravel (0.7 m land, 0.8 m sea)	Glacial clay	Till (2 m)
6 (II)							

Domain no. (type area no.) and QD on QD map	Average total QD depth (m)	Z1 – Surface-affected layer (average layer depth, m)	Z2 – Peat	Z3 – Clay gyttja, gyttja or recent fluvial sediments	Z4 – Postglacial sand/gravel, glaciofluvial sediments and/or artificial fill	Z5 – Glacial clay	Z6 – Till
Glacial clay	4.1 (land) 7.1 (sea)	Surface-affected layer (0.6)	–	–	Postglacial sand/gravel (0.7 m land, 0.8 m sea)	Glacial clay	Till (2 m)
Glacial clay with a thin surface layer of postglacial fine sand	4.1 (land) 7.1 (sea)	Surface-affected layer (0.6)	–	–	Postglacial sand/gravel (0.7 m land, 0.8 m sea)	Glacial clay	Till (2 m)
Glacial clay with a thin surface layer of postglacial medium sand-gravel	4.1 (land) 7.1 (sea)	Surface-affected layer (0.6)	–	–	Postglacial sand/gravel (0.7 m land, 0.8 m sea)	Glacial clay	Till (2 m)
Clay-silt (unspecified)	4.1 (land) 7.1 (sea)	Surface-affected layer (0.6)	–	–	Postglacial sand/gravel (0.7 m land, 0.8 m sea)	Glacial clay	Till (2 m)
Postglacial fine sand	4.1 (land) 7.1 (sea)	Surface-affected layer (0.6)	–	–	Postglacial fine sand (0.7 m land, 0.8 m sea)	Glacial clay	Till (2 m)
Postglacial sand	4.1 (land) 7.1 (sea)	Surface-affected layer (0.6)	–	–	Postglacial sand (0.7 m land, 0.8 m sea)	Glacial clay	Till (2 m)
Postglacial sand with a thin surface layer of peat	4.1 (only land)	Surface-affected layer (0.6)	–	–	Postglacial sand (0.7 m land, 0.8 m sea)	Glacial clay	Till (2 m)
Postglacial medium sand-gravel	7.1 (only sea)	Surface-affected layer (0.6)	–	–	Postglacial medium sand-gravel (0.7 m land, 0.8 m sea)	Glacial clay	Till (2 m)
Postglacial gravel with a thin surface layer of peat	4.1 (only land)	Surface-affected layer (0.6)	–	–	Postglacial gravel (0.7 m land, 0.8 m sea)	Glacial clay	Till (2 m)
Postglacial gravel	4.1 (land) 7.1 (sea)	Surface-affected layer (0.6)	–	–	Postglacial gravel (0.7 m land, 0.8 m sea)	Glacial clay	Till (2 m)
Glacial clay with thin surface layer of peat	4.1 (only land)	Surface-affected layer (0.6)	–	–	Postglacial sand/gravel (0.7 m land, 0.8 m sea)	Glacial clay	Till (2 m)
Glacial silt	4.1 (land) 7.1 (sea)	Surface-affected layer (0.6)	–		Postglacial sand/gravel (0.7 m land, 0.8 m sea)	Glacial clay	Till (2 m)
7 (III)							
Glaciofluvial sediments, shallow	4.1	Surface-affected layer (0.6)	–	–	Glaciofluvial sediments (3.5)		
8 (III)							
Glaciofluvial sediments, deep (the Tuna esker)	13.8	Surface-affected layer (0.6)	–	–	Glaciofluvial sediments (13.2)	–	–
9 (no type area)							
Artificial fill	5	Surface-affected layer (0.6)	–	–	Artificial fill (4.4)	–	–

Table A5-5. Preliminary data-based assignment of hydrogeological properties to different types of QD, arranged in layers Z1-Z6 according to the regolith depth and stratigraphy model /Sohlenius and Hedenström 2008/. The assignment should be considered as a starting point for quantitative water-flow modeling. K_h = horizontal hydraulic conductivity ($m \cdot s^{-1}$), K_h/K_v = anisotropy ratio (–), S_y = specific yield (–), and S_s = specific storage coefficient (m^{-1}). SAL = surface-affected layer, PSG = postglacial sand/gravel, GS = glaciofluvial sediments, AF = artificial fill, GLC = glacial clay, and GC/CG = gyttja clay/clay gyttja. In the first column, (G) denotes that the properties are based on "generic" data and therefore are considered uncertain. (S) denotes that the properties are supported by site data and are considered more certain. (G/S) means that there is some site-data support. For layer Z6, the first set of parameter values tentatively applies to areas with a total QD depth less than 10 m, and the second set to areas with a total QD depth larger than 10 m. /Werner et al. 2008/.

Domain no. (type area no.)		Z1	Z2	Z3	Z4	Z5	Z6
QD on QD map							
1 (I)							
Rock outcrops	QD	SAL (G)	–	–	–	–	–
	K_h	$4 \cdot 10^{-4}$					
	K_h/K_v	1					
	S_y	0.10					
	S_s	$5 \cdot 10^{-3}$					
2 (I)							
Till	QD	SAL (G)	–	–	–	–	Till (S)
	K_h	$4 \cdot 10^{-4}$					$4 \cdot 10^{-5}$ / $4 \cdot 10^{-4}$
	K_h/K_v	1					1
	S_y	0.15					0.05 / 0.10
	S_s	$1 \cdot 10^{-3}$					$1 \cdot 10^{-3}$ / $5 \cdot 10^{-3}$
Till with a thin surface layer of peat	QD	SAL (peat) (G/S)	–	–	–	–	Till (S)
	K_h	$3 \cdot 10^{-6}$					$4 \cdot 10^{-5}$ / $4 \cdot 10^{-4}$
	K_h/K_v	1					1
	S_y	0.24					0.05 / 0.10
	S_s	$5 \cdot 10^{-2}$					$1 \cdot 10^{-3}$ / $5 \cdot 10^{-3}$
Postglacial shingle	QD	SAL (shingle) (G)	–	–	–	–	Till (S)
	K_h	$1 \cdot 10^{-2}$					$4 \cdot 10^{-5}$ / $4 \cdot 10^{-4}$
	K_h/K_v	1					1
	S_y	0.25					0.05 / 0.10
	S_s	0.025					$1 \cdot 10^{-3}$ / $5 \cdot 10^{-3}$
Boulder deposit	QD	SAL (G)	–	–	–	–	Till (S)
	K_h	$4 \cdot 10^{-4}$					$4 \cdot 10^{-5}$ / $4 \cdot 10^{-4}$
	K_h/K_v	1					1
	S_y	0.15					0.05 / 0.10
	S_s	$1 \cdot 10^{-3}$					$1 \cdot 10^{-3}$ / $5 \cdot 10^{-3}$
3 (II)							
Gyttja clay/clay gyttja (GC/CG)	QD	SAL (G)	–	GC/CG (G)	PSG (G/S)	GLC (G)	Till (S)
	K_h	$4 \cdot 10^{-4}$		$1 \cdot 10^{-7}$	$5 \cdot 10^{-3}$	$1 \cdot 10^{-8}$	$4 \cdot 10^{-5}$ / $4 \cdot 10^{-4}$
	K_h/K_v	1		1	1	1	1
	S_y	0.10		0.03	0.25	0.03	0.05 / 0.10
	S_s	$5 \cdot 10^{-3}$		$6 \cdot 10^{-3}$	0.025	$6 \cdot 10^{-3}$	$1 \cdot 10^{-3}$ / $5 \cdot 10^{-3}$
Gyttja	QD	SAL (G)	–	Gyttja (G)	PSG (G/S)	GC	Till (S)
	K_h	$4 \cdot 10^{-4}$		$1 \cdot 10^{-8}$	$5 \cdot 10^{-3}$	$1 \cdot 10^{-8}$	$4 \cdot 10^{-5}$ / $4 \cdot 10^{-4}$
	K_h/K_v	1		1	1	1	1
	S_y	0.10		0.03	0.25	0.03	0.05 / 0.10
	S_s	$5 \cdot 10^{-3}$		$6 \cdot 10^{-3}$	0.025	$6 \cdot 10^{-3}$	$1 \cdot 10^{-3}$ / $5 \cdot 10^{-3}$

Domain no. (type area no.)		Z1	Z2	Z3	Z4	Z5	Z6
QD on QD map							
Gyttja clay/ clay gyttja (GC/ CG) with a thin surface layer of peat	QD	SAL (peat) (G/S)	–	GC/CG (G)	PSG (G/S)	GLC (G)	Till (S)
	K_h	$3 \cdot 10^{-6}$		$1 \cdot 10^{-7}$	$5 \cdot 10^{-3}$	$1 \cdot 10^{-8}$	$4 \cdot 10^{-5}$ / $4 \cdot 10^{-4}$
	K_h/K_v	1		1	1	1	1
	S_y	0.24		0.03	0.25	0.03	0.05 / 0.10
	S_s	$5 \cdot 10^{-2}$		$6 \cdot 10^{-3}$	0.025	$6 \cdot 10^{-3}$	$1 \cdot 10^{-3}$ / $5 \cdot 10^{-3}$
Recent fluvial sediments	QD	SAL (G)	–	GC/CG (G)	PSG (G/S)	GLC (G)	Till (S)
	K_h	$4 \cdot 10^{-4}$		$1 \cdot 10^{-7}$	$5 \cdot 10^{-3}$	$1 \cdot 10^{-8}$	$4 \cdot 10^{-5}$ / $4 \cdot 10^{-4}$
	K_h/K_v	1		1	1	1	1
	S_y	0.10		0.03	0.25	0.03	0.05 / 0.10
	S_s	$5 \cdot 10^{-3}$		$6 \cdot 10^{-3}$	0.025	$6 \cdot 10^{-3}$	$1 \cdot 10^{-3}$ / $5 \cdot 10^{-3}$
Gyttja clay/ clay gyttja (GC/ CG) with a thin surface layer of sand-gravel	QD	SAL (sand-gravel) (G/S)	–	GC/CG(G)	PSG (G/S)	GLC (G)	Till (S)
	K_h	$5 \cdot 10^{-3}$		$1 \cdot 10^{-7}$	$5 \cdot 10^{-3}$	$1 \cdot 10^{-8}$	$4 \cdot 10^{-5}$ / $4 \cdot 10^{-4}$
	K_h/K_v	1		1	1	1	1
	S_y	0.25		0.03	0.25	0.03	0.05 / 0.10
	S_s	0.025		$6 \cdot 10^{-3}$	0.025	$6 \cdot 10^{-3}$	$1 \cdot 10^{-3}$ / $5 \cdot 10^{-3}$
4 (I)							
Peat, shallow (fen peat, bog peat, and unspecified peat)	QD	–	Peat (G/S)	–	–	–	Till (S)
	K_h		$3 \cdot 10^{-6}$				$4 \cdot 10^{-5}$ / $4 \cdot 10^{-4}$
	K_h/K_v		1				1
	S_y		0.24				0.05 / 0.10
	S_s		$5 \cdot 10^{-2}$				$1 \cdot 10^{-3}$ / $5 \cdot 10^{-3}$
5 (II)							
Peat, deep (fen peat, bog peat, and unspecified peat)	QD	–	Peat (G/S)	GC/CG (G)	PSG (G/S)	GLC (G)	Till (S)
	K_h		$3 \cdot 10^{-6}$	$1 \cdot 10^{-7}$	$5 \cdot 10^{-3}$	$1 \cdot 10^{-8}$	$4 \cdot 10^{-5}$ / $4 \cdot 10^{-4}$
	K_h/K_v		1	1	1	1	1
	S_y		0.24	0.03	0.25	0.03	0.05 / 0.10
	S_s		$5 \cdot 10^{-2}$	$6 \cdot 10^{-3}$	0.025	$6 \cdot 10^{-3}$	$1 \cdot 10^{-3}$ / $5 \cdot 10^{-3}$
6 (II)							
Glacial clay (GLC)	QD	SAL (G)	–	–	PSG (G/S)	GLC (G)	Till (S)
	K_h	$4 \cdot 10^{-4}$			$5 \cdot 10^{-3}$	$1 \cdot 10^{-8}$	$4 \cdot 10^{-5}$ / $4 \cdot 10^{-4}$
	K_h/K_v	1			1	1	1
	S_y	0.10			0.25	0.03	0.05 / 0.10
	S_s	$5 \cdot 10^{-3}$			0.025	$6 \cdot 10^{-3}$	$1 \cdot 10^{-3}$ / $5 \cdot 10^{-3}$
Glacial clay (GLC) with a thin surface layer of postglacial fine sand	QD	SAL (G)	–	–	PSG (G/S)	GLC	Till (S)
	K_h	$5 \cdot 10^{-4}$			$5 \cdot 10^{-3}$	$1 \cdot 10^{-8}$	$4 \cdot 10^{-5}$ / $4 \cdot 10^{-4}$
	K_h/K_v	1			1	1	1
	S_y	0.25			0.25	0.03	0.05 / 0.10
	S_s	0.025			0.025	$6 \cdot 10^{-3}$	$1 \cdot 10^{-3}$ / $5 \cdot 10^{-3}$
Glacial clay with a thin surface layer of post-glacial medium sand-gravel	QD	SAL (G)	–	–	PSG (G/S)	GLC (G)	Till (S)
	K_h	$5 \cdot 10^{-3}$			$5 \cdot 10^{-3}$	$1 \cdot 10^{-8}$	$4 \cdot 10^{-5}$ / $4 \cdot 10^{-4}$
	K_h/K_v	1			1	1	1
	S_y	0.25			0.25	0.03	0.05 / 0.10
	S_s	0.025			0.025	$6 \cdot 10^{-3}$	$1 \cdot 10^{-3}$ / $5 \cdot 10^{-3}$
Clay-silt (unspecified)	QD	SAL (G)	–	–	PSG (G/S)	GLC(G)	Till (S)
	K_h	$4 \cdot 10^{-4}$			$5 \cdot 10^{-3}$	$1 \cdot 10^{-8}$	$4 \cdot 10^{-5}$ / $4 \cdot 10^{-4}$
	K_h/K_v	1			1	1	1
	S_y	0.10			0.25	0.03	0.05 / 0.10
	S_s	$5 \cdot 10^{-3}$			0.025	$6 \cdot 10^{-3}$	$1 \cdot 10^{-3}$ / $5 \cdot 10^{-3}$

Domain no. (type area no.)		Z1	Z2	Z3	Z4	Z5	Z6
QD on QD map							
Postglacial fine sand (PFS)	QD	SAL (G)	–	–	PFS (G/S)	GLC (G)	Till (S)
	K_h	$4 \cdot 10^{-4}$			$5 \cdot 10^{-4}$	$1 \cdot 10^{-8}$	$4 \cdot 10^{-5}$ / $4 \cdot 10^{-4}$
	K_h/K_v	1			1	1	1
	S_y	0.10			0.25	0.03	0.05 / 0.10
	S_s	$5 \cdot 10^{-3}$			0.025	$6 \cdot 10^{-3}$	$1 \cdot 10^{-3}$ / $5 \cdot 10^{-3}$
Postglacial sand (PS)	QD	SAL (G)	–	–	PS (G/S)	GC (G)	Till (S)
	K_h	$4 \cdot 10^{-4}$			$1 \cdot 10^{-3}$	$1 \cdot 10^{-8}$	$4 \cdot 10^{-5}$ / $4 \cdot 10^{-4}$
	K_h/K_v	1			1	1	1
	S_y	0.10			0.25	0.03	0.05 / 0.10
	S_s	$5 \cdot 10^{-3}$			0.025	$6 \cdot 10^{-3}$	$1 \cdot 10^{-3}$ / $5 \cdot 10^{-3}$
Postglacial sand (PS) with a thin surface layer of peat	QD	SAL (G)	–	–	PS	GLC (G)	Till (S)
	K_h	$3 \cdot 10^{-6}$			$1 \cdot 10^{-3}$	$1 \cdot 10^{-8}$	$4 \cdot 10^{-5}$ / $4 \cdot 10^{-4}$
	K_h/K_v	1			1	1	1
	S_y	0.24			0.25	0.03	0.05 / 0.10
	S_s	$5 \cdot 10^{-2}$			0.025	$6 \cdot 10^{-3}$	$1 \cdot 10^{-3}$ / $5 \cdot 10^{-3}$
Postglacial medium sand-gravel	Q	SAL (G)	–	–	Postglacial medium sand-gravel (G/S)	GLC(G)	Till (S)
	K_h	$4 \cdot 10^{-4}$			$5 \cdot 10^{-3}$	$1 \cdot 10^{-8}$	$4 \cdot 10^{-5}$ / $4 \cdot 10^{-4}$
	K_h/K_v	1			1	1	1
	S_y	0.10			0.25	0.03	0.05 / 0.10
	S_s	$5 \cdot 10^{-3}$			0.025	$6 \cdot 10^{-3}$	$1 \cdot 10^{-3}$ / $5 \cdot 10^{-3}$
Postglacial gravel (PG) with a thin surface layer of peat	QD	SAL (G)	–	–	PG (G/S)	GLC (G)	Till (S)
	K_h	$3 \cdot 10^{-6}$			$1 \cdot 10^{-2}$	$1 \cdot 10^{-8}$	$4 \cdot 10^{-5}$ / $4 \cdot 10^{-4}$
	K_h/K_v	1			1	1	1
	S_y	0.24			0.25	0.03	0.05 / 0.10
	S_s	$5 \cdot 10^{-2}$			0.025	$6 \cdot 10^{-3}$	$1 \cdot 10^{-3}$ / $5 \cdot 10^{-3}$
Postglacial gravel (PG)	QD	SAL (G)	–	–	PG (G/S)	GLC (G)	Till (S)
	K_h	$4 \cdot 10^{-4}$			$1 \cdot 10^{-2}$	$1 \cdot 10^{-8}$	$4 \cdot 10^{-5}$ / $4 \cdot 10^{-4}$
	K_h/K_v	1			1	1	1
	S_y	0.10			0.25	0.03	0.05 / 0.10
	S_s	$5 \cdot 10^{-3}$			0.025	$6 \cdot 10^{-3}$	$1 \cdot 10^{-3}$ / $5 \cdot 10^{-3}$
Glacial clay (GLC) with thin surface layer of peat	QD	SAL (G)	–	–	PSG (G/S)	GLC (G)	Till (S)
	K_h	$3 \cdot 10^{-6}$			$5 \cdot 10^{-3}$	$1 \cdot 10^{-8}$	$4 \cdot 10^{-5}$ / $4 \cdot 10^{-4}$
	K_h/K_v	1			1	1	1
	S_y	0.24			0.25	0.03	0.05 / 0.10
	S_s	$5 \cdot 10^{-2}$			0.025	$6 \cdot 10^{-3}$	$1 \cdot 10^{-3}$ / $5 \cdot 10^{-3}$
Glacial silt	QD	SAL (G)	–		PSG (G/S)	GLC (G)	Till (S)
	K_h	$4 \cdot 10^{-4}$			$5 \cdot 10^{-3}$	$1 \cdot 10^{-8}$	$4 \cdot 10^{-5}$ / $4 \cdot 10^{-4}$
	K_h/K_v	1			1	1	1
	S_y	0.10			0.25	0.03	0.05 / 0.10
	S_s	$5 \cdot 10^{-3}$			0.025	$6 \cdot 10^{-3}$	$1 \cdot 10^{-3}$ / $5 \cdot 10^{-3}$
7 (III)							
Glaciofluvial sediments (GS), shallow	QD	SAL (G)	–	–	GS (G/S)	–	–
	K_h	$4 \cdot 10^{-4}$			$5 \cdot 10^{-3}$		
	K_h/K_v	1			1		
	S_y	0.10			0.25		
	S_s	$5 \cdot 10^{-3}$			0.025		
8 (III)							

Domain no. (type area no.)		Z1	Z2	Z3	Z4	Z5	Z6
QD on QD map							
Glaciofluvial sediments (GS), deep (Tuna esker)	QD	SAL (G)	–	–	GS (G/S)	–	–
	K_h	$4 \cdot 10^{-4}$			$5 \cdot 10^{-3}$		
	K_h/K_v	1			1		
	S_y	0.10			0.25		
	S_s	$5 \cdot 10^{-3}$			0.025		
9 (no type area)	QD						
Artificial fill (AF)	QD	SAL (G)	–	–	AF (G)	–	–
	K_h	$4 \cdot 10^{-4}$			$4 \cdot 10^{-5}$		
	K_h/K_v	1			1		
	S_y	0.10			0.05		
	S_s	$5 \cdot 10^{-3}$			$1 \cdot 10^{-3}$		

Appendix 6

A6 Properties for deformation zones after and before calibration

A6.1 Properties of deformation zones after calibration for full model depth, depth zones

The definition of hydraulic properties used in the central **calibrated case** for the each deformation zone is specified in Table A6-1. The depth variation was **implemented in CONNECTFLOW** as a step-wise change.

Table A6-1. Depth variation of hydraulic conductivity K (m/s) and the used thickness, b_h (m), in HCD for elevation intervals used for groundwater flow and solute transport in the central calibration case. All elevations are in m RHB 70.

Deformation zone	b_h (m)	Hydraulic conductivity K (m/s) for depth interval (m RHB 70)									
		0 to –150	–150 to –400	–400 to –650	–650 to –800	–800 to –1,000	–1,000 to –1,200	–1,200 to –1,400	–1,400 to –1,600	–1,600 to –1,800	–1,800 to –2,200
hlx28_dz1	10	5.00E-07	5.47E-08	1.55E-08	1.88E-09	7.80E-10	2.84E-10	1.04E-10	3.78E-11	1.38E-11	1.00E-11
klx03_dz1b	10	5.00E-07	5.47E-08	1.55E-08	1.88E-09	7.80E-10	2.84E-10	1.04E-10	3.78E-11	1.38E-11	1.00E-11
klx03_dz1c	10	5.00E-07	5.47E-08	1.55E-08	1.88E-09	7.80E-10	2.84E-10	1.04E-10	3.78E-11	1.38E-11	1.00E-11
klx04_dz6b	14	3.57E-07	3.91E-08	1.11E-08	1.35E-09	5.57E-10	2.03E-10	7.41E-11	2.70E-11	1.00E-11	1.00E-11
klx04_dz6c	30	1.67E-07	1.82E-08	5.17E-09	6.28E-10	2.60E-10	9.48E-11	3.46E-11	1.26E-11	1.00E-11	1.00E-11
klx07_dz10	10	5.00E-07	5.47E-08	1.55E-08	1.88E-09	7.80E-10	2.84E-10	1.04E-10	3.78E-11	1.38E-11	1.00E-11
klx07_dz11	30	1.67E-07	1.82E-08	5.17E-09	6.28E-10	2.60E-10	9.48E-11	3.46E-11	1.26E-11	1.00E-11	1.00E-11
klx07_dz12	47	1.06E-07	1.16E-08	3.30E-09	4.01E-10	1.66E-10	6.05E-11	2.21E-11	1.00E-11	1.00E-11	1.00E-11
klx07_dz13	10	5.00E-07	5.47E-08	1.55E-08	1.88E-09	7.80E-10	2.84E-10	1.04E-10	3.78E-11	1.38E-11	1.00E-11
klx07_dz7	30	1.67E-07	1.82E-08	5.17E-09	6.28E-10	2.60E-10	9.48E-11	3.46E-11	1.26E-11	1.00E-11	1.00E-11
klx07_dz9	10	5.00E-07	5.47E-08	1.55E-08	1.88E-09	7.80E-10	2.84E-10	1.04E-10	3.78E-11	1.38E-11	1.00E-11
klx08_dz1	27	1.85E-07	2.03E-08	5.74E-09	6.98E-10	2.89E-10	1.05E-10	3.84E-11	1.40E-11	1.00E-11	1.00E-11
klx08_dz10	11	4.54E-07	4.97E-08	1.41E-08	1.71E-09	7.09E-10	2.59E-10	9.43E-11	3.44E-11	1.25E-11	1.00E-11
klx08_dz6	10	5.00E-07	5.47E-08	1.55E-08	1.88E-09	7.80E-10	2.84E-10	1.04E-10	3.78E-11	1.38E-11	1.00E-11
klx09_dz10	25	2.00E-07	2.19E-08	6.20E-09	7.54E-10	3.12E-10	1.14E-10	4.15E-11	1.51E-11	1.00E-11	1.00E-11
klx09_dz14	9	5.97E-07	6.53E-08	1.85E-08	2.25E-09	9.31E-10	3.40E-10	1.24E-10	4.52E-11	1.65E-11	1.00E-11
klx09_dz9	6	5.45E-06	5.96E-07	1.69E-07	2.05E-08	8.50E-09	3.10E-09	1.13E-09	4.13E-10	1.50E-10	5.49E-11
klx09e_dz2	22	2.27E-07	2.49E-08	7.05E-09	8.57E-10	3.54E-10	1.29E-10	4.72E-11	1.72E-11	1.00E-11	1.00E-11

Deformation zone	b_h (m)	Hydraulic conductivity K (m/s) for depth interval (m RHB 70)									
		0 to –150	–150 to –400	–400 to –650	–650 to –800	–800 to –1,000	–1,000 to –1,200	–1,200 to –1,400	–1,400 to –1,600	–1,600 to –1,800	–1,800 to –2,200
klx09f_dz1	14	3.57E-07	3.91E-08	1.11E-08	1.35E-09	5.57E-10	2.03E-10	7.41E-11	2.70E-11	1.00E-11	1.00E-11
klx10c_dz3	10	5.00E-07	5.47E-08	1.55E-08	1.88E-09	7.80E-10	2.84E-10	1.04E-10	3.78E-11	1.38E-11	1.00E-11
klx10c_dz7	10	5.00E-07	5.47E-08	1.55E-08	1.88E-09	7.80E-10	2.84E-10	1.04E-10	3.78E-11	1.38E-11	1.00E-11
klx11_dz11	20	2.50E-07	2.73E-08	7.75E-09	9.42E-10	3.90E-10	1.42E-10	5.19E-11	1.89E-11	1.00E-11	1.00E-11
klx16_dz6	1	5.40E-05	5.91E-06	1.68E-06	2.04E-07	8.43E-08	3.07E-08	1.12E-08	4.09E-09	1.49E-09	5.44E-10
klx18_dz9	10	5.00E-07	5.47E-08	1.55E-08	1.88E-09	7.80E-10	2.84E-10	1.04E-10	3.78E-11	1.38E-11	1.00E-11
klx19_dz2	4	1.42E-05	1.55E-06	4.40E-07	5.35E-08	2.21E-08	8.08E-09	2.95E-09	1.07E-09	3.92E-10	1.43E-10
klx19_dz5-8_dolerite	45	9.99E-07	1.09E-07	3.10E-08	3.77E-09	1.56E-09	5.69E-10	2.08E-10	7.57E-11	2.76E-11	1.01E-11
klx21b_dz10-12	10	5.00E-07	5.47E-08	1.55E-08	1.88E-09	7.80E-10	2.84E-10	1.04E-10	3.78E-11	1.38E-11	1.00E-11
klx28_dz1	13	3.84E-07	4.21E-08	1.19E-08	1.45E-09	6.00E-10	2.19E-10	7.98E-11	2.91E-11	1.06E-11	1.00E-11

Deformation zone (ZSM)	b_h (m)	Hydraulic conductivity K (m/s) for depth interval (m RHB 70)									
		0 to –150	–150 to –400	–400 to –650	–650 to –800	–800 to –1,000	–1,000 to –1,200	–1,200 to –1,400	–1,400 to –1,600	–1,600 to –1,800	–1,800 to –2,200
zsmew002a	50	1.29E-06	1.61E-07	5.39E-08	7.49E-09	3.48E-09	1.45E-09	6.05E-10	2.52E-10	1.05E-10	4.39E-11
zsmew007a	50	6.95E-05	5.15E-06	1.49E-07	5.50E-09	2.31E-09	8.54E-10	3.16E-10	1.17E-10	4.33E-11	1.60E-11
zsmew007c	50	1.72E-07	1.97E-08	5.90E-09	7.51E-10	3.24E-10	1.24E-10	4.72E-11	1.80E-11	1.00E-11	1.00E-11
ZSMEW009A	12	7.15E-07	8.19E-08	2.46E-08	3.13E-09	1.35E-09	5.15E-10	1.97E-10	7.51E-11	2.87E-11	1.10E-11
zsmew013a	45	1.43E-06	1.79E-07	5.99E-08	8.32E-09	3.87E-09	1.61E-09	6.73E-10	2.80E-10	1.17E-10	4.87E-11
zsmew014a	10	5.00E-07	5.47E-08	1.55E-08	1.88E-09	7.80E-10	2.84E-10	1.04E-10	3.78E-11	1.38E-11	1.00E-11
ZSMEW020A	50	1.29E-06	1.61E-07	5.39E-08	7.49E-09	3.48E-09	1.45E-09	6.05E-10	2.52E-10	1.05E-10	4.39E-11
ZSMEW038A	10	6.43E-06	8.05E-07	2.70E-07	3.75E-08	1.74E-08	7.26E-09	3.03E-09	1.26E-09	5.26E-10	2.19E-10
ZSMEW076A	31	2.06E-06	2.57E-07	8.62E-08	1.20E-08	5.57E-09	2.32E-09	9.68E-10	4.03E-10	1.68E-10	7.01E-11
ZSMEW114A	25	2.59E-06	3.25E-07	1.09E-07	1.51E-08	7.02E-09	2.93E-09	1.22E-09	5.09E-10	2.12E-10	8.84E-11
zsmew120a	50	1.72E-07	1.97E-08	5.90E-09	7.51E-10	3.24E-10	1.24E-10	4.72E-11	1.80E-11	1.00E-11	1.00E-11
ZSMEW129A	20	3.28E-06	4.10E-07	1.37E-07	1.91E-08	8.87E-09	3.70E-09	1.54E-09	6.42E-10	2.68E-10	1.12E-10
ZSMEW190A	17	5.18E-07	5.93E-08	1.78E-08	2.27E-09	9.76E-10	3.73E-10	1.42E-10	5.44E-11	2.08E-11	1.00E-11
ZSMEW200A	17	4.91E-07	5.63E-08	1.69E-08	2.15E-09	9.27E-10	3.54E-10	1.35E-10	5.16E-11	1.97E-11	1.00E-11
ZSMEW230A	18	4.75E-07	5.44E-08	1.63E-08	2.08E-09	8.96E-10	3.42E-10	1.31E-10	4.99E-11	1.91E-11	1.00E-11
ZSMEW240A	50	1.29E-06	1.61E-07	5.39E-08	7.49E-09	3.48E-09	1.45E-09	6.05E-10	2.52E-10	1.05E-10	4.39E-11
ZSMEW305A	19	4.47E-07	5.12E-08	1.54E-08	1.96E-09	8.43E-10	3.22E-10	1.23E-10	4.70E-11	1.79E-11	1.00E-11
zsmew316a	30	2.14E-06	2.68E-07	8.98E-08	1.25E-08	5.81E-09	2.42E-09	1.01E-09	4.21E-10	1.75E-10	7.31E-11
zsmew900a	25	2.00E-07	2.19E-08	6.20E-09	7.54E-10	3.12E-10	1.14E-10	4.15E-11	1.51E-11	1.00E-11	1.00E-11
zsmew900b	25	2.00E-07	2.19E-08	6.20E-09	7.54E-10	3.12E-10	1.14E-10	4.15E-11	1.51E-11	1.00E-11	1.00E-11
ZSMEW904A	50	1.29E-06	1.61E-07	5.39E-08	7.49E-09	3.48E-09	1.45E-09	6.05E-10	2.52E-10	1.05E-10	4.39E-11
ZSMEW905A	21	3.04E-06	3.80E-07	1.27E-07	1.77E-08	8.23E-09	3.43E-09	1.43E-09	5.96E-10	2.48E-10	1.04E-10
ZSMEW906A	50	1.29E-06	1.61E-07	5.39E-08	7.49E-09	3.48E-09	1.45E-09	6.05E-10	2.52E-10	1.05E-10	4.39E-11
ZSMEW907A	50	1.29E-06	1.61E-07	5.39E-08	7.49E-09	3.48E-09	1.45E-09	6.05E-10	2.52E-10	1.05E-10	4.39E-11
ZSMEW936A	11	7.76E-07	8.89E-08	2.67E-08	3.40E-09	1.46E-09	5.59E-10	2.14E-10	8.16E-11	3.12E-11	1.19E-11
zsmew946a	10	2.77E-06	9.81E-08	6.79E-09	2.68E-10	4.13E-11	1.00E-11	1.00E-11	1.00E-11	1.00E-11	1.00E-11

Deformation zone (ZSM)	b_h (m)	Hydraulic conductivity K (m/s) for depth interval (m RHB 70)									
		0 to –150	–150 to –400	–400 to –650	–650 to –800	–800 to –1,000	–1,000 to –1,200	–1,200 to –1,400	–1,400 to –1,600	–1,600 to –1,800	–1,800 to –2,200
zsmne004a	50	8.97E-07	8.32E-08	1.92E-08	1.97E-09	7.06E-10	2.18E-10	6.75E-11	2.08E-11	1.00E-11	1.00E-11
zsmne005a	50	8.97E-07	8.32E-08	1.92E-08	1.97E-09	7.06E-10	2.18E-10	6.75E-11	2.08E-11	1.00E-11	1.00E-11
zsmne006a	50	1.13E-05	8.08E-07	1.35E-07	1.08E-08	3.09E-09	7.41E-10	1.77E-10	4.25E-11	1.02E-11	1.00E-11
ZSMNE008A	39	1.15E-06	1.06E-07	2.45E-08	2.52E-09	9.03E-10	2.79E-10	8.62E-11	2.67E-11	1.00E-11	1.00E-11
ZSMNE010A	34	1.31E-06	1.21E-07	2.80E-08	2.88E-09	1.03E-09	3.19E-10	9.86E-11	3.05E-11	1.00E-11	1.00E-11
zsmne011a	50	8.97E-07	8.32E-08	1.92E-08	1.97E-09	7.06E-10	2.18E-10	6.75E-11	2.08E-11	1.00E-11	1.00E-11
zsmne012a	50	2.90E-06	3.15E-07	8.82E-08	1.06E-08	4.36E-09	1.58E-09	5.71E-10	2.06E-10	7.46E-11	2.70E-11
zsmne015a	10	5.00E-07	5.47E-08	1.55E-08	1.88E-09	7.80E-10	2.84E-10	1.04E-10	3.78E-11	1.38E-11	1.00E-11
zsmne018a	50	9.99E-08	1.09E-08	3.10E-09	3.77E-10	1.56E-10	5.69E-11	2.08E-11	1.00E-11	1.00E-11	1.00E-11
zsmne019a	20	2.24E-06	2.08E-07	4.79E-08	4.93E-09	1.77E-09	5.46E-10	1.69E-10	5.21E-11	1.61E-11	1.00E-11
zsmne021a	40	1.12E-06	1.04E-07	2.40E-08	2.47E-09	8.83E-10	2.73E-10	8.43E-11	2.61E-11	1.00E-11	1.00E-11
zsmne022a	28	1.61E-06	1.49E-07	3.43E-08	3.54E-09	1.27E-09	3.91E-10	1.21E-10	3.73E-11	1.15E-11	1.00E-11
ZSMNE024A	50	3.37E-05	3.67E-07	5.83E-09	7.07E-11	1.00E-11	1.00E-11	1.00E-11	1.00E-11	1.00E-11	1.00E-11
ZSMNE024B	16	1.06E-04	1.15E-06	1.83E-08	2.22E-10	1.22E-11	1.00E-11	1.00E-11	1.00E-11	1.00E-11	1.00E-11
ZSMNE031A	15	2.99E-06	2.77E-07	6.39E-08	6.58E-09	2.35E-09	7.28E-10	2.25E-10	6.95E-11	2.15E-11	1.00E-11
ZSMNE031B	19	2.64E-07	2.89E-08	8.20E-09	9.97E-10	4.12E-10	1.50E-10	5.49E-11	2.00E-11	1.00E-11	1.00E-11
ZSMNE032A	26	1.70E-06	1.58E-07	3.64E-08	3.74E-09	1.34E-09	4.14E-10	1.28E-10	3.96E-11	1.22E-11	1.00E-11
ZSMNE033A	30	1.50E-06	1.40E-07	3.21E-08	3.31E-09	1.18E-09	3.66E-10	1.13E-10	3.50E-11	1.08E-11	1.00E-11
ZSMNE034A	29	1.55E-06	1.44E-07	3.31E-08	3.41E-09	1.22E-09	3.77E-10	1.16E-10	3.60E-11	1.11E-11	1.00E-11
ZSMNE036A	23	1.94E-06	1.80E-07	4.15E-08	4.27E-09	1.53E-09	4.73E-10	1.46E-10	4.51E-11	1.39E-11	1.00E-11
zsmne040a	20	2.50E-07	2.73E-08	7.75E-09	9.42E-10	3.90E-10	1.42E-10	5.19E-11	1.89E-11	1.00E-11	1.00E-11
ZSMNE062A	17	2.97E-07	3.25E-08	9.21E-09	1.12E-09	4.63E-10	1.69E-10	6.16E-11	2.25E-11	1.00E-11	1.00E-11
zsmne063a	10	5.00E-07	5.47E-08	1.55E-08	1.88E-09	7.80E-10	2.84E-10	1.04E-10	3.78E-11	1.38E-11	1.00E-11
zsmne065a	10	5.00E-07	5.47E-08	1.55E-08	1.88E-09	7.80E-10	2.84E-10	1.04E-10	3.78E-11	1.38E-11	1.00E-11
ZSMNE073A	36	1.24E-06	1.15E-07	2.65E-08	2.73E-09	9.77E-10	3.02E-10	9.33E-11	2.88E-11	1.00E-11	1.00E-11
zsmne079a	10	4.48E-06	4.16E-07	9.58E-08	9.87E-09	3.53E-09	1.09E-09	3.37E-10	1.04E-10	3.22E-11	1.00E-11
ZSMNE081A	21	2.18E-06	2.02E-07	4.66E-08	4.80E-09	1.72E-09	5.31E-10	1.64E-10	5.07E-11	1.57E-11	1.00E-11
ZSMNE095A	23	1.96E-06	1.82E-07	4.19E-08	4.32E-09	1.55E-09	4.78E-10	1.48E-10	4.56E-11	1.41E-11	1.00E-11
ZSMNE096A	17	2.90E-07	3.18E-08	9.01E-09	1.10E-09	4.53E-10	1.65E-10	6.03E-11	2.20E-11	1.00E-11	1.00E-11

Deformation zone (ZSM)	b_h (m)	Hydraulic conductivity K (m/s) for depth interval (m RHB 70)									
		0 to –150	–150 to –400	–400 to –650	–650 to –800	–800 to –1,000	–1,000 to –1,200	–1,200 to –1,400	–1,400 to –1,600	–1,600 to –1,800	–1,800 to –2,200
zsmne107a	35	1.28E-05	1.19E-06	2.74E-08	2.82E-09	1.01E-09	3.12E-10	9.64E-11	2.98E-11	1.00E-11	1.00E-11
zsmne108a	10	5.00E-07	5.47E-08	1.55E-08	1.88E-09	7.80E-10	2.84E-10	1.04E-10	3.78E-11	1.38E-11	1.00E-11
ZSMNE132A	28	1.61E-06	1.49E-07	3.44E-08	3.54E-09	1.27E-09	3.92E-10	1.21E-10	3.74E-11	1.16E-11	1.00E-11
ZSMNE133A	24	1.84E-06	1.71E-07	3.93E-08	4.05E-09	1.45E-09	4.48E-10	1.38E-10	4.28E-11	1.32E-11	1.00E-11
ZSMNE185A	24	1.89E-06	1.75E-07	4.03E-08	4.15E-09	1.48E-09	4.59E-10	1.42E-10	4.38E-11	1.35E-11	1.00E-11
ZSMNE210A	21	2.11E-06	1.95E-07	4.50E-08	4.63E-09	1.66E-09	5.12E-10	1.58E-10	4.89E-11	1.51E-11	1.00E-11
ZSMNE210B	28	1.62E-06	1.50E-07	3.46E-08	3.56E-09	1.28E-09	3.94E-10	1.22E-10	3.76E-11	1.16E-11	1.00E-11
ZSMNE218A	50	8.97E-07	8.32E-08	1.92E-08	1.97E-09	7.06E-10	2.18E-10	6.75E-11	2.08E-11	1.00E-11	1.00E-11
ZSMNE229A	20	2.24E-06	2.07E-07	4.78E-08	4.92E-09	1.76E-09	5.44E-10	1.68E-10	5.20E-11	1.61E-11	1.00E-11
ZSMNE257A	27	1.67E-06	1.55E-07	3.57E-08	3.67E-09	1.31E-09	4.06E-10	1.26E-10	3.88E-11	1.20E-11	1.00E-11
ZSMNE258A	26	1.71E-06	1.59E-07	3.66E-08	3.77E-09	1.35E-09	4.17E-10	1.29E-10	3.98E-11	1.23E-11	1.00E-11
ZSMNE259A	28	1.59E-06	1.47E-07	3.40E-08	3.50E-09	1.25E-09	3.87E-10	1.20E-10	3.70E-11	1.14E-11	1.00E-11
ZSMNE267A	23	1.99E-06	1.84E-07	4.24E-08	4.37E-09	1.56E-09	4.84E-10	1.49E-10	4.62E-11	1.43E-11	1.00E-11
ZSMNE286A	27	1.67E-06	1.55E-07	3.57E-08	3.68E-09	1.32E-09	4.07E-10	1.26E-10	3.89E-11	1.20E-11	1.00E-11
ZSMNE289A	21	2.11E-06	1.95E-07	4.50E-08	4.64E-09	1.66E-09	5.13E-10	1.58E-10	4.90E-11	1.51E-11	1.00E-11
ZSMNE295A	31	1.43E-06	1.33E-07	3.06E-08	3.15E-09	1.13E-09	3.49E-10	1.08E-10	3.33E-11	1.03E-11	1.00E-11
ZSMNE302A	24	1.84E-06	1.70E-07	3.92E-08	4.04E-09	1.45E-09	4.47E-10	1.38E-10	4.27E-11	1.32E-11	1.00E-11
ZSMNE307A	18	2.79E-07	3.06E-08	8.66E-09	1.05E-09	4.36E-10	1.59E-10	5.80E-11	2.12E-11	1.00E-11	1.00E-11
ZSMNE308A	24	1.85E-06	1.72E-07	3.95E-08	4.07E-09	1.46E-09	4.50E-10	1.39E-10	4.30E-11	1.33E-11	1.00E-11
ZSMNE313A	50	8.97E-07	8.32E-08	1.92E-08	1.97E-09	7.06E-10	2.18E-10	6.75E-11	2.08E-11	1.00E-11	1.00E-11
ZSMNE901A	25	1.78E-06	1.65E-07	3.80E-08	3.92E-09	1.40E-09	4.33E-10	1.34E-10	4.14E-11	1.28E-11	1.00E-11
ZSMNE903A	25	1.81E-06	1.68E-07	3.88E-08	3.99E-09	1.43E-09	4.42E-10	1.36E-10	4.22E-11	1.30E-11	1.00E-11
ZSMNE909A	17	2.90E-07	3.17E-08	9.00E-09	1.09E-09	4.53E-10	1.65E-10	6.02E-11	2.20E-11	1.00E-11	1.00E-11
ZSMNE910A	22	2.05E-06	1.90E-07	4.39E-08	4.52E-09	1.62E-09	5.00E-10	1.54E-10	4.77E-11	1.47E-11	1.00E-11
ZSMNE911A	50	8.97E-07	8.32E-08	1.92E-08	1.97E-09	7.06E-10	2.18E-10	6.75E-11	2.08E-11	1.00E-11	1.00E-11
ZSMNE912A	31	1.46E-06	1.35E-07	3.11E-08	3.20E-09	1.15E-09	3.54E-10	1.09E-10	3.38E-11	1.05E-11	1.00E-11
ZSMNE913A	50	8.97E-07	8.32E-08	1.92E-08	1.97E-09	7.06E-10	2.18E-10	6.75E-11	2.08E-11	1.00E-11	1.00E-11
ZSMNE914A	50	8.97E-07	8.32E-08	1.92E-08	1.97E-09	7.06E-10	2.18E-10	6.75E-11	2.08E-11	1.00E-11	1.00E-11
ZSMNE915A	19	2.57E-07	2.81E-08	7.96E-09	9.68E-10	4.00E-10	1.46E-10	5.33E-11	1.94E-11	1.00E-11	1.00E-11

Deformation zone (ZSM)	b_h (m)	Hydraulic conductivity K (m/s) for depth interval (m RHB 70)									
		0 to –150	–150 to –400	–400 to –650	–650 to –800	–800 to –1,000	–1,000 to –1,200	–1,200 to –1,400	–1,400 to –1,600	–1,600 to –1,800	–1,800 to –2,200
zsmne930a	5	8.97E-06	8.32E-07	1.92E-07	1.97E-08	7.06E-09	2.18E-09	6.75E-10	2.08E-10	6.44E-11	1.99E-11
ZSMNE940A	16	3.07E-07	3.36E-08	9.53E-09	1.16E-09	4.79E-10	1.75E-10	6.38E-11	2.33E-11	1.00E-11	1.00E-11
ZSMNE941A	22	2.06E-06	1.91E-07	4.41E-08	4.54E-09	1.62E-09	5.02E-10	1.55E-10	4.79E-11	1.48E-11	1.00E-11
zsmne942a	15	1.21E-06	1.20E-07	3.02E-08	3.32E-09	1.26E-09	4.16E-10	1.38E-10	4.54E-11	1.50E-11	1.00E-11
zsmne944a	10	5.00E-07	5.47E-08	5.17E-09	1.88E-09	7.80E-10	2.84E-10	1.04E-10	3.78E-11	1.38E-11	1.00E-11
zsmns001a	50	2.76E-06	2.73E-07	6.85E-08	7.54E-09	2.86E-09	9.45E-10	3.12E-10	1.03E-10	3.41E-11	1.13E-11
zsmns001b	50	2.76E-06	2.73E-07	6.85E-08	7.54E-09	2.86E-09	9.45E-10	3.12E-10	1.03E-10	3.41E-11	1.13E-11
zsmns001c	50	8.27E-06	9.11E-07	6.85E-08	7.54E-09	2.86E-09	9.45E-10	3.12E-10	1.03E-10	3.41E-11	1.13E-11
zsmns001d	50	2.76E-06	2.73E-07	6.85E-08	7.54E-09	2.86E-09	9.45E-10	3.12E-10	1.03E-10	3.41E-11	1.13E-11
zsmns001e	50	2.76E-06	2.73E-07	6.85E-08	7.54E-09	2.86E-09	9.45E-10	3.12E-10	1.03E-10	3.41E-11	1.13E-11
ZSMNS009A	25	1.79E-06	1.66E-07	3.83E-08	3.95E-09	1.41E-09	4.37E-10	1.35E-10	4.17E-11	1.29E-11	1.00E-11
ZSMNS017A	21	2.16E-06	2.00E-07	4.61E-08	4.75E-09	1.70E-09	5.26E-10	1.62E-10	5.02E-11	1.55E-11	1.00E-11
ZSMNS017B	20	1.90E-05	1.88E-06	4.71E-07	5.19E-08	1.97E-08	6.51E-09	2.15E-09	7.10E-10	2.35E-10	7.75E-11
zsmns046a	20	2.24E-06	2.08E-07	4.79E-08	4.93E-09	1.77E-09	5.46E-10	1.69E-10	5.21E-11	1.61E-11	1.00E-11
zsmns057a	20	2.24E-06	2.08E-07	4.79E-08	4.93E-09	1.77E-09	5.46E-10	1.69E-10	5.21E-11	1.61E-11	1.00E-11
zsmns059a	50	2.94E-06	2.91E-07	7.30E-08	8.04E-09	3.05E-09	1.01E-09	3.33E-10	1.10E-10	3.63E-11	1.20E-11
ZSMNS064A	50	8.97E-07	8.32E-08	1.92E-08	1.97E-09	7.06E-10	2.18E-10	6.75E-11	2.08E-11	1.00E-11	1.00E-11
ZSMNS071A	18	2.71E-07	2.97E-08	8.41E-09	1.02E-09	4.23E-10	1.54E-10	5.63E-11	2.05E-11	1.00E-11	1.00E-11
ZSMNS084A	32	1.40E-06	1.30E-07	2.99E-08	3.08E-09	1.10E-09	3.41E-10	1.05E-10	3.26E-11	1.01E-11	1.00E-11
ZSMNS085A	37	1.22E-06	1.13E-07	2.60E-08	2.67E-09	9.57E-10	2.96E-10	9.14E-11	2.82E-11	1.00E-11	1.00E-11
ZSMNS117A	17	2.98E-07	3.26E-08	9.25E-09	1.12E-09	4.65E-10	1.70E-10	6.19E-11	2.26E-11	1.00E-11	1.00E-11
zsmns141a	20	2.24E-06	2.08E-07	4.79E-08	4.93E-09	1.77E-09	5.46E-10	1.69E-10	5.21E-11	1.61E-11	1.00E-11
ZSMNS165A	18	2.81E-07	3.07E-08	8.70E-09	1.06E-09	4.38E-10	1.60E-10	5.83E-11	2.12E-11	1.00E-11	1.00E-11
ZSMNS182A	30	1.50E-06	1.39E-07	3.20E-08	3.29E-09	1.18E-09	3.64E-10	1.13E-10	3.48E-11	1.07E-11	1.00E-11
ZSMNS182B	30	1.48E-06	1.38E-07	3.17E-08	3.27E-09	1.17E-09	3.61E-10	1.12E-10	3.45E-11	1.07E-11	1.00E-11

Deformation zone (ZSM)	b_h (m)	Hydraulic conductivity K (m/s) for depth interval (m RHB 70)									
		0 to –150	–150 to –400	–400 to –650	–650 to –800	–800 to –1,000	–1,000 to –1,200	–1,200 to –1,400	–1,400 to –1,600	–1,600 to –1,800	–1,800 to –2,200
ZSMNS215A	16	3.08E-07	3.37E-08	9.56E-09	1.16E-09	4.81E-10	1.75E-10	6.40E-11	2.33E-11	1.00E-11	1.00E-11
ZSMNS221A	22	2.03E-06	1.88E-07	4.34E-08	4.47E-09	1.60E-09	4.94E-10	1.53E-10	4.72E-11	1.46E-11	1.00E-11
ZSMNS287A	34	1.32E-06	1.22E-07	2.82E-08	2.91E-09	1.04E-09	3.21E-10	9.93E-11	3.07E-11	1.00E-11	1.00E-11
ZSMNS291A	19	2.64E-07	2.89E-08	8.20E-09	9.97E-10	4.12E-10	1.50E-10	5.49E-11	2.00E-11	1.00E-11	1.00E-11
ZSMNS301A	19	2.67E-07	2.92E-08	8.28E-09	1.01E-09	4.16E-10	1.52E-10	5.54E-11	2.02E-11	1.00E-11	1.00E-11
ZSMNS916A	44	1.03E-06	9.56E-08	2.20E-08	2.27E-09	8.12E-10	2.51E-10	7.75E-11	2.40E-11	1.00E-11	1.00E-11
ZSMNS917A	50	8.97E-07	8.32E-08	1.92E-08	1.97E-09	7.06E-10	2.18E-10	6.75E-11	2.08E-11	1.00E-11	1.00E-11
ZSMNS918A	29	1.56E-06	1.45E-07	3.34E-08	3.44E-09	1.23E-09	3.81E-10	1.18E-10	3.63E-11	1.12E-11	1.00E-11
ZSMNS919A	50	8.97E-07	8.32E-08	1.92E-08	1.97E-09	7.06E-10	2.18E-10	6.75E-11	2.08E-11	1.00E-11	1.00E-11
ZSMNS920A	31	1.46E-06	1.36E-07	3.12E-08	3.22E-09	1.15E-09	3.56E-10	1.10E-10	3.40E-11	1.05E-11	1.00E-11
zsmns945a	10	4.48E-06	4.16E-07	9.58E-08	9.87E-09	3.53E-09	1.09E-09	3.37E-10	1.04E-10	3.22E-11	1.00E-11
zsmns947a	20	2.50E-07	2.73E-08	7.75E-09	9.42E-10	3.90E-10	1.42E-10	5.19E-11	1.89E-11	1.00E-11	1.00E-11
ZSMNW025A	10	5.00E-07	5.47E-08	1.55E-08	1.88E-09	7.80E-10	2.84E-10	1.04E-10	3.78E-11	1.38E-11	1.00E-11
ZSMNW027A	34	1.31E-06	1.21E-07	2.80E-08	2.88E-09	1.03E-09	3.18E-10	9.84E-11	3.04E-11	1.00E-11	1.00E-11
zsmnw042a-east	50	8.97E-07	8.32E-08	1.92E-08	1.97E-09	7.06E-10	2.18E-10	6.75E-11	2.08E-11	1.00E-11	1.00E-11
zsmnw042a-west	50	8.97E-07	8.32E-08	1.92E-08	1.97E-09	7.06E-10	2.18E-10	6.75E-11	2.08E-11	1.00E-11	1.00E-11
zsmnw047a	25	2.00E-07	2.19E-08	6.20E-09	7.54E-10	3.12E-10	1.14E-10	4.15E-11	1.51E-11	1.00E-11	1.00E-11
zsmnw052a	15	3.33E-07	3.65E-08	1.03E-08	1.26E-09	5.20E-10	1.90E-10	6.92E-11	2.52E-11	1.00E-11	1.00E-11
ZSMNW060A	32	1.39E-06	1.29E-07	2.96E-08	3.05E-09	1.09E-09	3.38E-10	1.04E-10	3.22E-11	1.00E-11	1.00E-11
ZSMNW066A	50	8.97E-07	8.32E-08	1.92E-08	1.97E-09	7.06E-10	2.18E-10	6.75E-11	2.08E-11	1.00E-11	1.00E-11
ZSMNW067A	50	8.97E-07	8.32E-08	1.92E-08	1.97E-09	7.06E-10	2.18E-10	6.75E-11	2.08E-11	1.00E-11	1.00E-11
ZSMNW068A	18	2.79E-07	3.05E-08	8.64E-09	1.05E-09	4.35E-10	1.59E-10	5.79E-11	2.11E-11	1.00E-11	1.00E-11
ZSMNW068B	22	2.04E-06	1.89E-07	4.36E-08	4.49E-09	1.61E-09	4.96E-10	1.53E-10	4.74E-11	1.46E-11	1.00E-11
ZSMNW068C	4	1.14E-06	1.25E-07	3.53E-08	4.29E-09	1.78E-09	6.48E-10	2.36E-10	8.62E-11	3.15E-11	1.15E-11
ZSMNW074A	33	1.35E-06	1.26E-07	2.89E-08	2.98E-09	1.07E-09	3.30E-10	1.02E-10	3.15E-11	1.00E-11	1.00E-11
ZSMNW075A	38	1.17E-06	1.08E-07	2.50E-08	2.57E-09	9.21E-10	2.85E-10	8.79E-11	2.72E-11	1.00E-11	1.00E-11
ZSMNW083A	16	3.03E-07	3.32E-08	9.40E-09	1.14E-09	4.73E-10	1.73E-10	6.29E-11	2.30E-11	1.00E-11	1.00E-11

Deformation zone (ZSM)	b_h (m)	Hydraulic conductivity K (m/s) for depth interval (m RHB 70)									
		0 to –150	–150 to –400	–400 to –650	–650 to –800	–800 to –1,000	–1,000 to –1,200	–1,200 to –1,400	–1,400 to –1,600	–1,600 to –1,800	–1,800 to –2,200
ZSMNW086A	22	2.04E-06	1.89E-07	4.36E-08	4.49E-09	1.61E-09	4.96E-10	1.53E-10	4.74E-11	1.46E-11	1.00E-11
zsmnw088a	20	2.24E-06	2.08E-07	4.79E-08	4.93E-09	1.77E-09	5.46E-10	1.69E-10	5.21E-11	1.61E-11	1.00E-11
ZSMNW089A	21	2.10E-06	1.95E-07	4.48E-08	4.62E-09	1.65E-09	5.11E-10	1.58E-10	4.88E-11	1.51E-11	1.00E-11
ZSMNW106A	17	2.93E-07	3.20E-08	9.08E-09	1.10E-09	4.57E-10	1.67E-10	6.08E-11	2.22E-11	1.00E-11	1.00E-11
ZSMNW113A	30	1.47E-06	1.36E-07	3.14E-08	3.24E-09	1.16E-09	3.58E-10	1.11E-10	3.42E-11	1.06E-11	1.00E-11
zsmnw119a	10	4.48E-06	4.16E-07	9.58E-08	9.87E-09	3.53E-09	1.09E-09	3.37E-10	1.04E-10	3.22E-11	1.00E-11
ZSMNW123A	32	1.39E-06	1.29E-07	2.96E-08	3.05E-09	1.09E-09	3.37E-10	1.04E-10	3.22E-11	1.00E-11	1.00E-11
ZSMNW126A	37	1.23E-06	1.14E-07	2.62E-08	2.70E-09	9.66E-10	2.99E-10	9.23E-11	2.85E-11	1.00E-11	1.00E-11
ZSMNW126B	36	1.26E-06	1.17E-07	2.69E-08	2.77E-09	9.91E-10	3.06E-10	9.47E-11	2.93E-11	1.00E-11	1.00E-11
ZSMNW131A	50	8.97E-07	8.32E-08	1.92E-08	1.97E-09	7.06E-10	2.18E-10	6.75E-11	2.08E-11	1.00E-11	1.00E-11
ZSMNW173A	21	2.11E-06	1.96E-07	4.51E-08	4.65E-09	1.66E-09	5.14E-10	1.59E-10	4.91E-11	1.52E-11	1.00E-11
ZSMNW178A	41	1.08E-06	1.00E-07	2.31E-08	2.38E-09	8.53E-10	2.64E-10	8.15E-11	2.52E-11	1.00E-11	1.00E-11
ZSMNW184A	16	3.03E-07	3.32E-08	9.40E-09	1.14E-09	4.73E-10	1.73E-10	6.29E-11	2.30E-11	1.00E-11	1.00E-11
ZSMNW202A	16	3.08E-07	3.37E-08	9.55E-09	1.16E-09	4.81E-10	1.75E-10	6.39E-11	2.33E-11	1.00E-11	1.00E-11
ZSMNW206A	19	2.69E-07	2.94E-08	8.34E-09	1.01E-09	4.19E-10	1.53E-10	5.58E-11	2.04E-11	1.00E-11	1.00E-11
ZSMNW222A	27	1.67E-06	1.55E-07	3.57E-08	3.68E-09	1.32E-09	4.07E-10	1.26E-10	3.88E-11	1.20E-11	1.00E-11
ZSMNW233A	19	2.58E-07	2.83E-08	8.02E-09	9.75E-10	4.03E-10	1.47E-10	5.37E-11	1.96E-11	1.00E-11	1.00E-11
ZSMNW235A	20	2.24E-06	2.07E-07	4.78E-08	4.92E-09	1.76E-09	5.44E-10	1.68E-10	5.20E-11	1.61E-11	1.00E-11
ZSMNW245A	23	1.94E-06	1.80E-07	4.15E-08	4.27E-09	1.53E-09	4.73E-10	1.46E-10	4.51E-11	1.39E-11	1.00E-11
ZSMNW247A	16	3.09E-07	3.38E-08	9.59E-09	1.17E-09	4.82E-10	1.76E-10	6.42E-11	2.34E-11	1.00E-11	1.00E-11
ZSMNW251A	20	2.50E-07	2.74E-08	7.76E-09	9.43E-10	3.90E-10	1.42E-10	5.19E-11	1.89E-11	1.00E-11	1.00E-11
ZSMNW254A	49	9.08E-07	8.42E-08	1.94E-08	2.00E-09	7.15E-10	2.21E-10	6.83E-11	2.11E-11	1.00E-11	1.00E-11
ZSMNW261A	22	2.01E-06	1.86E-07	4.29E-08	4.42E-09	1.58E-09	4.89E-10	1.51E-10	4.67E-11	1.44E-11	1.00E-11
ZSMNW263A	16	3.09E-07	3.38E-08	9.59E-09	1.17E-09	4.82E-10	1.76E-10	6.42E-11	2.34E-11	1.00E-11	1.00E-11
ZSMNW269A	21	2.11E-06	1.96E-07	4.51E-08	4.65E-09	1.66E-09	5.14E-10	1.59E-10	4.91E-11	1.52E-11	1.00E-11
ZSMNW280A	20	2.24E-06	2.07E-07	4.78E-08	4.92E-09	1.76E-09	5.44E-10	1.68E-10	5.20E-11	1.61E-11	1.00E-11
ZSMNW294A	23	1.97E-06	1.83E-07	4.21E-08	4.34E-09	1.55E-09	4.79E-10	1.48E-10	4.58E-11	1.41E-11	1.00E-11
ZSMNW312A	50	9.00E-07	8.34E-08	1.92E-08	1.98E-09	7.09E-10	2.19E-10	6.77E-11	2.09E-11	1.00E-11	1.00E-11
ZSMNW312B	12	4.04E-07	4.42E-08	1.25E-08	1.52E-09	6.30E-10	2.30E-10	8.38E-11	3.06E-11	1.11E-11	1.00E-11

Deformation zone (ZSM)	b_h (m)	Hydraulic conductivity K (m/s) for depth interval (m RHB 70)									
		0 to –150	–150 to –400	–400 to –650	–650 to –800	–800 to –1,000	–1,000 to –1,200	–1,200 to –1,400	–1,400 to –1,600	–1,600 to –1,800	–1,800 to –2,200
ZSMNW312C	17	3.00E-07	3.28E-08	9.30E-09	1.13E-09	4.68E-10	1.71E-10	6.22E-11	2.27E-11	1.00E-11	1.00E-11
ZSMNW321A	21	2.17E-06	2.01E-07	4.63E-08	4.77E-09	1.71E-09	5.27E-10	1.63E-10	5.04E-11	1.56E-11	1.00E-11
ZSMNW322A	50	8.97E-07	8.32E-08	1.92E-08	1.97E-09	7.06E-10	2.18E-10	6.75E-11	2.08E-11	1.00E-11	1.00E-11
ZSMNW921A	25	1.76E-06	1.63E-07	3.77E-08	3.88E-09	1.39E-09	4.29E-10	1.33E-10	4.10E-11	1.27E-11	1.00E-11
ZSMNW922A	18	2.80E-07	3.07E-08	8.69E-09	1.06E-09	4.37E-10	1.59E-10	5.82E-11	2.12E-11	1.00E-11	1.00E-11
ZSMNW923A	37	1.20E-06	1.11E-07	2.56E-08	2.63E-09	9.43E-10	2.91E-10	9.00E-11	2.78E-11	1.00E-11	1.00E-11
ZSMNW925A	28	1.62E-06	1.50E-07	3.45E-08	3.55E-09	1.27E-09	3.93E-10	1.21E-10	3.75E-11	1.16E-11	1.00E-11
zsmnw928a	10	5.00E-07	5.47E-08	1.55E-08	1.88E-09	7.80E-10	2.84E-10	1.04E-10	3.78E-11	1.38E-11	1.00E-11
zsmnw929a	20	2.24E-06	2.08E-07	4.79E-08	4.93E-09	1.77E-09	5.46E-10	1.69E-10	5.21E-11	1.61E-11	1.00E-11
zsmnw931a	50	8.97E-07	8.32E-08	1.92E-08	1.97E-09	7.06E-10	2.18E-10	6.75E-11	2.08E-11	1.00E-11	1.00E-11
ZSMNW931B	38	1.19E-06	1.10E-07	2.53E-08	2.61E-09	9.34E-10	2.89E-10	8.92E-11	2.76E-11	1.00E-11	1.00E-11
ZSMNW933A	22	2.02E-06	1.87E-07	4.31E-08	4.44E-09	1.59E-09	4.92E-10	1.52E-10	4.69E-11	1.45E-11	1.00E-11
ZSMNW937A	17	2.88E-07	3.15E-08	8.92E-09	1.08E-09	4.49E-10	1.64E-10	5.97E-11	2.18E-11	1.00E-11	1.00E-11
ZSMNW943A	17	2.88E-07	3.15E-08	8.92E-09	1.08E-09	4.49E-10	1.64E-10	5.97E-11	2.18E-11	1.00E-11	1.00E-11

A6.2 Properties of deformation zones before calibration for full model depth, depth zones

The definition of **initial hydraulic properties before calibration** for the each deformation zone is specified in Table A6-2. The depth variation was **implemented in CONNECTFLOW** as a step-wise change.

Table A6-2. Depth variation of hydraulic conductivity K (m/s) and the used thickness, bh (m), in HCD for elevation intervals used for groundwater flow and solute transport before calibration. All elevations are in m RHB 70.

Deformation zone	b_h (m)	Hydraulic conductivity K (m/s) for depth interval (m RHB 70)									
		0 to –150	–150 to –400	–400 to –650	–650 to –800	–800 to –1,000	–1,000 to –1,200	–1,200 to –1,400	–1,400 to –1,600	–1,600 to –1,800	–1,800 to –2,200
hlx28_dz1	10	5.00E-07	1.82E-07	5.17E-08	1.88E-08	7.80E-09	2.84E-09	1.04E-09	3.78E-10	1.38E-10	5.04E-11
klx03_dz1b	10	5.00E-07	1.82E-07	5.17E-08	1.88E-08	7.80E-09	2.84E-09	1.04E-09	3.78E-10	1.38E-10	5.04E-11
klx03_dz1c	10	5.00E-07	1.82E-07	5.17E-08	1.88E-08	7.80E-09	2.84E-09	1.04E-09	3.78E-10	1.38E-10	5.04E-11
klx04_dz6b	14	3.57E-07	1.30E-07	3.69E-08	1.35E-08	5.57E-09	2.03E-09	7.41E-10	2.70E-10	9.86E-11	3.60E-11
klx04_dz6c	30	1.67E-07	6.08E-08	1.72E-08	6.28E-09	2.60E-09	9.48E-10	3.46E-10	1.26E-10	4.60E-11	1.68E-11
klx07_dz10	10	5.00E-07	1.82E-07	5.17E-08	1.88E-08	7.80E-09	2.84E-09	1.04E-09	3.78E-10	1.38E-10	5.04E-11
klx07_dz11	30	1.67E-07	6.08E-08	1.72E-08	6.28E-09	2.60E-09	9.48E-10	3.46E-10	1.26E-10	4.60E-11	1.68E-11
klx07_dz12	47	1.06E-07	3.88E-08	1.10E-08	4.01E-09	1.66E-09	6.05E-10	2.21E-10	8.05E-11	2.94E-11	1.07E-11
klx07_dz13	10	5.00E-07	1.82E-07	5.17E-08	1.88E-08	7.80E-09	2.84E-09	1.04E-09	3.78E-10	1.38E-10	5.04E-11
klx07_dz7	30	1.67E-07	6.08E-08	1.72E-08	6.28E-09	2.60E-09	9.48E-10	3.46E-10	1.26E-10	4.60E-11	1.68E-11
klx07_dz9	10	5.00E-07	1.82E-07	5.17E-08	1.88E-08	7.80E-09	2.84E-09	1.04E-09	3.78E-10	1.38E-10	5.04E-11
klx08_dz1	27	1.85E-07	6.75E-08	1.91E-08	6.98E-09	2.89E-09	1.05E-09	3.84E-10	1.40E-10	5.11E-11	1.86E-11
klx08_dz10	11	4.54E-07	1.66E-07	4.70E-08	1.71E-08	7.09E-09	2.59E-09	9.43E-10	3.44E-10	1.25E-10	4.58E-11
klx08_dz6	10	5.00E-07	1.82E-07	5.17E-08	1.88E-08	7.80E-09	2.84E-09	1.04E-09	3.78E-10	1.38E-10	5.04E-11
klx09_dz10	25	2.00E-07	7.29E-08	2.07E-08	7.54E-09	3.12E-09	1.14E-09	4.15E-10	1.51E-10	5.52E-11	2.01E-11
klx09_dz14	9	5.97E-07	2.18E-07	6.17E-08	2.25E-08	9.31E-09	3.40E-09	1.24E-09	4.52E-10	1.65E-10	6.01E-11
klx09_dz9	6	5.45E-06	1.99E-06	5.63E-07	2.05E-07	8.50E-08	3.10E-08	1.13E-08	4.13E-09	1.50E-09	5.49E-10
klx09e_dz2	22	2.27E-07	8.29E-08	2.35E-08	8.57E-09	3.54E-09	1.29E-09	4.72E-10	1.72E-10	6.27E-11	2.29E-11
klx09f_dz1	14	3.57E-07	1.30E-07	3.69E-08	1.35E-08	5.57E-09	2.03E-09	7.41E-10	2.70E-10	9.86E-11	3.60E-11
klx10c_dz3	10	5.00E-07	1.82E-07	5.17E-08	1.88E-08	7.80E-09	2.84E-09	1.04E-09	3.78E-10	1.38E-10	5.04E-11
klx10c_dz7	10	5.00E-07	1.82E-07	5.17E-08	1.88E-08	7.80E-09	2.84E-09	1.04E-09	3.78E-10	1.38E-10	5.04E-11
klx11_dz11	20	2.50E-07	9.11E-08	2.58E-08	9.42E-09	3.90E-09	1.42E-09	5.19E-10	1.89E-10	6.90E-11	2.52E-11
klx16_dz6	1	5.40E-05	1.97E-05	5.59E-06	2.04E-06	8.43E-07	3.07E-07	1.12E-07	4.09E-08	1.49E-08	5.44E-09
klx18_dz9	10	5.00E-07	1.82E-07	5.17E-08	1.88E-08	7.80E-09	2.84E-09	1.04E-09	3.78E-10	1.38E-10	5.04E-11
klx19_dz2	4	1.42E-05	5.18E-06	1.47E-06	5.35E-07	2.21E-07	8.08E-08	2.95E-08	1.07E-08	3.92E-09	1.43E-09
klx19_dz5-8_dolerite	45	9.99E-07	3.65E-07	1.03E-07	3.77E-08	1.56E-08	5.69E-09	2.08E-09	7.57E-10	2.76E-10	1.01E-10
klx21b_dz10-12	10	5.00E-07	1.82E-07	5.17E-08	1.88E-08	7.80E-09	2.84E-09	1.04E-09	3.78E-10	1.38E-10	5.04E-11
klx28_dz1	13	3.84E-07	1.40E-07	3.97E-08	1.45E-08	6.00E-09	2.19E-09	7.98E-10	2.91E-10	1.06E-10	3.87E-11

Deformation zone (ZSM)	b_h (m)	Hydraulic conductivity K (m/s) for depth interval (m RHB 70)									
		0 to –150	–150 to –400	–400 to –650	–650 to –800	–800 to –1,000	–1,000 to –1,200	–1,200 to –1,400	–1,400 to –1,600	–1,600 to –1,800	–1,800 to –2,200
zsmew002a	50	1.29E-06	5.36E-07	1.80E-07	7.49E-08	3.48E-08	1.45E-08	6.05E-09	2.52E-09	1.05E-09	4.39E-10
zsmew007a	50	1.39E-06	5.15E-07	1.49E-07	5.50E-08	2.31E-08	8.54E-09	3.16E-09	1.17E-09	4.33E-10	1.60E-10
zsmew007c	50	1.72E-07	6.55E-08	1.97E-08	7.51E-09	3.24E-09	1.24E-09	4.72E-10	1.80E-10	6.89E-11	2.63E-11
ZSMEW009A	12	7.15E-07	2.73E-07	8.20E-08	3.13E-08	1.35E-08	5.15E-09	1.97E-09	7.51E-10	2.87E-10	1.10E-10
zsmew013a	45	1.43E-06	5.96E-07	2.00E-07	8.32E-08	3.87E-08	1.61E-08	6.73E-09	2.80E-09	1.17E-09	4.87E-10
zsmew014a	10	5.00E-07	1.82E-07	5.17E-08	1.88E-08	7.80E-09	2.84E-09	1.04E-09	3.78E-10	1.38E-10	5.04E-11
ZSMEW020A	50	1.29E-06	5.36E-07	1.80E-07	7.49E-08	3.48E-08	1.45E-08	6.05E-09	2.52E-09	1.05E-09	4.39E-10
ZSMEW038A	10	6.43E-06	2.68E-06	8.98E-07	3.75E-07	1.74E-07	7.26E-08	3.03E-08	1.26E-08	5.26E-09	2.19E-09
ZSMEW076A	31	2.06E-06	8.57E-07	2.87E-07	1.20E-07	5.57E-08	2.32E-08	9.68E-09	4.03E-09	1.68E-09	7.01E-10
ZSMEW114A	25	2.59E-06	1.08E-06	3.62E-07	1.51E-07	7.02E-08	2.93E-08	1.22E-08	5.09E-09	2.12E-09	8.84E-10
zsmew120a	50	1.72E-07	6.55E-08	1.97E-08	7.51E-09	3.24E-09	1.24E-09	4.72E-10	1.80E-10	6.89E-11	2.63E-11
ZSMEW129A	20	3.28E-06	1.37E-06	4.57E-07	1.91E-07	8.87E-08	3.70E-08	1.54E-08	6.42E-09	2.68E-09	1.12E-09
ZSMEW190A	17	5.18E-07	1.98E-07	5.93E-08	2.27E-08	9.76E-09	3.73E-09	1.42E-09	5.44E-10	2.08E-10	7.94E-11
ZSMEW200A	17	4.91E-07	1.88E-07	5.63E-08	2.15E-08	9.27E-09	3.54E-09	1.35E-09	5.16E-10	1.97E-10	7.53E-11
ZSMEW230A	18	4.75E-07	1.81E-07	5.45E-08	2.08E-08	8.96E-09	3.42E-09	1.31E-09	4.99E-10	1.91E-10	7.29E-11
ZSMEW240A	50	1.29E-06	5.36E-07	1.80E-07	7.49E-08	3.48E-08	1.45E-08	6.05E-09	2.52E-09	1.05E-09	4.39E-10
ZSMEW305A	19	4.47E-07	1.71E-07	5.12E-08	1.96E-08	8.43E-09	3.22E-09	1.23E-09	4.70E-10	1.79E-10	6.85E-11
zsmew316a	30	2.14E-06	8.94E-07	2.99E-07	1.25E-07	5.81E-08	2.42E-08	1.01E-08	4.21E-09	1.75E-09	7.31E-10
zsmew900a	25	2.00E-07	7.29E-08	2.07E-08	7.54E-09	3.12E-09	1.14E-09	4.15E-10	1.51E-10	5.52E-11	2.01E-11
zsmew900b	25	2.00E-07	7.29E-08	2.07E-08	7.54E-09	3.12E-09	1.14E-09	4.15E-10	1.51E-10	5.52E-11	2.01E-11
ZSMEW904A	50	1.29E-06	5.36E-07	1.80E-07	7.49E-08	3.48E-08	1.45E-08	6.05E-09	2.52E-09	1.05E-09	4.39E-10
ZSMEW905A	21	3.04E-06	1.27E-06	4.24E-07	1.77E-07	8.23E-08	3.43E-08	1.43E-08	5.96E-09	2.48E-09	1.04E-09
ZSMEW906A	50	1.29E-06	5.36E-07	1.80E-07	7.49E-08	3.48E-08	1.45E-08	6.05E-09	2.52E-09	1.05E-09	4.39E-10
ZSMEW907A	50	1.29E-06	5.36E-07	1.80E-07	7.49E-08	3.48E-08	1.45E-08	6.05E-09	2.52E-09	1.05E-09	4.39E-10
ZSMEW936A	11	7.76E-07	2.96E-07	8.90E-08	3.40E-08	1.46E-08	5.59E-09	2.14E-09	8.16E-10	3.12E-10	1.19E-10
zsmew946a	10	2.77E-06	3.27E-07	2.26E-08	2.68E-09	4.13E-10	4.88E-11	1.00E-11	1.00E-11	1.00E-11	1.00E-11

Deformation zone (ZSM)	b_h (m)	Hydraulic conductivity K (m/s) for depth interval (m RHB 70)									
		0 to –150	–150 to –400	–400 to –650	–650 to –800	–800 to –1,000	–1,000 to –1,200	–1,200 to –1,400	–1,400 to –1,600	–1,600 to –1,800	–1,800 to –2,200
zsmne004a	50	8.97E-07	2.77E-07	6.39E-08	1.97E-08	7.06E-09	2.18E-09	6.75E-10	2.08E-10	6.44E-11	1.99E-11
zsmne005a	50	8.97E-07	2.77E-07	6.39E-08	1.97E-08	7.06E-09	2.18E-09	6.75E-10	2.08E-10	6.44E-11	1.99E-11
zsmne006a	50	1.13E-05	2.69E-06	4.51E-07	1.08E-07	3.09E-08	7.41E-09	1.77E-09	4.25E-10	1.02E-10	2.43E-11
ZSMNE008A	39	1.15E-06	3.54E-07	8.17E-08	2.52E-08	9.03E-09	2.79E-09	8.62E-10	2.67E-10	8.24E-11	2.55E-11
ZSMNE010A	34	1.31E-06	4.05E-07	9.33E-08	2.88E-08	1.03E-08	3.19E-09	9.86E-10	3.05E-10	9.41E-11	2.91E-11
zsmne011a	50	8.97E-07	2.77E-07	6.39E-08	1.97E-08	7.06E-09	2.18E-09	6.75E-10	2.08E-10	6.44E-11	1.99E-11
zsmne012a	50	2.90E-06	1.05E-06	2.94E-07	1.06E-07	4.36E-08	1.58E-08	5.71E-09	2.06E-09	7.46E-10	2.70E-10
zsmne015a	10	5.00E-07	1.82E-07	5.17E-08	1.88E-08	7.80E-09	2.84E-09	1.04E-09	3.78E-10	1.38E-10	5.04E-11
zsmne018a	50	9.99E-08	3.65E-08	1.03E-08	3.77E-09	1.56E-09	5.69E-10	2.08E-10	7.57E-11	2.76E-11	1.01E-11
zsmne019a	20	2.24E-06	6.93E-07	1.60E-07	4.93E-08	1.77E-08	5.46E-09	1.69E-09	5.21E-10	1.61E-10	4.98E-11
zsmne021a	40	1.12E-06	3.46E-07	7.98E-08	2.47E-08	8.83E-09	2.73E-09	8.43E-10	2.61E-10	8.05E-11	2.49E-11
zsmne022a	28	1.61E-06	4.96E-07	1.14E-07	3.54E-08	1.27E-08	3.91E-09	1.21E-09	3.73E-10	1.15E-10	3.57E-11
ZSMNE024A	50	3.37E-05	1.22E-06	1.94E-08	7.07E-10	3.89E-11	2.00E-12	2.00E-12	2.00E-12	2.00E-12	2.00E-12
ZSMNE024B	16	1.06E-04	3.85E-06	6.11E-08	2.22E-09	1.22E-10	6.29E-12	6.29E-12	6.29E-12	6.29E-12	6.29E-12
ZSMNE031A	15	2.99E-06	9.24E-07	2.13E-07	6.58E-08	2.35E-08	7.28E-09	2.25E-09	6.95E-10	2.15E-10	6.64E-11
ZSMNE031B	19	2.64E-07	9.64E-08	2.73E-08	9.97E-09	4.12E-09	1.50E-09	5.49E-10	2.00E-10	7.30E-11	2.66E-11
ZSMNE032A	26	1.70E-06	5.26E-07	1.21E-07	3.74E-08	1.34E-08	4.14E-09	1.28E-09	3.96E-10	1.22E-10	3.78E-11
ZSMNE033A	30	1.50E-06	4.65E-07	1.07E-07	3.31E-08	1.18E-08	3.66E-09	1.13E-09	3.50E-10	1.08E-10	3.34E-11
ZSMNE034A	29	1.55E-06	4.79E-07	1.10E-07	3.41E-08	1.22E-08	3.77E-09	1.16E-09	3.60E-10	1.11E-10	3.44E-11
ZSMNE036A	23	1.94E-06	6.00E-07	1.38E-07	4.27E-08	1.53E-08	4.73E-09	1.46E-09	4.51E-10	1.39E-10	4.31E-11
zsmne040a	20	2.50E-07	9.11E-08	2.58E-08	9.42E-09	3.90E-09	1.42E-09	5.19E-10	1.89E-10	6.90E-11	2.52E-11
ZSMNE062A	17	2.97E-07	1.08E-07	3.07E-08	1.12E-08	4.63E-09	1.69E-09	6.16E-10	2.25E-10	8.20E-11	2.99E-11
zsmne063a	10	5.00E-07	1.82E-07	5.17E-08	1.88E-08	7.80E-09	2.84E-09	1.04E-09	3.78E-10	1.38E-10	5.04E-11
zsmne065a	10	5.00E-07	1.82E-07	5.17E-08	1.88E-08	7.80E-09	2.84E-09	1.04E-09	3.78E-10	1.38E-10	5.04E-11
ZSMNE073A	36	1.24E-06	3.84E-07	8.84E-08	2.73E-08	9.77E-09	3.02E-09	9.33E-10	2.88E-10	8.91E-11	2.75E-11
zsmne079a	10	4.48E-06	1.39E-06	3.19E-07	9.87E-08	3.53E-08	1.09E-08	3.37E-09	1.04E-09	3.22E-10	9.95E-11
ZSMNE081A	21	2.18E-06	6.74E-07	1.55E-07	4.80E-08	1.72E-08	5.31E-09	1.64E-09	5.07E-10	1.57E-10	4.84E-11
ZSMNE095A	23	1.96E-06	6.07E-07	1.40E-07	4.32E-08	1.55E-08	4.78E-09	1.48E-09	4.56E-10	1.41E-10	4.36E-11
ZSMNE096A	17	2.90E-07	1.06E-07	3.00E-08	1.10E-08	4.53E-09	1.65E-09	6.03E-10	2.20E-10	8.02E-11	2.93E-11
zsmne107a	35	1.28E-06	3.96E-07	9.12E-08	2.82E-08	1.01E-08	3.12E-09	9.64E-10	2.98E-10	9.20E-11	2.84E-11
zsmne108a	10	5.00E-07	1.82E-07	5.17E-08	1.88E-08	7.80E-09	2.84E-09	1.04E-09	3.78E-10	1.38E-10	5.04E-11
ZSMNE132A	28	1.61E-06	4.98E-07	1.15E-07	3.54E-08	1.27E-08	3.92E-09	1.21E-09	3.74E-10	1.16E-10	3.57E-11

Deformation zone (ZSM)	b_h (m)	Hydraulic conductivity K (m/s) for depth interval (m RHB 70)									
		0 to –150	–150 to –400	–400 to –650	–650 to –800	–800 to –1,000	–1,000 to –1,200	–1,200 to –1,400	–1,400 to –1,600	–1,600 to –1,800	–1,800 to –2,200
ZSMNE133A	24	1.84E-06	5.69E-07	1.31E-07	4.05E-08	1.45E-08	4.48E-09	1.38E-09	4.28E-10	1.32E-10	4.08E-11
ZSMNE185A	24	1.89E-06	5.83E-07	1.34E-07	4.15E-08	1.48E-08	4.59E-09	1.42E-09	4.38E-10	1.35E-10	4.18E-11
ZSMNE210A	21	2.11E-06	6.51E-07	1.50E-07	4.63E-08	1.66E-08	5.12E-09	1.58E-09	4.89E-10	1.51E-10	4.67E-11
ZSMNE210B	28	1.62E-06	5.00E-07	1.15E-07	3.56E-08	1.28E-08	3.94E-09	1.22E-09	3.76E-10	1.16E-10	3.59E-11
ZSMNE218A	50	8.97E-07	2.77E-07	6.39E-08	1.97E-08	7.06E-09	2.18E-09	6.75E-10	2.08E-10	6.44E-11	1.99E-11
ZSMNE229A	20	2.24E-06	6.91E-07	1.59E-07	4.92E-08	1.76E-08	5.44E-09	1.68E-09	5.20E-10	1.61E-10	4.96E-11
ZSMNE257A	27	1.67E-06	5.16E-07	1.19E-07	3.67E-08	1.31E-08	4.06E-09	1.26E-09	3.88E-10	1.20E-10	3.71E-11
ZSMNE258A	26	1.71E-06	5.30E-07	1.22E-07	3.77E-08	1.35E-08	4.17E-09	1.29E-09	3.98E-10	1.23E-10	3.80E-11
ZSMNE259A	28	1.59E-06	4.92E-07	1.13E-07	3.50E-08	1.25E-08	3.87E-09	1.20E-09	3.70E-10	1.14E-10	3.53E-11
ZSMNE267A	23	1.99E-06	6.14E-07	1.41E-07	4.37E-08	1.56E-08	4.84E-09	1.49E-09	4.62E-10	1.43E-10	4.41E-11
ZSMNE286A	27	1.67E-06	5.17E-07	1.19E-07	3.68E-08	1.32E-08	4.07E-09	1.26E-09	3.89E-10	1.20E-10	3.71E-11
ZSMNE289A	21	2.11E-06	6.51E-07	1.50E-07	4.64E-08	1.66E-08	5.13E-09	1.58E-09	4.90E-10	1.51E-10	4.68E-11
ZSMNE295A	31	1.43E-06	4.43E-07	1.02E-07	3.15E-08	1.13E-08	3.49E-09	1.08E-09	3.33E-10	1.03E-10	3.18E-11
ZSMNE302A	24	1.84E-06	5.68E-07	1.31E-07	4.04E-08	1.45E-08	4.47E-09	1.38E-09	4.27E-10	1.32E-10	4.08E-11
ZSMNE307A	18	2.79E-07	1.02E-07	2.89E-08	1.05E-08	4.36E-09	1.59E-09	5.80E-10	2.12E-10	7.71E-11	2.81E-11
ZSMNE308A	24	1.85E-06	5.72E-07	1.32E-07	4.07E-08	1.46E-08	4.50E-09	1.39E-09	4.30E-10	1.33E-10	4.11E-11
ZSMNE313A	50	8.97E-07	2.77E-07	6.39E-08	1.97E-08	7.06E-09	2.18E-09	6.75E-10	2.08E-10	6.44E-11	1.99E-11
ZSMNE901A	25	1.78E-06	5.50E-07	1.27E-07	3.92E-08	1.40E-08	4.33E-09	1.34E-09	4.14E-10	1.28E-10	3.95E-11
ZSMNE903A	25	1.81E-06	5.61E-07	1.29E-07	3.99E-08	1.43E-08	4.42E-09	1.36E-09	4.22E-10	1.30E-10	4.03E-11
ZSMNE909A	17	2.90E-07	1.06E-07	3.00E-08	1.09E-08	4.53E-09	1.65E-09	6.02E-10	2.20E-10	8.01E-11	2.92E-11
ZSMNE910A	22	2.05E-06	6.35E-07	1.46E-07	4.52E-08	1.62E-08	5.00E-09	1.54E-09	4.77E-10	1.47E-10	4.56E-11
ZSMNE911A	50	8.97E-07	2.77E-07	6.39E-08	1.97E-08	7.06E-09	2.18E-09	6.75E-10	2.08E-10	6.44E-11	1.99E-11
ZSMNE912A	31	1.46E-06	4.50E-07	1.04E-07	3.20E-08	1.15E-08	3.54E-09	1.09E-09	3.38E-10	1.05E-10	3.23E-11
ZSMNE913A	50	8.97E-07	2.77E-07	6.39E-08	1.97E-08	7.06E-09	2.18E-09	6.75E-10	2.08E-10	6.44E-11	1.99E-11
ZSMNE914A	50	8.97E-07	2.77E-07	6.39E-08	1.97E-08	7.06E-09	2.18E-09	6.75E-10	2.08E-10	6.44E-11	1.99E-11
ZSMNE915A	19	2.57E-07	9.36E-08	2.65E-08	9.68E-09	4.00E-09	1.46E-09	5.33E-10	1.94E-10	7.09E-11	2.59E-11
zsmne930a	5	8.97E-06	2.77E-06	6.39E-07	1.97E-07	7.06E-08	2.18E-08	6.75E-09	2.08E-09	6.44E-10	1.99E-10
ZSMNE940A	16	3.07E-07	1.12E-07	3.18E-08	1.16E-08	4.79E-09	1.75E-09	6.38E-10	2.33E-10	8.49E-11	3.10E-11
ZSMNE941A	22	2.06E-06	6.37E-07	1.47E-07	4.54E-08	1.62E-08	5.02E-09	1.55E-09	4.79E-10	1.48E-10	4.58E-11
zsmne942a	15	1.21E-06	4.01E-07	1.01E-07	3.32E-08	1.26E-08	4.16E-09	1.38E-09	4.54E-10	1.50E-10	4.96E-11
zsmne944a	10	5.00E-07	1.82E-07	5.17E-08	1.88E-08	7.80E-09	2.84E-09	1.04E-09	3.78E-10	1.38E-10	5.04E-11

Deformation zone (ZSM)	b_h (m)	Hydraulic conductivity K (m/s) for depth interval (m RHB 70)									
		0 to –150	–150 to –400	–400 to –650	–650 to –800	–800 to –1,000	–1,000 to –1,200	–1,200 to –1,400	–1,400 to –1,600	–1,600 to –1,800	–1,800 to –2,200
zsmns001a	50	2.76E-06	9.11E-07	2.28E-07	7.54E-08	2.86E-08	9.45E-09	3.12E-09	1.03E-09	3.41E-10	1.13E-10
zsmns001b	50	2.76E-06	9.11E-07	2.28E-07	7.54E-08	2.86E-08	9.45E-09	3.12E-09	1.03E-09	3.41E-10	1.13E-10
zsmns001c	50	2.76E-06	9.11E-07	2.28E-07	7.54E-08	2.86E-08	9.45E-09	3.12E-09	1.03E-09	3.41E-10	1.13E-10
zsmns001d	50	2.76E-06	9.11E-07	2.28E-07	7.54E-08	2.86E-08	9.45E-09	3.12E-09	1.03E-09	3.41E-10	1.13E-10
zsmns001e	50	2.76E-06	9.11E-07	2.28E-07	7.54E-08	2.86E-08	9.45E-09	3.12E-09	1.03E-09	3.41E-10	1.13E-10
ZSMNS009A	25	1.79E-06	5.54E-07	1.28E-07	3.95E-08	1.41E-08	4.37E-09	1.35E-09	4.17E-10	1.29E-10	3.98E-11
ZSMNS017A	21	2.16E-06	6.68E-07	1.54E-07	4.75E-08	1.70E-08	5.26E-09	1.62E-09	5.02E-10	1.55E-10	4.79E-11
ZSMNS017B	20	1.90E-05	6.27E-06	1.57E-06	5.19E-07	1.97E-07	6.51E-08	2.15E-08	7.10E-09	2.35E-09	7.75E-10
zsmns046a	20	2.24E-06	6.93E-07	1.60E-07	4.93E-08	1.77E-08	5.46E-09	1.69E-09	5.21E-10	1.61E-10	4.98E-11
zsmns057a	20	2.24E-06	6.93E-07	1.60E-07	4.93E-08	1.77E-08	5.46E-09	1.69E-09	5.21E-10	1.61E-10	4.98E-11
zsmns059a	50	2.94E-06	9.71E-07	2.43E-07	8.04E-08	3.05E-08	1.01E-08	3.33E-09	1.10E-09	3.63E-10	1.20E-10
ZSMNS064A	50	8.97E-07	2.77E-07	6.39E-08	1.97E-08	7.06E-09	2.18E-09	6.75E-10	2.08E-10	6.44E-11	1.99E-11
ZSMNS071A	18	2.71E-07	9.89E-08	2.80E-08	1.02E-08	4.23E-09	1.54E-09	5.63E-10	2.05E-10	7.49E-11	2.73E-11
ZSMNS084A	32	1.40E-06	4.33E-07	9.98E-08	3.08E-08	1.10E-08	3.41E-09	1.05E-09	3.26E-10	1.01E-10	3.11E-11
ZSMNS085A	37	1.22E-06	3.75E-07	8.65E-08	2.67E-08	9.57E-09	2.96E-09	9.14E-10	2.82E-10	8.73E-11	2.70E-11
ZSMNS117A	17	2.98E-07	1.09E-07	3.08E-08	1.12E-08	4.65E-09	1.70E-09	6.19E-10	2.26E-10	8.24E-11	3.00E-11
zsmns141a	20	2.24E-06	6.93E-07	1.60E-07	4.93E-08	1.77E-08	5.46E-09	1.69E-09	5.21E-10	1.61E-10	4.98E-11
ZSMNS165A	18	2.81E-07	1.02E-07	2.90E-08	1.06E-08	4.38E-09	1.60E-09	5.83E-10	2.12E-10	7.75E-11	2.83E-11
ZSMNS182A	30	1.50E-06	4.63E-07	1.07E-07	3.29E-08	1.18E-08	3.64E-09	1.13E-09	3.48E-10	1.07E-10	3.32E-11
ZSMNS182B	30	1.48E-06	4.59E-07	1.06E-07	3.27E-08	1.17E-08	3.61E-09	1.12E-09	3.45E-10	1.07E-10	3.30E-11
ZSMNS215A	16	3.08E-07	1.12E-07	3.19E-08	1.16E-08	4.81E-09	1.75E-09	6.40E-10	2.33E-10	8.51E-11	3.10E-11
ZSMNS221A	22	2.03E-06	6.27E-07	1.45E-07	4.47E-08	1.60E-08	4.94E-09	1.53E-09	4.72E-10	1.46E-10	4.50E-11
ZSMNS287A	34	1.32E-06	4.08E-07	9.40E-08	2.91E-08	1.04E-08	3.21E-09	9.93E-10	3.07E-10	9.48E-11	2.93E-11
ZSMNS291A	19	2.64E-07	9.64E-08	2.73E-08	9.97E-09	4.12E-09	1.50E-09	5.49E-10	2.00E-10	7.30E-11	2.66E-11
ZSMNS301A	19	2.67E-07	9.73E-08	2.76E-08	1.01E-08	4.16E-09	1.52E-09	5.54E-10	2.02E-10	7.37E-11	2.69E-11
ZSMNS916A	44	1.03E-06	3.19E-07	7.34E-08	2.27E-08	8.12E-09	2.51E-09	7.75E-10	2.40E-10	7.40E-11	2.29E-11
ZSMNS917A	50	8.97E-07	2.77E-07	6.39E-08	1.97E-08	7.06E-09	2.18E-09	6.75E-10	2.08E-10	6.44E-11	1.99E-11
ZSMNS918A	29	1.56E-06	4.83E-07	1.11E-07	3.44E-08	1.23E-08	3.81E-09	1.18E-09	3.63E-10	1.12E-10	3.47E-11
ZSMNS919A	50	8.97E-07	2.77E-07	6.39E-08	1.97E-08	7.06E-09	2.18E-09	6.75E-10	2.08E-10	6.44E-11	1.99E-11
ZSMNS920A	31	1.46E-06	4.52E-07	1.04E-07	3.22E-08	1.15E-08	3.56E-09	1.10E-09	3.40E-10	1.05E-10	3.24E-11
zsmns945a	10	4.48E-06	1.39E-06	3.19E-07	9.87E-08	3.53E-08	1.09E-08	3.37E-09	1.04E-09	3.22E-10	9.95E-11
zsmns947a	20	2.50E-07	9.11E-08	2.58E-08	9.42E-09	3.90E-09	1.42E-09	5.19E-10	1.89E-10	6.90E-11	2.52E-11

Deformation zone (ZSM)	b_h (m)	Hydraulic conductivity K (m/s) for depth interval (m RHB 70)									
		0 to –150	–150 to –400	–400 to –650	–650 to –800	–800 to –1,000	–1,000 to –1,200	–1,200 to –1,400	–1,400 to –1,600	–1,600 to –1,800	–1,800 to –2,200
ZSMNW025A	10	5.00E-07	1.82E-07	5.17E-08	1.88E-08	7.80E-09	2.84E-09	1.04E-09	3.78E-10	1.38E-10	5.04E-11
ZSMNW027A	34	1.31E-06	4.04E-07	9.32E-08	2.88E-08	1.03E-08	3.18E-09	9.84E-10	3.04E-10	9.40E-11	2.90E-11
zsmnw042a-east	50	8.97E-07	2.77E-07	6.39E-08	1.97E-08	7.06E-09	2.18E-09	6.75E-10	2.08E-10	6.44E-11	1.99E-11
zsmnw042a-west	50	8.97E-07	2.77E-07	6.39E-08	1.97E-08	7.06E-09	2.18E-09	6.75E-10	2.08E-10	6.44E-11	1.99E-11
zsmnw047a	25	2.00E-07	7.29E-08	2.07E-08	7.54E-09	3.12E-09	1.14E-09	4.15E-10	1.51E-10	5.52E-11	2.01E-11
zsmnw052a	15	3.33E-07	1.22E-07	3.44E-08	1.26E-08	5.20E-09	1.90E-09	6.92E-10	2.52E-10	9.20E-11	3.36E-11
ZSMNW060A	32	1.39E-06	4.29E-07	9.88E-08	3.05E-08	1.09E-08	3.38E-09	1.04E-09	3.22E-10	9.96E-11	3.08E-11
ZSMNW066A	50	8.97E-07	2.77E-07	6.39E-08	1.97E-08	7.06E-09	2.18E-09	6.75E-10	2.08E-10	6.44E-11	1.99E-11
ZSMNW067A	50	8.97E-07	2.77E-07	6.39E-08	1.97E-08	7.06E-09	2.18E-09	6.75E-10	2.08E-10	6.44E-11	1.99E-11
ZSMNW068A	18	2.79E-07	1.02E-07	2.88E-08	1.05E-08	4.35E-09	1.59E-09	5.79E-10	2.11E-10	7.70E-11	2.81E-11
ZSMNW068B	22	2.04E-06	6.30E-07	1.45E-07	4.49E-08	1.61E-08	4.96E-09	1.53E-09	4.74E-10	1.46E-10	4.53E-11
ZSMNW068C	4	1.14E-06	4.15E-07	1.18E-07	4.29E-08	1.78E-08	6.48E-09	2.36E-09	8.62E-10	3.15E-10	1.15E-10
ZSMNW074A	33	1.35E-06	4.19E-07	9.65E-08	2.98E-08	1.07E-08	3.30E-09	1.02E-09	3.15E-10	9.73E-11	3.01E-11
ZSMNW075A	38	1.17E-06	3.61E-07	8.33E-08	2.57E-08	9.21E-09	2.85E-09	8.79E-10	2.72E-10	8.40E-11	2.60E-11
ZSMNW083A	16	3.03E-07	1.11E-07	3.13E-08	1.14E-08	4.73E-09	1.73E-09	6.29E-10	2.30E-10	8.37E-11	3.05E-11
ZSMNW086A	22	2.04E-06	6.30E-07	1.45E-07	4.49E-08	1.61E-08	4.96E-09	1.53E-09	4.74E-10	1.46E-10	4.53E-11
zsmnw088a	20	2.24E-06	6.93E-07	1.60E-07	4.93E-08	1.77E-08	5.46E-09	1.69E-09	5.21E-10	1.61E-10	4.98E-11
ZSMNW089A	21	2.10E-06	6.49E-07	1.49E-07	4.62E-08	1.65E-08	5.11E-09	1.58E-09	4.88E-10	1.51E-10	4.66E-11
ZSMNW106A	17	2.93E-07	1.07E-07	3.03E-08	1.10E-08	4.57E-09	1.67E-09	6.08E-10	2.22E-10	8.09E-11	2.95E-11
ZSMNW113A	30	1.47E-06	4.54E-07	1.05E-07	3.24E-08	1.16E-08	3.58E-09	1.11E-09	3.42E-10	1.06E-10	3.26E-11
zsmnw119a	10	4.48E-06	1.39E-06	3.19E-07	9.87E-08	3.53E-08	1.09E-08	3.37E-09	1.04E-09	3.22E-10	9.95E-11
ZSMNW123A	32	1.39E-06	4.28E-07	9.87E-08	3.05E-08	1.09E-08	3.37E-09	1.04E-09	3.22E-10	9.96E-11	3.08E-11
ZSMNW126A	37	1.23E-06	3.79E-07	8.74E-08	2.70E-08	9.66E-09	2.99E-09	9.23E-10	2.85E-10	8.81E-11	2.72E-11
ZSMNW126B	36	1.26E-06	3.89E-07	8.96E-08	2.77E-08	9.91E-09	3.06E-09	9.47E-10	2.93E-10	9.04E-11	2.79E-11
ZSMNW131A	50	8.97E-07	2.77E-07	6.39E-08	1.97E-08	7.06E-09	2.18E-09	6.75E-10	2.08E-10	6.44E-11	1.99E-11
ZSMNW173A	21	2.11E-06	6.53E-07	1.50E-07	4.65E-08	1.66E-08	5.14E-09	1.59E-09	4.91E-10	1.52E-10	4.69E-11
ZSMNW178A	41	1.08E-06	3.35E-07	7.71E-08	2.38E-08	8.53E-09	2.64E-09	8.15E-10	2.52E-10	7.78E-11	2.40E-11
ZSMNW184A	16	3.03E-07	1.11E-07	3.13E-08	1.14E-08	4.73E-09	1.73E-09	6.29E-10	2.30E-10	8.37E-11	3.05E-11
ZSMNW202A	16	3.08E-07	1.12E-07	3.18E-08	1.16E-08	4.81E-09	1.75E-09	6.39E-10	2.33E-10	8.51E-11	3.10E-11
ZSMNW206A	19	2.69E-07	9.80E-08	2.78E-08	1.01E-08	4.19E-09	1.53E-09	5.58E-10	2.04E-10	7.43E-11	2.71E-11
ZSMNW222A	27	1.67E-06	5.16E-07	1.19E-07	3.68E-08	1.32E-08	4.07E-09	1.26E-09	3.88E-10	1.20E-10	3.71E-11
ZSMNW233A	19	2.58E-07	9.43E-08	2.67E-08	9.75E-09	4.03E-09	1.47E-09	5.37E-10	1.96E-10	7.14E-11	2.60E-11

Deformation zone (ZSM)	b_h (m)	Hydraulic conductivity K (m/s) for depth interval (m RHB 70)									
		0 to –150	–150 to –400	–400 to –650	–650 to –800	–800 to –1,000	–1,000 to –1,200	–1,200 to –1,400	–1,400 to –1,600	–1,600 to –1,800	–1,800 to –2,200
ZSMNW235A	20	2.24E-06	6.91E-07	1.59E-07	4.92E-08	1.76E-08	5.44E-09	1.68E-09	5.20E-10	1.61E-10	4.97E-11
ZSMNW245A	23	1.94E-06	6.00E-07	1.38E-07	4.27E-08	1.53E-08	4.73E-09	1.46E-09	4.51E-10	1.39E-10	4.31E-11
ZSMNW247A	16	3.09E-07	1.13E-07	3.20E-08	1.17E-08	4.82E-09	1.76E-09	6.42E-10	2.34E-10	8.54E-11	3.11E-11
ZSMNW251A	20	2.50E-07	9.13E-08	2.59E-08	9.43E-09	3.90E-09	1.42E-09	5.19E-10	1.89E-10	6.91E-11	2.52E-11
ZSMNW254A	49	9.08E-07	2.81E-07	6.47E-08	2.00E-08	7.15E-09	2.21E-09	6.83E-10	2.11E-10	6.52E-11	2.02E-11
ZSMNW261A	22	2.01E-06	6.21E-07	1.43E-07	4.42E-08	1.58E-08	4.89E-09	1.51E-09	4.67E-10	1.44E-10	4.46E-11
ZSMNW263A	16	3.09E-07	1.13E-07	3.20E-08	1.17E-08	4.82E-09	1.76E-09	6.42E-10	2.34E-10	8.54E-11	3.11E-11
ZSMNW269A	21	2.11E-06	6.52E-07	1.50E-07	4.65E-08	1.66E-08	5.14E-09	1.59E-09	4.91E-10	1.52E-10	4.69E-11
ZSMNW280A	20	2.24E-06	6.91E-07	1.59E-07	4.92E-08	1.76E-08	5.44E-09	1.68E-09	5.20E-10	1.61E-10	4.96E-11
ZSMNW294A	23	1.97E-06	6.09E-07	1.40E-07	4.34E-08	1.55E-08	4.79E-09	1.48E-09	4.58E-10	1.41E-10	4.37E-11
ZSMNW312A	50	9.00E-07	2.78E-07	6.41E-08	1.98E-08	7.09E-09	2.19E-09	6.77E-10	2.09E-10	6.46E-11	2.00E-11
ZSMNW312B	12	4.04E-07	1.47E-07	4.17E-08	1.52E-08	6.30E-09	2.30E-09	8.38E-10	3.06E-10	1.11E-10	4.07E-11
ZSMNW312C	17	3.00E-07	1.09E-07	3.10E-08	1.13E-08	4.68E-09	1.71E-09	6.22E-10	2.27E-10	8.28E-11	3.02E-11
ZSMNW321A	21	2.17E-06	6.70E-07	1.54E-07	4.77E-08	1.71E-08	5.27E-09	1.63E-09	5.04E-10	1.56E-10	4.81E-11
ZSMNW322A	50	8.97E-07	2.77E-07	6.39E-08	1.97E-08	7.06E-09	2.18E-09	6.75E-10	2.08E-10	6.44E-11	1.99E-11
ZSMNW921A	25	1.76E-06	5.45E-07	1.26E-07	3.88E-08	1.39E-08	4.29E-09	1.33E-09	4.10E-10	1.27E-10	3.91E-11
ZSMNW922A	18	2.80E-07	1.02E-07	2.90E-08	1.06E-08	4.37E-09	1.59E-09	5.82E-10	2.12E-10	7.74E-11	2.82E-11
ZSMNW923A	37	1.20E-06	3.70E-07	8.53E-08	2.63E-08	9.43E-09	2.91E-09	9.00E-10	2.78E-10	8.60E-11	2.66E-11
ZSMNW925A	28	1.62E-06	4.99E-07	1.15E-07	3.55E-08	1.27E-08	3.93E-09	1.21E-09	3.75E-10	1.16E-10	3.58E-11
zsmnw928a	10	5.00E-07	1.82E-07	5.17E-08	1.88E-08	7.80E-09	2.84E-09	1.04E-09	3.78E-10	1.38E-10	5.04E-11
zsmnw929a	20	2.24E-06	6.93E-07	1.60E-07	4.93E-08	1.77E-08	5.46E-09	1.69E-09	5.21E-10	1.61E-10	4.98E-11
zsmnw931a	50	8.97E-07	2.77E-07	6.39E-08	1.97E-08	7.06E-09	2.18E-09	6.75E-10	2.08E-10	6.44E-11	1.99E-11
ZSMNW931B	38	1.19E-06	3.67E-07	8.44E-08	2.61E-08	9.34E-09	2.89E-09	8.92E-10	2.76E-10	8.52E-11	2.63E-11
ZSMNW933A	22	2.02E-06	6.24E-07	1.44E-07	4.44E-08	1.59E-08	4.92E-09	1.52E-09	4.69E-10	1.45E-10	4.48E-11
ZSMNW937A	17	2.88E-07	1.05E-07	2.97E-08	1.08E-08	4.49E-09	1.64E-09	5.97E-10	2.18E-10	7.94E-11	2.90E-11
ZSMNW943A	17	2.88E-07	1.05E-07	2.97E-08	1.08E-08	4.49E-09	1.64E-09	5.97E-10	2.18E-10	7.94E-11	2.90E-11

A6.3 Calculated and calibrated hydraulic properties for deformation zones, limited depth and 100 m intervals

In Table A6-3 the hydraulic properties are calculated for **100 m sections** using the depth trend functions and then adjusted as in the central **calibrated case**, but for a limited depth.

Table A6-3. Depth variation of hydraulic conductivity K (m/s) and the used thickness, bh (m), in HCD for elevation intervals used for groundwater flow and solute transport in the central calibration case in 100 m steps, but for a limited depth. All elevations are in m RHB 70.

Deformation zone	b_h (m)	Hydraulic conductivity K (m/s) for depth interval (m RHB 70)									
		0 to –100	–100 to –200	–200 to –300	–300 to –400	–400 to –500	–500 to –600	–600 to –700	–700 to –800	–800 to –900	–900 to –1,000
hlx28_dz1	10	5.67E-07	2.23E-07	6.20E-08	3.75E-08	2.26E-08	1.37E-08	5.50E-09	1.66E-09	1.00E-09	6.06E-10
klx03_dz1b	10	5.67E-07	2.23E-07	6.20E-08	3.75E-08	2.26E-08	1.37E-08	5.50E-09	1.66E-09	1.00E-09	6.06E-10
klx03_dz1c	10	5.67E-07	2.23E-07	6.20E-08	3.75E-08	2.26E-08	1.37E-08	5.50E-09	1.66E-09	1.00E-09	6.06E-10
klx04_dz6b	14	4.05E-07	1.59E-07	4.43E-08	2.68E-08	1.62E-08	9.76E-09	3.93E-09	1.19E-09	7.17E-10	4.33E-10
klx04_dz6c	30	1.89E-07	7.42E-08	2.07E-08	1.25E-08	7.54E-09	4.56E-09	1.83E-09	5.54E-10	3.34E-10	2.02E-10
klx07_dz10	10	5.67E-07	2.23E-07	6.20E-08	3.75E-08	2.26E-08	1.37E-08	5.50E-09	1.66E-09	1.00E-09	6.06E-10
klx07_dz11	30	1.89E-07	7.42E-08	2.07E-08	1.25E-08	7.54E-09	4.56E-09	1.83E-09	5.54E-10	3.34E-10	2.02E-10
klx07_dz12	47	1.21E-07	4.73E-08	1.32E-08	7.97E-09	4.81E-09	2.91E-09	1.17E-09	3.54E-10	2.14E-10	1.29E-10
klx07_dz13	10	5.67E-07	2.23E-07	6.20E-08	3.75E-08	2.26E-08	1.37E-08	5.50E-09	1.66E-09	1.00E-09	6.06E-10
klx07_dz7	30	1.89E-07	7.42E-08	2.07E-08	1.25E-08	7.54E-09	4.56E-09	1.83E-09	5.54E-10	3.34E-10	2.02E-10
klx07_dz9	10	5.67E-07	2.23E-07	6.20E-08	3.75E-08	2.26E-08	1.37E-08	5.50E-09	1.66E-09	1.00E-09	6.06E-10
klx08_dz1	27	2.10E-07	8.24E-08	2.30E-08	1.39E-08	8.38E-09	5.06E-09	2.04E-09	6.15E-10	3.72E-10	2.24E-10
klx08_dz10	11	5.15E-07	2.02E-07	5.64E-08	3.41E-08	2.06E-08	1.24E-08	5.00E-09	1.51E-09	9.12E-10	5.51E-10
klx08_dz6	10	5.67E-07	2.23E-07	6.20E-08	3.75E-08	2.26E-08	1.37E-08	5.50E-09	1.66E-09	1.00E-09	6.06E-10
klx09_dz10	25	2.27E-07	8.90E-08	2.48E-08	1.50E-08	9.05E-09	5.47E-09	2.20E-09	6.65E-10	4.01E-10	2.42E-10
klx09_dz14	9	6.77E-07	2.66E-07	7.41E-08	4.47E-08	2.70E-08	1.63E-08	6.57E-09	1.98E-09	1.20E-09	7.24E-10
klx09_dz9	6	6.18E-06	2.43E-06	6.76E-07	4.08E-07	2.47E-07	1.49E-07	6.00E-08	1.81E-08	1.09E-08	6.61E-09
klx09e_dz2	22	2.58E-07	1.01E-07	2.82E-08	1.70E-08	1.03E-08	6.21E-09	2.50E-09	7.55E-10	4.56E-10	2.75E-10
klx09f_dz1	14	4.05E-07	1.59E-07	4.43E-08	2.68E-08	1.62E-08	9.76E-09	3.93E-09	1.19E-09	7.17E-10	4.33E-10
klx10c_dz3	10	5.67E-07	2.23E-07	6.20E-08	3.75E-08	2.26E-08	1.37E-08	5.50E-09	1.66E-09	1.00E-09	6.06E-10
klx10c_dz7	10	5.67E-07	2.23E-07	6.20E-08	3.75E-08	2.26E-08	1.37E-08	5.50E-09	1.66E-09	1.00E-09	6.06E-10
klx11_dz11	20	2.83E-07	1.11E-07	3.10E-08	1.87E-08	1.13E-08	6.83E-09	2.75E-09	8.31E-10	5.02E-10	3.03E-10
klx16_dz6	1	6.13E-05	2.41E-05	6.71E-06	4.05E-06	2.45E-06	1.48E-06	5.95E-07	1.80E-07	1.08E-07	6.55E-08
klx18_dz9	10	5.67E-07	2.23E-07	6.20E-08	3.75E-08	2.26E-08	1.37E-08	5.50E-09	1.66E-09	1.00E-09	6.06E-10
klx19_dz2	4	1.61E-05	6.32E-06	1.76E-06	1.06E-06	6.43E-07	3.88E-07	1.56E-07	4.72E-08	2.85E-08	1.72E-08
klx19_dz5-8_dolerite	45	1.13E-06	4.45E-07	1.24E-07	7.49E-08	4.53E-08	2.73E-08	1.10E-08	3.32E-09	2.01E-09	1.21E-09
klx21b_dz10-12	10	5.67E-07	2.23E-07	6.20E-08	3.75E-08	2.26E-08	1.37E-08	5.50E-09	1.66E-09	1.00E-09	6.06E-10
klx28_dz1	13	4.36E-07	1.71E-07	4.77E-08	2.88E-08	1.74E-08	1.05E-08	4.23E-09	1.28E-09	7.72E-10	4.66E-10

Deformation zone (ZSM)	b_h (m)	Hydraulic conductivity K (m/s) for depth interval (m RHB 70)									
		0 to –100	–100 to –200	–200 to –300	–300 to –400	–400 to –500	–500 to –600	–600 to –700	–700 to –800	–800 to –900	–900 to –1,000
zsmew002a	50	1.44E-06	6.02E-07	1.80E-07	1.16E-07	7.48E-08	4.83E-08	2.08E-08	6.71E-09	4.34E-09	2.80E-09
zsmew007a	50	7.87E-05	2.87E-05	1.11E-05	3.55E-06	2.16E-07	1.31E-07	4.39E-08	4.86E-09	2.96E-09	1.80E-09
zsmew007c	50	1.93E-07	7.77E-08	2.22E-08	1.37E-08	8.47E-09	5.23E-09	2.16E-09	6.66E-10	4.12E-10	2.54E-10
ZSMEW009A	12	8.06E-07	3.24E-07	9.24E-08	5.71E-08	3.53E-08	2.18E-08	8.98E-09	2.78E-09	1.72E-09	1.06E-09
zsmew013a	45	1.60E-06	6.69E-07	1.99E-07	1.29E-07	8.32E-08	5.37E-08	2.31E-08	7.46E-09	4.82E-09	3.11E-09
zsmew014a	10	5.67E-07	2.23E-07	6.20E-08	3.75E-08	2.26E-08	1.37E-08	5.50E-09	1.66E-09	1.00E-09	6.06E-10
ZSMEW020A	50	1.44E-06	6.02E-07	1.80E-07	1.16E-07	7.48E-08	4.83E-08	2.08E-08	6.71E-09	4.34E-09	2.80E-09
ZSMEW038A	10	7.18E-06	3.01E-06	8.98E-07	5.80E-07	3.74E-07	2.42E-07	1.04E-07	3.36E-08	2.17E-08	1.40E-08
ZSMEW076A	31	2.29E-06	9.63E-07	2.87E-07	1.85E-07	1.20E-07	7.72E-08	3.32E-08	1.07E-08	6.93E-09	4.47E-09
ZSMEW114A	25	2.89E-06	1.21E-06	3.62E-07	2.34E-07	1.51E-07	9.74E-08	4.19E-08	1.35E-08	8.74E-09	5.64E-09
zsmew120a	50	1.93E-07	7.77E-08	2.22E-08	1.37E-08	8.47E-09	5.23E-09	2.16E-09	6.66E-10	4.12E-10	2.54E-10
ZSMEW129A	20	3.65E-06	1.53E-06	4.57E-07	2.95E-07	1.90E-07	1.23E-07	5.29E-08	1.71E-08	1.10E-08	7.12E-09
ZSMEW190A	17	5.84E-07	2.34E-07	6.69E-08	4.13E-08	2.55E-08	1.58E-08	6.50E-09	2.01E-09	1.24E-09	7.68E-10
ZSMEW200A	17	5.54E-07	2.22E-07	6.35E-08	3.92E-08	2.42E-08	1.50E-08	6.17E-09	1.91E-09	1.18E-09	7.28E-10
ZSMEW230A	18	5.36E-07	2.15E-07	6.14E-08	3.79E-08	2.35E-08	1.45E-08	5.97E-09	1.85E-09	1.14E-09	7.05E-10
ZSMEW240A	50	1.44E-06	6.02E-07	1.80E-07	1.16E-07	7.48E-08	4.83E-08	2.08E-08	6.71E-09	4.34E-09	2.80E-09
ZSMEW305A	19	5.04E-07	2.02E-07	5.77E-08	3.57E-08	2.21E-08	1.36E-08	5.62E-09	1.74E-09	1.07E-09	6.63E-10
zsmew316a	30	2.39E-06	1.00E-06	2.99E-07	1.93E-07	1.25E-07	8.05E-08	3.47E-08	1.12E-08	7.23E-09	4.67E-09
zsmew900a	25	2.27E-07	8.90E-08	2.48E-08	1.50E-08	9.05E-09	5.47E-09	2.20E-09	6.65E-10	4.01E-10	2.42E-10
zsmew900b	25	2.27E-07	8.90E-08	2.48E-08	1.50E-08	9.05E-09	5.47E-09	2.20E-09	6.65E-10	4.01E-10	2.42E-10
ZSMEW904A	50	1.44E-06	6.02E-07	1.80E-07	1.16E-07	7.48E-08	4.83E-08	2.08E-08	6.71E-09	4.34E-09	2.80E-09
ZSMEW905A	21	3.39E-06	1.42E-06	4.24E-07	2.74E-07	1.77E-07	1.14E-07	4.91E-08	1.59E-08	1.02E-08	6.61E-09
ZSMEW906A	50	1.44E-06	6.02E-07	1.80E-07	1.16E-07	7.48E-08	4.83E-08	2.08E-08	6.71E-09	4.34E-09	2.80E-09
ZSMEW907A	50	1.44E-06	6.02E-07	1.80E-07	1.16E-07	7.48E-08	4.83E-08	2.08E-08	6.71E-09	4.34E-09	2.80E-09
ZSMEW936A	11	8.75E-07	3.52E-07	1.00E-07	6.20E-08	3.83E-08	2.37E-08	9.75E-09	3.01E-09	1.86E-09	1.15E-09
zsmew946a	10	3.61E-06	8.08E-07	1.28E-07	4.40E-08	1.51E-08	5.20E-09	1.19E-09	2.05E-10	7.04E-11	2.42E-11

Deformation zone (ZSM)	b_h (m)	Hydraulic conductivity K (m/s) for depth interval (m RHB 70)									
		0 to –100	–100 to –200	–200 to –300	–300 to–400	–400 to –500	–500 to –600	–600 to –700	–700 to –800	–800 to –900	–900 to –1,000
zsmne004a	50	1.04E-06	3.75E-07	9.63E-08	5.35E-08	2.98E-08	1.65E-08	6.13E-09	1.70E-09	9.47E-10	5.27E-10
zsmne005a	50	1.04E-06	3.75E-07	9.63E-08	5.35E-08	2.98E-08	1.65E-08	6.13E-09	1.70E-09	9.47E-10	5.27E-10
zsmne006a	50	1.35E-05	4.28E-06	9.66E-07	4.73E-07	2.31E-07	1.13E-07	3.69E-08	9.04E-09	4.42E-09	2.16E-09
ZSMNE008A	39	1.33E-06	4.80E-07	1.23E-07	6.85E-08	3.81E-08	2.12E-08	7.84E-09	2.18E-09	1.21E-09	6.73E-10
ZSMNE010A	34	1.52E-06	5.48E-07	1.41E-07	7.82E-08	4.35E-08	2.42E-08	8.96E-09	2.49E-09	1.38E-09	7.69E-10
zsmne011a	50	1.04E-06	3.75E-07	9.63E-08	5.35E-08	2.98E-08	1.65E-08	6.13E-09	1.70E-09	9.47E-10	5.27E-10
zsmne012a	50	3.29E-06	1.29E-06	3.57E-07	2.15E-07	1.29E-07	7.77E-08	3.11E-08	9.36E-09	5.63E-09	3.38E-09
zsmne015a	10	5.67E-07	2.23E-07	6.20E-08	3.75E-08	2.26E-08	1.37E-08	5.50E-09	1.66E-09	1.00E-09	6.06E-10
zsmne018a	50	1.13E-07	4.45E-08	1.24E-08	7.49E-09	4.53E-09	2.73E-09	1.10E-09	3.32E-10	2.01E-10	1.21E-10
zsmne019a	20	2.60E-06	9.38E-07	2.41E-07	1.34E-07	7.44E-08	4.14E-08	1.53E-08	4.26E-09	2.37E-09	1.32E-09
zsmne021a	40	1.30E-06	4.69E-07	1.20E-07	6.69E-08	3.72E-08	2.07E-08	7.66E-09	2.13E-09	1.18E-09	6.58E-10
zsmne022a	28	1.86E-06	6.72E-07	1.72E-07	9.59E-08	5.33E-08	2.96E-08	1.10E-08	3.05E-09	1.70E-09	9.43E-10
ZSMNE024A	50	5.10E-05	6.32E-06	5.56E-07	1.06E-07	2.02E-08	3.85E-09	4.90E-10	4.67E-11	1.00E-11	1.00E-11
ZSMNE024B	16	1.60E-04	1.98E-05	1.75E-06	3.33E-07	6.35E-08	1.21E-08	1.54E-09	1.47E-10	2.80E-11	1.00E-11
ZSMNE031A	15	3.46E-06	1.25E-06	3.21E-07	1.78E-07	9.92E-08	5.51E-08	2.04E-08	5.68E-09	3.16E-09	1.76E-09
ZSMNE031B	19	3.00E-07	1.18E-07	3.28E-08	1.98E-08	1.20E-08	7.23E-09	2.91E-09	8.79E-10	5.31E-10	3.20E-10
ZSMNE032A	26	1.97E-06	7.12E-07	1.83E-07	1.02E-07	5.65E-08	3.14E-08	1.16E-08	3.23E-09	1.80E-09	9.99E-10
ZSMNE033A	30	1.74E-06	6.30E-07	1.62E-07	8.98E-08	4.99E-08	2.78E-08	1.03E-08	2.86E-09	1.59E-09	8.84E-10
ZSMNE034A	29	1.79E-06	6.48E-07	1.66E-07	9.25E-08	5.14E-08	2.86E-08	1.06E-08	2.94E-09	1.64E-09	9.10E-10
ZSMNE036A	23	2.25E-06	8.13E-07	2.09E-07	1.16E-07	6.44E-08	3.58E-08	1.33E-08	3.69E-09	2.05E-09	1.14E-09
zsmne040a	20	2.83E-07	1.11E-07	3.10E-08	1.87E-08	1.13E-08	6.83E-09	2.75E-09	8.31E-10	5.02E-10	3.03E-10
ZSMNE062A	17	3.37E-07	1.32E-07	3.68E-08	2.23E-08	1.34E-08	8.12E-09	3.27E-09	9.87E-10	5.96E-10	3.60E-10
zsmne063a	10	5.67E-07	2.23E-07	6.20E-08	3.75E-08	2.26E-08	1.37E-08	5.50E-09	1.66E-09	1.00E-09	6.06E-10
zsmne065a	10	5.67E-07	2.23E-07	6.20E-08	3.75E-08	2.26E-08	1.37E-08	5.50E-09	1.66E-09	1.00E-09	6.06E-10
ZSMNE073A	36	1.44E-06	5.19E-07	1.33E-07	7.41E-08	4.12E-08	2.29E-08	8.48E-09	2.36E-09	1.31E-09	7.29E-10
zsmne079a	10	5.19E-06	1.88E-06	4.82E-07	2.68E-07	1.49E-07	8.27E-08	3.07E-08	8.52E-09	4.74E-09	2.63E-09
ZSMNE081A	21	2.53E-06	9.13E-07	2.34E-07	1.30E-07	7.24E-08	4.02E-08	1.49E-08	4.14E-09	2.30E-09	1.28E-09
ZSMNE095A	23	2.27E-06	8.21E-07	2.11E-07	1.17E-07	6.51E-08	3.62E-08	1.34E-08	3.73E-09	2.07E-09	1.15E-09
ZSMNE096A	17	3.29E-07	1.29E-07	3.61E-08	2.18E-08	1.32E-08	7.94E-09	3.20E-09	9.66E-10	5.83E-10	3.52E-10
zsmne107a	35	1.48E-05	5.36E-06	2.61E-06	7.65E-07	4.25E-08	2.36E-08	8.76E-09	2.43E-09	1.35E-09	7.52E-10
zsmne108a	10	5.67E-07	2.23E-07	6.20E-08	3.75E-08	2.26E-08	1.37E-08	5.50E-09	1.66E-09	1.00E-09	6.06E-10

Deformation zone (ZSM)	b_h (m)	Hydraulic conductivity K (m/s) for depth interval (m RHB 70)									
		0 to –100	–100 to –200	–200 to –300	–300 to–400	–400 to –500	–500 to –600	–600 to –700	–700 to –800	–800 to –900	–900 to –1,000
ZSMNE132A	28	1.87E-06	6.74E-07	1.73E-07	9.61E-08	5.34E-08	2.97E-08	1.10E-08	3.06E-09	1.70E-09	9.46E-10
ZSMNE133A	24	2.13E-06	7.70E-07	1.98E-07	1.10E-07	6.11E-08	3.39E-08	1.26E-08	3.50E-09	1.94E-09	1.08E-09
ZSMNE185A	24	2.18E-06	7.89E-07	2.02E-07	1.13E-07	6.26E-08	3.48E-08	1.29E-08	3.58E-09	1.99E-09	1.11E-09
ZSMNE210A	21	2.44E-06	8.81E-07	2.26E-07	1.26E-07	6.99E-08	3.88E-08	1.44E-08	4.00E-09	2.22E-09	1.24E-09
ZSMNE210B	28	1.88E-06	6.78E-07	1.74E-07	9.67E-08	5.37E-08	2.99E-08	1.11E-08	3.08E-09	1.71E-09	9.51E-10
ZSMNE218A	50	1.04E-06	3.75E-07	9.63E-08	5.35E-08	2.98E-08	1.65E-08	6.13E-09	1.70E-09	9.47E-10	5.27E-10
ZSMNE229A	20	2.59E-06	9.36E-07	2.40E-07	1.34E-07	7.42E-08	4.13E-08	1.53E-08	4.25E-09	2.36E-09	1.31E-09
ZSMNE257A	27	1.93E-06	6.99E-07	1.79E-07	9.96E-08	5.54E-08	3.08E-08	1.14E-08	3.17E-09	1.76E-09	9.80E-10
ZSMNE258A	26	1.98E-06	7.17E-07	1.84E-07	1.02E-07	5.69E-08	3.16E-08	1.17E-08	3.26E-09	1.81E-09	1.01E-09
ZSMNE259A	28	1.84E-06	6.66E-07	1.71E-07	9.49E-08	5.28E-08	2.93E-08	1.09E-08	3.02E-09	1.68E-09	9.34E-10
ZSMNE267A	23	2.30E-06	8.32E-07	2.13E-07	1.19E-07	6.59E-08	3.67E-08	1.36E-08	3.78E-09	2.10E-09	1.17E-09
ZSMNE286A	27	1.94E-06	7.00E-07	1.80E-07	9.99E-08	5.55E-08	3.09E-08	1.14E-08	3.18E-09	1.77E-09	9.83E-10
ZSMNE289A	21	2.44E-06	8.82E-07	2.26E-07	1.26E-07	6.99E-08	3.89E-08	1.44E-08	4.00E-09	2.23E-09	1.24E-09
ZSMNE295A	31	1.66E-06	6.00E-07	1.54E-07	8.55E-08	4.75E-08	2.64E-08	9.80E-09	2.72E-09	1.51E-09	8.41E-10
ZSMNE302A	24	2.13E-06	7.69E-07	1.97E-07	1.10E-07	6.09E-08	3.39E-08	1.26E-08	3.49E-09	1.94E-09	1.08E-09
ZSMNE307A	18	3.17E-07	1.24E-07	3.47E-08	2.09E-08	1.26E-08	7.64E-09	3.08E-09	9.29E-10	5.61E-10	3.39E-10
ZSMNE308A	24	2.14E-06	7.74E-07	1.99E-07	1.10E-07	6.14E-08	3.41E-08	1.26E-08	3.52E-09	1.95E-09	1.09E-09
ZSMNE313A	50	1.04E-06	3.75E-07	9.63E-08	5.35E-08	2.98E-08	1.65E-08	6.13E-09	1.70E-09	9.47E-10	5.27E-10
ZSMNE901A	25	2.06E-06	7.45E-07	1.91E-07	1.06E-07	5.91E-08	3.28E-08	1.22E-08	3.38E-09	1.88E-09	1.05E-09
ZSMNE903A	25	2.10E-06	7.59E-07	1.95E-07	1.08E-07	6.02E-08	3.35E-08	1.24E-08	3.45E-09	1.92E-09	1.07E-09
ZSMNE909A	17	3.29E-07	1.29E-07	3.60E-08	2.17E-08	1.31E-08	7.93E-09	3.19E-09	9.64E-10	5.82E-10	3.52E-10
ZSMNE910A	22	2.38E-06	8.59E-07	2.20E-07	1.23E-07	6.81E-08	3.79E-08	1.40E-08	3.90E-09	2.17E-09	1.21E-09
ZSMNE911A	50	1.04E-06	3.75E-07	9.63E-08	5.35E-08	2.98E-08	1.65E-08	6.13E-09	1.70E-09	9.47E-10	5.27E-10
ZSMNE912A	31	1.69E-06	6.09E-07	1.56E-07	8.69E-08	4.83E-08	2.68E-08	9.95E-09	2.77E-09	1.54E-09	8.55E-10
ZSMNE913A	50	1.04E-06	3.75E-07	9.63E-08	5.35E-08	2.98E-08	1.65E-08	6.13E-09	1.70E-09	9.47E-10	5.27E-10
ZSMNE914A	50	1.04E-06	3.75E-07	9.63E-08	5.35E-08	2.98E-08	1.65E-08	6.13E-09	1.70E-09	9.47E-10	5.27E-10
ZSMNE915A	19	2.91E-07	1.14E-07	3.19E-08	1.92E-08	1.16E-08	7.02E-09	2.83E-09	8.53E-10	5.15E-10	3.11E-10
zsmne930a	5	1.04E-05	3.75E-06	9.63E-07	5.35E-07	2.98E-07	1.65E-07	6.13E-08	1.70E-08	9.47E-09	5.27E-09
ZSMNE940A	16	3.48E-07	1.37E-07	3.81E-08	2.30E-08	1.39E-08	8.40E-09	3.38E-09	1.02E-09	6.17E-10	3.73E-10
ZSMNE941A	22	2.39E-06	8.63E-07	2.21E-07	1.23E-07	6.84E-08	3.80E-08	1.41E-08	3.92E-09	2.18E-09	1.21E-09
zsmne942a	15	1.40E-06	5.21E-07	1.38E-07	7.95E-08	4.57E-08	2.63E-08	1.01E-08	2.89E-09	1.66E-09	9.55E-10
zsmne944a	10	5.67E-07	2.23E-07	1.03E-07	3.75E-08	7.54E-09	4.56E-09	2.75E-09	1.66E-09	1.00E-09	6.06E-10

Deformation zone (ZSM)	b_h (m)	Hydraulic conductivity K (m/s) for depth interval (m RHB 70)									
		0 to –100	–100 to –200	–200 to –300	–300 to –400	–400 to –500	–500 to –600	–600 to –700	–700 to –800	–800 to –900	–900 to –1,000
zsmns001a	50	3.17E-06	1.18E-06	3.14E-07	1.80E-07	1.04E-07	5.96E-08	2.28E-08	6.56E-09	3.77E-09	2.17E-09
zsmns001b	50	3.17E-06	1.18E-06	3.14E-07	1.80E-07	1.04E-07	5.96E-08	2.28E-08	6.56E-09	3.77E-09	2.17E-09
zsmns001c	50	9.50E-06	3.64E-06	1.78E-06	6.01E-07	1.04E-07	5.96E-08	2.28E-08	6.56E-09	3.77E-09	2.17E-09
zsmns001d	50	3.17E-06	1.18E-06	3.14E-07	1.80E-07	1.04E-07	5.96E-08	2.28E-08	6.56E-09	3.77E-09	2.17E-09
zsmns001e	50	3.17E-06	1.18E-06	3.14E-07	1.80E-07	1.04E-07	5.96E-08	2.28E-08	6.56E-09	3.77E-09	2.17E-09
ZSMNS009A	25	2.08E-06	7.51E-07	1.93E-07	1.07E-07	5.95E-08	3.31E-08	1.23E-08	3.41E-09	1.89E-09	1.05E-09
ZSMNS017A	21	2.50E-06	9.04E-07	2.32E-07	1.29E-07	7.17E-08	3.98E-08	1.48E-08	4.10E-09	2.28E-09	1.27E-09
ZSMNS017B	20	2.18E-05	8.15E-06	2.16E-06	1.24E-06	7.14E-07	4.11E-07	1.57E-07	4.52E-08	2.60E-08	1.49E-08
zsmns046a	20	2.60E-06	9.38E-07	2.41E-07	1.34E-07	7.44E-08	4.14E-08	1.53E-08	4.26E-09	2.37E-09	1.32E-09
zsmns057a	20	2.60E-06	9.38E-07	2.41E-07	1.34E-07	7.44E-08	4.14E-08	1.53E-08	4.26E-09	2.37E-09	1.32E-09
zsmns059a	50	3.38E-06	1.26E-06	3.35E-07	1.92E-07	1.11E-07	6.36E-08	2.44E-08	7.00E-09	4.02E-09	2.31E-09
ZSMNS064A	50	1.04E-06	3.75E-07	9.63E-08	5.35E-08	2.98E-08	1.65E-08	6.13E-09	1.70E-09	9.47E-10	5.27E-10
ZSMNS071A	18	3.07E-07	1.21E-07	3.36E-08	2.03E-08	1.23E-08	7.41E-09	2.98E-09	9.01E-10	5.44E-10	3.29E-10
ZSMNS084A	32	1.62E-06	5.87E-07	1.51E-07	8.37E-08	4.65E-08	2.59E-08	9.58E-09	2.66E-09	1.48E-09	8.23E-10
ZSMNS085A	37	1.41E-06	5.08E-07	1.30E-07	7.25E-08	4.03E-08	2.24E-08	8.31E-09	2.31E-09	1.28E-09	7.13E-10
ZSMNS117A	17	3.38E-07	1.33E-07	3.70E-08	2.24E-08	1.35E-08	8.15E-09	3.28E-09	9.91E-10	5.99E-10	3.62E-10
zsmns141a	20	2.60E-06	9.38E-07	2.41E-07	1.34E-07	7.44E-08	4.14E-08	1.53E-08	4.26E-09	2.37E-09	1.32E-09
ZSMNS165A	18	3.18E-07	1.25E-07	3.48E-08	2.10E-08	1.27E-08	7.67E-09	3.09E-09	9.33E-10	5.63E-10	3.40E-10
ZSMNS182A	30	1.73E-06	6.26E-07	1.61E-07	8.93E-08	4.97E-08	2.76E-08	1.02E-08	2.84E-09	1.58E-09	8.79E-10
ZSMNS182B	30	1.72E-06	6.21E-07	1.59E-07	8.86E-08	4.93E-08	2.74E-08	1.01E-08	2.82E-09	1.57E-09	8.72E-10
ZSMNS215A	16	3.50E-07	1.37E-07	3.83E-08	2.31E-08	1.40E-08	8.43E-09	3.39E-09	1.02E-09	6.19E-10	3.74E-10
ZSMNS221A	22	2.35E-06	8.49E-07	2.18E-07	1.21E-07	6.73E-08	3.74E-08	1.39E-08	3.86E-09	2.14E-09	1.19E-09
ZSMNS287A	34	1.53E-06	5.53E-07	1.42E-07	7.88E-08	4.38E-08	2.44E-08	9.03E-09	2.51E-09	1.39E-09	7.75E-10
ZSMNS291A	19	3.00E-07	1.18E-07	3.28E-08	1.98E-08	1.20E-08	7.23E-09	2.91E-09	8.79E-10	5.31E-10	3.20E-10
ZSMNS301A	19	3.03E-07	1.19E-07	3.31E-08	2.00E-08	1.21E-08	7.30E-09	2.94E-09	8.87E-10	5.36E-10	3.24E-10
ZSMNS916A	44	1.19E-06	4.31E-07	1.11E-07	6.15E-08	3.42E-08	1.90E-08	7.05E-09	1.96E-09	1.09E-09	6.05E-10
ZSMNS917A	50	1.04E-06	3.75E-07	9.63E-08	5.35E-08	2.98E-08	1.65E-08	6.13E-09	1.70E-09	9.47E-10	5.27E-10
ZSMNS918A	29	1.81E-06	6.54E-07	1.68E-07	9.33E-08	5.19E-08	2.88E-08	1.07E-08	2.97E-09	1.65E-09	9.18E-10
ZSMNS919A	50	1.04E-06	3.75E-07	9.63E-08	5.35E-08	2.98E-08	1.65E-08	6.13E-09	1.70E-09	9.47E-10	5.27E-10
ZSMNS920A	31	1.69E-06	6.12E-07	1.57E-07	8.72E-08	4.85E-08	2.70E-08	9.99E-09	2.78E-09	1.54E-09	8.58E-10
zsmns945a	10	5.19E-06	1.88E-06	4.82E-07	2.68E-07	1.49E-07	8.27E-08	3.07E-08	8.52E-09	4.74E-09	2.63E-09
zsmns947a	20	2.83E-07	1.11E-07	3.10E-08	1.87E-08	1.13E-08	6.83E-09	2.75E-09	8.31E-10	5.02E-10	3.03E-10

Deformation zone (ZSM)	b_h (m)	Hydraulic conductivity K (m/s) for depth interval (m RHB 70)									
		0 to –100	–100 to –200	–200 to –300	–300 to –400	–400 to –500	–500 to –600	–600 to –700	–700 to –800	–800 to –900	–900 to –1,000
ZSMNW025A	10	5.67E-07	2.23E-07	6.20E-08	3.75E-08	2.26E-08	1.37E-08	5.50E-09	1.66E-09	1.00E-09	6.06E-10
ZSMNW027A	34	1.52E-06	5.48E-07	1.40E-07	7.81E-08	4.34E-08	2.41E-08	8.94E-09	2.49E-09	1.38E-09	7.68E-10
zsmnw042a-east	50	1.04E-06	3.75E-07	9.63E-08	5.35E-08	2.98E-08	1.65E-08	6.13E-09	1.70E-09	9.47E-10	5.27E-10
zsmnw042a-west	50	1.04E-06	3.75E-07	9.63E-08	5.35E-08	2.98E-08	1.65E-08	6.13E-09	1.70E-09	9.47E-10	5.27E-10
zsmnw047a	25	2.27E-07	8.90E-08	2.48E-08	1.50E-08	9.05E-09	5.47E-09	2.20E-09	6.65E-10	4.01E-10	2.42E-10
zsmnw052a	15	3.78E-07	1.48E-07	4.14E-08	2.50E-08	1.51E-08	9.11E-09	3.67E-09	1.11E-09	6.69E-10	4.04E-10
ZSMNW060A	32	1.61E-06	5.81E-07	1.49E-07	8.28E-08	4.60E-08	2.56E-08	9.48E-09	2.64E-09	1.47E-09	8.15E-10
ZSMNW066A	50	1.04E-06	3.75E-07	9.63E-08	5.35E-08	2.98E-08	1.65E-08	6.13E-09	1.70E-09	9.47E-10	5.27E-10
ZSMNW067A	50	1.04E-06	3.75E-07	9.63E-08	5.35E-08	2.98E-08	1.65E-08	6.13E-09	1.70E-09	9.47E-10	5.27E-10
ZSMNW068A	18	3.16E-07	1.24E-07	3.46E-08	2.09E-08	1.26E-08	7.62E-09	3.07E-09	9.26E-10	5.60E-10	3.38E-10
ZSMNW068B	22	2.36E-06	8.53E-07	2.19E-07	1.22E-07	6.77E-08	3.76E-08	1.39E-08	3.88E-09	2.15E-09	1.20E-09
ZSMNW068C	4	1.29E-06	5.07E-07	1.41E-07	8.54E-08	5.16E-08	3.11E-08	1.25E-08	3.79E-09	2.29E-09	1.38E-09
ZSMNW074A	33	1.57E-06	5.67E-07	1.45E-07	8.09E-08	4.49E-08	2.50E-08	9.26E-09	2.57E-09	1.43E-09	7.95E-10
ZSMNW075A	38	1.35E-06	4.89E-07	1.26E-07	6.98E-08	3.88E-08	2.16E-08	7.99E-09	2.22E-09	1.24E-09	6.87E-10
ZSMNW083A	16	3.44E-07	1.35E-07	3.76E-08	2.27E-08	1.37E-08	8.29E-09	3.34E-09	1.01E-09	6.09E-10	3.68E-10
ZSMNW086A	22	2.36E-06	8.53E-07	2.19E-07	1.22E-07	6.77E-08	3.76E-08	1.39E-08	3.87E-09	2.15E-09	1.20E-09
zsmnw088a	20	2.60E-06	9.38E-07	2.41E-07	1.34E-07	7.44E-08	4.14E-08	1.53E-08	4.26E-09	2.37E-09	1.32E-09
ZSMNW089A	21	2.43E-06	8.78E-07	2.25E-07	1.25E-07	6.96E-08	3.87E-08	1.43E-08	3.99E-09	2.22E-09	1.23E-09
ZSMNW106A	17	3.32E-07	1.30E-07	3.63E-08	2.19E-08	1.33E-08	8.01E-09	3.22E-09	9.73E-10	5.88E-10	3.55E-10
ZSMNW113A	30	1.70E-06	6.15E-07	1.58E-07	8.78E-08	4.88E-08	2.71E-08	1.01E-08	2.79E-09	1.55E-09	8.63E-10
zsmnw119a	10	5.19E-06	1.88E-06	4.82E-07	2.68E-07	1.49E-07	8.27E-08	3.07E-08	8.52E-09	4.74E-09	2.63E-09
ZSMNW123A	32	1.61E-06	5.80E-07	1.49E-07	8.28E-08	4.60E-08	2.56E-08	9.48E-09	2.63E-09	1.46E-09	8.14E-10
ZSMNW126A	37	1.42E-06	5.14E-07	1.32E-07	7.32E-08	4.07E-08	2.26E-08	8.39E-09	2.33E-09	1.30E-09	7.21E-10
ZSMNW126B	36	1.46E-06	5.27E-07	1.35E-07	7.51E-08	4.18E-08	2.32E-08	8.60E-09	2.39E-09	1.33E-09	7.39E-10
ZSMNW131A	50	1.04E-06	3.75E-07	9.63E-08	5.35E-08	2.98E-08	1.65E-08	6.13E-09	1.70E-09	9.47E-10	5.27E-10
ZSMNW173A	21	2.45E-06	8.84E-07	2.27E-07	1.26E-07	7.01E-08	3.90E-08	1.44E-08	4.01E-09	2.23E-09	1.24E-09
ZSMNW178A	41	1.25E-06	4.53E-07	1.16E-07	6.47E-08	3.59E-08	2.00E-08	7.41E-09	2.06E-09	1.14E-09	6.36E-10
ZSMNW184A	16	3.44E-07	1.35E-07	3.76E-08	2.27E-08	1.37E-08	8.29E-09	3.34E-09	1.01E-09	6.09E-10	3.68E-10
ZSMNW202A	16	3.49E-07	1.37E-07	3.82E-08	2.31E-08	1.39E-08	8.42E-09	3.39E-09	1.02E-09	6.18E-10	3.73E-10
ZSMNW206A	19	3.05E-07	1.20E-07	3.34E-08	2.02E-08	1.22E-08	7.35E-09	2.96E-09	8.94E-10	5.40E-10	3.26E-10

Deformation zone (ZSM)	b_h (m)	Hydraulic conductivity K (m/s) for depth interval (m RHB 70)									
		0 to –100	–100 to –200	–200 to –300	–300 to –400	–400 to –500	–500 to –600	–600 to –700	–700 to –800	–800 to –900	–900 to –1,000
ZSMNW222A	27	1.93E-06	6.99E-07	1.79E-07	9.97E-08	5.54E-08	3.08E-08	1.14E-08	3.17E-09	1.76E-09	9.81E-10
ZSMNW233A	19	2.93E-07	1.15E-07	3.21E-08	1.94E-08	1.17E-08	7.07E-09	2.85E-09	8.59E-10	5.19E-10	3.13E-10
ZSMNW235A	20	2.59E-06	9.36E-07	2.40E-07	1.34E-07	7.42E-08	4.13E-08	1.53E-08	4.25E-09	2.36E-09	1.31E-09
ZSMNW245A	23	2.25E-06	8.13E-07	2.09E-07	1.16E-07	6.44E-08	3.58E-08	1.33E-08	3.69E-09	2.05E-09	1.14E-09
ZSMNW247A	16	3.51E-07	1.38E-07	3.84E-08	2.32E-08	1.40E-08	8.45E-09	3.40E-09	1.03E-09	6.21E-10	3.75E-10
ZSMNW251A	20	2.84E-07	1.11E-07	3.11E-08	1.88E-08	1.13E-08	6.84E-09	2.75E-09	8.32E-10	5.02E-10	3.03E-10
ZSMNW254A	49	1.05E-06	3.80E-07	9.75E-08	5.42E-08	3.01E-08	1.67E-08	6.21E-09	1.73E-09	9.59E-10	5.33E-10
ZSMNW261A	22	2.33E-06	8.41E-07	2.16E-07	1.20E-07	6.67E-08	3.71E-08	1.37E-08	3.82E-09	2.12E-09	1.18E-09
ZSMNW263A	16	3.51E-07	1.38E-07	3.84E-08	2.32E-08	1.40E-08	8.45E-09	3.40E-09	1.03E-09	6.21E-10	3.75E-10
ZSMNW269A	21	2.45E-06	8.84E-07	2.27E-07	1.26E-07	7.01E-08	3.89E-08	1.44E-08	4.01E-09	2.23E-09	1.24E-09
ZSMNW280A	20	2.59E-06	9.36E-07	2.40E-07	1.33E-07	7.42E-08	4.13E-08	1.53E-08	4.25E-09	2.36E-09	1.31E-09
ZSMNW294A	23	2.28E-06	8.24E-07	2.12E-07	1.18E-07	6.54E-08	3.63E-08	1.35E-08	3.74E-09	2.08E-09	1.16E-09
ZSMNW312A	50	1.04E-06	3.77E-07	9.66E-08	5.37E-08	2.99E-08	1.66E-08	6.15E-09	1.71E-09	9.50E-10	5.28E-10
ZSMNW312B	12	4.58E-07	1.80E-07	5.01E-08	3.03E-08	1.83E-08	1.10E-08	4.44E-09	1.34E-09	8.10E-10	4.89E-10
ZSMNW312C	17	3.40E-07	1.33E-07	3.72E-08	2.25E-08	1.36E-08	8.20E-09	3.30E-09	9.97E-10	6.02E-10	3.64E-10
ZSMNW321A	21	2.51E-06	9.07E-07	2.33E-07	1.29E-07	7.19E-08	4.00E-08	1.48E-08	4.12E-09	2.29E-09	1.27E-09
ZSMNW322A	50	1.04E-06	3.75E-07	9.63E-08	5.35E-08	2.98E-08	1.65E-08	6.13E-09	1.70E-09	9.47E-10	5.27E-10
ZSMNW921A	25	2.04E-06	7.38E-07	1.89E-07	1.05E-07	5.85E-08	3.25E-08	1.21E-08	3.35E-09	1.86E-09	1.04E-09
ZSMNW922A	18	3.18E-07	1.25E-07	3.48E-08	2.10E-08	1.27E-08	7.66E-09	3.08E-09	9.32E-10	5.63E-10	3.40E-10
ZSMNW923A	37	1.39E-06	5.01E-07	1.29E-07	7.15E-08	3.97E-08	2.21E-08	8.18E-09	2.27E-09	1.26E-09	7.03E-10
ZSMNW925A	28	1.87E-06	6.76E-07	1.73E-07	9.64E-08	5.36E-08	2.98E-08	1.10E-08	3.07E-09	1.71E-09	9.48E-10
zsmnw928a	10	5.67E-07	2.23E-07	6.20E-08	3.75E-08	2.26E-08	1.37E-08	5.50E-09	1.66E-09	1.00E-09	6.06E-10
zsmnw929a	20	2.60E-06	9.38E-07	2.41E-07	1.34E-07	7.44E-08	4.14E-08	1.53E-08	4.26E-09	2.37E-09	1.32E-09
zsmnw931a	50	1.04E-06	3.75E-07	9.63E-08	5.35E-08	2.98E-08	1.65E-08	6.13E-09	1.70E-09	9.47E-10	5.27E-10
ZSMNW931B	38	1.37E-06	4.96E-07	1.27E-07	7.08E-08	3.94E-08	2.19E-08	8.11E-09	2.25E-09	1.25E-09	6.96E-10
ZSMNW933A	22	2.34E-06	8.45E-07	2.17E-07	1.21E-07	6.70E-08	3.73E-08	1.38E-08	3.84E-09	2.13E-09	1.19E-09
ZSMNW937A	17	3.26E-07	1.28E-07	3.57E-08	2.16E-08	1.30E-08	7.86E-09	3.17E-09	9.56E-10	5.77E-10	3.49E-10
ZSMNW943A	17	3.26E-07	1.28E-07	3.57E-08	2.16E-08	1.30E-08	7.86E-09	3.17E-09	9.56E-10	5.77E-10	3.49E-10

A6.4 Calculated properties of deformation zones before calibration for limited model depth and 100 m intervals

In Table A6-4, the **initial hydraulic properties before calibration** are calculated for **100 m sections** using the depth trend functions for a limited model depth.

Table A6-4. Depth variation of hydraulic conductivity K (m/s) and the used thickness, bh (m), in HCD for elevation intervals used for groundwater flow and solute transport in the central case before calibration. Values calculated for 100 m sections. All elevations are in m RHB 70.

Deformation zone	b_h (m)	Hydraulic conductivity K (m/s) for depth interval (m RHB 70)									
		0 to –100	–100 to –200	–200 to –300	–300 to –400	–400 to –500	–500 to –600	–600 to –700	–700 to –800	–800 to –900	–900 to –1,000
hlx28_dz1	10	5.67E-07	3.42E-07	2.07E-07	1.25E-07	7.54E-08	4.56E-08	2.75E-08	1.66E-08	1.00E-08	6.06E-09
klx03_dz1b	10	5.67E-07	3.42E-07	2.07E-07	1.25E-07	7.54E-08	4.56E-08	2.75E-08	1.66E-08	1.00E-08	6.06E-09
klx03_dz1c	10	5.67E-07	3.42E-07	2.07E-07	1.25E-07	7.54E-08	4.56E-08	2.75E-08	1.66E-08	1.00E-08	6.06E-09
klx04_dz6b	14	4.05E-07	2.45E-07	1.48E-07	8.92E-08	5.39E-08	3.25E-08	1.97E-08	1.19E-08	7.17E-09	4.33E-09
klx04_dz6c	30	1.89E-07	1.14E-07	6.89E-08	4.16E-08	2.51E-08	1.52E-08	9.17E-09	5.54E-09	3.34E-09	2.02E-09
klx07_dz10	10	5.67E-07	3.42E-07	2.07E-07	1.25E-07	7.54E-08	4.56E-08	2.75E-08	1.66E-08	1.00E-08	6.06E-09
klx07_dz11	30	1.89E-07	1.14E-07	6.89E-08	4.16E-08	2.51E-08	1.52E-08	9.17E-09	5.54E-09	3.34E-09	2.02E-09
klx07_dz12	47	1.21E-07	7.28E-08	4.40E-08	2.66E-08	1.60E-08	9.69E-09	5.85E-09	3.54E-09	2.14E-09	1.29E-09
klx07_dz13	10	5.67E-07	3.42E-07	2.07E-07	1.25E-07	7.54E-08	4.56E-08	2.75E-08	1.66E-08	1.00E-08	6.06E-09
klx07_dz7	30	1.89E-07	1.14E-07	6.89E-08	4.16E-08	2.51E-08	1.52E-08	9.17E-09	5.54E-09	3.34E-09	2.02E-09
klx07_dz9	10	5.67E-07	3.42E-07	2.07E-07	1.25E-07	7.54E-08	4.56E-08	2.75E-08	1.66E-08	1.00E-08	6.06E-09
klx08_dz1	27	2.10E-07	1.27E-07	7.66E-08	4.63E-08	2.79E-08	1.69E-08	1.02E-08	6.15E-09	3.72E-09	2.24E-09
klx08_dz10	11	5.15E-07	3.11E-07	1.88E-07	1.14E-07	6.86E-08	4.14E-08	2.50E-08	1.51E-08	9.12E-09	5.51E-09
klx08_dz6	10	5.67E-07	3.42E-07	2.07E-07	1.25E-07	7.54E-08	4.56E-08	2.75E-08	1.66E-08	1.00E-08	6.06E-09
klx09_dz10	25	2.27E-07	1.37E-07	8.27E-08	5.00E-08	3.02E-08	1.82E-08	1.10E-08	6.65E-09	4.01E-09	2.42E-09
klx09_dz14	9	6.77E-07	4.09E-07	2.47E-07	1.49E-07	9.01E-08	5.44E-08	3.29E-08	1.98E-08	1.20E-08	7.24E-09
klx09_dz9	6	6.18E-06	3.73E-06	2.25E-06	1.36E-06	8.22E-07	4.97E-07	3.00E-07	1.81E-07	1.09E-07	6.61E-08
klx09e_dz2	22	2.58E-07	1.56E-07	9.40E-08	5.68E-08	3.43E-08	2.07E-08	1.25E-08	7.55E-09	4.56E-09	2.75E-09
klx09f_dz1	14	4.05E-07	2.45E-07	1.48E-07	8.92E-08	5.39E-08	3.25E-08	1.97E-08	1.19E-08	7.17E-09	4.33E-09
klx10c_dz3	10	5.67E-07	3.42E-07	2.07E-07	1.25E-07	7.54E-08	4.56E-08	2.75E-08	1.66E-08	1.00E-08	6.06E-09
klx10c_dz7	10	5.67E-07	3.42E-07	2.07E-07	1.25E-07	7.54E-08	4.56E-08	2.75E-08	1.66E-08	1.00E-08	6.06E-09
klx11_dz11	20	2.83E-07	1.71E-07	1.03E-07	6.24E-08	3.77E-08	2.28E-08	1.38E-08	8.31E-09	5.02E-09	3.03E-09
klx16_dz6	1	6.13E-05	3.70E-05	2.24E-05	1.35E-05	8.15E-06	4.92E-06	2.97E-06	1.80E-06	1.08E-06	6.55E-07
klx18_dz9	10	5.67E-07	3.42E-07	2.07E-07	1.25E-07	7.54E-08	4.56E-08	2.75E-08	1.66E-08	1.00E-08	6.06E-09
klx19_dz2	4	1.61E-05	9.72E-06	5.87E-06	3.55E-06	2.14E-06	1.29E-06	7.81E-07	4.72E-07	2.85E-07	1.72E-07
klx19_dz5-8_dolerite	45	1.13E-06	6.85E-07	4.14E-07	2.50E-07	1.51E-07	9.11E-08	5.50E-08	3.32E-08	2.01E-08	1.21E-08
klx21b_dz10-12	10	5.67E-07	3.42E-07	2.07E-07	1.25E-07	7.54E-08	4.56E-08	2.75E-08	1.66E-08	1.00E-08	6.06E-09
klx28_dz1	13	4.36E-07	2.63E-07	1.59E-07	9.61E-08	5.80E-08	3.50E-08	2.12E-08	1.28E-08	7.72E-09	4.66E-09

Deformation zone (ZFM)	b_h (m)	Hydraulic conductivity K (m/s) for depth interval (m RHB 70)									
		0 to –100	–100 to –200	–200 to –300	–300 to –400	–400 to –500	–500 to –600	–600 to –700	–700 to –800	–800 to –900	–900 to –1,000
zsmew002a	50	1.44E-06	9.27E-07	5.98E-07	3.86E-07	2.49E-07	1.61E-07	1.04E-07	6.71E-08	4.34E-08	2.80E-08
zsmew007a	50	1.57E-06	9.58E-07	5.83E-07	3.55E-07	2.16E-07	1.31E-07	7.99E-08	4.86E-08	2.96E-08	1.80E-08
zsmew007c	50	1.93E-07	1.20E-07	7.39E-08	4.57E-08	2.82E-08	1.74E-08	1.08E-08	6.66E-09	4.12E-09	2.54E-09
ZSMEW009A	12	8.06E-07	4.98E-07	3.08E-07	1.90E-07	1.18E-07	7.27E-08	4.49E-08	2.78E-08	1.72E-08	1.06E-08
zsmew013a	45	1.60E-06	1.03E-06	6.65E-07	4.29E-07	2.77E-07	1.79E-07	1.16E-07	7.46E-08	4.82E-08	3.11E-08
zsmew014a	10	5.67E-07	3.42E-07	2.07E-07	1.25E-07	7.54E-08	4.56E-08	2.75E-08	1.66E-08	1.00E-08	6.06E-09
ZSMEW020A	50	1.44E-06	9.27E-07	5.98E-07	3.86E-07	2.49E-07	1.61E-07	1.04E-07	6.71E-08	4.34E-08	2.80E-08
ZSMEW038A	10	7.18E-06	4.63E-06	2.99E-06	1.93E-06	1.25E-06	8.05E-07	5.20E-07	3.36E-07	2.17E-07	1.40E-07
ZSMEW076A	31	2.29E-06	1.48E-06	9.56E-07	6.18E-07	3.99E-07	2.57E-07	1.66E-07	1.07E-07	6.93E-08	4.47E-08
ZSMEW114A	25	2.89E-06	1.87E-06	1.21E-06	7.79E-07	5.03E-07	3.25E-07	2.10E-07	1.35E-07	8.74E-08	5.64E-08
zsmew120a	50	1.93E-07	1.20E-07	7.39E-08	4.57E-08	2.82E-08	1.74E-08	1.08E-08	6.66E-09	4.12E-09	2.54E-09
ZSMEW129A	20	3.65E-06	2.36E-06	1.52E-06	9.83E-07	6.35E-07	4.10E-07	2.65E-07	1.71E-07	1.10E-07	7.12E-08
ZSMEW190A	17	5.84E-07	3.61E-07	2.23E-07	1.38E-07	8.51E-08	5.26E-08	3.25E-08	2.01E-08	1.24E-08	7.68E-09
ZSMEW200A	17	5.54E-07	3.42E-07	2.12E-07	1.31E-07	8.08E-08	4.99E-08	3.09E-08	1.91E-08	1.18E-08	7.28E-09
ZSMEW230A	18	5.36E-07	3.31E-07	2.05E-07	1.26E-07	7.82E-08	4.83E-08	2.99E-08	1.85E-08	1.14E-08	7.05E-09
ZSMEW240A	50	1.44E-06	9.27E-07	5.98E-07	3.86E-07	2.49E-07	1.61E-07	1.04E-07	6.71E-08	4.34E-08	2.80E-08
ZSMEW305A	19	5.04E-07	3.11E-07	1.92E-07	1.19E-07	7.35E-08	4.54E-08	2.81E-08	1.74E-08	1.07E-08	6.63E-09
zsmew316a	30	2.39E-06	1.54E-06	9.97E-07	6.44E-07	4.16E-07	2.68E-07	1.73E-07	1.12E-07	7.23E-08	4.67E-08
zsmew900a	25	2.27E-07	1.37E-07	8.27E-08	5.00E-08	3.02E-08	1.82E-08	1.10E-08	6.65E-09	4.01E-09	2.42E-09
zsmew900b	25	2.27E-07	1.37E-07	8.27E-08	5.00E-08	3.02E-08	1.82E-08	1.10E-08	6.65E-09	4.01E-09	2.42E-09
ZSMEW904A	50	1.44E-06	9.27E-07	5.98E-07	3.86E-07	2.49E-07	1.61E-07	1.04E-07	6.71E-08	4.34E-08	2.80E-08
ZSMEW905A	21	3.39E-06	2.19E-06	1.41E-06	9.13E-07	5.89E-07	3.80E-07	2.46E-07	1.59E-07	1.02E-07	6.61E-08
ZSMEW906A	50	1.44E-06	9.27E-07	5.98E-07	3.86E-07	2.49E-07	1.61E-07	1.04E-07	6.71E-08	4.34E-08	2.80E-08
ZSMEW907A	50	1.44E-06	9.27E-07	5.98E-07	3.86E-07	2.49E-07	1.61E-07	1.04E-07	6.71E-08	4.34E-08	2.80E-08
ZSMEW936A	11	8.75E-07	5.41E-07	3.34E-07	2.07E-07	1.28E-07	7.89E-08	4.88E-08	3.01E-08	1.86E-08	1.15E-08
zsmew946a	10	3.61E-06	1.24E-06	4.27E-07	1.47E-07	5.05E-08	1.73E-08	5.96E-09	2.05E-09	7.04E-10	2.42E-10

Deformation zone (ZFM)	b_h (m)	Hydraulic conductivity K (m/s) for depth interval (m RHB 70)									
		0 to –100	–100 to –200	–200 to –300	–300 to –400	–400 to –500	–500 to –600	–600 to –700	–700 to –800	–800 to –900	–900 to –1,000
zsmne004a	50	1.04E-06	5.77E-07	3.21E-07	1.78E-07	9.92E-08	5.51E-08	3.07E-08	1.70E-08	9.47E-09	5.27E-09
zsmne005a	50	1.04E-06	5.77E-07	3.21E-07	1.78E-07	9.92E-08	5.51E-08	3.07E-08	1.70E-08	9.47E-09	5.27E-09
zsmne006a	50	1.35E-05	6.58E-06	3.22E-06	1.58E-06	7.71E-07	3.77E-07	1.85E-07	9.04E-08	4.42E-08	2.16E-08
ZSMNE008A	39	1.33E-06	7.38E-07	4.10E-07	2.28E-07	1.27E-07	7.05E-08	3.92E-08	2.18E-08	1.21E-08	6.73E-09
ZSMNE010A	34	1.52E-06	8.44E-07	4.69E-07	2.61E-07	1.45E-07	8.06E-08	4.48E-08	2.49E-08	1.38E-08	7.69E-09
zsmne011a	50	1.04E-06	5.77E-07	3.21E-07	1.78E-07	9.92E-08	5.51E-08	3.07E-08	1.70E-08	9.47E-09	5.27E-09
zsmne012a	50	3.29E-06	1.98E-06	1.19E-06	7.16E-07	4.31E-07	2.59E-07	1.56E-07	9.36E-08	5.63E-08	3.38E-08
zsmne015a	10	5.67E-07	3.42E-07	2.07E-07	1.25E-07	7.54E-08	4.56E-08	2.75E-08	1.66E-08	1.00E-08	6.06E-09
zsmne018a	50	1.13E-07	6.85E-08	4.14E-08	2.50E-08	1.51E-08	9.11E-09	5.50E-09	3.32E-09	2.01E-09	1.21E-09
zsmne019a	20	2.60E-06	1.44E-06	8.03E-07	4.46E-07	2.48E-07	1.38E-07	7.66E-08	4.26E-08	2.37E-08	1.32E-08
zsmne021a	40	1.30E-06	7.22E-07	4.01E-07	2.23E-07	1.24E-07	6.89E-08	3.83E-08	2.13E-08	1.18E-08	6.58E-09
zsmne022a	28	1.86E-06	1.03E-06	5.75E-07	3.20E-07	1.78E-07	9.88E-08	5.49E-08	3.05E-08	1.70E-08	9.43E-09
ZSMNE024A	50	5.10E-05	9.72E-06	1.85E-06	3.53E-07	6.74E-08	1.28E-08	2.45E-09	4.67E-10	8.90E-11	1.70E-11
ZSMNE024B	16	1.60E-04	3.05E-05	5.82E-06	1.11E-06	2.12E-07	4.04E-08	7.70E-09	1.47E-09	2.80E-10	5.34E-11
ZSMNE031A	15	3.46E-06	1.92E-06	1.07E-06	5.95E-07	3.31E-07	1.84E-07	1.02E-07	5.68E-08	3.16E-08	1.76E-08
ZSMNE031B	19	3.00E-07	1.81E-07	1.09E-07	6.60E-08	3.99E-08	2.41E-08	1.45E-08	8.79E-09	5.31E-09	3.20E-09
ZSMNE032A	26	1.97E-06	1.10E-06	6.09E-07	3.39E-07	1.88E-07	1.05E-07	5.82E-08	3.23E-08	1.80E-08	9.99E-09
ZSMNE033A	30	1.74E-06	9.69E-07	5.39E-07	2.99E-07	1.66E-07	9.25E-08	5.14E-08	2.86E-08	1.59E-08	8.84E-09
ZSMNE034A	29	1.79E-06	9.97E-07	5.54E-07	3.08E-07	1.71E-07	9.52E-08	5.29E-08	2.94E-08	1.64E-08	9.10E-09
ZSMNE036A	23	2.25E-06	1.25E-06	6.95E-07	3.86E-07	2.15E-07	1.19E-07	6.64E-08	3.69E-08	2.05E-08	1.14E-08
zsmne040a	20	2.83E-07	1.71E-07	1.03E-07	6.24E-08	3.77E-08	2.28E-08	1.38E-08	8.31E-09	5.02E-09	3.03E-09
ZSMNE062A	17	3.37E-07	2.03E-07	1.23E-07	7.42E-08	4.48E-08	2.71E-08	1.63E-08	9.87E-09	5.96E-09	3.60E-09
zsmne063a	10	5.67E-07	3.42E-07	2.07E-07	1.25E-07	7.54E-08	4.56E-08	2.75E-08	1.66E-08	1.00E-08	6.06E-09
zsmne065a	10	5.67E-07	3.42E-07	2.07E-07	1.25E-07	7.54E-08	4.56E-08	2.75E-08	1.66E-08	1.00E-08	6.06E-09
ZSMNE073A	36	1.44E-06	7.99E-07	4.44E-07	2.47E-07	1.37E-07	7.63E-08	4.24E-08	2.36E-08	1.31E-08	7.29E-09
zsmne079a	10	5.19E-06	2.89E-06	1.61E-06	8.92E-07	4.96E-07	2.76E-07	1.53E-07	8.52E-08	4.74E-08	2.63E-08
ZSMNE081A	21	2.53E-06	1.40E-06	7.81E-07	4.34E-07	2.41E-07	1.34E-07	7.45E-08	4.14E-08	2.30E-08	1.28E-08
ZSMNE095A	23	2.27E-06	1.26E-06	7.03E-07	3.91E-07	2.17E-07	1.21E-07	6.71E-08	3.73E-08	2.07E-08	1.15E-08
ZSMNE096A	17	3.29E-07	1.99E-07	1.20E-07	7.26E-08	4.38E-08	2.65E-08	1.60E-08	9.66E-09	5.83E-09	3.52E-09
zsmne107a	35	1.48E-06	8.25E-07	4.59E-07	2.55E-07	1.42E-07	7.88E-08	4.38E-08	2.43E-08	1.35E-08	7.52E-09
zsmne108a	10	5.67E-07	3.42E-07	2.07E-07	1.25E-07	7.54E-08	4.56E-08	2.75E-08	1.66E-08	1.00E-08	6.06E-09
ZSMNE132A	28	1.87E-06	1.04E-06	5.76E-07	3.20E-07	1.78E-07	9.90E-08	5.50E-08	3.06E-08	1.70E-08	9.46E-09

Deformation zone (ZFM)	b_h (m)	Hydraulic conductivity K (m/s) for depth interval (m RHB 70)									
		0 to –100	–100 to –200	–200 to –300	–300 to –400	–400 to –500	–500 to –600	–600 to –700	–700 to –800	–800 to –900	–900 to –1,000
ZSMNE133A	24	2.13E-06	1.18E-06	6.59E-07	3.66E-07	2.04E-07	1.13E-07	6.29E-08	3.50E-08	1.94E-08	1.08E-08
ZSMNE185A	24	2.18E-06	1.21E-06	6.75E-07	3.75E-07	2.09E-07	1.16E-07	6.44E-08	3.58E-08	1.99E-08	1.11E-08
ZSMNE210A	21	2.44E-06	1.36E-06	7.54E-07	4.19E-07	2.33E-07	1.29E-07	7.20E-08	4.00E-08	2.22E-08	1.24E-08
ZSMNE210B	28	1.88E-06	1.04E-06	5.80E-07	3.22E-07	1.79E-07	9.96E-08	5.53E-08	3.08E-08	1.71E-08	9.51E-09
ZSMNE218A	50	1.04E-06	5.77E-07	3.21E-07	1.78E-07	9.92E-08	5.51E-08	3.07E-08	1.70E-08	9.47E-09	5.27E-09
ZSMNE229A	20	2.59E-06	1.44E-06	8.01E-07	4.45E-07	2.47E-07	1.38E-07	7.65E-08	4.25E-08	2.36E-08	1.31E-08
ZSMNE257A	27	1.93E-06	1.07E-06	5.97E-07	3.32E-07	1.85E-07	1.03E-07	5.71E-08	3.17E-08	1.76E-08	9.80E-09
ZSMNE258A	26	1.98E-06	1.10E-06	6.13E-07	3.41E-07	1.90E-07	1.05E-07	5.86E-08	3.26E-08	1.81E-08	1.01E-08
ZSMNE259A	28	1.84E-06	1.02E-06	5.69E-07	3.16E-07	1.76E-07	9.78E-08	5.44E-08	3.02E-08	1.68E-08	9.34E-09
ZSMNE267A	23	2.30E-06	1.28E-06	7.11E-07	3.95E-07	2.20E-07	1.22E-07	6.79E-08	3.78E-08	2.10E-08	1.17E-08
ZSMNE286A	27	1.94E-06	1.08E-06	5.99E-07	3.33E-07	1.85E-07	1.03E-07	5.72E-08	3.18E-08	1.77E-08	9.83E-09
ZSMNE289A	21	2.44E-06	1.36E-06	7.54E-07	4.19E-07	2.33E-07	1.30E-07	7.20E-08	4.00E-08	2.23E-08	1.24E-08
ZSMNE295A	31	1.66E-06	9.23E-07	5.13E-07	2.85E-07	1.58E-07	8.81E-08	4.90E-08	2.72E-08	1.51E-08	8.41E-09
ZSMNE302A	24	2.13E-06	1.18E-06	6.57E-07	3.65E-07	2.03E-07	1.13E-07	6.28E-08	3.49E-08	1.94E-08	1.08E-08
ZSMNE307A	18	3.17E-07	1.91E-07	1.16E-07	6.98E-08	4.22E-08	2.55E-08	1.54E-08	9.29E-09	5.61E-09	3.39E-09
ZSMNE308A	24	2.14E-06	1.19E-06	6.62E-07	3.68E-07	2.05E-07	1.14E-07	6.32E-08	3.52E-08	1.95E-08	1.09E-08
ZSMNE313A	50	1.04E-06	5.77E-07	3.21E-07	1.78E-07	9.92E-08	5.51E-08	3.07E-08	1.70E-08	9.47E-09	5.27E-09
ZSMNE901A	25	2.06E-06	1.15E-06	6.37E-07	3.54E-07	1.97E-07	1.09E-07	6.09E-08	3.38E-08	1.88E-08	1.05E-08
ZSMNE903A	25	2.10E-06	1.17E-06	6.50E-07	3.61E-07	2.01E-07	1.12E-07	6.20E-08	3.45E-08	1.92E-08	1.07E-08
ZSMNE909A	17	3.29E-07	1.99E-07	1.20E-07	7.25E-08	4.38E-08	2.64E-08	1.60E-08	9.64E-09	5.82E-09	3.52E-09
ZSMNE910A	22	2.38E-06	1.32E-06	7.35E-07	4.09E-07	2.27E-07	1.26E-07	7.02E-08	3.90E-08	2.17E-08	1.21E-08
ZSMNE911A	50	1.04E-06	5.77E-07	3.21E-07	1.78E-07	9.92E-08	5.51E-08	3.07E-08	1.70E-08	9.47E-09	5.27E-09
ZSMNE912A	31	1.69E-06	9.37E-07	5.21E-07	2.90E-07	1.61E-07	8.95E-08	4.98E-08	2.77E-08	1.54E-08	8.55E-09
ZSMNE913A	50	1.04E-06	5.77E-07	3.21E-07	1.78E-07	9.92E-08	5.51E-08	3.07E-08	1.70E-08	9.47E-09	5.27E-09
ZSMNE914A	50	1.04E-06	5.77E-07	3.21E-07	1.78E-07	9.92E-08	5.51E-08	3.07E-08	1.70E-08	9.47E-09	5.27E-09
ZSMNE915A	19	2.91E-07	1.76E-07	1.06E-07	6.41E-08	3.87E-08	2.34E-08	1.41E-08	8.53E-09	5.15E-09	3.11E-09
zsmne930a	5	1.04E-05	5.77E-06	3.21E-06	1.78E-06	9.92E-07	5.51E-07	3.07E-07	1.70E-07	9.47E-08	5.27E-08
ZSMNE940A	16	3.48E-07	2.10E-07	1.27E-07	7.68E-08	4.64E-08	2.80E-08	1.69E-08	1.02E-08	6.17E-09	3.73E-09
ZSMNE941A	22	2.39E-06	1.33E-06	7.38E-07	4.10E-07	2.28E-07	1.27E-07	7.05E-08	3.92E-08	2.18E-08	1.21E-08
zsmne942a	15	1.40E-06	8.02E-07	4.61E-07	2.65E-07	1.52E-07	8.75E-08	5.03E-08	2.89E-08	1.66E-08	9.55E-09
zsmne944a	10	5.67E-07	3.42E-07	2.07E-07	1.25E-07	7.54E-08	4.56E-08	2.75E-08	1.66E-08	1.00E-08	6.06E-09

Deformation zone (ZFM)	b_h (m)	Hydraulic conductivity K (m/s) for depth interval (m RHB 70)									
		0 to –100	–100 to –200	–200 to –300	–300 to –400	–400 to –500	–500 to –600	–600 to –700	–700 to –800	–800 to –900	–900 to –1,000
zsmns001a	50	3.17E-06	1.82E-06	1.05E-06	6.01E-07	3.46E-07	1.99E-07	1.14E-07	6.56E-08	3.77E-08	2.17E-08
zsmns001b	50	3.17E-06	1.82E-06	1.05E-06	6.01E-07	3.46E-07	1.99E-07	1.14E-07	6.56E-08	3.77E-08	2.17E-08
zsmns001c	50	3.17E-06	1.82E-06	1.05E-06	6.01E-07	3.46E-07	1.99E-07	1.14E-07	6.56E-08	3.77E-08	2.17E-08
zsmns001d	50	3.17E-06	1.82E-06	1.05E-06	6.01E-07	3.46E-07	1.99E-07	1.14E-07	6.56E-08	3.77E-08	2.17E-08
zsmns001e	50	3.17E-06	1.82E-06	1.05E-06	6.01E-07	3.46E-07	1.99E-07	1.14E-07	6.56E-08	3.77E-08	2.17E-08
ZSMNS009A	25	2.08E-06	1.15E-06	6.42E-07	3.57E-07	1.98E-07	1.10E-07	6.13E-08	3.41E-08	1.89E-08	1.05E-08
ZSMNS017A	21	2.50E-06	1.39E-06	7.73E-07	4.30E-07	2.39E-07	1.33E-07	7.38E-08	4.10E-08	2.28E-08	1.27E-08
ZSMNS017B	20	2.18E-05	1.25E-05	7.21E-06	4.14E-06	2.38E-06	1.37E-06	7.87E-07	4.52E-07	2.60E-07	1.49E-07
zsmns046a	20	2.60E-06	1.44E-06	8.03E-07	4.46E-07	2.48E-07	1.38E-07	7.66E-08	4.26E-08	2.37E-08	1.32E-08
zsmns057a	20	2.60E-06	1.44E-06	8.03E-07	4.46E-07	2.48E-07	1.38E-07	7.66E-08	4.26E-08	2.37E-08	1.32E-08
zsmns059a	50	3.38E-06	1.94E-06	1.12E-06	6.41E-07	3.69E-07	2.12E-07	1.22E-07	7.00E-08	4.02E-08	2.31E-08
ZSMNS064A	50	1.04E-06	5.77E-07	3.21E-07	1.78E-07	9.92E-08	5.51E-08	3.07E-08	1.70E-08	9.47E-09	5.27E-09
ZSMNS071A	18	3.07E-07	1.86E-07	1.12E-07	6.77E-08	4.09E-08	2.47E-08	1.49E-08	9.01E-09	5.44E-09	3.29E-09
ZSMNS084A	32	1.62E-06	9.03E-07	5.02E-07	2.79E-07	1.55E-07	8.62E-08	4.79E-08	2.66E-08	1.48E-08	8.23E-09
ZSMNS085A	37	1.41E-06	7.82E-07	4.35E-07	2.42E-07	1.34E-07	7.47E-08	4.15E-08	2.31E-08	1.28E-08	7.13E-09
ZSMNS117A	17	3.38E-07	2.04E-07	1.23E-07	7.45E-08	4.50E-08	2.72E-08	1.64E-08	9.91E-09	5.99E-09	3.62E-09
zsmns141a	20	2.60E-06	1.44E-06	8.03E-07	4.46E-07	2.48E-07	1.38E-07	7.66E-08	4.26E-08	2.37E-08	1.32E-08
ZSMNS165A	18	3.18E-07	1.92E-07	1.16E-07	7.01E-08	4.23E-08	2.56E-08	1.54E-08	9.33E-09	5.63E-09	3.40E-09
ZSMNS182A	30	1.73E-06	9.64E-07	5.36E-07	2.98E-07	1.66E-07	9.20E-08	5.12E-08	2.84E-08	1.58E-08	8.79E-09
ZSMNS182B	30	1.72E-06	9.56E-07	5.31E-07	2.95E-07	1.64E-07	9.13E-08	5.07E-08	2.82E-08	1.57E-08	8.72E-09
ZSMNS215A	16	3.50E-07	2.11E-07	1.28E-07	7.70E-08	4.65E-08	2.81E-08	1.70E-08	1.02E-08	6.19E-09	3.74E-09
ZSMNS221A	22	2.35E-06	1.31E-06	7.26E-07	4.04E-07	2.24E-07	1.25E-07	6.94E-08	3.86E-08	2.14E-08	1.19E-08
ZSMNS287A	34	1.53E-06	8.50E-07	4.73E-07	2.63E-07	1.46E-07	8.12E-08	4.51E-08	2.51E-08	1.39E-08	7.75E-09
ZSMNS291A	19	3.00E-07	1.81E-07	1.09E-07	6.60E-08	3.99E-08	2.41E-08	1.45E-08	8.79E-09	5.31E-09	3.20E-09
ZSMNS301A	19	3.03E-07	1.83E-07	1.10E-07	6.67E-08	4.03E-08	2.43E-08	1.47E-08	8.87E-09	5.36E-09	3.24E-09
ZSMNS916A	44	1.19E-06	6.64E-07	3.69E-07	2.05E-07	1.14E-07	6.34E-08	3.52E-08	1.96E-08	1.09E-08	6.05E-09
ZSMNS917A	50	1.04E-06	5.77E-07	3.21E-07	1.78E-07	9.92E-08	5.51E-08	3.07E-08	1.70E-08	9.47E-09	5.27E-09
ZSMNS918A	29	1.81E-06	1.01E-06	5.60E-07	3.11E-07	1.73E-07	9.61E-08	5.34E-08	2.97E-08	1.65E-08	9.18E-09
ZSMNS919A	50	1.04E-06	5.77E-07	3.21E-07	1.78E-07	9.92E-08	5.51E-08	3.07E-08	1.70E-08	9.47E-09	5.27E-09
ZSMNS920A	31	1.69E-06	9.41E-07	5.23E-07	2.91E-07	1.62E-07	8.99E-08	5.00E-08	2.78E-08	1.54E-08	8.58E-09
zsmns945a	10	5.19E-06	2.89E-06	1.61E-06	8.92E-07	4.96E-07	2.76E-07	1.53E-07	8.52E-08	4.74E-08	2.63E-08
zsmns947a	20	2.83E-07	1.71E-07	1.03E-07	6.24E-08	3.77E-08	2.28E-08	1.38E-08	8.31E-09	5.02E-09	3.03E-09

Deformation zone (ZFM)	b_h (m)	Hydraulic conductivity K (m/s) for depth interval (m RHB 70)									
		0 to –100	–100 to –200	–200 to –300	–300 to –400	–400 to –500	–500 to –600	–600 to –700	–700 to –800	–800 to –900	–900 to –1,000
ZSMNW025A	10	5.67E-07	3.42E-07	2.07E-07	1.25E-07	7.54E-08	4.56E-08	2.75E-08	1.66E-08	1.00E-08	6.06E-09
ZSMNW027A	34	1.52E-06	8.42E-07	4.68E-07	2.60E-07	1.45E-07	8.05E-08	4.47E-08	2.49E-08	1.38E-08	7.68E-09
zsmnw042a-east	50	1.04E-06	5.77E-07	3.21E-07	1.78E-07	9.92E-08	5.51E-08	3.07E-08	1.70E-08	9.47E-09	5.27E-09
zsmnw042a-west	50	1.04E-06	5.77E-07	3.21E-07	1.78E-07	9.92E-08	5.51E-08	3.07E-08	1.70E-08	9.47E-09	5.27E-09
zsmnw047a	25	2.27E-07	1.37E-07	8.27E-08	5.00E-08	3.02E-08	1.82E-08	1.10E-08	6.65E-09	4.01E-09	2.42E-09
zsmnw052a	15	3.78E-07	2.28E-07	1.38E-07	8.33E-08	5.03E-08	3.04E-08	1.83E-08	1.11E-08	6.69E-09	4.04E-09
ZSMNW060A	32	1.61E-06	8.93E-07	4.96E-07	2.76E-07	1.53E-07	8.53E-08	4.74E-08	2.64E-08	1.47E-08	8.15E-09
ZSMNW066A	50	1.04E-06	5.77E-07	3.21E-07	1.78E-07	9.92E-08	5.51E-08	3.07E-08	1.70E-08	9.47E-09	5.27E-09
ZSMNW067A	50	1.04E-06	5.77E-07	3.21E-07	1.78E-07	9.92E-08	5.51E-08	3.07E-08	1.70E-08	9.47E-09	5.27E-09
ZSMNW068A	18	3.16E-07	1.91E-07	1.15E-07	6.96E-08	4.21E-08	2.54E-08	1.53E-08	9.26E-09	5.60E-09	3.38E-09
ZSMNW068B	22	2.36E-06	1.31E-06	7.30E-07	4.06E-07	2.26E-07	1.25E-07	6.97E-08	3.88E-08	2.15E-08	1.20E-08
ZSMNW068C	4	1.29E-06	7.80E-07	4.71E-07	2.85E-07	1.72E-07	1.04E-07	6.27E-08	3.79E-08	2.29E-08	1.38E-08
ZSMNW074A	33	1.57E-06	8.72E-07	4.85E-07	2.70E-07	1.50E-07	8.33E-08	4.63E-08	2.57E-08	1.43E-08	7.95E-09
ZSMNW075A	38	1.35E-06	7.53E-07	4.18E-07	2.33E-07	1.29E-07	7.19E-08	4.00E-08	2.22E-08	1.24E-08	6.87E-09
ZSMNW083A	16	3.44E-07	2.08E-07	1.25E-07	7.58E-08	4.58E-08	2.76E-08	1.67E-08	1.01E-08	6.09E-09	3.68E-09
ZSMNW086A	22	2.36E-06	1.31E-06	7.30E-07	4.06E-07	2.26E-07	1.25E-07	6.97E-08	3.87E-08	2.15E-08	1.20E-08
zsmnw088a	20	2.60E-06	1.44E-06	8.03E-07	4.46E-07	2.48E-07	1.38E-07	7.66E-08	4.26E-08	2.37E-08	1.32E-08
ZSMNW089A	21	2.43E-06	1.35E-06	7.51E-07	4.18E-07	2.32E-07	1.29E-07	7.17E-08	3.99E-08	2.22E-08	1.23E-08
ZSMNW106A	17	3.32E-07	2.01E-07	1.21E-07	7.32E-08	4.42E-08	2.67E-08	1.61E-08	9.73E-09	5.88E-09	3.55E-09
ZSMNW113A	30	1.70E-06	9.47E-07	5.26E-07	2.93E-07	1.63E-07	9.04E-08	5.03E-08	2.79E-08	1.55E-08	8.63E-09
zsmnw119a	10	5.19E-06	2.89E-06	1.61E-06	8.92E-07	4.96E-07	2.76E-07	1.53E-07	8.52E-08	4.74E-08	2.63E-08
ZSMNW123A	32	1.61E-06	8.93E-07	4.96E-07	2.76E-07	1.53E-07	8.52E-08	4.74E-08	2.63E-08	1.46E-08	8.14E-09
ZSMNW126A	37	1.42E-06	7.90E-07	4.39E-07	2.44E-07	1.36E-07	7.54E-08	4.19E-08	2.33E-08	1.30E-08	7.21E-09
ZSMNW126B	36	1.46E-06	8.10E-07	4.50E-07	2.50E-07	1.39E-07	7.74E-08	4.30E-08	2.39E-08	1.33E-08	7.39E-09
ZSMNW131A	50	1.04E-06	5.77E-07	3.21E-07	1.78E-07	9.92E-08	5.51E-08	3.07E-08	1.70E-08	9.47E-09	5.27E-09
ZSMNW173A	21	2.45E-06	1.36E-06	7.56E-07	4.20E-07	2.34E-07	1.30E-07	7.22E-08	4.01E-08	2.23E-08	1.24E-08
ZSMNW178A	41	1.25E-06	6.97E-07	3.88E-07	2.16E-07	1.20E-07	6.66E-08	3.70E-08	2.06E-08	1.14E-08	6.36E-09
ZSMNW184A	16	3.44E-07	2.08E-07	1.25E-07	7.57E-08	4.57E-08	2.76E-08	1.67E-08	1.01E-08	6.09E-09	3.68E-09
ZSMNW202A	16	3.49E-07	2.11E-07	1.27E-07	7.70E-08	4.65E-08	2.81E-08	1.70E-08	1.02E-08	6.18E-09	3.73E-09
ZSMNW206A	19	3.05E-07	1.84E-07	1.11E-07	6.72E-08	4.06E-08	2.45E-08	1.48E-08	8.94E-09	5.40E-09	3.26E-09
ZSMNW222A	27	1.93E-06	1.08E-06	5.98E-07	3.32E-07	1.85E-07	1.03E-07	5.71E-08	3.17E-08	1.76E-08	9.81E-09

Deformation zone (ZFM)	b_h (m)	Hydraulic conductivity K (m/s) for depth interval (m RHB 70)									
		0 to –100	–100 to –200	–200 to –300	–300 to –400	–400 to –500	–500 to –600	–600 to –700	–700 to –800	–800 to –900	–900 to –1,000
ZSMNW233A	19	2.93E-07	1.77E-07	1.07E-07	6.46E-08	3.90E-08	2.36E-08	1.42E-08	8.59E-09	5.19E-09	3.13E-09
ZSMNW235A	20	2.59E-06	1.44E-06	8.01E-07	4.45E-07	2.47E-07	1.38E-07	7.65E-08	4.25E-08	2.36E-08	1.31E-08
ZSMNW245A	23	2.25E-06	1.25E-06	6.95E-07	3.86E-07	2.15E-07	1.19E-07	6.64E-08	3.69E-08	2.05E-08	1.14E-08
ZSMNW247A	16	3.51E-07	2.12E-07	1.28E-07	7.72E-08	4.67E-08	2.82E-08	1.70E-08	1.03E-08	6.21E-09	3.75E-09
ZSMNW251A	20	2.84E-07	1.71E-07	1.04E-07	6.25E-08	3.78E-08	2.28E-08	1.38E-08	8.32E-09	5.02E-09	3.03E-09
ZSMNW254A	49	1.05E-06	5.85E-07	3.25E-07	1.81E-07	1.00E-07	5.58E-08	3.10E-08	1.73E-08	9.59E-09	5.33E-09
ZSMNW261A	22	2.33E-06	1.29E-06	7.19E-07	4.00E-07	2.22E-07	1.24E-07	6.87E-08	3.82E-08	2.12E-08	1.18E-08
ZSMNW263A	16	3.51E-07	2.12E-07	1.28E-07	7.72E-08	4.66E-08	2.82E-08	1.70E-08	1.03E-08	6.21E-09	3.75E-09
ZSMNW269A	21	2.45E-06	1.36E-06	7.56E-07	4.20E-07	2.34E-07	1.30E-07	7.22E-08	4.01E-08	2.23E-08	1.24E-08
ZSMNW280A	20	2.59E-06	1.44E-06	8.00E-07	4.45E-07	2.47E-07	1.38E-07	7.64E-08	4.25E-08	2.36E-08	1.31E-08
ZSMNW294A	23	2.28E-06	1.27E-06	7.05E-07	3.92E-07	2.18E-07	1.21E-07	6.73E-08	3.74E-08	2.08E-08	1.16E-08
ZSMNW312A	50	1.04E-06	5.79E-07	3.22E-07	1.79E-07	9.95E-08	5.53E-08	3.08E-08	1.71E-08	9.50E-09	5.28E-09
ZSMNW312B	12	4.58E-07	2.76E-07	1.67E-07	1.01E-07	6.09E-08	3.68E-08	2.22E-08	1.34E-08	8.10E-09	4.89E-09
ZSMNW312C	17	3.40E-07	2.05E-07	1.24E-07	7.49E-08	4.52E-08	2.73E-08	1.65E-08	9.97E-09	6.02E-09	3.64E-09
ZSMNW321A	21	2.51E-06	1.40E-06	7.76E-07	4.31E-07	2.40E-07	1.33E-07	7.41E-08	4.12E-08	2.29E-08	1.27E-08
ZSMNW322A	50	1.04E-06	5.77E-07	3.21E-07	1.78E-07	9.92E-08	5.51E-08	3.07E-08	1.70E-08	9.47E-09	5.27E-09
ZSMNW921A	25	2.04E-06	1.14E-06	6.31E-07	3.51E-07	1.95E-07	1.08E-07	6.03E-08	3.35E-08	1.86E-08	1.04E-08
ZSMNW922A	18	3.18E-07	1.92E-07	1.16E-07	7.00E-08	4.23E-08	2.55E-08	1.54E-08	9.32E-09	5.63E-09	3.40E-09
ZSMNW923A	37	1.39E-06	7.71E-07	4.29E-07	2.38E-07	1.32E-07	7.36E-08	4.09E-08	2.27E-08	1.26E-08	7.03E-09
ZSMNW925A	28	1.87E-06	1.04E-06	5.78E-07	3.21E-07	1.79E-07	9.93E-08	5.52E-08	3.07E-08	1.71E-08	9.48E-09
zsmnw928a	10	5.67E-07	3.42E-07	2.07E-07	1.25E-07	7.54E-08	4.56E-08	2.75E-08	1.66E-08	1.00E-08	6.06E-09
zsmnw929a	20	2.60E-06	1.44E-06	8.03E-07	4.46E-07	2.48E-07	1.38E-07	7.66E-08	4.26E-08	2.37E-08	1.32E-08
zsmnw931a	50	1.04E-06	5.77E-07	3.21E-07	1.78E-07	9.92E-08	5.51E-08	3.07E-08	1.70E-08	9.47E-09	5.27E-09
ZSMNW931B	38	1.37E-06	7.64E-07	4.24E-07	2.36E-07	1.31E-07	7.29E-08	4.05E-08	2.25E-08	1.25E-08	6.96E-09
ZSMNW933A	22	2.34E-06	1.30E-06	7.23E-07	4.02E-07	2.23E-07	1.24E-07	6.90E-08	3.84E-08	2.13E-08	1.19E-08
ZSMNW937A	17	3.26E-07	1.97E-07	1.19E-07	7.19E-08	4.34E-08	2.62E-08	1.58E-08	9.56E-09	5.77E-09	3.49E-09
ZSMNW943A	17	3.26E-07	1.97E-07	1.19E-07	7.19E-08	4.34E-08	2.62E-08	1.58E-08	9.56E-09	5.77E-09	3.49E-09

Appendix 7

A7 Upscaling the Hydrogeological DFN to produce an ECPM model for Forsmark and Laxemar

A7.1 Introduction

The power-law fracture size distribution and fracture transmissivity distribution parameters derived through the calibration procedures described in /Rhén et al. 2008/ are intended for use in modelling flow and transport using a DFN concept. However much of the hydro-geological modelling within the SDM, for both Forsmark and Laxemar, uses equivalent porous continuum medium (ECPM) modelling based on upscaling the underlying DFN model. For the SDM Laxemar and SDM Forsmark regional-scale groundwater flow modelling ECPM models have been constructed of the sites using elements of 20–40 m in the local-scale and about 100 m on the regional-scale.

The upscaling methodology produces a directional hydraulic conductivity tensor, fracture kinematic porosity and other transport properties (such as the connected fracture surface area per unit volume). In CONNECTFLOW a flux-based upscaling method is used that requires several flow calculations through a DFN model in different directions. There are several methodological factors which may affect the results of upscaling calculations. Some of these are described, and their affect on upscaling results quantified below.

For heterogeneous fracture systems block scale hydraulic properties have a strong dependence on the block scale considered. On the scale of a deposition hole, i.e. a few metres, the hydraulic properties depend heavily on the intensity and transmissivity distribution of individual fractures, whereas bulk flows on scales of hundreds of metres are controlled by a network system of fractures, and hence is more homogenised.

It is usually only feasible to work with DFN models of not more than a few tens of millions of fractures; hence it is often necessary to truncate the fracture size distribution at some lower limit. Although the density of fractures increases with decreasing fracture size, the smaller fractures tend to be less well-connected and, for the semi-correlated and correlated models, tend to be less transmissive. Therefore neglecting the smaller fractures may only involve a small approximation. Hence another objective of studying block-scale ECPM properties is to determine appropriate truncation limits on the size of fractures generated that will not have a significant effect on the upscaled properties. This was investigated in SDM Laxemar and SDM Forsmark: We found that a reasonable rule of thumb was that if r_{min} was less than a quarter of the block size, the upscaling results were stable with respect to reducing r_{min}.

Kinematic porosity has less scale dependence, but the truncation of fracture size, r_{min}, in the fractures generated has more of an affect than was the case for hydraulic conductivity.

Use of a ‘guard-zone’ is a refinement of the upscaling methodology. The aim is to simulate flow through a slightly larger domain than the block size required for the ECPM properties, but then calculate the flux responses through the correct block size. The reason for this is to avoid over-prediction of hydraulic conductivity from flows through fractures that just cut the corner of the block but that are unrepresentative of flows through the in situ fracture network. The use of a guard-zone can reduce the calculated hydraulic conductivity of a block significantly. The sensitivity of the regional and block upscaling results to the use of a guard-zone are considered in this appendix.

A7.2 Upscaling methodology.

Figure A7-1 shows an illustration of how flow is calculated in a DFN model (a 2D network is shown for simplicity). To calculate equivalent hydraulic conductivity for the block shown, the flux through the network is calculated for a linear head gradient in each of the axial directions. Due to the variety of connections across the network, several flow-paths are possible, and may result in cross-flows non-parallel to the head gradient. Cross-flows are a common characteristic of DFN models and can be approximated in an ECPM by an anisotropic hydraulic conductivity. In 3D, ConnectFlow uses six components to characterise the symmetric hydraulic conductivity tensor. Using the DFN flow simulations, the fluxes through each face of the block are calculated for each head gradient direction. The hydraulic conductivity tensor is

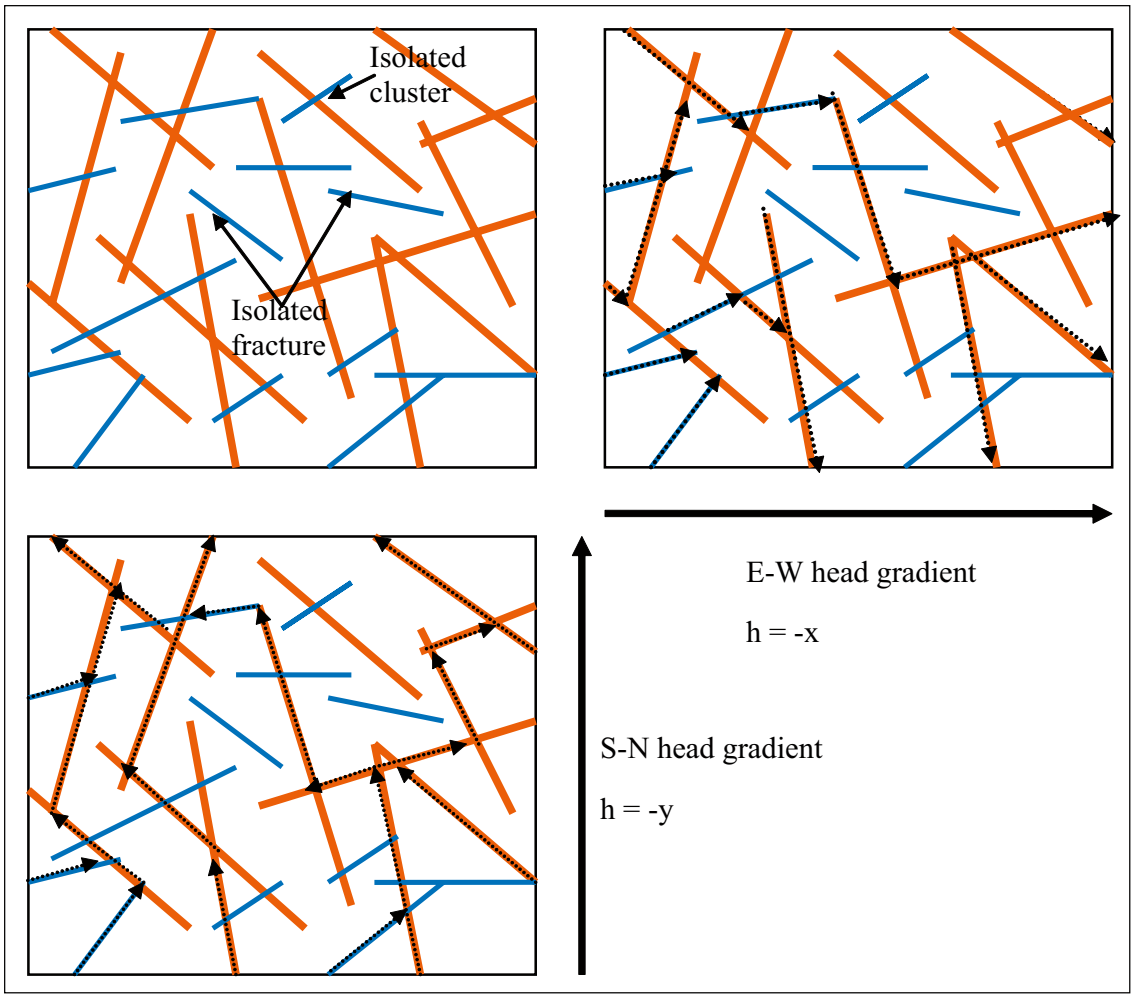

Figure A7-1. *2D illustration of flow through a network of fractures. A random network of fractures with variable length and transmissivity is shown top left (orange fractures are large transmissivity, blue are low). Top right: flow-paths for a linear head gradient E-W decreasing along the x-axis. Bottom left: flow-paths through the network for a linear head gradient S-N decreasing along the y-axis.*

then derived by a least-squares fit to these flux responses for the fixed head gradients. Other authors /La Pointe 1995/ have only considered the components of the equivalent hydraulic conductivity parallel to the coordinate axes using a head difference between opposite faces and no-flow on the other faces. This leads to a poor representation of blocks in which the network connections, and hence flow, are mostly between adjacent faces rather than between opposite faces. The effective hydraulic conductivity assigned to such blocks may be essentially zero, even though the flow-paths through the block may contribute significantly to the overall flow through the network.

In 3D, the blocks have to be hexahedra (cuboids), but the upscaling method can be applied to an array of sub-blocks within a much larger DFN domain by performing the upscaling on each sub-block in sequence. The upscaling method is typically used in one of two ways:

- To obtain the statistical distribution of hydraulic conductivity on a given block scale a DFN model is generated for a much larger domain, and then ECPM properties are calculated for an array of sub-blocks of equal size and shape to give an ensemble of properties. (This method is used to obtain the results described here).
- To obtain an ECPM model for a local- or regional-scale grid, a DFN model is generated within the grid domain, and the upscaling is performed within each grid element to derive the ECPM properties element by element.

A detailed description of the upscaling method to calculate the ECPM hydraulic conductivity tensor is given in /Jackson et al. 2000/. Briefly, the method can be summarised by the following steps:

- Define a sub-block within a DFN model.
- Identify the fractures that are either completely inside or cut the block.
- Calculate the connections between these fractures and their connection to the faces of the block.
- Remove isolated fractures and isolated fracture clusters, and dead-end fractures if specified.
- Specify a linear head gradient parallel to each coordinate axis on all the faces of the block.
- Calculate the flow through the network and the flux through each face of the block for each axial head gradient.
- Fit a symmetric anisotropic hydraulic conductivity tensor that best fits (least-squares) the flux response of the network.
- Fracture kinematic porosity is calculated as the sum (over all fractures that are connected on the scale of the block) of fracture area within the block multiplied by the transport aperture of the fracture ($e_t = 0.705\ T^{0.404}$ /Hjerne et al. 2009/.

One important aspect of this approach is that the properties are calculated on a particular scale, that of the blocks, and that a connectivity analysis of the network is performed only on the scale of the block. Bulk flows across many blocks will depend on the correlation and variability of properties between blocks.

One refinement of the upscaling methodology is to simulate flow through a slightly larger domain than the block size required for the ECPM properties, but then calculate the flux responses through the correct block size. The reason for this is to avoid over-prediction of hydraulic conductivity from flows through fractures that just cut the corner of the block but that are unrepresentative of flows through the in situ fracture network. This method is illustrated in Figure A7-2. The area around the block is known as a 'guard-zone', and an appropriate choice for its thickness is about half a fracture length. The problem is most significant in sparse heterogeneous networks in which the flux through the network of fractures is affected by 'bottlenecks' through low transmissivity fractures, and is quite different to the flux through single fractures.

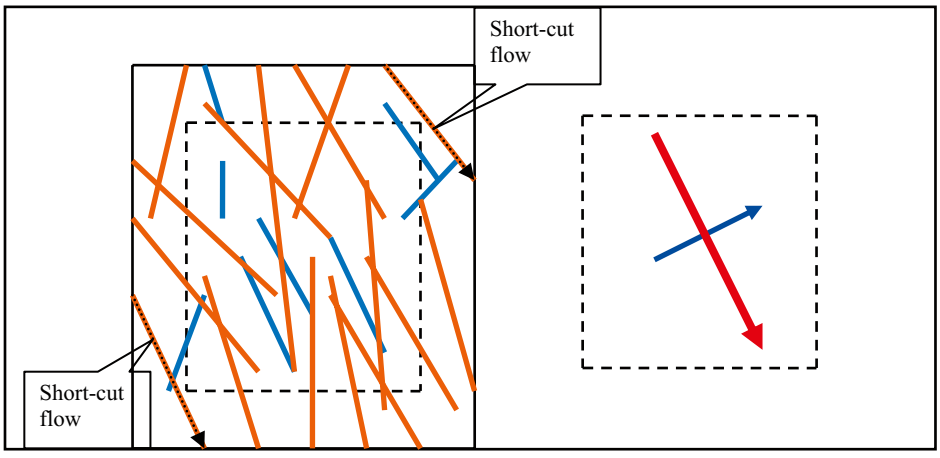

Figure A7-2. *2D sketch of how block-scale hydraulic conductivity can be over-estimated using a linear head gradient by high transmissivity fractures that cut across a corner of the block. By simulating flow through a larger domain, but only calculating the flux through the required block size (dashed block) then fluxes more consistent with flow through an in situ network are obtained. The ECPM hydraulic conductivities are then calculated for the dashed block to give principal components (right). The red arrow is the maximum component, blue the minimum.*

A7.1 Results of upscaling: Laxemar.

The results of the upscaling calculations on the block scale are displayed in Figure A7-3 and Figure A7-4. The results of the regional upscaling are shown in Table A7-1. The effect of including a guard zone in the calculationsis to reduce the hydraulic conductivities by up to a factor of 3. The variation in hydraulic conductivities bewteen blocks is also increased, whilst the percentage of blocks that are hydraulically active is deceased. These effects are less pronounced in the results of upscaling the regional model compared to the block models due to a smaller guard zone being used. This was neccesary in order to make the calculations tractable.

A7.2 Results of upscaling: Forsmark.

Equivalent calculations were made for Forsmark to quantify how sensitive the Hydrogeological DFN for that site /Follin et al. 2007b/ is to the use of a guard zone. The results of the upscaling calculations on the block scale are displayed in Figure A7-5 and Figure A7-6. The results of the regional upscaling are shown in Table A7-2. The effect of including a guard zone in the calculationsis to reduce the hydraulic conductivities by up to a factor of 3. The variation in hydraulic conductivities bewteen blocks is also increased, whilst the percentage of blocks that are hydraulically active is deceased. These effects are less pronounced in the results of upscaling the regional model compared to the block models due to a smaller guard zone being used. This was neccesary in order to make the calculations tractable.

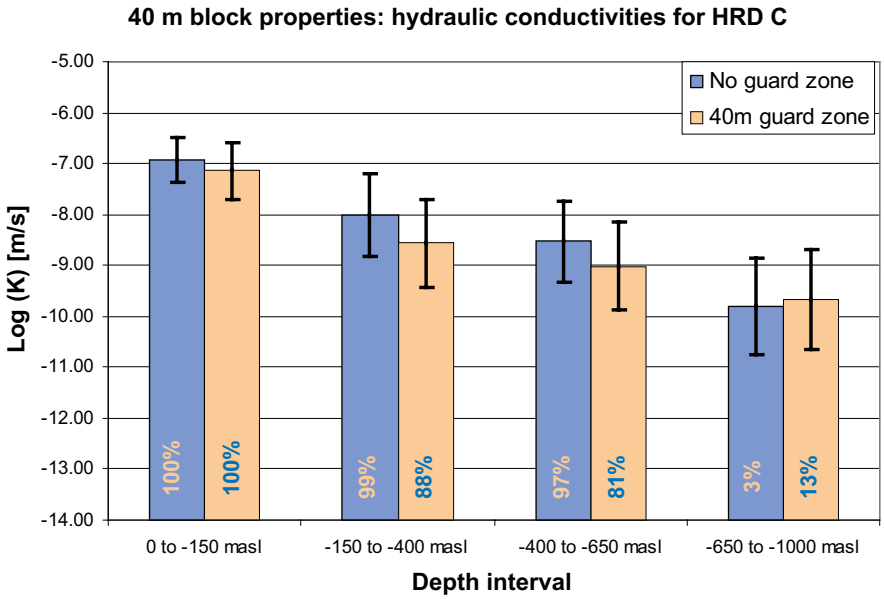

Figure A7-3. *Histogram comparing 40 m block-scale hydraulic conductivities by depth zone, using a guard-zone of 40 m around the block and without a guard zone. The DFN model used is for HRD_C, semi-correlated transmissivity model, for OPO fractures. The height of the column is the mean Log (hydraulic conductivity) of the blocks that are hydraulically active. The error bars are the standard deviation of Log (hydraulic conductivity) of the blocks that are hydraulically active. The number at the base of each column is the percentage of blocks that are hydraulically active in 3D.*

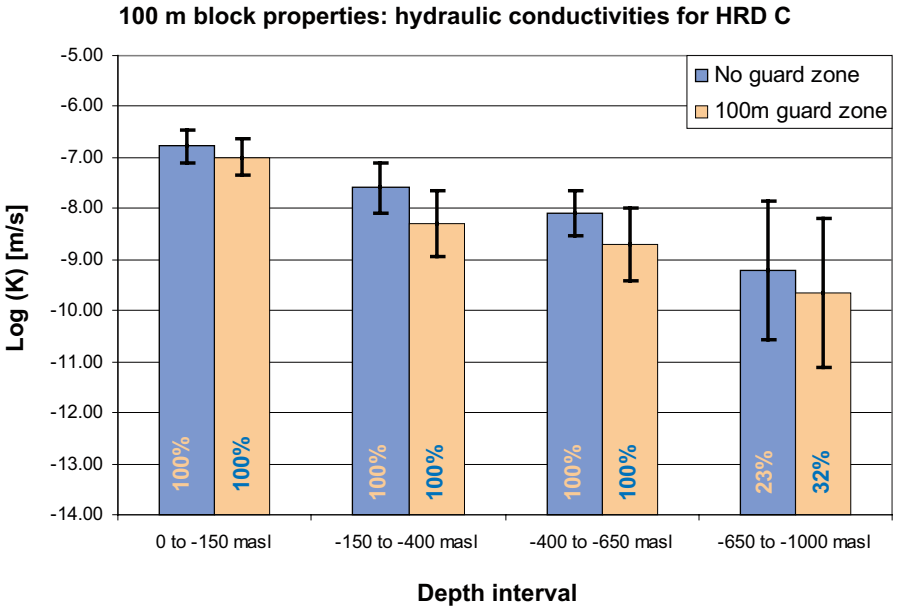

Figure A7-4. *Histogram comparing 100 m block-scale hydraulic conductivities by depth zone, using a guard-zone of 100 m around the block and without a guard zone. The DFN model used is for HRD_C, semi-correlated transmissivity model, for OPO fractures. The height of the column is the mean Log (hydraulic conductivity) of the blocks that are hydraulically active. The error bars are the standard deviation of Log (hydraulic conductivity) of the blocks that are hydraulically active. The number at the base of each column is the percentage of blocks that are hydraulically active in 3D.*

Table A7-1. A comparison of 40 m upscaling results, on one realization of the Laxemar regional DFN model, with and without a guard zone.

	Using a guard zone (20 m)			Without a guard zone		
	Log_{10} Hydraulic conductivity (ms/)			Log_{10} Hydraulic conductivity (ms/)		
	mean K_{eff}	std K_{eff}	% active	mean K_{eff}	std K_{eff}	% active
HRD_C						
0 to –150 m.a.s.l.	–7.32	0.59	100.0%	–7.14	0.47	100.0%
–150 to –400 m.a.s.l.	–8.18	0.94	89.1%	–7.85	0.80	98.6%
–400 to –650 m.a.s.l.	–8.58	0.90	80.1%	–8.34	0.78	95.2%
–650 to –1,000 m.a.s.l.	–8.16	1.16	17.5%	–8.27	1.10	26.4%
HRD_EW007						
0 to –150 m.a.s.l.	–7.08	0.38	100.0%	–7.03	0.34	100.0%
–150 to –400 m.a.s.l.	–7.34	0.49	100.0%	–7.22	0.41	100.0%
–400 to –650 m.a.s.l.	–8.09	0.67	98.7%	–7.91	0.49	99.9%
–650 to –1,000 m.a.s.l.	–8.77	0.93	14.4%	–8.80	0.87	22.6%
HRD_W						
0 to –150 m.a.s.l.	–6.94	0.61	100.0%	–6.82	0.49	100.0%
–150 to –400 m.a.s.l.	–7.92	0.97	83.3%	–7.75	0.81	96.4%
–400 to –650 m.a.s.l.	–8.51	0.97	65.9%	–8.37	0.93	85.5%
–650 to –1,000 m.a.s.l.	–8.29	1.05	10.1%	–8.45	0.96	14.7%
HRD_N						
0 to –150 m.a.s.l.	–6.49	0.43	100.0%	–6.42	0.38	100.0%
–150 to –400 m.a.s.l.	–7.19	0.75	99.5%	–7.01	0.53	100.0%
–400 to –650 m.a.s.l.	–8.33	0.80	86.3%	–8.16	0.67	97.4%
–650 to –1,000 m.a.s.l.	–8.70	0.83	21.0%	–8.93	0.87	39.6%

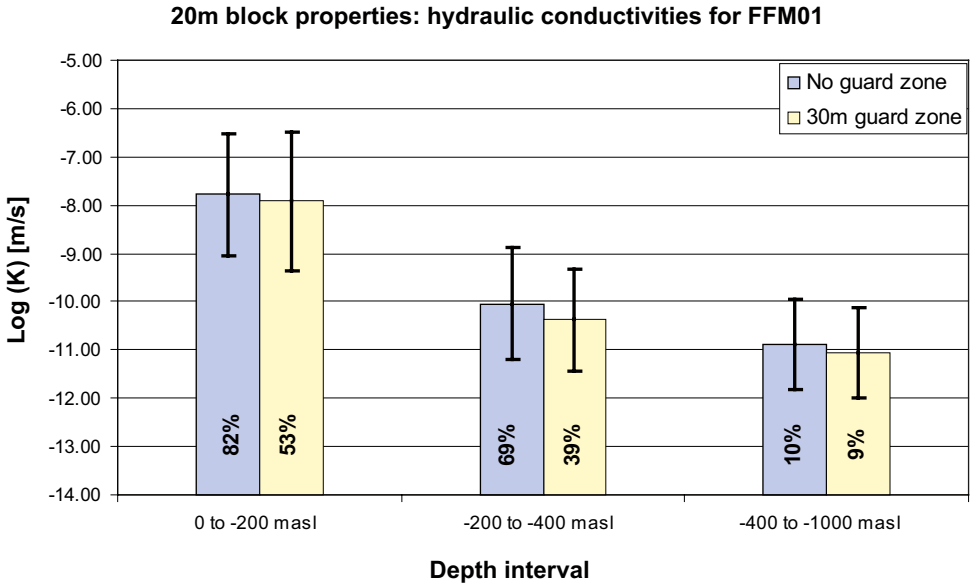

Figure A7-5. *Histogram comparing 20 m block-scale hydraulic conductivities by depth zone, using a guard-zone of 30 m around the block and without a guard zone. The DFN model used is for FFM01, semi-correlated transmissivity model. The height of the column is the mean Log (hydraulic conductivity) of the blocks that are hydraulically active. The error bars are the standard deviation of Log (hydraulic conductivity) of the blocks that are hydraulically active. The number at the base of each column is the percentage of blocks that are hydraulically active ion 3D.*

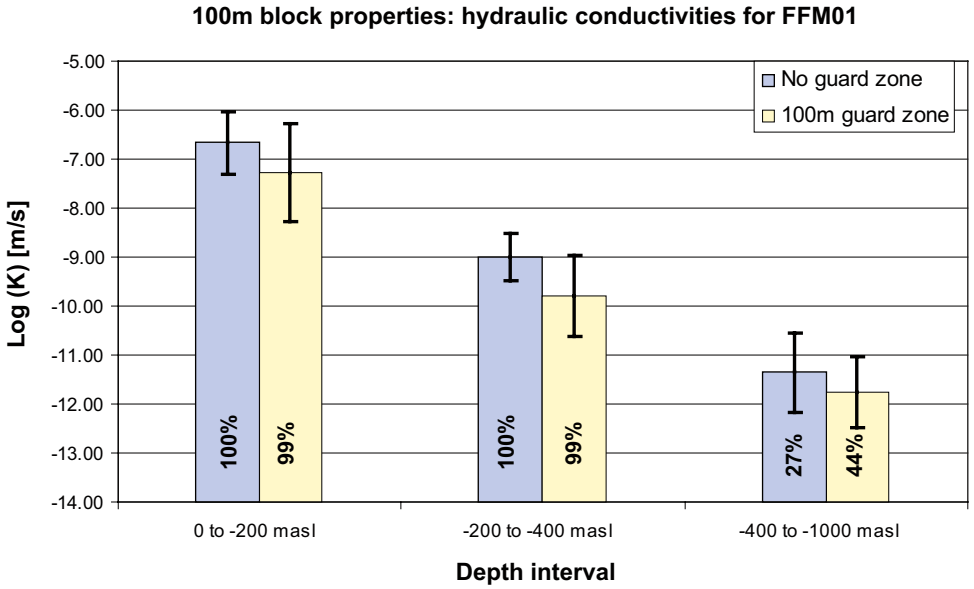

Figure A7-6. *Histogram comparing 100 m block-scale hydraulic conductivities by depth zone, using a guard-zone of 100 m around the block and without a guard zone. The DFN model used is for FFM01, semi-correlated transmissivity. The height of the column is the mean Log (hydraulic conductivity) of the blocks that are hydraulically active. The error bars are the standard deviation of Log (hydraulic conductivity) of the blocks that are hydraulically active. The number at the base of each column is the percentage of blocks that are hydraulically active in 3D.*

Table A7-2. A comparison of 20 m upscaling results, on one realization of the Forsmark regional DFN model, with and without a guard zone.

	Using a guard zone (10 m)			Without a guard zone		
	Log_{10} Hydraulic conductivity (ms/)			Log_{10} Hydraulic conductivity (ms/)		
	mean K_{eff}	std K_{eff}	% active	mean K_{eff}	std K_{eff}	% active
FFM01						
0 to –200 m.a.s.l.	–7.96	1.18	62.8%	–7.92	1.08	86.1%
–200 to –400 m.a.s.l.	–9.45	1.01	54.3%	–9.47	0.96	77.9%
–400 to –1,000 m.a.s.l.	–10.45	1.05	17.7%	–10.67	1.01	30.1%
FFM02						
0 to –200 m.a.s.l.	–8.51	0.99	84.1%	–8.22	0.84	97.3%
–200 to –400 m.a.s.l.	–8.69	0.99	79.0%	–8.29	0.79	96.8%
FFM03						
0 to –200 m.a.s.l.	–8.96	0.87	58.6%	–8.91	0.82	82.1%
–200 to –400 m.a.s.l.	–8.88	0.82	57.5%	–8.85	0.79	81.1%
–400 to –1,000 masl	–9.21	0.78	32.1%	–9.18	0.75	57.2%
FFM04						
0 to –200 m.a.s.l.	–8.74	0.83	59.3%	–8.67	0.81	81.0%
–200 to –400 m.a.s.l.	–8.62	0.79	55.3%	–8.60	0.78	79.6%
–400 to –1,000 m.a.s.l.	–8.76	0.70	37.6%	–8.84	0.68	59.9%
FFM05						
0 to –200 m.a.s.l.	–8.86	0.92	60.3%	–8.82	0.87	83.5%
–200 to –400 m.a.s.l.	–8.82	0.86	53.8%	–8.84	0.83	77.2%
–400 to –1,000 m.a.s.l.	–8.98	0.73	39.6%	–9.06	0.71	60.4%
FFM06						
0 to –200 m.a.s.l.	–7.62	1.36	64.2%	–7.66	1.22	87.6%
–200 to –400 m.a.s.l.	–9.49	1.07	48.2%	–9.51	1.01	75.2%
–400 to –1,000 m.a.s.l.	–10.53	0.98	19.6%	–10.74	0.96	33.0%

A8 Comparison of natural groundwater heads.

Profiles of environmental head predicted in core drilled boreholes using the base case model are compared with measured values taken as an average over a packer interval are shown in Figure A8-1 through Figure A8-13. Here, the boreholes are grouped by HRD.

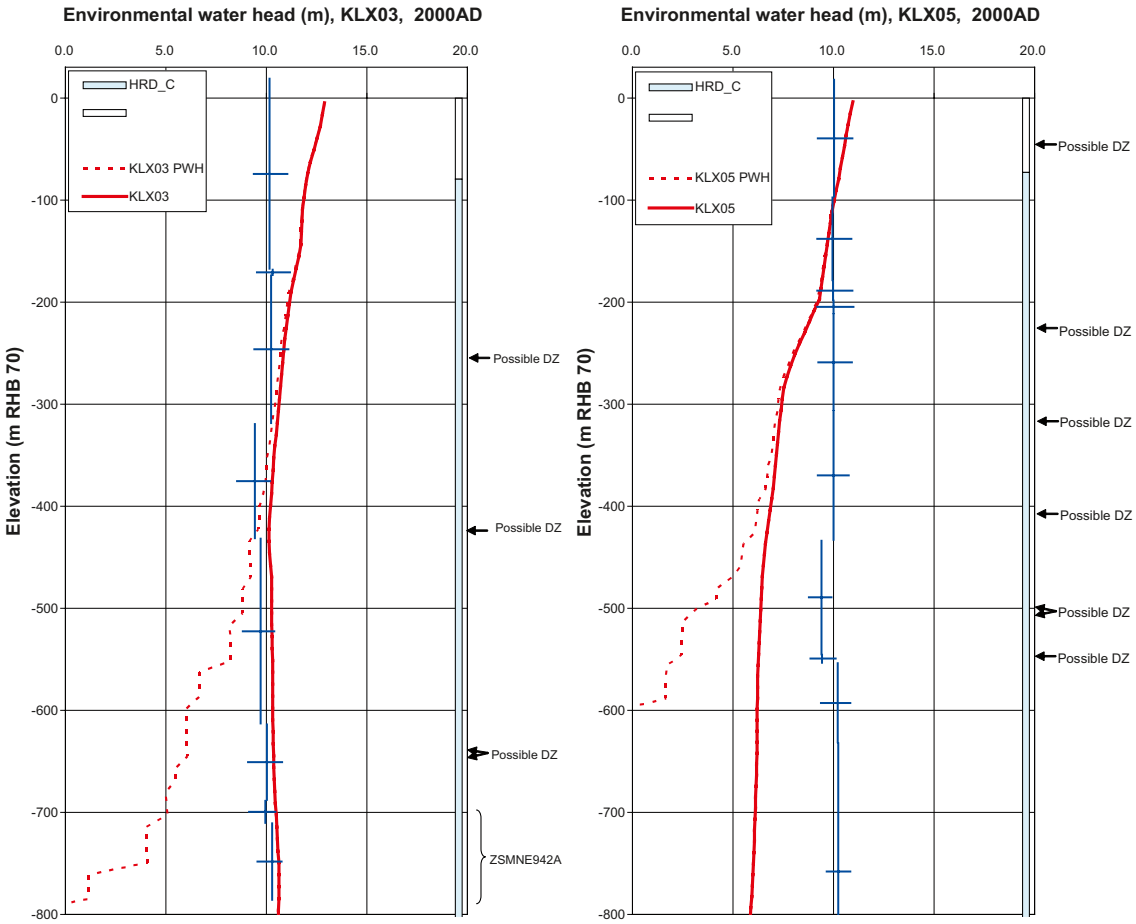

Figure A8-1. *Modelled environmental-water head (solid red line) and point-water head (dotted red line) in KLX03 and KLX05 in HRD_C compared to environmental-water heads (blue crossed lines, centre showing midpoint of the section, vertical line showing the extent of the section and horizontal line showing the temporal variation of the measured head) calculated from measured point-water head data in sections along the borehole. At the right hand side, the prevailing hydraulic rock domains are shown as coloured bars along the borehole. Detected fractures/deformation zones are indicated at the intersection depth in the boreholes.*

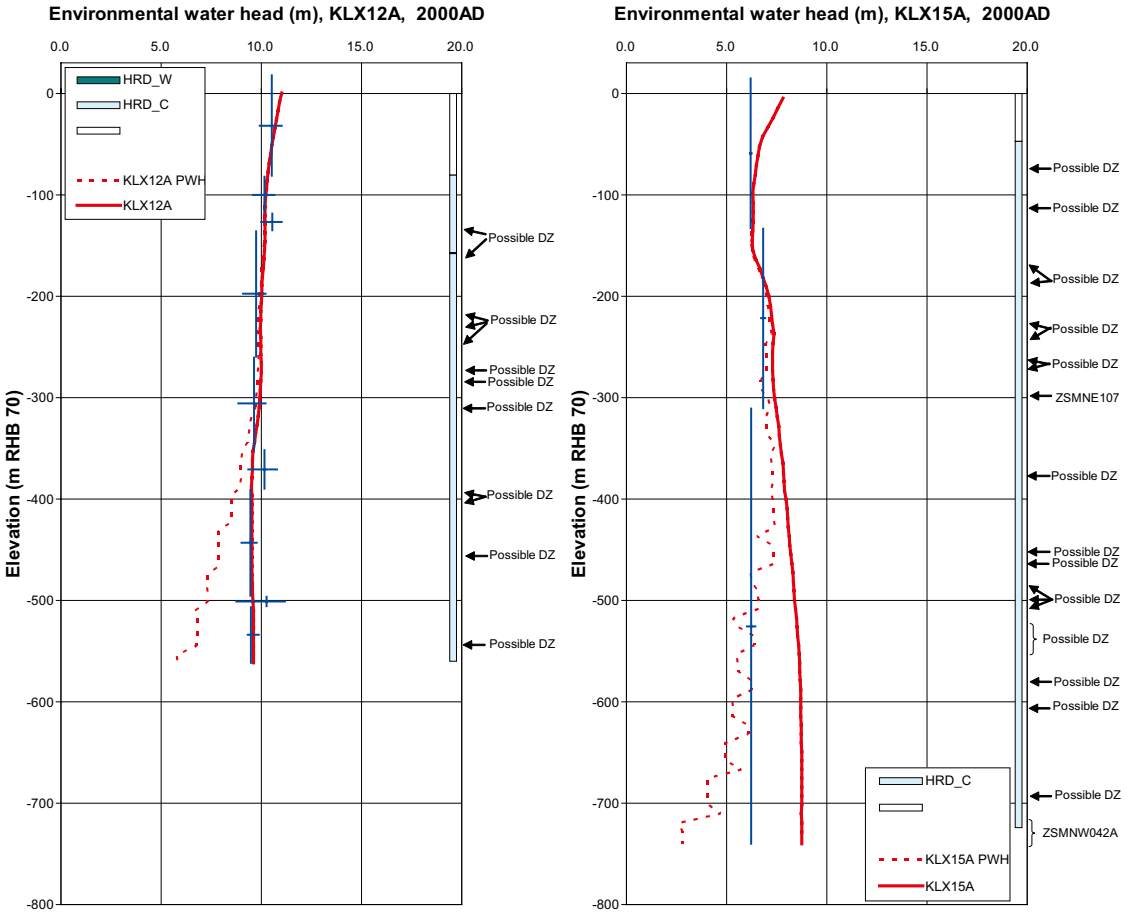

Figure A8-2. *Modelled environmental-water head (solid red line) and point-water head (dotted red line) in KLX12A and KLX15A in HRD_C compared to environmental-water heads (blue crossed lines, centre showing midpoint of the section, vertical line showing the extent of the section and horizontal line showing the temporal variation of the measured head) calculated from measured point-water head data in sections along the borehole. At the right hand side, the prevailing hydraulic rock domains are shown as coloured bars along the borehole. Detected fractures/deformation zones are indicated at the intersection depth in the boreholes.*

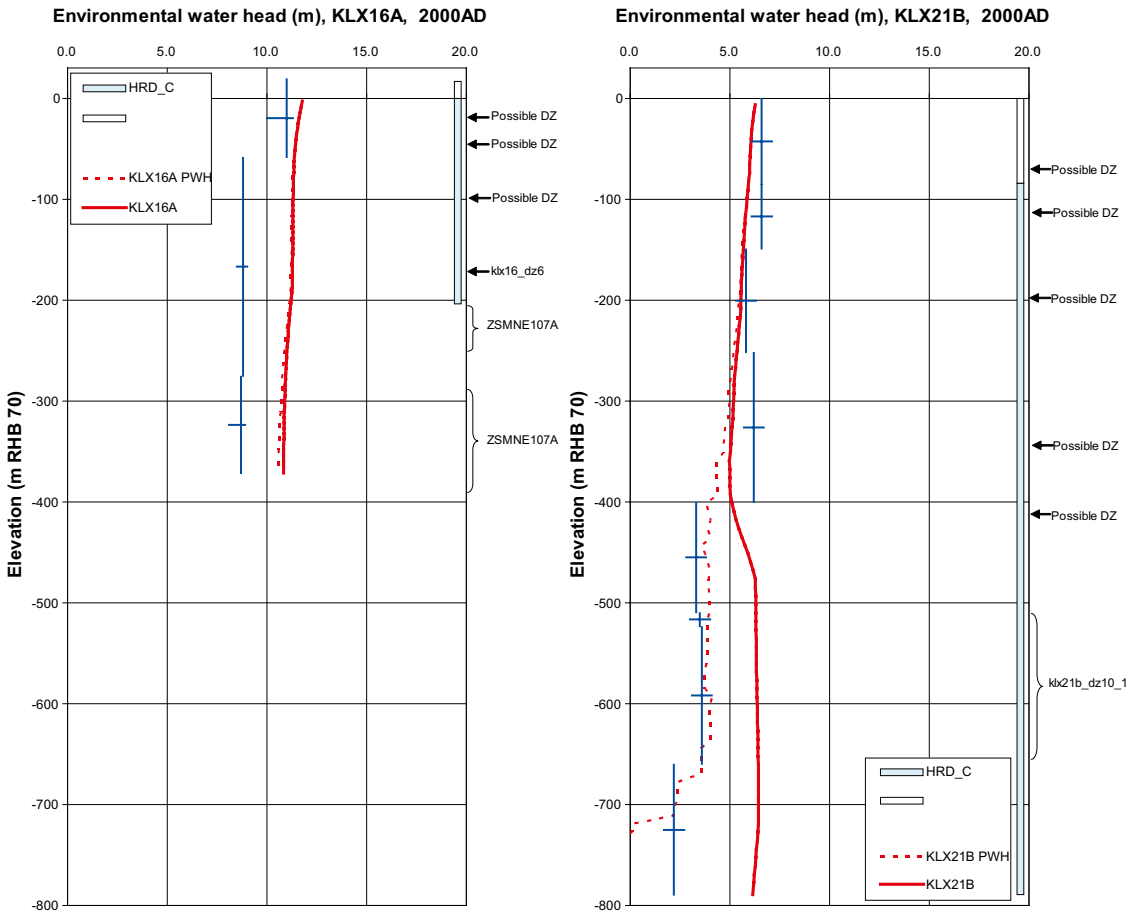

Figure A8-3. *Modelled environmental-water head (solid red line) and point-water head (dotted red line) in KLX16A and KLX21B in HRD_C compared to environmental-water heads (blue crossed lines, centre showing midpoint of the section, vertical line showing the extent of the section and horizontal line showing the temporal variation of the measured head) calculated from measured point-water head data in sections along the borehole. At the right hand side, the prevailing hydraulic rock domains are shown as coloured bars along the borehole. Detected fractures/deformation zones are indicated at the intersection depth in the boreholes.*

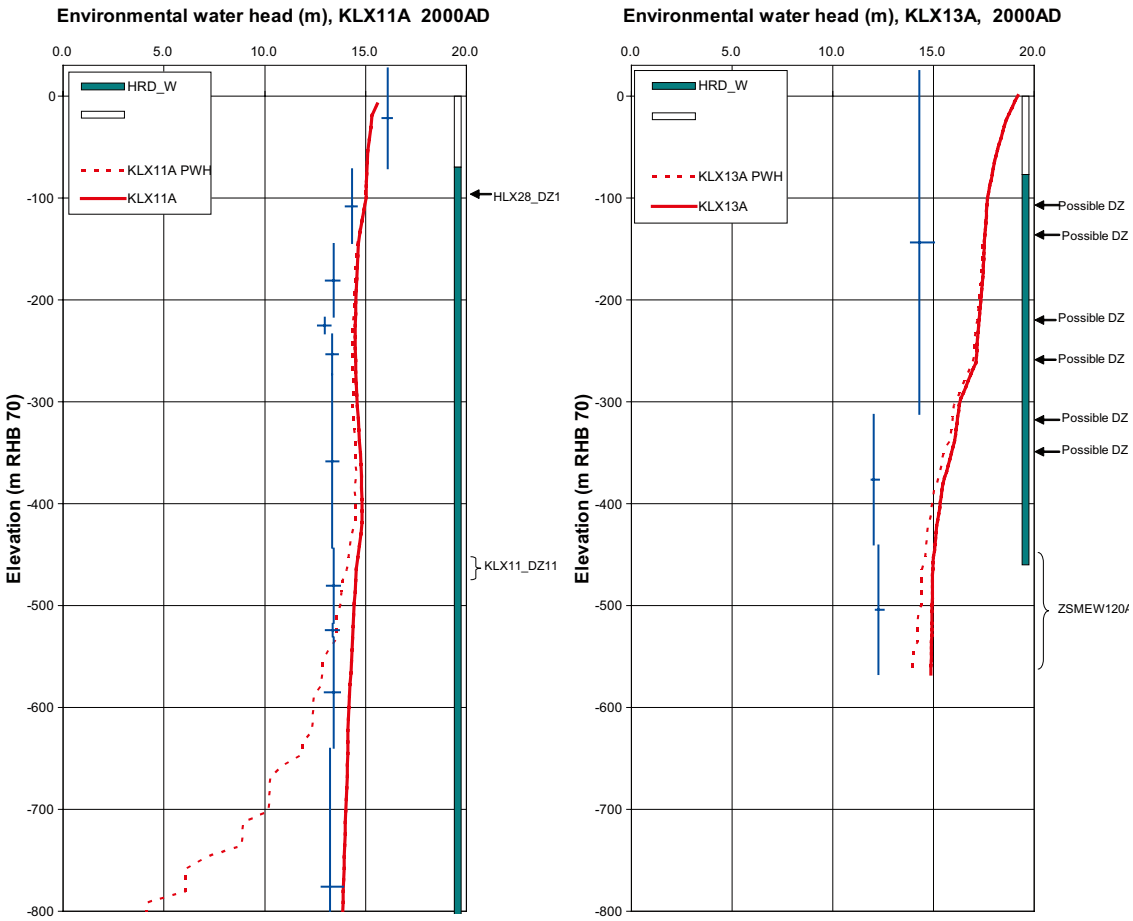

Figure A8-4. *Modelled environmental-water head (solid red line) and point-water head (dotted red line) in KLX11A and KLX13A in HRD_W compared to environmental-water heads (blue crossed lines, centre showing midpoint of the section, vertical line showing the extent of the section and horizontal line showing the temporal variation of the measured head) calculated from measured point-water head data in sections along the borehole. At the right hand side, the prevailing hydraulic rock domains are shown as coloured bars along the borehole. Detected fractures/deformation zones are indicated at the intersection depth in the boreholes.*

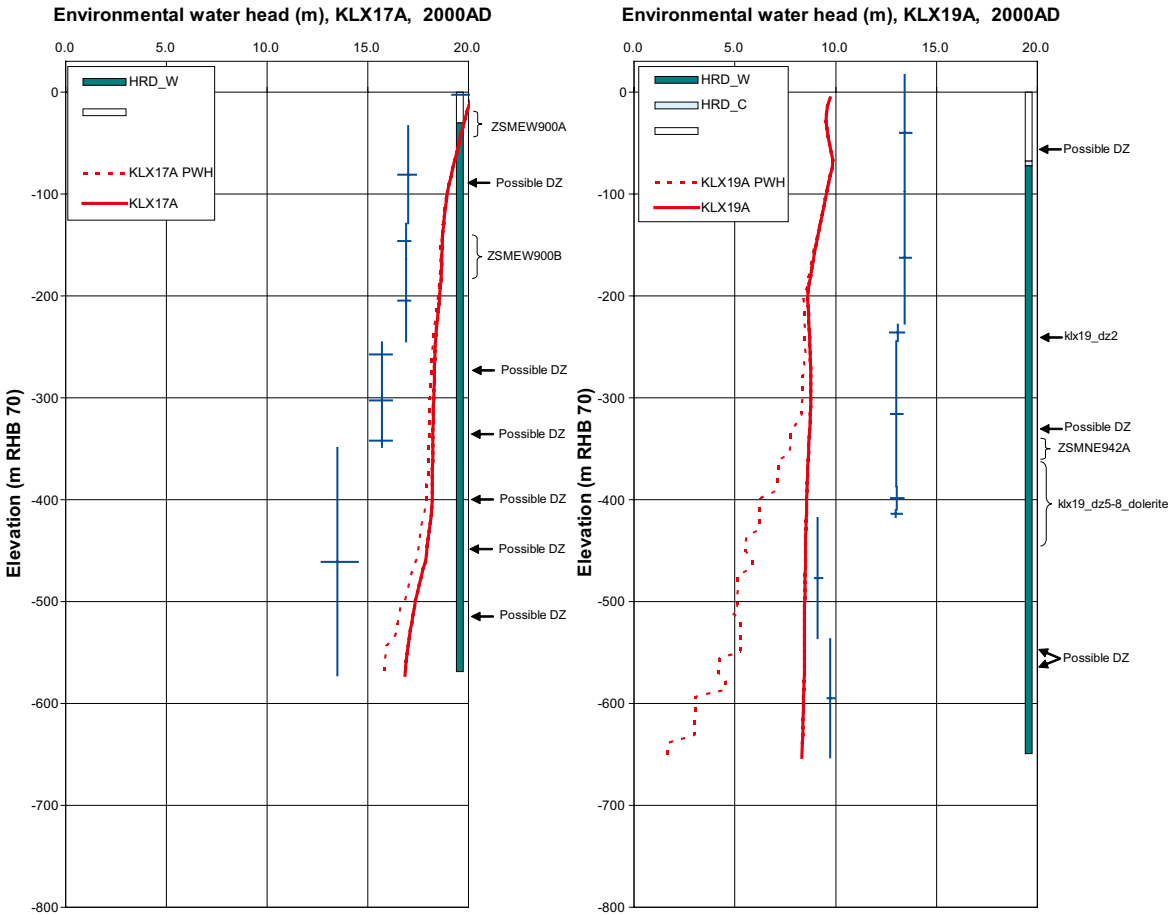

Figure A8-5. *Modelled environmental-water head (solid red line) and point-water head (dotted red line) in KLX17A and KLX19A in HRD_W compared to environmental-water heads (blue crossed lines, centre showing midpoint of the section, vertical line showing the extent of the section and horizontal line showing the temporal variation of the measured head) calculated from measured point-water head data in sections along the borehole. At the right hand side, the prevailing hydraulic rock domains are shown as coloured bars along the borehole. Detected fractures/deformation zones are indicated at the intersection depth in the boreholes.*

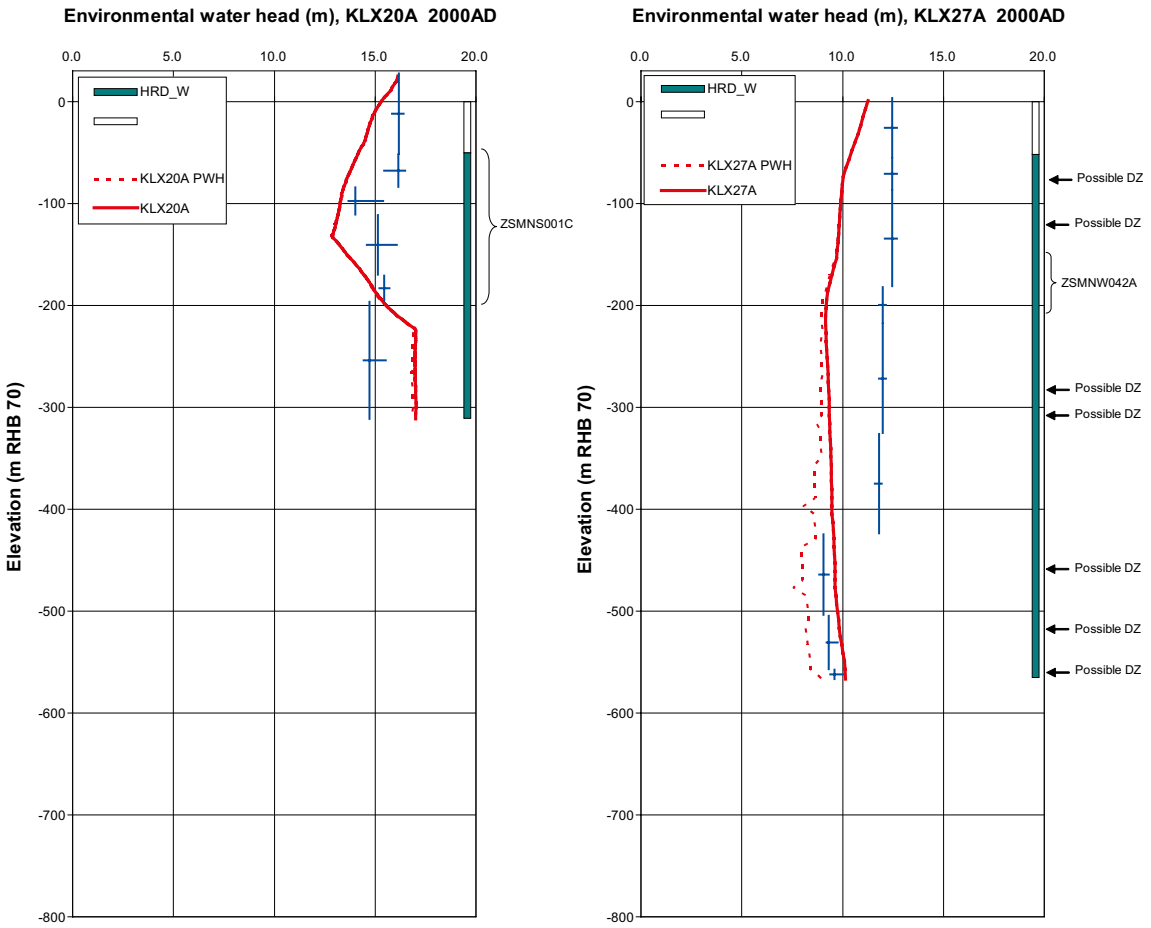

Figure A8-6. *Modelled environmental-water head (solid red line) and point-water head (dotted red line) in KLX20A and KLX27A in HRD_W compared to environmental-water heads (blue crossed lines, centre showing midpoint of the section, vertical line showing the extent of the section and horizontal line showing the temporal variation of the measured head) calculated from measured point-water head data in sections along the borehole. At the right hand side, the prevailing hydraulic rock domains are shown as coloured bars along the borehole. Detected fractures/deformation zones are indicated at the intersection depth in the boreholes.*

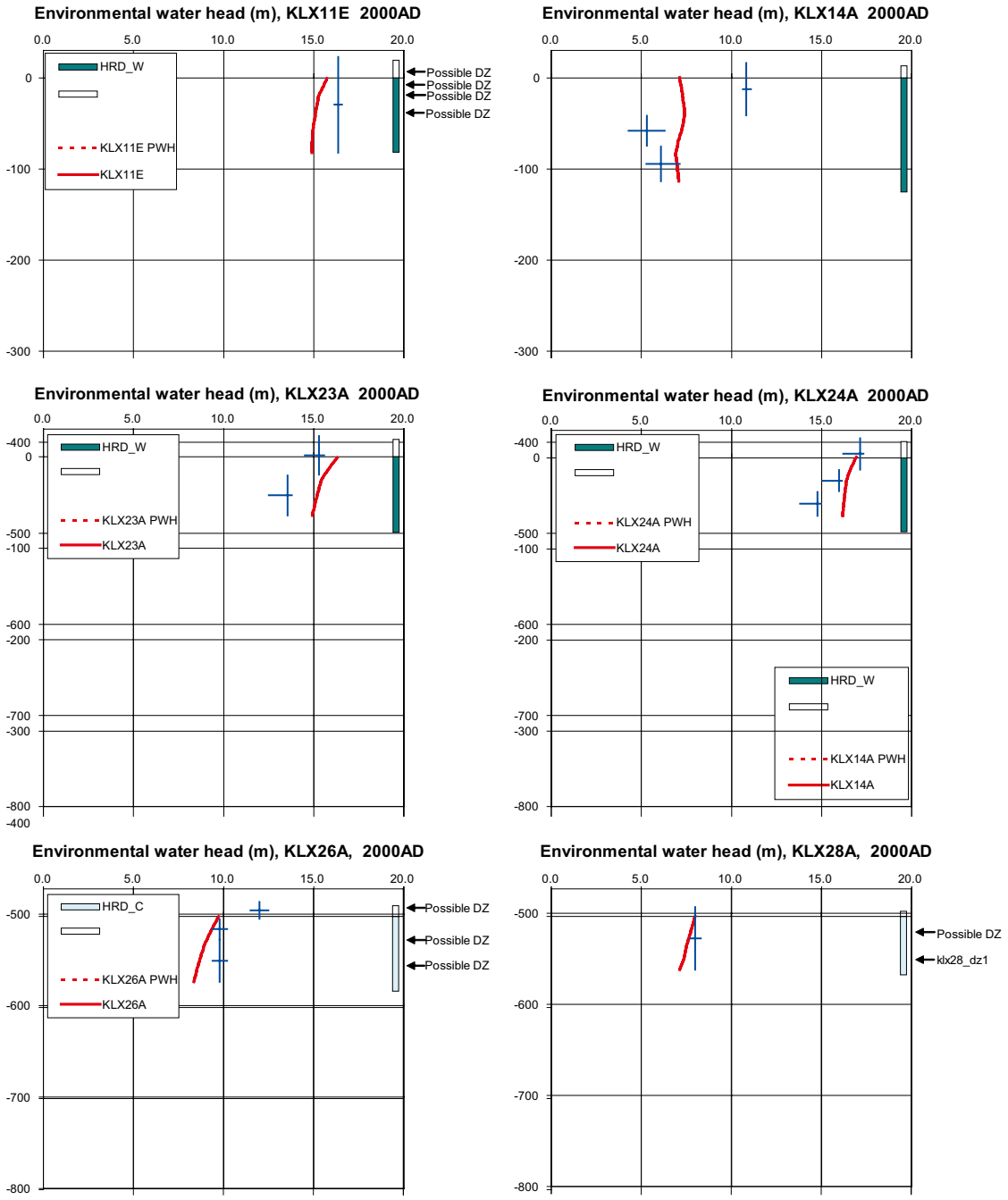

Figure A8-7. *Modelled environmental-water head (solid red line) and point-water head (dotted red line) in KLX11E, KLX14A, KLX23A, KLX24A in HRD_W; and KLX26A and KLX28A in HRD_ C compared to environmental-water heads (blue crossed lines, centre showing midpoint of the section, vertical line showing the extent of the section and horizontal line showing the temporal variation of the measured head) calculated from measured point-water head data in sections along the borehole. At the right hand side, the prevailing hydraulic rock domains are shown as coloured bars along the borehole. Detected fractures/ deformation zones are indicated at the intersection depth in the boreholes.*

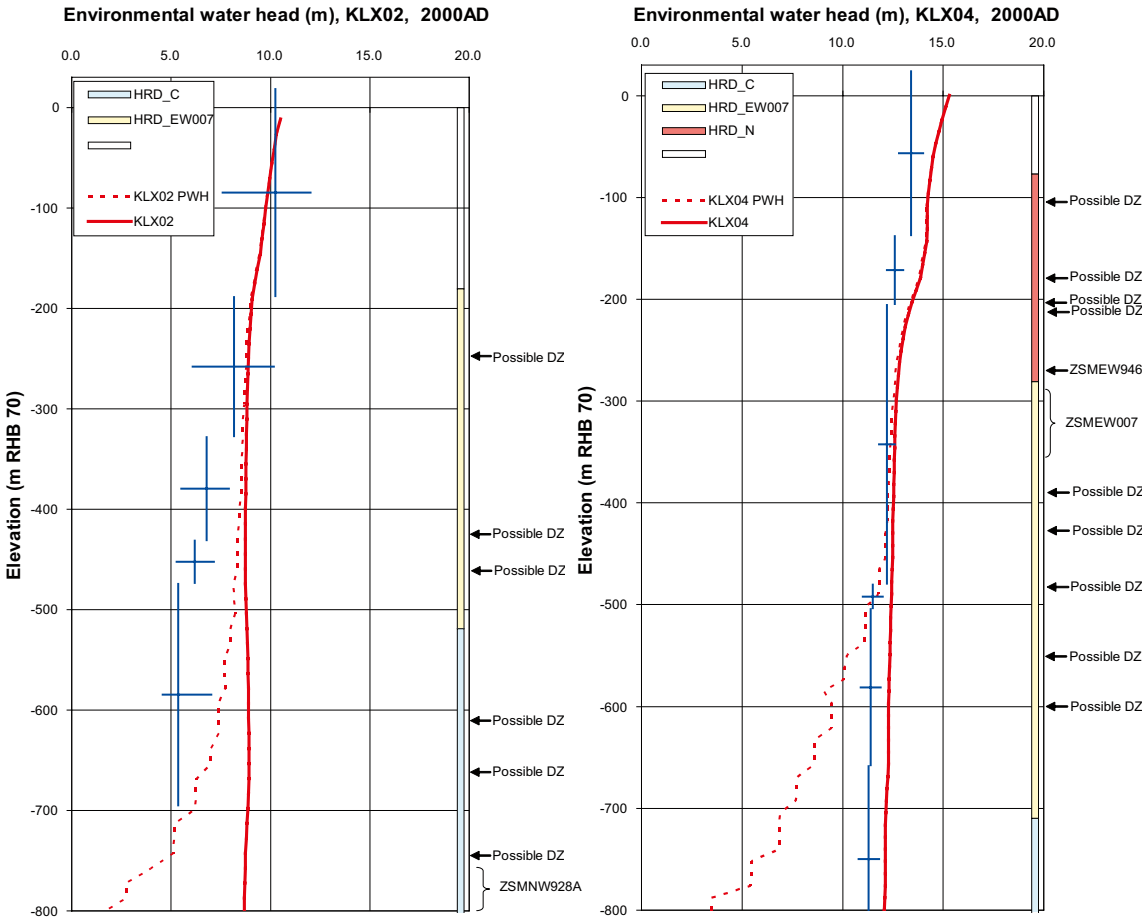

Figure A8-8. *Modelled environmental-water head (solid red line) and point-water head (dotted red line) in KLX02 and KLX04 in HRD_EW007 compared to environmental-water heads (blue crossed lines, centre showing midpoint of the section, vertical line showing the extent of the section and horizontal line showing the temporal variation of the measured head) calculated from measured point-water head data in sections along the borehole. At the right hand side, the prevailing hydraulic rock domains are shown as coloured bars along the borehole. Detected fractures/deformation zones are indicated at the intersection depth in the boreholes.*

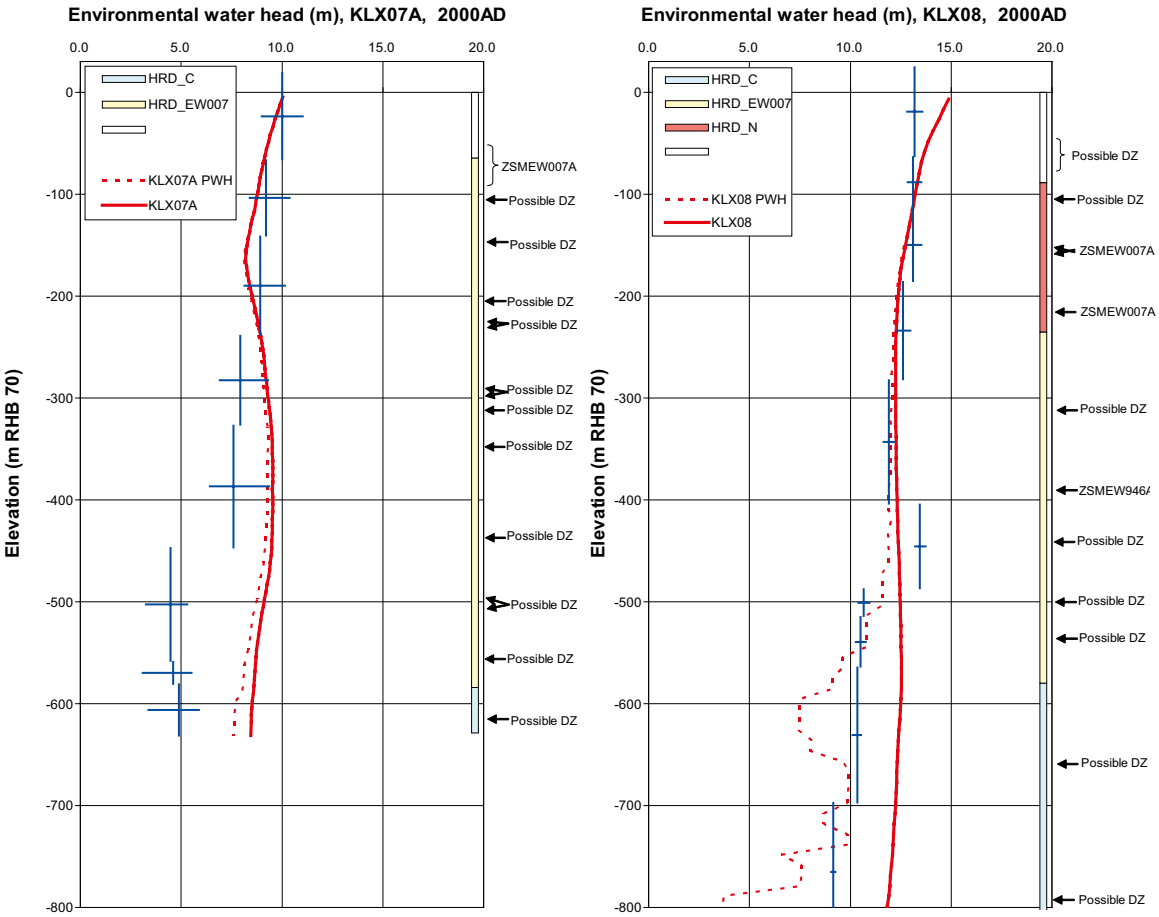

Figure A8-9. *Modelled environmental-water head (solid red line) and point-water head (dotted red line) in KLX07A and KLX08 in HRD_ EW007compared to environmental-water heads (blue crossed lines, centre showing midpoint of the section, vertical line showing the extent of the section and horizontal line showing the temporal variation of the measured head) calculated from measured point-water head data in sections along the borehole. At the right hand side, the prevailing hydraulic rock domains are shown as coloured bars along the borehole. Detected fractures/deformation zones are indicated at the intersection depth in the boreholes.*

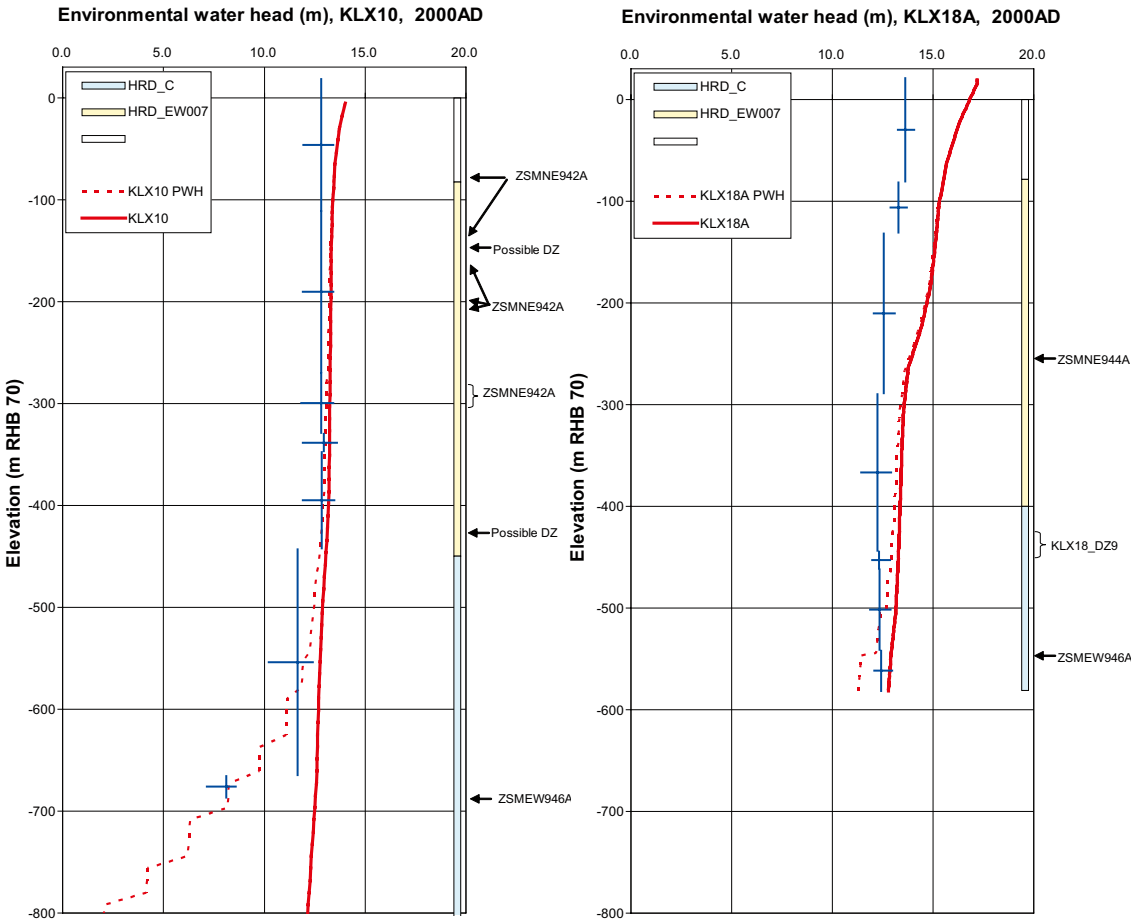

Figure A8-10. *Modelled environmental-water head (solid red line) and point-water head (dotted red line) in KLX10 and KLX18A in HRD_ EW007compared to environmental-water heads (blue crossed lines, centre showing midpoint of the section, vertical line showing the extent of the section and horizontal line showing the temporal variation of the measured head) calculated from measured point-water head data in sections along the borehole. At the right hand side, the prevailing hydraulic rock domains are shown as coloured bars along the borehole. Detected fractures/deformation zones are indicated at the intersection depth in the boreholes.*

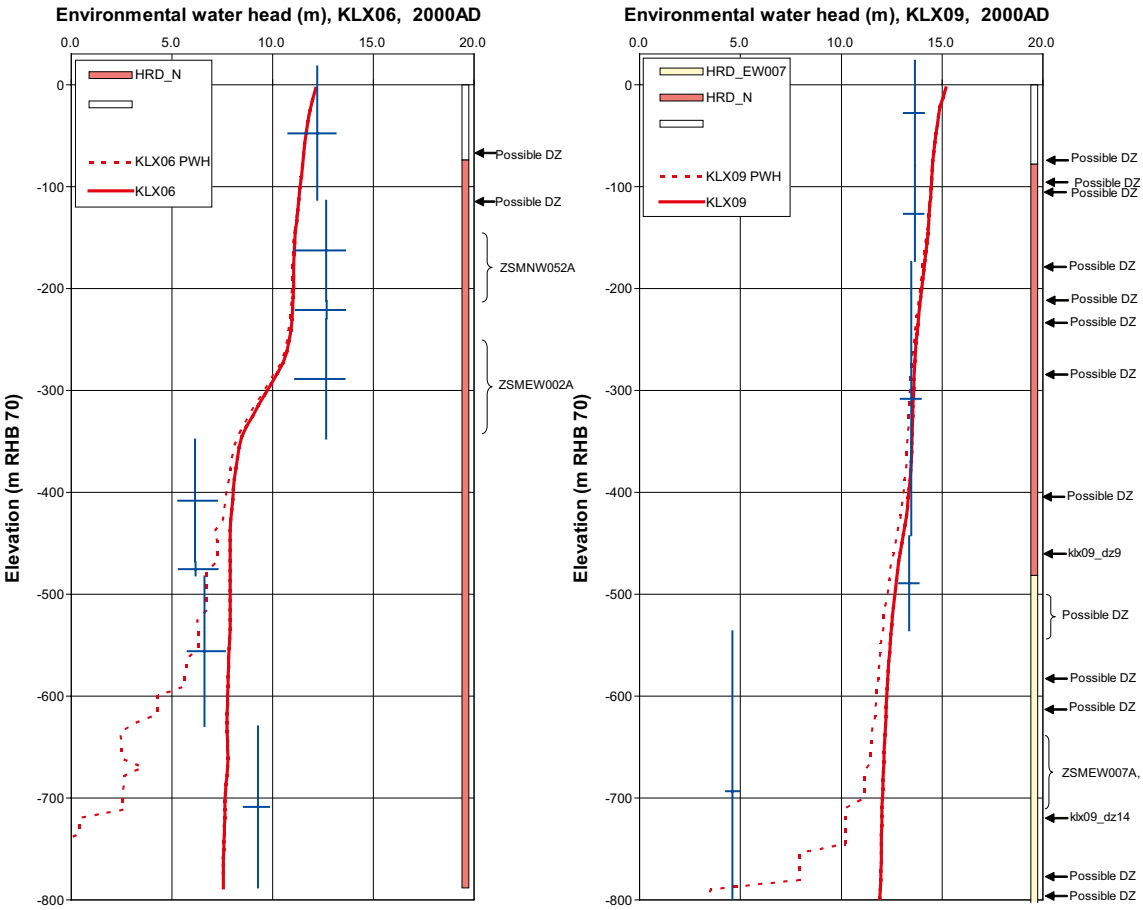

Figure A8-11. *Modelled environmental-water head (solid red line) and point-water head (dotted red line) in KLX06 and KLX09 in HRD_ N compared to environmental-water heads (blue crossed lines, centre showing midpoint of the section, vertical line showing the extent of the section and horizontal line showing the temporal variation of the measured head) calculated from measured point-water head data in sections along the borehole. At the right hand side, the prevailing hydraulic rock domains are shown as coloured bars along the borehole. Detected fractures/deformation zones are indicated at the intersection depth in the boreholes.*

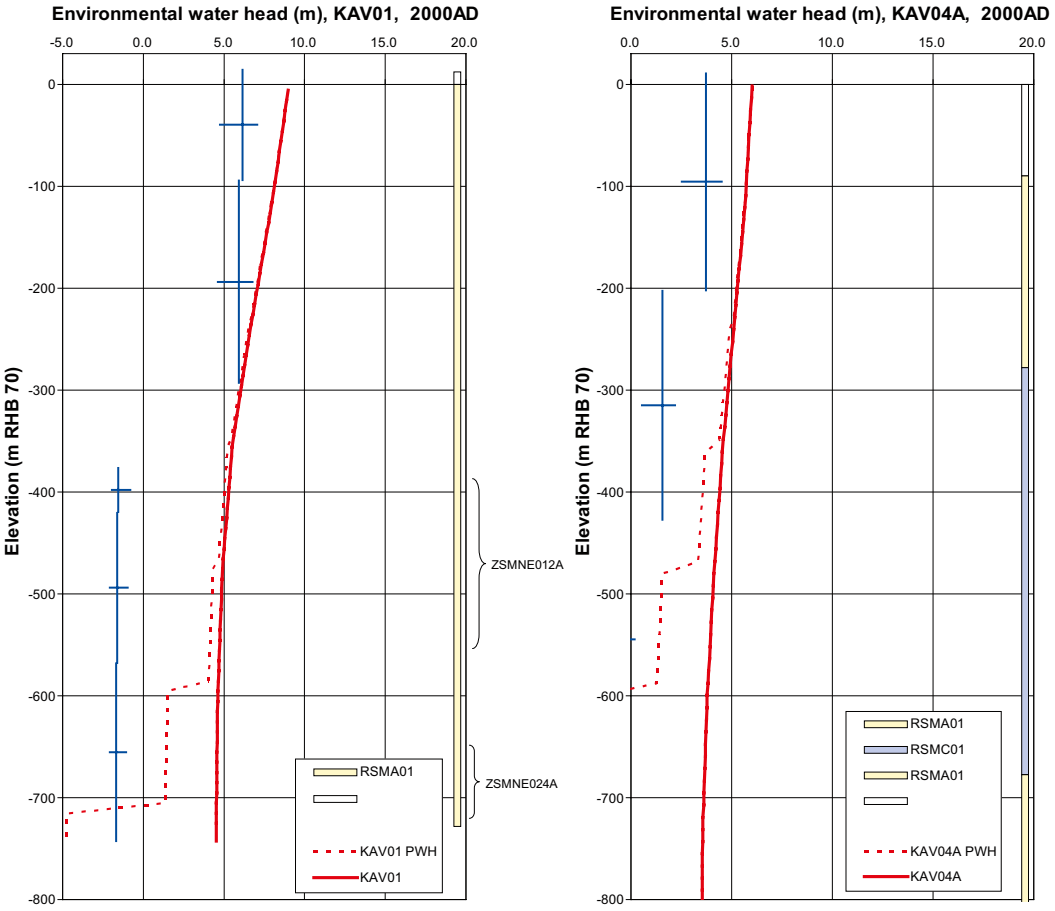

Figure A8-12. *Modelled environmental-water head (solid red line) and point-water head (dotted red line) in KAV01 and KAV04A in HRD_N compared to environmental-water heads (blue crossed lines, centre showing midpoint of the section, vertical line showing the extent of the section and horizontal line showing the temporal variation of the measured head) calculated from measured point-water head data in sections along the borehole. At the right hand side, the prevailing hydraulic rock domains are shown as coloured bars along the borehole. Detected fractures/deformation zones are indicated at the intersection depth in the boreholes.*

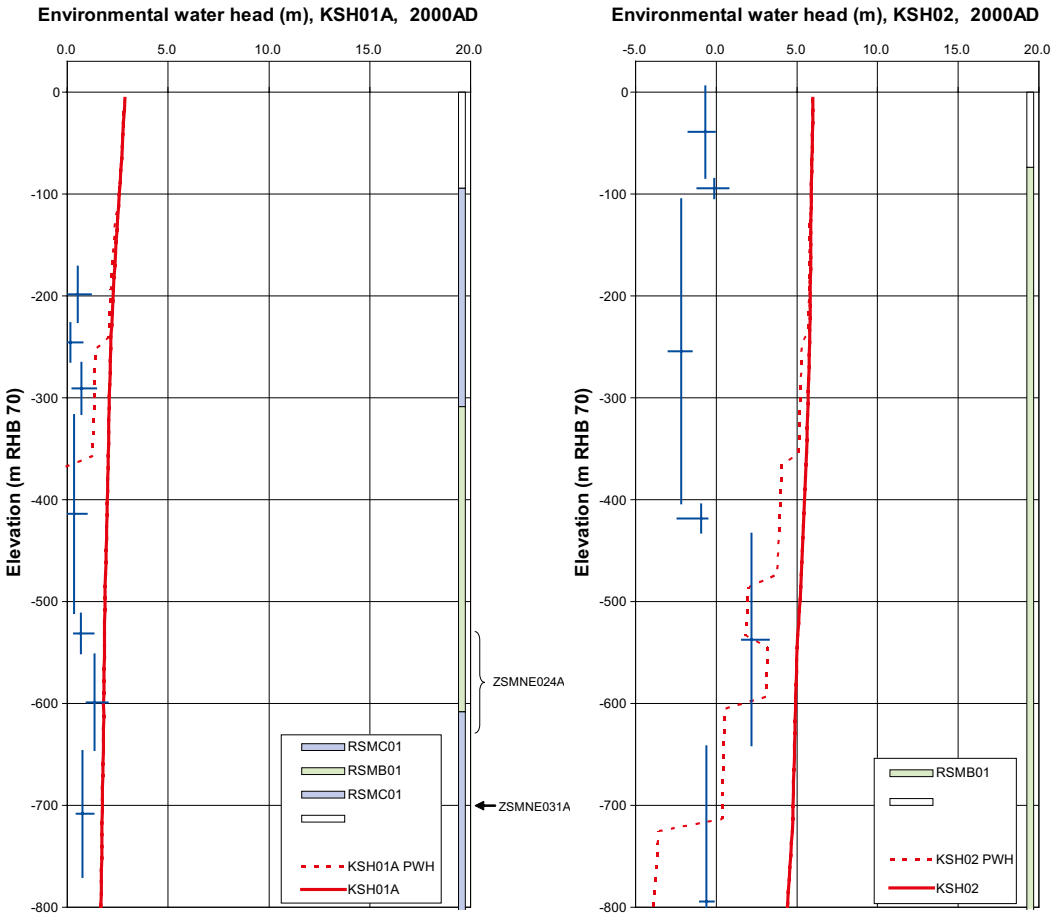

Figure A8-13. *Modelled environmental-water head (solid red line) and point-water head (dotted red line) in KSH01A and KSH02 in HRD_ BC compared to environmental-water heads (blue crossed lines, centre showing midpoint of the section, vertical line showing the extent of the section and horizontal line showing the temporal variation of the measured head) calculated from measured point-water head data in sections along the borehole. At the right hand side, the prevailing hydraulic rock domains are shown as coloured bars along the borehole. Detected fractures/deformation zones are indicated at the intersection depth in the boreholes.*

Appendix 9

A9 Additional palaeohydrogeology results

This appendix presents additional results supporting Section 9.

A9.1 Comparison of reference water fractions in boreholes

The base case simulated mass fractions of the 5 references waters in the fracture water (solid lines) and porewater (dashed lines) for all the core drilled boreholes are presented in Figure A9-1 through Figure A9-6. The M3 interpreted mixing fractions, based on just 4 reference waters (meteoric water was not differentiated between Altered meteoric water, i.e. post-glacial origin, and Inter-glacial water in this analysis).

A9.2 Palaeo-hydrogeological cross-sections

Figure A9-7 shows the positions of the vertical sections used to visualise the palaeo-hydrogeological simulations for the base case. On these various chemical entities, such as reference water mass fractions, major ions and isotope ratios, are plotted along with the positions of nearby core-drilled boreholes. The distributions of Cl, $\delta^{18}O$ along with the magnitudes and direction of Darcy velocity are shown on each of the sections Hv1–Hv7 in Figure A9-8 through Figure A9-14.

A9.3 Illustrations of sensitivities

One aspect of the calibration process is illustrated in Figure A9-15 showing the simulated profiles of Cl, Br/Cl, $\delta^{18}O$ and HCO_3 in the boreholes within HRD_C for the variant based on uncalibrated hydraulic properties of HCD and HRD as specified in /Rhén et al. 2008/. Comparing this to Figure 9-3 for the base case it can be seen that Cl > 5,000 mg/l is about 200 m deeper for most boreholes in this variant with uncalibrated hydraulic properties., Likewise post-glacial meteoric, indicated by HCO_3, penetrates about 200 m deeper and there is very little of what could be considered a signature of *Glacial Water* left in any boreholes. Hence, this was not considered a viable model for palaeohydrogeological simulations and changed to the hydraulic properties were necessary. The improvement in the calibration of the base case was more dependent on the changes made to the HCD parameterisation, although there was significant dependency on the HRD also. Figure A9-16 is included to illustrate the sensitivity to the changes made to the HCD alone with only the transmissivity of the HCD reverted to uncalibrated values. Cl > 5,000 mg/l is about 50–200 m deeper in this uncalibrated HCD variant, especially in KLX15A. Post-glacial meteoric, indicated by HCO_3, penetrated 100–200 m deeper for this variant.

By contrast, the next two variants included improve the match with hydrochemistry. The first has an enhanced fracture surface area per unit volume, σ, in the solute transport equations by a factor 3 in the HCD, the second has the horizontal conductivity of the HRD increased by a factor 3 above –150 m (See Table 9-1). Results for boreholes within the Laxemar focused area for the first variant are shown in Figure A9-17 through Figure A9-20, and for the second variant in Figure A9-21 through Figure A9-24, and can be compared to Figure 9-3 through 9-6 for the base case. Enhanced fracture surface area in the HCD increases the magnitude of rock matrix diffusion in the deformation zones relative to the surrounding rock which retards any mixing fronts in these higher conductivity regions. HCO_3 and $\delta^{18}O$ are most sensitive to this variant, especially boreholes that intersect several HCD. The match to HCO_3 is significantly improved for KLX03, KLX05 and KLX13A. The match to $\delta^{18}O$ is significantly improved for KLX03, KLX04, KLX08, KLX13A and KLX19A. The increased hydraulic conductivity reduces the hydraulic gradients at depth and consequently preserves the groundwater composition at depth for longer. Cl is generally about 25–50 m shallower for this variant. A similar result is seen for post-glacial meteoric flushing indicated by HCO_3, although post-glacial meteoric flushing in KLX13A and KLX17A is still too deep.

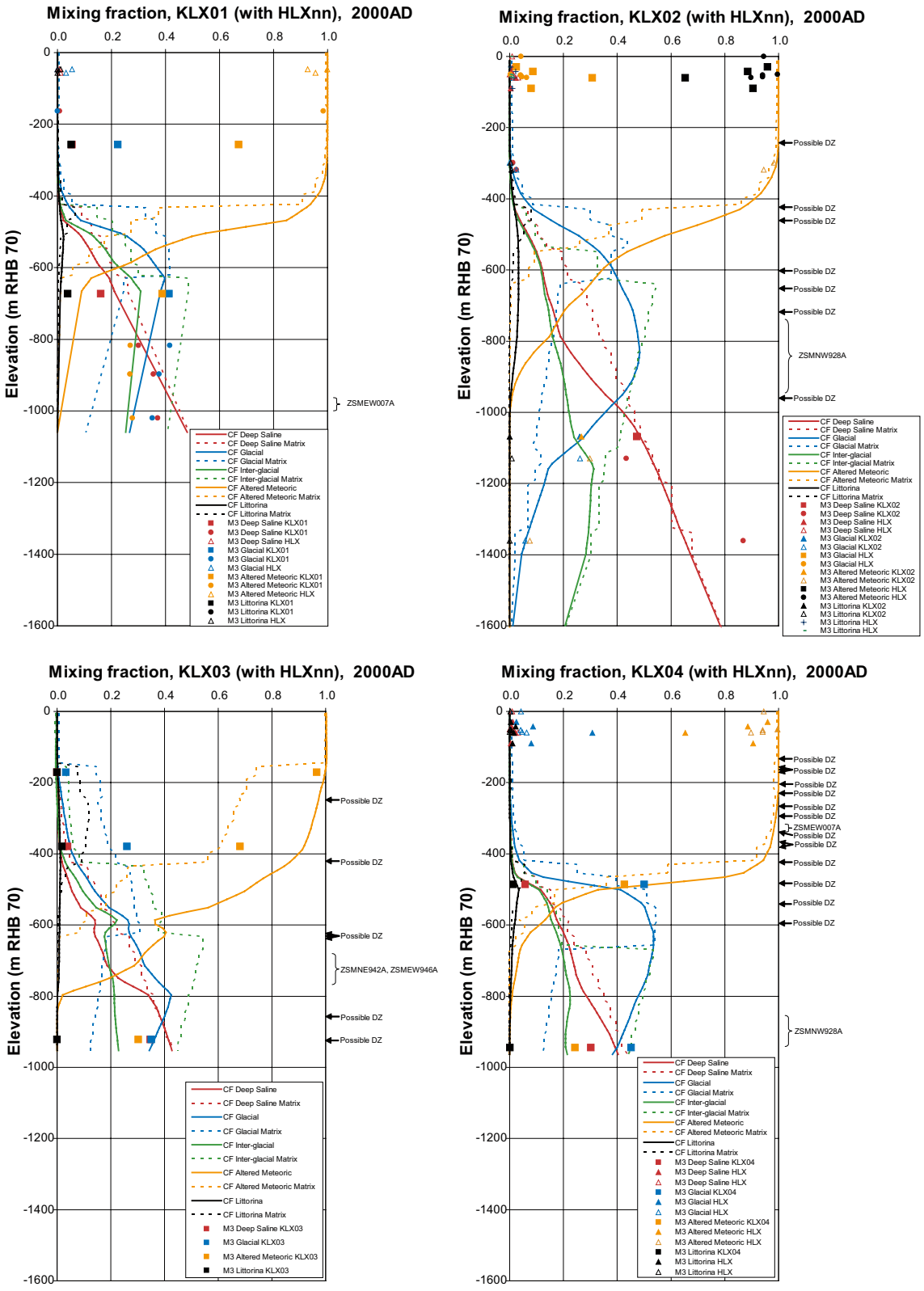

Figure A9-1. *Illustration of simulated mixtures of reference water mass fractions in boreholes KLX01, KLX02, KLX03 and KLX04. Solid lines show simulated reference water mass fractions for Brine, Littorina, Altered meteoric, Glacial and Inter-glacial in the fracture system; dashed correspond to the reference water mass fractions in the matrix. The points show the mixture of 4 reference waters (Brine, Littorina, Altered meteoric, Glacial and Inter-glacial) interpreted from groundwater samples by the M3 method.*

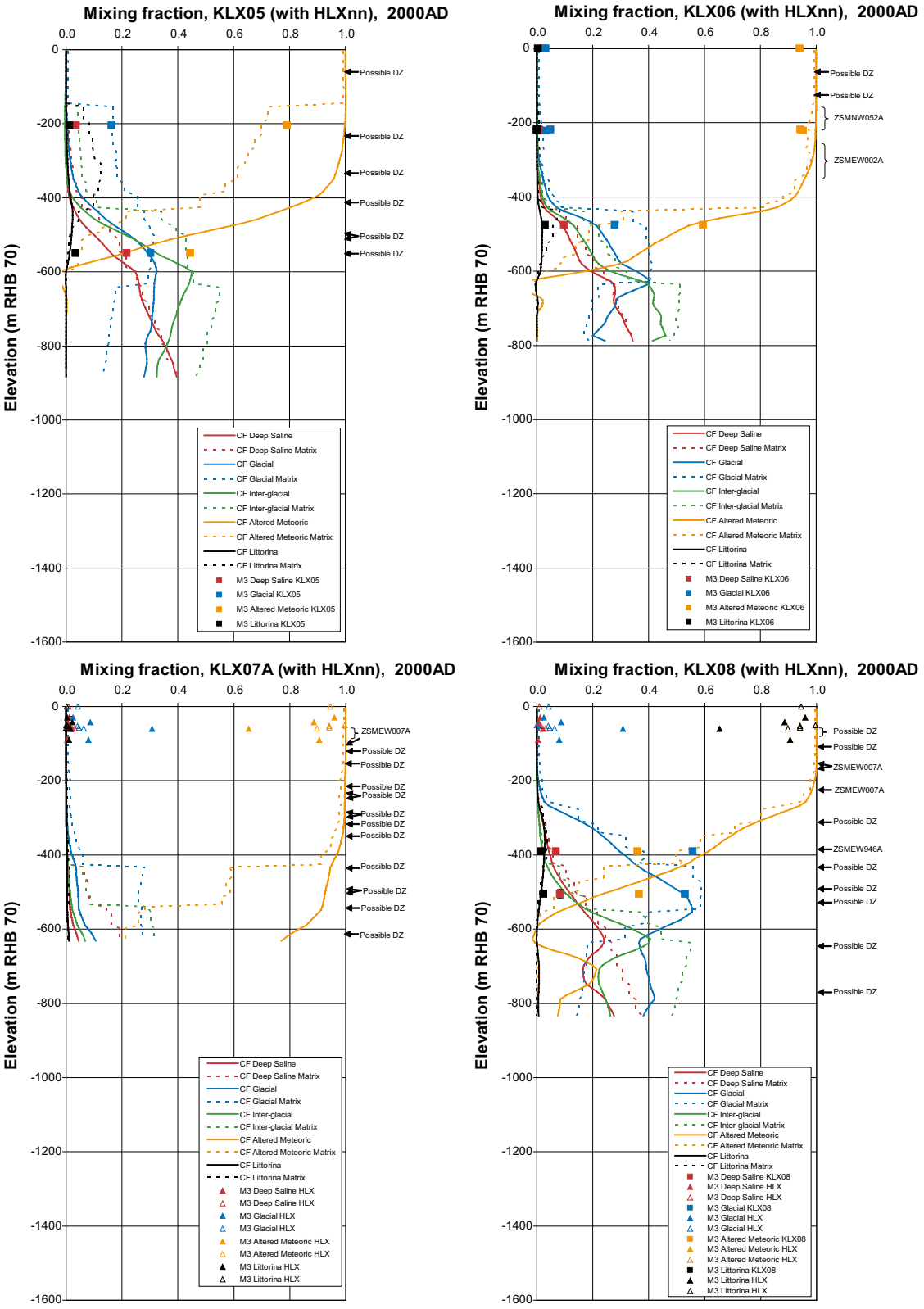

Figure A9-2. *Illustration of simulated mixtures of reference water mass fractions in boreholes KLX05, KLX06, KLX07A and KLX08. Solid lines show simulated reference water mass fractions for Brine, Littorina, Altered meteoric, Glacial and Inter-glacial in the fracture system; dashed correspond to the reference water mass fractions in the matrix. The points show the mixture of 4 reference waters (Brine, Littorina, Altered meteoric, Glacial and Inter-glacial) interpreted from groundwater samples by the M3 method.*

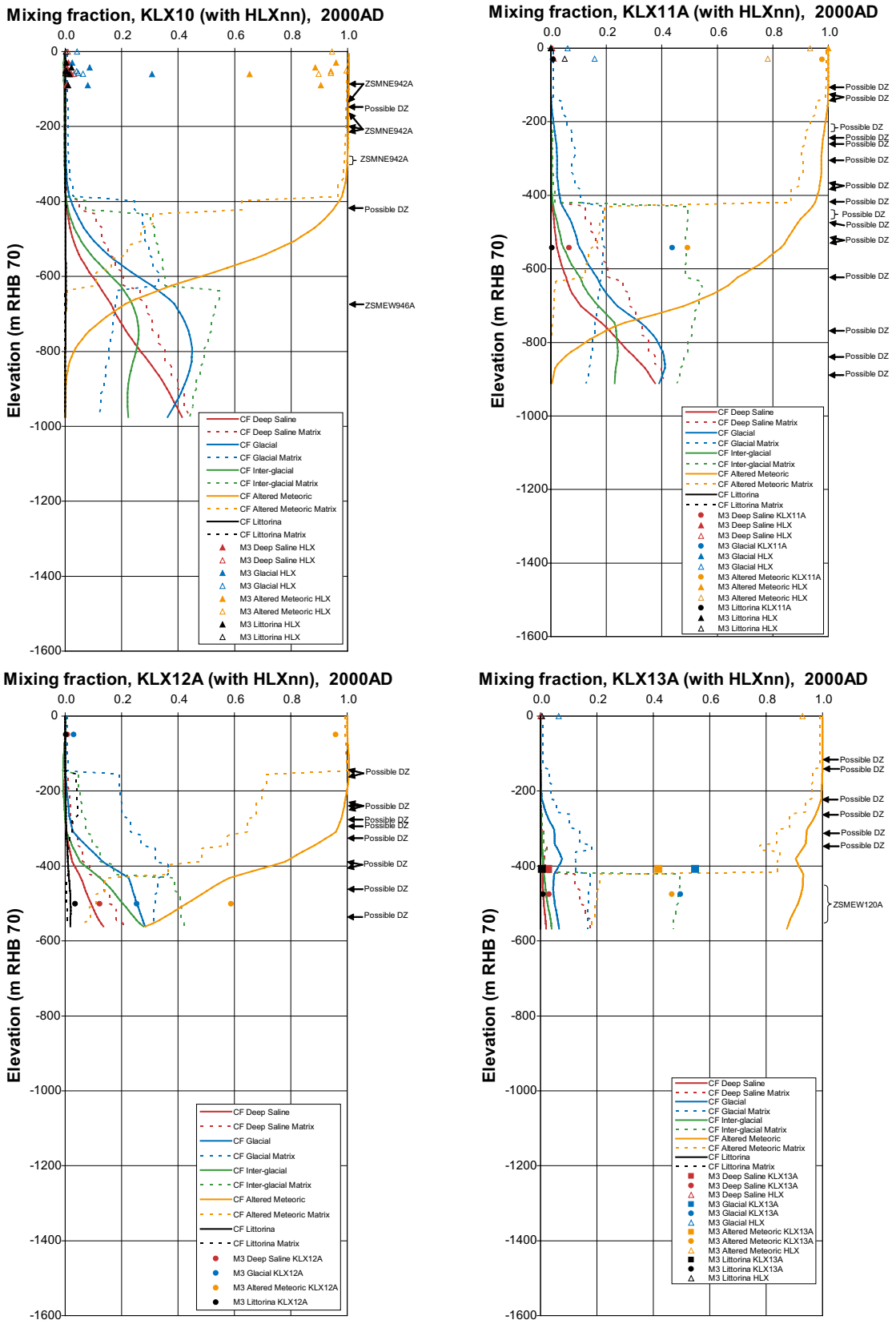

Figure A9-3. *Illustration of simulated mixtures of reference water mass fractions in boreholes KLX10, KLX11A, KLX12A and KLX13A. Solid lines show simulated reference water mass fractions for Brine, Littorina, Altered meteoric, Glacial and Inter-glacial in the fracture system; dashed correspond to the reference water mass fractions in the matrix. The points show the mixture of 4 reference waters (Brine, Littorina, Altered meteoric, Glacial and Inter-glacial) interpreted from groundwater samples by the M3 method.*

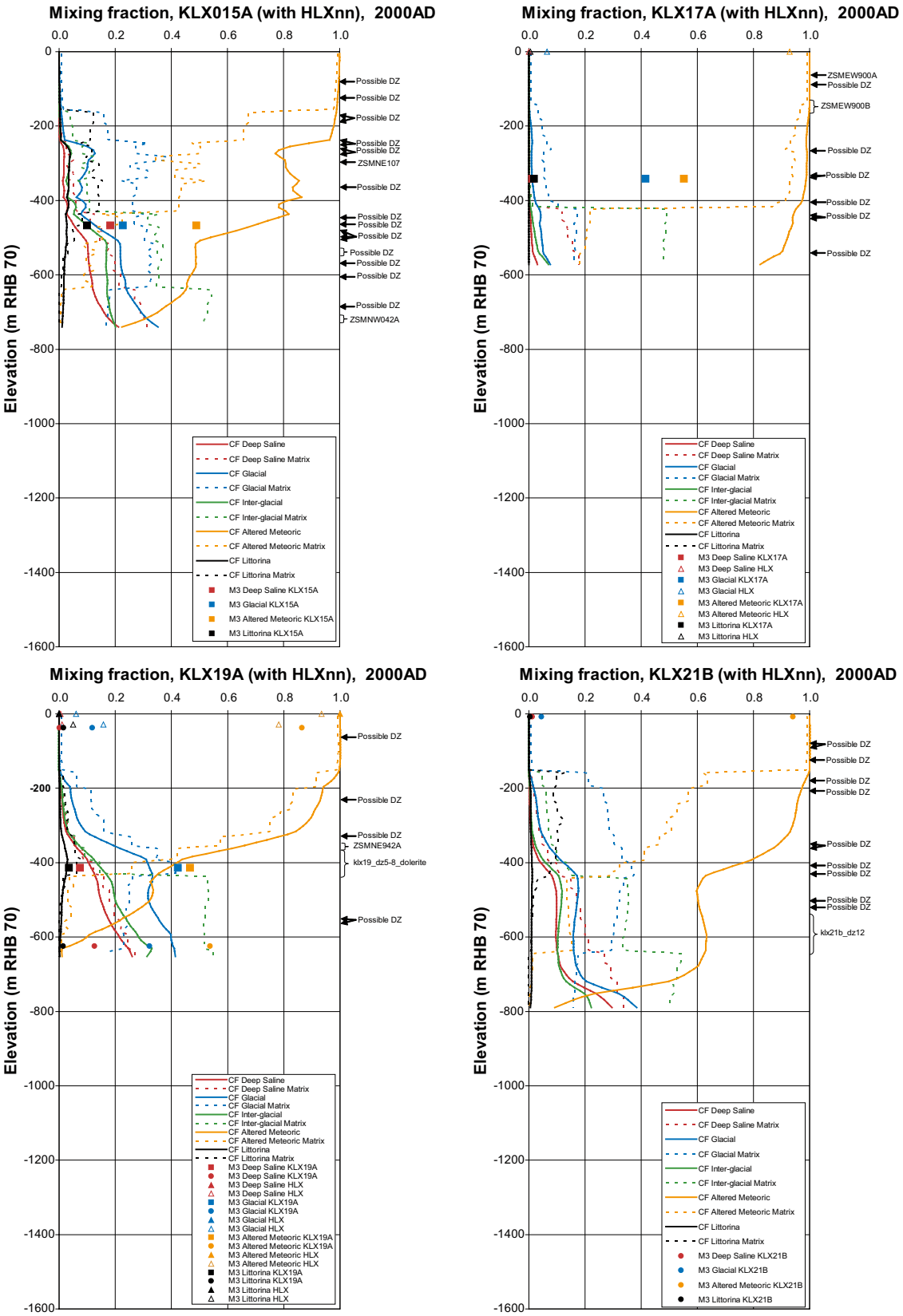

Figure A9-4. *Illustration of simulated mixtures of reference water mass fractions in boreholes KLX15A, KLX171A, KLX19A and KLX21B. Solid lines show simulated reference water mass fractions for Brine, Littorina, Altered meteoric, Glacial and Inter-glacial in the fracture system; dashed correspond to the reference water mass fractions in the matrix. The points show the mixture of 4 reference waters (Brine, Littorina, Altered meteoric, Glacial and Inter-glacial) interpreted from groundwater samples by the M3 method.*

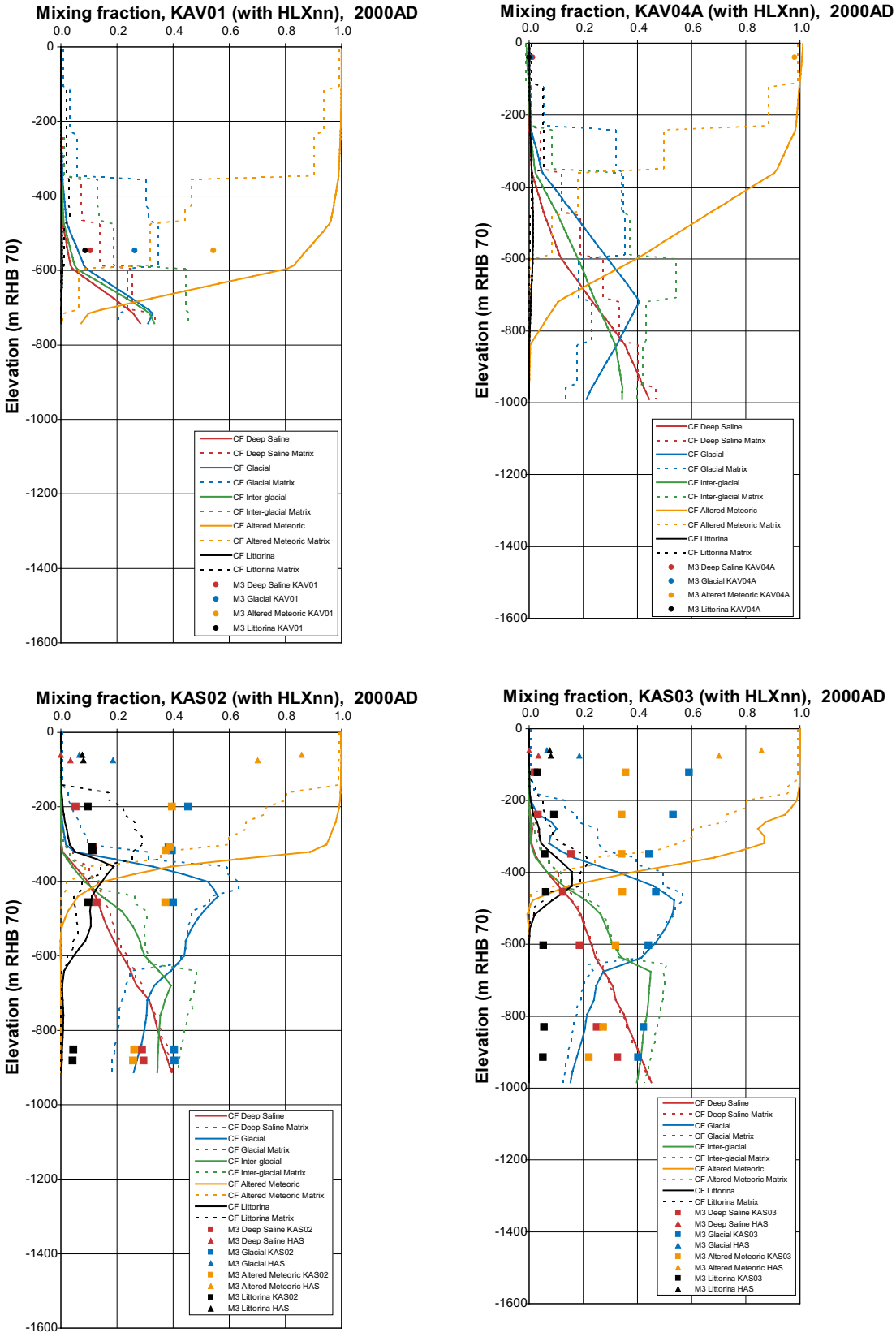

Figure A9-5. *Illustration of simulated mixtures of reference water mass fractions in boreholes KAV01, KAV04A, KAS02 and KAS03. Solid lines show simulated reference water mass fractions for Brine, Littorina, Altered meteoric, Glacial and Inter-glacial in the fracture system; dashed correspond to the reference water mass fractions in the matrix. The points show the mixture of 4 reference waters (Brine, Littorina, Altered meteoric, Glacial and Inter-glacial) interpreted from groundwater samples by the M3 method.*

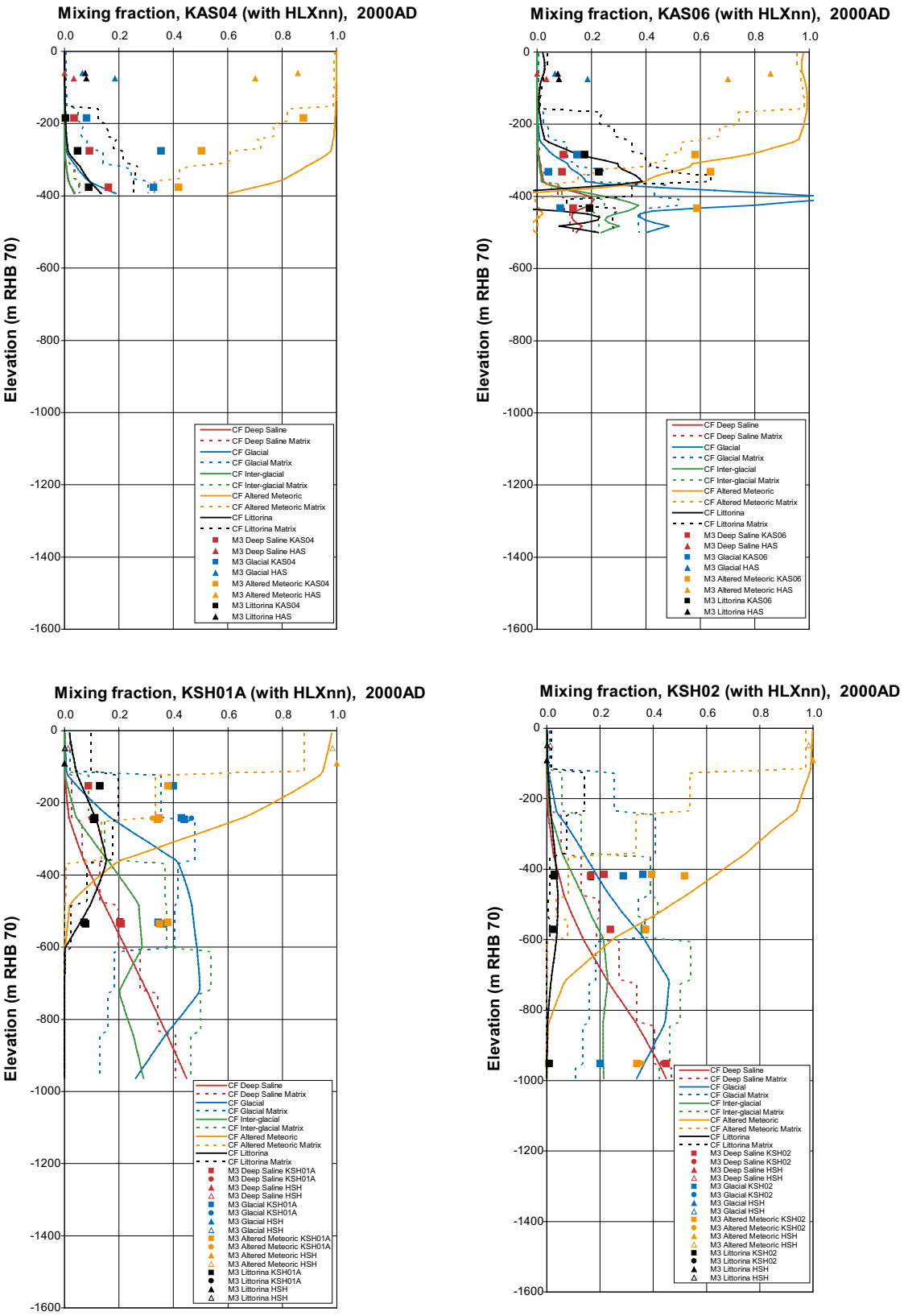

Figure A9-6. *Illustration of simulated mixtures of reference water mass fractions in boreholes KAS04, KAS06, KSH01A and KSH02. Solid lines show simulated reference water mass fractions for Brine, Littorina, Altered meteoric, Glacial and Inter-glacial in the fracture system; dashed correspond to the reference water mass fractions in the matrix. The points show the mixture of 4 reference waters (Brine, Littorina, Altered meteoric, Glacial and Inter-glacial) interpreted from groundwater samples by the M3 method.*

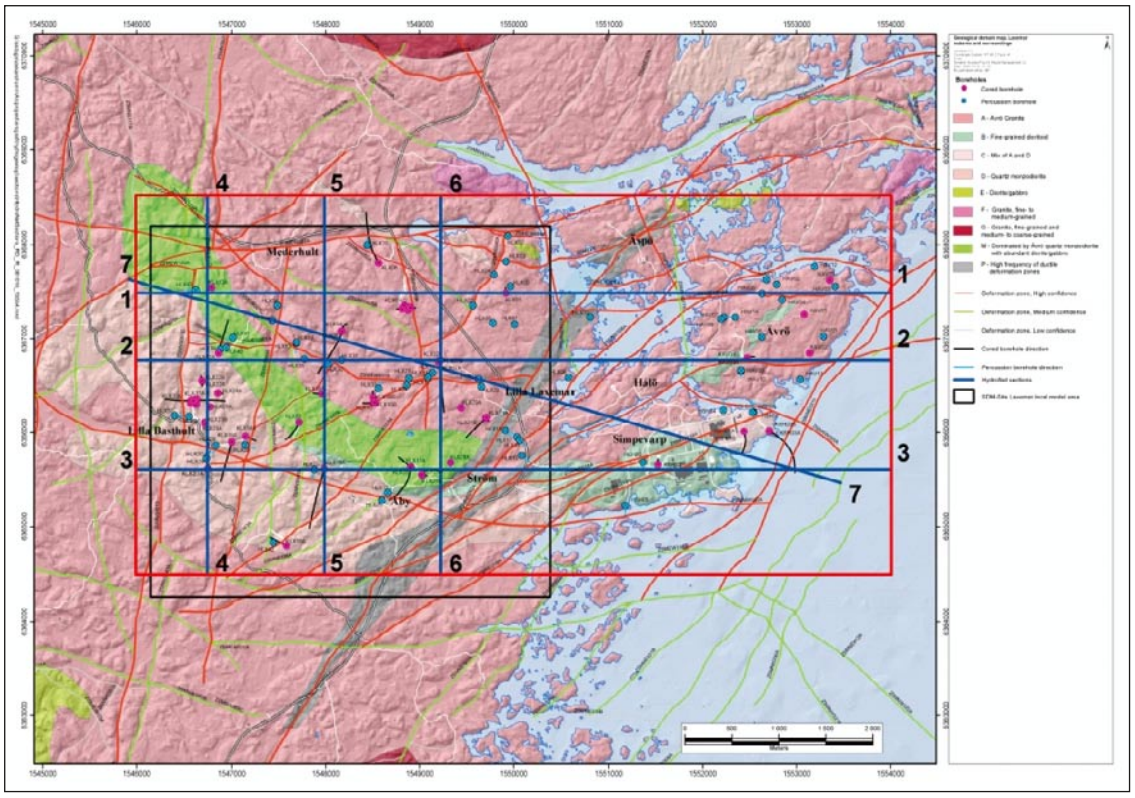

Figure A9-7. *Positions of vertical slices Hv1-7 used in the palaeo-hydrogeology plots shown in Figure A9-8 through Figure A9-14. The Laxemar local model area is shown by the black square. Hv1b-3b and Hv7b are limited to the east by the Laxemar local model area.*

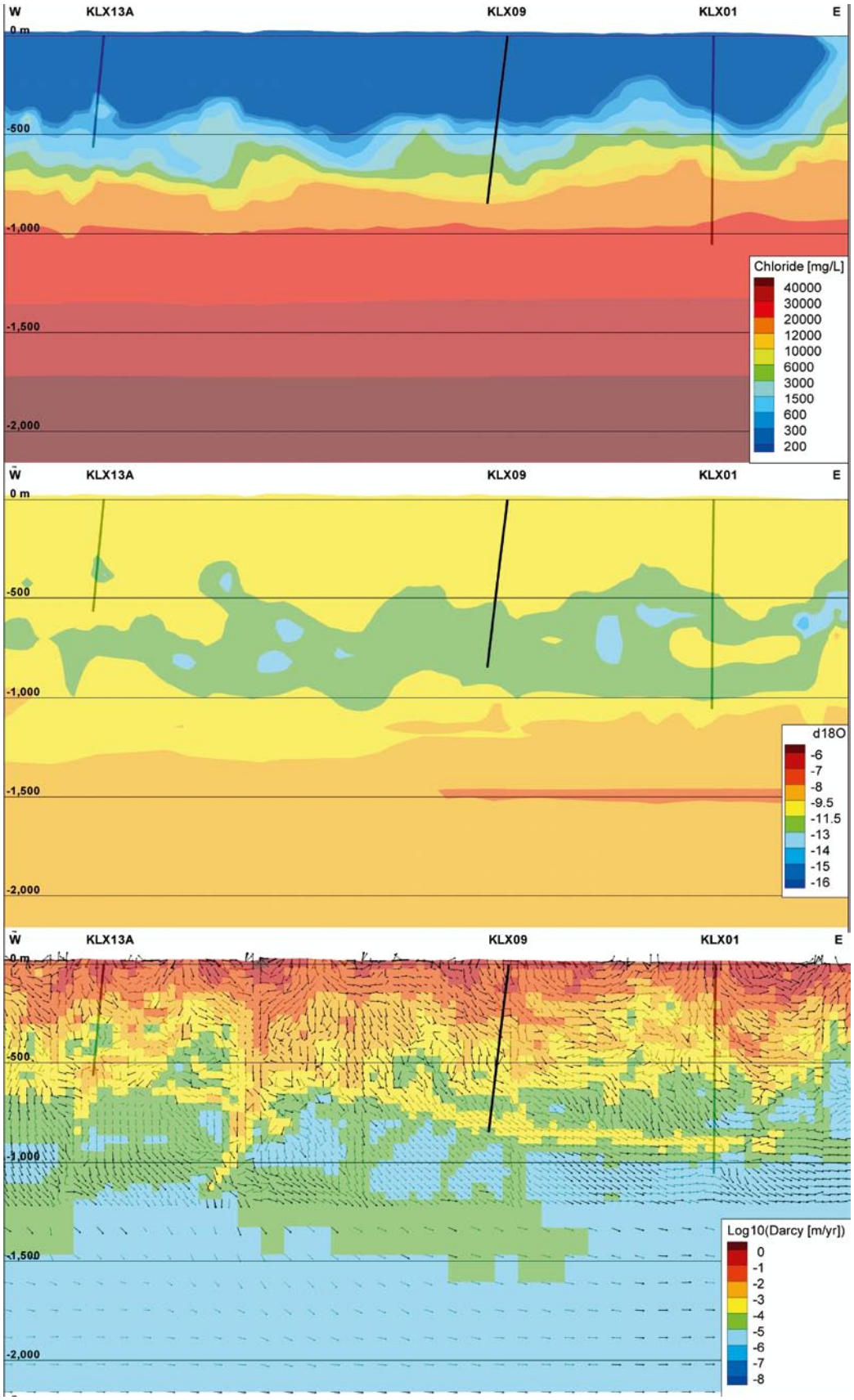

Figure A9-8. *Distribution of Cl (top), $\delta^{18}O$ (middle) and Darcy velocity (bottom) simulated by the base case vertical slice Hv1b.*

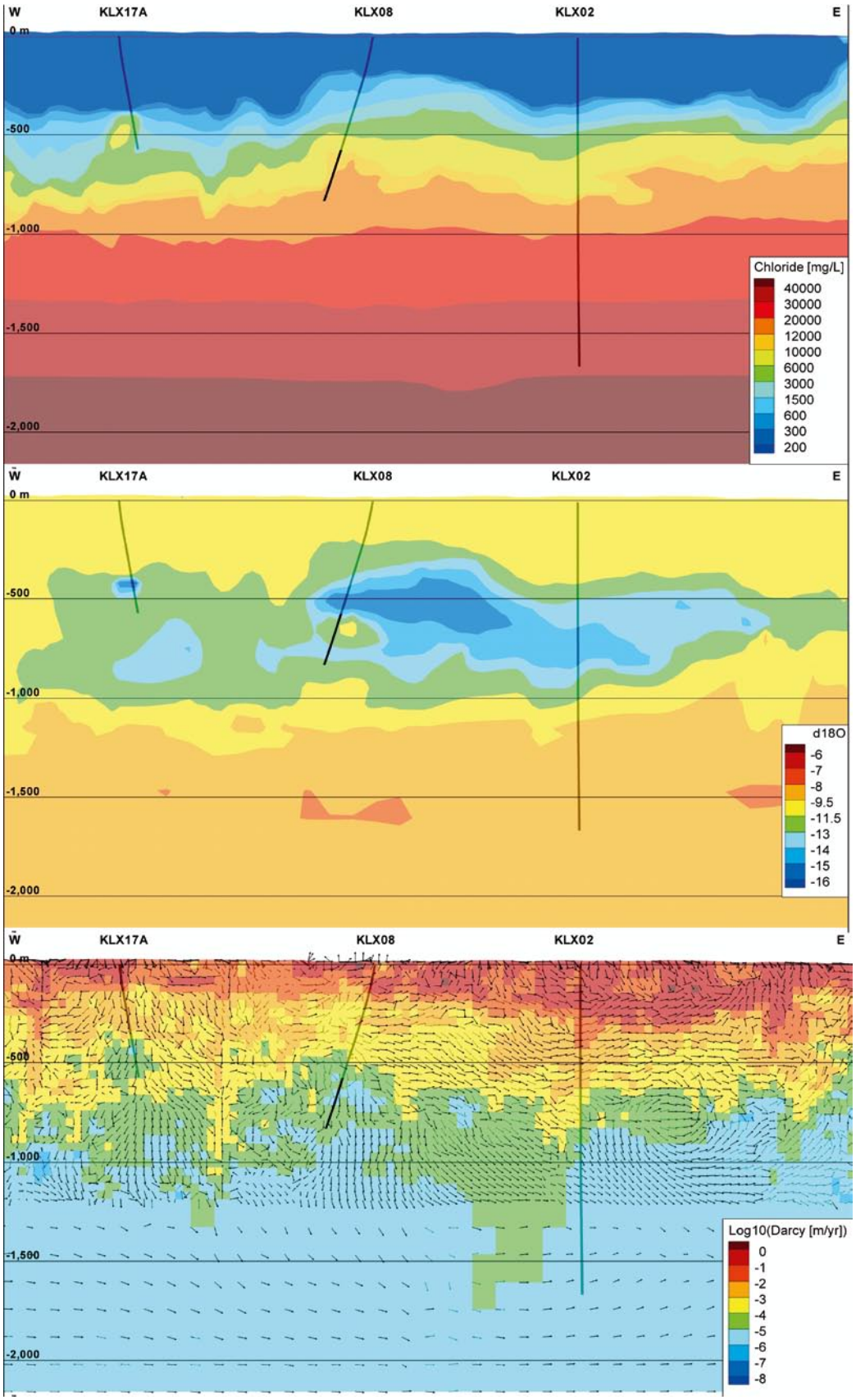

Figure A9-9. *Distribution of Cl (top), $\delta^{18}O$ (middle) and Darcy velocity (bottom) simulated by the base case vertical slice Hv2b.*

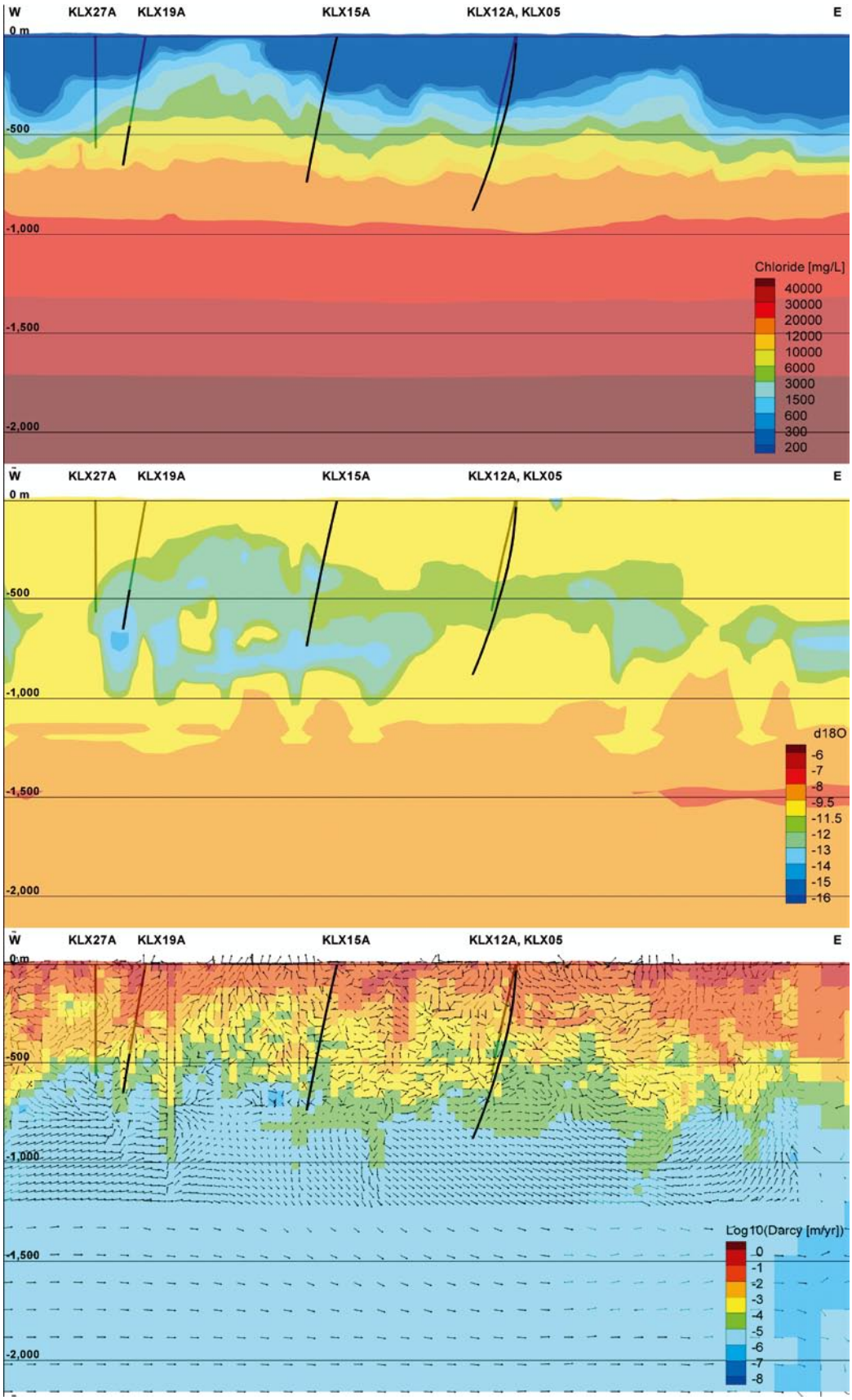

Figure A9-10. *Distribution of Cl (top), $\delta^{18}O$ (middle) and Darcy velocity (bottom) simulated by the base case vertical slice Hv3b.*

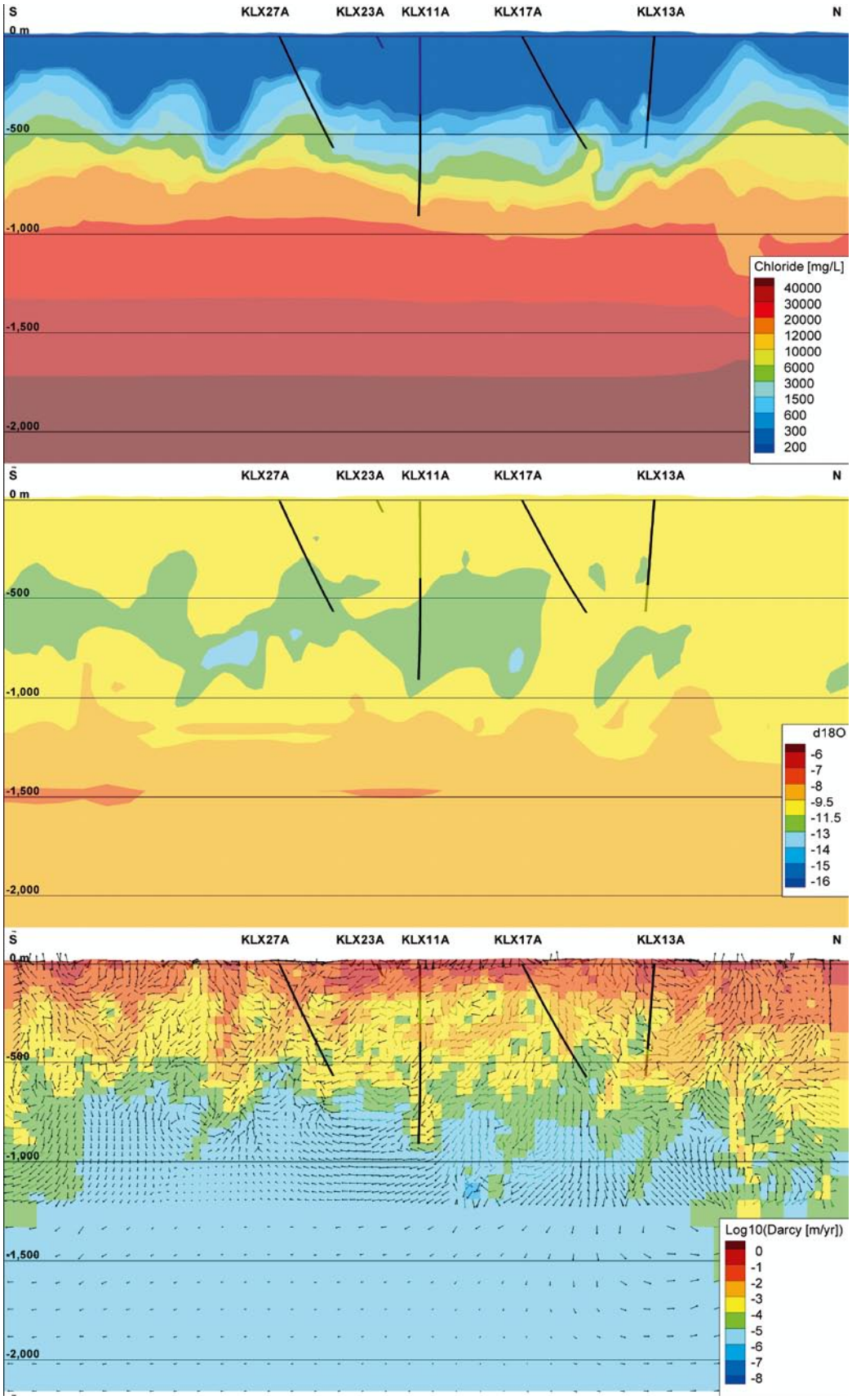

Figure A9-11. *Distribution of Cl (top), $\delta^{18}O$ (middle) and Darcy velocity (bottom) simulated by the base case vertical slice Hv4.*

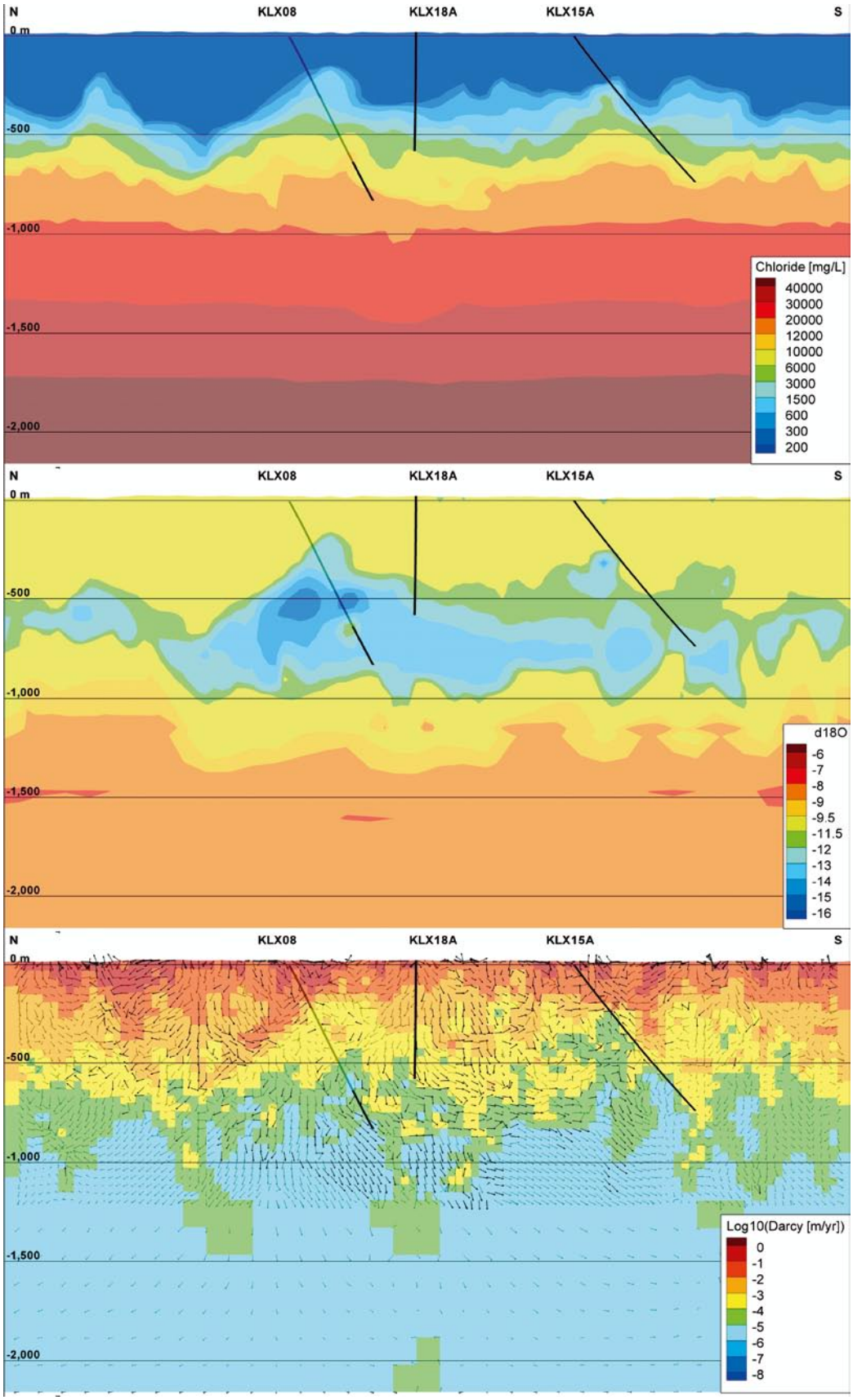

Figure A9-12. *Distribution of Cl (top), $\delta^{18}O$ (middle) and Darcy velocity (bottom) simulated by the base case vertical slice Hv5.*

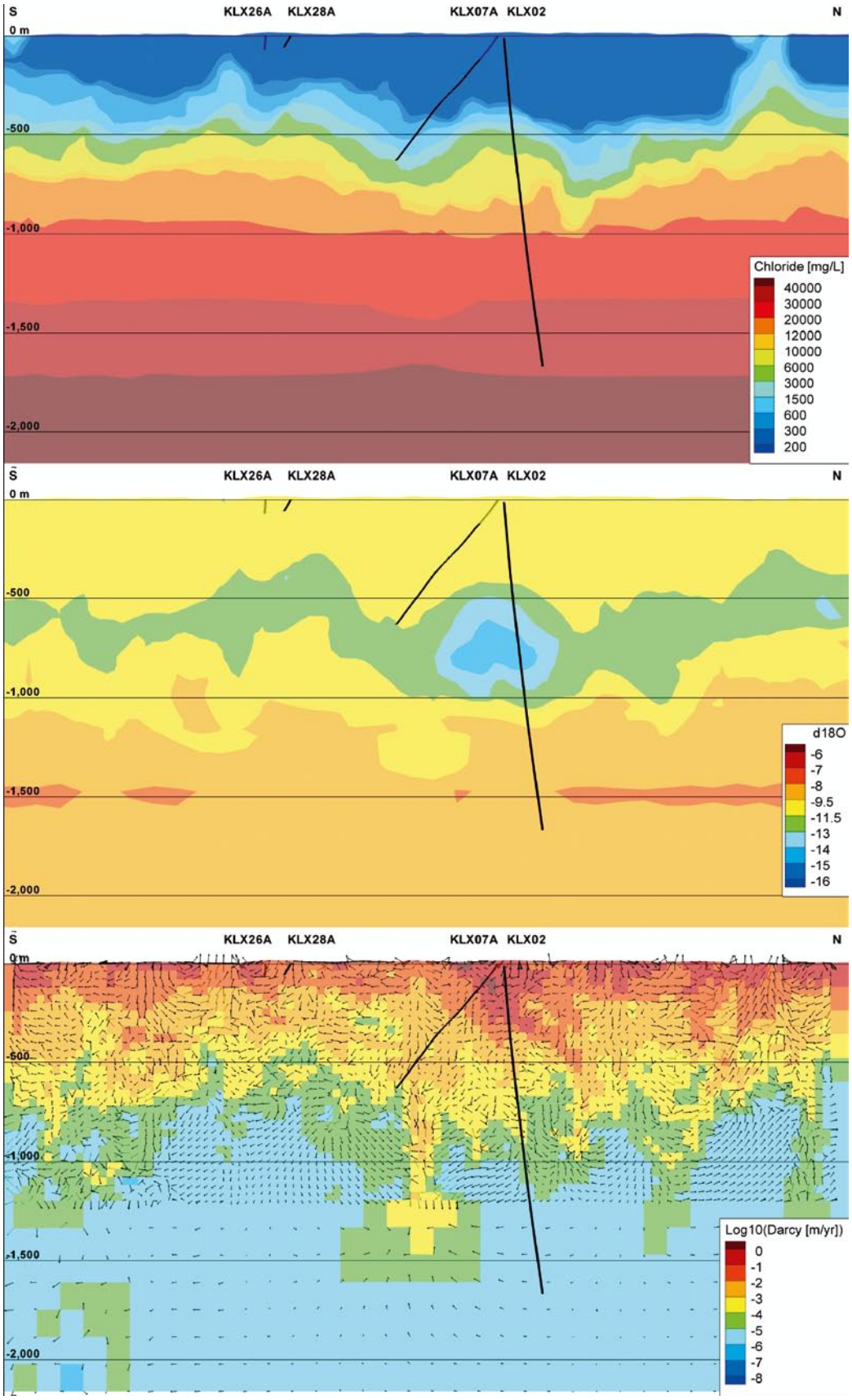

Figure A9-13. *Distribution of Cl (top), $\delta^{18}O$ (middle) and Darcy velocity (bottom) simulated by the base case vertical slice Hv6.*

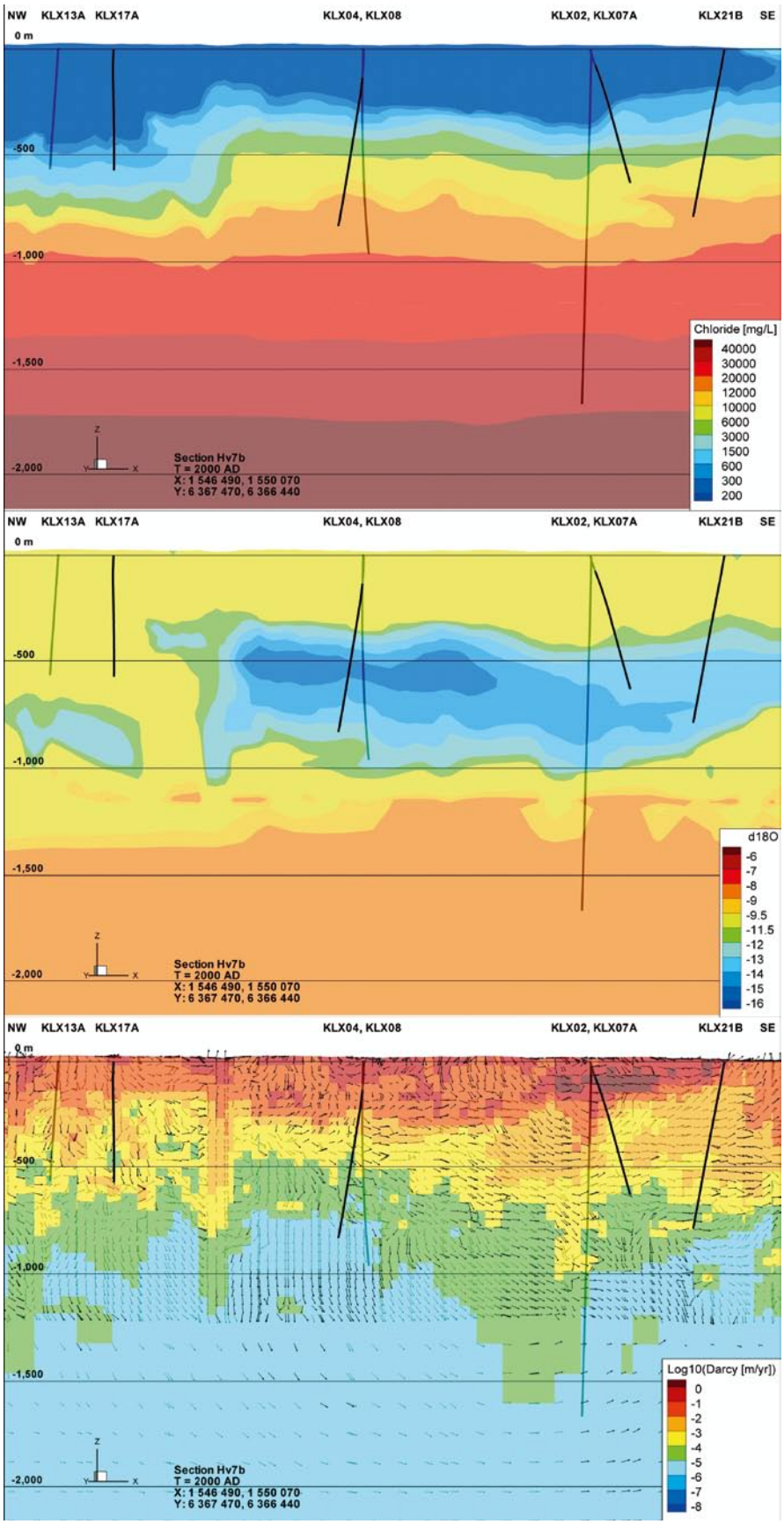

Figure A9-14. *Distribution of Cl (top), $\delta^{18}O$ (middle) and Darcy velocity (bottom) simulated by the base case vertical slice Hv7b.*

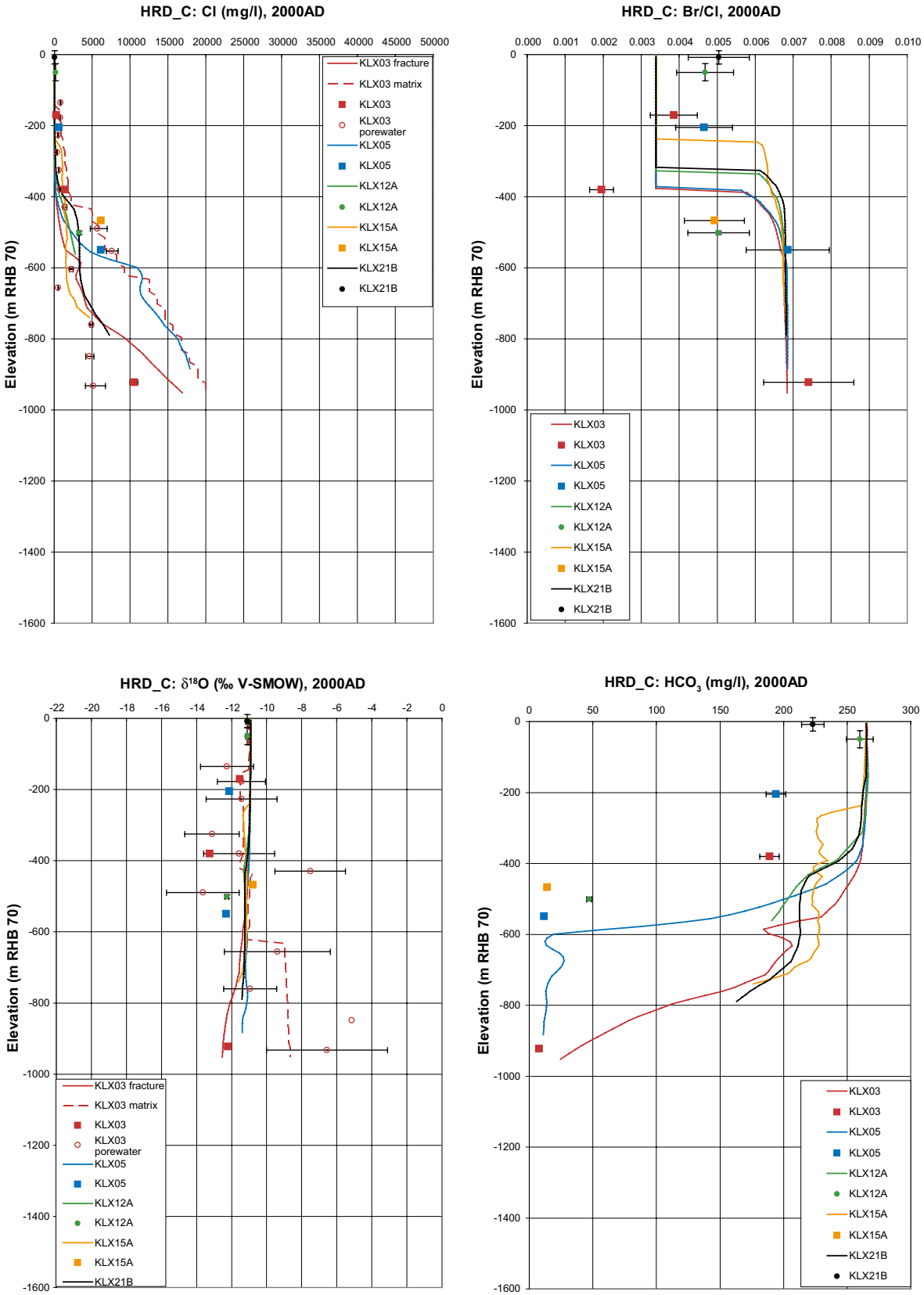

Figure A9-15. *Comparison of modelled and measured Cl, Br/Cl, $\delta^{18}O$ and HCO_3 in the fracture system for boreholes in HRD_C for the variant before calibration of HCD or HRD. Square symbols are used for Category 1–3 data, and small diamond symbols for the Category 4 data. The error bars on the data only indicate the laboratory analytical error. The solid lines show the complete distribution in the borehole simulated in the fracture system, and the dashed lines are for the matrix.*

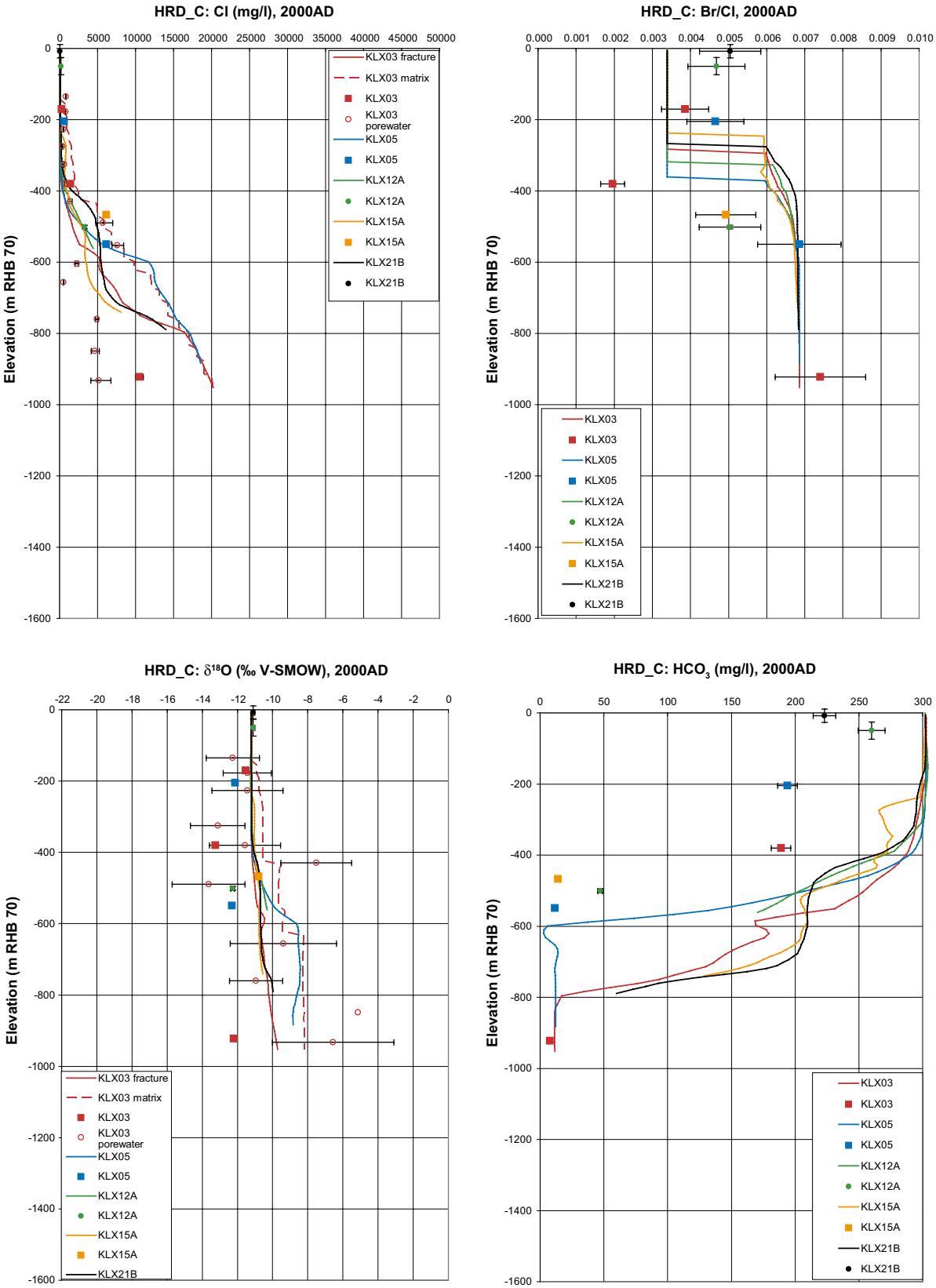

Figure A9-16. *Comparison of modelled and measured Cl, Br/Cl, $\delta^{18}O$ and HCO_3 in the fracture system for boreholes in HRD_C for the variant before calibration of HCD. Square symbols are used for Category 1–3 data, and small diamond symbols for the Category 4 data. The error bars on the data only indicate the laboratory analytical error. The solid lines show the complete distribution in the borehole simulated in the fracture system, and the dashed lines are for the matrix.*

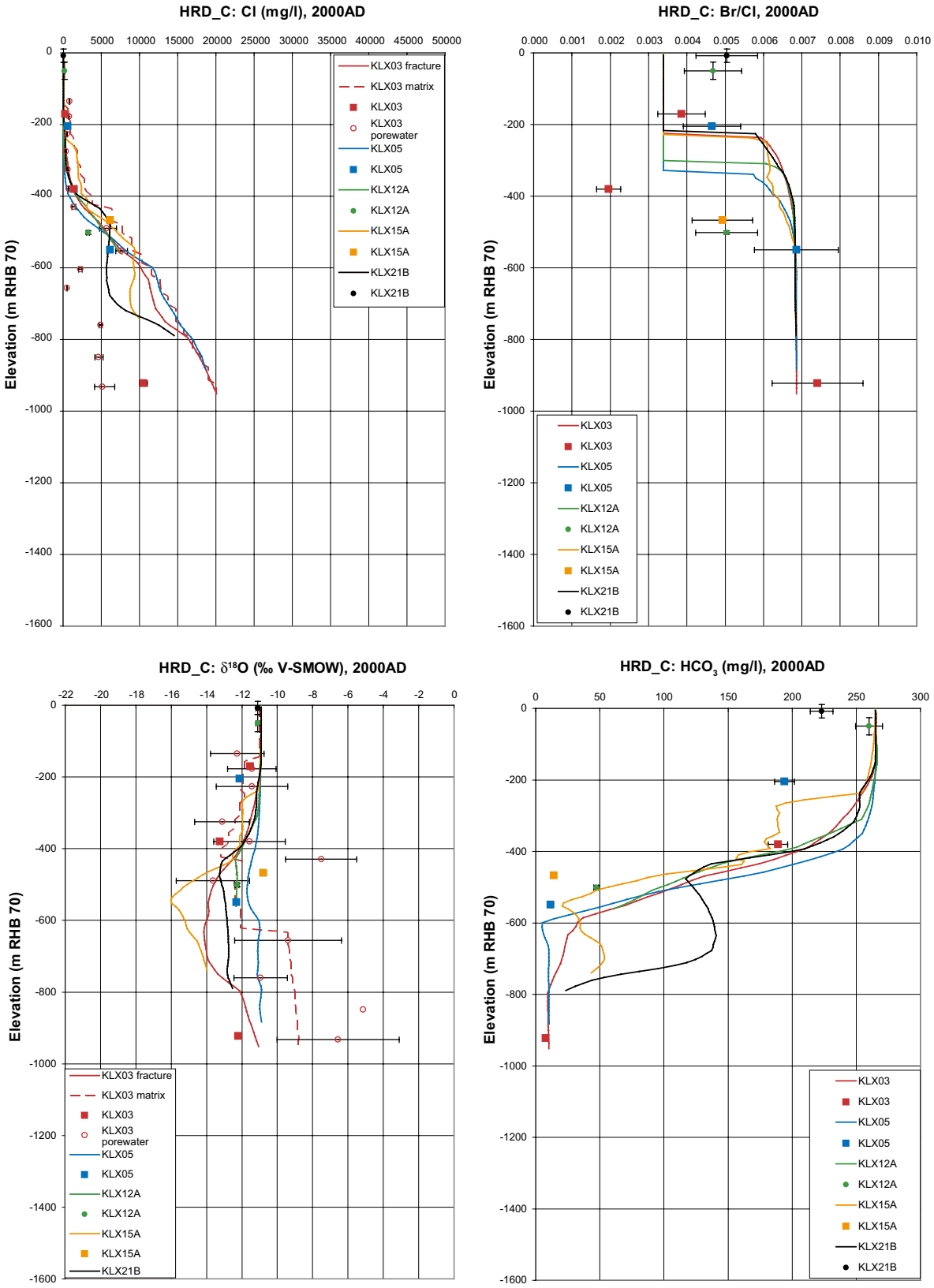

Figure A9-17. *Comparison of modelled and measured Cl, Br/Cl, $\delta^{18}O$ and HCO_3 in the fracture system for boreholes in HRD_C for the variant with enhanced fracture surface area, σ, in HCD. Square symbols are used for Category 1–3 data, and small diamond symbols for the Category 4 data. The error bars on the data only indicate the laboratory analytical error. The solid lines show the complete distribution in the borehole simulated in the fracture system, and the dashed lines are for the matrix.*

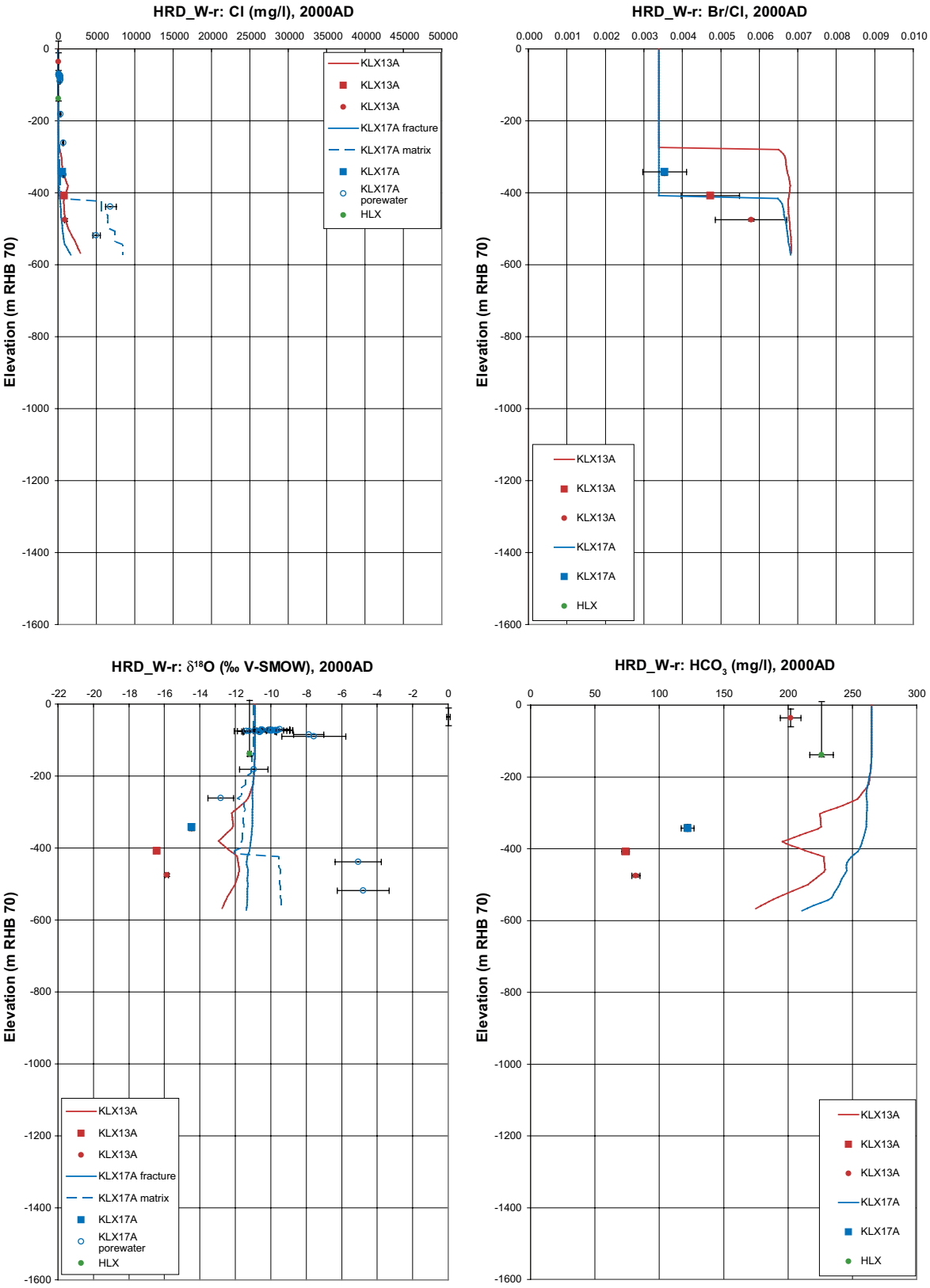

Figure A9-18. *Comparison of modelled and measured Cl, Br/Cl, $\delta^{18}O$ and HCO_3 in the fracture system for boreholes in HRD_W-recharge for the variant with enhanced fracture surface area, σ, in HCD. Square symbols are used for Category 1–3 data, and small diamond symbols for the Category 4 data. The error bars on the data only indicate the laboratory analytical error. The solid lines show the complete distribution in the borehole simulated in the fracture system, and the dashed lines are for the matrix.*

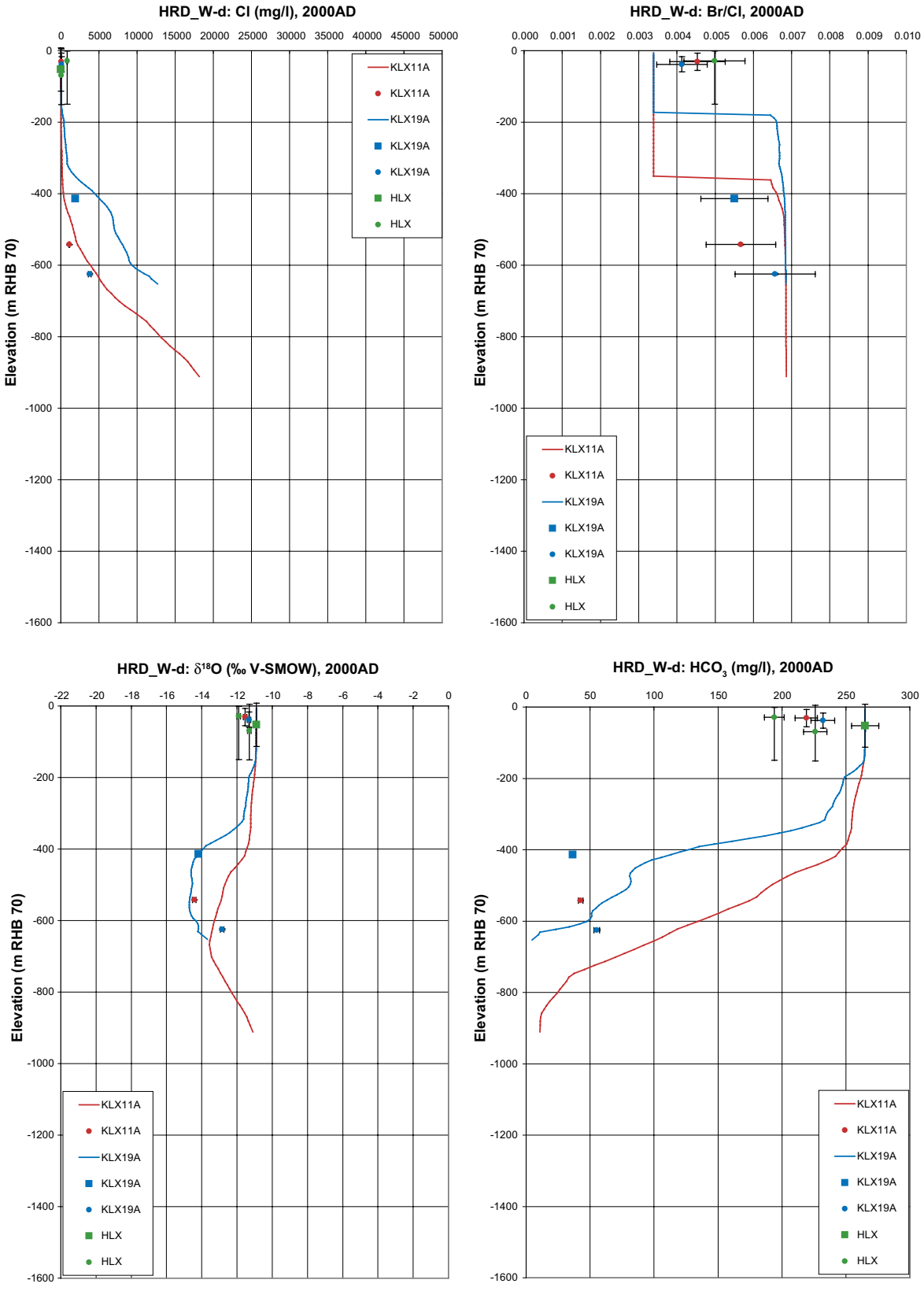

Figure A9-19. *Comparison of modelled and measured Cl, Br/Cl, $\delta^{18}O$ and HCO_3 in the fracture system for boreholes in HRD_W-discharge for the variant with enhanced fracture surface area, σ, in HCD. Square symbols are used for Category 1–3 data, and small diamond symbols for the Category 4 data. The error bars on the data only indicate the laboratory analytical error. The solid lines show the complete distribution in the borehole simulated in the fracture system, and the dashed lines are for the matrix.*

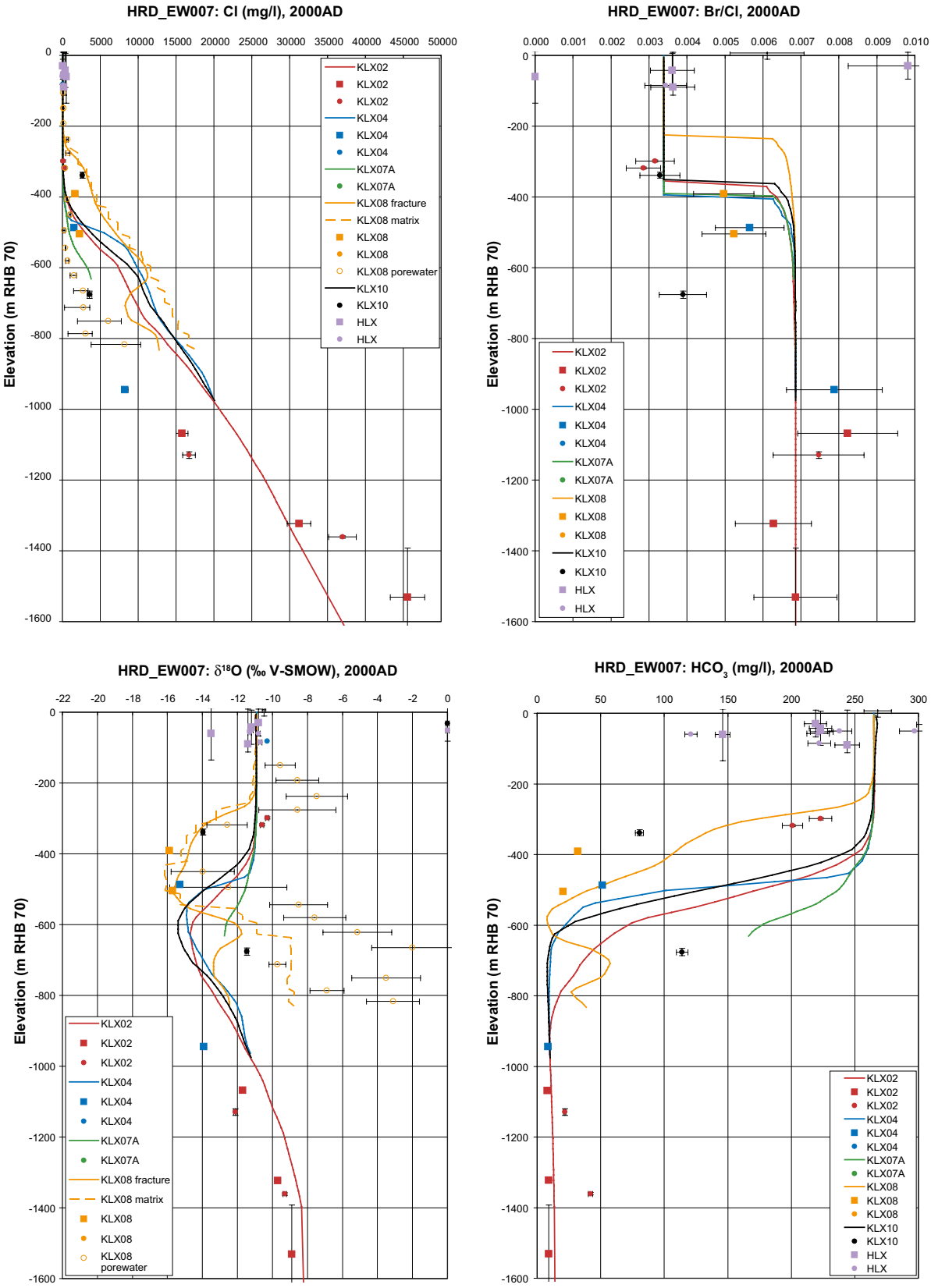

Figure A9-20. *Comparison of modelled and measured Cl, Br/Cl, $\delta^{18}O$ and HCO_3 in the fracture system for boreholes in HRD_EW007 for the variant with enhanced fracture surface area, σ, in HCD. Square symbols are used for Category 1–3 data, and small diamond symbols for the Category 4 data. The error bars on the data only indicate the laboratory analytical error. The solid lines show the complete distribution in the borehole simulated in the fracture system, and the dashed lines are for the matrix.*

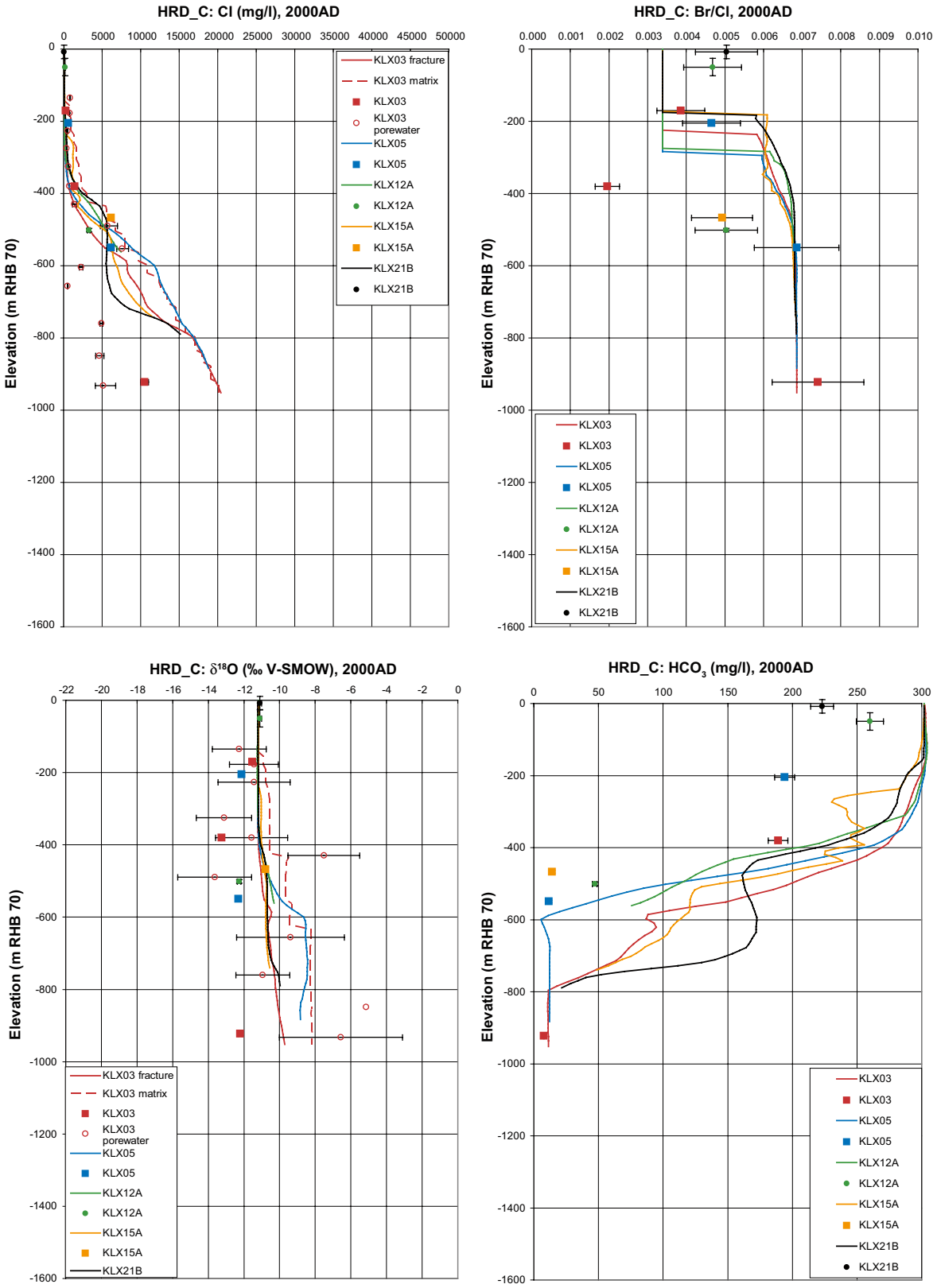

Figure A9-21. *Comparison of modelled and measured Cl, Br/Cl, $\delta^{18}O$ and HCO_3 in the fracture system for boreholes in HRD_C for the variant with $3\times K_h$ above –150 m. Square symbols are used for Category 1–3 data, and small diamond symbols for the Category 4 data. The error bars on the data only indicate the laboratory analytical error. The solid lines show the complete distribution in the borehole simulated in the fracture system, and the dashed lines are for the matrix.*

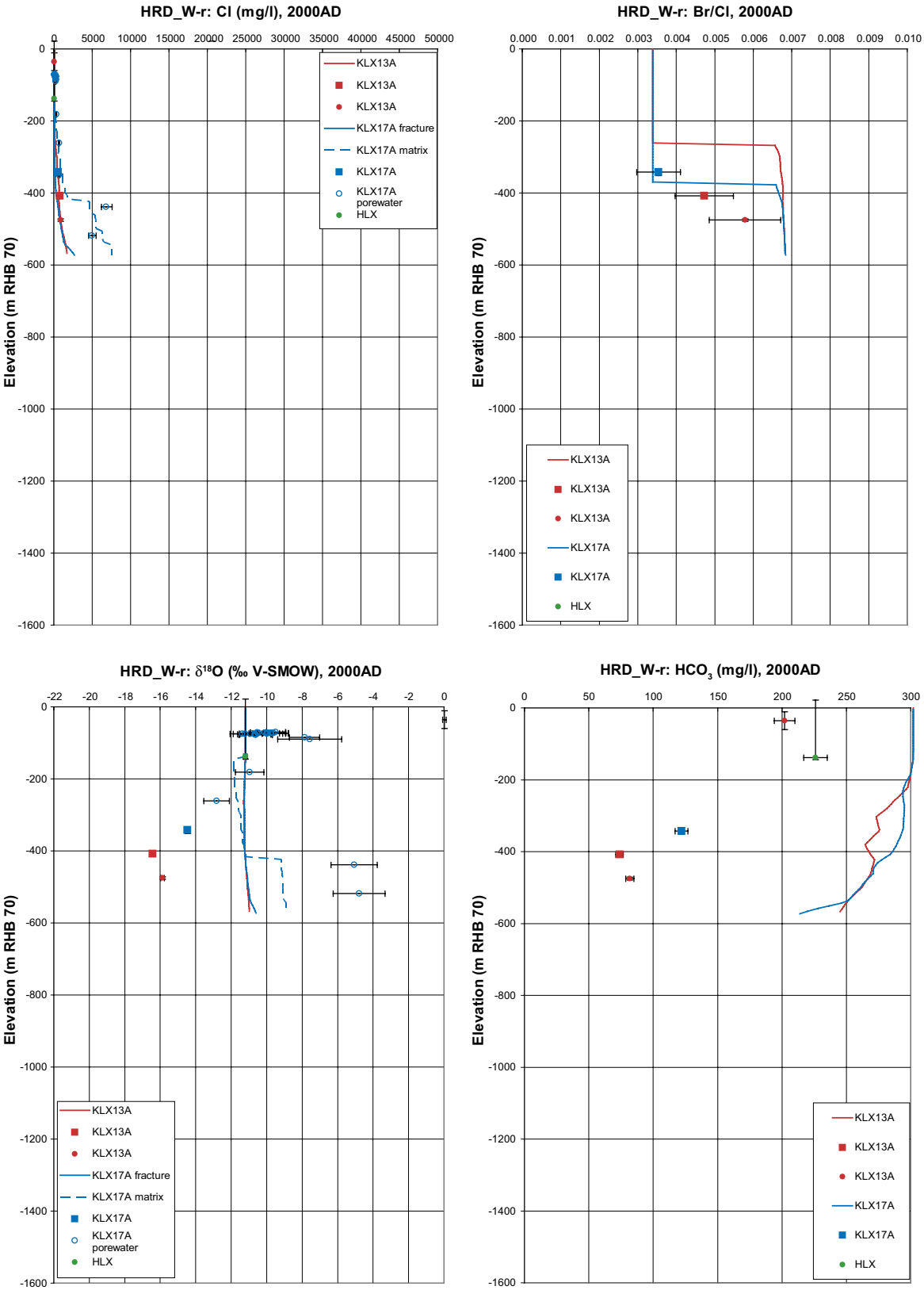

Figure A9-22. *Comparison of modelled and measured Cl, Br/Cl, $\delta^{18}O$ and HCO_3 in the fracture system for boreholes in HRD_W-recharge for the variant with $3\times K_h$ above –150 m. Square symbols are used for Category 1–3 data, and small diamond symbols for the Category 4 data. The error bars on the data only indicate the laboratory analytical error. The solid lines show the complete distribution in the borehole simulated in the fracture system, and the dashed lines are for the matrix.*

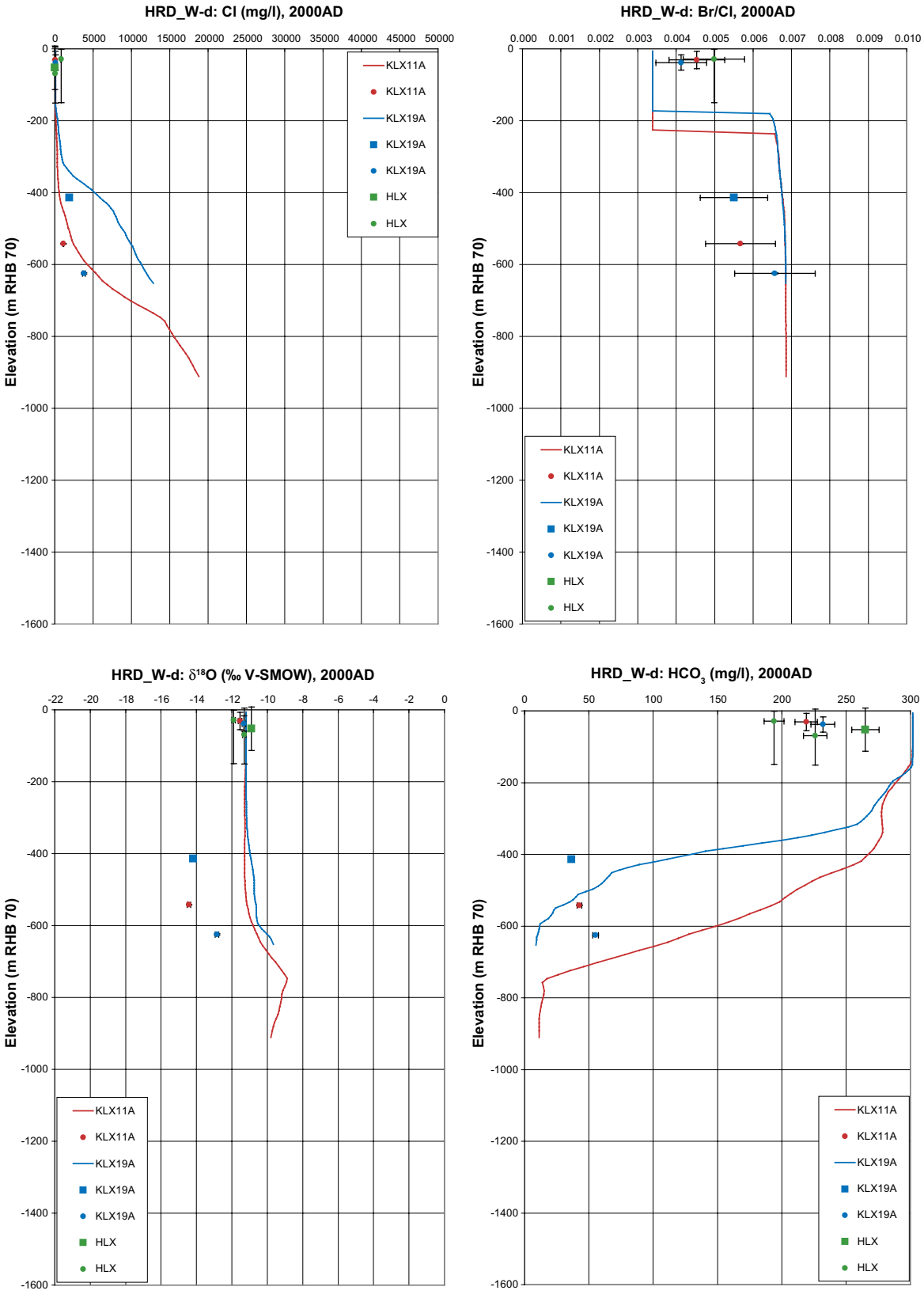

Figure A9-23. *Comparison of modelled and measured Cl, Br/Cl, $\delta^{18}O$ and HCO_3 in the fracture system for boreholes in HRD_W-discharge for the variant with 3×K_h above –150 m. Square symbols are used for Category 1–3 data, and small diamond symbols for the Category 4 data. The error bars on the data only indicate the laboratory analytical error. The solid lines show the complete distribution in the borehole simulated in the fracture system, and the dashed lines are for the matrix.*

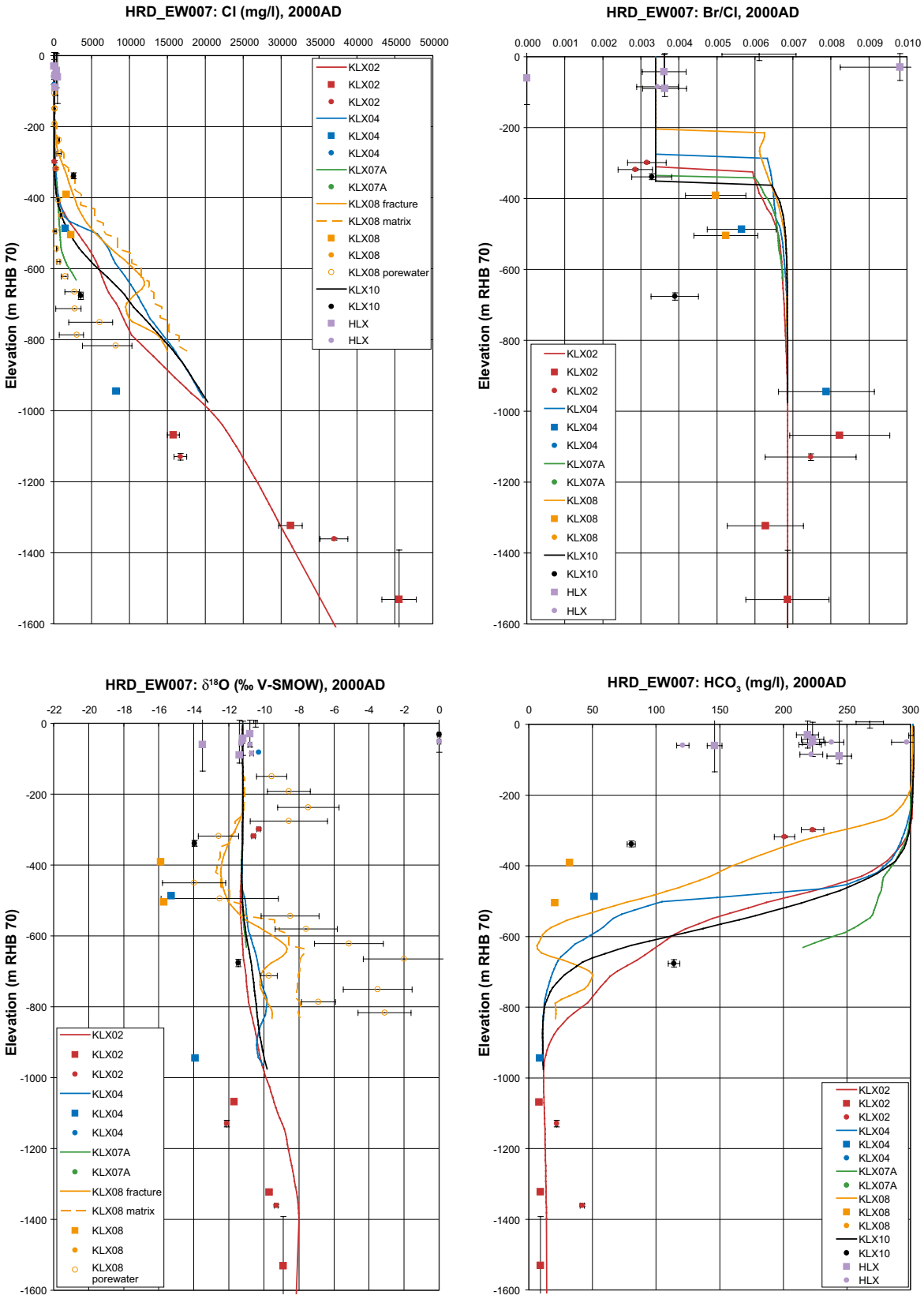

Figure A9-24. *Comparison of modelled and measured Cl, Br/Cl, $\delta^{18}O$ and HCO_3 in the fracture system for boreholes in HRD_EW007 for the variant with $3\times K_h$ above –150 m. Square symbols are used for Category 1–3 data, and small diamond symbols for the Category 4 data. The error bars on the data only indicate the laboratory analytical error. The solid lines show the complete distribution in the borehole simulated in the fracture system, and the dashed lines are for the matrix.*

A10 Tritium migration model

In Section 4.10.3 of /Laaksoharju et al. 2009/ it is concluded that a characteristic decrease in tritium at a depth of 100 to 150 m indicates the penetration of modern fresh meteoric. This appendix details how calculations of tritium migration were carried out by extending the models developed for simulating palaeohydrogeology to demonstrate consistency between the hydrogeological model and the above interpretation of hydrochemistry.

A10.1 Data delivery

In Figure A10-1, the sampled tritium concentrations in precipitation (rain and snow) from Hydrochemistry's "Extended Laxemar 2.3 data freeze of Nov 30 2007" /Laaksoharju et al. 2009/, are presented. Data were sampled over the period 2002-08-22 to 2007-08-13. It should be noted that these dates represent the date of input of the last data in a series of measurements. The sampled tritium data from boreholes in the delivery prior to 2002-01-01 have been discarded mainly because some earlier tritium data were contaminated due to excess of drilling water or due to leakage problems with the pumping equipment /Laaksoharju et al. 2009/. A simple linear fit to the data is also included in Figure A10-1 to indicate the average tritium levels in precipitation. It shows that the majority of background concentration of tritium in precipitation at Laxemar during the measurement period is between 9–15 TU, with an overall average about 12 TU. The total range is from 5 to 19 TU over the period considered.

In Figure A10-2 and Figure A10-3, the sampled tritium concentrations in all cored boreholes from the Hydrochemistry's "Extended Laxemar 2.3 data freeze of Nov 30 2007" are presented for the Laxemar subarea and Simpevarp subarea, respectively. The data have been coloured according to the categories used for quality representation. Category 1 (high quality) is indicated by orange circular markers.

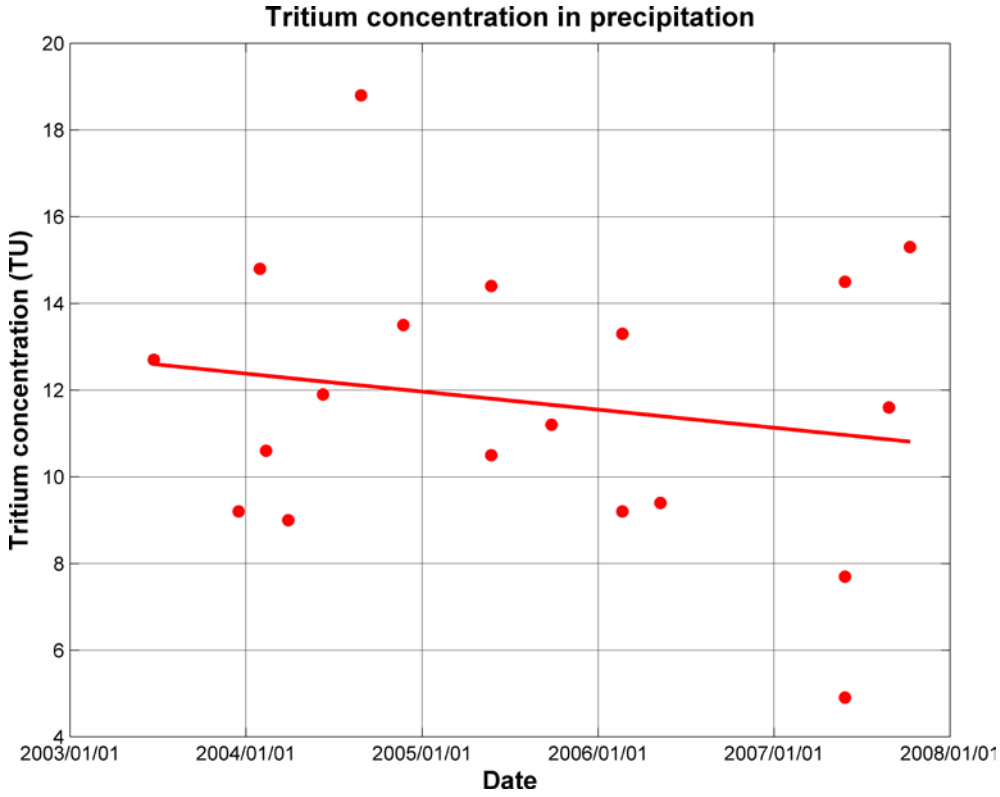

Figure A10-1. *Tritium concentrations measured in precipitation at Laxemar, from Hydrochemistry's in the period 2003–2008 "Extended Laxemar 2.3 data freeze of Nov 30 2007".*

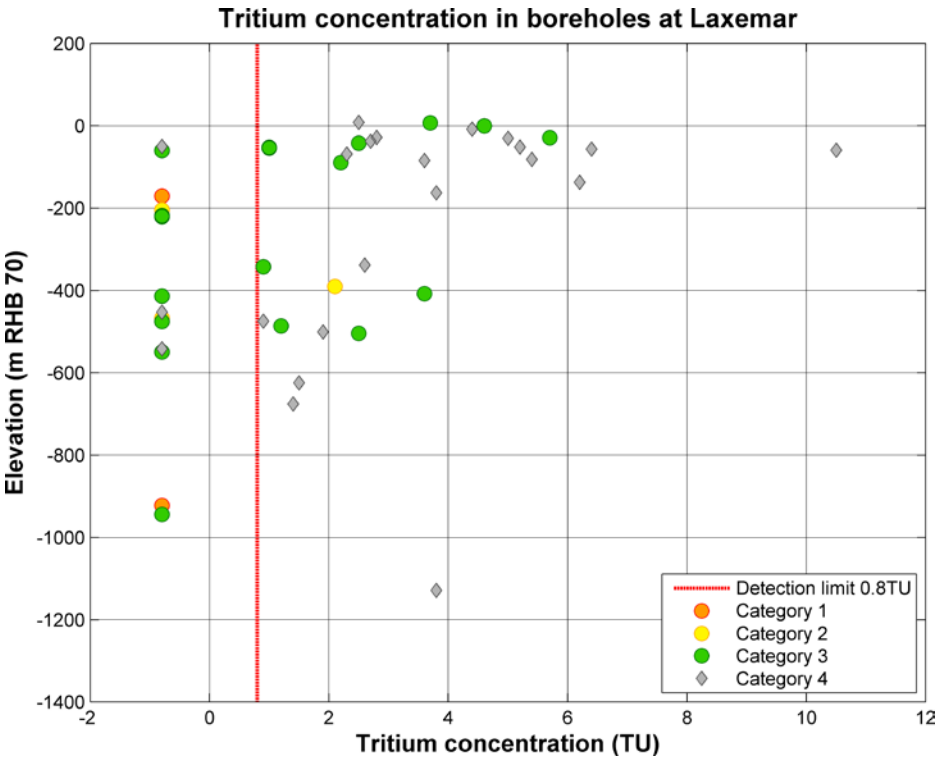

Figure A10-2. *Tritium concentrations shown at sampling elevation, measured in core and percussion drilled boreholes in the Laxemar subarea from the Extended Laxemar 2.3 data freeze (only data after 2002-01-01). Data has been coloured according to the categories used for quality representation. The limit of detection (0.8 TU) is indicated and the measurement uncertainty has been estimated to be 0.8 TU /Nilsson 2009/.*

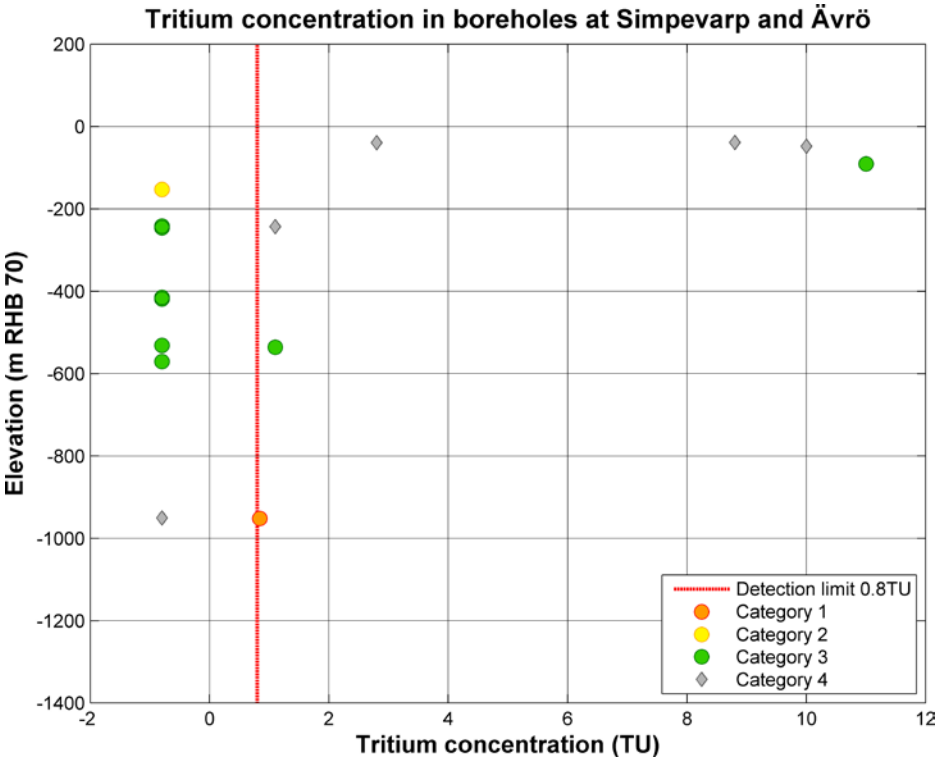

Figure A10-3. *Tritium concentrations shown at sampling elevation, measured in core and percussion drilled boreholes in the Simpevarp and Ävrö subareas from the Extended Laxemar 2.3 data freeze (only data after 2002-01-01). Data has been coloured according to the categories used for quality representation. The limit of detection (0.8 TU) is indicated and the measurement uncertainty has been estimated to be 0.8 TU /Nilsson 2009/.*

Category 2 (high quality) is indicated by yellow markers. Category 3 (intermediate quality) is indicated by green markers. The grey diamond shaped markers are used for Category 4 data (intermediate to low quality). The sampled elevations range from the surface down to –1,400 meter above sea level. The tritium concentrations in the cored boreholes range from 0 to 35 TU with the majority of values being less than about 12 TU.

A10.2 Period modelled

Tritium is formed naturally by cosmic rays in the upper atmosphere. The atomic bomb tests in the 1950's, 60's and 70's also produced large amounts of tritium, leading to much higher atmospheric concentrations than the natural background. There is a detailed record of atmospheric concentrations measured at Ottawa (see Figure A10-4). From this plot it appears that present background levels of tritium are around 10–15 Tritium Units (TU). The bomb tests led to tritium levels that at their peak in the early 60's were about 100 times greater than the actual ones. Records for other locations are less detailed. However, the available measurements for locations in Sweden appear to be consistent with the measurements at Ottawa (Canada), see. /Laaksoharju et al. 2004, cf Figure 4-6 therein/, although some variation between locations might be expected, e.g. due to variation in the amount of precipitation, particularly for the bomb test tritium.

Tritium is transferred from the atmosphere to the geosphere through precipitation, and it infiltrates into the groundwater system. Tritium has a very short half-life (12.43 years), and hence tritium that entered the groundwater system more than fifty years ago will have decreased by more than an order of magnitude (about a factor 16), and tritium that entered the groundwater system in precipitation more than a hundred years ago would have decreased by more than two orders of magnitude (about a factor 256). As the bomb test input started in the early 50's, as shown by the atmospheric concentrations presented in Figure A10-4, it is only necessary to consider migration of tritium since the 1950's. The natural background of tritium in precipitation prior to the bomb tests will now contribute less than 1 TU to the current groundwater concentrations, and in principle it could be neglected. However, in order to facilitate a comparison of the levels of tritium in groundwater due to the bomb test tritium with the levels due to the natural background, the calculations of tritium migration were carried out for a period

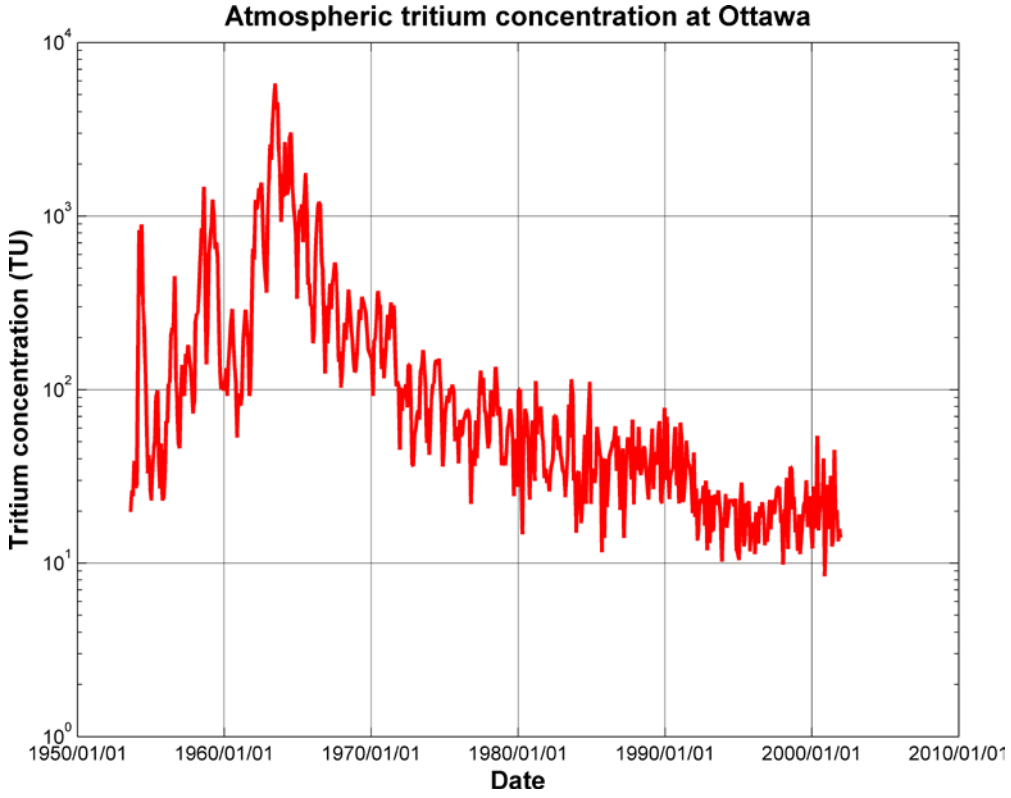

Figure A10-4. *Atmospheric concentrations of tritium measured at Ottawa (Canada) during the period 1950–2002.*

of 120 years (about ten tritium half lives) starting from 1890 AD. The results of the calculations therefore effectively provide results for an initial 60 year period with natural background levels of tritium in precipitation, and a 60 year period with the bomb-test tritium as well. (Carrying out the calculations in this way also ensured that the initial conditions for the calculations with the bomb-test tritium included are realistic, although this is not strictly necessary, for the reason discussed above.) It should be noted that the final time for the simulations is 2010 AD, but the results used for comparison are taken at 2005 AD, as 5 year time steps have been used and 2005 AD is the approximate mean time for the present measurements at Laxemar.

The time period modelled is short relative to the time-scale of natural evolutions of the regional groundwater flow such as sea-level and sea-water salinity changes that occur on time scales of thousands of years, and the results of the regional groundwater flow calculations were only saved every 1,000 years. Therefore, the flow and distributions of reference waters at the end of the transient regional groundwater flow calculation from 8000 BC to the present day, i.e. 2000 AD, were used as the initial conditions for the calculations of tritium migration. This introduced a small error, in that the change in the flow since 1890 AD and the present-day was effectively neglected. However, this change is small.

Using the conditions at the end of the transient regional groundwater flow as the initial conditions effectively takes the conditions in the rock matrix to be in equilibrium at the start of the tritium migration calculations. Provided that the distributions of the reference waters were not changing rapidly towards the end of the regional groundwater flow calculations, this will be a reasonable approximation.

A10.3 Boundary conditions

As indicated, calculations of tritium migration were carried out for the period since 1890 AD. The calculations used multi-component groundwater flow, with rock-matrix diffusion. Tritium enters the model through the top surface, where the boundary condition was effectively specified such that the flux of tritium was equal to the recharge flux of groundwater multiplied by the concentration of tritium in precipitation, which was obtained from the data shown in Figure A10-4.

The option for modelling multi-component flow allows for modelling of tracers (e.g. $\delta^{18}O$, δD) as well as the main groundwater constituents (e.g. Na, Cl), but it does not currently allow for decay. All tracers are modelled as conservative, in the same way as the main groundwater constituents. However, it is straightforward to deal with this.

The transport equation for a decaying radionuclide of concentration, C, that includes advection, dispersion and rock matrix diffusion has one extra term compared to Equation (7-8):

$$\frac{\partial(n_e \rho C)}{\partial t} + \nabla \cdot (\rho C \mathbf{q}) = \nabla \cdot (n_e \rho \mathbf{D} \cdot \nabla C) - \lambda n_e \rho C + \sigma \rho D_e \left. \frac{\partial c'}{\partial w} \right|_{w=0} \qquad \text{A10-1}$$

By using the transformation

$$C(\underline{x}, t) = C_m(\underline{x}, t) \times exp\left(-\lambda \left[t - t_{1890}\right]\right) \qquad \text{A10-2}$$

Equation (A10-2) can be converted to a transport equation for a conservative species of concentration, C_m, of the same form as Equation (7-8):

$$\frac{\partial(n_e \rho C_m)}{\partial t} + \nabla \cdot (\rho C_m \mathbf{q}) = \nabla \cdot (n_e \rho \mathbf{D} \cdot \nabla C_m) + \sigma \rho D_e \left. \frac{\partial c'_m}{\partial w} \right|_{w=0} \qquad \text{A10-3}$$

The time, $t_{1890,}$ is a time datum from which the tritium simulations are started, and λ is ln (2)/12.43. In order to use this transformation, the input boundary condition for tritium, C_{input}, entering at the top surface of the model must be transformed consistent with Equation (A10-2)

$$C_{input}(t_{input}) = C_{ottawa}(t_{input}) \times exp\left(\lambda \left[t_{input} - t_{1890}\right]\right) \qquad \text{A10-4}$$

where t_{input} is the time in years AD at the time under consideration, and C_{ottawa} is the atmospheric concentration of tritium at time, t_{input}. Equation (A10-4) implies an adjusted input concentration, C_{input}, of 10 TU at 1890 AD. Similarly, if at 1958 AD the atmospheric tritium concentration is 531 TU, then the adjusted input, C_{input}, is 23,540 TU.

The simulated tritium concentration calculated by solving Equation (A10-3) then has to be transformed back to account for decay using Equation (A10-2 For instance, a ConnectFlow, C_m, tritium value of 7,000 TU at 2005 AD would be decayed to give a final tritium result of 11.5 TU at 2005 AD.

Figure A10-5 shows the input tritium concentration used in the modelling after adjustment for decay, i.e. C_{input}. This is based on atmospheric tritium concentrations measured at Ottawa, given monthly, together with a simplified piecewise-constant approximation to this that was used in the modelling. An assumed background level of 10 TU was used in the simulations. For the piecewise-constant approximation of the Ottawa data series, a temporal discretisation of 1 year was used. In the calculations, the value corresponding to the end of a time-step was taken. In /Hartley et al. 2005/ the effect of changing the time step size was explored.

A10.4 Simulation results

An illustration of the simulated tritium concentrations at 2005 AD in the 3D palaeohydrogeology model is shown in Figure A10-6 on several cross-sections. As can bee seen tritium only penetrates the upper bedrock and maximum predicted tritium levels are about 15 TU around –100 m. The depth of penetration of tritium appears to be slightly less in the Laxemar subarea compared to areas further south or west, but this may just be a consequence of the higher grid resolution used in the Laxemar subarea. All results presented here account for decay, i.e. Equation (A10-2) has been applied to give C_{final}, and so the simulations results can be directly compared with measured values.

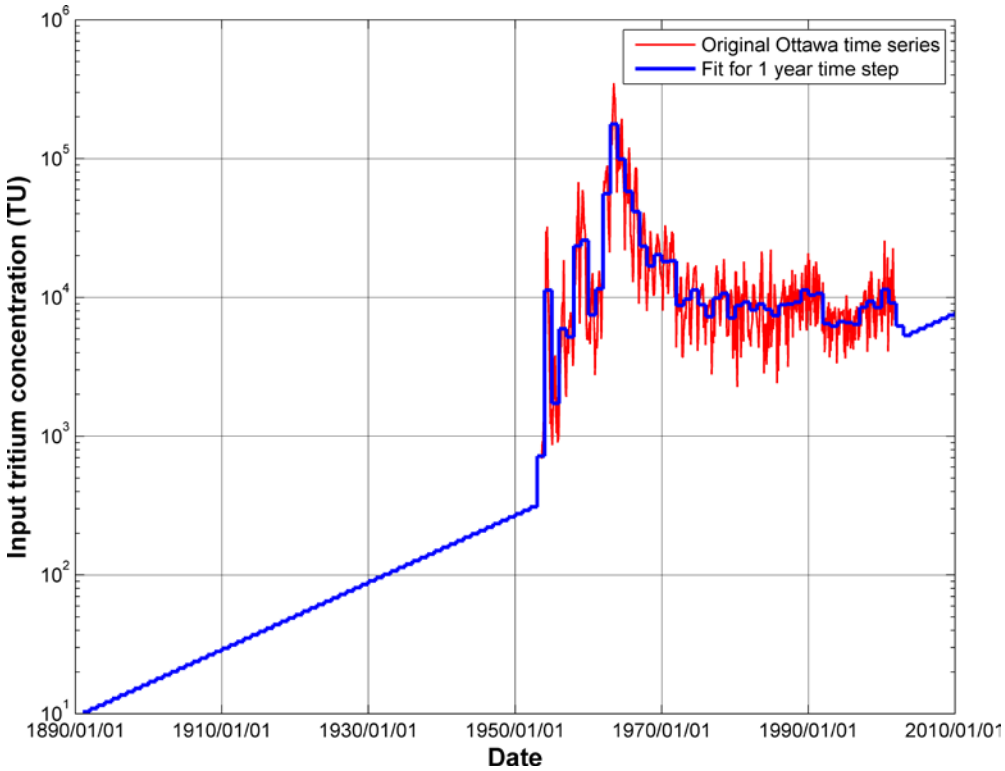

Figure A10-5. *The input tritium concentration adjusted for decay (i.e. C_{input} in Equation A10-1) used in ConnectFlow was based on the original time series for atmospheric tritium at Ottawa (red curve) averaged over one year time steps (blue curve). The adjustment for decay is made relative to a reference time of 1890 AD and continued until the end point for the modelling at 2010 AD.*

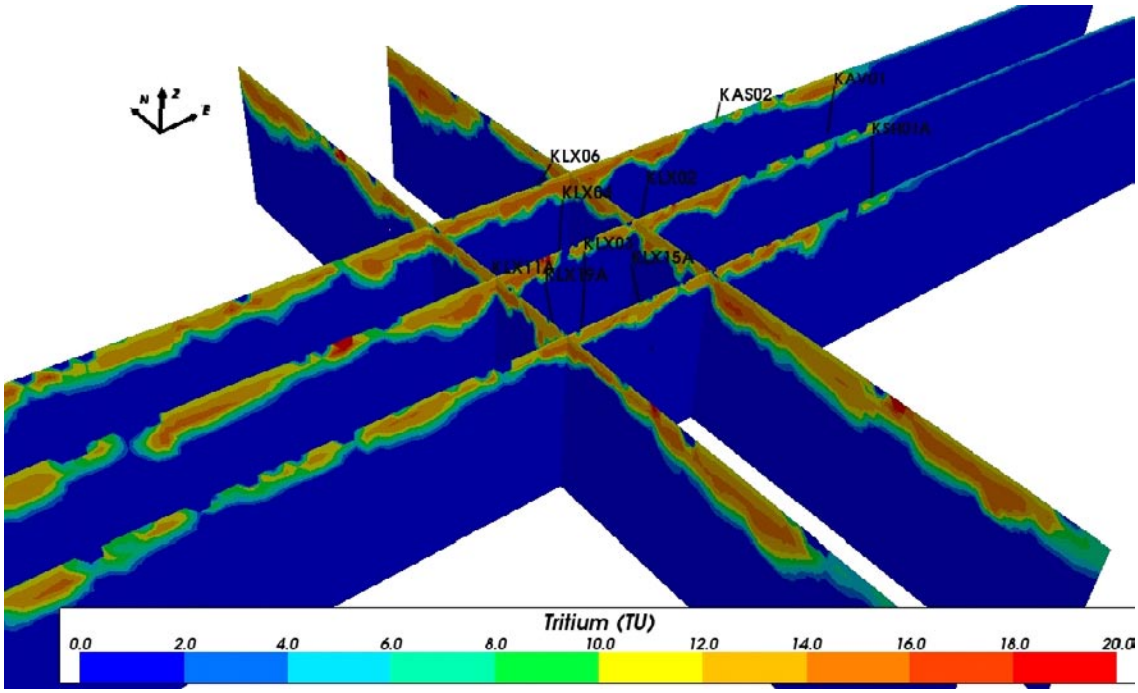

Figure A10-6. *The distribution of tritium concentration in the base case model at 2005 AD on 3 E-W and 2 N-S vertical cross-sections with the locations of selected core drilled boreholes superimposed. The model extends vertically down to –2,164 m.*

The confirmatory tests were made by comparing the modelled tritium concentrations at 2005 AD, corrected for radioactive decay, with the available data from boreholes. The results are presented for the base case described in Section 7 in Figure A10-7 and Figure A10-8 with simulated boreholes grouped according to hydraulic fracture domain and flow regime as is used in Section 9. Given the heterogeneity and discrete nature of the site, exact matches in individual boreholes and to each data point are not expected. What is sought is a broad consistency with the key characteristics seen in the penetration and levels of tritium suggested by the measurements. To this end, all simulated borehole tritium profiles demonstrate the characteristic fall in tritium levels below about –150 m to –200 m. Tritium levels at the surface are about 10 TU consistent with assumed average input from precipitation at present. Such levels have persisted for about the last 10 years. The slight peak at –100 m of 12–15 TU is a remnant of the bomb-test atmospheric tritium from 1950's and 1960's which by 2005 AD decayed to very similar levels as the background. Given, the rapid decay, the magnitude of this peak, and its existence, is sensitive to which exact year the simulated results are considered. For example, by 2010 AD the peak levels are reduced to about 10 TU and hence are indistinguishable from the tritium levels in recharge at the surface, as shown in Figure A10-9. There is little available data in depth ranges between –100 m to –200 m to confirm where such a peak might occur apart from the Simpevarp boreholes, HSH boreholes. What can be confirmed from these comparisons is that tritium levels are consistently predicted to be less than about 4 TU below about –250 m.

Two variant cases were considered to quantify sensitivities. These were the cases with an increased horizontal conductivity in the HRD above –150 m and the case with enhanced fracture surface area within HCD, which are described in Section 9.1.4. These cases were considered since they both appeared to give improvements over the base case model in predicting bicarbonate, which is also used as in indicator of infiltration of modern meteoric water. The sensitivities to these changes were moderate, although both gave a reduction in penetration of tritium of about 50 m for some of the boreholes considered.

In conclusion, simulations of tritium migration confirm the developed palaeohydrogeological models are generally consistent with the interpretation of hydrogeochemistry /Laaksoharju et al. 2009, Section 7.2.2/ that modern meteoric recharge from the last 50–60 years has penetrated the groundwater system to a depth of approximately 150 to 200 m.

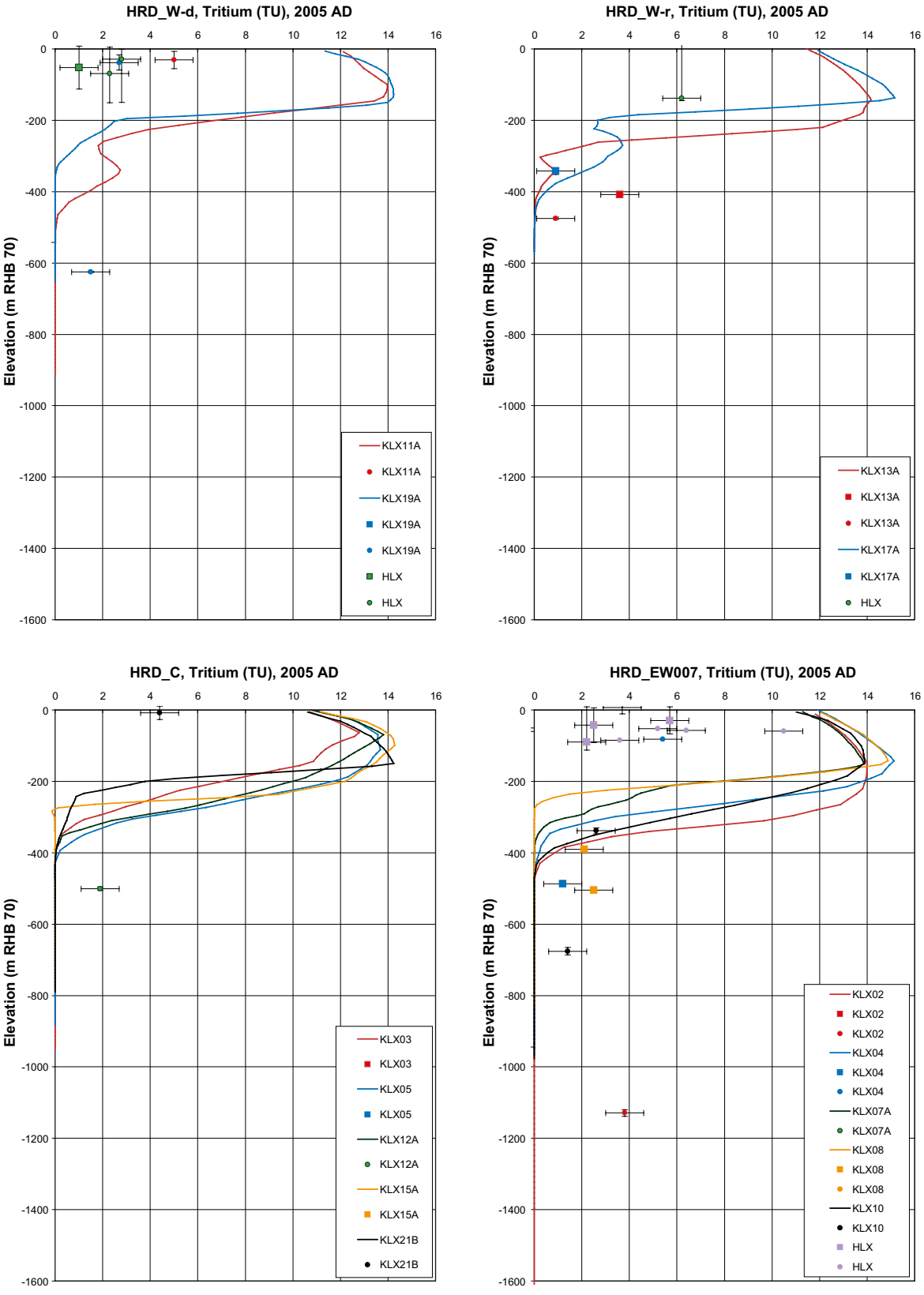

Figure A10-7. *Comparison of modelled and measured tritium in the fracture system for boreholes in HRD_W (-d = discharge areas, -r = recharge areas), HRD_C and HRD_EW007 for the base case calibrated model. Square symbols are used for Category 1–3 data, and small diamond symbols for the Category 4 data. The error bars on the data only indicate the laboratory analytical error. The solid lines show the complete distribution in the borehole simulated in the fracture system.*

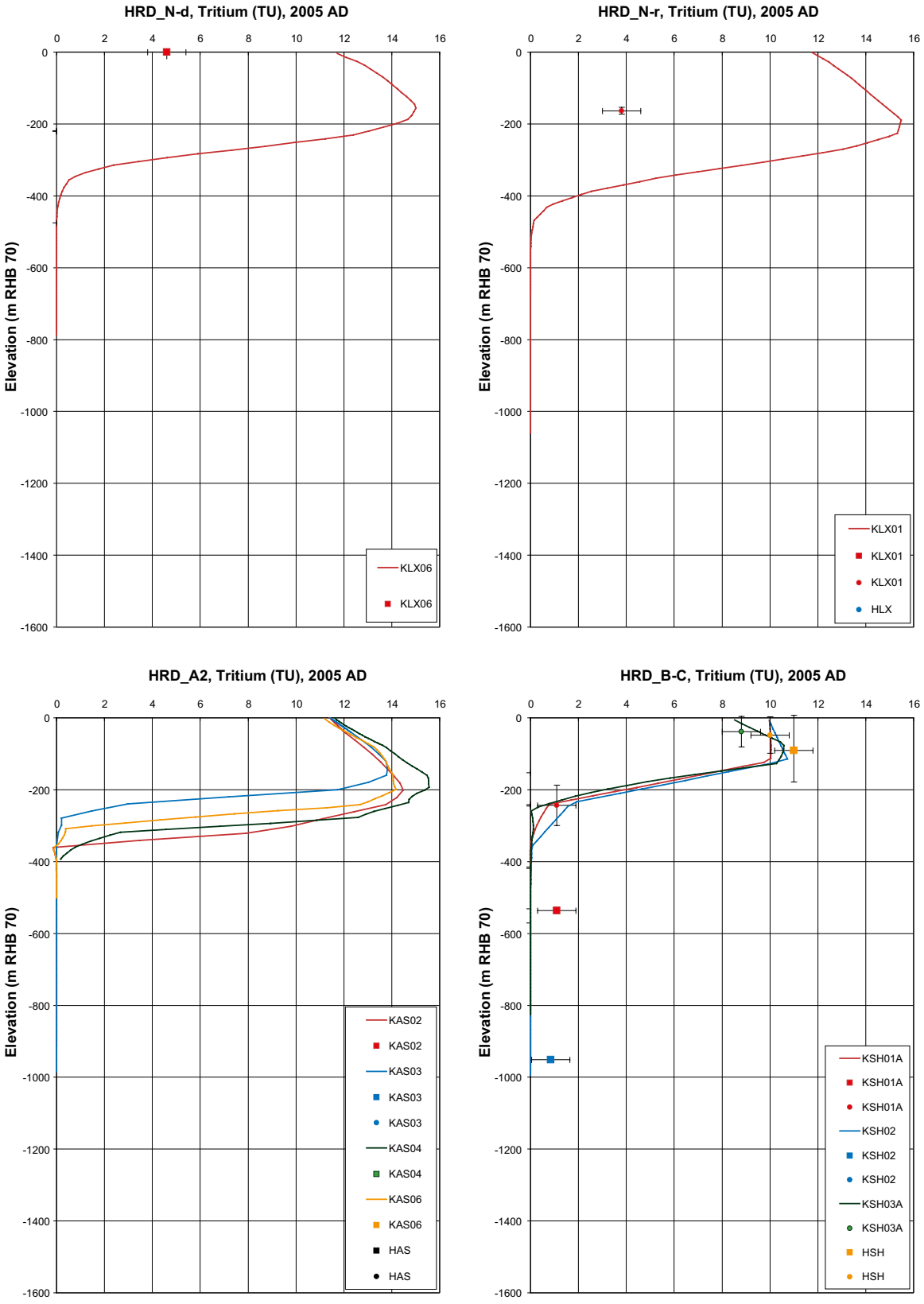

Figure A10-8. *Comparison of modelled and measured tritium in the fracture system for boreholes in HRD_N (-d = discharge areas, -r = recharge areas), HRD_A2 and HRD_B-C for the base case calibrated model. Square symbols are used for Category 1–3 data, and small diamond symbols for the Category 4 data. The error bars on the data only indicate the laboratory analytical error. The solid lines show the complete distribution in the borehole simulated in the fracture system.*

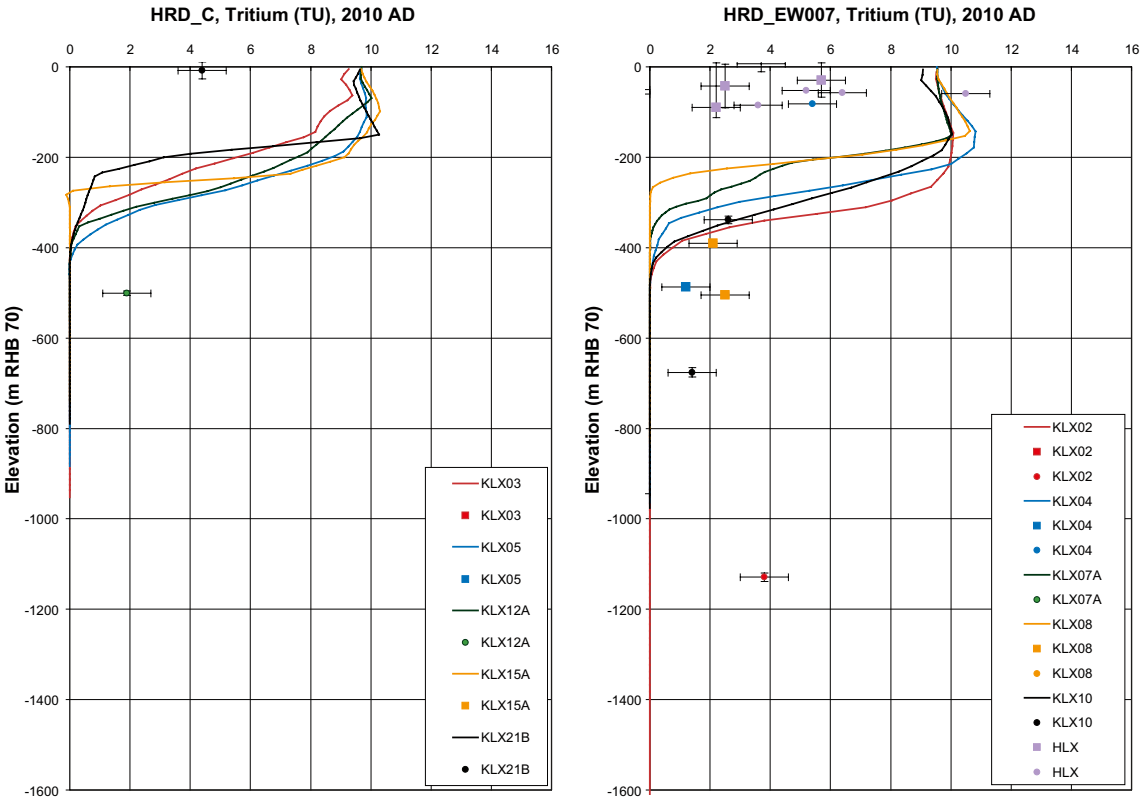

Figure A10-9. *Comparison of modelled and measured tritium in the fracture system for boreholes in HRD_C and HRD_EW007 for the base case calibrated model at 2010 AD. Square symbols are used for Category 1–3 data, and small diamond symbols for the Category 4 data. The error bars on the data only indicate the laboratory analytical error. The solid lines show the complete distribution in the borehole simulated in the fracture system.*